TECHNICAL TRANSACTIONS

CZASOPISMO TECHNICZNE

ELECTRICAL ENGINEERING

ELEKTROTECHNIKA

ISSUE 1-E (8)

ZESZYT 1-E (8)

YEAR 2015 (112)

ROK 2015 (112)

WYDAWNICTWO POLITECHNIKI KRAKOWSKIEJ

TECHNICAL TRANSACTIONS
ELECTRICAL ENGINEERING

CZASOPISMO TECHNICZNE
ELEKTROTECHNIKA

ISSUE 1-E (8)
YEAR 2015 (112)

ZESZYT 1-E (8)
ROK 2015 (112)

Basic version of each Technical Transactions magazine is its online version
Pierwotną wersją każdego zeszytu Czasopisma Technicznego jest jego wersja online
www.ejournals.eu/Czasopismo-Techniczne www.technicaltransactions.com www.czasopismotechniczne.pl

Series: Electrical Engineering
1-E/2015

TECHNICAL TRANSACTIONS | **CZASOPISMO TECHNICZNE**
ELECTRICAL ENGINEERING | ELEKTROTECHNIKA
1-E/2015

TOMASZ SIEŃKO, JERZY SZCZEPANIK, TADEUSZ J. SOBCZYK*

STUDY OF THE APPLICATION OF A MULTIPHASE MATRIX CONVERTER FOR THE INTERCONNECTION OF THE HIGH SPEED GENERATION TO THE GRID

STUDIUM UKŁADU PRZYŁĄCZENIA SZYBKOOBROTOWEGO UKŁADU GENERACYJNEGO OPARTEGO NA PRZEKSZTAŁTNIKU MATRYCOWYM DO SYSTEMU ELEKTROENERGETYCZNEGO

Abstract

The article shows a new field of application for the matrix converter (MC) as the interconnecting device between the high speed, permanent magnet generator and the grid. The converter works under the developed control algorithm based on a so called 'area based' approach. The device consists of a converter, a transformer (or transformers) and filters and is supposed to substitute or revolution decreasing gear box or DC link based power electronic converter. Several structures, including multiphase structures (3, 12 phase) were investigated and their properties were assessed using the results of Matlab Simulink based simulations. The simulations were performed using the standard Simulink models and the developed, simplified permanent magnet motor model. The results were very satisfactory, i.e. input waveforms distortions, output current and machine torque ripples were at acceptable levels for the multiphase structures and high frequency input. The waveform distortions were found to be a function of input frequency and the number of phases in the conversion device, but the structure of the converter was limited to a 12x12 structure for economic reasons.

Keywords: *matrix converter, permanent magnet machine, high speed co-generation unit*

Streszczenie

W artykule pokazano aplikację Przekształtnika Macierzowego (MC – *Matrix Converter*) jako układu synchronizującego pomiędzy wysokoobrotowym generatorem synchronicznym z magnesami trwałymi a Systemem Elektroenergetycznym. Przekształtnik jest sterowany za pomocą skonstruowanego jednookresowego algorytmu kontroli – jednego z algorytmów należących do klasy algorytmów obszarowych. W proponowanym urządzeniu, które składa się z transformatora (transformatorów), filtrów oraz przekształtnika, MC ma zastąpić przekładnię mechaniczną lub przekształtnik AC-DC-AC. Podstawowe symulacje obejmujące część elektryczną mikroturbiny (generator, przekształtnik, transformator, filtry) wykonano w programie MATLAB/Simulink. W ramach pracy na podstawie symulacji oceniano wpływ rozmiaru struktury MC (3-, 12-fazowa) na pracę generatora z magnesami trwałymi (składowa zmienna momentu elektrycznego) oraz poziom zniekształceń napięć i prądów. Zniekształcenia, które były funkcją rozmiaru struktury MC oraz prędkości obrotowej generatora, uznano za akceptowalne i łatwe do odfiltrowania dla struktury 12x12. Większych struktur nie rozpatrywano, gdyż koszt takich urządzeń byłby nieuzasadniony.

Słowa kluczowe: *przekształtnik macierzowy*, *generator z magnesami trwałymi*, *mały moduł ko-generacyjny*

DOI: 10.4467/2353737XCT.15.022.3822

* M.Sc. Eng. Tomasz Sieńko, Ph.D. Eng. Jerzy Szczepanik, Prof. D.Sc. Ph.D. Eng. Tadeusz J. Sobczyk, Institute of Electromechanical Energy Conversion, Faculty of Electrical and Computer Engineering, Cracow University of Technology.

1. Introduction

High parameter steam and gas miniturbines (mT) and microturbines (μT) are becoming an interesting option for small co-generation plants. The plants typically consist of high speed gas fueled turbines and generating units including transmissions for speed reduction and heat recovery systems or medium or high parameter boilers with high-speed steam turbines, transmissions (gear boxes), generators and heat exchangers to extract energy form the steam. The power range of such systems starts from 20–30 kW and goes up to 10 MW. Usually, the speed of the gas turbines ranges from 16 to 120 krpm. The speed of steam turbines (usually single stage turbines are used for small co-generation) depends on the parameters of the steam and on the turbine power and it ranges from 6 to 12 krpm. For all these arrangements, the combined cycle of work allows achieving high levels of efficiency at over 80%. The cogeneration unit structure usually involves the transmission decreasing the revolutions to match the generator's synchronous speed. For gas turbines, generators with a synchronous speed of 3000 rpm are used whereas for steam turbines, four pole generators with speeds of 1500 rpm are utilized. The typical performance of such units can be shown, for example, for the Capstone C-65 microturbine with an electrical efficiency of 29% for the nominal load of 65 kW and 70–112 kW of heat energy recovery depending on the type of heat recovery unit [1, 2].

In this research, it is proposed to replace the revolution decreasing gear box and 1500 or 3000 rpm generator with a high speed generator and electronic unit able to convert a high frequency alternating current into a 50 Hz current. The removal of the gear box and straight forward coupling of the turbine into the generator will decrease energy losses and will provide higher reliability of the mechanical part of the system. The changes will contain not only the generator (a permanent magnet high speed machine is proposed) but they also have to include the interconnection system to the grid. There are two basic structures of converters able to adapt high frequency generator output into a 50 Hz grid frequency: a structure based on AC-DC-AC conversion or a structure based on straightforward energy conversion. The first option is already in use and in this paper, the matrix converter (MC) is proposed as an alternative device.

2. The Structure and control algorithm for Matrix Converter

A NxM multi-phase matrix converter (MC) is an array of *N*x*M* fully controlled bi-directional switches (Fig. 1) able to convert *N* phase input voltages into *M* phase output voltages of different amplitude, phase and frequency than the input. Recently, due to its simplicity, the matrix converter (MC) has received a lot of attention. The main problems in large scale industrial application are the complexity of the control schemes, a large amount of low order harmonics in converter currents and their non-continuity.

The energy conversion in the MC is accomplished without the use of a DC current circuit or any energy storage elements between the converter input and the output. The matrix converter is a straightforward device which creates the output voltage as a combination of the input voltages.

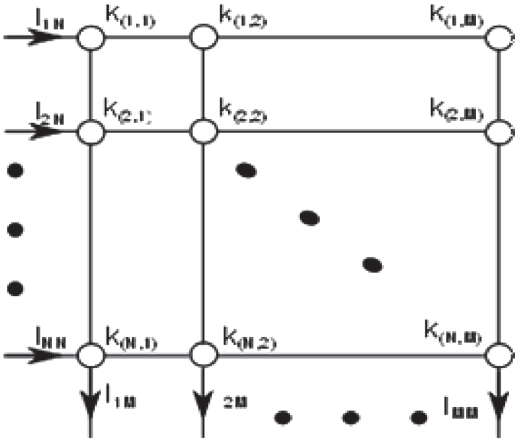

Fig. 1. The structure of the *N*x*M* matrix converter

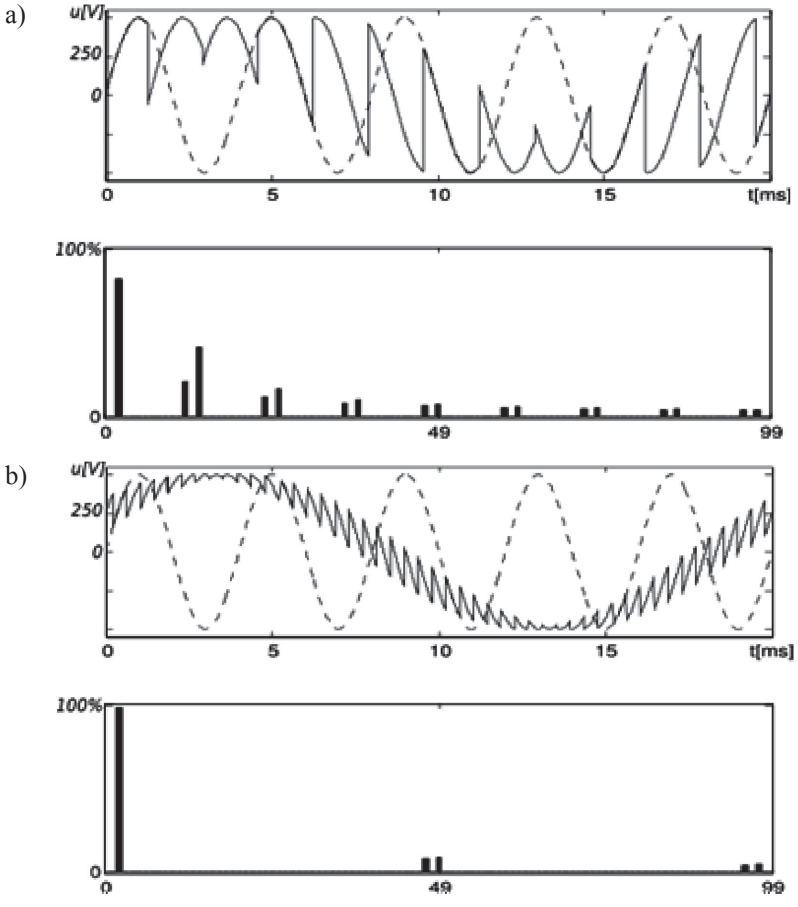

Fig. 2. Output voltage of 3x3 (a) and 12x12 (b) MC – (dotted line input voltage) and its FFT

In general, the output voltage $V_{mM}(t)$ for every m^{th} output phase can be written as:

$$V_{mM}(t) = \sum_{n=1}^{N} k_{(n,m)} V_{nN} \tag{1}$$

where:

$k_{(n,m)}$ – membership function for n^{th} input phase which determines when and how long the m^{th} output phase consists of n^{th} input phase,

V_{nN} – voltage for the n^{th} input phase.

The proposed in this research control single periodical algorithm [3, 4] is based on the so called 'area based algorithm' [5–7] and was chosen from among other possible algorithms developed by the authors. The algorithm, as opposed to other algorithms found in the literature, uses all fragments of the input sinusoids to create the shape of the output sinusoids, whereas the gross algorithms described in literature utilize only the parts of the input sinusoids which are close to the peaks of the waveforms [8–10]. The method of output waveform creation used by the proposed control technique can be clearly seen in Fig. 2a) for 3x3 MC structure and in Fig. 2b) for 12x12 MC structure. Any output phase can be connected at a certain instant to any input phase which creates ties not only for voltages but also for converter currents [11].

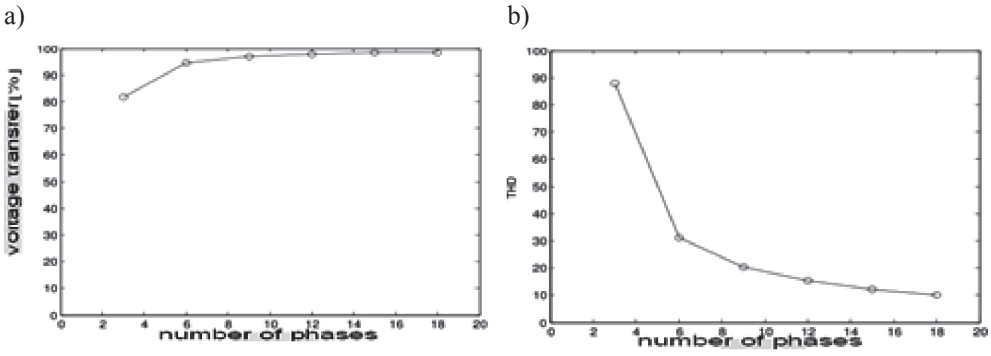

Fig. 3. Voltage transfer (a) and THD (b) as the function of the number of phases in MC square structure

The proposed multiphase structures (3x12, 12x12) have several advantages over the simple 3x3 structures – the voltage transfer of the MC increases, output voltage distortion and the rating of the switching elements decreases as its dimensions increase (Fig. 3). Moreover, in the proposed control procedure, the switching occurs between two adjoining input phases which minimize commutation problems. A square structure of the MC was chosen (the number of input phases is equal to the number of output phases) since for a proposed control scheme it enables a continuous current flow (currents without '0' periods) in all input and output phases. If the structure is not square and the simultaneous connection of two input phases into one output phase (or opposite) is not allowed due to a short circuit restriction at a certain instant, only the same number of input and output phases are connected, i.e. all phases from the side with the

lesser number of phases and not all phases from the side with the greater number of phases. This leaves some phases unconnected resulting in zero current periods.

In order to maximize MC power transfer and to minimize produced disturbances, it is necessary to switch on at a certain instant all possible switches without the creation of short circuits.

The investigated MC based grid connector structures include multiphase matrix arrangements (3x3, 3x12, 12x12) and transformers. The multiphase MC showed much better performance than three phase versions. The performance assessment was done for a much higher input frequency than output frequency and included voltage transfer, order of generated harmonics and THD coefficient.

It is worth noticing that for the investigated input frequency and 12x12 structure, the order of harmonics is close to the one produced by a 48 level converter which is a very complicated structure.

3. Simulation parameters and structure of the models

The performance of the proposed control scheme for a different structure of energy conversion paths was investigated using MATLAB/Simulink software and compared. The variations in the models included variations to the MC structure, generator and transformer models.

The models of the elements of the energy conversion systems (transformers, filters, equivalent models of power systems and power lines) were build using standard Simulink Libraries. The model of the permanent magnet generator (its electrical part) was developed using standard machine equations and taking several simplifications and assumptions such as sinusoidal distribution of the flux in the machine air gap into consideration, omitting mutual stator inductances and assuming phase shift of the N phase windings by $2\pi/N$:

$$\mathbf{U} = \omega \cdot \Psi \cdot \begin{bmatrix} \sin\vartheta \\ \sin\left(\vartheta - 2\pi/N\right) \\ \sin\left(\vartheta - 2(N-1)\pi/N\right) \end{bmatrix} - R_G \cdot \mathbf{I} - L_G \frac{\mathrm{d}}{\mathrm{d}t}\mathbf{I} \tag{2}$$

where:

$\mathbf{U}$ and $\mathbf{I}$ – matrixes of the generator voltages and currents (1xN),

Ψ – magnitude of the flux,

ϑ – actual position of a flux with respect to the first winding (the position of the rotor),

R_G, L_G – resistance and reactance of the generator.

The mechanical equation of rotor movement can be then expressed as:

$$J\frac{\mathrm{d}\omega}{dt} = T_m - T_e - D \cdot \omega \tag{3}$$

where:
J – moment of inertia,
T_m – mechanical torque applied to the rotor,
D – friction coefficient,
T_e – electrical torque.

The electrical torque is defined by the following equation:

$$T_e = p \cdot \frac{\delta}{\delta \vartheta} \mathbf{\Psi} \cdot \mathbf{I} \tag{4}$$

where $\mathbf{\Psi}$ – matrix of machine fluxes.

What for the stated assumptions results in the formula:

$$T_e = \omega \cdot \Psi(\sin \vartheta \cdot i_1 + \sin\left(\vartheta - \frac{2\pi}{N}\right) \cdot i_2 + ... + \sin\left(\vartheta - \frac{2(N-1)\pi}{N}\right) \cdot i_N) \tag{5}$$

The models of the multiphase transformers were developed using standard Simulink models and proper winding arrangements.

The speed of the generators in the presented simulation result was chosen in such a way that no inter-harmonic components are present in the current, voltage and torque waveforms

4. Simulation results of μT with 3x3 matrix converter

Several structures of the device were investigated and figure 4 shows the structure based on a 3x3 structure and transformer.

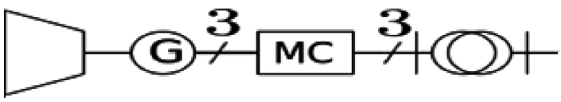

Fig. 4. Structure of 3x3 conversion device

Figures 5a) to 5c) illustrate selected results of simulations for a 3x3 structure. The waveforms of current, voltage and torque were chosen for the investigation.

The advantage of this structure is the use of typical elements (three phase generator MC and transformer) which result in the low cost of the connecting device.

The figures below show converter waveforms. All harmonics in the presented spectra were given with respect to the dominating one.

This device, however simple, produces a highly distorted generator current that results in a ripple in the generator torque. This highly distorted current will cause high losses in the generator core that will decrease the efficiency of the energy conversion. The generation unit output voltage, although not shown in this paper, also contains high level contents of high order harmonics and its shape is not acceptable.

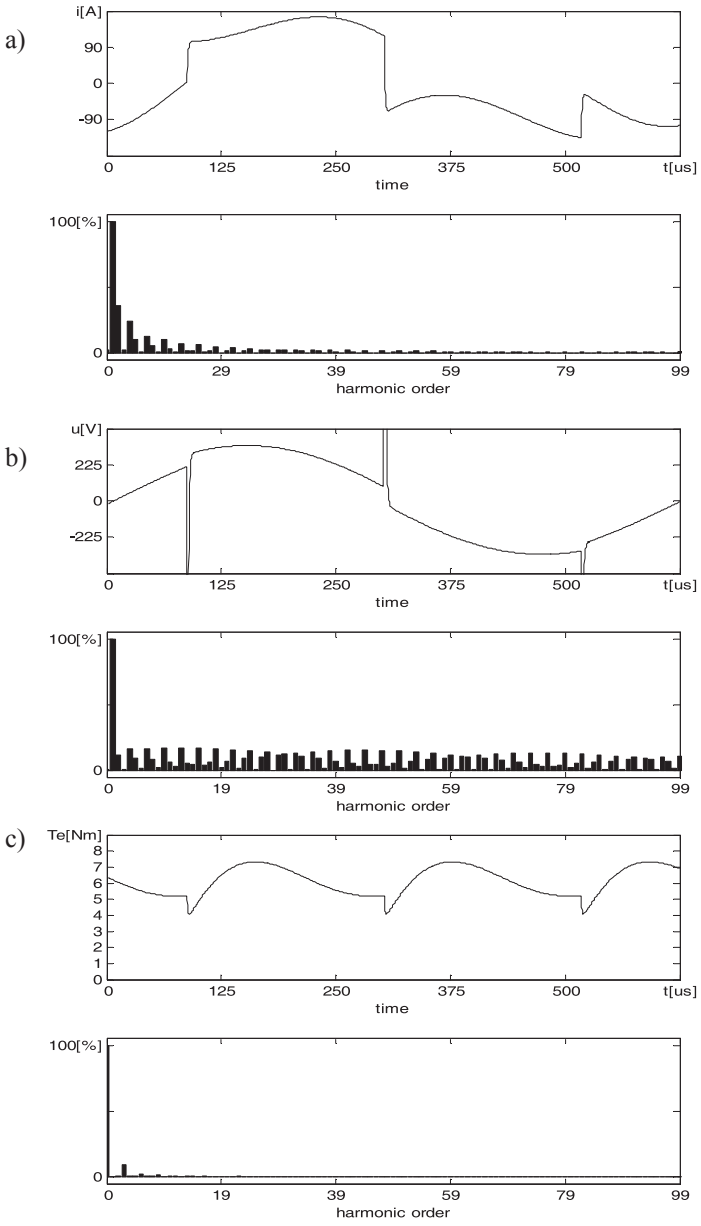

Fig. 5. Current (a), voltage (b) and electromagnetic torque of the generator (c) of μT with 3x3 MC

5. Simulation results of μT with 3x12 matrix converter

This device consists of the 36 switch MC structure (3x12) of a typical three phase generator and a non-typical 12x3 transformer.

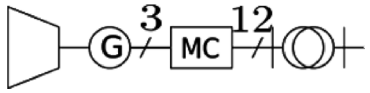

Fig. 6. Structure of 3x12 conversion device

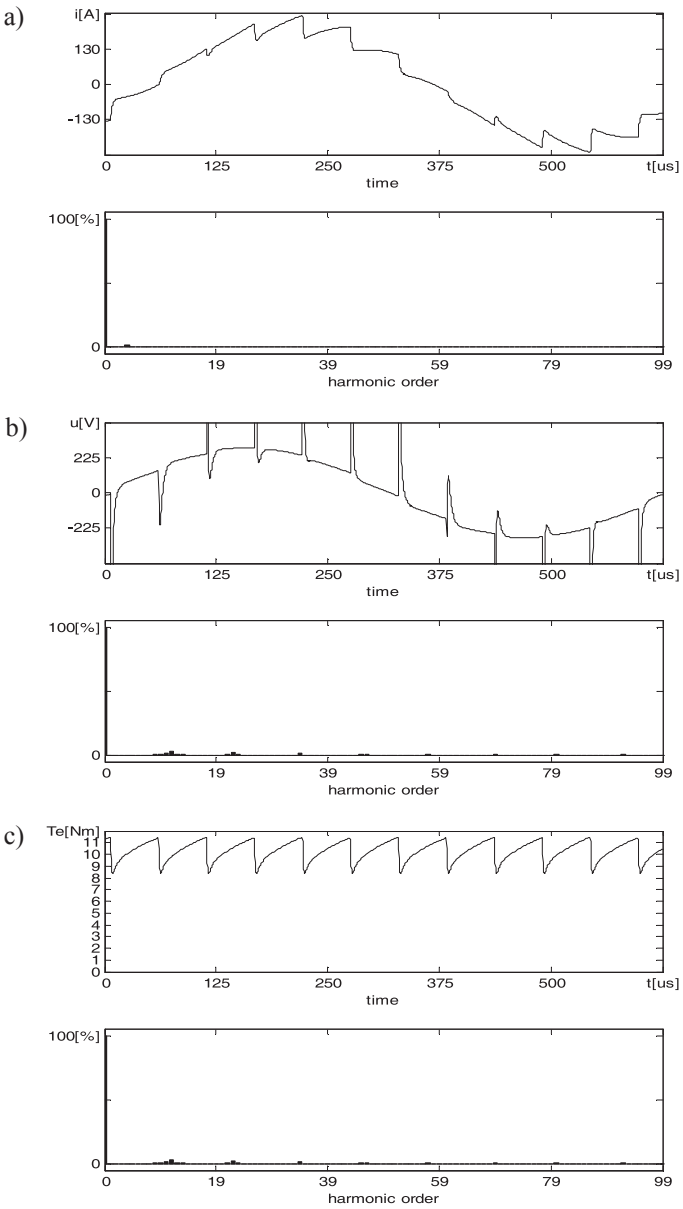

Fig. 7. Current (a), voltage (b) and electromagnetic torque of the generator (c) of μT with 3x12 MC

The disadvantages of this structure include rapid changes in the currents of the switches which results in rapid changes and over-voltages in generator output voltages.

4. Simulation results of μT with 12x12 matrix converter.

Fig. 8. Structure of 12x12 conversion device

The proposed structure is square and results in non '0' periods in converter currents i.e. for a proposed control 12 switches are always in the 'on' state.

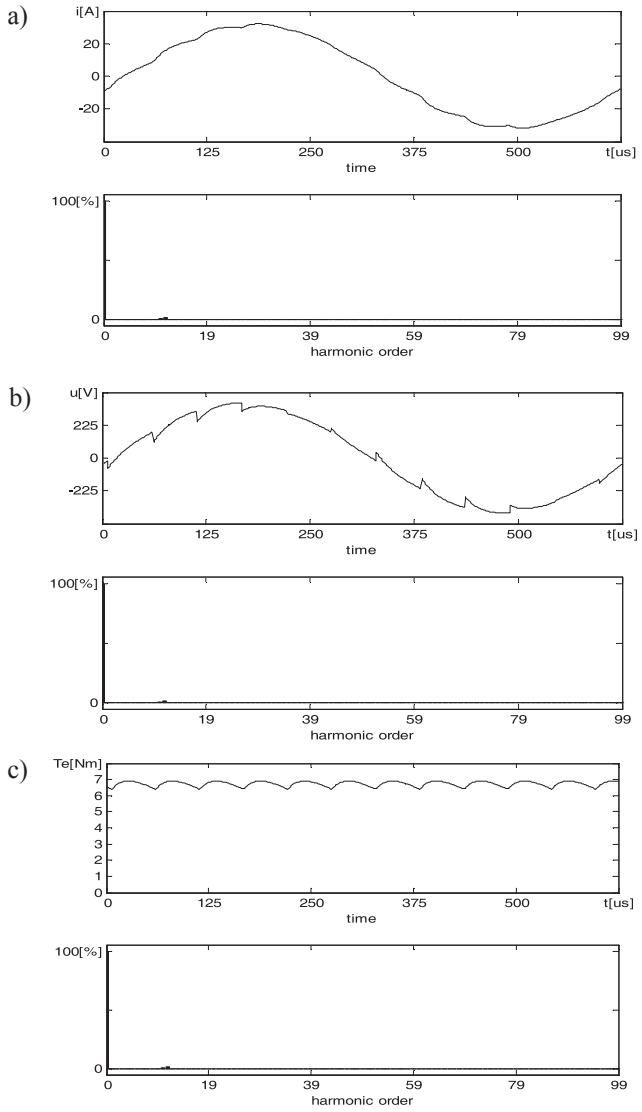

Fig. 9. Current (a), voltage (b) and electromagnetic torque of the generator (c) of μT with 12x12 MC

For this structure, the shape of the generator current and voltage is closer to the sinusoidal shape than for the previously considered structures what results in almost constant machine torque (Fig. 9c)). Thus, the expected machine losses are also smaller than for previously considered structures. However, the constructions of the generator and transformer are not typical and 144 switches are required to build the converter matrix.

5. Conclusions

This work shows a study of the implementation of MC as part of microturbine – grid connection devices. The paper includes the comparison of three different connector structures based on the comparison of generator currents, their terminal voltages and electromagnetic torque. A 3x3 structure achieves a fairly good performance if output voltages are considered (not shown in this research), but the shape of the input current influencing the electromechanical torque is not acceptable. Moreover, the sudden change between input phases (only three input phases) when creating output voltage, creates high over-voltages on converter switches. The current rating of the switches has to be relatively high since all power is transferred through only three phases and nine switches (three switches are working at any one time).

The 3x12 MC based structure shows much better properties than the 3x3 version (lower ripple in generator current and torque), but there are still large overvoltages visible in the generator terminal voltages

The best performance of the 12x12 MC working with a 12 phase generator and a 12x3 transformer is not a surprise, however, it requires special construction of a 12 phase generator and a 12x3 transformer as well as a large 144 element matrix hardware which is expensive when building a prototype. The alternative is a structure containing a 3 phase generator, two 12x3 transformers and a 12x12 MC structure. The problem lays within the construction of a high frequency 3x12 transformer which has to minimize its core losses, thus, this is not the same transformer as a transformer coupling a 12x12 MC to the grid.

It can be noted that the simulations were performed for a 1600 Hz input frequency and if this frequency decreases (speed of the turbine decreases), the advantage of multiphase structures over three phase ones increases.

The currents and the voltages at the grid side of the interconnection device were not analyzed in this paper which concentrated only on the influence of the MC on the generator working conditions.

References

[1] Boyce M.P., *Gas Turbine Engineering Handbook*, Elsevier Science 2006, ISBN 9780080456898.

[2] *Capstone Turbine Corporation*, http://www.capstoneturbine.com/ (access: 16.05.2013).

[3] Sieńko T., Sobczyk T., *Sposób sterowania przekształtnikiem macierzowym*, Polish Patent: P- 204643 PL (2010).

[4] Sobczyk T.J., Sienko T., *Matrix converters control for high speed generators*, Electric Machines and Drives, 2005, IEEE International Conference on y. 2005, pp. 1975–1980, doi: 10.1109/IEMDC.2005.195990.
[5] Sobczyk T.J., *Control strategy of matrix converters*, Proc. of European Conf. on Power Electronics and Applications (EPE), 1993, Vol. 4, pp. 93–97.
[6] Sobczyk T.J., *The matrix converter – a universal power electronic unit*, Prace Instytutu Elektrotechniki, 2002, pp. 5–21, ISSN 0032-6216.
[7] Sieńko T., Szczepanik J., *The Study of implementation of Multiphase Matrix Converter in Power System*, Przegląd Elektrotechniczny, 2013, nr 8.
[8] Friedli Th., Kolar J.W., *Milestones in Matrix Converter Research*, IEEJ Journal of Industry Applications, 2012, Vol. 1, pp. 2–14.
[9] Rodriguez J., Rivera M., Kolar J.W., Wheeler P.W., *A Review of Control and Modulation Methods for Matrix Converters*, Industrial Electronics, IEEE Transactions, 2012, Vol. 59, No. 1, pp. 58–70, ISSN 0278-0046.
[10] Casadei D., Serra G., Tani A., Zarri L., *A review on matrix converters*, Przegląd Elektrotechniczny, 2006, Vol. 82, No. 2, pp. 15–25, ISSN 0033-2097.
[11] Sieńko T., *Schemat zastępczy przekształtnika macierzowego dla stanów dynamicznych przy sterowaniu jednookresowym*, Czasopismo Techniczne, z. 1-E/2012, pp. 123–134.

TECHNICAL TRANSACTIONS | **CZASOPISMO TECHNICZNE**
ELECTRICAL ENGINEERING | ELEKTROTECHNIKA
1-E/2015

DARIUSZ BORKOWSKI*

CONTROL STRATEGY FOR MAXIMIZING CONVERSION EFFICIENCY OF A SMALL HYDROPOWER PLANT

STRATEGIA STEROWANIA MAŁĄ ELEKTROWNIĄ WODNĄ MAKSYMALIZUJĄCA SPRAWNOŚĆ PRZETWARZANIA

Abstract

An analysis of the energy conversion system which consists of a propeller water turbine, a permanent magnet synchronous generator and a power electronic converter is presented. The considered control strategy implements an optimizing technique that guarantees maximal average efficiency independently of hydrological condition changes through the constant search for optimal operation parameters. The water flow parameter, essential for objective function estimation, is eliminated by the dedicated control technique. The control method is implemented and tested in the model created in the Matlab/Simulink software. All characteristics and parameters were identified on a real small hydropower plant and on the special laboratory model.

Keywords: *small hydropower plant*, *variable speed operation*, *optimizing algorithm*

Streszczenie

W artykule analizowany jest tor przetwarzania energii, który składa się z turbiny śmigłowej, generatora synchronicznego z magnesami trwałymi oraz przekształtnika energoelektronicznego. Przedstawiono strategię sterowania opartą na metodach optymalizacji, która przez ciągłe poszukiwanie optymalnych parametrów pracy gwarantuje maksymalną sprawność przetwarzania niezależnie od zmiennych warunków hydrologicznych. Przez wybraną technikę sterowania wyeliminowano konieczność znajomości parametru przepływu wody niezbędnego do oszacowania funkcji celu. Strategia sterowania została zaimplementowana i przetestowana w modelu opracowanym z zastosowaniem oprogramowania Matlab/Simulink. Wszystkie charakterystyki i parametry zostały zidentyfikowane w rzeczywistym obiekcie małej elektrowni wodnej i na stanowisku laboratoryjnym.

Słowa kluczowe: *mała elektrownia wodna*, *zmienna prędkość obrotowa*, *algorytm optymalizacyjny*

DOI: 10.4467/2353737XCT.15.023.3823

* Ph.D. Eng. Dariusz Borkowski, Institute of Electromechanical Energy Conversion, Faculty of Electrical and Computer Engineering, Cracow University of Technology.

1. Introduction

The production of energy from renewable sources is of key importance for the energy security of Poland and European Union policy. According to the 2009/28/EC [1] directive, the European Union (Poland) should produce 20% (15%) of electrical energy from renewable energy sources by the end of 2020. The current share of these sources is estimated at 12.7% (9.5%) [2].

Small Hydropower Plants (SHPs) are objects rated up to 10 MW. Traditional solutions of energy conversion system for SHP are based on water turbines working at a constant speed (synchronous generators) or near constant speed (asynchronous generators). An interesting solution is to apply variable rotational speed operation to the system. The variable speed operation applied in hydropower plants improves the turbine operation range and increases energy conversion efficiency under changeable hydrological conditions [3]. This design simplifies a mechanical system but requires the application of a Power Electronic Unit (PEU) in the energy conversion system. The PEU is needed to match the generator and grid parameters and to control the power flow from the generator to the grid [3, 4]. Taking into account high efficiency under a wide range of loads, as well as a possible high pole number structure, the Permanent Magnet Synchronous Generator (PMSG) is the recommended type of generator. In Europe, and particularly in Poland, this type of solution is rare and is mainly of a prototype character [5, 6].

The variable speed operation can be especially effective in control demanding locations, where small changes in operation parameters significantly affect the energy production result. Such a situation especially concerns 'run-of-the-river' plants, where generating power depends on the actual hydrological conditions because the water storage is impossible or limited. Thus, changeable hydrological conditions throughout the year force the power plant to operate in a wide water flow and head range [7]. In this situation, the control strategy considerably affects the economic profitability of the SHP. Desirable regulation has to fulfill two main functions – maintaining the upper water level on a fixed level and adjusting the operation parameters in order to obtain the highest possible efficiency of the whole energy conversion system. The control of 'run-of-the-river' plants is difficult due to the continuously changeable hydrological conditions as well as turbine features caused by silt deposited in channels. Algorithms based upon fixed settings and operational characteristics are ineffective. Furthermore, the coefficient quality of the second task (efficiency) requires the actual water flow parameter, the measurement of which is difficult and expensive.

The control strategy presented in this paper solves the above mentioned problems by implementing optimizing methods and dedicated efficiency assessment methods avoiding the water flow parameter. The proposed solution is implemented and tested on the simulation model created in the Matlab/Simulink software. The energy conversion model is based on the real system installed in the SHP of 150 kW nominal power [6]. All characteristics and parameters are identified in this object and in the 30 kW laboratory model [8].

2. The structure of the SHP system

The analysed SHP system, presented in Fig. 1, consists of: guide vanes that control the water quantity Q flowing through the turbine; propeller turbine; permanent magnet synchronous generator (PMSG); power electronic unit (PEU); the controller.

As mentioned above, the regulation system of the 'run-of-the-river' plants has to fulfil two main functions. These tasks are performed by the two separate regulators.

The water level regulator maintains the upper water at a fixed level. The angle of the guide vanes α mainly influences the water flow quantity Q, thus, it was chosen as a control parameter. It is adjusted by the PI regulator based on the actual error ε between the actual H and set H_{set} water level.

The optimizing load controller has to select the optimal operation point of the system in order to obtain the highest possible efficiency of the whole energy conversion system. It adjusts the generator armature current I_g depending on the actual measuring parameters: water head H; guide vanes angle α; active power generated by the system P_s.

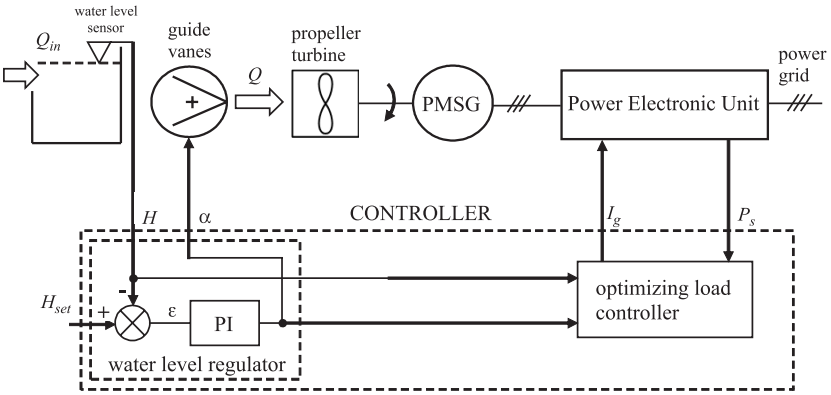

Fig. 1. Block diagram of the SHP system

3. Simulation model

The control process of the hydropower plant takes a long period of time due to the long-time constants of the water system. In order to accelerate simulation calculations, some simplifications are necessary. All elements of the energy conversion system are represented by their essential features: a steady state characteristics, time constants and efficiency functions.

The simulation model presented in Fig. 2 was created in the Matlab/Simulink software. The PI controller has a parallel form with the lower and upper saturation limit. The guide vanes block inserts the initial condition and rate limiter imitating the hydraulic system of position controlling.

The Hydroset subsystem (Fig. 3) models propeller turbine characteristics as a mechanical torque function T_t of guide vanes angle α, water level H and turbine speed n:

$$T_t = C_H \cdot \left(a_T(\alpha) \cdot n^2 + b_T(\alpha) \cdot n + c_T(\alpha) \right) \tag{1}$$

where:

C_H – water level coefficient [8],
$a_T(\alpha)$, $b_T(\alpha)$, $c_T(\alpha)$ – function coefficients approximated by a polynomial function of guide vanes angle [8].

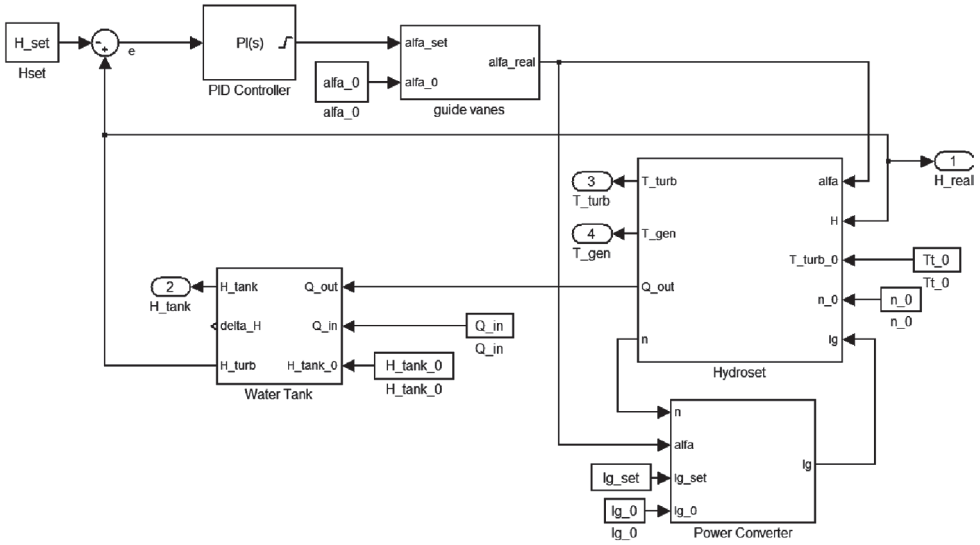

Fig. 2. Simulation model of SHP created in Matlab/Simulink

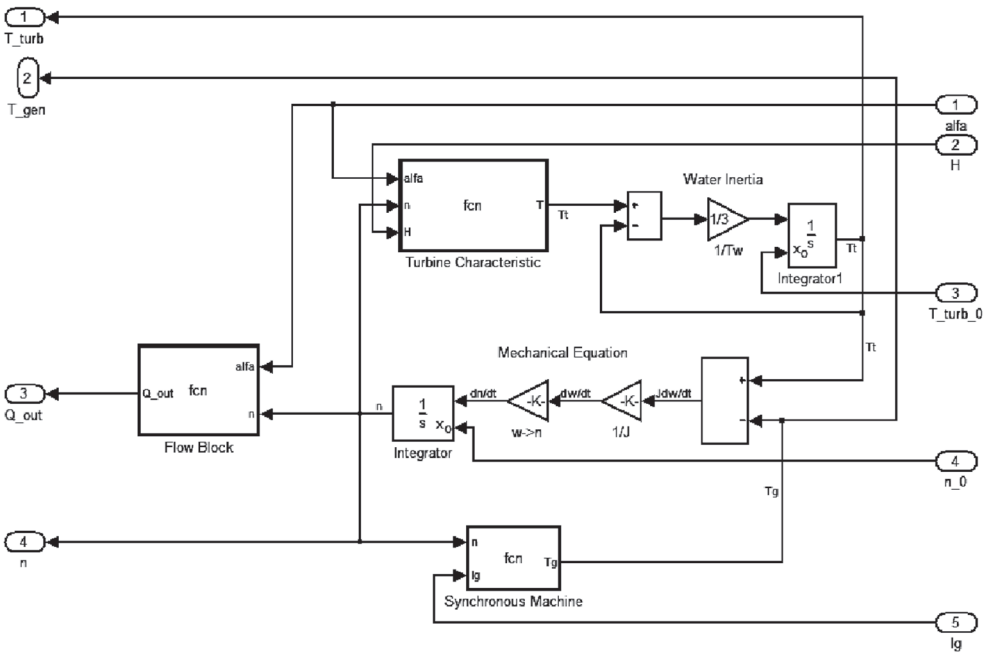

Fig. 3. Block diagram of Hydroset subsystem

The synchronous generator can be treated as a first order inertial object, where the generator armature current can be regarded as the system input, to which turbine torque is the system output. Taking into account linear relations between armature current and electromagnetic torque, the value of object gain is constant and independent on the generator speed.

The generator torque T_g and turbine torque T_t are compared in the mechanical equation from which the turbine speed n can be calculated. The parameter J is equal to the sum of the turbine and generator inertia.

$$J\frac{\mathrm{d}n}{\mathrm{d}t}=\frac{30}{\pi}\left(T_t-T_g\right) \tag{2}$$

The flow block calculates the water flow Q as a linear function of speed n with coefficients in the form of polynomial functions of angle:

$$Q=a_Q\left(\alpha\right)\cdot n+b_Q\left(\alpha\right) \tag{3}$$

All coefficients were calculated from the universal characteristic of the real propeller turbine (known as a hill chart) that presents efficiency isolines on a water flow-speed plane [9]. Dynamic behaviour of the turbine is caused by many elements, the most significant being the dynamic of the water mass. This time constant is a function of the water head and the volume of the inlet channel. The tests of real turbine operation allowed us to identify this parameter to be estimated at 3.5 seconds [9].

The PEU controls the generator electromagnetic torque T_g by its rms armature current I_g. The applied block (Power Converter) models the full-scale AC/DC/AC power converter consisting of: an uncontrolled rectifier; a DC-DC boost converter, which increases the DC voltage; the DC/AC converter with a DPC-SVM algorithm (Virtual Flux – Direct Power Control with SVM modulator) [4, 6]. The generator armature current corresponds to the rectifier DC current and is adjusted by the DC-DC boost converter. The time constant of the PEU is estimated to be about 1 second [8]. The efficiency of the PEU is sensitive to the value of the transferred power. It also changes depending on the generator speed but in a small range, thus, this variation has been neglected [6].

4. Optimizing control strategy

Due to the continuously changeable hydrological conditions, as well as the turbine features caused by silt deposited in the channels, algorithms based on the fixed settings and operational characteristics are ineffective [10]. For that reason, the special method using an optimizing algorithm has been implemented. The procedure starts from the non-optimal current value and tries to improve the conversion efficiency η by applying the gradient method.

$$\Delta I_g=k\cdot\frac{\partial\eta}{\partial I_g} \tag{4}$$

The quality coefficient (efficiency of the energy conversion system) is defined by the following formula:

$$\eta = \frac{P_s}{9.81 \cdot Q \cdot H} \tag{5}$$

where:
P_s – active power generated by the system,
Q – water flow through the turbine,
H – water head.

The control algorithm based on this quality coefficient is relatively fast and independent of the water flow regulator. However, it requires the actual value of the water flow which may be measured using very expensive devices. In some cases, these measurements are very inaccurate. One of the solutions to this problem is to simplify the quality coefficient. Let's assume that changes of the water flow of the river are slow compared to the regulation process (Q = const). Another assumption concerns the water level regulation. Let's activate the optimizing algorithm only after the PI regulator obtains the desired water level. In this situation, it is possible to write:

$$\frac{\partial \eta}{\partial I_g} \overset{Q,H=const}{=} \frac{\partial P_s}{\partial I_g} \tag{6}$$

Using the discretization Euler method of an order one, the formula (4) with substitution (6) may be written as follows:

$$I_{g(1)} = I_{g(0)} + k \cdot \frac{P_{s(0)} - P_{s(-1)}}{I_{g(0)} - I_{g(-1)}} \tag{7}$$

where the subscript brackets indicate the step number of optimizing algorithm l.

The procedure (Fig. 4) changes the initial values of current I_g following the direction of the gradient components multiplied by a positive factor k. The next step of optimizing the regulator is activated only when the water level error is smaller than or is equal to the limit value C_H (constant water level assumption). This time interval T_s (called inter-optimizing period) may be different after each step due to the varying initial conditions. However, it should be relatively small compared to changes of the river water flow to satisfy the constant water flow assumption. This is the way that the time limit (T_{lim}) was added. The example operation of the algorithm is presented in Fig. 5.
The simulated situation assumes the nominal water head and zero initial parameters. The water flow characterises a step change from 90% to 100% of nominal value in the 20th algorithm step. It can be noticed that the error value ε equals the limit value $C_H = 1 \cdot 10^{-5}$ in most of the periods. The rest of the periods have a higher error because they exceed the time limit $T_{\text{lim}} = 1000$ s.

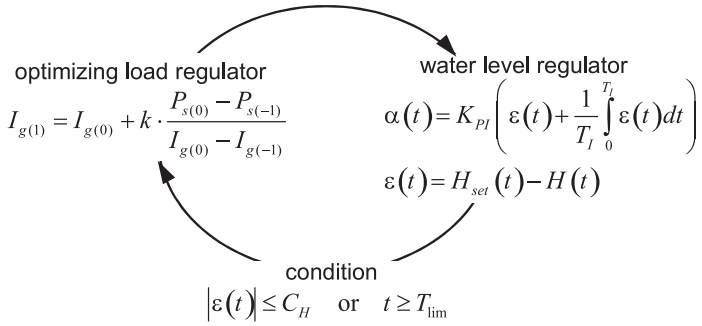

Fig. 4. Algorithm of control strategy

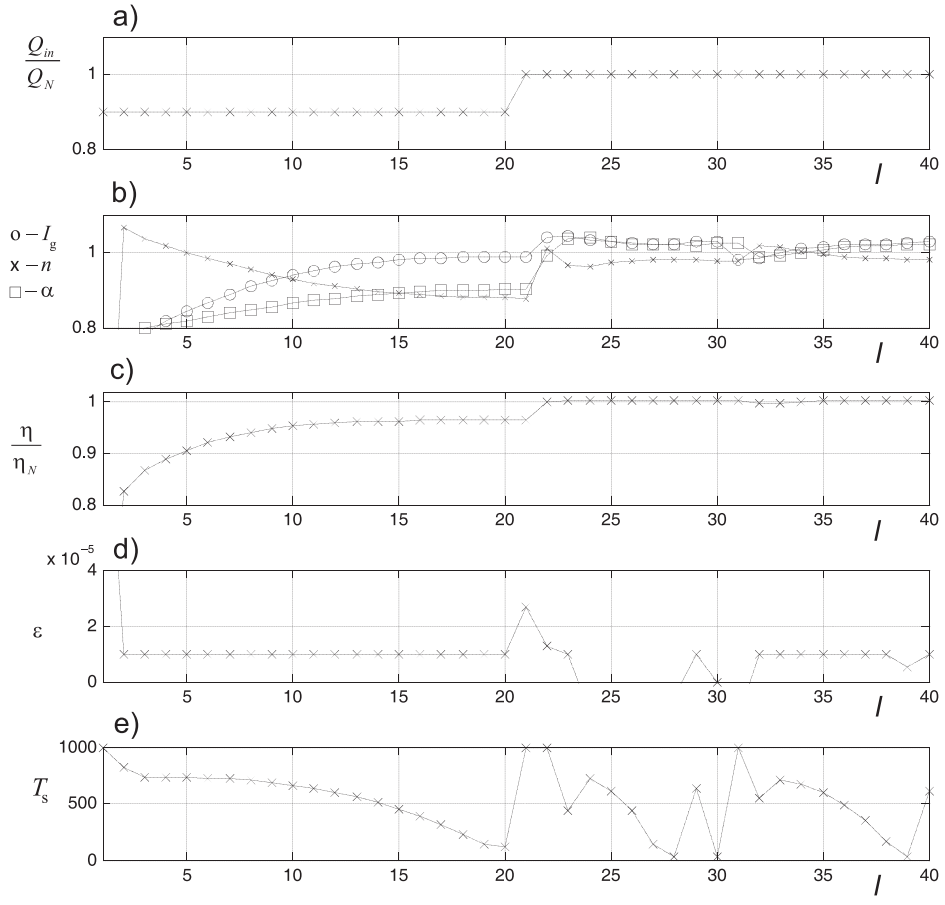

Fig. 5. Relative system state variables: a) water flow,, b) generator current (circle), speed (cross) and guide angle (square), c) total efficiency, d) regulator error, e) inter-optimizing period; for a certain algorithm step

Figure 6 presents the example inter-optimizing period between the 25th and 26th step of the optimizing algorithm. It is clearly visible that each step causes the impulse response of the system to the change of generator armature current.

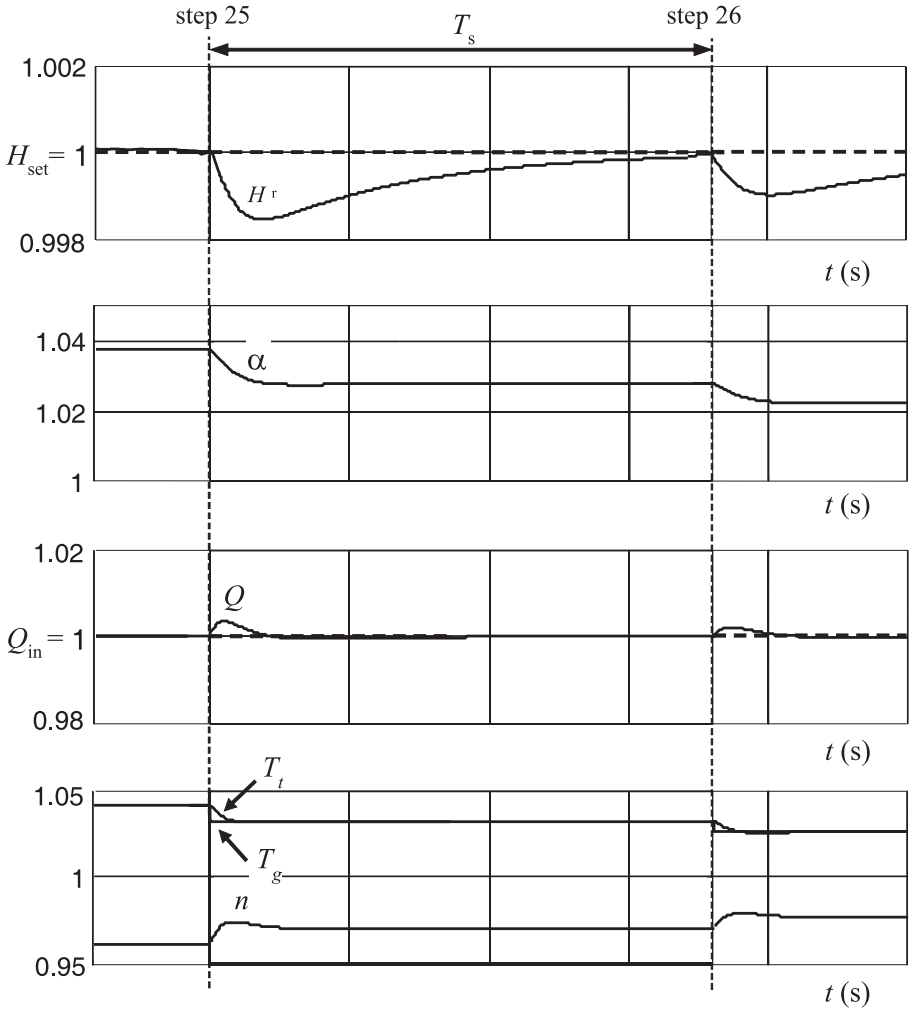

Fig. 6. Time domain system state variables during the example inter-optimizing period (T_s = 660 s) tuned by PI regulator

The optimizing method fulfils the main criterion of the control algorithm by obtaining the maximum efficiency of the whole system in the given hydrological conditions. This feature can be seen in Fig. 5c) and in the efficiency characteristic presented below (Fig. 7). The maximal efficiency is achieved after several algorithm steps. The continuous seeking process also provides optimal operation parameters after changes in the water flow value. This figure proves that the control algorithm maintains the constant water flow condition.

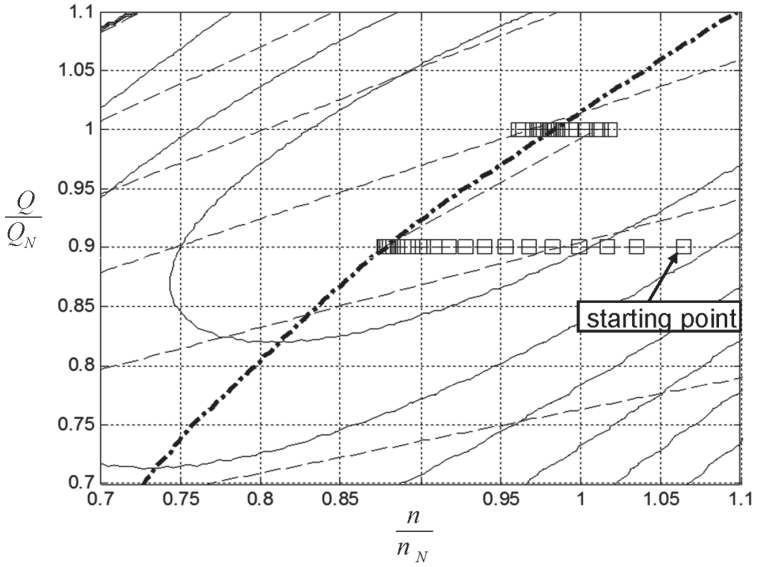

Fig. 7. Steady state algorithm steps (square markers) on the water flow – rotational speed plane (total efficiency isolines – solid line, guide angle lines – dashed line, maximal efficiency line – dash-dot line)

5. Summary

The changeable hydrological conditions and variable turbine parameters due to the ageing process as well as river pollution require adaptive control of 'run-of-the-river' plants. This paper presents the dedicated procedure based on the gradient method which tunes the generator armature current in order to obtain the highest possible efficiency. The gradient descent method applied in this paper can provide small step changes resulting in short periods of unsteady states. Thus, the optimal operation point may be obtained relatively fast. The drawback of this technique is the limitations of a target to the local extreme (minimum or maximum). Fortunately, the efficiency characteristic (quality function) of the investigated system is the convex function which means that any local extreme is also the global extreme.

The controller uses also the standard PI regulator which provides the desired upper water level. The introduced conditions defining the activation of the gradient procedure allow the quality function to be simplified. Due to this, water flow measurements (which are expensive and may be inaccurate) are not needed. This control algorithm can be easily implemented in the PLC controller with no installation of extra sensors.

The presented simulation results confirm the algorithm effectiveness and an application possibility on the real system.

References

[1] *Directive 2009/28/ec of the european parliament and of the council of 23 April 2009 on the promotion of the use of energy from renewable sources and amending and subsequently repealing Directives 2001/77/EC and 2003/30/EC*, Available: http://eurlex.europa.eu/LexUriServ/LexUriServ.do?uri=Oj:L:2009:140:0016:0062:en:PDF.

[2] *Report from the commission to the european parliament, the Council, the european economic and social committee and the Committee of the regions*, Brussels, 27.03.2013, Available: http://eurlex.europa.eu/LexUriServ/LexUriServ.do?uri=COM:2013:0175:FIN:EN:PDF.

[3] Fraile-Ardanuy J., Wilhelmi J.R., Fraile-Mora J.J., Perez J.I., *Variable-Speed Hydro Generation: Operational Aspects and Control*, IEEE Transactions on Energy Conversion, Vol. 21, No. 2, June 2006.

[4] Kaźmierkowski M., Krishnan R., Blaabjerg F., Irwin J., *Control In Power Electronics*, ACADEMIC PRESS, 2003, ISBN: 0–12–402772–5.

[5] *Status report on variable speed operation in small hydropower Austria: Energie publication*, 2000, Available: http://ec.europa.eu/energy/res/sectors/doc/small_hydro/statusreport_vspinshp_colour2.pdf.

[6] Borkowski D., Węgiel T., *Small Hydropower Plant with Integrated Turbine-Generators Working at Variable Speed*, IEEE Transactions on Energy Conversion, Vol. 28, No. 2, June 2013, pp. 452–459.

[7] Wijesinghe A., Lei Lai L., *Small hydro power plant analysis and development*, [in:] Proc. 4th Int. Conf. DRPT, 2011, pp. 25–30.

[8] Borkowski D., *Laboratory model of small hydropower plant with variable speed operation*, Zeszyty Problemowe – Maszyny Elektryczne, 2013, nr 3/(100), pp. 27–32.

[9] Borkowski D., Węgiel T., *Optymalizacja przetwarzania energii dla małych elektrowni wodnych z generatorami pracującymi ze zmienną prędkością obrotową*, Zeszyty Problemowe – Maszyny Elektryczne, 2011, nr 92, pp. 121–126.

TECHNICAL TRANSACTIONS | **CZASOPISMO TECHNICZNE**
ELECTRICAL ENGINEERING | ELEKTROTECHNIKA
1-E/2015

ŽELMÍRA FERKOVÁ, JÁN KAŇUCH*

SYNCHRONOUS MOTOR PROTOTYPE WITH AN EXTERNAL ROTOR USING PERMANENT MAGNETS

PROTOTYP SILNIKA SYNCHRONICZNEGO Z ZEWNĘTRZNYM WIRNIKIEM I MAGNESAMI TRWAŁYMI

Abstract

This paper presents the design, simulation and measurement of a synchronous motor prototype with an external rotor using permanent magnets. The motor was optimized for high-torque, in-wheel operation. Based on geometric dimensions, a 3D solid model was created. The electromagnetic design was calculated in ANSYS/RMxprt. A cross-section with graphical presentation of magnetic induction in particular parts of the electromagnetic circuits and the simulated and measured characteristics of the motor are shown.

Keywords: *synchronous motor*, *permanent magnet*, *ANSYS/RMxprt program*

Streszczenie

W artykule przedstawiono projekt, symulację i pomiar prototypu silnika synchronicznego z zewnętrznym wirnikiem z użyciem magnesów trwałych. Silnik został zoptymalizowany ze względu na wysoki moment do pracy w kole samochodu. Na podstawie wymiarów geometrycznych został utworzony trójwymiarowy (3-D) model silnika. Elektromagnetyczny projekt silnika został obliczony w programie ANSYS/RMxprt. W pracy zaprezentowano przekrój z graficznym przedstawieniem indukcji magnetycznej w poszczególnych częściach elektromagnetycznego obwodu oraz zasymulowane i zmierzone charakterystyki silnika.

Słowa kluczowe: *silnik synchroniczny*, *magnes trwały*, *program ANSYS/RMxprt*

DOI: 10.4467/2353737XCT.15.024.3824

* Ph.D. Eng. Ján Kaňuch, Assoc. professor, Ph.D. Eng. Želmíra Ferková, Department of Electrical Engineering and Mechatronic, Faculty of Electrical Engineering and Informatics, Technical University of Košice, Slovakia.

1. Introduction

Servo drives with permanent magnet (PM) motors fed from static inverters are finding applications on an increasing scale. PM servo motors with continuous output power of up to 15 kW at 1500 rpm are common. Rare-earth PMs have also been recently used in large power synchronous motors rated at more than 1 MW [1]. Synchronous motors operate at a constant speed in absolute synchronism with the line frequency or can also be supplied from a frequency converter. Currently, synchronous electric motors with permanent magnets (PM) and an external rotor are gradually applied in the drives of electric vehicles and are stored directly in the wheel.

Hub motors, also called in-wheel motors, were first patented in the 1880s. In 1899 the Viennese firm of Lohner & Co. built a car powered by battery-driven hub motors. This car was also unique as the world's first front wheel drive system. A news report at the time described the development of the first-ever transmissionless vehicle as a revolutionary innovation. The electric motor in the hubs of the front wheels had an output of 1.8 kW at 120 rpm [2].

2. The synchronous motor with PM external rotor – model and simulation

This chapter presents results of the electro-magnetic proposal for a synchronous motor with external rotor with permanent magnets, simulation of electromagnetic field motor and its operating characteristics. Basic electrical characteristics have been developed on the basis of operational requirements for the motor – these are shown in Table 1.

Table 1

The synchronous motor parameters

Parameter	*Value*
Rated power	3 kW
Rated voltage	3 x 82 V (Y)
Rated current	27 A
Rated torque	38 Nm
Synchronous speed	750 rpm

The electromagnetic design of the motor was calculated and optimized in ANSYS/RMxprt. Based on the required electrical parameters and the geometric dimensions resulting from the motor mount, a 3D model of electromagnetic circuit of the motor was designed in ANSYS/Maxwell (Fig. 1).

The following are simulation results of the synchronous electric motor with an external rotor and PM. The simulation of the electromagnetic field of the synchronous motor with PM is shown in Fig. 2. Figure 3 shows a simulation of the induced voltage in all three phases of the synchronous machine.

The simulation of the motor and load torque is shown in Fig. 4. The speed of synchronous motor was 750 rpm. The simulation of the motor speed and torque is shown in Fig. 5.

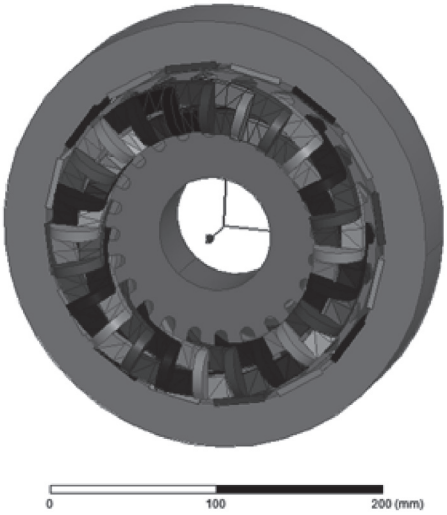

Fig. 1. The 3D model of synchronous motor with PM

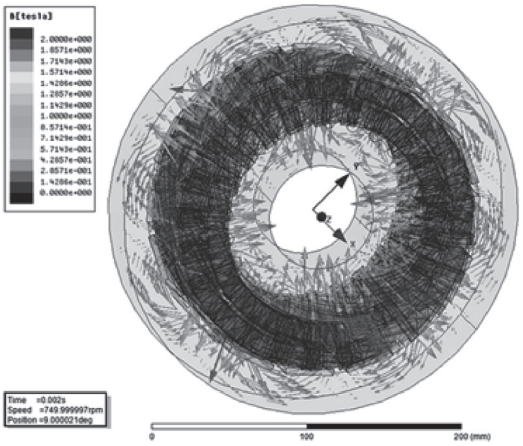

Fig. 2. Magnetic field of synchronous motor with PM

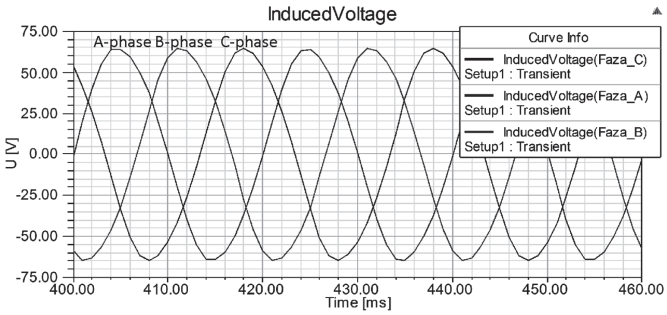

Fig. 3. Induced voltage calculated by ANSYS/Maxwell 3D

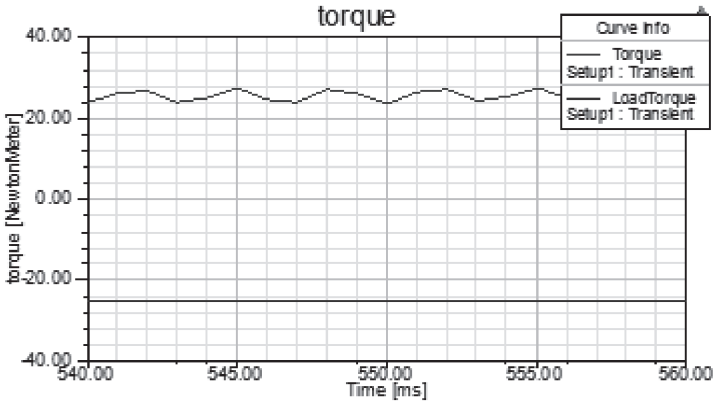

Fig. 4. Simulation of the motor and load torque calculated by ANSYS/Maxwell 3D

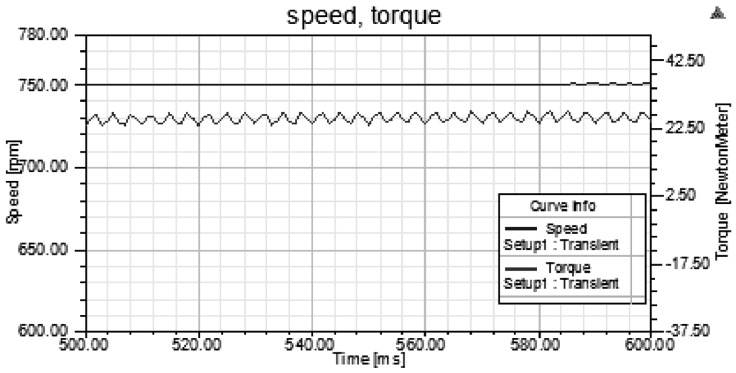

Fig. 5. Simulation of the motor speed and torque calculated by ANSYS/Maxwell 3D

3. Structural design of synchronous motor

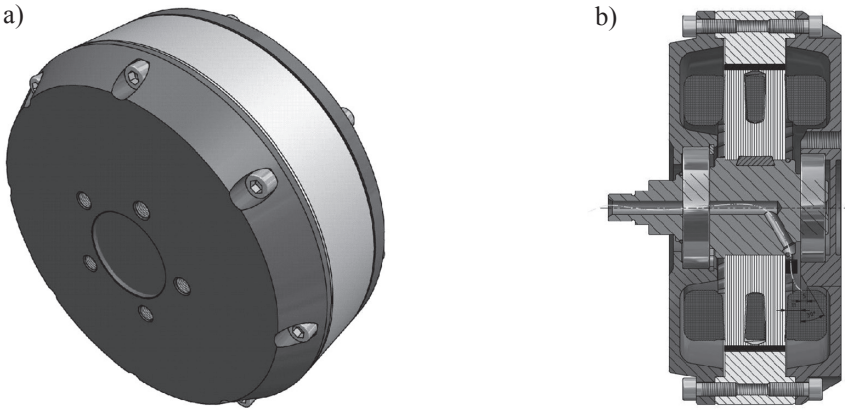

Fig. 6. 3D solid model of the synchronous motor

The construction and external dimensions of the motor are designed so that the motor can be easily positioned and mounted onto a traditional 14" steel rim wheel. The 3D solid model of the stator synchronous motor was created based on the geometric dimensions of the optimized simulation. Figure 6a) shows the general view of the 3D solid model of the synchronous motor with permanent magnets and the inverse rotor. A cross-sectional view of the synchronous motor is shown in Fig. 6b).

4. Measurement of synchronous motor prototype

Based on the structural design of the motor referred to in chapters 2 and 3, a functional prototype was devised. The synchronous motor was used for practical measurements in the laboratory, a photo of which is displayed in Figs. 7 and 8.

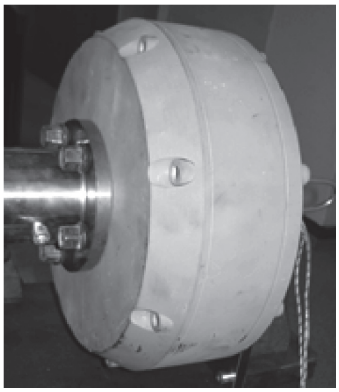

Fig. 7. The synchronous motor prototype

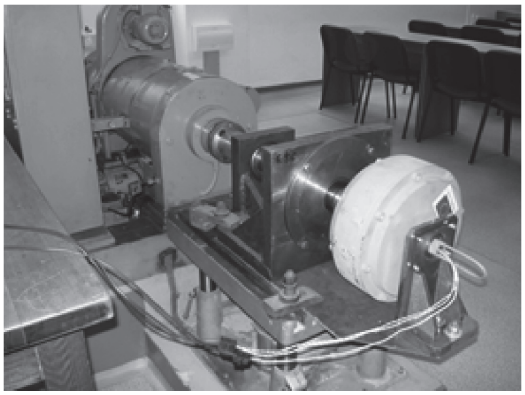

Fig. 8. Measurement of the synchronous motor prototype in the laboratory

4.1. Measurement of generator operation

When measured in a no load generator, the waveforms were recorded with an oscilloscope showing the voltage induced in individual phases. Figure 9 shows waveforms of induced voltages in the phases of the generator at a speed of 750 rpm.

When load is exerted on the generator (resistive load), its terminal voltage drops. In this measurement, the phase voltage reached 47.6 V (RMS) and the line-to-line voltage was 82.6 V (RMS). The frequency analysis of phase voltages (no load generator) is shown in Table 2.

Table 2

Frequency analysis of phase voltages

Order	U1[%H01]	U2[%H01]	U3[%H01]
1	100	100	100
3	2.2	2.2	2.3
5	1.4	1.4	1.5
7	-	0.1	-

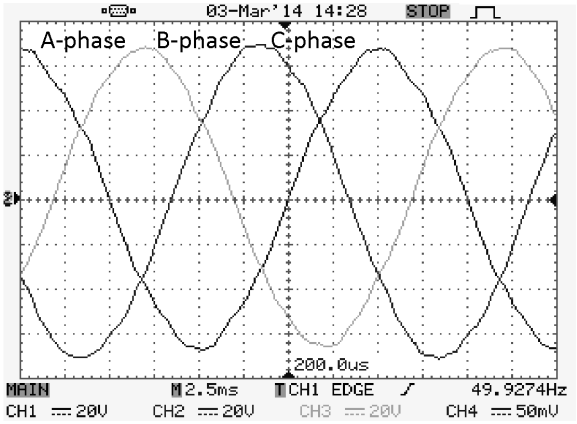

Fig. 9. The measured induced voltages

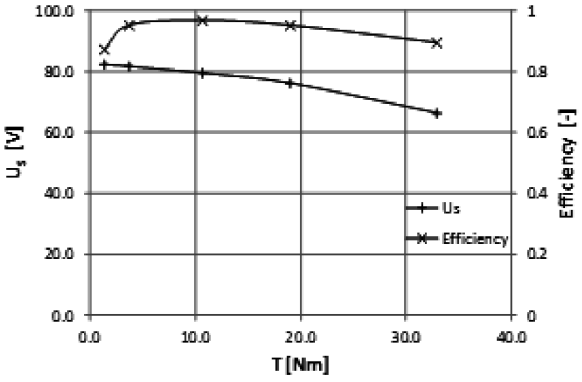

Fig. 10. Measured quantities for loads on the generator

When a load is exerted on the generator (resistive load), its terminal voltage drops. A plot of the terminal voltage and efficiency versus mechanical torque for a generator speed of 750 rpm is shown in Fig. 10. The measured quantities are indicated by crosses. Whilst the average efficiency is 94%, the voltage drop is up to 19%.

Figure 11 shows waveforms of voltage in the first phase and of the load current. The generator is loaded with a constant current of 20 A (RMS). Frequency analysis of phase currents (for load current of 20 A) is shown in Table 3.

Table 3

Frequency analysis of phase currents

Order	I1[%H01]	I2[%H01]	I3[%H01]
1	100	100	100
3	–	–	0.2
5	1.2	1.2	1.2
7	–	0.1	–

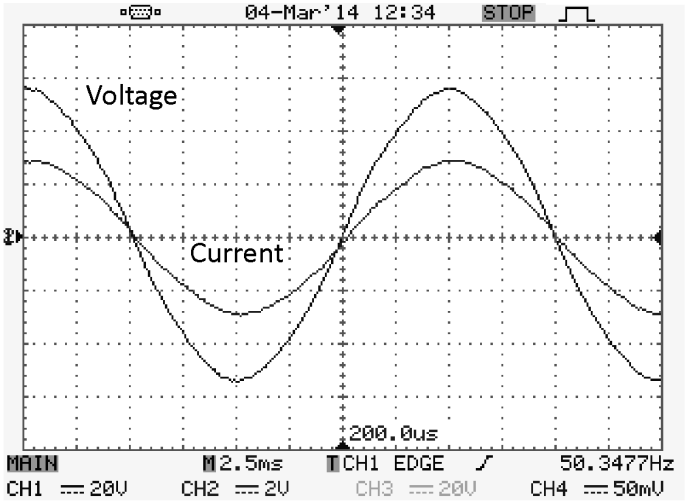

Fig. 11. Measured waveforms of voltage and current

4.2. Measurement of load motor operation

When measuring the synchronous machine in load motor operation, the machine is connected to a rated supply voltage of 82 V (RMS), with a frequency of 50 Hz. During loading of the motor, the supply voltage remains constant.

The synchronous motor was operating at a constant speed (750 rpm) and was loaded by a torque. At a constant mechanical speed, the mechanical output power is equivalent to mechanical torque on the shaft. The plot of motor torque is shown in Fig. 12, the input power and the mechanical power supplied to the rated voltage versus the phase current for a motor speed of 750 rpm. The measured quantities are indicated by crosses.

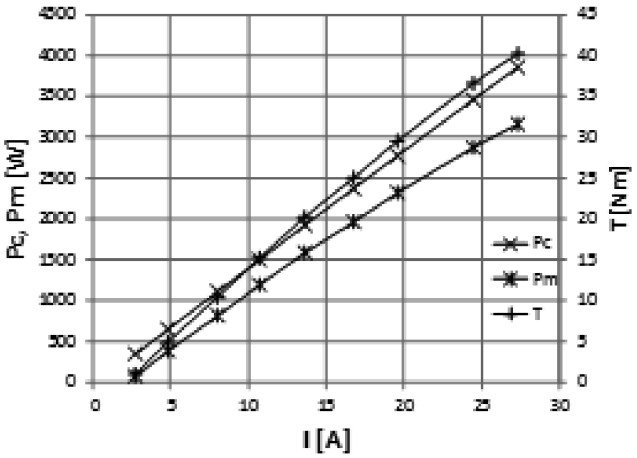

Fig. 12. Measured waveforms of torque and the powers

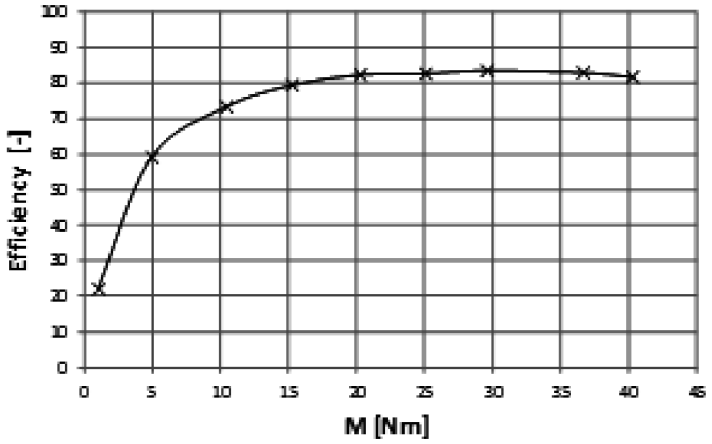

Fig. 13. Measured efficiency of synchronous motor

Figure 13 shows the plot of efficiency versus mechanical torque for synchronous motor speed of 750 and rated supply voltage of 82 V (RMS). The measured quantities are indicated by crosses. Figure 14 shows waveforms of supply voltage in the first phase and current of the motor. The motor is loaded with a constant torque of 1 Nm.

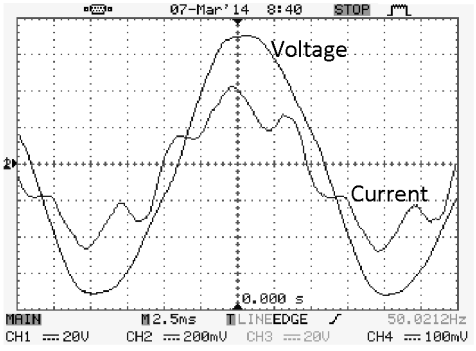

Fig. 14. Measured waveforms of supply voltage and current – $T = 1$ Nm

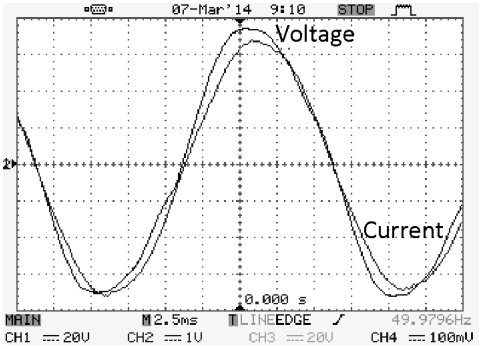

Fig. 15. Measured waveforms of supply voltage and current – $T = 36.6$ Nm

If the motor is loaded with a small torque ($T = 1$ Nm), then the waveform of the motor current contains higher harmonics and is very inharmonic. The motor operates under excitation.

Figure 15 shows waveforms of supply voltage in the first phase and current of the motor, if the motor is loaded with a constant torque of 36.6 Nm and operates as over-excited. If the motor is loaded with a rated torque, then the waveform of the motor current contains lower values of the higher harmonics and is roughly sinusoidal. Frequency analysis of phase voltages (for load motor torque – 36.6 Nm) is shown in Table 4.

Table 4

Frequency analysis of phase voltages

Order	U1[%H01]	U2[%H01]	U3[%H01]
1	100	100	100
3	2.5	2.2	2.0
5	4.2	4.5	4.6
7	1.3	1.8	1.2

Frequency analysis of phase currents (for load motor torque – 36.6 Nm) is shown in Table 5.

Table 5

Frequency analysis of phase currents

Order	I1[%H01]	I2[%H01]	I3[%H01]
1	100	100	100
3	0.6	0.3	0.4
5	1.2	1.0	1.2
7	0.4	0.4	0.5

4. Conclusion

This paper presents initial results of the simulation and measurement of a synchronous machine prototype with an external rotor and permanent magnets. When the synchronous machine works as a generator (resistive load), efficiency is higher than 90%. Efficiency of the synchronous motor is higher than 80% (for load torque higher than 15 Nm). The motor is designed to triple the torque overload. The maximum measured load torque of the synchronous motor was 40.2 Nm. The synchronous motor is designed to withstand three times the torque overload and is intended for in-wheel operation. Therefore, it is anticipated that future measurements will be performed of a synchronous machine supplied with a variable frequency converter.

5. Acknowledgment

We support research activities in Slovakia. This project is co-financed from EU funds. This paper was developed within the Project: “Centrum excelentnosti integrovaného výskumu a využitia progresívnych materiálov a technológií v oblasti automobilovej elektroniky”, ITMS 26220120055. (50%)

This work was supported in part of the Scientific Agency under the contract No: VEGA 1/0121/15. (50%)

References

[1] Gieras J.F., Wind M., *Permanent magnet motor technology – Design and Applications*, Ohio 2002.

[2] *Ferdinand Porsche (1875–1951)*, http://stuttcars.com/about-porsche/ferdinand-porsche.

[3] Skala B., *The Heat and Cooling of Electronically Switching Synchronous Machine as a Main Drive of a Car*, International Conference on Applied Electronics Location, Pilsen, Czech Republic, 7.08.2011.

[4] Miksiewicz R., *Właściwości silnika bezszczotkowego prądu stałego z magnesami trwałymi o różnych rozpiętościach uzwojeń stojana*, Zeszyty Problemowe – Maszyny Elektryczne, 2010, nr 87, Katowice, p. 215.

[5] Kacprzyk J., *Rozmyte programownie dynamiczne*, [in:] P. Kulczycki, O. Hryniewicz, J. Kacprzyk (eds.), *Techniki informacyjne w badaniach systemowych*, WNT, Warszawa 2007, pp. 231–282.

[6] Glinka T., Jakubiec M., *Silniki elektryczne z magnesami trwałymi umieszczonymi na wirniku*, Zeszyty Problemowe – Maszyny Elektryczne, 2005, nr 71, Katowice, p. 103.

[7] Kisielewski P., Antal M., Gierak D., Zalas P., *Zastosowanie magnesów trwałych w silnikach elektrycznych dużej mocy*, Zeszyty Problemowe – Maszyny Elektryczne, 2011, nr 92, Katowice, p. 187.

[8] Rossa R., *Zastosowanie metody polowo-obwodowej do obliczania parametrów silników synchronicznych z magnesami trwałymi przy pracy synchronicznej*, Zeszyty Problemowe – Maszyny Elektryczne, 2005, nr 72, Katowice.

[9] Bernatt J., Stanisław G., *Nowe rozwiązanie konstrukcyjne dwubiegunowej prądnicy synchronicznej z magnesami trwałymi*, Zeszyty Problemowe – Maszyny Elektryczne, 2005, nr 72, Katowice.

[10] Pistelok P., Kądziołka T., *Nowa seria wysokosprawnych dwubiegunowych generatorów synchronicznych wzbudzanych magnesami trwałymi*, Zeszyty Problemowe – Maszyny Elektryczne, 2013, nr 100, cz. II, Katowice, p. 65.

[11] Pyrhönen L., Jokinenm T., Hrabovcová V., *Design of Rotating Electrical Machines*, John Wiley & Sons Ltd, 2008, p. 512.

[12] Zawilak J., Zawilak T., *Minimization of higher harmonics in line-start permanent magnet synchronous motor*, Micromachines and servosys-tems, MiS ’06, International XV Symposium, Soplicowo, Sept. 2006, pp. 201–207.

[13] Salminen P., *Fractional slot permanent magnet synchronous motors for low speed applications*, Diss. Lappeenranta University of Technology, Lappeenrannan teknillinen yliopisto, 2004, p. 198.

TECHNICAL TRANSACTIONS | **CZASOPISMO TECHNICZNE**
ELECTRICAL ENGINEERING | ELEKTROTECHNIKA
1-E/2015

TOMASZ LERCH*, TOMASZ MATRAS**

MODELING THE PHENOMENON OF FREE AND FORCED MAGNETIZATION IN THREE-PHASE TRANSFORMERS

MODELOWANIE ZJAWISKA MAGNESOWANIA SWOBODNEGO I WYMUSZONEGO W TRANSFORMATORACH TRÓJFAZOWYCH

A b s t r a c t

This article presents the results of modeling the phenomenon of free and forced magnetization in three-phase, three-legged transformers. The no-load state of the transformer has been modeled using the program including a circuit model of the transformer. The results obtained have been compared with measurements carried out in the laboratory for the various circuits connection of the transformer.

Keywords: *transformer*, *free and forced magnetization*

S t r e s z c z e n i e

Artykuł przedstawia wyniki modelowania zjawiska magnesowania swobodnego i wymuszonego w transformatorach trójfazowych trójkolumnowych. Stan biegu jałowego transformatora modelowano za pomocą programów zawierających modele obwodowe transformatorów. Otrzymane wyniki porównywano z pomiarami przeprowadzonymi w laboratorium dla różnych układów połączeń transformatora.

Słowa kluczowe: *transformator*, *magnesowanie swobodne i wymuszone*

DOI: 10.4467/2353737XCT.15.025.3825

* Ph.D. Eng. Tomasz Lerch, assistant professor, Department of Power Electronics and Energy Control Systems, Faculty of Electrical Engineering, Automatics, Computer Science and Biomedical Engineering, AGH University of Science and Technology.

** M.Sc. Eng. Tomasz Matras, Enprom Sp. z o.o. [Ltd], Krzeszowice.

1. Introduction

The aim of this study was the modeling of the phenomenon of free and forced magnetization in three-phase transformers. For this purpose, the available programs, EMTP-ATP and Matlab-Simulink have been used for simulation of transients of the transformers. The programs take into account the unsymmetrical construction and non-linearity of the magnetic core. The calculation of currents and voltages has been performed for selected winding connections of the transformer.

Supplying the transformer winding with sinusoidal voltage, the magnetic flux and flux density are also sinusoidal. The relationship between flux density and no-load current for the ferromagnetic transformer core describes a hysteresis loop. Therefore, Fourier decomposition of the magnetizing current contains odd harmonics which are related to the amplitude of the saturation of the core. Such a case is called free magnetization of the transformer. If the higher harmonics of the current cannot flow in the transformer windings, especially the third one, then magnetic flux is deformed. Such a case is called a forced magnetization [3, 4].

2. No-load current of the transformer

Registrations of no-load current were performed for a three-phase, three-legged transformer with a capacity of S_N = 10 kVA. To register, Hall effect current transducers and a PC with a data acquisition card were used. An example of the no-load current waveform during free magnetization (*Y*0*y* connection) is shown in Fig. 1. Registration was performed for the selected windings connection where free and forced magnetization are present. The analysis of harmonic currents in each phase for *Y*0*y* and *Yy* windings connection are shown in Fig. 2.

The analysis of the currents shows that the third and fifth harmonics have the largest share of magnetizing current of the transformer besides the basic harmonic. It can also be noted that the amplitude of the fifth harmonic hardly depends on the windings connections. The third harmonic can flow to the windings of the transformer only in the four-wire system (*Y*0*y*).

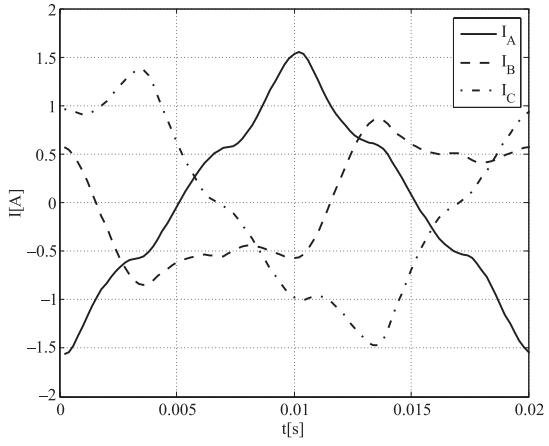

Fig. 1. No-load current – free magnetization

In the current spectrum of the three-wire system (*Yy*), current component with a frequency of 150 Hz can also be seen, but it does not create the zero-order system. In this case, the phase angles of phases A and C are identical while phase B is in antiphase to them. The current component of 150 Hz in the *Yy* connection system is caused by asymmetry of the three-legged transformer core.

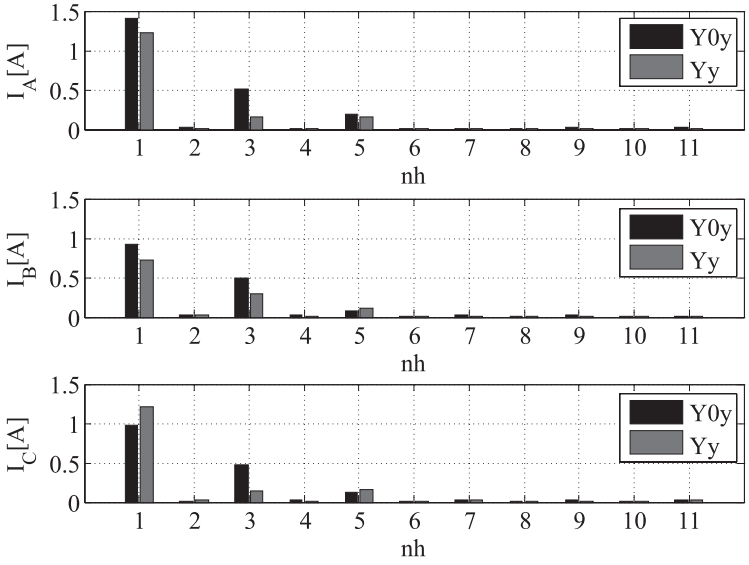

Fig. 2. Spectrum of no-load currents

3. Modeling of no-load current of the transformer

To model the studied phenomenon, available computational packages EMTP-ATP and Matlab-Simulink has been used. Models available in these packages allow to take into account non-linearity of magnetization characteristics of the transformer core.

ATP (Alternative Transients Program) is a non-commercial version of the EMTP (Electromagnetic Transients Program) developed in the frame of open access to the program. ATP is the universal program for the digital simulation of transient states of electromagnetic phenomena.

In the ATP package, there are two types of transformer models – a simplified model of SAT (saturable) and the hybrid model XFMR that takes into account the geometry of the transformer.

The SAT model takes into account the non-linear magnetization characteristic of the core. The input data for the primary and secondary side needed for simulation are: voltage; winding resistance; inductance; resistance for zero sequence. In the model, the windings connection and the number of columns of the core are also declared. Characteristics of magnetization are entered as a secondary side voltage dependence of the no-load primary side current of the transformer.

The operation of the XFMR model consist of topologically correct mapping of the substitute windings disposed on the surface of the core [6]. Individual branches are established for magnetizing yokes and columns depending on their length and area. Characteristics of the magnetization are described by the Frolich equation whose coefficients are adapted to the measurement data. This improves the extrapolation of saturation over the range of the measurement data. In the model also are taken into account the shunt capacities and dependence the winding resistance on the frequency.

The equivalent circuit model of the transformer takes into account four main aspects: the leakage inductance; windings capacitance; core nonlinearity; the impact of the frequency on winding resistance. This scheme is shown in Fig. 3.

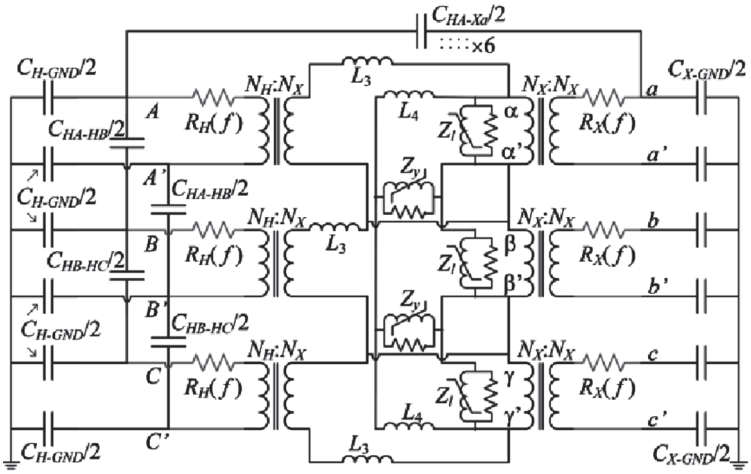

Fig. 3. Equivalent circuit of three-phase three-legged transformer

Matlab-Simulink is a software package for modeling, simulation and analysis of dynamic systems. Linear and nonlinear systems can be implemented and modeled in continuous or discrete time. After defining the model, the simulations are carried out using the integral method selected from the package menu or by typing the appropriate commands in the MATLAB command window. The transformer model used for simulation is defined by the parameters of the equivalent circuit and the characteristics of magnetization. This model does not take into account the asymmetry of the construction of the three-legged transformer core [5].

4. Simulation of no-load current of the transformer

Simulations were performed for two winding connections of the transformer – *Yy* where the magnetization is forced and *Y*0*y* where the magnetization is free. Both system connections have been simulated using the program EMTP-ATP model SAT and XFMR and Matlab-Simulink. The results of the simulation in each case were compared with laboratory measurements.

The first case concerns the forced magnetization in system *Yy*. Figure 4 shows the results of a SAT model simulation summarized with measurements results.

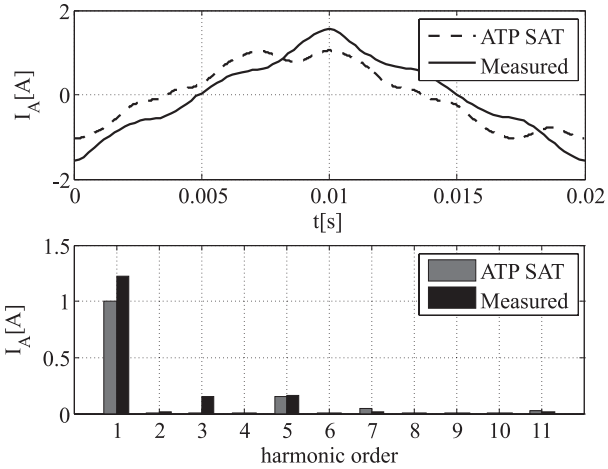

Fig. 4. *Yy* connection SAT model

Using the SAT model, where the construction of the transformer is given in a simplified manner, the calculated no-load current (in terms of amplitude and harmonic content) deviates from the measured current waveform. In particular, the simulated current waveform does not contain a 150 Hz component.

For the same case of study, but using the XFMR model, the calculated no-load current very well reflects the measured current waveform. This current waveform is shown in Fig. 5. The model which takes into account the core structure and the location of the individual windings better appoints the amplitude of the waveform and amplitude spectrum, including the component of frequency 150 Hz.

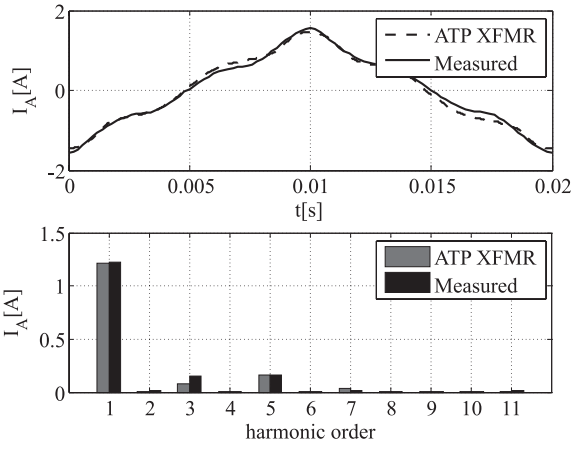

Fig. 5. *Yy* connection XFMR model

The no-load current for free magnetization has been simulated also using the model available in Matlab-Simulink. The simulation results are shown in Fig. 6.

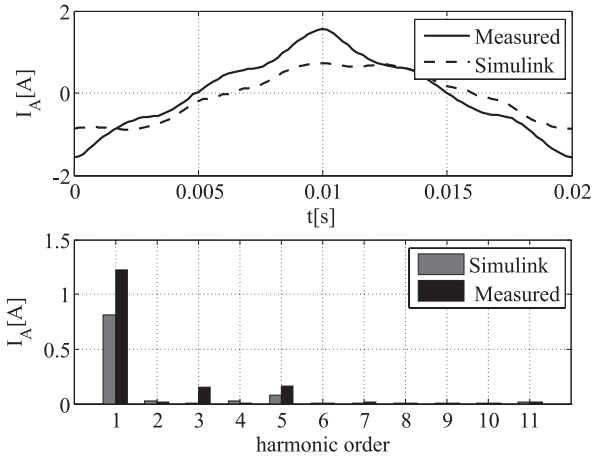

Fig. 6. *Yy* connection Simulink model

The transformer model available in Matlab-Simulink does not take into account the asymmetry and structure of the core. The waveforms are calculated only on the basis of equivalent circuit parameters and the magnetizing characteristics. As can seen in the above figure, this approach does not allow us to properly determine the amplitude and harmonic content of the current.

A second series of simulations was performed for the *Y0y* connection, i.e., for the case of the free magnetization. For this case, there is a closed path for the third harmonic current flow through the neutral wire as shown in the waveform in Fig. 2. The results of simulations performed on the SAT model EMTP-ATP package are shown in Fig. 7.

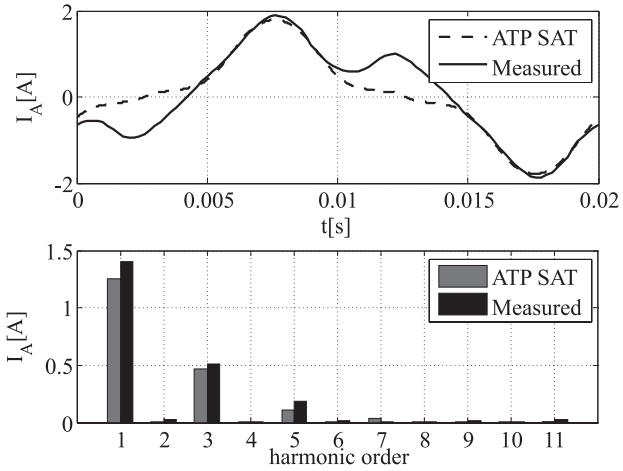

Fig. 7. *Y0y* connection SAT model

The harmonic analysis shows that in the case of the free magnetization, the no-load current has been calculated with a small error when compared to the results of the *Yy* connection (Fig. 4). Quite opposite results has been obtained using the model XFMR. Comparing the results obtained for the *Y0y* connection (shown in Fig. 8) with the results of the *Yy* connection (Fig. 5), it shows that in the case of the free magnetization, the model gives results significantly different from the measured. Despite consideration of the core geometry and winding arrangement in the model, the value of the third harmonic current (dominant in the case of the free magnetization), is several times smaller than the measured one.

The simulation results of no-load current using the model available in Matlab-Simulink (Fig. 9) are different from the measured waveforms as in the previous case. The model that does not consider the core geometry and winding arrangement gives correct results in any of the tested cases in terms of amplitude and harmonic current components.

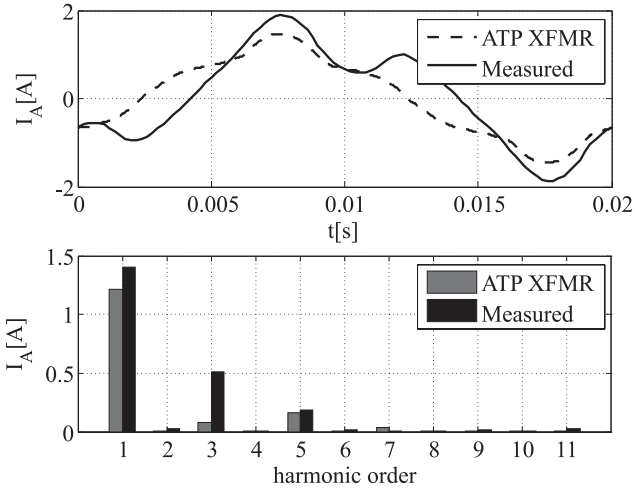

Fig. 8. *Y0y* connection XFMR model

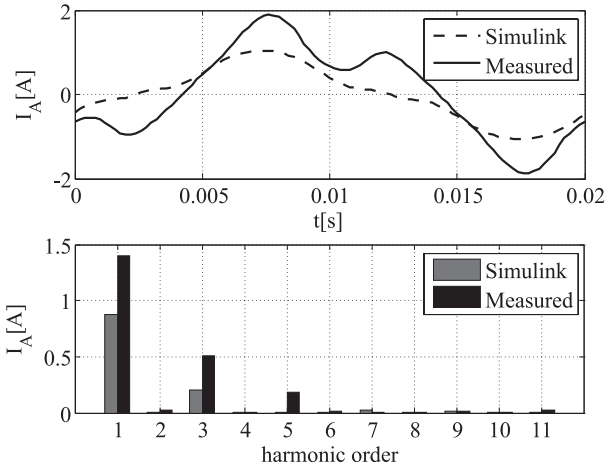

Fig. 9. *Y0y* connection Simulink model

5. Conclusion

Modeling the phenomenon of free and forced magnetization for three-phase three-legged transformers is a difficult issue because the core asymmetry and nonlinearity of the magnetizing characteristic has to be considered [1, 2]. It turns out, however, that the simulation results of the no-load current obtained using advanced models as XMFR type may be far from the measured. From the performed research, it can be concluded that the development of a universal circuit model of a three-phase three-legged transformer that allows us to simulate the phenomenon of free and forced magnetization for the various circuits connection is very difficult or even impossible.

References

[1] Chen X.S., Neudorfer P., *Digital model for transient studies of a three-phase five-legged trans-former*, IEE Proceedings C (Generation, Transmission and Distribution), Vol. 139, Issue 4, July 1992, pp. 351–358.
[2] Furgał J., *Symulacje prądów załączania transformatorów*, Przegląd Elektrotechniczny, 7.08.2007.
[3] Jezierski E., *Transformatory: budowa i projektowanie*, Wydawnictwa Naukowo-Techniczne, Warszawa 1963.
[4] Plamitzer A., *Maszyny elektryczne*, Wydawnictwa Naukowo-Techniczne, Warszawa 1982.
[5] Tomera M., *Wprowadzenie do Simulinka*, http://am.gdynia.pl/~tomera/ts/simulink_lab.pdf.
[6] Opis pakietu EMTP, http://www.emtp.org/.

TECHNICAL TRANSACTIONS | **CZASOPISMO TECHNICZNE**
ELECTRICAL ENGINEERING | ELEKTROTECHNIKA
1-E/2015

ALEJANDRO FERNÁNDEZ GÓMEZ, MACIEJ SUŁOWICZ, TADEUSZ J. SOBCZYK*

THE INFLUENCE OF MECHANICAL FAULTS ON INDUCTION MACHINES WITH ELECTRICAL FAULTS

WPŁYW USZKODZEŃ MECHANICZNYCH W SILNIKU INDUKCYJNYM NA OCENĘ USZKODZEŃ ELEKTRYCZNYCH

Abstract

The study of the interaction between faults of different natures is a crucial step for the development of effective systems for fault detection. The analysis of the electrical signals using the actual motor current signature analysis (MCSA) techniques may lead to different results and, as a consequence, an incorrect diagnosis of the fault due to the fact that the non-linear interactions between both faults are difficult to predict with high precision. The relationship between the electrical and mechanical components has been extensively studied in the past, but despite the progress made, the introduction of new control systems or the nonlinearities presented in the electrical machine, still makes it hard to diagnose faults. The study below attempts to show the evolution of the induction motor signatures when electrical and mechanical faults occur simultaneously. The Fourier analysis of the signatures presented in this paper indicates that the typical analysis carried out to diagnose the state of the electrical machine may be interpreted as an indicator of a different type of fault.

Keywords: *induction motors*, *broken bar*, *mechanical fault*, *Fourier*, *Simulink*

Streszczenie

Badanie interakcji występujących między efektami różnej natury uszkodzeń jest kluczowym krokiem w rozwoju efektywnych systemów diagnostycznych do wykrywania uszkodzeń maszyn indukcyjnych. Analiza prądu stojana z wykorzystaniem metody MCSA (*Motor Current Signature Analysis*) może prowadzić do różnych wyników i w konsekwencji do błędnego rozpoznania uszkodzenia. Spowodowane jest to tym, że nieliniowe interakcje pomiędzy rozmaitymi uszkodzeniami są trudne do przewidzenia i oszacowania z wystarczającą dokładnością. Relacje między charakterystycznymi komponentami uszkodzeń elektrycznych i mechanicznych zostały już dość dobrze zbadane w przeszłości, ale mimo to wciąż sprawiają trudności w zdiagnozowaniu poszczególnych uszkodzeń. Zawarte w artykule wyniki analiz stanowią próbę ukazania rozwoju charakterystycznych składowych w widmach prądu stojana silnika indukcyjnego podczas równoczesnego występowania zakłóceń elektrycznych i mechanicznych. Przedstawione w pracy analizy widmowe charakterystycznych cech tych uszkodzeń dowodzą, że typowa analiza przeprowadzona na podstawie metody MCSA może wpłynąć na błędne określenie stanu maszyny i złą interpretację uzyskanych wyników przez wskazanie innego typu uszkodzenia niż to, które rzeczywiście wystąpiło.

Słowa kluczowe: *silnik indukcyjny*, *uszkodzony pręt klatki*, *uszkodzenie mechaniczne*, *Fourier*, *Simulink*

DOI: 10.4467/2353737XCT.15.026.3826

* M.Sc. Alejandro Fernández Gómez, Ph.D. Eng. Maciej Sułowicz, Prof. D.Sc. Ph.D. Eng. Tadeusz J. Sobczyk, Institute on Electromechanical Energy Conversion, Faculty of Electrical and Computer Engineering, Cracow University of Technology.

1. Introduction

The fault diagnosis of electrical motors is a topic frequently discussed in relation to industrial solutions, especially in those cases in which high power machines run the production process. The scientific community together with industry have dealt with this challenge for many years now, but there is still no global solution available due to the evolution of the industry. For instance, the development of new drives for electrical motors brought new difficulties in the condition monitoring and fault diagnosis.

It is well known that the sideband components around the fundamental frequency $(1 \pm 2s)f_0$ for $k = \pm 1, \pm 2, \pm 3\ldots$ are typically used as an indicator of electrical faults and mechanical faults, and they depend on the torque demanded by the load.

However, the study and analysis of those components have been considered insufficient to detect faults in some cases, in which authors suggested complementary studies of other components of the stator currents, electromagnetic toque or rotor speed [1–4]. In [5], the authors suggest the use of the component at a frequency of $(5 - 4\ s)\ f_0$ in order to detect rotor faults due to the fact that this component increases with the number of broken bars whereas it remains almost unchangeable for the inertia of the motor-load unit as well as for supply voltage distortion or unbalance. In [6], the components around the principal slot harmonic PHS have been considered in order to detect the mechanical unbalance.

Nevertheless, those studies have not considered the possible effects on the frequency magnitudes that may happen when two of these faults occur simultaneously due to the interactions existing between electrical and mechanical components of the electrical machine.

In large scale motors at nominal conditions, the slip is rather small and the frequency sidebands are in a range of few Hertz. However, low frequency components are also a typical effect when a fault occurs in turbo-machinery, for instance, surges in centrifugal compressors. Surge is a phenomenon in which mass flow oscillations are produced due to the rise of pressure and rotational speed of the compressor, causing and alternating the component in the compressor's torque [7]. This phenomenon appears when the operation point of the compressor exceeds the stability limit in the compressor's map and may cause severe damage to the machine. In big compressors, i.e. 7–8 MW power, the surge frequency is about 1–2 Hz [8].

The objective of this work is to show the alterations produced in the frequency spectrum, when the above faults affect the whole system at once, of the sideband components around the main frequency, considering resonances due to the fact that characteristic frequencies of both faults may be equal. The load, the inertia of the system, the magnitude and phase of the mechanical load and the severity of the rotor fault have been considered.

The results have shown big differences in the magnitudes of sidebands as a function of the mechanical load conditions. Simulink has been selected as a platform to develop faulty dynamic models of induction motors (IM) based on the effect of main magneto-motive forces.

2. Models

2.2. Internal electrical fault – Broken Bar

A broken or incipient broken bar is one of the common faults in induction motors. When rotor defects appear, the symmetry is lost inducing additional components in the motor current the frequency of which is $(1 - 2s)f_0$. This frequency is responsible for the appearance of a torque ripple at a frequency of $2\,sf_0$. The ripple in the torque creates a new current in the stator windings at a frequency of $(1 + 2s)f_0$, hence, a new magnetic field arises with a frequency respect to rotor $3sf_0$. The interaction between magneto motive forces of the stator and rotor (MMF's) due to cage asymmetry, give rise to frequency components $(1 \pm 2s)f_0$ for $k = \pm1, \pm2, \pm3\ldots$ in the current spectrum. The magnitude of the components is lessened more and more for the inertia of the machine. Because of that, fault detection is focused on $(1 \pm 2s)f_0$.

The asymmetry of the cage is modeled increasing the resistance of the element affected by the fault. The change of the resistance is typically estimated by an increase of 20 times the initial value, therefore, an additional term of the rotor resistance will appear. It is well known that asymmetry and symmetry coefficients are used to indicate the increase of the cage resistance [9]. The use of this model is limited as it is only valid for those cases in which the slip remains closer to the nominal slip, otherwise, the matrix of inductance should also be changed.

The model for the internal electrical fault is described as follows:

$$\frac{\mathrm{d}}{\mathrm{d}t}\begin{bmatrix}\Psi_{sd}\\ \Psi_{sq}\\ \Psi'_{rd}\\ \Psi'_{r'q}\end{bmatrix}+\begin{bmatrix}-\omega_s\cdot\Psi_{sq}\\ \omega_s\cdot\Psi_{sd}\\ -\omega_r\cdot\Psi'_{rq}\\ \omega_r\cdot\Psi'_{rd}\end{bmatrix}+[\mathbf{R}]\cdot\begin{bmatrix}i_{sd}\\ i_{sq}\\ i'_{rd}\\ i'_{rq}\end{bmatrix}=\begin{bmatrix}u_{sd}\\ u_{sq}\\ 0\\ 0\end{bmatrix} \tag{1}$$

$$[\mathbf{R}]=\begin{bmatrix}R_s & 0 & 0 & 0\\ 0 & R_s & 0 & 0\\ 0 & 0 & R'^{p}_{r}\cdot\left(1+k_s+k_{as}\cdot\cos\left(2\cdot\gamma_r\right)\right) & R'^{p}_{r}\cdot k_{as}\cdot\sin\left(2\cdot\gamma_r\right)\\ 0 & 0 & R'^{p}_{r}\cdot k_{as}\cdot\sin\left(2\cdot\gamma_r\right) & R'^{p}_{r}\cdot\left(1+k_s-k_{as}\cdot\cos\left(2\cdot\gamma_r\right)\right)\end{bmatrix} \tag{2}$$

$$\begin{bmatrix}\Psi_{sd}\\ \Psi_{sq}\\ \Psi'_{rd}\\ \Psi'_{r'q}\end{bmatrix}=\begin{bmatrix}L_{\sigma s}+L_m & 0 & L_m & 0\\ 0 & L_{\sigma s}+L_m & 0 & L_m\\ L_m & 0 & L_{\sigma r}+L_{\boldsymbol{m}} & 0\\ 0 & L_m & 0 & L_{\sigma r}+L_m\end{bmatrix}\cdot\begin{bmatrix}i_{sd}\\ i_{sq}\\ i'_{rd}\\ i'_{rq}\end{bmatrix} \tag{3}$$

where:
Ψ_{sd} – the stator and rotor fluxes in the *d–q* components,
i_{sd} – the stator and rotor currents,
$w_{s,\,r}$ – the stator and rotor speed,
u_{sd} – the stator voltages,
R_s – the stator resistance,
$R_r^{'p}$ – the equivalent rotor resistance,
γ_r – the rotor rotational angle,
$L_{\sigma s,r}$ – the stator and rotor leakage inductance,
L_m – the mutual inductance,
k_s – the symmetry factor,
k_{as} – the asymmetry factor.

For the purpose of clarity, the equations used have been transformed into components *d–q* and stator and rotor fluxes have been chosen as state variables.

One broken bar has been considered in the analysis, hence, the corresponding value of k_s and k_{as} is 0.0291.

2.3. Generic Mechanical Fault

Electrical motors are the main component of a large variety of industries connected to a wide range of machinery. Their functionality is often affected by a malfunction in the load causing severe damage if it is not detected quickly, especially in high power machines. For example, an unbalanced rotation shaft due to a fault in the gearbox or a broken ball in a bearing creates an additional torque and in some cases, an asymmetry in the air-gap.

The reaction of the induction motor due to this type of fault can be studied through a set of two mechanical equations together with additional torque components, time or angle dependent.

$$J\frac{\mathrm{d}\omega_r}{\mathrm{d}t} + D\frac{\mathrm{d}\varphi}{\mathrm{d}t} = T_{ele} - T_z \tag{4}$$

$$\frac{\mathrm{d}\varphi}{\mathrm{d}t} = \omega_r \tag{5}$$

where:
J – the moment of inertia of the rotor plus the load,
D – the dumping term,
T_{ele} – the electromechanical torque,
T_z – the resistive torque in shaft,
φ – the geometrical angle of the rotor,
ω_r – the mechanical speed of the rotor.

Usually, the dumping term can be neglected.

In order to study the effects of a generic mechanical fault, T_z has been defined as the sum of a constant component plus an alternating component T_{AC}, in which the main harmonic has only been considered, with adjustable frequency f_z. The amplitude of T_{AC} has been defined under the assumption of the same effects over the electromagnetic torque as the broken bar.

$$T_z^{'} = T_z + T_{AC} \cdot \sin\left(2\pi f_0 + \alpha_z\right) \tag{6}$$

Where f_0 is the net frequency and α_z is the phase of the mechanical oscillation.

3. Results

In the previous sections, the relationship between the two sideband components close to the main net frequency is explained. The objective of the experiments is to clarify what the changes in magnitude are of the two components bringing light to the following challenges:

- If the mechanical frequency f_{BB} with a value of $2s\,f_0$ creates additional components at the same frequency as the broken bar, what can be expected in terms of magnitude when both faults occur simultaneously?
- The mechanical fault depends on the magnitude of the oscillating component as well as the phase. Considering frequencies f_z and f_{BB} have the same value, what would the behavior of components be if the mechanical fault phase is different?

Experiments were conducted in a 4 kW motor and the results are discussed in the following sections. However, the simulation results were obtained for a 2000 kW motor with the purpose of confirming that the same consequences can be expected independently of the motor size. Discrete induction machine models based on the Euler forward method were used in Simulink with a time step of 1e-5 (Simulation parameters: fix step and discrete solver). The following induction motor with the following rated data was chosen: P_N = 2000 kW; n_N = 2980 rpm; U_N = 6kV; I_N = 227 A; p = 1; N = 36 rotor bars; J = 34 kgm^2.

For the benefit of clarity, the Fourier spectrum of the stator phase currents was referred to the magnitude of the 50 Hz component (rms * 1e-5).

3.1. Evolution of Broken Bar component magnitude

A ripple with a characteristic frequency can be observed in the stator currents due to both types of faults. The simulations were carried out considering the same fault severity. Therefore, the amplitude of the mechanical alternating component produces a ripple in the electromagnetic torque equivalent to the broken bar effects. The following figures and tables show the evolution of $(1 \pm 2s)f_0$ components magnitude.

The load of the machine is one of the factors with more influence on the diagnosis and evolution of certain types of fault. For instance, the magnitude of the sidebands due to broken bar changes according to the load. The analysis has been carried out for different load scenarios considering the phase angle α_z equal to zero, loaded with 100%, 75% and 50% of the nominal torque. On the other hand, for greater slips, fluctuations in the speed reflected in

the $(1 - 2s)f_0$ component disappear as well as the component itself, hence, the influence of the machine inertia was also considered.

A filter was applied and the net frequency removed from the Fourier spectra of the stator phase currents.

Figures 1–3 show changes in the magnitude of the $(1 \pm 2s)f_0$ components in the linear scale as a function of the mechanical fault frequency f_z, which decreased from 4.5 Hz to 1.5 Hz, and the moment of inertia equal to twice the inertia of the induction motor (notice that red indicates the frequency component due to mechanical fault).

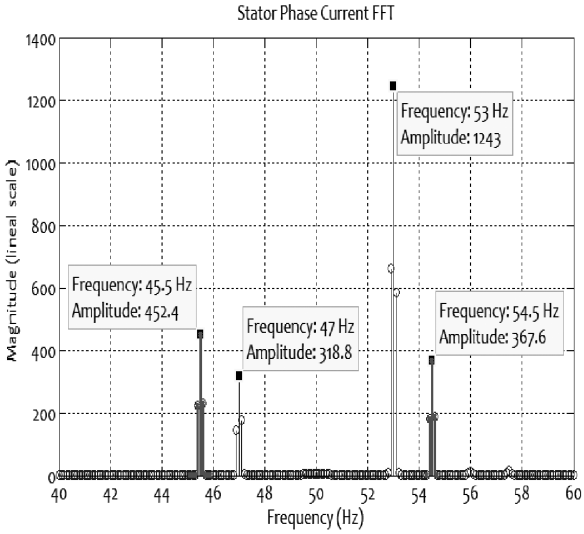

Fig. 1. Fourier Spectra of Phase current A: 100% Nominal torque and f_z = 4.5 Hz

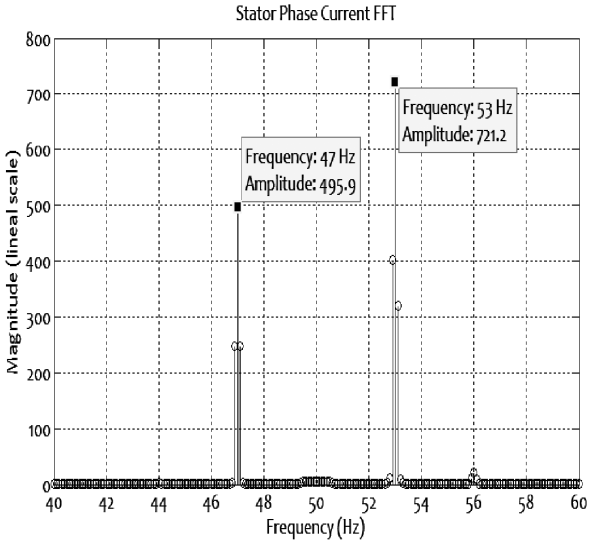

Fig. 2. Fourier Spectra of Phase current A: 100% Nominal torque and f_z = 3 Hz

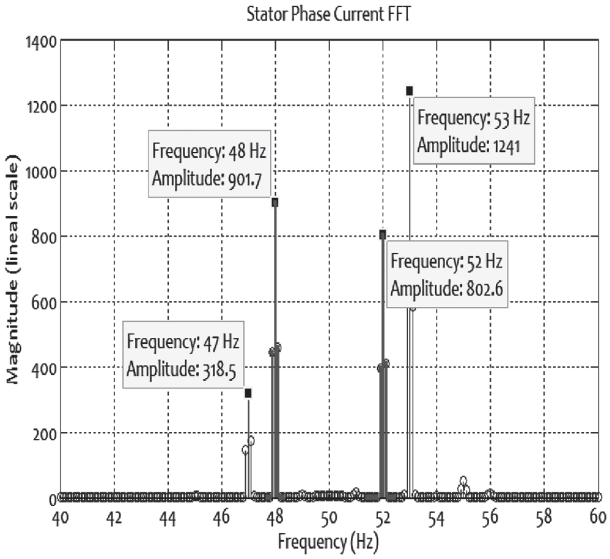

Fig. 3. Fourier Spectra of Phase current A: 100% Nominal torque and f_z = 2 Hz

Table 1 completes the analysis showing the changes of the frequencies do not included in the previous figures.

Table 1

Magnitude of $(1 \pm 2s)f_0$ component for inertia twice the motor inertia

f_{BB}/f_z	4.5 Hz	4 Hz	3.5 Hz	3 Hz	2.5 Hz	2 Hz
47 Hz 100% Tn	318.77	318.76	318.75	496	318.53	318.46
53 Hz 100% Tn	1242.55	1242.5	1242.34	721.07	1241.9	1241.22

It can be noted that the magnitude of the components only change considerably when the mechanical frequency is equal to the broken bar frequency independent of the load. In case of a different load, the same tendency can be observed. However, this effect is attenuated when the inertia of the systems is increased. In addition, the magnitude of the mechanical fault components increased as expected.

3.1. Evolution of Broken Bar component magnitude due to phase changes

According to the previous experiment, the magnitude of the sidebands $(1 \pm 2s)f_0$ changes if the frequency of both faults is equal. The second simulations explore how the phase may also change the magnitude.

Changing the phase of the alternating component of the mechanical load from 0 to 2π in ten steps, Fig. 4 shows the effects on the component's amplitude for equal severity faults, nominal torque, J twice the motor inertia and f_z = 3 Hz.

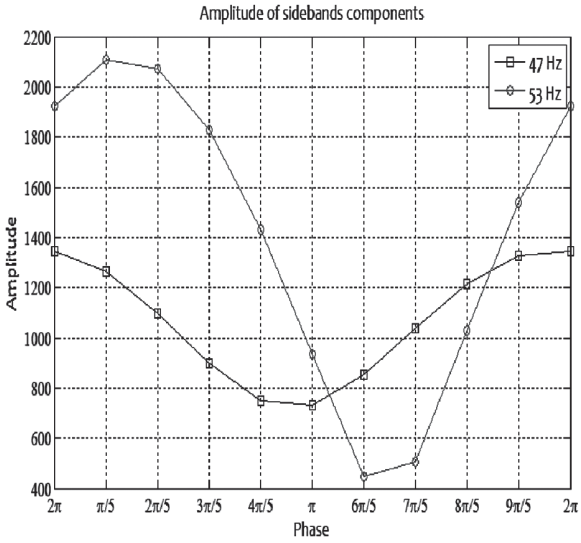

Fig. 4. Evolution of Sideband's Amplitude regarding mechanical phase

The alternation between both components which has the greater value due to phase changes can be observed. A modulation of low frequency of the stator phase currents has also been observed in the simulations. The resolution of the Fourier spectra used is 0.1 Hz and the component of that modulation could not be observed in the spectrum. Figure 5 shows the modulation (note the time scale). Figure 6 shows the presence of the ripple at 3 Hz due to fault. Figure 7 shows that the modulation is also present if f_z suffers slight changes (3.1 Hz) and it is divided in two: a) the left side shows the ripple at frequency 3.1 Hz as Fig. 6; b) the right side shows the modulation of the stator currents as Fig. 5.

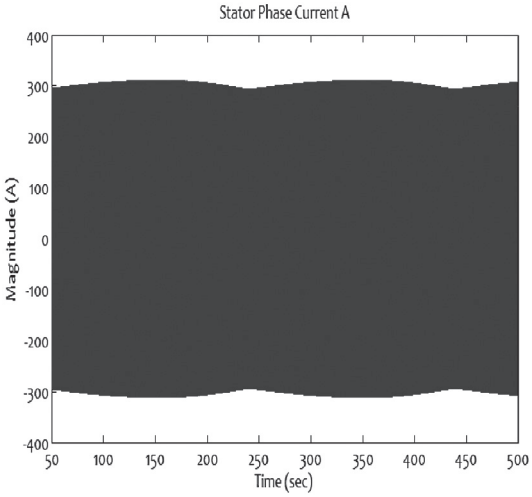

Fig. 5. Phase current modulation f_z = 3 Hz

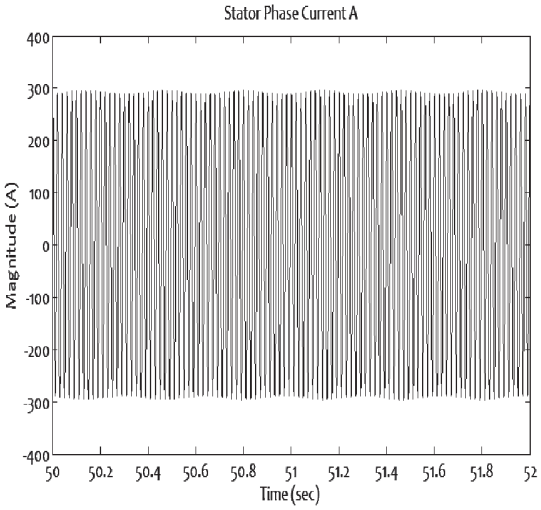

Fig. 6. Phase current modulation f_z = 3 Hz zoom

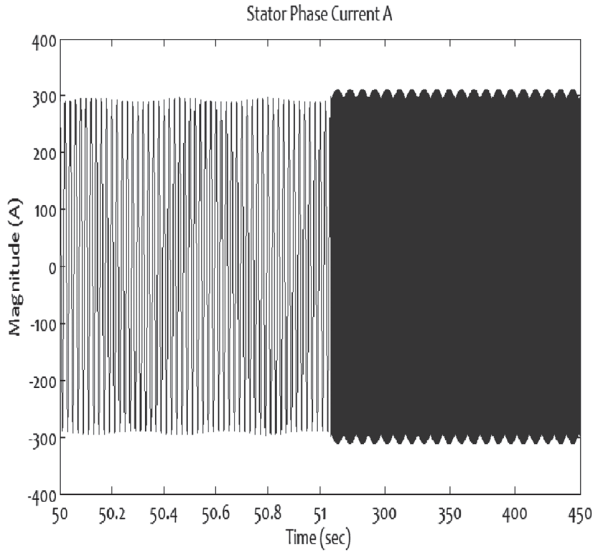

Fig. 7. Phase current modulation f_z = 3.1 Hz zoom

3.3. Experimental results

A qualitative analysis of the results shown in subchapter 3.1 was carried out with a motor of rated data P_N = 4 kW, n_N = 1480 rpm, U_N = 400 V, I_N = 2.6 A, p = 2, N = 28 rotor bars and J = 0.019 kgm^2. The mechanical fault was created controlling the field winding current of a DC motor by a power electronic converter, hence, the resistive torque applied to the motor for a given frequency f_z.

Figures 8–11 show the current spectrum for the following faults – one broken bar and one broken bar plus mechanical fault with an amplitude of 10% of the nominal torque and frequencies f_z equal to 6 Hz, 5.2 Hz and 4 Hz respectively.

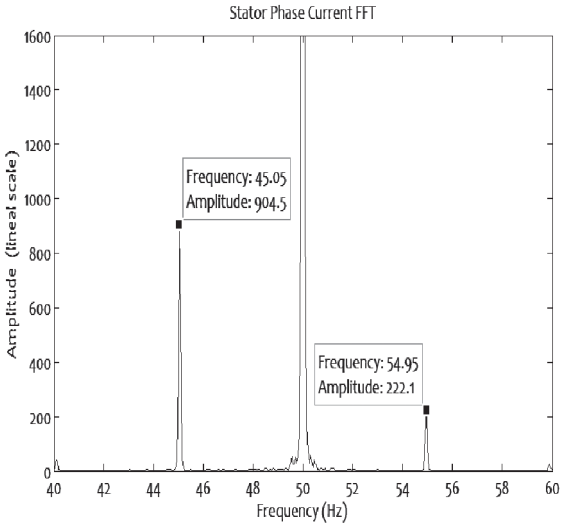

Fig. 8. Fourier Spectra of Phase current A: Broken Bar at 100% Nominal torque

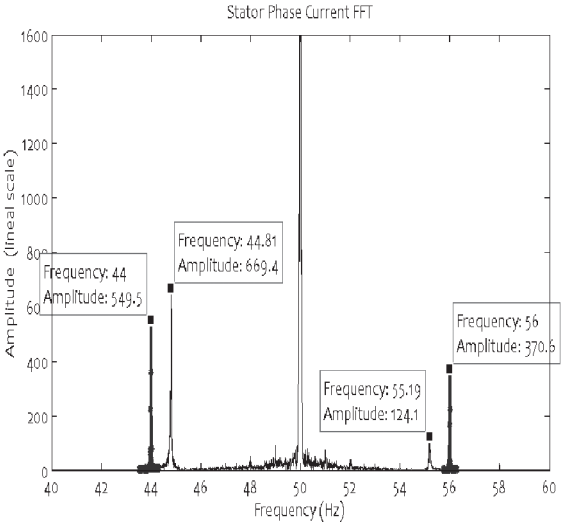

Fig. 9. Fourier Spectra of Phase current A: Broken Bar and f_z = 6 Hz

The evolution of the sidebands $(1 \pm 2s)f_0$ agrees with the simulation results. The amplitude of the broken bar is lower if the mechanical fault arises (Fig. 8). The amplitude of both mechanical components is greater when f_z is lower than f_{BB} as it has been shown in Figs. 1 and 3. Finally, if f_z reaches the value of f_{BB}, the difference between amplitudes of both sidebands, resulted from the sum of both fault effects, is reduced as it has been shown in Fig. 2.

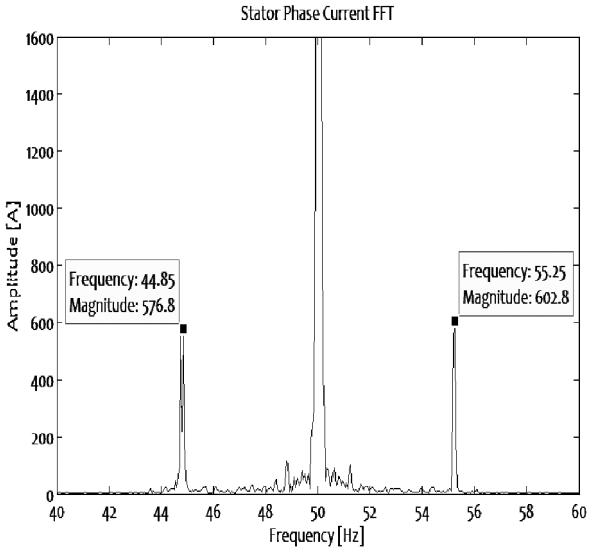

Fig. 10. Fourier Spectra of Phase current A: Broken Bar and f_z = 5.2 Hz

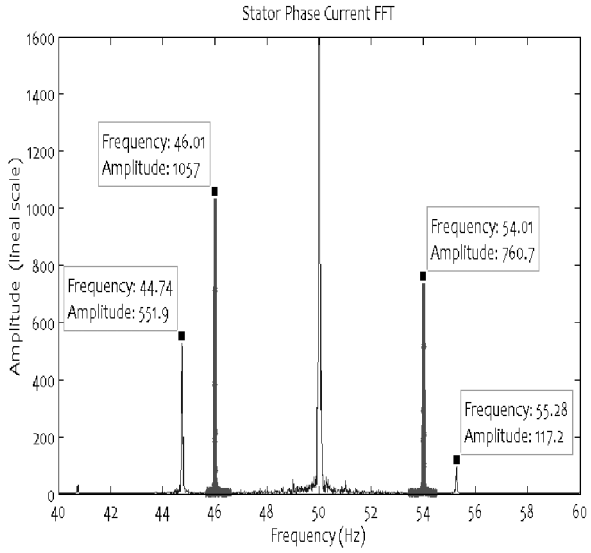

Fig. 11. Fourier Spectra of Phase current A: Broken Bar and f_z = 4 Hz

4. Conclusions

The aim of the paper is to study which phenomena occur in the induction motor when two of the commonest faults appear simultaneously – one broken bar and a mechanical fault. The MCSA technique was applied to study the evolution of the sideband frequencies $(1 \pm 2s)f_0$ extensively

used for the diagnosis of both faults. Changes in magnitudes were studied in order to reveal the behavior of the motor. The Fourier spectrum has shown differences regarding the faults applied and load conditions. Simulink was used as a platform for the development of IM models.

Simulations have shown that the magnitude of the sidebands $(1 \pm 2s)f_0$ only changed when mechanical fault frequency f_z reached the same value as the broken bar frequency f_{BB}. The experimental results confirmed, qualitatively, the evolution shown in the simulation results.

According to the simulation results, the phase of the mechanical fault has an important role, leading to possible misinterpretation of the results derived from the IM diagnosis due to changes in the sideband amplitudes.

One of the techniques applied to detect the presence of the broken bar or incipient broken bar in electrical motors consisted of studying the differences between the magnitudes of the two sidebands $(1 \pm 2s)f_0$ establishing global fault indicators [1, 10]. The presence of a mechanical fault produces variations in magnitudes that may alter the value of the indicator leading to incorrect diagnosis.

It is worth mentioning that the high difference between sideband components can be attributed to cases where more than one bar was damaged.

Future research may be focused on studying systems which not only include a model of the electrical machine plus a generic mechanical fault, but also the mechanical load driven, due to the fact that nowadays, industry demands solutions customized for individual systems. The inclusion of electrical machine models in the studies carried out to evaluate failures in turbo-machinery could point out that damage could be increased due to electrical faults and vice versa.

References

[1] Didier G., Ternisien E., Caspary O., Razik H., *Fault detection of broken rotor bars in induction motor using a global fault index*, Industry Applications, IEEE Transactions, 2006, Vol. 42, No. 1, pp. 79–88.

[2] Concari C., Franceschini G., Tassoni C., *Discerning mechanical load unbalances from rotor faults in induction machines through current space vector components*, IECON 2010 – 36th Annual Conference on IEEE Industrial Electronics Society, 2010, pp. 2609–2614.

[3] Bellini A., Concari C., Franceschini G., Lorenzani E., Tassoni C., Toscani A., *Thorough understanding and experimental validation of current sideband components in induction machines rotor monitoring*, IEEE Industrial Electronics, IECON 32nd Annual Conference, 2006, pp. 4957–4962.

[4] Martins Cunha C.C., Lyra R.O.C., Filho B.C., *Simulation and analysis of induction machines with rotor asymmetries*, Industry Applications, IEEE Transactions, 2005, Vol. 41, No. 1, pp. 18–24.

[5] Bossio G.R., De Angelo C.H., Pezzani C.M., Bossio J.M., Garcia G.O., *Evaluation of harmonic current sidebands for broken bar diagnosis in induction motors*, Diagnostics for Electric Machines, Power Electronics and Drives, SDEMPED IEEE International Symposium, 2009, pp. 1–6.

[6] Salah M., Bacha K., Chaari A., *Stator current analysis of a squirrel cage motor running under mechanical unbalance condition*, En Systems, Signals & Devices (SSD), 10th International Multi-Conference, 2013, IEEE, pp. 1–6.

[7] Giampaolo T., *Compressor Handbook: Principles and Practice*, The Fairmont Press, Inc., 2010.

[8] Gravdahl J.T., Egeland O., Vataland S., *Drive torque actuation in active surge control of centrifugal compressors*, Automatica, 2002, Vol. 38, No. 11, pp. 1881–1893.

[9] Fernández Gómez A.J., Sobczyk T.J., *Motor current signature analysis apply for external mechanical fault and cage asymmetry in induction motors*, Diagnostics for Electric Machines, Power Electronics and Drives (SDEMPED), 9th IEEE International Symposium, 2013, pp. 136–141.

[10] Bellini A., Filippetti F., Franceschini G., Tassoni C., Kliman G.B., *Quantitative evaluation of induction motor broken bars by means of electrical signature analysis*, IEEE Tran. on Ind. Appl., 2001, Vol. 37, No. 5, pp. 1248–1255.

TECHNICAL TRANSACTIONS | **CZASOPISMO TECHNICZNE**
ELECTRICAL ENGINEERING | ELEKTROTECHNIKA
1-E/2015

ANDRZEJ HERBST*

TWO CONSTRUCTIONS OF IE4 EFFICIENCY CLASS SYNCHRONOUS MOTORS WITH DISTRIBUTED AND CONCENTRATED WINDING

DWIE KONSTRUKCJE SILNIKA SYNCHRONICZNEGO O SPRAWNOŚCI KLASY IE4: Z UZWOJENIEM ROZŁOŻONYM I SKUPIONYM

A b s t r a c t

This paper takes into consideration two PMSM motors of size 80 with very similar efficiency and output power. In the article, design differences between a classic 4 pole/24 tooth motor with distributed winding and a 10 pole/12 tooth motor with concentrated winding are shown. Calculations and tests results are also presented for both machines.

Keywords: *PMSM motor*, *distributed winding*, *concentrated winding*

S t r e s z c z e n i e

W artykule przedstawiono dwa silniki synchroniczne z magnesami trwałymi o wzniosie wału 80 mm z bardzo podobną sprawnością i mocą wyjściową. Artykuł skupia się na pokazaniu różnic między konstrukcjami silnika 4-biegunowego/24-żłobkowego z uzwojeniem rozłożonym a 10-polowego/12-żłobkowego z uzwojeniem skupionym. Przedstawiono również wyniki obliczeń oraz badań obu maszyn.

Słowa kluczowe: *silnik PMSM*, *uzwojenie rozłożone*, *uzwojenie skupione*

DOI: 10.4467/2353737XCT.15.027.3827

* M.Sc. Eng. Andrzej Herbst, NORD GmbH, Germany.

1. Introduction

Due to many advantages of relatively small motors (up to 95% for 1.5 kW, 1500 rpm) such as the high efficiency possibilities, continuous operation without fan, supply by converter with sensorless algorithms and flat surface housing, synchronous motors with rare earths magnets are more and more common on the market. When we add the fact that the price of such a motor is similar to an IE3 asynchronous motor, a PMSM becomes the best choice for a variable speed drives. What is more, an IE4 PMSM motor can be one or two sizes smaller compared to IE3 asynchronous machines. Up until now, except for high performance servo motors, designers were utilizing standard lamination packages for synchronous motors – either PMSM or reluctance. This means that the cage rotor from classic, asynchronous motors was taken out and a new synchronous package was designed. This is an easy and cheap way to lead a quite good motor into production. Even without the optimal shape of stator, efficiency improvement is high enough to fulfil the new standard, e.g. higher IE class. Such an idea has one important advantage – the winding is also the same. No additional effort need be made to design the new winding technology. Usually, up to 3 kW, 1500 rpm motors consist of 4 poles. In the range of 3 up to 10 kW, 6 or 8 pole variants are also popular. It must be said that these machines are not optimized in order to minimize the amount of materials and maximize the power to weight factor. So the optimal shape of motor's cross section will vary from original asynchronous one.

2. Test objects and design software

This comparison takes as a base two synchronous motors with 0.75 kW power at a speed of 1500 RPM and an efficiency of 90%. In the described cases, both constructions have rotor with inserted magnets and sinusoidal EMF. Figure 1 shows a 4 pole example.

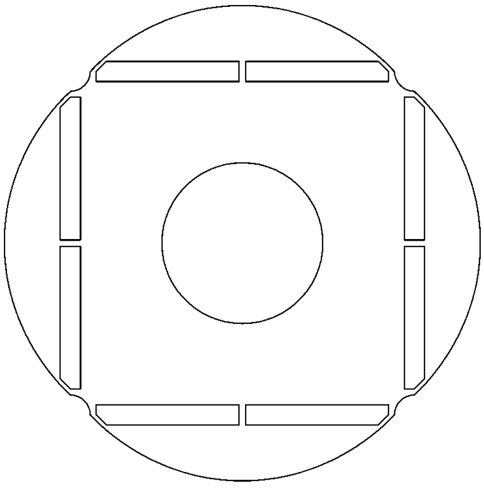

Fig. 1. Investigated 4 poles rotor geometry

Of course, this is one of several possible geometries [1], but with this inserted type, sinusoidal-pole is an internal, company standard. The construction has important advantages like ease of manufacturing the package and the magnet's assembly. Geometry of the stator as well as the winding is classic – like in 4 pole, 24 slot asynchronous motors, where q (number of slots per pole, per phase) is 2. For motor size 80, this is the most common case. It has the best ratio between material usage (weight) and efficiency (asynchronous machine). The second motor has similar rotor construction – see Fig. 2. Stator consists of 12 slots – which makes q equal to 0.4. This is shown in Fig. 3. For two layers winding (one coil for each tooth) winding factor is 0.933. A 10 pole, 12 tooth construction was chosen because it gives the best ratio between manufacturing costs, material usage, balanced magnetic pull and relatively low iron losses [2]. As low supply voltage frequency as 125 Hz at nominal speed is also an advantage for sensorless algorithms – processor of converter is fast enough to work with such a motor even at 3000 RPM (250 Hz). Where 400 Hz is a maximum frequency of an industrial standard. Let's look closer to the calculation's idea for both motors. Usually, worldwide there is one similar method to create universal software for designing efficient, material-saving motor in a short time.

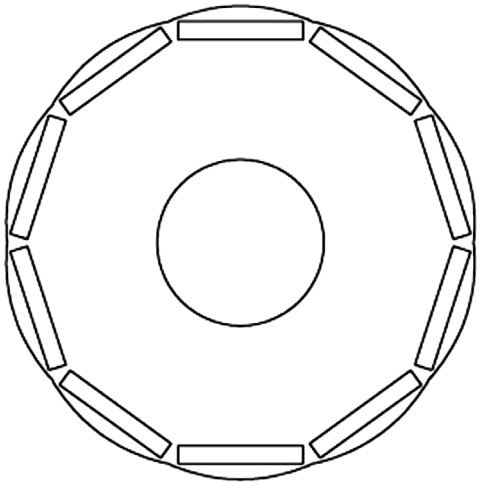

Fig. 2. Investigated 10 poles rotor geometry

The method is to combine mathematical language software with a program for finite-element calculations [3, 4]. Such a combination guarantees ease and high flexibility when changing the construction of the investigated model, such as the type of rotor or magnet material as well as the geometrical dimensions. The finite elements method (when well adjusted) shows great sensitivity when calculating cogging torque or the EMK. Nowadays, every synchronous motor should not only have a high efficiency factor but also a low THD of EMF, low cogging torque and low torque ripples. These help to achieve stable control of the frequency converter. Having already a few years of experience and reliable software, the designer can rely on it and omit the analytical method. In the software used for simulation, the problems are divided into two groups – cases with the current and without current.

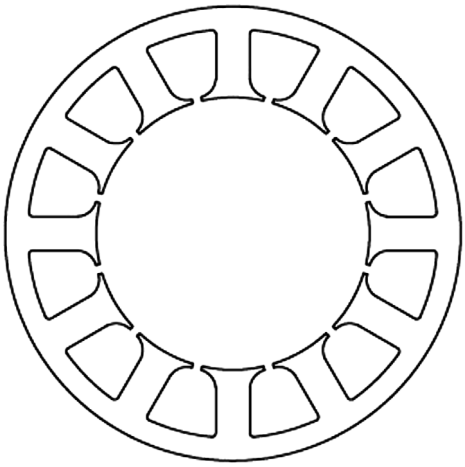

Fig. 3. Investigated 12 teeth stator geometry

In the first group, the user can investigate what follows: torque over angle characteristic (with DC currents in winding); normal torque characteristic + iron losses (AC currents in winding); inductance over angle characteristic (DC currents in winding) [5]. In the second group, two tests could be performed – cogging torque and EMF. A written script allows the user to choose which problem will be solved.

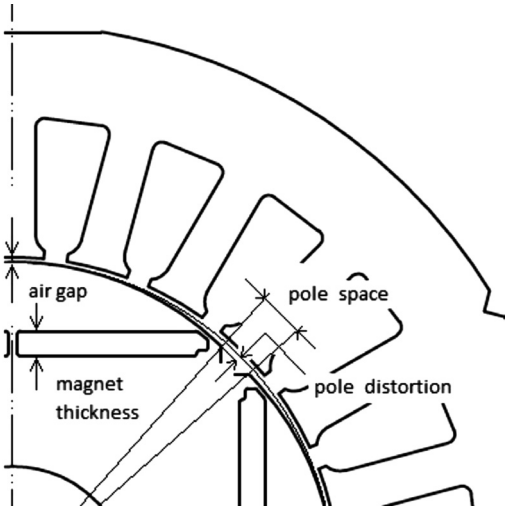

Fig. 4. Design variables of both rotors

Usually, all of them must be executed to check certain construction in a full aspect. As is mentioned above, in the case of 4 pole motors, only the rotor was optimized. The mechanical parameters which were a subject of the optimization of both rotors are shown in Fig. 4. The air gap, which is not a part of rotor, is also taken into consideration here.

In case of the 10 pole, 12 tooth motor, the next four parameters of stator were investigated: tooth wide; tooth high; joke high; slot enter gap. In the next part of the article, ranges of all the variables are shown.

3. Design results and tests results.

For the first rotor, Table 1 shows the range of investigation. Outside these ranges, some parameters from THD, cogging torque, average torque or torque ripples are poor. Such parameterisation makes the design process easier and faster. For all variables, vectors with possible values were created. The length of the stack, because of the standard for asynchronous motors, was kept at 60 mm.

Table 1

Range of variables for 4 poles rotor

Name of variable	Range of variable
Pole space [part of pole]	[0.06 : 0.005 : 0.09]
Magnet thickness [mm]	[2 2.5]
Air gap [mm]	[0.3 0.4 0.5 0.6]
Pole distortion [mm]	[1.3 : 0.1 : 1.7]

These ranges could look a little bit too narrow but it was found that such steps between values are precise enough to find final, optimized construction [6]. Previously, wider ranges of variables were also investigated with poorer mesh quality. The range of investigation of the second motor can be seen in Table 2. Also in this case, the ranges of some variables were cut. Wider ranges cause a longer calculation time because the number of construction rises very fast.

Table 2

Range of variables for 10 poles rotor

Name of variable	Range of variable
Pole space [part of pole]	[0.06 : 0.001 : 0.1]
Magnets thickness [mm]	[2 2.5]
Air gap [mm]	[0.3 0.4 0.5]
Pole distortion [mm]	[0.4 : 0.2 : 1]
Stator inner diam. [mm]	[60 : 1 : 72]
Stator's tooth wide [mm]	[7 : 1 : 12]
Stator's joke high [mm]	[5 : 1 : 8]
Slot entry gap [mm]	[2 : 0.2 : 3]

In the case of 10 pole, 12 tooth construction, the package length was not a variable but was adjusted (calculated) after the optimization process to achieve the requested efficiency. In the next figures, a comparison between fem simulations and real measurements for both motors is presented. Firstly, Figs. 5 and 6 show torque against angle curves.

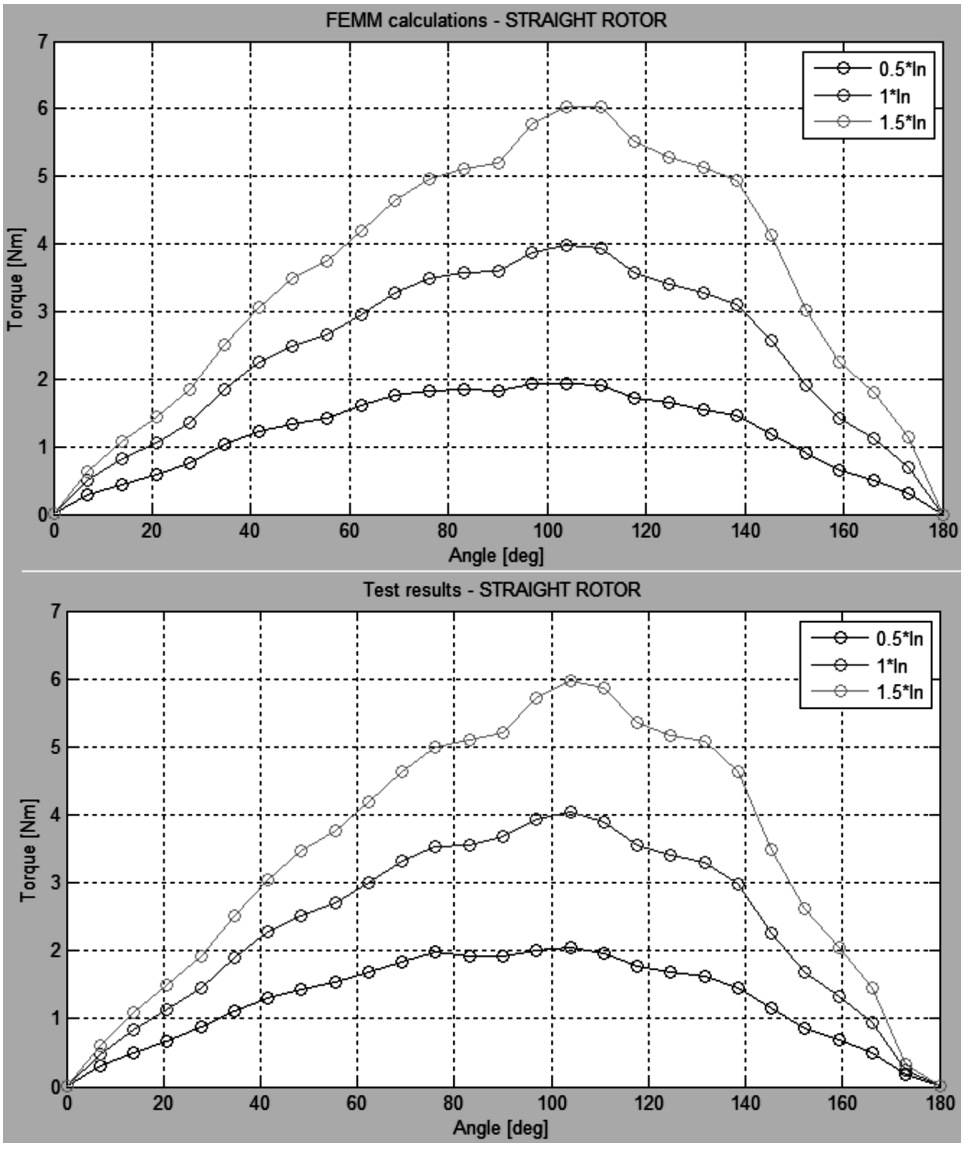

Fig. 5. Torque against angle, 4 poles (0.5xIn, In, 1.5xIn)

In this certain case, two phases were supplied with a DC current. During this test, the shaft was blocked and gradually turned with the help of a high ratio worm gearbox. Such a test is very useful to compare finite element torque analysis with real prototype measurements.

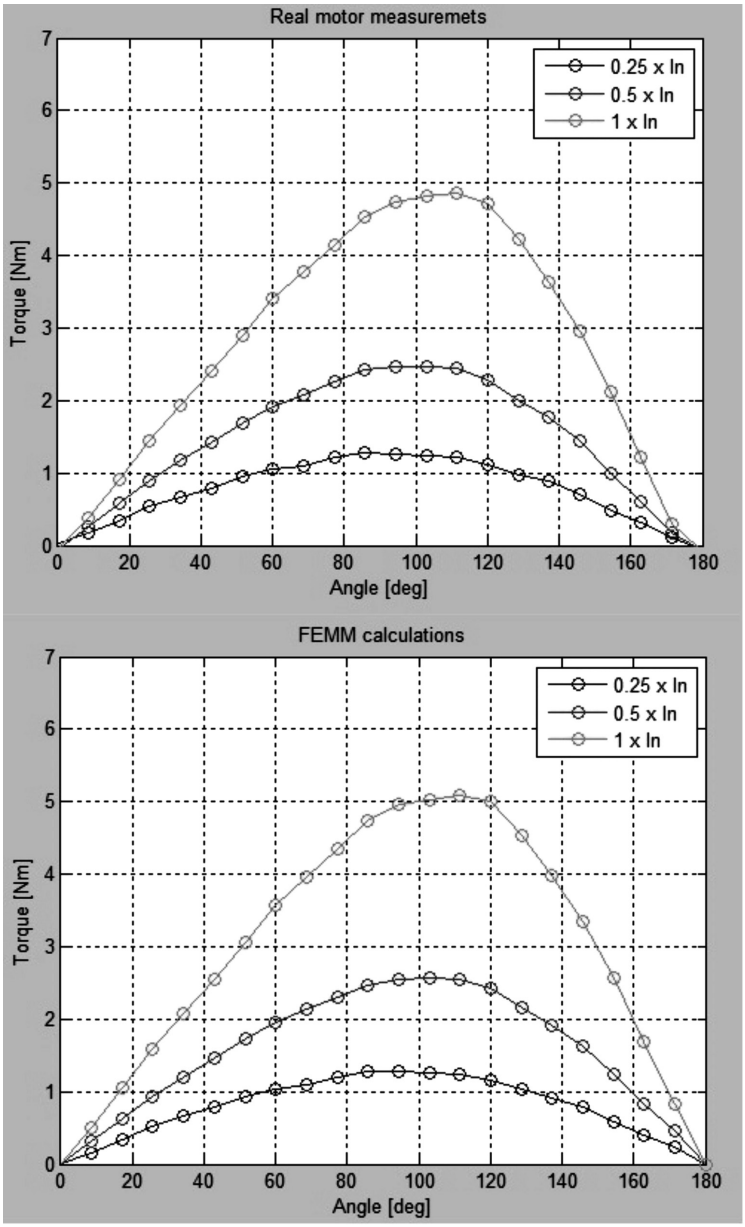

Fig. 6. Torque against angle, 10 poles (In, 0.5xIn, 0.25xIn)

It avoids some influences which are sometimes not predictable during normal test runs with a converter. In Tables 4 and 5, the efficiencies for different load points of both motors are shown. As can be seen, the main assumption relating to efficiency was fulfilled for two machines. A level of 90% is reached for the rated power at the rated speed. At the end of this paragraph, in Table 3, mechanical parameters of each construction are shown.

In motors with concentrated windings, the problem of vibrations and noise can be significant. Magnetic pull due to the relatively thin stator's joke is able to bend the housing and the stator. In the construction with 4 poles and 24 slots, there are four periods of electromagnetic pull around the motor. But in the construction with 10 poles and 12 teeth, there are only two periods of electromagnetic pull around the motor. As long as the motor is optimized for high efficiency, the air gap must be thin. Due to the thin air gap, all mechanical stresses are not smoothed. So the problem of increased noise was seen during the first tests either with or without load. So the noise tests were carried out to measure and to compare the 10 pole motor to the 4 pole motor. It can be easly seen (Fig. 7) that the 10 pole motor is not a perfect construction. From the beginning it looked as if the main sources of the sound were bearing covers and the fan cover. Therefore, the special bearing covers were designed and tested. As can be seen, the improvement is significant at around 5 dB for load condition. In the near future, a second prototype will be finished. Stator will be segmented which will probably improve the damping factor of the mechanical vibrations. Additionally, winding's filling factor is higher for the segmented stator compared to one-piece construction.

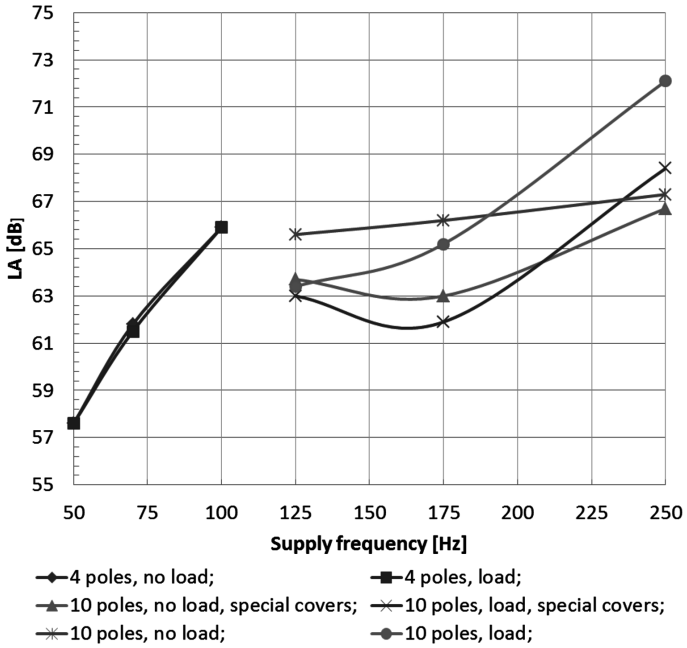

Fig. 7. Level of noise, 1 m distance. Speed range is 1500–3000 RPM for both motors

4. Conclusion and comments

The conducted research shows that the finite element method could be the only one during the whole design process. One time written software is flexible. Could be useful for few types of topologies of the machine. Additionally, the accuracy is high enough to rely on software in

the case of electromagnetic torque, EMK, cogging torque. Iron and mechanical losses must be calculated in an analytical way. The electromagnetic model in this case will be a source of flux density in the steel. Of course, special parameters (factors) dependent on mechanical features like steel type, punching process, assembly process must be taken into account in the equations. Comparison shows that for PMSM rather fractional slots winding is more proper. The differences between these two motors in material usage are huge. By using concentrated winding, where losses in the end winding part are drastically decreased, current density in the wire could be fully exploited. This fact leads to length and weight reduction of the motor.

Table 3

Mechanical parameters of optimized constructions

Parameter	4 poles	10 poles
Stator outer diameter	120 mm	120 mm
Stator inner diameter	70 mm	68 mm
Air gap	0.5 mm	0.5 mm
Package length	60 mm	30 mm
End winding high	28 mm	9 mm
Active part length	116 mm	48 mm
Magnet thickness	2.5 mm	2.5 mm
Pole distortion	1.7 mm	0.8 mm
Stator's tooth wide	4.8 mm	10 mm
Stator's joke high	10 mm	7 mm
Slot entry gap	2.3 mm	2.8 mm
Pole space	0.075	0.068
Magnet amount	170g	106g
Magnet type	N38SH	N38SH
Steel amount	3.8 kg	1.6 kg
Steel type	M400-50A	M330-35A
Copper amount	1.4 kg	0.55 kg

Additionally, costs are reduced, which is an important consequence. Nowadays, winding technology is so advanced that the production process of such winding is easy and cheap both, in needle winding and in the separated tooth method.

Table 4

Efficiency measurements, 4 poles motor

Load	20%	40%	60%	80%	100%	120%	140%
Eficiency	85.5%	91.1%	91%	90.9%	90%	88.9%	87.8%

Table 5

Efficiency measurements, 10 poles motor

Load	25%	50%	75%	100%	125%
Eficiency	88.1%	91.7%	91.7%	90.7%	89.2%

Motors with fractional slots winding provide a good opportunity for future downsizing of drives. This is a very important fact for customers and machine designers. Despite few important advantages, further research must be done in the mechanical area. Especially in the case of motors with power above 1–1.5 kW, a well-designed housing is required – otherwise, fractional slot construction can create high noise and vibrations.

References

[1] Salminen P., *Fractional slot permanent magnet synchronous motors for low speed applications*, Ph.D. thesis, Lappenranta University of Technology, 2004.
[2] Skaar S.E., Krovel O., Nilssen R., *Distribution, coil-span and winding factors for PM machines with concentrated windigs*, Publications of NTNU, 2008.
[3] Bianchi N., *Electrical machine analysis using finite elements*, CRC Press, 2005.
[4] Reece A.B.J., Preston T.W., *Finite element method in electrical power engineering*, Oxford Science Publications, 2000.
[5] Weizhong F., *Permanent Magnet Synchronous Machines with Fractional Slot and Concentrated Winding Configuration*, Ph.D. thesis, Cranfield University, 2011.
[6] Salminen P., Libert F., *Torque ripple of permanent magnet machines with concentrated Winding*, ISEF, 2005.

TECHNICAL TRANSACTIONS | **CZASOPISMO TECHNICZNE**
ELECTRICAL ENGINEERING | ELEKTROTECHNIKA
1-E/2015

LUCJAN SETLAK*

OVERVIEW OF AIRCRAFT TECHNOLOGY SOLUTIONS COMPATIBLE WITH THE CONCEPT OF MEA

PRZEGLĄD ROZWIĄZAŃ TECHNOLOGICZNYCH SAMOLOTU ZGODNYCH Z KONCEPCJĄ *MORE ELECTRIC AIRCRAFT* (MEA)

Abstract

The purpose of this paper is to present some selected issues relating to the alternative application of the perspective concept on the plane board MEA (More Electric Aircraft), instead of the traditional solution, in terms of power (pneumatic and hydraulic systems). In the context of the analysis of this trend, particular attention is paid to the major advantages that aeroplanes have, made in accordance with the new technology and problems in autonomous systems of electricity generation (electric power grid of aircraft). Considering that the largest growth of the above trend of electric aircraft (MEA) applies to civil aviation, the most important role in this paper was assigned to civilian aircraft (Boeing, Airbus) in the context of power distribution in electro-energy systems. In addition, a review of air sources of electricity (electric power) generation was made for particular types of energy sources (generators, generator-starters, transformers, converters, etc.) and advanced on-board autonomous power systems ASE (Autonomous Electric Power Systems), used in most modern aircraft constructions (passenger and military aircraft). In the final part of this paper, based on a literature review of electric aircraft concepts (MEA) and a brief analysis, the main conclusions arising from the application of this trend in modern aviation are presented.

Keywords: *More Electric Aircraft*, *Aircraft Electric Power Systems*, *electric machines*

Streszczenie

Przedmiotem niniejszego artykułu jest przedstawienie wybranych zagadnień związanych z alternatywnym zastosowaniem na pokładzie samolotu perspektywicznej koncepcji MEA (*More Electric Aircraft*) zamiast rozwiązania tradycyjnego w zakresie zasilania (układy pneumatyczne i hydrauliczne). W kontekście analizy tego trendu szczególną uwagę zwrócono na główne zalety samolotów wykonanych zgodnie z nową technologią oraz na problematykę autonomicznych systemów wytwarzania energii elektrycznej (sieć elektroenergetyczna samolotu). W związku z tym, że największy rozwój omawianego trendu zelektryfikowanego samolotu (MEA) dotyczy lotnictwa cywilnego, najistotniejszą rolę w niniejszej pracy przypisano samolotom cywilnym (Boeing, Airbus) w kontekście rozdziału mocy w systemach elektroenergetycznych. Ponadto dokonano przeglądu lotniczych źródeł wytwarzania energii elektrycznej (mocy) dla poszczególnych rodzajów źródeł energii elektrycznej (prądnice, prądnico-rozruszniki, transformatory, przetworniki itp.) oraz zaawansowanych pokładowych autonomicznych systemów elektroenergetycznych ASE (*Autonomous Electric Power Systems*), stosowanych w najnowocześniejszych konstrukcjach lotniczych (samoloty pasażerskie i wojskowe). W końcowej części artykułu, na podstawie przeglądu literatury przedmiotu z zakresu koncepcji zelektryfikowanego samolotu (MEA) oraz krótkiej analizy, przedstawiono główne wnioski wynikające z zastosowania powyższego trendu we współczesnym lotnictwie.

Słowa kluczowe: *MEA*, *lotnicze elektryczne systemy zasilania*, *maszyny elektryczne*

DOI: 10.4467/2353737XCT.15.028.3828

* Ph.D. Eng. Lucjan Setlak, Avionics, Department of Aviation, Air Force Academy Deblin, Poland.

1. Introduction

A dynamic development of electrical machines in both civil aviation (A-380, B-787) and army aviation (F-22 Raptor, F-35) can be observed – this is caused by the introduction of modern technologies, PES (Power Electronic Systems) [2], devices and materials [1, 3] as well as advanced avionic devices and systems. These changes are related to the realization of the More Electric Aircraft concept (MEA), which was formed as a part of wider concept – MOET (More Open Electrical Technology). The idea of the MEA concept is to replace pneumatic and hydraulic devices with electrical devices. As a result, instead of having three different generation and distribution systems onboard modern aircraft, there is only one used – an electrical system. The most significant as well as most important benefits of the development described above are: increase of reliability; decrease of operational cost; limitation of harmful substances emission. Therefore, the MEA concept will probably be fully adapted in the near future in the area of aircraft power, especially on civilian aircraft. In modern aircraft electrical power systems, designed according to the MEA concept, universal, high voltage and hybrid connections of DC systems and AC systems should be used. Thus, both generation and distribution of electrical power onboard an aircraft are essential types of multilevel processing of electrical power. Electrical systems (DC and AC) of modern aircraft use a variety of voltages. These are four types in use: 405 VAC variable frequency; 200 VAC constant frequency; 28 VDC; 270 VDC.

2. Electrical power generation by autonomic electrical systems

The range and level of power used in different types of technologically advanced aircraft gradually increased for many years, as can be seen in the Figs. 1 and 2.

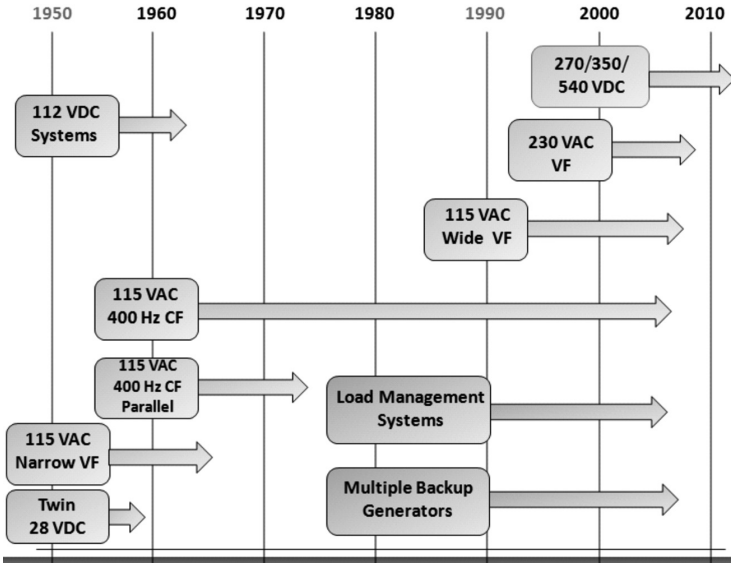

Fig. 1. Electro-energy Systems Evolution of Aircraft [4]

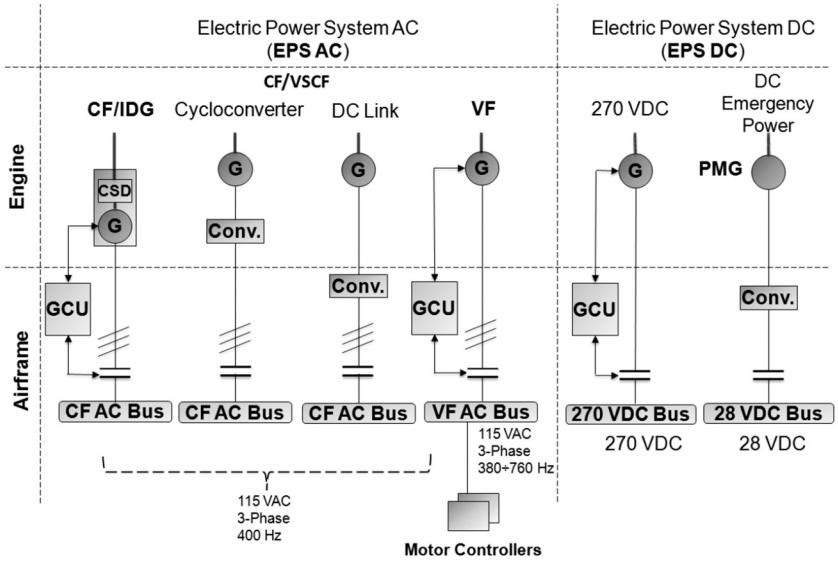

Fig. 2. Electrical Power Generation Types [4]

Examples of generators in use and types of autonomic electrical systems are summarized in Table 1.

Table 1

Recent civil and military aircraft power systems developments [4]

Generation Type	Civil Application		Military Application	
IDG/ CF [115 VAC/ 400 Hz]	B777	2x120 kVA	Eurofighter Typhoon	
	A340	4x90 kVA		
	B737NG	2x90 kVA		
	MD-12	4x120 kVA		
	B747-X	4x120 kVA		
	B717	2x40 kVA		
	B767/400	2x120 kVA		
VSCF (Cyclo-converter) [115 VAC/ 400 Hz]			F18C/D	2x40/ 45 kVA
			F18E/F	2x60/ 65 kVA
VSC (DC Link) [115 VAC/ 400 Hz]	B777 (Backup)	2x20 kVA		
	MD-90	2x75 kVA		
VF [115 VAC/ 380÷760 Hz Typical]	Cobal Ex	4x40 kVA	Boeing JSF	2x50 kVA
	Horizon	4x25 kVA		
	A380	4x150 kVA		
VF [230 VAC]	B787	4x250 kVA		
270 VDC			F-22 Raptor LM F-35	2x70 kVA

It was dictated by the MEA concept as well as the dissemination of digital technology, the intensive development of which led to revolutionary changes in the field of signal processing. From 1940 to 1950, the standard voltage of electrical sources (generators, starter/generators) was 28 VDC. Batteries (1 or 2 units) were an emergency power source in the case of primary power sources damage and protected essential loads – this increased the safety of flight. In turn, the voltage of 200 VAC was dedicated to power AC loads. This type of voltage (200 VAC) with a constant frequency, was in use from 1960. Variable frequency generators began to be used in aviation from 1990 as a power source for high power loads and as a standby generator. Variable speed, constant frequency power sources started to be used in aircraft from 1990. The need to use these sources was caused primarily by problems encountered in maintaining constant generator speed during changes to the main engine speed – CSD (Constant Speed Drive) – by use of standard AC electrical sources (115 VAC constant frequency at 400 Hz generators), because it needs to use complex hydromechanical gear. Power generated in this way by AC variable frequency generators is being processed to 115 VAC at 400 Hz by power converters. These systems are being used on technologically advanced civil aircrafts (Boeing, Airbus). The mentioned companies intensively increase the range and level of power being used on their latest aeroplanes, such as 800 kVA on the Airbus A-380 and 1400 kVA on the Boeing B-787. Analysis of the chosen power systems are described below in an appropriate order.

2.1. Constant Frequency/IDG Generating System (CF/IDG)

Integrated drive generators used on conventional aircraft have a constant speed, obtained by complex hydromechanical gear and processed by the source presented in Fig. 3 (1). Initially, AC generators worked at 115 VAC in 400 Hz electrical systems. The task of the hydromechanical gear in CF/IDG systems is to maintain a constant generator speed at variable main engine speeds. The disadvantage of this solution is the high operational cost caused by the hydromechanical gear.

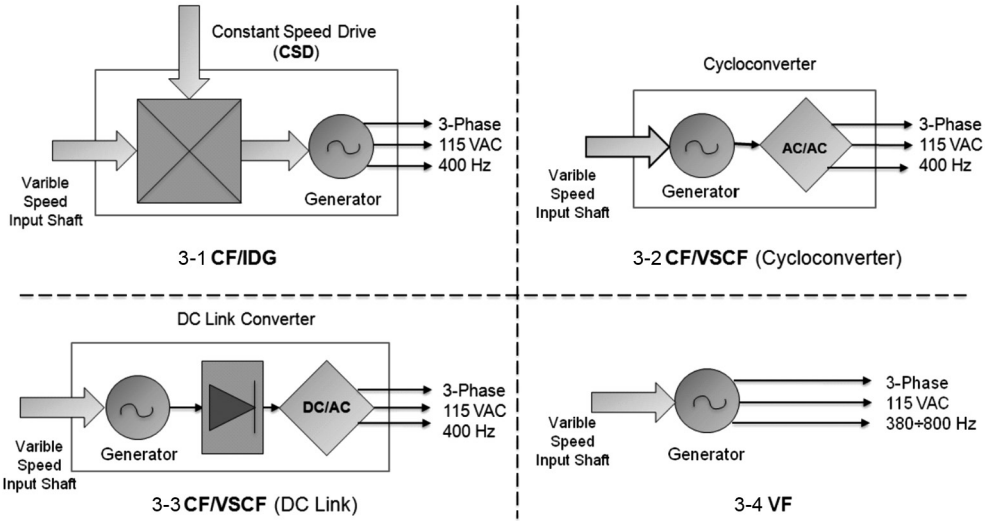

Fig. 3. Electric Power Generation Development of Civil Aircraft [4, 5]

2.2. CF/VSCF Generating System

Due to the fact that in this solution, engine output speed is variable, output frequency of the generator is also variable. To supply AC power with a constant frequency of 400 Hz, there is a DC converter (DC Link) applied in the electric circuit between the generator and the load of the AC converter – this is presented in Fig. 3 (2). For this purpose, AC/DC and DC/AC converters or cycloconverters (AC/AC converter) as shown in Fig. 3 (3). CF/VSCF system, converting variable frequency power from the AC generator to 115 VAC at 400 Hz by using power electronic converters was applied in civil aircrafts (B-737, A-340). Using a DC link can gain additional benefits in terms of supplying high power loads and charging batteries.

2.3. VF Generating System

In VF generating systems, engine speed is variable, therefore, the frequency of the generator is also variable in the range 380–800 Hz, with an output voltage of 200 V. It should be noticed that variable frequency in the VF generating system is the simplest, the cheapest and the most reliable form of generating power. Moreover, AC voltages have a significant impact on aircraft subsystems, such as engines, controlling devices and protecting devices existing on the aircraft [4, 5].

2.4. Auxiliary Power Unit (APU)

APU (Auxiliary Power Unit) power, being used by aircraft systems in normal flight conditions is generated by AC generators driven by the main engines. The aircraft electrical system is powered by two engines driving the generators controlled by an integrated drive, e.g. GEN1 (first generator) is driven by the first engine, whereas GEN2 (second generator) is driven by the second engine. The third AC generator 3x200 V at 400 Hz is driven by the APU generator, which is able to replace one or two main generators (GEN1 and GEN2).

2.5. Emergency Power Source (Emergency Generator)

RAT (Ram Air Turbine) or fuel cells are emergency sources of power in case of main generators or APU (Auxiliary Power Unit) damage. An emergency AC generator with output voltage of 3x200 V at 400 Hz is driven by a hydraulic RAT system, designed for automatic emergency powering (in case of all main generators damage). Fuel cells are used as an emergency DC power source. For proper operation, it needs the power supply from converters, whereas batteries are used to provide emergency power in the case of alternative or emergency power source damage.

2.6. Ground Power Unit (GPU)

In order to perform maintenance on the ground – a ground power unit (GPU) is necessary for technical maintenance and to check each system in voltage state. The GPU is powered by a 3-phase 200 VAC at 400 Hz voltage, as in the case of supplying by AC generators.

3. Electrical power generation by autonomic electrical systems

3.1. Conventional Solution

Electrical system structures depend primarily on the purpose and type of aircraft (civil or military), level of load power, types of electrical power (voltages) necessary to supply loads and quality requirements of aircraft user. An example of the conventional aircraft electrical system of a Boeing B-767 is presented in Fig. 4.

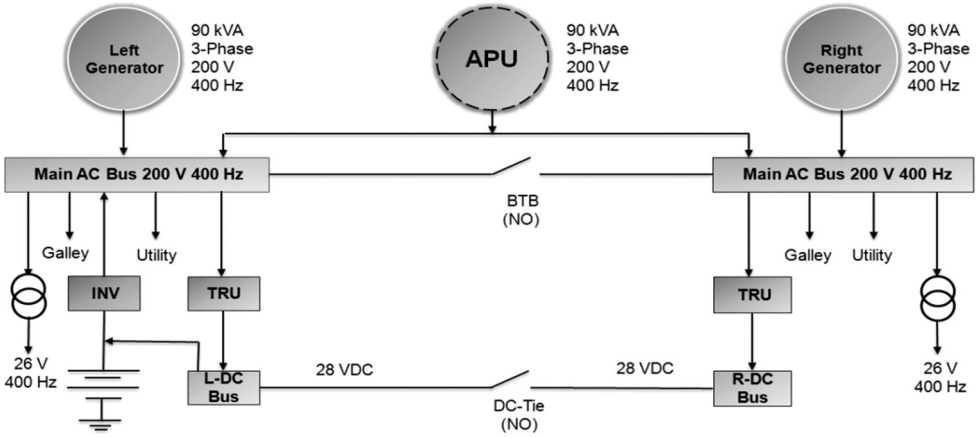

Fig. 4. Conventional B-767 Aircraft Power Distribution System [4, 6]

Conventional aircraft electrical systems have different structures depending on the composition of the electrical power sources and the type of converters – it can be designed as one-channel, two-channel or mixed. DC power is provided by a generator or a starter/generator (DC power system) and brushless generator (AC power system). In the case of a DC system, power is provided by a DC generator, which is driven by the main engine (main gearbox) directly. In multiengine aircraft, DC generators are used, working parallel with electrochemical cells (batteries) enabled. Converters (machine or static) provide AC power with constant frequency and different values of voltage. Different solutions in conventional aircraft are electrical system structures with AC generator (in this variant there is no main source of DC power such as generator or starter/generator). In this solution, electrical power is generated by a primary source of power which is a 3-phase AC generator with collector rings 200 VAC or 3x200/115 VAC at 400 Hz. These generators are driven by the main engine (main gearbox, which is the typical source of power with constant speed), while the DC power, essential to supply loads and to load the battery, is converted by a rectifying system (transforming and rectifying device), which is a secondary DC power source.

3.2. More Electric Aircraft (MEA) Concept

In modern aircraft electrical power system, called Power-By-Wire (PBW), MEA and latest perspective trend AEA (All Electric Aircraft) it is assumed that the only and most important power is electrical power (aircraft partially or fully electrified). Moreover, most conventional systems (heavy and unreliable hydraulic and pneumatic systems) will be replaced by electromechanical or electrohydraulic equivalents, increasing the reliability of the aircraft and reducing operational cost. Advanced PES (Power Electronic Systems), controlling systems, engine drives and electric machines affect the development of advanced technologies which use a CF/VSCF generating system. The main benefit of this solution is usage of improved and more efficient systems (starter/generators) which can operate in motor mode, providing a starting function for engines of jet-propelled aircraft. Other advantages of a CF/VSCF generating system are improved reliability, decreased service and maintenance costs and a shorter work cycle. This systems uses 3-phase, synchronous AC generators and solid-state converters. Converters of this type consist of a rectifier (converting AC power to DC power), an intermediate circuit and an inverter (converting DC power into constant frequency 3-phase AC power). The power distribution of a CF/VSCF generating system is presented in Fig. 5.

In the generating mode of a CF/VSCF system, aircraft engines with variable speed provide mechanical power to the input of the electrical generator. Then, the electrical generator provides AC power with variable frequency to the bidirectional power converter, which provides constant frequency AC power to the main bus. In motor mode constant frequency AC system, through bidirectional power converter, provide power to input of electrical motor, which operate as starter of aircraft engine. In addition, synchronous, induction, switch reluctance electrical machines competes with CF/VSCF generating systems with starter/generators with 270 VDC voltage is presented in Fig. 6.

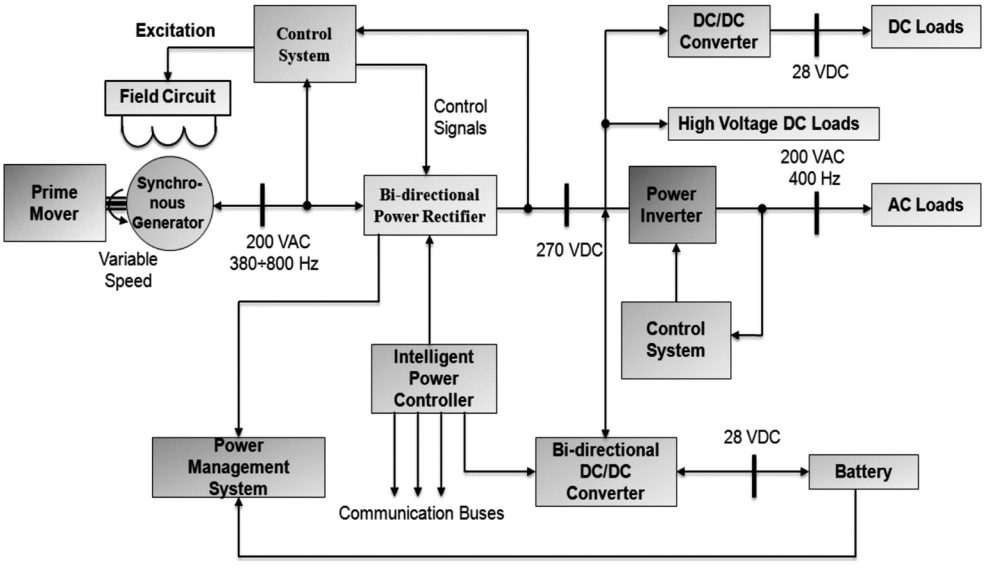

Fig. 5. More Electric Aircraft (MEA) Power Distribution System [6]

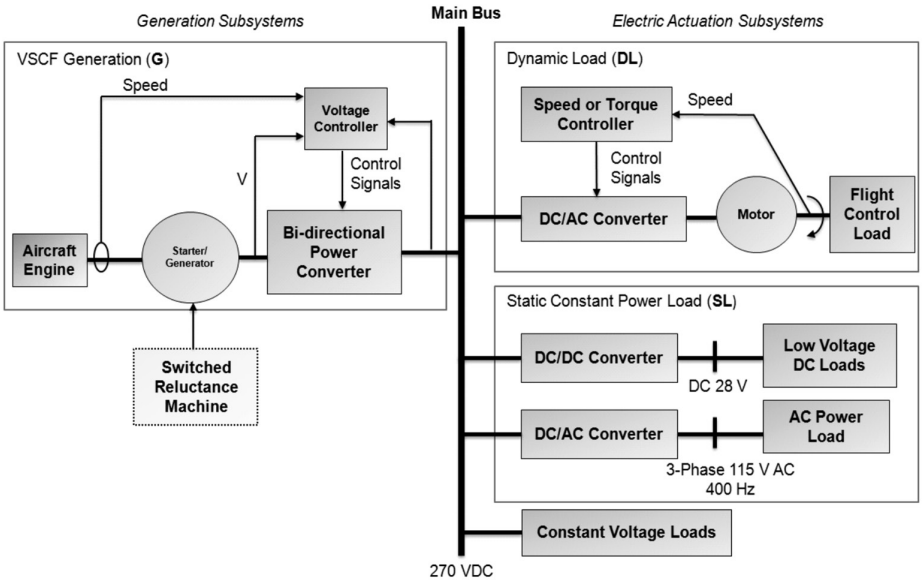

Fig. 6. 270 DC Power System for MEA [7]

3.3. Technologically advanced developments of modern aircrafts (B-787, A-380)

The distribution system on modern aircrafts B-787/A-380, presented in Fig. 7 consists of a main generator, with 1 MVA range of power and an auxiliary power unit, with a 450 kVA range of power.

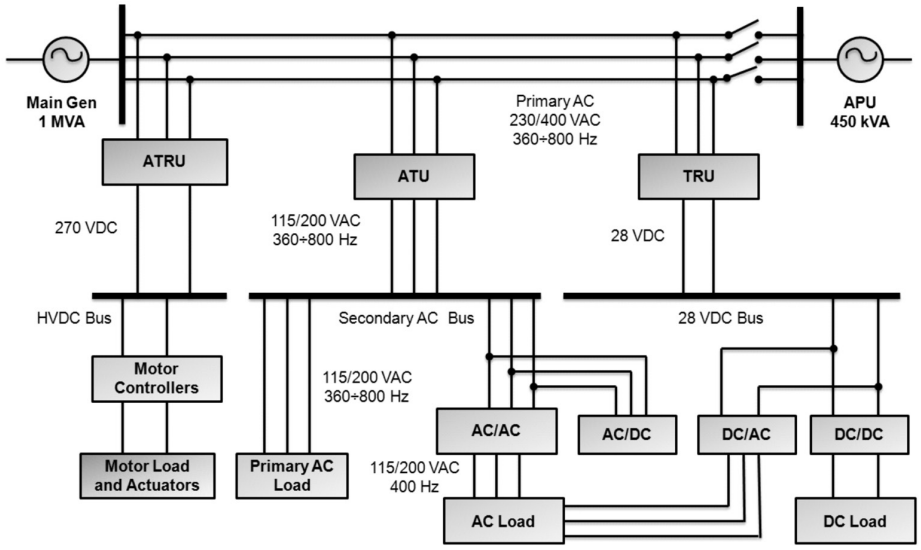

Fig. 7. B-787/A-380 Aircraft Power Distribution System [4, 7]

The primary AC bus is characterized by a high range of voltage with a value of 400 V and a frequency between 360 and 800 Hz, instead of 200 V in previous systems. The primary AC bus supply high voltage DC bus with 270 HVDC (High Voltage Direct Current) through the autotransformer of the ATRU (Auto-Transformer Rectifier Unit), standby AC bus with a voltage of 200 V and a frequency between 360 and 800 Hz through the ATU (Auto Transformer Unit), the 28 VDC bus through the TRU (Transformer Rectifier Unit) and the main AC loads. When an emergency power source is enabled, the main electrical power distribution system focuses input electrical powers, which may be provided by the main generator, APU, GPU or RAT.

4. Conclusions

With the development of advanced technology in the field of electrical machines (MEA technology) they began to look for solutions that would be able to meet the demands of today's aircraft in the context of power and electricity generation (PES, switch reluctance starter/generators 270 VDC). MEA technology is the future trend of the aircraft, as elements of its development are the ecological, economic and quality factors, which are also its main advantages. The replacement of mechanical, hydraulic and pneumatic power onboard the aircraft with one kind of energy (electrical) is the most important innovation of MEA/AEA technology. Based on the findings of the European aircraft energy optimization project, POA (Power Optimized Aircraft) and using a local onboard DC distribution system PDS (Power Distribution System) provides opportunities to reach the optimal benefits by individual onboard subsystems, which include: reducing the weight of actuator systems; increased equipment reliability; easier maintenance; lower operating costs; increased flight safety. Thus, the PDS is a local network of aircraft supplying important receivers, systems, installations and onboard systems necessary for the safety of the flight e.g. flight control, landing system, fire protection, anti-icing systems, etc. This article reviews chosen solutions of power systems and signaled an analysis of electricity distribution management of advanced power systems for both conventional aircrafts as well as those compatible with the MEA technology and modern constructions (A-380, B-787) which showed that MEA/AEA concepts are feasible in the near future. In addition, these aircraft are characterized by a higher power range, generated by onboard sources. For MEA aircraft, it is a power of 1 MVA, while for conventional aircraft – 90 kVA. Furthermore, systems advanced in terms of power electronic (PES) i.e. electronic switches and control devices are able to generate and manage the onboard energy of the multi-voltage power and a variable and constant frequency. Aiming towards solutions of aircraft compatible with the concept of MEA, it should be noted that it is characterized by the performance of the entire aircraft, increased reliability, flexibility and efficiency. In summary, MEA technology is continually evaluated and has a huge potential in terms of weight, quality and operating costs, while traditional systems, sources and applications are on the line, which distance from the curve continuously decreases (asymptotic growth).

References

[1] Ronkowski M., Michna M., Kostro G., Kutt F., *Maszyny elektryczne wokół nas*, Politechnika Gdańska, 2009/2010.

[2] Gong G., Drofenik U., Kolar J.W., *12-Pulse Rectifier for More Electric Aircraft Applications*, ETH Zurich, Power Electronic Systems Laboratory, ICIT, 2003.

[3] Wiak S., Pyć A., Pyć M., *Electrical machines in the military More Electric Aircraft and their impact on the environment*, Przegląd Elektrotechniczny, 2012, R. 88, nr 7a.

[4] Moir I., Seabridge A., *Aircraft Systems: Mechanical, Electrical, and avionics subsystems integration*, 3th ed., John Wiley & Sons, Ltd, 2008.

[5] Corcau J.I., Dinca L., *On using PEMFC for Electrical Power Generation on More Electric Aircraft*, International Journal of Electronics and Electrical Engineering, 2012, No. 6.

[6] Eid A., Abdel-Salam M., El-Kishky H., El-Mohandes T., *Simulation and transient analysis of conventional and advanced aircraft electric power systems with harmonics mitigation*, Electric Power Systems Research, 2009, No. 79.

[7] Emandi K., Ehsani M., *Aircraft power systems: technology, state of the art, and future trends*, Aerospace and Electronic Systems Magazine, IEEE, 2000.

TECHNICAL TRANSACTIONS | **CZASOPISMO TECHNICZNE**
ELECTRICAL ENGINEERING | ELEKTROTECHNIKA
1-E/2015

JANUSZ KOŁODZIEJ, MARCIN KOWOL, TOMASZ GARBIEC*

AN ANALYSIS OF THE INFLUENCE OF SELECTED DESIGN AND MATERIAL PARAMETERS ON HIGH-SPEED EDDY-CURRENT BRAKE PERFORMANCE

ANALIZA WPŁYWU WYBRANYCH PARAMETRÓW KONSTRUKCYJNYCH I MATERIAŁOWYCH NA PRACĘ WYSOKOOBROTOWEJ HAMOWNICY INDUKCYJNEJ

A b s t r a c t

This paper presents an analysis of the influence of utilizing rotor materials of different magnetization and conductivity on steady-state torque-speed characteristics for a high-speed eddy--current brake. The analysis involves rotors of different active lengths, with or without axial slits and a copper layer on the surface. The calculations were carried out using two and three--dimensional numerical models, partially verified on the laboratory test-stand.

Keywords: *electromagnetic brake*, *eddy currents*, *finite element method*

S t r e s z c z e n i e

Artykuł prezentuje wyniki analizy wpływu użycia różnych materiałów wirnika o różnej krzywej magnesowania i konduktywności na charakterystyki mechaniczne wysokoobrotowej hamownicy wiroprądowej. Analiza obejmuje wirniki o różnych długościach czynnych z nacięciami osiowymi lub bez nacięć osiowych oraz warstwy miedzi na powierzchni. Obliczenia są prowadzone z zastosowaniem dwu- i trójwymiarowych modeli numerycznych, częściowo zweryfikowanych na stanowisku pomiarowym.

Słowa kluczowe: *hamownica indukcyjna*, *prądy wirowe*, *metoda elementów skończonych*

DOI: 10.4467/2353737XCT.15.029.3829

* Ph.D. Eng. Janusz Kołodziej, Ph.D. Eng. Marcin Kowol, Ph.D. Eng. Tomasz Garbiec, Faculty of Electrical Engineering, Automatic Control and Informatics, Opole University of Technology.

1. Introduction

In the most cases, eddy currents in massive elements of electromechanical converters deteriorate in their performance and efficiency. However, there is a group of converters of which the principle of operation relies upon utilizing the eddy currents induced by magnetic field. This group contains eddy-current brakes of which the main advantage is converting mechanical energy into heat without physical contact [1–3]. This type of device is successfully used as brakes in tracked vehicles and high-speed turns, providing a very high value of braking torque, minimum noise emission as well as reliable operation. Because of the aftermentioned properties, eddy-current brakes are especially useful in the measurement of the torque of devices operating at very high rotational speeds e.g. electric motors designed for driving vacuum cleaners, centrifuges or compressors.

An example of a such an application was presented in previous works by authors [4, 5] where the designed eddy-current brake was used for carrying out torque measurements on the low-power motor operating at rotational speeds of up to 100 000 rpm. In this paper, investigations on this brake will be continued and will involve an analysis of the influence of using different rotor materials on torque-speed characteristics. For that purpose, numerical models of the brake will be used. The main objective of this study, being the continuation of work [5], is searching for methods of improving the brake performance by utilization appropriate rotor material.

2. Design parameters and numerical models

The considered brake consists of two main elements. The stator is made of a steel sheet (M400-50A) and equipped with two pairs of symmetrically spaced coils with different numbers of turns (z_1 = 85 and z_2 = 120) generating a constant magnetic field of two poles. The winding is supplied from a DC power supply with a current of rated value I_N = 10 A. During operation of the brake, a tangential force is acting on the armature. This force is measured using force transducers and gained by the electronic unit, and consequently the braking torque is also measured. Bearing in mind the specific operating conditions of the brake (working at very high rotational speeds) the rotor diameter was calculated so as to maintain a working air-gap width of δ = 2 mm. The wide air-gap facilitates the positioning and alignment of the rotor in relation to the stationary stator sheet package.

For the investigation carried out on this work, two rotors made of steel with various material properties were produced. DC-magnetization characteristics of these steel rotors are illustrated in Fig. 1. The rotor materials with various magnetization characteristics also differ in their electrical conductivity. The conductivity of steel A (high carbon) is of 2.43 MS/m, while of steel B (low carbon) of 5.74 MS/m.

Due to the specific geometry of the analyzed converter (see. Fig. 2), the authors focused mainly on utilizing three-dimensional models for carrying out the investigation. However, because of the very long time duration of the execution of these models, it was justified to use a two-dimensional model in the preliminary calculations. In such models, it was necessary to take into account the so-called rotor-end effect (presence of the current density vector components that are perpendicular to the shaft axis) [6]. Based on the literature study, it can

be stated that one of the most commonly used methods for taking into account the end-effects in the two-dimensional models is to apply in computations the effective conductivity of the material being a product of the real conductivity of the rotor material and the so-called rotor-end factor. It is possible to determine its value either by using analytical or numerical methods. Considering the specific structure of the rotor, the authors applied the rotor-end factor in computations obtained analytically, based on the simple formula given by O'Kelly [7]:

$$k_e = \frac{L_z}{L_z + \tau}, \tag{1}$$

where:
k_e – rotor-end factor,
L_z – active length of the rotor,
τ – length of the arc on the rotor surface for whose chord is equal to the stator tooth width.

The rotor-end factor for the 2D model determined by using the abovementioned formula gives value of 0.52. The results obtained from this model will be compared in the next section with the results from a three-dimensional model and measurements.

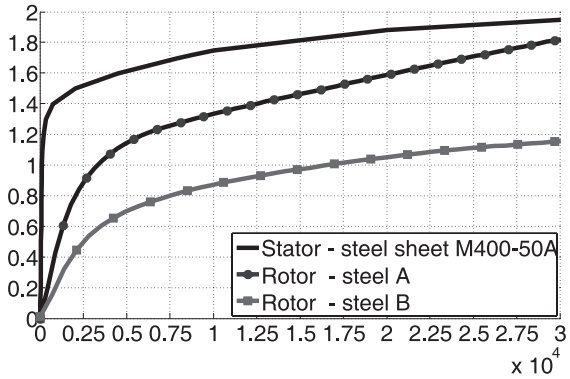

Fig. 1. Magnetization characteristics of the used materials

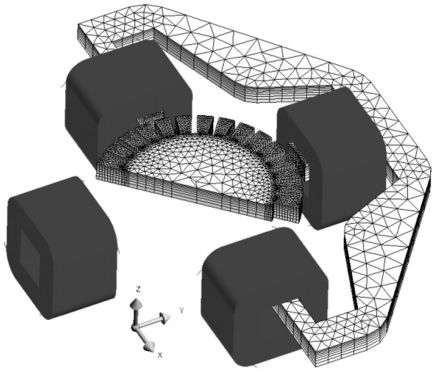

Fig. 2. Three-dimensional model of the brake

3. Calculation results

3.1. Homogenous rotors

The first step of the research was to perform a series of computer simulations for a basic structure of the solid rotor using the two and three-dimensional models and comparing their results with the results of the measurement on the physical model (Fig. 3).

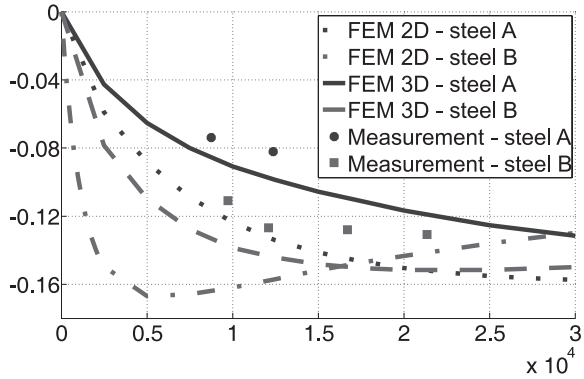

Fig. 3. Steady-state braking torque vs. speed for the brake for the rotor with a basic construction (the uniform solid rotor of the length equal to the stator core length)

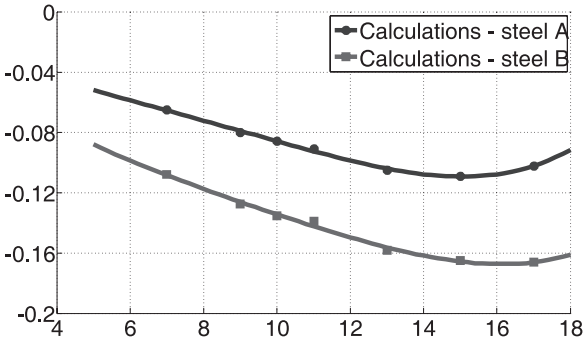

Fig. 4. Braking torque vs. active rotor length for the brake equipped with the uniform rotor at rated speed

As can be seen from the plot above, there are significant differences in the results of the calculations by the two and three-dimensional models. This proved that the physical phenomenon in the analyzed device (the rotor-end effect especially) cannot be modeled properly using the two-dimensional model. Hence, the three-dimensional model must be used for further computations. It is supposed that the main reason for the discrepancies in the calculation results by the 3D models and the measurement results is that the hysteresis losses in the rotor were neglected in computations. From the analysis of the results presented earlier in the plot, it can be observed that, from the point of view of the braking torque value, better electric properties of the rotor material are much more important than its magnetic properties.

The authors also carried out a series of simulations to determine the effect of changing the active length of the rotor on the produced braking torque. The active length of the rotor adopted as a parameter for simulation was varied as $L_Z \in$ <5.18> mm. The results obtained from the calculations are shown in Fig. 4.

The most interesting conclusion from the analysis of the calculation results is the non-monotonic nature of the braking torque variation as a function of rotor length. The length corresponding to the extreme of the above-mentioned function varies depending on the type of steel.

In conclusion, the analysis of the characteristics (Figs. 3 and 4) allows us to make an unambiguous choice of selecting rotor material (steel B), keeping in mind the most important parameter – the maximum braking torque value.

3.2. Rotors with copper coating

Searching for other methods to increase the braking torque, the authors also investigated the impact of modifying the structure of the rotor by applying a copper layer coating to its surface. Preliminary computational results suggesting the effectiveness of such a solution are presented in the paper [5]. The copper ring, in contrast to the steel, has a much higher electrical conductivity while maintaining the diamagnetic properties. While keeping a constant air-gap length, the utilization of the thick layer of copper results in the introduction of an additional reluctance, and significant increase of the rotor equivalent conductivity ratio at the same time. The calculations for the two types of steel and different thickness copper rings are presented in Fig. 5.

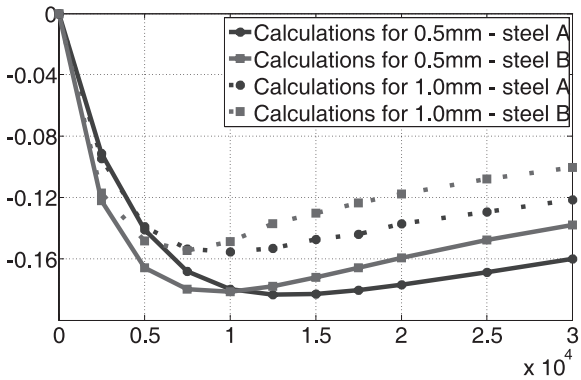

Fig. 5. Steady-state braking torque vs. speed for the brake with the rotors coated by thin copper layer

Utilization of an additional material (copper) resulted in an increase in the value of the braking torque. As can be seen, the position of the extremum of the developed torque was considerable shifted simultaneously. This is caused by significant weakening of the main flux produced by the winding due to the eddy currents induced in the copper layer.

From the authors point of view, an interesting problem, is the determination of the optimal copper layer thickness coating the rotor. The performed series of numerical simulations allowed for the accurate determination of this value. However, in this case, limitations associated with the maximum current density in the copper area should be kept in mind; hence,

it is impossible to exceed the certain minimum thickness of copper coating. The calculation results for the selected analyzed materials are shown in Fig. 6.

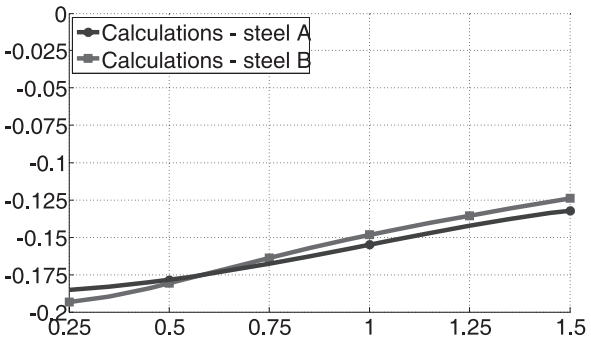

Fig. 6. Braking torque vs. thickness of the copper layer at rated speed

3.3. Rotors with axial slits on the surface

The brake analyzed in the paper belongs to the group of devices with solid rotors. In the case of solid-rotor induction machines, one of the methods for improving the operational performance, widely described in the literature, is to make a series of axial slits on the rotor surface [6, 8]. This results in a significant increase in the depth of the magnetic field penetration into the rotor, and as a consequence, an increase in torque values [8].

Because of significant differences between the construction of a typical solid-rotor induction machine and the considered brake, the authors decided to analyze its performance when it is equipped with the slitted rotor shown in Fig. 7.

The new structure has 30 slits with a depth of 7 mm, distributed symmetrically on the rotor circumference. Other structural parameters of the model remained unchanged.

The obtained results of numerical calculations for the modified structure of the rotor are shown and compared with the basic rotor structures in Fig. 8.

Unfortunately, the characteristics illustrate a decrease rather than an increase of braking torque. The reason for this should be sought in the very small ratio of active length of rotor in relation to its outer diameter. Another cause for the reduction in the value of the torque is the

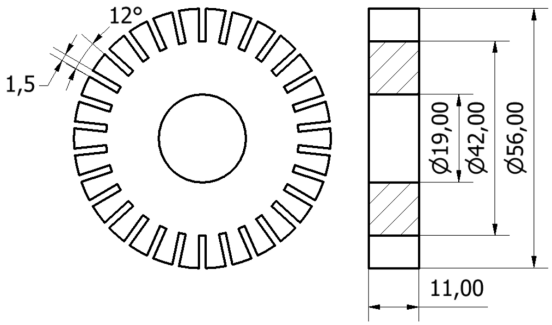

Fig. 7. Slitted rotor

characteristic structure of the brake stator. A small area of the stator pole shoe is associated with a relatively large dispersion of the main flux. Exemplary density distributions of eddy currents induced on the disc are shown in Fig. 9.

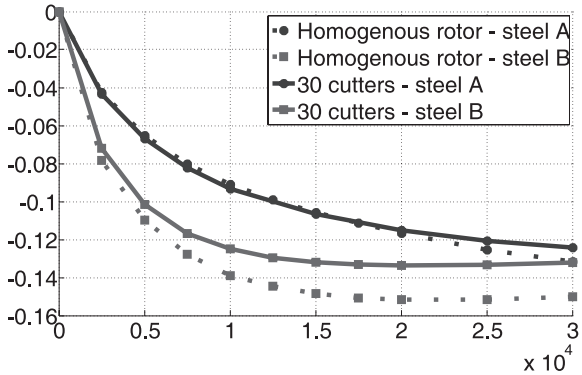

Fig. 8. Comparison of steady-state braking torque vs. speed characteristics for the brake with uniform and slitted rotors

4. Summary

The main issue posed in this study was to analyse the effect of using different rotor materials on high-speed induction brake performance. The calculation results were partly verified by taking measures on the test-stand. The two-dimensional models were already omitted at an early stage of the research and full analysis in three dimensional space was carried out. On the basis of the characteristics, the effect of material parameters on the brake operating conditions was clearly defined. Among the most interesting results, the dependence of the braking torque on the rotor length with the clear extremum can be mentioned. The positive effect of an additional copper layer (0.2–0.5 mm) on the mechanical characteristics of the brake has been confirmed.

It was also shown that it is inappropriate to perform slits on the surface of the rotor. In such a case, the observed decrease in the braking torque is mainly caused by a small ratio of the active length to the rotor diameter and narrow pole shoes. The only positive result for this modification is to improve the coefficient of heat dissipation to the environment associated with the increased heat exchange surface with the air. The obtained results of the simulation allow designing a new rotor with increased active length, coated with a thin copper layer – this would significantly improve the achievable braking torque. However, it should be emphasized that it is advisable to apply the optimization methods to determine the most appropriate structural parameters of the rotor in terms of braking torque. The most important conclusion from the investigation is that a high value of electrical conductivity of the rotor material is much more important than its good magnetic properties. This is because of a relatively high length of air-gap resulting in the linearizing of the brake magnetic circuit.

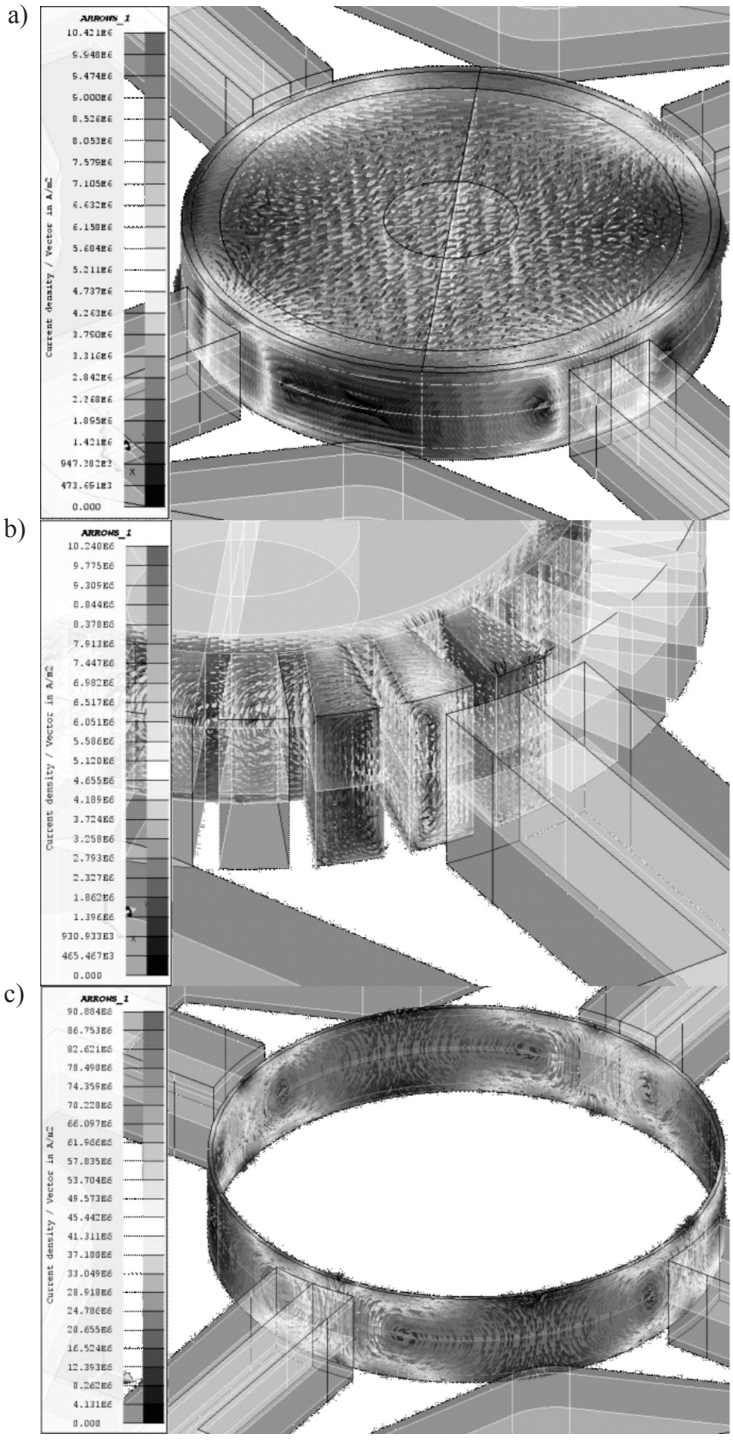

Fig. 9. Current density distribution a) uniform rotor, b) slitted rotor, c) rotor with copper layer

References

[1] Srivastava R.K., Kumar S., *An alternative approach for calculation of braking force of an eddy-current brake*, IEEE Trans. Magn., 2009, Vol. 45, No. 1, pp. 150–154.

[2] Gay S.E., Ehsani M., *Parametric analysis of eddy-current brake performance by 3-D Finite-Element analysis*, IEEE Trans. Magn., 2006, Vol. 42, No. 2, pp. 319–328.

[3] Gulbahce M.O., Kocabas D.A., Habir I., *Finite elements analysis of an small Power Eddy-current brake*, Mechatronika, 15th International Symposium, 5–7 Dec. 2012.

[4] Jagieła M., Kowol M., Kołodziej J., Łukaniszyn M., Cichoń K., Skrzypek K., *Design, analysis and testing of high-speed eddy-current brake/dynamometer*, XXII Symposium Electromagnetic Phenomena in Nonlinear Circuits, EPNC 2012, June 26–29, 2012, Pula, Croatia, pp. 19–20.

[5] Garbiec T., Kowol M., Kołodziej J., *Design considerations of high-speed eddy-current brake*, Archives of Electrical Engineering, 2014, Vol. 63, No. 2, pp. 295–304.

[6] Jagieła M., Garbiec T., *Evaluation of rotor-end factors in the solid rotor induction motors*, IEEE Transactions on Magnetics, January 2012, Vol. 48, No. 1, pp. 137–142.

[7] O'Kelly D., *Theory and performance of solid-rotor induction and hysteresis machines*, IEE Proc., May 1976, Vol. 123, No. 5, pp. 421–428.

[8] Huppunen J., *High-speed solid-rotor induction machine – electromagnetic calculation and design*, Ph.D. Diss., Acta Universitatis Lappeenrantaensis, Lappeenranta, 2004.

TECHNICAL TRANSACTIONS | **CZASOPISMO TECHNICZNE**
ELECTRICAL ENGINEERING | ELEKTROTECHNIKA
1-E/2015

MARCIN KOWOL, JANUSZ KOŁODZIEJ, MARIAN ŁUKANISZYN*

AN ANALYSIS OF MAGNETIC GEAR PERFORMANCE

ANALIZA PRACY PRZEKŁADNI MAGNETYCZNEJ

Abstract

Continuous development of technology determines the search for new solutions in the field of electric machine design with improved electromechanical properties. In recent years, there has been an increased interest in passive and active magnetic gears. This paper presents the design, operation and performance analysis of the modified magnetic gear. The new prototype magnetic gear allows obtaining a ratio of 4:1 or 5:1. For the analyzed construction, two and three-dimensional numerical models are developed for which the series of the magnetic field calculations are carried out . The characteristics of the magnetic torque vs. angle position of the inner rotor with respect to the intermediate ring (modulation ring) and the outer rotor are determined and compared. The examples of flux density distributions for the analyzed converter construction are presented. The calculation results are verified with measurements on the prototype.

Keywords: *magnetic gear*, *finite element method*

Streszczenie

Ciągły rozwój techniki determinuje poszukiwanie nowych rozwiązań konstrukcyjnych maszyn elektrycznych o poprawionych parametrach elektromechanicznych. W ostatnim czasie można zauważyć wzrost zainteresowania pasywnymi oraz aktywnymi przekładniami magnetycznymi. W niniejszej pracy przedstawiono budowę, zasadę działania oraz analizę pracy zmodyfikowanej przekładni magnetycznej. Zbudowano prototyp przetwornika momentu umożliwiającego uzyskanie przełożenia 4:1 lub 5:1. Dla analizowanej konstrukcji opracowano dwu- oraz trójwymiarowe modele numeryczne, dla których wykonano szereg obliczeń polowych. Wyznaczono oraz porównano charakterystyki momentu magnetycznego w funkcji kąta położenia wirnika wewnętrznego względem pierścienia pośredniczącego (modulującego) oraz wirnika zewnętrznego. Przedstawiono przykładowe rozkłady indukcji magnetycznej dla analizowanej konstrukcji przekładni. Wyniki obliczeń zostały zweryfikowane z pomiarami na prototypie przetwornika.

Słowa kluczowe: *przekładnia magnetyczna*, *metoda elementów skończonych*

DOI: 10.4467/2353737XCT.15.030.3830

* Ph.D. Eng. Marcin Kowol, Ph.D. Eng. Janusz kołodziej, Ph.D. Eng. Marian Łukaniszyn, Faculty of Electrical Engineering, Automatic Control and Informatics, Opole University of Technology.

1. Introduction

Magnetic gears offer plenty of potential benefits, including: physical isolation between the driver and the receiver, reduction of noise and vibration levels, protection against overload and contactless torque transmission [1–4]. They do not require periodic inspections or maintenance checks, which significantly helps reduce operating costs. Conventional magnetic gear, illustrated in Fig. 1a), has a simple construction. It consists of a low and high-speed rotor, on which permanent magnets are mounted. It should be noted that the rotor contact interface is reduced significantly, this causes heavy losses in the magnetic circuit. Therefore, the gear efficiency decreases, as well as, the transmitted torque density is not sufficient for practical application, and it does not exceed 10 kNm/m^3 for this type of designs [1, 3].

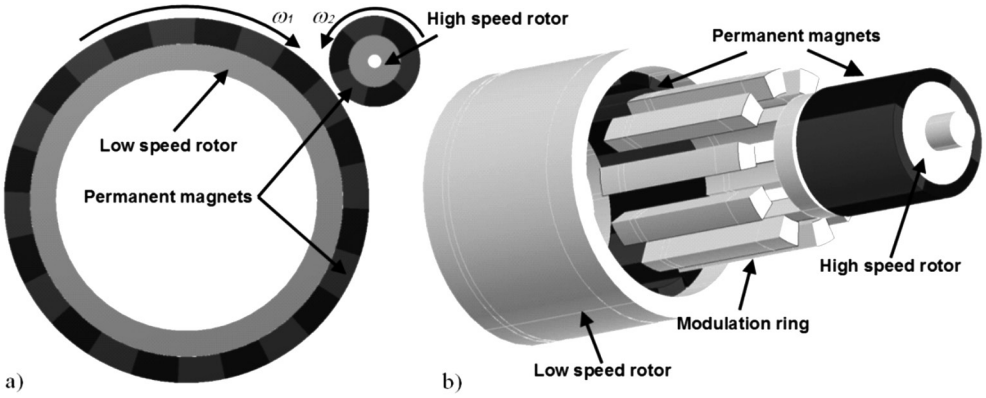

Fig. 1. Example of magnetic gear a) base construction [4], b) modified construction

This paper presents a modified magnetic gear, which can compete against certain mechanical constructions. A schematic diagram of magnetic gear is shown in Fig. 1b). The machine consists of external and internal rotors with permanent magnets mounted on the entire circumference and the intermediate ring formed of ferromagnetic poles. Additionally, by using the high-energy permanent magnets, it is possible to obtain a density of the transferred torque level of 150 kNm/m^3 [1, 4].

2. Operating principle

The operating principle of the analysed magnetic gear is described in detail by the authors of previous work [4]. In order to enable the magnetic torque transmission at various speeds, one of the aforementioned components of the machine must be locked with respect to the others. During the design stage, it must be determined which element will be driven and which one will be locked. This has a significant impact on the value of the final drive ratio, while every possible configuration gives another gear ratio. Relationships that allow choosing the number of internal and external rotor magnets and the number of ferromagnetic pole pieces for a given gear drive, have been derived on the basis of distri-

bution analysis of the modulated magnetic field produced by permanent magnets in the air gap [1–4]. The next stage of the designing process is to determine the number of pole pairs within one of the permanent magnet rotors and to indicate pole pieces of the intermediate ring. On this basis, by using the formula (1), we can calculate the number of pole pairs within the second rotor.

$$p_{rz} = p_s - p_{rw} \tag{1}$$

where:
p_{rz}, p_{rw} – number of pole pairs in the outer rotor and inner rotor,
p_s – number of pole pairs in the modulation ring.

Considering the operating state during which the modulating ring is locked and the internal rotor is being driven, the magnetic gear ratio (i_r), is given by:

$$i_r = \frac{p_s - p_{rw}}{p_{rw}} = \frac{p_{rz}}{p_{rw}} \tag{2}$$

Under such conditions, the external rotor will rotate in the opposite direction to the internal rotor. On the other hand, during the operating state (in which the external rotor is locked), the intermediary ring will be rotating in the direction of the internal rotor, and the gear ratio is determined by the formula:

$$i_r = \frac{p_s}{p_{rw}} \tag{3}$$

3. Physical model

The prototype of the magnetic gear on the test stand illustrates Fig. 2. Basic parameters are listed in Table 1.

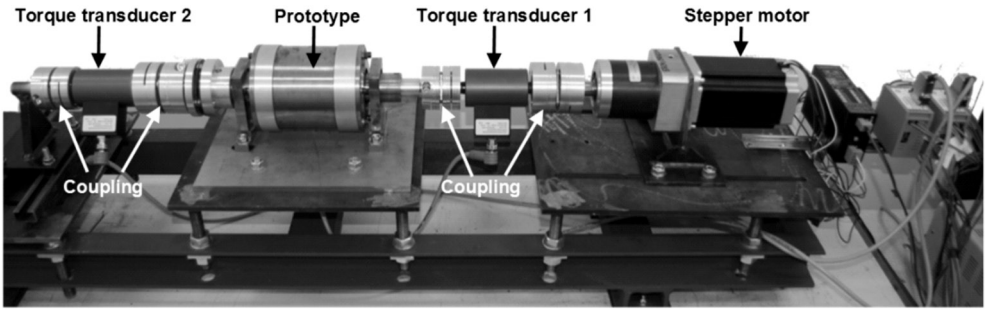

Fig. 2. Test bench for torque measurement

Table 1

Basic parameters of the designed gear

Inner rotor outer diameter	50 mm
Modulation ring inner diameter	54 mm
Modulation ring outer diameter	74 mm
Outer rotor inner diameter	78 mm
Outer rotor outer diameter	104 mm
Permanent magnets height	5 mm
Gear active length	50 mm

The external rotor has fixed neodymium magnets producing a magnetic field of eight pole-pairs; while the internal rotor of two pole-pairs. The number of ferromagnetic pole pieces in the modulation ring is ten. For easy measurement, it was assumed that the intermediary ring will be locked. For intermediary ring being locked, the gear ratio, according to the formula (2), is 4:1, while for the external rotor being locked, the gear ratio, based on the equation (3), is 5:1.

4. Numerical models

To carry out verification of the computations results, two and three-dimensional field models were developed (see Fig. 3). Calculations were carried out using the finite element method. In both models, eddy currents and magnetic hysteresis effects were neglected. The base point in the analysis is the angular position of the rotors where the magnetic moment is zero.

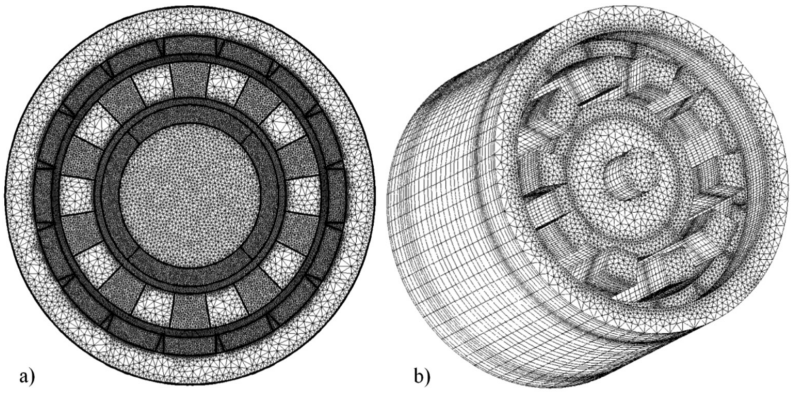

Fig. 3. Finite element mesh for a) two-dimensional model b) three-dimensional model (version B)

Due to the fact that the gear outer diameter is twice as large as the active length, 3D numerical models were developed to validate computation results from the two-dimensional model. In the first model (version A), it was assumed that the cross-section of the gear is the same along its whole length. The second model includes the actual dimensions of ferromagnetic elements, which can significantly affect the operation of the converter.

The difference between these two models lies in the length of intermediate ring pole pieces, which in model B is much greater than the length of permanent magnets. Of course, adaptation of those differences increase computational costs because it is impossible to impose symmetry and periodicity boundary conditions.

5. Simulation results and measurement verification

A series of computer simulations was carried out by using the developed numerical models. Calculations results of the magnetic torque have been verified on the prototype. For this purpose, a test-stand was built, which consists of: a prototype of the magnetic gear; two torque transducers equipped with encoders and terminals allowing for capturing the measurement data; a stepper motor with a planetary gearbox; the stepper motor controller; a system designed by the authors for stepper motor control and data acquisition. Figures 4–6 show characteristics of the magnetic torque acting on particular elements of the converter as a function of the rotation angle of the internal rotor. Based on the calculation results, the highest torque value (T_{max}) of which the gear can be loaded is obtained for the 45-degree angular displacement of the internal rotor with respect to the external rotor or intermediary ring. When the maximum value of the torque is exceeded, the magnetic gear stops. Table 2 lists the obtained computation results for the developed models and specifies their percentage change in terms of the measured magnetic torque (ΔT_{max}).

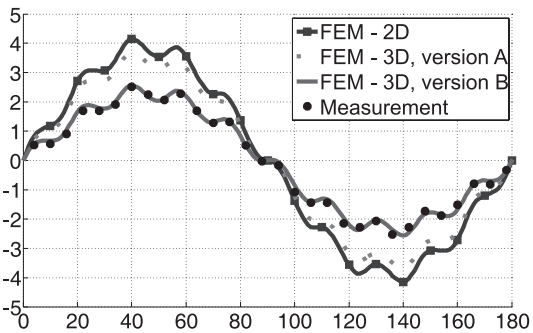

Fig. 4. Magnetic torque acting on the inner rotor vs. its angular displacement when the outer rotor and intermediary ring are locked

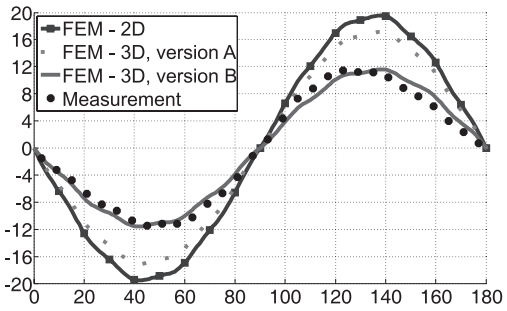

Fig. 5. Magnetic torque acting on the intermediary ring vs. angular displacement of the inner rotor when the outer rotor and intermediary ring are locked

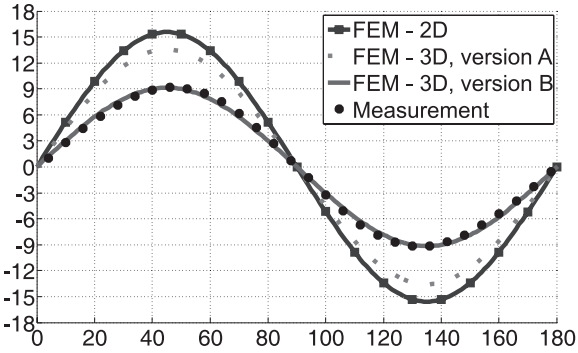

Fig. 6. Magnetic torque acting on outer rotor vs. angular displacement of the inner rotor when the outer rotor and intermediary ring are locked

Table 2

Magnetic torque peak values comparison

	Inner rotor		Intermediary ring		Outer rotor	
	T_{max} [Nm]	ΔT_{max} [%]	T_{max} [Nm]	ΔT_{max} [%]	T_{max} [Nm]	ΔT_{max} [%]
FEM 2D	4.21	+64.5	19.46	+69.9	15.56	+68.8
FEM 3D (version A)	3.72	+45.3	16.80	+46.6	13.63	+47.5
FEM 3D (version B)	2.59	+1.6	11.25	-1.8	9.20	-0.4
Measurement	2.56	-	11.46	-	9.24	-

Figures 7–9 show the change of the magnetic torque acting on particular elements of the gear when the intermediate ring is locked and the external rotor is loaded by the maximum torque value.

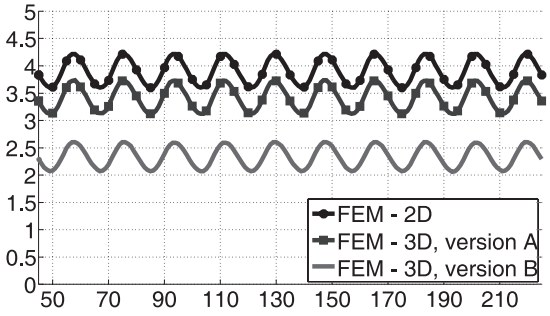

Fig. 7. Magnetic torque acting on the inner rotor vs. its angular displacement when the outer rotor is unlocked

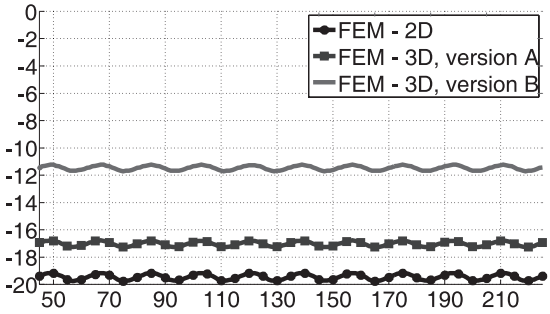

Fig. 8. Magnetic torque acting on the intermediary ring vs. angular displacement of the inner rotor when the outer rotor is unlocked

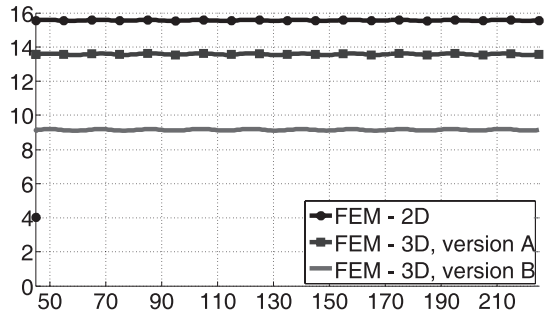

Fig. 9. Magnetic torque acting on the outer ring vs. angular displacement of the inner rotor when the outer rotor is unlocked

The change of the external rotor rotation angle with respect to the internal rotor was computed according to the formula:

$$\alpha_z = -\frac{p_{rw}}{p_{rz}}\alpha_w \tag{4}$$

where:
α_w, α_z – displacement angle of the inner and outer rotors, respectively.

Tables 3–5 provide a comparison of the most relevant parameters for all models. Furthermore, for calculation purposes, a parameter describing the electromagnetic torque ripples (ε) was introduced, which is described by the formula shown below:

$$\varepsilon = \frac{T_{\max} - T_{\min}}{2T_{av}} \cdot 100\% \tag{5}$$

where:
$T_{\min}$ – the lowest value of torque,
T_{av} – the average value of torque.

Table 3

Torque values for the inner rotor

	FEM 2D	FEM 3D (version A)	FEM 3D (version B)
T_{max} [Nm]	4.21	3.72	2.60
T_{min} [Nm]	3.59	3.12	2.06
T_{av} [Nm]	3.89	3.41	2.33
ε [%]	7.98	8.87	11.56

Table 4

Torque values for the intermediary ring

	FEM 2D	FEM 3D (version A)	FEM 3D (version B)
T_{max} [Nm]	19.75	17.29	11.72
T_{min} [Nm]	19.18	16.81	11.25
T_{av} [Nm]	19.46	17.04	11.48
ε [%]	1.47	1.43	2.05

Table 5

Torque values for the outer rotor

	FEM 2D	FEM 3D (version A)	FEM 3D (version B)
T_{max} [Nm]	15.60	13.63	9.20
T_{min} [Nm]	15.53	13.52	9.10
T_{av} [Nm]	15.57	13.58	9.15
ε [%]	0.22	0.39	0.55

Figure 10 represents angular change of magnetic torque acting on the intermediary ring with no load on the gear. Exemplary flux density distributions at the same angular position for the three-dimensional models are illustrated in Fig. 11.

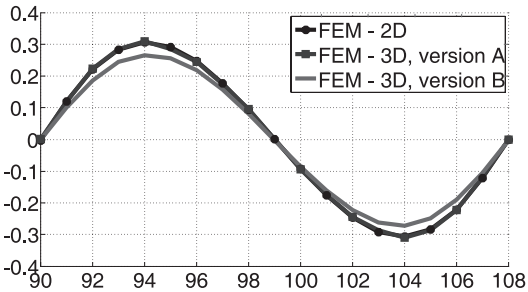

Fig. 10. Magnetic torque acting on the intermediary ring vs. angular displacement of the inner rotor when the outer rotor is unlocked

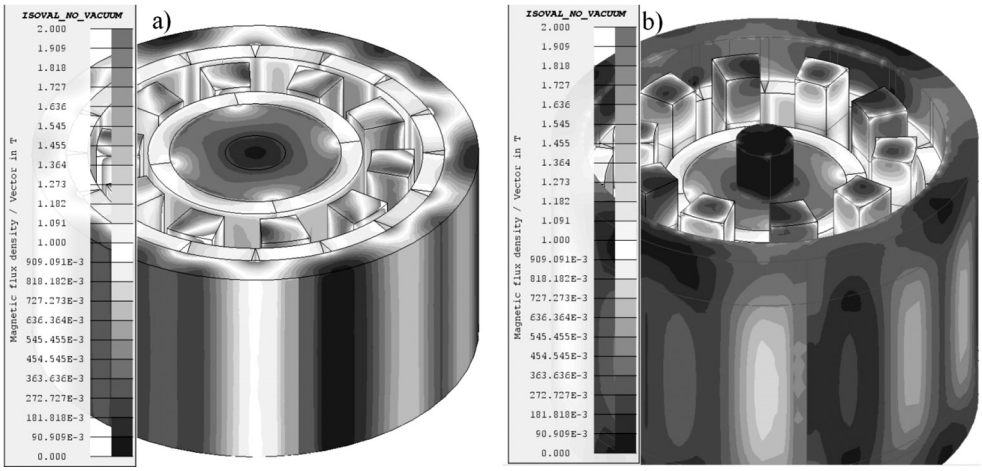

Fig. 11. Example of magnetic flux density distribution computed using 3D numerical model a) version A, b) version B

6. Summary

The paper describes the design and operation of the magnetic gear allowing for substantial increases in the torque transmission level. Significant impact of the length of the pole pieces in the modulation ring on the magnetic torque value was shown. Torque density in the 2D model equals 39.6 kNm/m^3 while in the 3D model in version A, it is 34.6 kNm/m^3 and in version B, it is 15.3 kNm/m^3. Such large discrepancies in torque density values are caused by an improper design of the converter. However, it should be noted that the constructed machine is the first prototype built in the Chair of Electrical Machines at the Technical University of Opole. Further research study will involve works on the design improvement and optimization of the magnetic circuit.

References

[1] Atallah K., Howe D., A *novel high-performance magnetic gear*, Transactions on Magnetics, IEEE, Jul. 2001, Vol. 37, No. 4, pp. 2844–2846.

[2] Atallah K., Calverley S., Howe D., *Design, analysis and realization of a high--performance magnetic gear*, IEE Proc. Electric Power Appllication, 2004, Vol. 151, No. 2, pp. 135–143.

[3] Niguchi N., Hirata K., *Cogging Torque Analysis of Magnetic Gear*, Transactions on Industrial Electronics, 2012, IEEE, Vol. 59, pp. 2189–2197.

[4] Kowol M., Kołodziej J., Łukaniszyn M., *Analiza pola magnetycznego w przekładni magnetycznej*, Zeszyty Problemowe – Maszyny Elektryczne, 2013, nr 100(3), Komel, pp. 163–168.

TECHNICAL TRANSACTIONS | **CZASOPISMO TECHNICZNE**
ELECTRICAL ENGINEERING | ELEKTROTECHNIKA
1-E/2015

PIOTR MYNAREK, MARCIN KOWOL*

THERMAL ANALYSIS OF A PMSM USING FEA AND LUMPED PARAMETER MODELING

ANALIZA CIEPLNA SILNIKA PMSM ZA POMOCĄ METODY ELEMENTÓW SKOŃCZONYCH ORAZ SCHEMATU CIEPLNEGO

Abstract

Permanent magnet synchronous motors are often used in hybrid electric vehicles due to the high power density. Overheating in a PMSM motor can cause negative effects on the work of permanent magnets and a significant shortening of the life of the machine due to the phenomenon of the thermal ageing of insulation. Therefore, it is extremely important to know the exact temperature distribution in different parts of the electrical machine under various operating conditions. This paper presents a lumped parameter thermal model and FE model of a permanent magnet synchronous motor. A method for the homogenization of a stator winding is also described. In order to validate the accuracy of the calculation results, measurements on the physical model of the machine were carried out.

Keywords: *PMSM*, *thermal analysis*, *homogenization*

Streszczenie

Silniki synchroniczne z magnesami trwałymi dzięki dużej gęstości mocy są coraz chętniej wykorzystywane w różnych gałęziach przemysłu. Zbyt duże nagrzewanie silnika PMSM może wpływać negatywnie na pracę magnesów trwałych oraz spowodować skrócenie czasu życia maszyny w wyniku termicznego starzenia się izolacji. Dlatego też niezmiernie ważna jest dokładna znajomość rozkładu temperatury w poszczególnych częściach maszyny elektrycznej, w różnych jej stanach pracy. W artykule przedstawiono analizę cieplną silnika synchronicznego z magnesami trwałymi przeprowadzoną metodą schematów cieplnych, jak również metodą elementów skończonych (MES). Opisano także metodę homogenizacji uzwojeń wsypywanych. Wyniki symulacji komputerowych zostały zweryfikowane pomiarowo na obiekcie rzeczywistym silnika.

Słowa kluczowe: *silnik PMSM*, *analiza cieplna*, *homogenizacja*

DOI: 10.4467/2353737XCT.15.031.3831

* Ph.D. Eng. Piotr Mynarek, Ph.D. Eng. Marcin Kowol, Faculty of Electrical Engineering, Automatic Control and Informatics, Opole University of Technology.

1. Introduction

New constructional solutions applied by aircraft and automotive industries use electric motors more and more often. Such solutions allow more energy efficient processing and the reduction of emissions. One of the major factors when selecting the most appropriate electric motor for the propulsion system is the power density, therefore, permanent magnet synchronous motors are increasingly being used [3]. Rotor design solutions give the possibility to develop the highest possible density torque in a relatively small volume. In addition, PMSM are characterized by high efficiency and a wide range of power at constant rotational speed.

Placing an electric motor, for example in a compartment in a vehicle, causes significant deterioration of cooling conditions. Therefore, an accurate knowledge of the temperature distribution in different parts of the electric motor during its various operating conditions is an extremely important issue. Thermal analysis of electric motors primarily uses the lumped parameter thermal models [3, 4] and the finite elements method (FEM) [1, 6]. This paper presents a permanent magnet synchronous motor based on both calculation methods. The application of both methods enables an effective analysis of the machine.

2. Determination of power losses

The research subject of the study is SMKwsg90M8 motor with the start-up frequency and parameters presented in Table 1.

Table 1

Selected parameters of the machine

Physical size	U_n [V]	I_n [A]	P_n [kW]	n_n [rev/obr]	η [%]
Value	400	3.7	2	2200	91

During the first stage of the research work, power losses in the analysed motor were determined. For this purpose, a numerical model was built, which, together with the discretization mesh, is shown in Fig. 1. During the building of the field model of the analysed motor, periodic boundary conditions were applied, thus limiting the calculation area to one fourth of the volume of the entire machine. This procedure allowed a significant reduction in the computation cost needed to solve the problem.

The main sources of heating in synchronous machines come from the heating effect according to Joule's law and core losses. Omitting the skin and proximity effects, losses occurring in the windings can be determined in accordance with the formula:

$$\Delta P_{cu} = RI^2 \tag{1}$$

where:
R – the phase resistance,
I – the phase current.

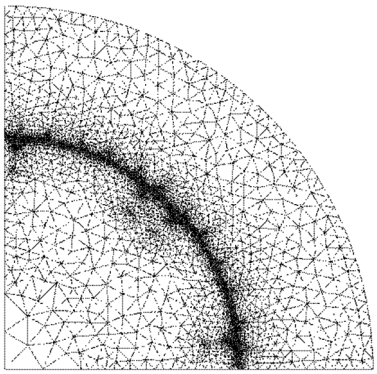

Fig. 1. Discretization mesh in cross-section of the motor

The second major thermal source in electric motors comes from iron losses ΔP_{Fe}. Due to the fact that the object of the research study is a synchronous motor, the losses are mainly formed in the stator. Losses in the rotor are smaller and caused by higher harmonics of magnetic flux density. Iron losses were estimated by using Bertotti's formula considering the losses from the hysteresis loop, eddy current and excess losses [6]. Coefficients of hysteresis and excess losses have been estimated on the basis of electrical steel sheet losses given in the manufacturer's specifications.

$$\Delta P_{Fe} = \iiint_V (k_h B_m^2 f\, k_f + \frac{1}{T}\int_0^T \left[\sigma \frac{d^2}{12}\left(\frac{\mathrm{d}B}{\mathrm{d}t}(t)\right)^2 + k_e \left(\frac{\mathrm{d}B}{\mathrm{d}t}(t)\right)^{\frac{3}{2}} \right] k_f \mathrm{d}t)\mathrm{d}V \qquad (2)$$

where:
k_h – the hysteresis coefficient,
B_m – maximum flux density excursion over an electrical cycle,
f – the frequency,
k_f – the packing factor of the laminated core pack,
σ – the electric conductivity,
d – the thickness of a single sheet of lamination,
k_e – the excess loss coefficient,
V – the volume of the region.

Using formula (2), losses ΔP_{Fe} are calculated in each element of the discretisation mesh being formed in the 2D model for a particular region, and then averaged across the volume of the region. Losses were determined for three characteristic areas of the machine, specifically, the yoke, stator teeth and rotor. Table 2 lists power losses for the selected working state of the analyzed machine.

Table 2

Calculated loss in PMSM

Load on the motor ($n = n_N$)	Losses ΔP_{Cu} [W]	Losses ΔP_{Fe} [W]		
		Stator teeth	Stator yoke	Rotor
T_l = 8.70 Nm	64.89	40.6	21.8	11.6

3. Estimation of the heat transfer coefficient

One of the major problems in thermal analysis is the proper consideration of heat transfer intensity in the analyzed object. The most convenient method of considering this is to apply Newton's boundary condition. The application of Newton's boundary condition of cooling directly allows considering the intensity of cooling in the form of heat transfer coefficient α. However, the correctly calculating the coefficient gives rise to many problems. Therefore, this study proposes the estimation of the heat transfer coefficient based on calibration measurements. This approach enables determining the searched value for the specific motor housing in every typical point, that is for a motor housing fin and for gaps between the fins. Furthermore, it is possible to determine the dependence between α coefficient and the motor rotational speed, rather than the coolant velocity. It is undoubtedly more practical and intuitive when performing thermal analysis for a particular state of the machine.

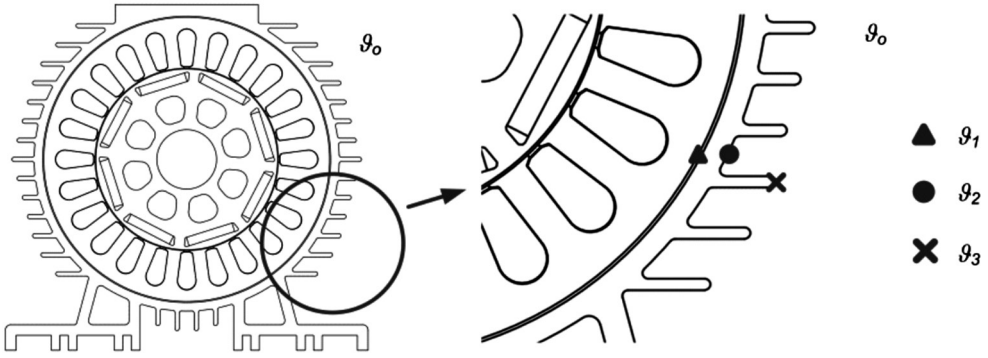

Fig. 2. Cross-section of motor along with marked measuring points, where: ϑ_1 – temperature between stator and motor housing; ϑ_2 – motor housing temperature between cooling fins; ϑ_3 – fin temperature; ϑ_o – ambient temperature

According to Newton's condition of heating, the heat flux q being transferred in a solid object equals the flux being transferred to the ambient.

$$q_\alpha = \lambda \left.\frac{\partial \vartheta}{\partial n}\right|_F = \alpha\left(\vartheta_F - \vartheta_o\right) \tag{3}$$

By measuring the temperature at the points shown in Fig. 2, it is possible to designate coefficient α with satisfactory accuracy. Based on temperatures ϑ_1 and ϑ_2 (ϑ_3), as well as when the exact dimensions of the housing are known, the heat transferred within the solid object can be determined. Considering the heat flux, surface and ambient temperatures, by using the equation (3), the heat transfer coefficient for the motor housing between cooling fins (4), although separately – just for the cooling fins (5) can be determined.

$$\alpha_o = \frac{\vartheta_1 - \vartheta_2}{\left(\frac{d_1}{\lambda_1} + \frac{d_2}{\lambda_2}\right)\left(\vartheta_2 - \vartheta_o\right)} \tag{4}$$

where:
d_1, d_2 – air layer thickness (of housing),
λ_1, λ_2 – coefficient of the air thermal conductivity (aluminum).

$$\alpha_z = \frac{\vartheta_1 - \vartheta_3}{\left(\frac{d_1}{\lambda_1} + \frac{d_2'}{\lambda_2}\right)\left(\vartheta_3 - \vartheta_o\right)} \tag{5}$$

where: d'_2 – housing layer thickness together with the high typical for the cooling fin.

On the basis of the performed measurements, the heat transfer coefficients were determined at both typical points on the motor housing as a function of the rotational speed. Figure 3 indicates measurement results and an approximate relationship of the α coefficient as a function of motor rotational speed.

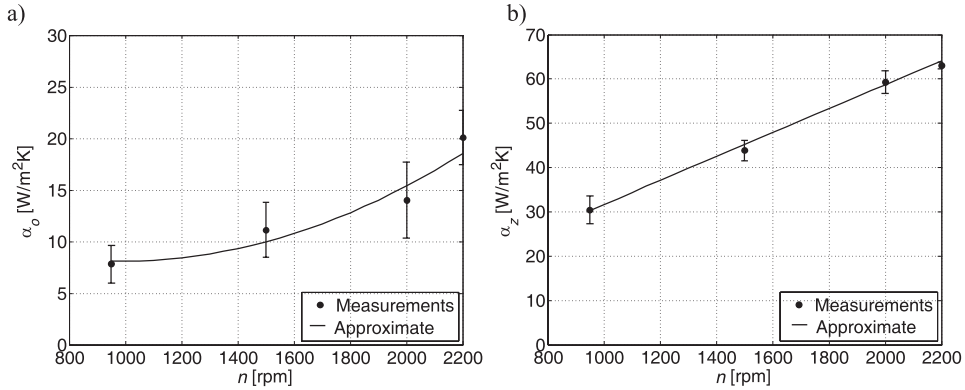

Fig. 3. Dependency of heat transfer coefficient for a housing between cooling fins (a) and for a single cooling fin (b) as a function of motor rotational speed

4. Homogenization of windings

In terms of heating, a sensitive area in permanent magnet synchronous motors is the stator winding as the highest temperature occurs here. Proper modeling of the windings, in particular windings with randomly wound insulated coil, causes many problems because of the high complexity of the object's structure [5]. In order to determine thermal conductivity of the impregnated winding (λ_{iw}) for the analysed motor, it was decided to design two coils: one impregnated and one non-impregnated, both placed in a segment of the stator (Fig. 4a). Coil winding data and stator segment dimensions correspond to the technical data of the analyzed machine. In both coils, five K-type thermocouples ($T1$–$T5$) were placed along the height of the slots (Fig. 4b).

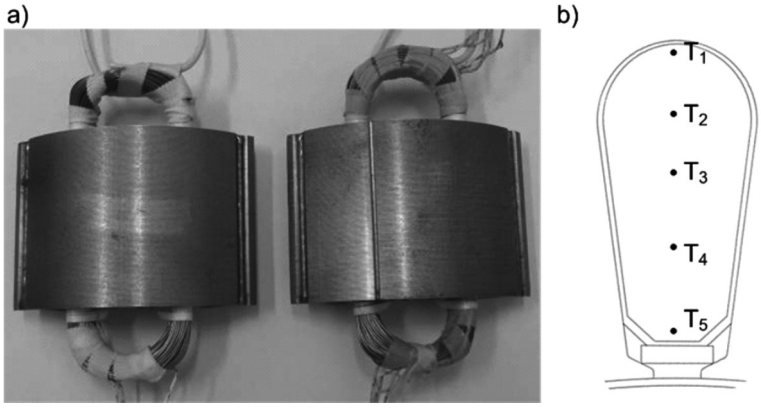

Fig. 4. Constructed coils (a) and arrangement of the thermocouples in the coil (b)

Figure 5 shows schematic diagram of the proposed method for determining the thermal conductivity of an impregnated winding.

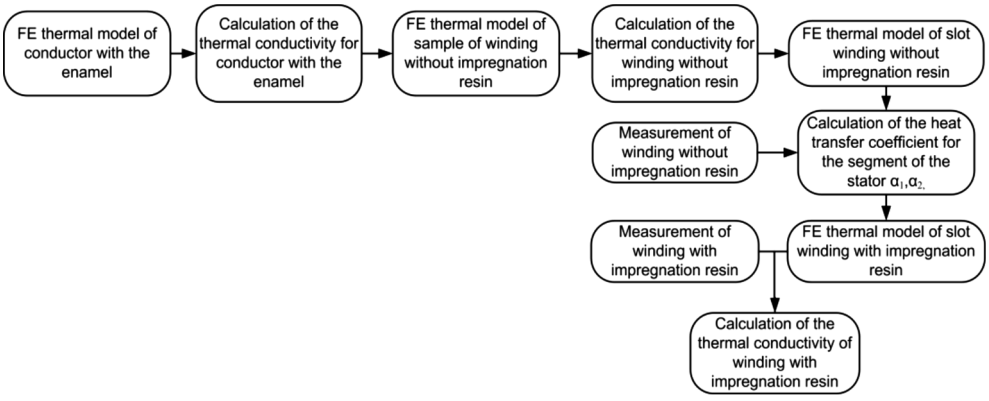

Fig. 5. The proposed method for determining the thermal conductivity of impregnated windings

In order to determine the equivalent thermal conductivity of conductors with enamel, the formula presented below was used:

$$\lambda_{ec} = \left(\frac{d' - \delta_e}{2\delta_e} \right) \lambda_e \tag{6}$$

where:
d' – diameter of the conductor with enamel,
δ_e – thickness of the enamel layer,
λ_e – thermal conductivity of enamel.

The thermal conductivity of non-impregnated winding $\lambda_{ni\,w} = 0.1$ W/(mK), along the *OX* axis as well as the *OY* axis. This coefficient was calculated based on the numerical model of the winding sample with filling coefficient similar to the one, as in the case of the real winding – $k = 51\%$ (Fig. 6) and adapted in the Fourier's law (7) [1].

$$\lambda_{ni\,w\,x} = \frac{q_x \cdot d}{\vartheta_1 - \vartheta_2} \tag{7}$$

where:
q_x – heat flux transferred across the wall,
l – the thickness of the wall,
ϑ_1, ϑ_2 – the temperatures of the walls,
$\lambda_{ni\,w\,x}$ – thermal conductivity of the non-impregnated winding in the *x*-axis direction.

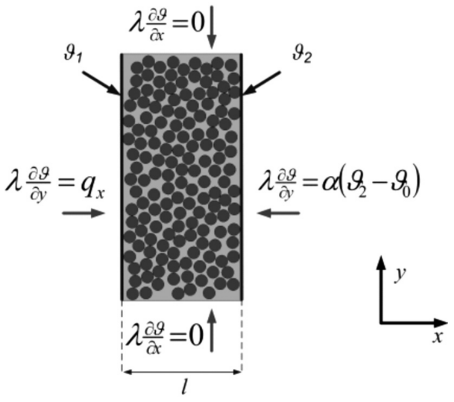

Fig. 6. FE model of the winding sample

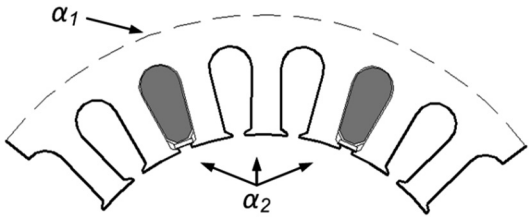

Fig. 7. The values of the coefficient of heat transfer for stator segment

As the values of power losses occurring in the non-impregnated coil and the thermal conductivity were known, the heat transfer coefficient α for the segment of the core was estimated. For the analysed measuring object of the outer layer of the core, the estimated coefficient α is α_1 = 10 W/(m^{2}K), while for the other layers, it is α_2 = 6 W/(m^{2}K) (Fig. 8).

While maintaining the same measurement conditions for both coils, it is possible to also adopt the designated heat transfer coefficients for the impregnated coil. Then, based on the field model of the impregnated coil and measurement results, the impregnated winding thermal conductivity coefficient λ_{iw}, was estimated, for which the value is λ_{iw} = 0.18 W/(mK).

5. Lumped parameter thermal model of PMSM

The mathematical model, by which the transient thermal analysis of the analysed PMSM was carried out, was built on the basis of a lumped parameter thermal method. In this model, the following assumptions were adopted: the machine is symmetrical; mechanical losses are omitted; the thermal transfer coefficient is averaged in respect to the entire machine housing surface.

Particular heat transfer paths between respective elements of the analysed machine have assigned corresponding thermal resistance. The thermal resistance for heat transfer in the conductivity state was determined based on the formula [7]:

$$R_{th} = \frac{h}{\lambda S} \tag{8}$$

where:
h – active length that is parallel to the heat flux,
λ – thermal conductivity,
S – cross-sectional area that is normal to the heat flux.

While the thermal resistance value for convection phenomena was based on the following formula:

$$R_{th} = \frac{1}{\alpha S_c} \tag{9}$$

where:
α – convective heat transfer coefficient,
S_c – heat transfer surface area.

The model considers the thermal capacity of the motor's individual components, which was computed from:

$$C_{th} = c_w \rho V \tag{10}$$

where:
c_w – specific heat capacity,
ρ – density,
V – volume.

A PMSM mathematical model in the form of a thermal circuit was implemented in PLECS software (Fig. 8).

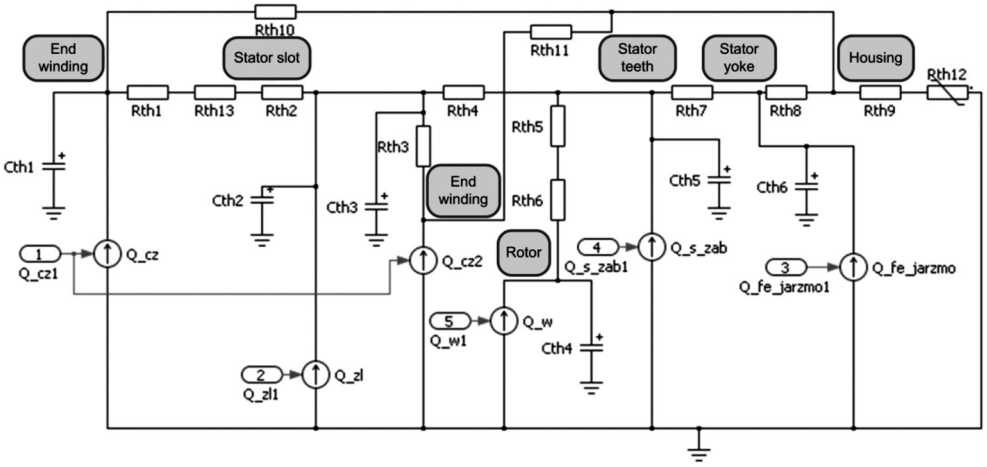

Fig. 8. Thermal model of the analysed motor in PLECS toolbox

By using the thermal circuit, a number of computer simulations for different PMSM operating states were performed. The results obtained are verified by measurements performed on the real object of the motor. For this purpose, a measuring stand was built based on the authors' data acquisition system – this is described in detail in [2]. Figures 9 and 10 show temperature changes at selected measuring points, for nominal motor operating conditions.

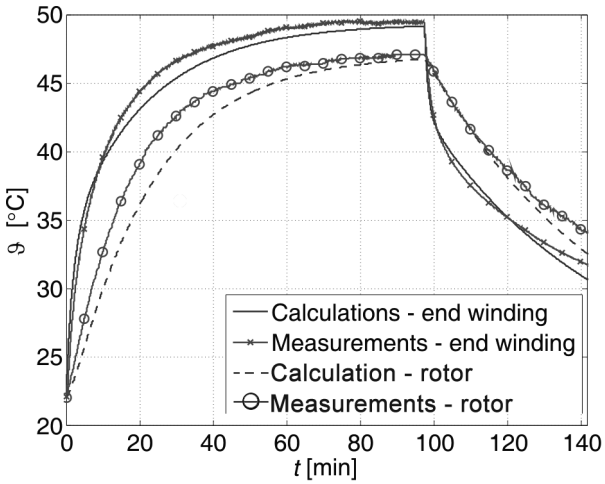

Fig. 9. Temperature change in the end winding and in the rotor (heating and cooling process)

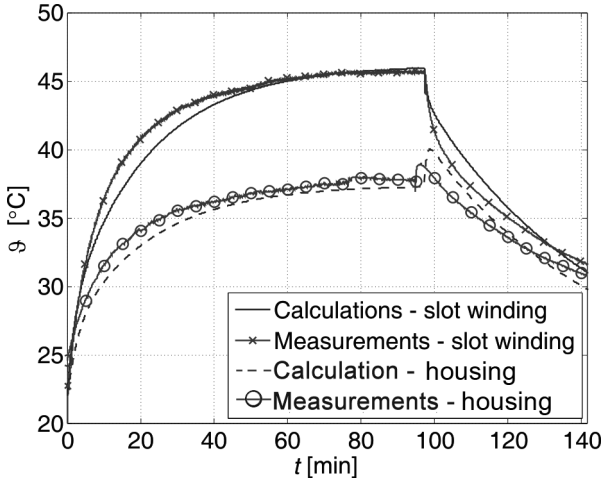

Fig. 10. Temperature change in winding slots and on the motor housing (heating and cooling process)

6. Thermal calculations of PMSM by using field model

The stage of the research study on the analysed motor, thermal analysis in steady state was carried out. For this purpose, a two-dimensional field model was built. During the construction process of the analysed motor field model, symmetry conditions were applied, thus limiting the calculation area to one-eighth of the machine's entire volume, which allowed reducing the numerical costs. The model adopts similar simplifying assumptions to the thermal circuit model. The further adopted value of the heat transfer coefficient was adjusted by the surface heat transfer coefficient and thermal resistance of the housing, which allowed omission of the motor housing parameter.

Table 3 lists computer simulation results carried out on the developed two mathematical models with measurement results performed on the real object of the motor.

Table 3

The results of calculations and measurements

Measuring point	Calculations lumped parameter models ϑ_{LP} [°C]	Calculations MES ϑ_{MES} [°C]	Measurement ϑ_m [°C]
End-winding	48.6	–	49.4
Stator slot	46.8	47.1	45.6
Rotor	46.1	46.5	47.1
Housing	36.9	38.7	38.4

7. Conclusions

This paper has presented permanent magnet synchronous thermal. Satisfactory convergence with measurements performed on the actual physical motor was obtained. The presented thermal modeling operating method of the analysed motor combines advantages of field models and lumped parameter models. The lumped element models allow obtaining temperature increments in particular parts of the machine at relatively low numerical costs. However, it should be noted that determining a thermal equivalent circuit and thermal parameters is a relatively difficult task, especially for windings. On the other hand, field models allow obtaining accurate temperature distribution in the machine, which enables determining local high temperature spots.

References

[1] Idoughi L., Mininger X., Bouillault F., Bernard L., Hoang E., *Thermal Model with Winding Homogenization and FIT Discretization for Stator Slot*, IEEE Transactions on Magnetics, December 2011, Vol. 47, No. 12, pp. 4822–4826.

[2] Kowol M., Mynarek P., Kołodziej J., *Application of LabVIEW environment for permanent magnet synchronous motor testing*, Poznan University of Technology, Academic Journals, Electrical Enginnering, Computer Applications in Electrical Enginnering, Issue 75, Poznań 2013, pp. 49–56.

[3] Lee B., Kim K., Jung J., Hong J., Kim Y., *Temperature Estimation of IPMSM Using Thermal Equivalent Circuit*, IEEE Transactions on Magnetics, November 2012, Vol. 48, No. 11, pp. 2949–2952.

[4] Nategh S., Wallmark, O., Leksell M., Zhao S., *Thermal Analysis of a PMaSRM Using Partial FEA and Lumped Parameter Modeling*, IEEE Transactions on Energy Conversion, June 2012, Vol. 27, No. 2, pp. 477–488.

[5] Simpson N., Wrobel R., Mellor P.H., *Estimation of Equivalent Thermal Parameters of Impregnated Electrical Windings*, IEEE Transactions on Industry Applications, Nov.–Dec. 2013, Vol. 49, No. 6, pp. 2505–2515.

[6] Wrobel R., Mellor P.H., McNeill N., Staton D.A., *Thermal Performance of an Open--Slot Modular-Wound Machine with External Rotor*, IEEE Transactions on Energy Conversion, 2010, Vol. 25, No. 2, pp. 403–411.

[7] Wrobel R., Mellor P.H., *Thermal Design of High-Energy-Density Wound Components*, IEEE Transactions on Industrial Electronics, September 2011, Vol. 58, No. 9, pp. 4096–4104.

TECHNICAL TRANSACTIONS | **CZASOPISMO TECHNICZNE**
ELECTRICAL ENGINEERING | ELEKTROTECHNIKA
1-E/2015

PIOTR BOGUSZ*

INFLUENCE OF CONTROL PARAMETERS ON PROPERTIES OF THE HIGH SPEED TWO-PHASE SWITCHED RELUCTANCE DRIVE

WPŁYW PARAMETRÓW STEROWANIA NA WŁAŚCIWOŚCI WYSOKOOBROTOWEGO NAPĘDU Z DWUPASMOWYM SILNIKIEM RELUKTANCYJNYM PRZEŁĄCZALNYM

Abstract

Two-phase switched reluctance motors are distinguished by their very simple design and belong to the group of high-speed motors. At high rotational speeds, losses in the core of a 4/2-pole switched reluctance machine are much lower than those occurring in a SRM with a larger number of phases. Unfortunately, a flaw of such a solution consists of a difficulty to obtain the starting torque in certain rotor positions. This occurs in the case of a symmetrical stator and rotor layout. To obtain the starting torque in any rotor position, an asymmetric design of rotor has been employed. In the framework of this study, a simulation model of such a machine was developed with the use of which motor characteristics were obtained for two specific working points, namely for very low and very high rotor speeds. Special attention was also focused on the problem of voltage control at high rotor speeds. On the grounds of the obtained results, an analysis of properties of the examined drive was performed from the point of view of the development of a practical control circuit for a two-phase SRM.

Keywords: *high speed drive*, *switched reluctance motor*, *simulation model*

Streszczenie

Dwupasmowe silniki reluktancyjne przełączalne charakteryzują się bardzo prostą konstrukcją i należą do grupy silników wysokoobrotowych. Przy dużych prędkościach wirowania wirnika w maszynie SRM 4/2 w rdzeniu występują znacznie mniejsze straty w porównaniu do SRM o większej liczbie pasm. Niestety wadą tego rozwiązania jest problem z uzyskaniem w każdym położeniu wirnika momentu rozruchowego, tak jak w przypadku symetrycznej konstrukcji stojana i wirnika. Aby uzyskać moment rozruchowy w każdym położeniu, zastosowano niesymetryczną budowę wirnika. W ramach niniejszej pracy zbudowano model symulacyjny omawianej maszyny, za pomocą którego uzyskano wyniki badań dla dwóch przypadków pracy, tj. dla bardzo małych i bardzo dużych prędkości wirowania wirnika. Zwrócono również uwagę na problem regulacji napięcia przy dużych prędkościach wirnika. Na podstawie uzyskanych wyników przeprowadzono analizę właściwości tego napędu pod kątem opracowania praktycznego układu sterownika dla dwupasmowego silnika SRM.

Słowa kluczowe: *napęd wysokoobrotowy*, *silnik reluktancyjny przełączalny*, *model symulacyjny*

DOI: 10.4467/2353737XCT.15.032.3832

* D.Sc. Eng. Piotr Bogusz, Dept. of Electrodynamics and Electrical Machine Systems, Faculty of Electrical and Computer Engineering, Rzeszow University of Technology.

1. Introduction

In household appliances such as vacuum cleaners, juice extractors, and food processors, ac commutator motors are commonly used. Drives of this type have a number of flaws, including, among other things, the generation of electromagnetic interference, susceptibility to failures, and lower efficiency compared to brushless drives. An alternative solution allowing potentially to supplant commutator motors are switched reluctance machines (SRM) distinguished by their very simple construction, absence of commutators, absence of windings and permanent magnets on rotor. Additionally, motors of this type have very good properties including a wide range speed control and are characterized with a higher efficiency compared to commutator motors. Drives employing SRMs, in view of the simple design of their rotors, are very suitable for use in high-speed appliances [1–3]. Flaws of drives of this type include their relatively large torque pulsation and high noise levels relating to the pulsed supply of windings. Recently, a number of studies were published on high-speed drives with switched reluctance motors [2–7]. In general, high-speed SRM drives are constructed as two-phase 4/2-pole machines as such designs allow reducing the switching frequency and as a consequence, reduce losses in the motor core. Limiting the number of motor phases to two means a significant reduction of costs relating to control as less power transistors and diodes are required which represent the most costly items on the list of control system components. In high-speed drives designed, for example, for vacuum cleaner suction units where the motor operates in a single-channel mode, it is possible to use a two-phase SRM with an asymmetric rotor. A characteristic feature of such a solution is the possibility to produce torque in any rotor position, contrary to two-phase SRM designs with a symmetric rotor [3–5]. An important issue is the control method selected for such a motor. In paper [6], a specific technique for torque pulsation minimization at high rotor rotational speeds is proposed, while paper [7] discloses a solution for a SRM controller utilizing a signal processor.

The purpose of this paper is to present results obtained from simulations and preliminary laboratory tests of a two-phase 4/2-pole high-speed SRM with an asymmetric rotor. Simulations were aimed at the determination of the effect of control parameters on the performance of the drive. Knowledge of the control parameters allowed in turn to develop algorithms optimizing the performance of the drive at a specific design working point. The designed and constructed control module was based on a microprocessor circuit allowing for convenient implementation of the control algorithm.

2. Mathematical model

Neglecting eddy currents in the stator and rotor cores and assuming that in the case of non-linearity of the magnetic circuit, the associated flux vector $\boldsymbol{\psi}$ depends on the rotor position θ and on N currents in individual machine winding phases $i_1, ..., i_N$ according to definition:

$$\boldsymbol{\psi}(\theta,\mathbf{i}) \stackrel{def}{=} \left[\psi_1(\theta,i_1,...,i_N), ..., \psi_N(\theta,i_1,...,i_N) \right]^T, \tag{1}$$

equations describing a N-phase SRM can be written as follows:

$$\mathbf{u} = \mathbf{R}\,\mathbf{i} + \frac{\mathrm{d}}{\mathrm{d}t}\boldsymbol{\psi}(\theta, \mathbf{i}) \,, \tag{2}$$

$$J\frac{\mathrm{d}\omega}{\mathrm{d}t} + D\omega + T_L = T_e \,, \tag{3}$$

$$\frac{\mathrm{d}\theta}{\mathrm{d}t} = \omega \,, \tag{4}$$

$$T_e = \frac{\partial W_c^*(\theta, \mathbf{i})}{\partial \theta} \,, \tag{5}$$

where:
$\mathbf{u} = [u_1, ..., u_N]$,
$\mathbf{i} = [i_1, ..., i_N]$,
$\mathbf{R} = \mathrm{diag}[R_1, ..., R_N]$,
θ – the rotor position angle,
ω – rotor angular speed,
J – rotor's moment of inertia,
D – coefficient of viscous friction,
T_L – load torque,
T_e – motor electromagnetic torque,
$W_c^*(\theta, \mathbf{i})$ – total magnetic field co-energy in the machine's air gap.

3. Simulation model

The subject of simulation studies was the two-phase switched reluctance motor with stepper air gap of the rotor. The geometry of the motor is presented in Fig. 1. As the motor has an asymmetric structure, flux-current-angle and torque-current-angle characteristics for the full electric cycle were employed in the simulation model and calculated with the use of FEM. These characteristics for selected phase current values are presented in Fig. 2. As it follows from Fig. 2, the motor can produce a positive torque value within the rotor position range $0° \le \theta \le 110°$. As the motor is designed to be supplied directly from 230 V electric power grid, apart from the motor model and the controlled converter, a bridge rectifier was used. The simulation model was developed in the MATLAB/Simulink environment with the use of the SimPowerSystems library.

Fig. 1. Geometry of the 4/2 SRM: (a) stator, (b) rotor

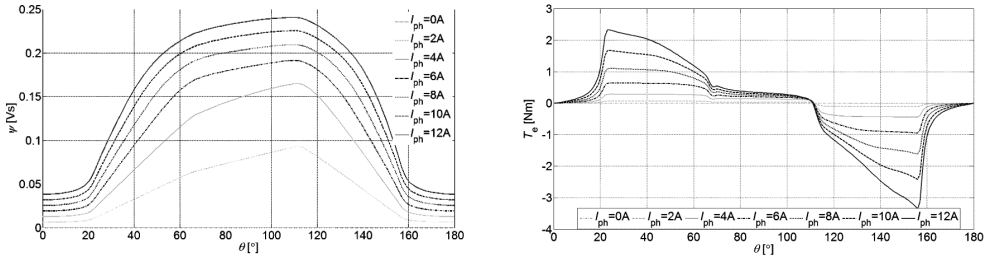

a) b)

Fig. 2. Characteristics of a 4/2 SRM: a) $\psi = f(\theta)$, b) $T_e = f(\theta)$ for different values of current i_{ph}

Parameters of the examined motor are listed in Table 1.

Table 1

Parameters of the examined SRM

Number of stator teeth, *Ns*	4
Number of rotor teeth, N_r	2
Nominal voltage	325 V dc
Nominal rotor speed, n_N	45 000 rpm
Nominal power, P_N	700 W

A block diagram of the simulation model developed for the examined motor is presented in Fig. 3.

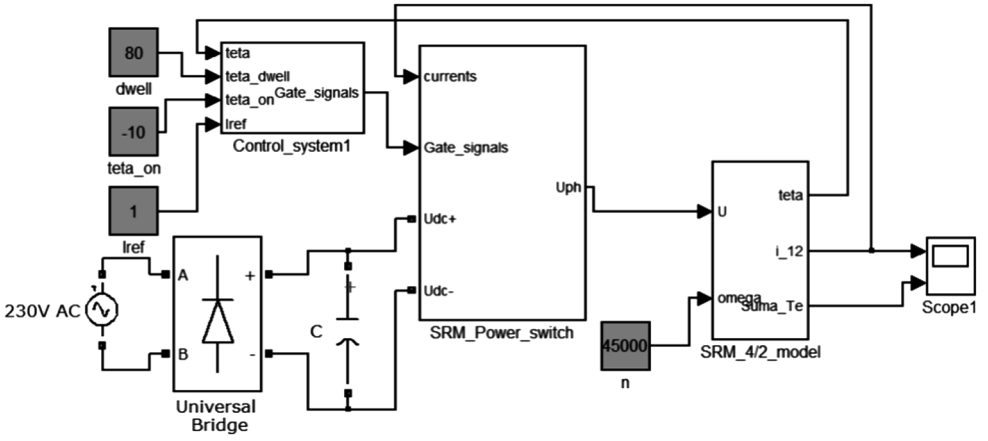

Fig. 3. A block diagram of SRM drive simulation model

The examined motor is designed to be used in a drive for vacuum cleaner suction where high starting torque is not necessary. The angle $\theta = 0°$ was selected as corresponding to the unaligned position of the rotor.

4. Simulation results

4.1. Static characteristics

4.1.1. Supply range $\theta_{supply} = 90°$

Waveforms of the resultant motor torque with idealized square shapes of phase currents i_{ph1} and i_{ph2} for which the maximum value was adopted to be 6 A, for the supply range $\theta_{supply} = 90°$, and turn-on angles $\theta_{on} = 0°$ and 20°, are presented in Fig. 4. Comparing waveforms presented in Figs. 4a) and b), it can be observed that with windings supplied in such a way that $\theta_{on} = 0°$ and $\theta_{supply} = 90°$, there are points in which the starting torque equals 0. In cases where motor windings are supplied with a delay of 20° (counting from the unaligned position of the rotor), the minimum torque value is $T_{emin} = 0.1$ Nm. This means that a 20° turn-on delay results in a significant increase in the motor starting torque; moreover, the torque has a nonzero value in any position of the rotor.

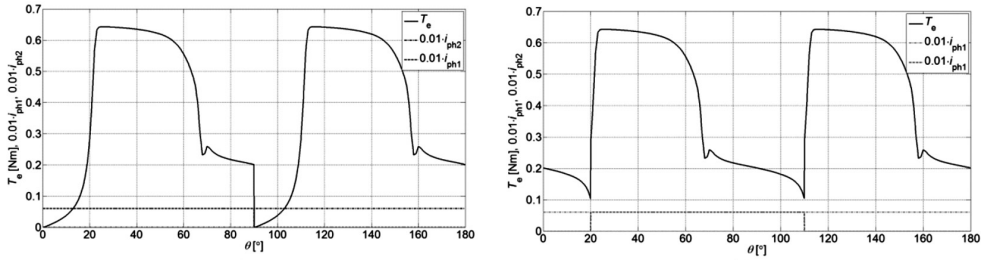

Fig. 4. Motor torque waveforms for the supply angle $\theta_{supply} = 90°$ and the turn-on angle: a) $\theta_{on} = 0°$, b) $\theta_{on} = 20°$

4.1.2. Supply range $\theta_{supply} = 110°$

The examined motor achieves the largest starting torque when the turn-on angle is $\theta_{on} = 0°$, and the supply range $\theta_{supply} = 110°$.

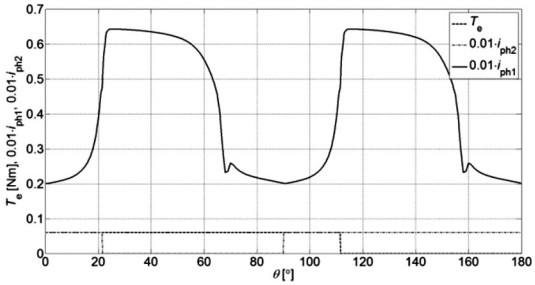

Fig. 5. The motor torque waveform for the supply range $\theta_{supply} = 110°$ and the turn-on angle $\theta_{on} = 0°$

For these parameters, the minimum torque value is T_{emin} = 0.2 Nm. The torque waveform for this case is presented in Fig. 5. When θ_{supply} = 110° and θ_{on} = 0°, the minimum starting torque value is twice as high compared to the case θ_{supply} = 90° and θ_{on} = 20°.

4.2. Motor steady-state operation

4.2.1. Low-speed operation

Plots of the torque average value (T_{eav}), supply current (I_{dcav}), T_{eav}/I_{dcav} ratio, and the torque minimum value (T_{emin}) as functions of the turn-on angle are shown in Fig. 6. The characteristics have been determined for motor speed n = 100 rpm and different supply ranges (θ_{supply}) that were changed within the interval from 90° to 110°, with phase currents limited to I_{ref} = 6 A.

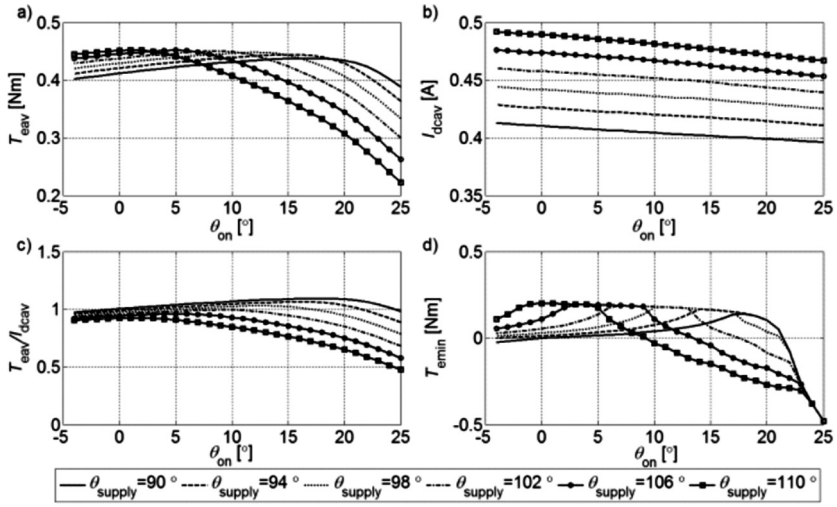

Fig. 6. Functional relationships for different supply ranges (θ_{supply}): a) $T_{eav} = f(\theta_{on})$, b) $I_{dcav} = f(\theta_{on})$, c) $T_{eav}/I_{dcav} = f(\theta_{on})$, d) $T_{emin} = f(\theta_{on})$, at n = 100 rpm; I_{ref} = 6 A

It follows from Fig. 6a) that it is possible to maintain the average torque produced by the motor on the level T_{eav} = 0.45 Nm, with phase current amplitude set to 6 A for various combinations of the turn-on angle and supply range values. A parameter very important for motor performance at starting is the minimum torque value T_{emin}, presented in Fig. 6d) as a function of the turn-on angle for different supply ranges. Delaying the winding turn-on position by angles larger than 20° results in a rapid decrease of the minimum torque value. The maximum T_{eav}/I_{dcav} ratio occurs for the supply range θ_{supply} = 90° and the turn-on angle θ_{on} = 20° (Fig. 6c)). The supply current value I_{dcav} as a function of the turn-on angle for different supply ranges is presented in Fig. 6b).

4.2.2. Nominal operating point

The examined motor is designed to operate at nominal speed n_N = 45 000 rpm and output mechanical power P_N = 700 W. To ensure an adequate amount of the produced torque with increasing speed, it is necessary to change the control position angles. This mainly follows from increase of back-EMF. Figure 7 shows waveforms of phase currents (i_{ph1}, i_{ph2}), phase torques (T_{eph1}, T_{eph2}), and the total electromagnetic current (T_e) of the motor determined under the following conditions: U_{dc} = 325 V; n = 45 000 rpm; $\theta_{on} = -7°$; $\theta_{supply} = 90°$ (Fig. 7a)) and $\theta_{supply} = 70°$ (Fig. 7b)). At high rotor speeds, reduction of the supply range from 90° to 70° results in an increase of the produced torque average value because phase currents decay before the dropping inductance zone. When the motor is supplied at its nominal operating point with a supply range of 70°, no negative torque occurs – this can be clearly seen by comparing waveforms of torques T_{eph1} and T_{eph2} in Figs. 7a) and b).

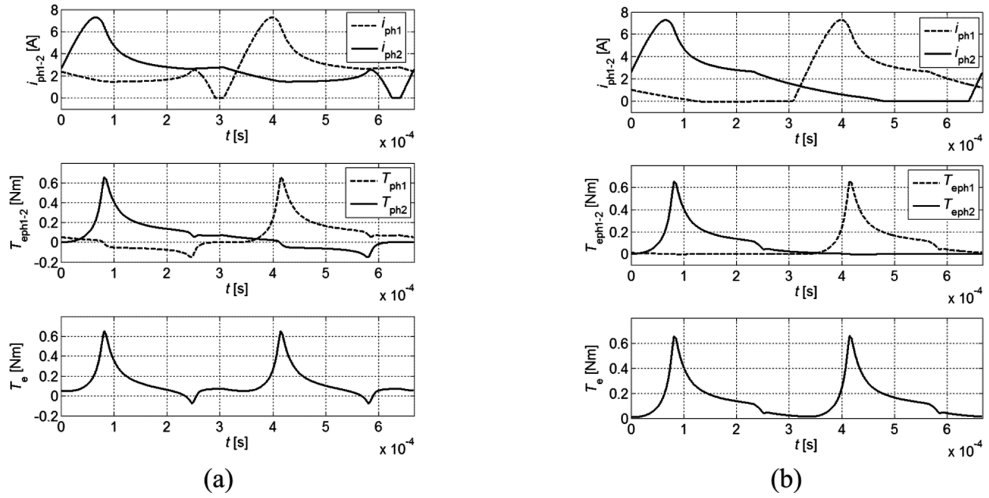

Fig. 7. Waveforms of phase currents i_{ph1}, i_{ph2}, phase torques T_{eph1}, T_{eph2}, and total torque T_e for motor speed n = 45 000 rpm, voltage U_{dc} = 325 V, turn-on angle $\theta_{on} = -7°$, and two different supply ranges: a) $\theta_{supply} = 90°$, b) $\theta_{supply} = 70°$

4.3. PWM control

In Figure 8, waveforms of phase currents i_{ph1}, i_{ph2} and phase voltages u_{ph1}, u_{ph2} are shown for two PWM signal carrier wave frequencies f_{PWM} = 8 kHz (Fig. 8a)) and f_{PWM} = 16 kHz (Fig. 8b)) at the duty cycle δ = 0.8. The waveforms were determined for motor speed n = 39 000 rpm, U_{dc} = 325 V, $\theta_{on} = -3°$, and $\theta_{supply} = 70°$.

It can be seen that at the frequency f_{PWM} = 8 kHz, a significant asymmetry of phase currents appears resulting from too small a ratio of the carrier wave frequency f_{PWM} to the individual phase switching frequency f_{switch}. For motor speed n = 39 000 rpm, f_{switch} = 1.3 kHz, and the ratio f_{PWM}/f_{switch} = 6.15. Doubling the frequency f_{PWM} significantly reduces change vari-

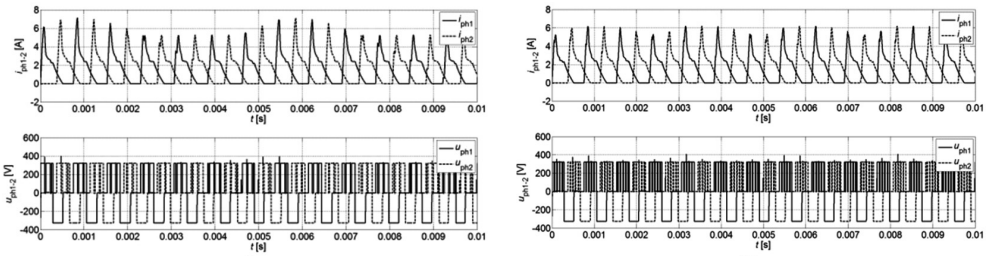

Fig. 8. Waveforms of phase currents (i_{ph1}, i_{ph2}) and voltages (u_{ph1}, u_{ph2}) determined for motor speed n = 39 000 rpm and frequencies: a) f_{PWM} = 8 kHz, b) f_{PWM} = 16 kHz

ability of phase current maximum values, although the changes are still clearly visible (Fig. 8b)). When developing a controller for SRM, it should be considered that with increasing switching frequency, losses in power transistor circuits also significantly increase.

4.4. Motor starting

In order to simulate the conditions prevailing in the examined machine at starting, the simulation model of Fig. 3 was complemented with the equation of torques (3). To limit the source current at starting, a limitation on the phase current maximum values was introduced. Such a phase current limit has been set to I_{ref} = 10 A. Phase currents and motor speed as functions of time at motor starting are plotted in Fig. 9.

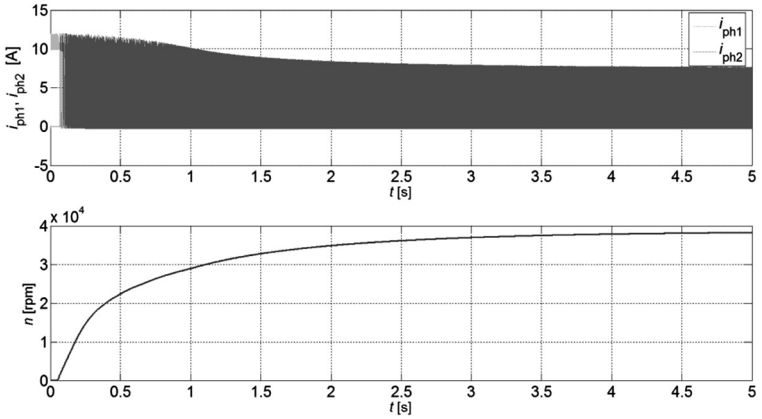

Fig. 9. Phase currents and motor speed as functions of time at the start of two-phase SRM

5. Experimental test

Based on results obtained from simulation, a controller for the two-phase SRM was developed and constructed. A view of the controller together with the tested motor is shown in Fig. 10.

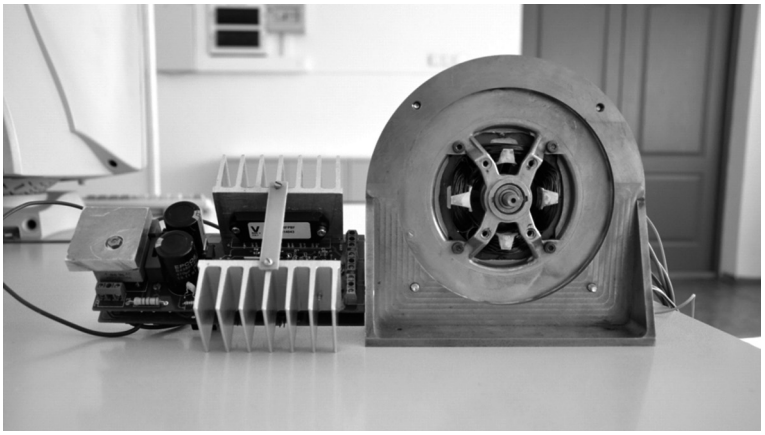

Fig. 10. A view of the 4/2 SRM together with controller

Figs. 11a) and b) present oscillograms registered in the course of the preliminary examination of the motor. The oscillograms were taken at the supply voltage lowered to $U_{dc} = 52$ V.

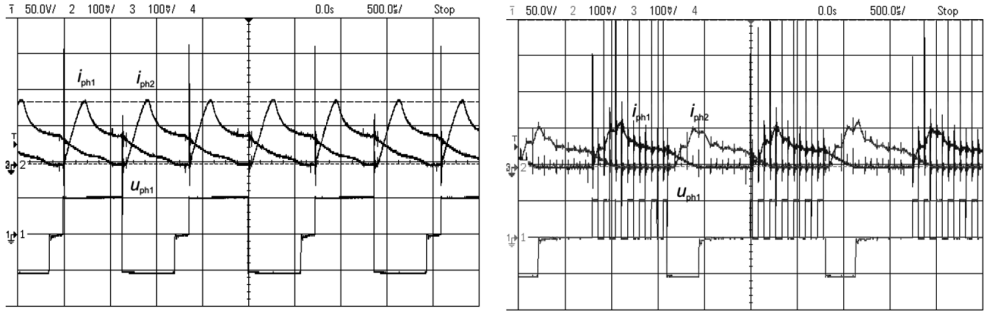

Fig. 11. Phase currents and phase voltage oscillograms for $U_{dc} = 52$ V, $\theta_{on} = -5°$, $\theta_{supply} = 85°$: a) $\delta = 100\%$, $n = 23\,634$ rpm, b) $\delta = 40\%$, $n = 16\,514$ rpm

Figure 11a) shows an oscillogram taken under single-pulse control, while Fig. 11b) presents an oscillogram corresponding to control with the PWM method ($\delta = 40\%$).

6. Conclusions

With the use of the mathematical model of the SRM presented above, a simulation model of a high-speed 4/2-pole two-phase SRM with an asymmetric rotor was developed in the MATLAB/Simulink environment. The model was used for carrying out simulations aimed at the determination of performance of the motor at very low rotor speeds (motor starting) as well as at revs close to the nominal speed. The obtained results are expected to be useful in the development of an uncomplicated and inexpensive controller for motors of that type. On the grounds of the obtained results, it can be stated that:

– In the course of motor starting, the supply range should fall into the 90° to 110° bracket in order to ensure sufficient starting torque, whereas the turn-on angle should be properly adapted to the supply range.
– At high rotor speeds, the introduction of speed control by means of a supply voltage with the use of the pulse width modulation method requires the use of a PWM signal carrier wave of high frequency (> 16 kHz); otherwise, a very large asymmetry of phase currents occurs. It must be remembered that an excessively high PWM signal frequency results in significant losses in the converter circuit.
– With PWM control and at high rotor speeds, significant asymmetry of phase currents occurs, therefore, speed control in such circumstances should be exercised by appropriate change of the turn-on angle.

References

[1] Hamdy R., Fletcher J.E., Williams B.W., *Bidirectional starting of a symmetry two-phase switched reluctance machine*, IEEE Transactions on Energy Conversion, 2000, Vol. 15(2), pp. 211–217.

[2] Wen Ding, Ling Liu, Jianyong Lou, *Design and control of a high-speed switched reluctance machine with conical magnetic bearings for aircraft application*, Electric Power Applications, IET, 2013, Vol. 7(3), pp. 179–190.

[3] Khater M.M., Afifi W.A., Ei-Khazendar M.A., *Operating performances of a two-phase switched reluctance motor*, 11th International Power Systems Conference, MEPCON 2006, Vol. 2, pp. 636–642.

[4] Wróbel K., Tomczewski K., *Jednoczesna optymalizacja kształtu obwodu magnetycznego i parametrów zasilania przełączalnego silnika reluktancyjnego* [*Simultaneous optimization of the magnetic circuit shape and supply parameters of the switched reluctance motor*], Przegląd Elektrotechniczny, 2009, Vol. 85(3), pp. 107–110.

[5] Bogusz P., Korkosz M., Prokop J., *Analiza rozwiązań konstrukcyjnych silników reluktancyjnych przełączalnych przeznaczonych do napędów wysokoobrotowych* [*An analysis of switched reluctance motor solutions designed for high-speed drives*], Zeszyty Problemowe – Maszyny Elektryczne, 2012, No. 1(94), pp. 25–31.

[6] So-Yeon Ahn, Jin-Woo Ahn, Dong-Hee Lee, *A Novel Torque Controller Design for High Speed SRM using Negative Torque Compensator*, IEEE 8th International Conference on Power Electronics and ECCE Asia (ICPE & ECCE), 2011, pp. 937–944.

[7] Qingqing Ma, Daqiang Bi, Baoming Ge, *Digital Control Issue of High Speed Switched Reluctance Motor*, IEEE International Symposium on Industry Electronics (ISIE), 2012, pp. 641–646.

TECHNICAL TRANSACTIONS | **CZASOPISMO TECHNICZNE**
ELECTRICAL ENGINEERING | ELEKTROTECHNIKA
1-E/2015

WOJCIECH BURLIKOWSKI, ZYGMUNT KOWALIK*

ERROR ANALYSIS IN MATHEMATICAL MODEL OF ELECTROMECHANICAL ACTUATOR USING HAMILTONIAN EQUATIONS

ANALIZA BŁĘDU W MODELU MATEMATYCZNYM PRZETWORNIKA ELEKTROMECHANICZNEGO WYKORZYSTUJĄCYM RÓWNANIA HAMILTONA

A b s t r a c t

This paper presents a methodology of error analysis in a mathematical model of an electromechanical actuator using Hamiltonian equations in the description of energy conversion. As the basic quantity in numerical algorithms, the coenergy of magnetic field E_{cm} is employed. The reason for the application of coenergy as a state function is the explicitness of its value for a given set of state variables, resulting from neglecting eddy currents and hysteresis phenomenon in the model.

Keywords: *electrical machines*, *Hamiltonian equations*, *error analysis*, *relative error*

S t r e s z c z e n i e

W artykule przedstawiono metodykę analizy błędu w modelu matematycznym przetwornika elektromechanicznego wykorzystującym równania Hamiltona w opisie przemiany elektromechanicznej. Jako podstawowej wielkości w algorytmie obliczeniowym użyto koenergii pola magnetycznego E_{cm}. Wykorzystano w tym celu jednoznaczność określenia wartości koenergii dla danej wartości zmiennych stanu, wynikającą z pominięcia w modelu prądów wirowych oraz zjawiska histerezy.

Słowa kluczowe: *maszyny elektryczne*, *równania Hamiltona*, *analiza błędu*, *błąd względny*
DOI: 10.4467/2353737XCT.15.033.3833

* D.Sc. Ph.D. Eng. Wojciech Burlikowski, M.Sc. Eng. Zygmunt Kowalik, Department of Mechatronics, Faculty of Electrical Engineering, Silesian University of Technology, Gliwice.

1. Introduction

In the case of electromechanical actuators, the main advantage of the Hamiltonian model compared to equivalent Lagrangian model is the canonical form of its equations [11]. This feature is particularly important in the computer implementation of this model due to the possible application of discrete databases concerning only currents and flux linkages as the input values. These values can be obtained using numerical analysis (e.g. using the finite elements method FEM [3, 4]) or through measurements. Due to the lack of a method for determining magnetic field coenergy by measurements, it is assumed that it is not available during the mathematical model construction, although there are numerical methods for its determination [8].

2. Error sources

Independently of the method for determining the input values, in the simulation model there are possible errors, the sources of which are:

a) simplicial approximation – this is a topological method of current-flux characteristic approximation based on the triangulation of the discrete databases which define this characteristic,
b) uncertainty of currents and flux values related to numerical (using FEM, [8]) or measurement [10] errors.

In this paper, an error resulting from the first source mentioned above is analysed. As the measure of this error, a local deviation ΔE_{cm} from explicitness of the coenergy computation inside a single simplex from a triangulated current set is taken [1, 3, 6]. The obtained results are compared with a mathematically equivalent reciprocity principle, relating to the symmetry of the dynamic inductance matrix in the case of an electromechanical actuator [11]. The mechanical equation was not considered as the analysis concerns a constant rotor angular position $\vartheta = \text{const}$ (Fig. 1).

3. Canonical equations

In the paper, a 3-phase synchronous reluctance machine SynRM with wye-connected stator windings without neutral wire is analysed as an exemplary electromechanical actuator (Fig. 1) [2]. The differential equation describing an electrical part of the model is:

$$\mathbf{e} = \frac{\mathrm{d}\Psi}{\mathrm{d}t} + \mathbf{R}\mathbf{i} \tag{1}$$

where:
$\mathbf{i} = [i_A, i_B]^T$ – the generalized currents vector,
$\Psi = [\psi_{AC}, \psi_{BC}]^T = [\psi_A - \psi_C, \psi_B - \psi_C]^T$ – the generalized flux linkages vector,
$\mathbf{e} = [e_{AC}, e_{BC}]^T$ – the generalized external voltages vector,
$\mathbf{R}$ – resistance matrix.

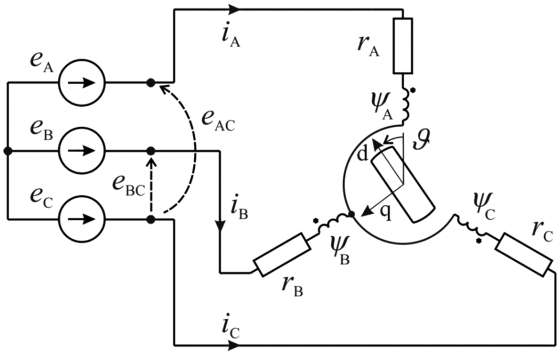

Fig. 1. A scheme of a SynRM machine

The choice of considering the wye-connected stator windings without neutral wire is made because of its great practical importance, as well as it ensuring the lowest possible state space dimension $N = 2$, which allows the electromechanical system as a whole to be graphically analysed [4].

Obtaining a set of canonical equations based on equation (1) requires setting state variables and dependent variables. The choice leads to one of the two forms of canonical equations [4, 11]:

a) Hamilton equations, in which flux linkages are state variables (such a model is called HMEA – Hamiltonian Model of Electromechanical Actuator):

$$\frac{\mathrm{d}\Psi}{\mathrm{d}t} = \mathbf{e} - \mathbf{R}\mathbf{i}\left(\vartheta, \Psi\right) \tag{2}$$

b) Lagrange equations, in which **currents** are state variables:

$$\frac{\mathrm{d}\mathbf{i}}{\mathrm{d}t} = \left(\mathbf{L}_d\left(\vartheta, \mathbf{i}\right)\right)^{-1}\left(\mathbf{e} - \left(\omega\frac{\partial\Psi\left(\vartheta, \mathbf{i}\right)}{\partial\vartheta} + \mathbf{R}\mathbf{i}\right)\right) \tag{3}$$

where:
ω – mechanical angular velocity of the rotor,
$\mathbf{L}_d(\vartheta, \mathbf{i})$ – dynamic inductance matrix [11].

4. Synergy features used in HMEA

In the considered electromechanical system, there are no elements that store potential energy. In this case, coenergy E_{cm} can be expressed as a scalar product of two generalized quantities relating to the magnetic field:

$$E_{cm}(\vartheta,\mathbf{i}) = \int_0^{\mathbf{i}} \Psi \cdot \mathrm{d}\mathbf{i} \tag{4}$$

Due to the fact that coenergy is a state function of the considered system, its change along a closed path equals zero:

$$\oint \Psi \cdot \mathrm{d}\mathbf{i} = 0 \tag{5}$$

It allows a flux linkage vector field defined in the current space **RI** (which is, for $N = 2$, a subspace of a three-dimensional Euclidean space $\boldsymbol{E}^3$ with a standard basis $\left[\vec{e}_{i\mathrm{A}} \quad \vec{e}_{i\mathrm{B}} \quad \vec{e}_{i\mathrm{C}}\right]$) to be interpreted as a curless field (Stokes' theorem):

$$\operatorname{rot}\Psi = \begin{vmatrix} \vec{e}_{i\mathrm{A}} & \vec{e}_{i\mathrm{B}} & \vec{e}_{i\mathrm{C}} \\ \dfrac{\partial}{\partial i_{\mathrm{A}}} & \dfrac{\partial}{\partial i_{\mathrm{B}}} & 0 \\ \psi_{\mathrm{AC}} & \psi_{\mathrm{BC}} & 0 \end{vmatrix} = \mathbf{0} \tag{6}$$

which yields:

$$\vec{e}_{i\mathrm{C}}\left(\frac{\partial\psi_{\mathrm{AC}}}{\partial i_{\mathrm{B}}} - \frac{\partial\psi_{\mathrm{BC}}}{\partial i_{\mathrm{A}}}\right) = \mathbf{0} \tag{7}$$

and is equivalent to the symmetry of the dynamic inductance matrix $\mathbf{L}_d(\vartheta, \mathbf{i})$ of the analysed system.

5. Discrete model of the electromechanical actuator

The discrete model is formulated using data collected by a numerical analysis using the FEM method and a FEMM computer program [7]. A FEM model of a prototype SynRM machine was created. This prototype machine is based on a stator from a mass produced RSg 80-4A induction motor by the BESEL company. Its basic characteristic features, fundamental for a mathematical model construction, are as follows:

- Rated current $I_n = 2.2$ A,
- Number of stator poles $2p = 4$,
- Number of stator slots $Q_s = 36$,
- Number of rotor poles $Q_r = 4$,
- Rotor's length $l_r = 72$ mm,
- Number of turns per slot $z_s = 90$,
- Air gap length $\delta = 0.25$ mm.

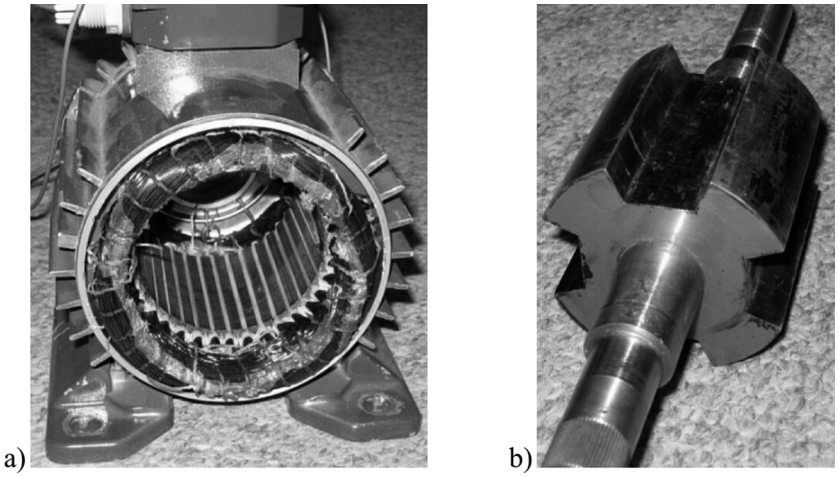

Fig. 2. A pictorial view of a stator (a) and a rotor (b) of a modeled SynRM machine

The numerical analysis was made for a currents set I^k, which is a Cartesian product of a sequence $I = \{-4\text{ A}; -3.5\text{ A}; \ldots; 4\text{ A}\}$, i.e. $I^k = I \times I$. For each point $\mathbf{i}_p \in I^k$ (Fig. 3) a flux linkages vector $\mathbf{\Psi}_p$ was computed, thus constructing a set $\Psi^k = \{\mathbf{\Psi}_1, \mathbf{\Psi}_1, \ldots, \mathbf{\Psi}_K\}$, K – number of points (Fig. 4). The set Ψ^k is a subset of a flux linkage space $\mathbf{R\Psi} \subset E^N$.

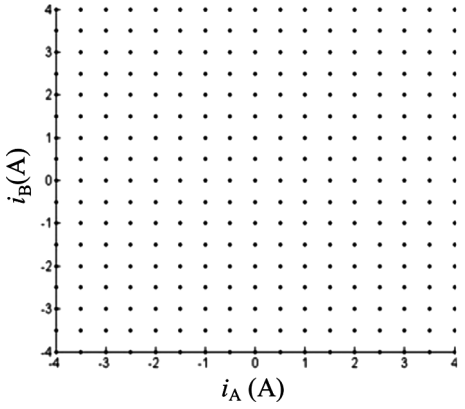

Fig. 3. Currents set I^k

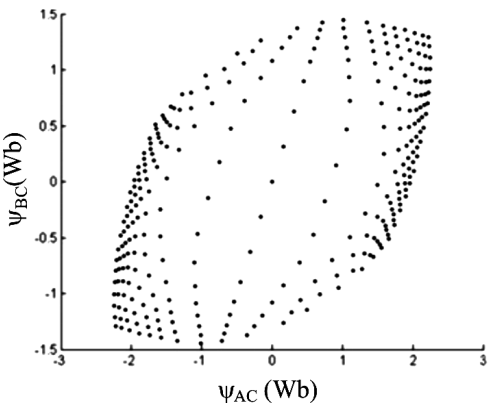

Fig. 4. Flux linkages set Ψ^k

6. Error definition in HMEA

Due to a homeomorphism between currents space **RI** and flux linkages space **RΨ**, coming from assumed uniqueness of magnetization characteristic, further analysis concerns a T^k triangulation defined on a set I^k using Delaunay algorithm (Fig. 5) [1, 6]. The triangulation result is a simplex grid (which are triangles for $N = 2$), which enables flux linkage computation in every point of space **RI** using the simplicial approximation [3, 6].

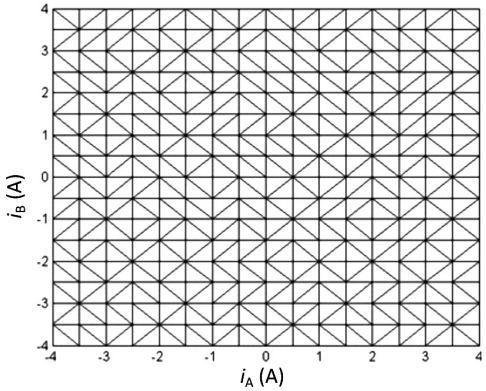

Fig. 5.Currents subspace triangulation $T^k(I^k)$

Because flux linkage values, obtained either from numerical analysis or measurements, are taken with an error and because of the use of simplicial approximation, coenergy in every simplex is computed with an error. Therefore, the influence of this error value generated by both of the aforementioned factors on the computed integral values needs to be explored [9]. As a measure of this error, a local deviation ΔE_{cm} from explicitness of the coenergy computation inside each simplex $\Delta^k_{I,j}$ of the triangulated currents set is used:

$$\oint_{\partial S_I} \Psi \cdot \mathbf{di} = \Delta E_{cm} \tag{8}$$

where:
∂S_I – analysed simplex boundary (Fig. 6).

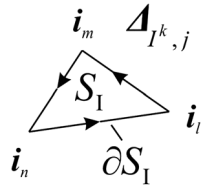

Fig. 6. A Simplex S_I in the currents subspace

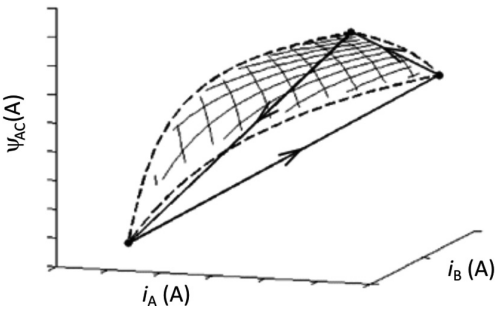

Fig. 7. Graphical interpretation of the error related to the curvature of the current-flux characteristic

The ΔE_{cm} value is equal to 0 for an accurate values of currents and flux linkages (dashed line, Fig. 7). For a linear approximation of a current-flux characteristic an error appears (solid line, Fig. 7).

The exact measure of an error for a given simplex $\Delta_{I^k,j}$ is a relative error value expressed as [10]:

$$\delta E_{cm} = \frac{\Delta E_{cm}}{\bar{E}_{cm}} \tag{9}$$

where $\bar{E}_{cm}$ – average value of coenergy in a given simplex (Fig. 6).

For simplicity, $\bar{E}_{cm}$ is defined as an arithmetical average of the coenergy value in the vertices of a given simplex [4].

7. Error definition in a Lagrangian model

Similar to the HMEA, a relative error in a model based on Lagrange equations was defined. As a measure of it, a violation rate of the reciprocity principle was chosen. This error is related to the symmetry of the dynamic inductance matrix:

$$\Delta L_d = \frac{\partial \psi_{\mathrm{AC}}}{\partial i_{\mathrm{B}}} - \frac{\partial \psi_{\mathrm{BC}}}{\partial i_{\mathrm{A}}} \tag{10}$$

According to equations (5) and (7), this value is an analogue to the ΔE_{cm} parameter expressed by equation (8). The relative error value is defined as:

$$\delta L_d = 2\frac{\Delta L_d}{\left(\left|\frac{\partial \psi_{\mathrm{AC}}}{\partial i_{\mathrm{B}}}\right| + \left|\frac{\partial \psi_{\mathrm{BC}}}{\partial i_{\mathrm{A}}}\right|\right)} \tag{11}$$

In formulas (10) and (11) for the derivatives approximation a central difference algorithm is used [9].

8. Computational results

In Figures 8–10, it can be seen that in both cases, the absolute error value is the largest at the transition between the linear area of the current-flux characteristic and the area in which magnetic saturation is observed (Fig. 10).

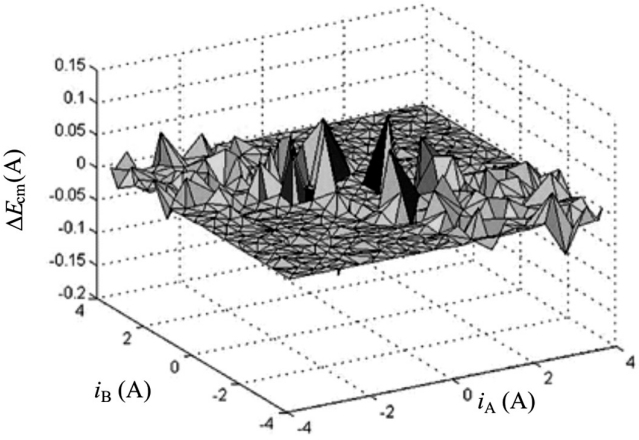

Fig. 8. Absolute error in HMEA

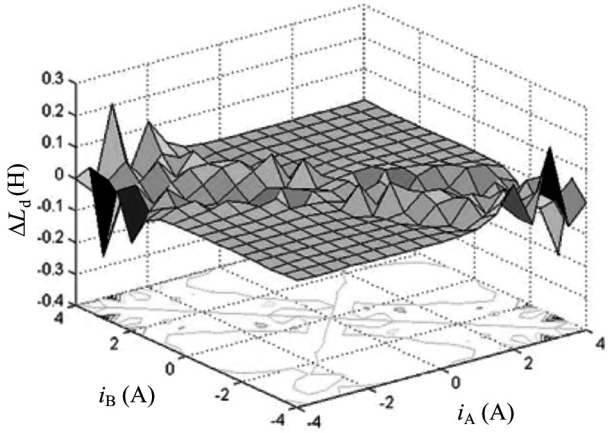

Fig. 9. Absolute error in the Lagrangian model

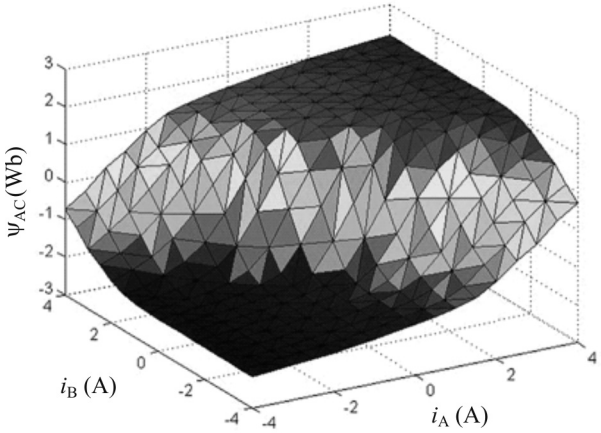

Fig. 10. Current flux characteristic $\psi_{AC}(i_A, i_B, \vartheta = 30°)$

This result is as expected as in this region, the curvature of the current-flux characteristic is the highest (Fig. 10). These results are consistent with the computed relative error values in the HMEA model (Fig. 11). In the case of the Lagrangian model, a relative error distribution is far from prediction (Fig. 12).

For computation, a rotor angular position $\vartheta = 30°$ is chosen, as a coupling between generalized windings is the largest for this angular position [3, 4].

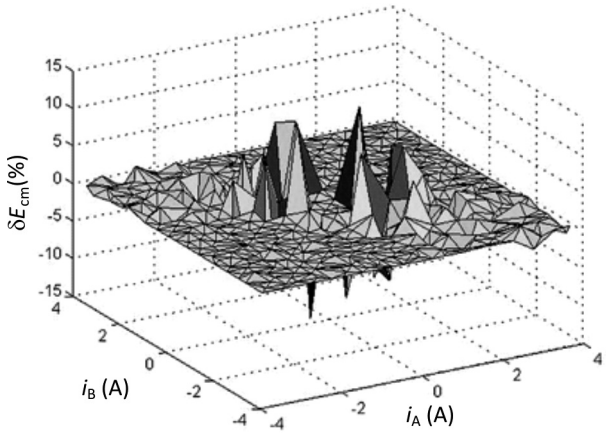

Fig. 11. Relative error in HMEA

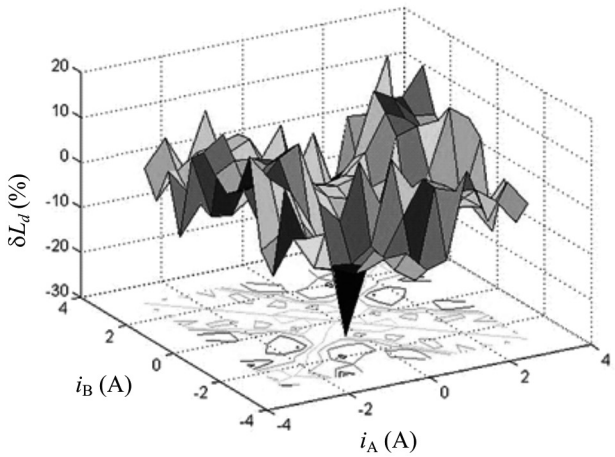

Fig. 12. Relative error in Lagrange model

9. Conclusions

General conclusions that come from the comparison between relative errors in both the HMEA and Lagrangian model are as follows:

a) relative error range is similar in both cases (15%–20%),
b) a possible simple algorithm of error minimization can be used in HMEA (barycentric subdivision [6]) due to the lack of necessity of complicated numerical differentiation [9]. This results in a reduction of the region, where computed errors are the largest, to the region of the highest curvature of the current-flux characteristic (Fig. 10),
c) there is a necessity for much more precise methods for computing elements of dynamic inductance matrix in the Lagrangian model. It has to be done probably as early as during FEM numerical analysis [5],
d) in case of the Lagrangian model, a relative error distribution is stochastic in the whole analysed currents subspace (Fig. 12), which makes its minimization harder, as it requires increased database accuracy in the whole considered range.

References

[1] Agoston M.K., *Computer Graphics and Geometric Modeling – Mathematics*, Springer, 2005.
[2] Boldea I., Tutelea L., *Electric machines: steady state, transients and design with Matlab*, CRC Press, 2009.
[3] Burlikowski W., *Reluctance motor mathematical model in natural reference frame using hamiltonian equations – simulational analysis*, Zeszyty Problemowe – Maszyny Elektryczne, 2011, nr 93, BOBRME Komel, pp. 19–24.
[4] Burlikowski W., *Zastosowanie formalizmu Hamiltona w opisie przetwornika elektromechanicznego na przykładzie silnika reluktancyjnego*, Zeszyty Naukowe Politechniki Śląskiej „Elektryka", Monografia, z. 373, Gliwice 2012.
[5] Demenko A., Hameyer K., *Field and field-circuit description of electrical machines*, Proc. of EPE-PEMC 2008, pp. 2412–2419.
[6] Kuratowski K., *Wstęp do teorii mnogości i topologii*, PWN, Warszawa 2004.
[7] Meeker D., *Finite Element Method Magnetics. User's Manual*, ver. 4.2, 2007.
[8] Meunier G. et al., *The Finite Element Method for Electromagnetic Modeling*, ISTE Ltd, 2008.
[9] Ralston A., *Wstęp do analizy numerycznej*, wyd. 3, PWN, Warszawa 1983.
[10] Skubis T., *Opracowanie wyników pomiarów: przykłady*, Wydawnictwo Politechniki Śląskiej, Gliwice 2003.
[11] Sobczyk T.J., *Metodyczne aspekty modelowania maszyn elektrycznych prądu przemiennego*, WNT, Warszawa 2004.

TECHNICAL TRANSACTIONS | **CZASOPISMO TECHNICZNE**
ELECTRICAL ENGINEERING | ELEKTROTECHNIKA
1-E/2015

ADRIAN MLOT*, MARIUSZ KORKOSZ**, MARIAN ŁUKANISZYN*

A SINGLE-PHASE SLOTLESS AXIAL-FLUX LOW-POWER GENERATOR WITH FERRITE MAGNETS

BEZŻŁOBKOWY 1-FAZOWY GENERATOR MAŁEJ MOCY O STRUMIENIU OSIOWYM Z MAGNESAMI FERRYTOWYMI

Abstract

The design and development of an axial-flux ferrite magnet slotless generator for use in a small-scale wind turbine is described. The 4/4-pole single-phase machine is designed for simplicity and ease of manufacture and it consists of one slotless stator disc. The generator produces approx. 12 W at 1000 rpm with electrical efficiency of up to 46%. Because the efficiency of the machine is important, the power curve characteristics and voltage produced by the generator are investigated. The presented generator should generate sufficient output DC voltage to charge 4 to 5 batteries of 12 volt each. Finally, the finite element (FE) results are compared with measurements on a prototype. The calculated values coincide to a strong degree with the experimental results.

Keywords: *single-phase axial-flux machine*, *ferrite magnet generator*, *wind turbine application*, *efficiency*

Streszczenie

Przedmiotem badań w niniejszym artykule jest prototyp generatora tarczowego, przewidzianego do zastosowania w małej elektrowni wiatrowej. Przedstawiono pomiary i obliczenia numeryczne ważniejszych parametrów funkcjonalnych, takich jak: sprawność, moc wyjściowa i moment elektromagnetyczny generatora tarczowego z magnesami ferrytowymi o strumieniu osiowym. Zbudowany prototyp generatorów o 4 biegunach stojana i wirnika posiada jednofazowe uzwojenie bezżłobkowe. W badanym generatorze zastosowano magnesy ferrytowe o przekroju prostokątnym oraz cewki owalne. Zasadniczym parametrem generatora jest napięcie rotacji, które powinno być wystarczająco wysokie do naładowania określonej liczby akumulatorów. W zamieszczonych poniżej rozważniach pominięto wpływ napięcia i rezystancji wewnętrznej baterii na parametry generatora. Analiza ta będzie kontynuowana w przyszłych badaniach. Do obliczeń pola magnetycznego zastosowano metodę trójwymiarową (3-D) opartą na metodzie elementów skończonych (MES).

Słowa kluczowe: *generatory jednofazowe ze strumieniem osiowym*, *małe turbiny wiatrowe*, *sprawność*

DOI: 10.4467/2353737XCT.15.034.3834

* Ph.D. Eng. Adrian Mlot, Prof. D.Sc. Ph.D. Eng. Marian Lukaniszyn, Faculty of Electrical Engineering, Automatic Control and Informatics, Opole University of Technology.

** D.Sc. Ph.D. Eng. Mariusz Korkosz, Faculty of Electrical and Computer Engineering, Rzeszow University of Technology.

1. Introduction

Permanent magnet (PM) machines offer many unique features. There are two different designs of the machine – radial and axial-flux PM motors. Axial-flux PM machines have a number of distinct advantages over radial-flux machines. They can be designed to have a higher power to weight ratio resulting in less core material. They are also smaller in size than their radial-flux concepts and have disc shaped rotor and stator structures [8–10, 12, 14–17]. Those are important features of axial-flux machines, because suitable shape and size to match the space limitation is crucial for many applications such as electric vehicles, wind turbines etc. [1–7, 11]. The end-windings are quite short which results in making the copper loss of the axial-flux machine smaller (for example, the torus non-slotted structure of the machine). The axial-flux machine can be built as the slotted or non-slotted stator core structures which consist of the stack of laminated steel. They can be constructed in single-stator-single-rotor or multiple-stator-multiple-rotor forms. The rotor can be manufactured with a surface mounted PM machine or an axial flux interior PM machine (an interior magnet structure). Possible axial flux machine structures operating as a motor or generator have been reported in the literature [8–10, 12, 14–17].

The basic and simplest axial-flux structure is the single-rotor and single-stator topology with surface mounted PMs – this machine is presented in this paper as a generator. The machine is a single-phase generator and can be used to generate power in single-phase electric power systems. It is a three-blade wind turbine for use in homes, boats, yachts, light poles, advertising signs etc. The prototype of the wind turbine is shown in Fig. 1a).

The objective of this paper is to examine the axial-flux generator and compare finite element analysis (FEA) with measurements of the electromagnetic torque, output power vs. DC output current at load operation. Additionally, the DC output voltage generated by the wind generator and the efficiency are also investigated. The required DC output voltage of the generator should be suitable to recharge 3 to 5 batteries of 12 V each.

2. Axial-flux generator prototype

The prototype presented in Fig. 1b) consists of the non-slotted stator core as a stack of laminated steel discs. The stator of the machine is made as a wound core. Coils are connected in series and placed into the disc. The space between the coils and the stator disc is filled with epoxy resin to increase robustness and provide a better heat conduction. The rotor structure is formed by surface mounted ferrite magnets, a rotor core formed from a solid steel disk and shaft.

The generator is designed for small outer diameters. Electromagnetic torque is a function of the outer diameter in axial-flux machines. The required torque can be achieved by using multi-stage axial-flux machine structures. This could be easier to assemble and even better torque and power densities could be obtained. The initial aim was to build the machine in such a way that it remained cheap and light. In this case, the authors decided to use thicker ferrite magnets (12.5 mm) rather than build the multi-stage axial-flux generator structure. The one-phase 4-pole stator and 4-pole rotor topology is shown in Fig. 2.

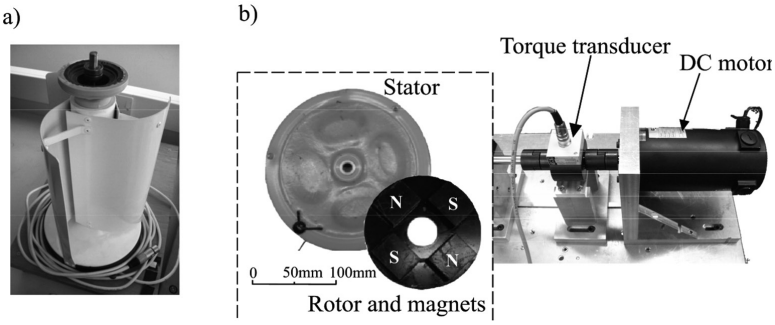

Fig. 1. 3 bladed wind turbine (a) and disassembled a one-phase 4-pole axial-flux generator with test rig (b)

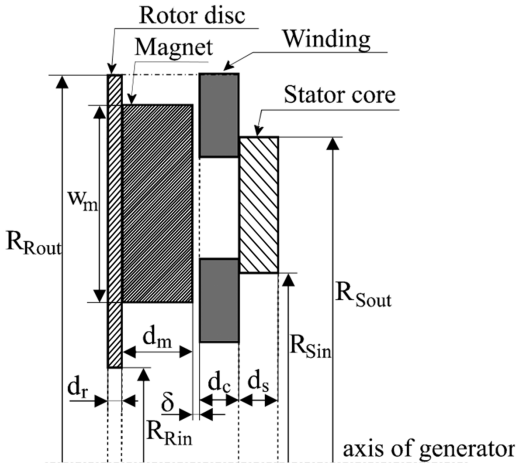

Fig. 2. Single-stator, single-rotor topology of single-phase axial-flux magnet generator

The main dimensions and material specifications of the axial-flux generator are given in Table 1.

Table 1

Dimensions and material specifications of generator

Type of magnet	**Ferrite**
Thickness of magnet (d_m)	12.5 mm
High of magnet (w_m)	35 mm
Width of magnet (l_m)	45 mm
Remanent flux density of the magnets	0.4 T
Outer radius of rotor core/magnet (R_{Rout})	69.2 mm
Inner radius of rotor core/magnet (R_{Rin})	17.2 mm
Thickness of rotor core (d_r)	2.5 mm
Outer radius of stator core (R_{Sout})	58 mm

Table 1 con.

Inner radius of stator core(R_{Sin})	34 mm
Thickness of stator core (d_s)	7 mm
Turn number per coil (n_t)	500
Number of rotor/stator pole	4/4
Thickness of coil (d_c)	7 mm
Air-gap (stator-magnet) (δ)	1.5 mm
Resistance of phase (in series)	78.6 Ω

3. FEA model of single-phase generator

A 3-D FEA model of the generator consists of 4 oval shaped coils connected in series, and 4 square shaped magnets. The 3-D model of the generator has repetitive patterns, then it is possible to model a fraction of the basis geometry such as a ¼ part of the whole generator topology as is shown in Fig. 3a). From a physical point of view, periodicity boundary conditions are set. A single-phase alternating circuit connected through the rectifier circuits produces direct voltage. The DC voltage terminals are connected to the resistive load as shown in Fig. 3b). Here, the battery voltage with internal resistance is neglected and will be investigated in future work.

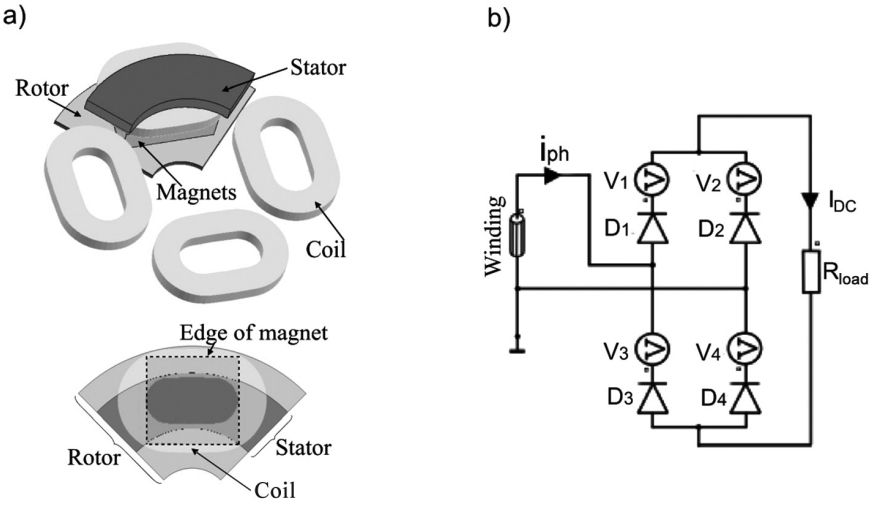

Fig. 3. 3-D FEA model of 1-phase, 4-pole axial-flux generator (a) and the electric circuit producing direct voltage for the wind turbine application with resistive load (b)

4. FEA results and experimental study of the permanent magnet generators

The localized maximum flux distribution in the axial-flux generator is found to be greater in the rotor disk area of the core at approximately 150% of that in the stator disc. The peak value of the flux density at the rotor core is 1.5 T. In this case, at high speed operation the magnet temperature can increase rapidly. The remanent flux density (B_r) of the magnet will then decrease and that will decrease the torque, and consequently, the power and efficiency of the machine. To lower the risk of demagnetization, the size/shape of magnets should be redesigned and/or the thickness of the rotor disc should be increased. Furthermore, the flux density distribution in the air-gap is also shown in Fig. 4.

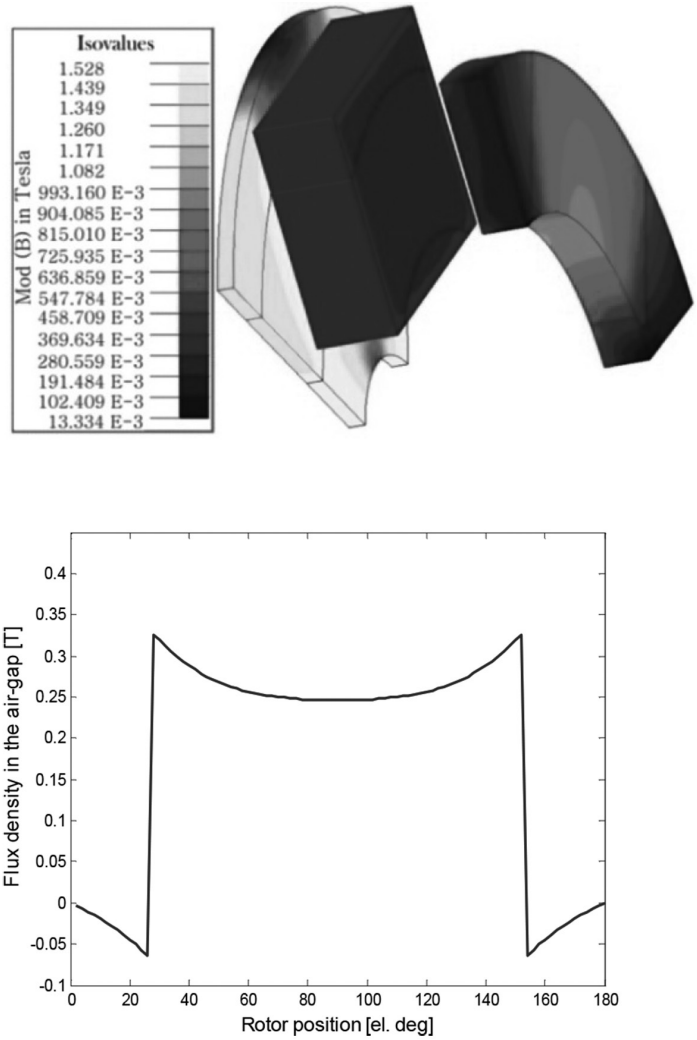

Fig. 4. Flux density distribution in the wind generator and in the air-gap at 1000 rpm under no-load operation

The open-circuit and load characteristics for different rotational speeds are measured. The single-phase load as a diode rectifier with resistive load is connected to the terminal of the generator (Fig. 3). The electromagnetic torque calculated and measured at open-circuit line voltage and the load operation at 1000 rpm is shown in Fig. 5.

Another interesting curve is the one shown in Fig. 6 which depicts the power extracted from the generator as a function of DC current at varied rotor speeds. The dashed red line connects the peak points of all the power curves, and represents the maximum power extraction curve. It clearly shows that the curve rises very quickly as the speed of the generator increases by spinning machine representing a wind.

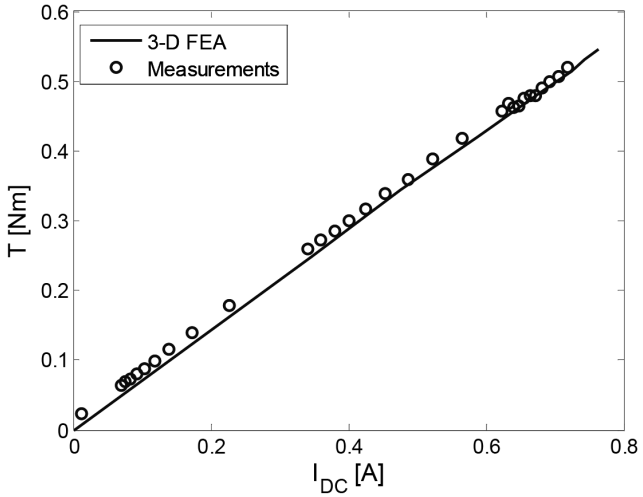

Fig. 5. Measurements and finite element analysis of electromagnetic torque vs. DC output current

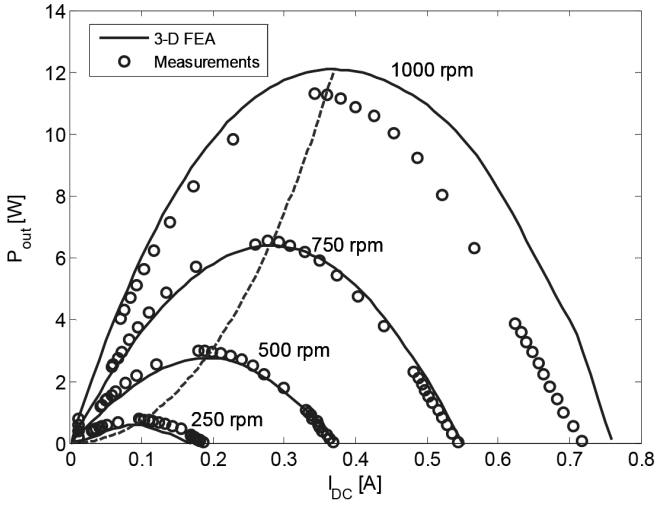

Fig. 6. Measurements and finite element analysis of wind generator output power vs. DC current at varied rotor speed

In the case of the resistive load, the measured voltage of the prototype ferrite magnet generator is about 66 V, the calculated value is 62 V at high speed. The computed data strongly agree with the experimental measurements. The difference may be caused by the magnet temperatures, which differ from those predicted. The calculated line voltages and the output power tended to differ from experimentally measured values by 0.5–20%. This is caused mainly by the fact that the experiment starts from a low speed at the open-circuit operation to the high load operation, therefore, experimental temperatures of the magnets are relatively lower than the temperature set in the FEA model at the first stage of tests. At 1000 rpm, the magnet was already preheated, so the measured power is relatively lower than the predicted values during the test. The working temperature of the load operation is neglected in the finite element analysis and the temperature is set to 25°C.

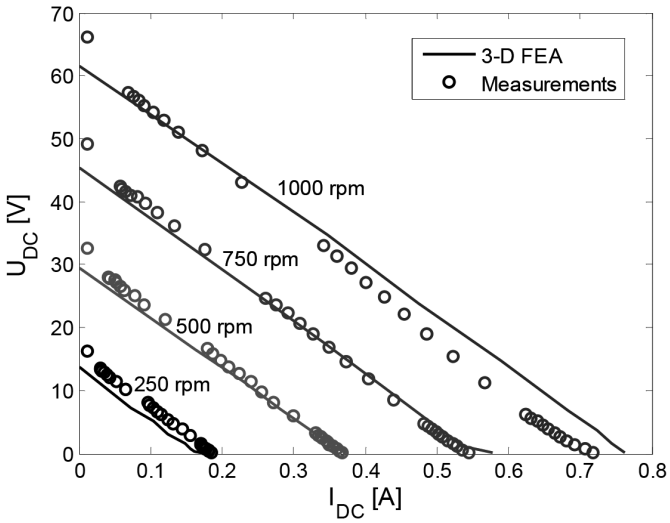

Fig. 7. Measurements and calculations of DC output voltage at varied speed versus DC output current when the terminals of the wind generator are connected to the resistive load

The stiffness characteristic of the presented generator depicted in Fig. 7 is low, owing to the high winding resistance being (R_{ph} = 78.6 Ω) of the small size generator.

The efficiency of the axial flux generator can be calculated as:

$$\eta = \frac{P_{\text{out}}}{P_{\text{in}}} \cdot 100\% \tag{1}$$

where:
P_{out}, P_{in} – the output and input power.

The input power P_{in} is calculated as the sum of mechanical power on the shaft and mechanical losses. Mechanical power of the rotating machine can be expressed as $P_{\text{mech}} = T \cdot \omega$, where T – average electromagnetic torque (Nm), ω – angular velocity (rad/s), and mechanical

losses are assumed to be dependent upon speed. The losses of winding and losses in the rectifier circuit are also taken into account. Because the axial-flux generator operates at a low electrical frequency, the iron losses are very small and can be neglected.

The results of the efficiency vs. DC current at various speeds in the range 250 rpm to 1000 rpm are presented in Fig. 8. It is shown that at 1000 rpm, the efficiency of the investigated generator is $\eta = 45\%$.

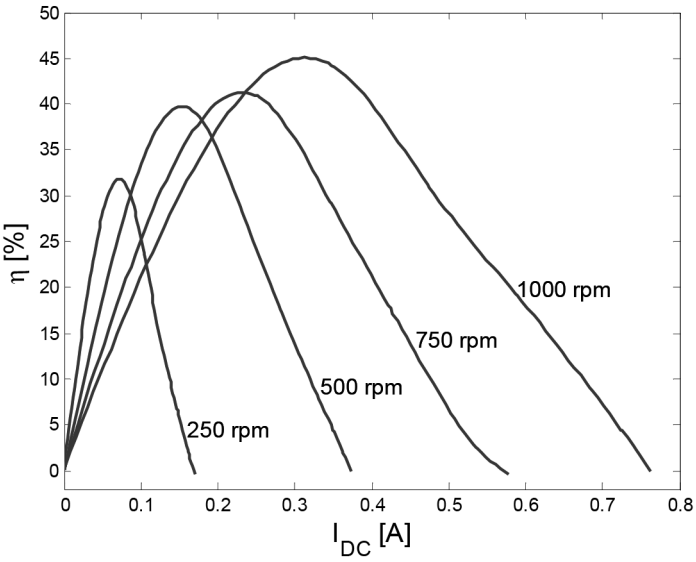

Fig. 8. Efficiency of the axial-flux generator vs. DC current at varied speed

From Figs. 6 and 8, it can be seen that the peaks of the output power and the peaks of the efficiency are roughly at the same DC load currents.

5. Conclusion and future work

This paper has presented the design of a small power axial-flux generator with permanent magnets for small-size wind turbine applications. The concept has comprised a very simple design such as simple wind blades, a disc generator and an electric rectifier circuit. The whole small-scale wind power application has the capability to be manufactured in a small workshop. To calculate the efficiency, mechanical characteristics and output voltage vs. loaded DC current at varied rotor speeds were carried out by using the 3-D software package based on a finite element analysis. The FEA calculation of the electromagnetic torque and output power were verified with measurements to be in strong agreement. The differences between FEA and measurements may be caused by the magnet temperatures.

In the first stage of the experimental tests, the input mechanical energy was fed to drive the rotor of the investigated generator which can change mechanical energy into electrical

energy. The results show that the rotor speed of 1000 rpm while the wind generator terminals were connected to the resistivity load, produce a direct current voltage equal to 62 V at a very low resistivity load, with the efficiency of the generator equal to $\eta = 45\%$, the output DC current equal to 0.34 A, and the power output equal to 12 W.

The most common application of wind turbines is battery charging through a diode rectifier. In this research, the balance of power across the AC and DC sides was investigated without a battery connection. Here, the power supplied to the battery and the DC current to the battery was neglected. The battery voltage and internal resistance can affect current I_{DC} during charging and affect the torque [6, 10]. In future work, the battery internal resistance and battery voltage will be connected to the terminals of the diode rectifier system to investigate the power to the battery.

Acknowledgment

The authors would like to express their gratitude to the Electrical Machine Laboratory, Department of Electrical & Electronic Engineering, University of Bristol, UK, for the support in accessing the experimental axial flux wind generator.

References

[1] Parviainen A., Pyrhonen J., Kontkanen P., *Axial flux PM generator with concentrated winding for small wind power applications*, Electric Machines and Drives, IEEE, 2005, pp. 1187–1191.

[2] Vansompel H., Sergeant P., Dupre L., *Optimized design considering the mass influence of an axial flux permanent-magnet synchronous generator with concentrated pole windings*, IEEE Transactions on Magnetics, Vol. 46(12), December 2010, pp. 4101–4107.

[3] Khan M.A., Pillay P., Batane N.R., Morrison D.J., *FPGA Prototyping a composite SMC/steel axial-flux PM wind generator*, Industry Applications Conference, 41st IAS Annual Meeting, IEEE, Vol. 5, October 2006, pp. 2374–2381.

[4] Hsieh Min-Fu, Dorrell D.G., Ekram S., *Cogging torque reduction in axial flux machines for small wind turbines*, Industrial Electronics, 35th Annual Conference, IEEE, November 2009, pp. 4435–4439.

[5] Ani S.O., Polinder H., Ferreira J.A., *Energy yield of two generator system for small wind turbine application*, IEEE International Electric Machines and Drives Conference, IEMDC, May 2011, pp. 735–740.

[6] Louie H., *Experiences in the construction of open source low technology off-grid wind turbines*, Power and Energy Society General Meeting, IEEE, July 2011, pp. 1–7.

[7] Andriollo M., Bertoli M., Martinelli G., Morini A., Torella A., *Permanent magnet axial flux disc generator for small wind turbines*, Electrical Machines, ICEM, IEEE, September 2008, pp. 1–6.

[8] Gerlando A., Foglia G., IacchettiM., Perini R., *Axial flux PM machines with concentrated armature windings: Design analysis and test validation of wind energy generators*, IEEE Transactions on Industrial Electronics, Vol. 58(9), September 2011, pp. 3795–3805.

[9] Yicheng C., Pragasen P., *Axial-flux PM wind generator with a soft magnetic composite core*, Industry Applications Conference, Fourtieth IAS Annual Meeting, IEEE, Vol. 1, October 2005, pp. 231–237.
[10] Javadi S., Mirsalim M., *Design and analysis of 42-V coreless axial-flux permanent--magnet generators for automotive applications*, IEEE Transactions on Magnetics, Vol. 46(4), April 2010, pp. 1015–1023.
[11] Bumby J.R., Stannard N., Dominy J., McLeod N., A *permanent magnet generator for small scale wind and water turbines*, IEEE, September 2008, pp. 1–6.
[12] Mendrela E., Moch J., Paduch P., *Właściwości elektromechaniczne bezszczotkowego silnika tarczowego prądu stałego*, Prace Naukowe Instytutu Maszyn, Napędów i Pomiarów Elektrycznych Politechniki Wrocławskiej, Nr 50, Studia i Materiały, Nr 22, 2000, pp. 189–198.
[13] Glinka T., Wolnik T., Król E., *Silnik tarczowy z wirnikiem wewnętrznym – obliczenia obwodu elektromagnetycznego*, Zeszyty Problemowe – Maszyny Elektryczne, Nr 92, 2011, pp. 23–28.
[14] Glinka T., Król E., Wolnik T., *Model polowy bezrdzeniowej maszyny tarczowej*, Zeszyty Problemowe – Maszyny Elektryczne, Nr 86, 2010, pp. 187–190.
[15] Glinka T., Tomaszkiewicz W., *Silniki tarczowe*, Zeszyty Problemowe – Maszyny Elektryczne, Nr 80, 2008, pp. 232–237.
[16] Glinka T., Jakubiec M., *Rozwiązania silników tarczowych*, Zeszyty Problemowe – Maszyny Elektryczne, Nr 77, 2007, pp. 243–249.
[17] Glinka T., Król E., Białas A., Wolnik T., *Silniki tarczowe z magnesami trwałymi*, Zeszyty Problemowe – Maszyny Elektryczne, Nr 87, 2010, pp. 63–68.
[18] Cierzniewski P., *Bezrdzeniowy silnik tarczowy z magnesami trwałymi*, Zeszyty Problemowe – Maszyny Elektryczne, Nr 77, 2007, pp. 161–166.
[19] Hosseini S.M., Agha-Mirsalim M., Mirzaei M., *Design, prototyping and analysis of a low-cost disk permanent magnet generator with rectangular flat-shaped magnets*, Iranian Journal of Science and Technology, Transaction B, Engineering, No. B3, 2008, pp. 191–203.
[20] Flux 11.1 Documentation, 2012, Cedrat Group.
[21] Giangrande P., Cupertino F., Pellegrino G., Ronchetto D., Gerada C., Sumner M., *Analysis of two-part rotor, axial flux permanent magnet machines*, Energy Conversion Congress and Exposition (ECCE), IEEE, September 2011, pp. 1576–1581.

TECHNICAL TRANSACTIONS | **CZASOPISMO TECHNICZNE**
ELECTRICAL ENGINEERING | ELEKTROTECHNIKA
1-E/2015

PIOTR BOGUSZ, MARIUSZ KORKOSZ, JAN PROKOP*

ANALYSIS OF THE INFLUENCE OF WINDING CONFIGURATION ON THE PROPERTIES OF A SWITCHED RELUCTANCE MOTOR

ANALIZA WPŁYWU KONFIGURACJI UZWOJEŃ BIEGUNÓW NA WŁAŚCIWOŚCI SILNIKA RELUKTANCYJNEGO PRZEŁĄCZALNEGO

A b s t r a c t

In this paper, the series configuration of pole winding connections in each phase of a three--phase 12/8 switched reluctance motor was analyzed. Based on the simulation model, the effect of magnetic couplings on motor properties was determined. Static characteristics were obtained for NNSS and NSNS configurations. Voltage, current, and electromagnetic torque waveforms were determined. Simulation results were verified through laboratory tests.

Keywords: *switched reluctance motor*, *three-phase motor*, *winding pole configurations*

S t r e s z c z e n i e

W niniejszym artykule analizowano konfigurację szeregową uzwojeń biegunów każdego pasma trójpasmowego silnika reluktancyjnego przełączalnego 12/8. Na podstawie modelu symulacyjnego określono wpływ sprzężeń magnetycznych na właściwości silnika. Dla konfiguracji NNSS i SNS zostały wyznaczone charakterystyki statyczne. Wyznaczono też przebiegi czasowe napięć, prądów oraz momentu elektromagnetycznego. Dokonano weryfikacji laboratoryjnej.

Słowa kluczowe: *silnik reluktancyjny przełączalny*, *silnik trójpasmowy*, *konfiguracja uzwojeń biegunów*

DOI: 10.4467/2353737XCT.15.035.3835

* Ph.D. Eng. Piotr Bogusz, D.Sc. Ph.D. Eng. Mariusz Korkosz, D.Sc. Ph.D. Eng. Jan Prokop, Faculty of Electrical and Computer Engineering, Rzeszow University of Technology, Poland.

1. Introduction

With increasing the number of poles per phase in a switched reluctance motor (SRM), the number of possible configurations of the connection of winding poles also increases. In the standard version of the switched reluctance machine, two pole winding configurations, (serial and parallel) are possible [1]. At the same time, the presence of a higher number of poles per phase and a higher number of phases results in the multiplication of the number of possible ways of particular pole windings supply [2–5].

The purpose of the paper is to present the results of the analysis on the influence of configuration on poles windings connected in series in a 12/8 switched reluctance motor on its static properties and current waveforms.

With the serial connection, there are two basic configurations possible for each of the phases, NNSS and NSNS. For each of these phase configurations, a number of variants is available in which individual pole windings can be supplied. For selected pole winding supply configuration, simulations were carried out aimed at the evaluation of the effect of magnetic couplings between individual motor phases from which voltage, current, and electromagnetic torque waveforms were determined. In laboratory conditions, current and voltage waveforms were registered under specific motor supplying conditions for a selected pole winding supplying configuration. Finally, example mechanical characteristics of the motor were determined.

2. Motor parameters and poles windings configuration

A physical model of the switched reluctance motor was developed in the course of an earlier research project [6]. It allows the obtaining of any configuration of windings. Table 1 summarizes selected parameters of the motor prototype constituting the subject of the tests.

Table 1

Selected parameters of the examined motor

Number of phases	3
Number of stator poles	12
Number of rotor poles	8
Rated power	1 kW
Rated voltage	300 V
Rated speed	30 000 rpm
Magnetic material	M470-50A

Assuming that pole windings of each phase in a 12/8-pole three-phase SRM are connected in series, two basic configurations of pole windings can be distinguished, NNSS and NSNS. Figure 1 shows both pole winding supply configurations considered here in the basic version of types NNNNNNSSSSSS (Fig. 1a)) and NNNSSSNNNSSS (Fig. 1c)). Additionally, Figs.

1b) and d) depict configurations in which input terminals of individual phases are shifted with respect to each other, i.e. configurations NSSNNSSNNSSN and NSNSNSNSNSNS, respectively. The phase denoted as *Ph*1 comprises poles A1–A4, while phases *Ph*2 and *Ph*3 include poles B1–B4 and C1–C4, respectively.

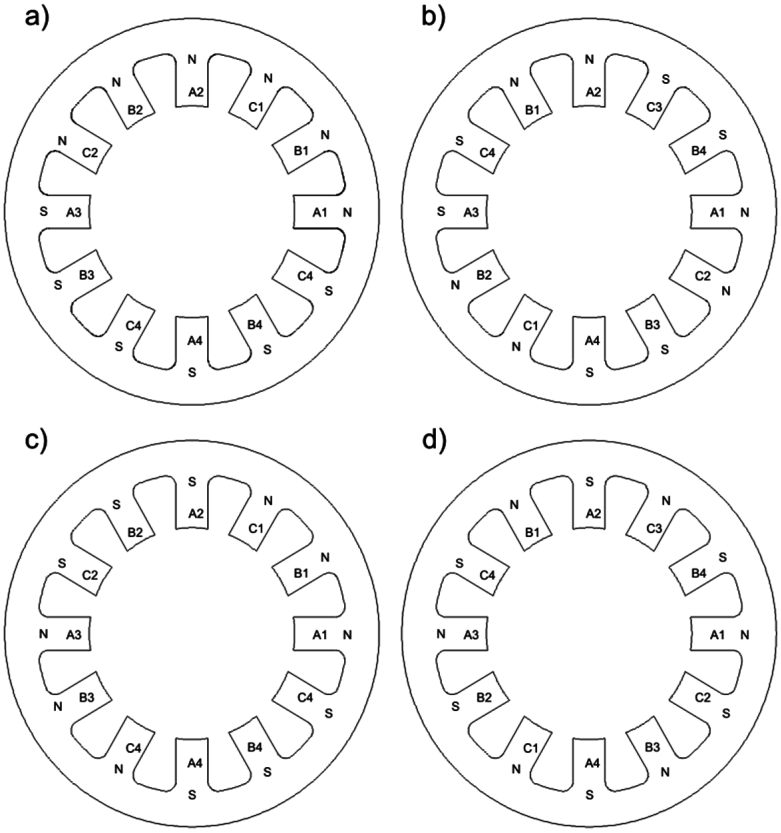

Fig. 1. The considered pole winding supplying configurations in the three-phase 12/8-pole SRM

3. Simulations – determination of static characteristics

The numerical model of the SRM has been developed in a computer program based on the finite element method [7]. Figure 2 presents plots of electromagnetic torque average value T_{eav} as a function of current I in one of the motor phases for the analyzed winding supplying configurations, i.e. NNSS and NSNS.

The analyzed configurations (NNSS, NSNS) don't have much effect on the produced electromagnetic torque value in the motor design considered herein. The main flux ψ_{11} determined as a function of the rotor position θ is shown in Fig. 3, while the coupled fluxes ψ_{12} and ψ_{13} are plotted in Figs. 4 and 5, respectively.

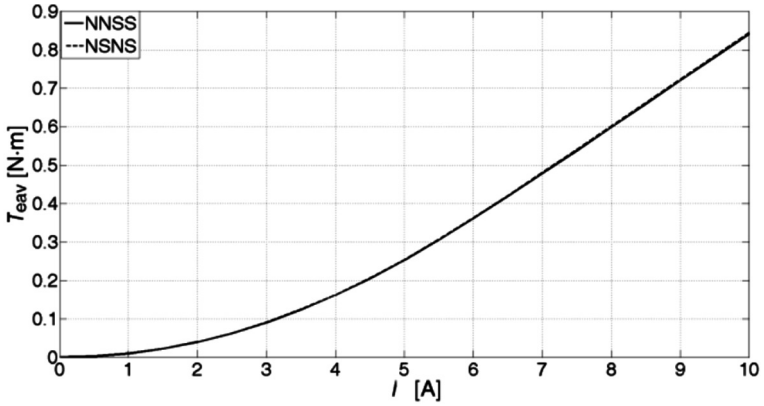

Fig. 2. The electromagnetic torque T_{eav} as a function of rotor position θ at I = var for configurations NNSS and NSNS

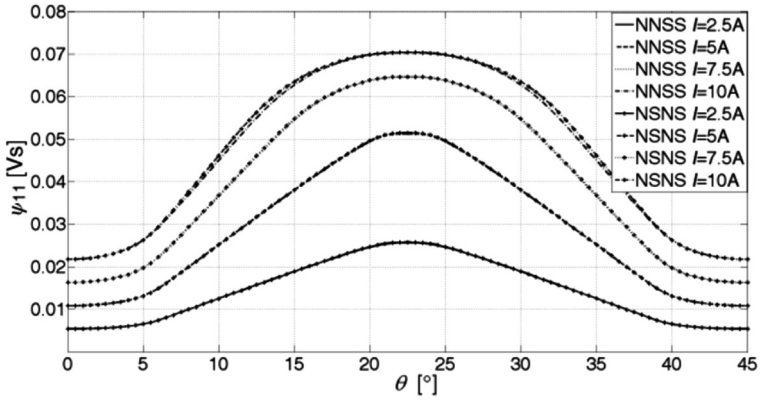

Fig. 3. The main flux ψ_{11} as a function of rotor position θ at I = var for configurations NNSS and NSNS

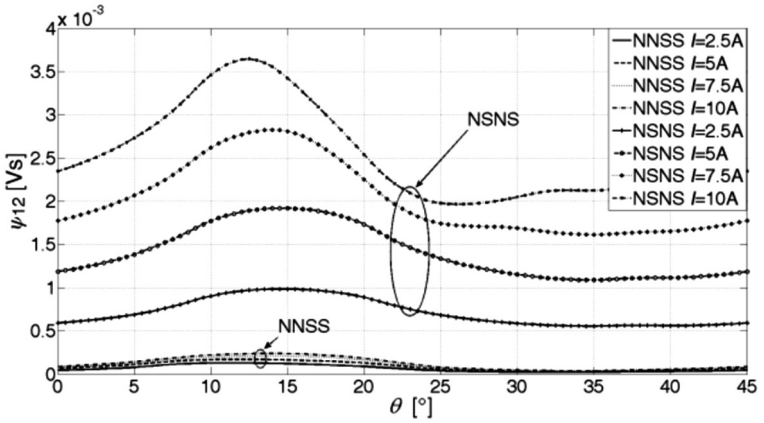

Fig. 4. The main flux ψ_{12} as a function of rotor position θ at I = var for configurations NNSS and NSNS

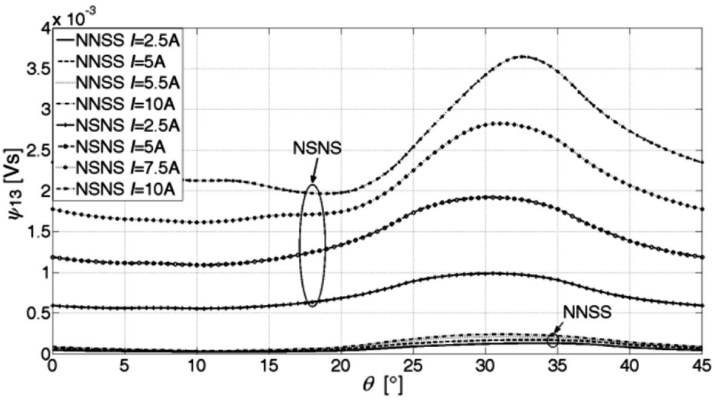

Fig. 5. The coupled flux ψ_{13} as a function of rotor position θ at I = var for configurations NNSS and NSNS

The main flux ψ_{11} depends only in a small degree on the pole winding configuration type. In the case of configuration NSNS, a slightly larger value of the coupled flux is obtained in any aligned position of the rotor. Nevertheless, it can be stated that both the electromagnetic torque and the main torque do not depend on the phase pole configuration scheme.

The issue looks slightly different in the case of coupled fluxes ψ_{12} and ψ_{13}. In the case of configuration NSNS, significantly higher magnetic coupling occurs between individual phases.

4. Simulations – determination of current and electromagnetic torque instantaneous values

To determine waveforms of the electromagnetic torque and currents in individual phases, a field-circuit model was employed. Calculations were carried out with the following assumptions: supply voltage U_{dc} = 60 V; turn-on angle θ_{on} = –1.25°; turn-off angle θ_{off} = 15°; speed n = 3000 rpm; winding temperature T = 70°C; full magnetic and electric symmetry of all motor phases. For all configurations depicted in Fig. 1, the electromagnetic torque T_e and phase currents i_{ph} were determined as functions of the rotor position θ. Figures 6 and 7 show plots of the electromagnetic torque T_e as a function of the rotor position θ for configuration NNSS (Fig. 6) in two variants, NNNNNNSSSSSS and NSSNNSSNNSSN, and for configuration NSNS (Fig. 7) in variants NNNSSSNNNSSS and NSNSNSNSNSNS.

Phase currents i_{ph} as functions of the rotor position θ are shown in Figs. 8 and 9 for configuration NNSS in variants NNNNNNSSSSSS and NSSNNSSNNSSN and for configuration NSNS in variants NNNSSSNNNSSS and NSNSNSNSNSNS, respectively.

For configuration NNSS in variant NSSNNSSNNSSN and configuration NSNS in variant NSNSNSNSNSNS, the obtained functional dependence of the electromagnetic torque and phase currents on rotor position were very close to each other. At the same time, configuration NSNS is much more sensitive to the scheme of phase placement along the stator magnetic circuit. This is confirmed by values of flux couplings between individual motor phases determined in Section 3 above. At the same time, configuration NNSS is more resistant to the effect of mutual magnetic couplings in the case of variant NNNNNNSSSSSS.

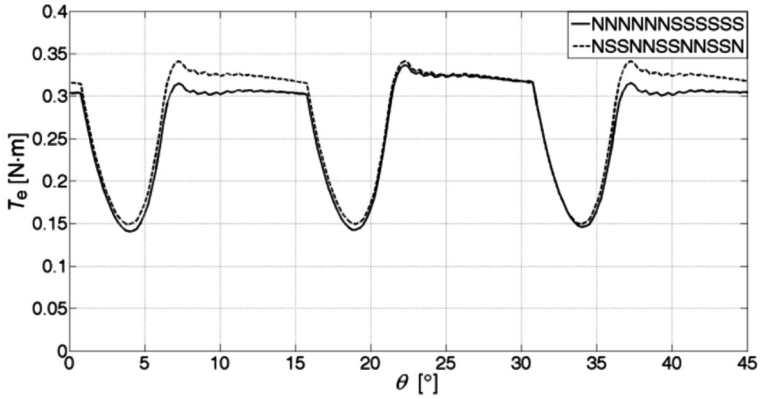

Fig. 6. Electromagnetic torque T_e as a function of the rotor position θ at rotor speed n = 3000 rpm for configuration NNSS in two variants

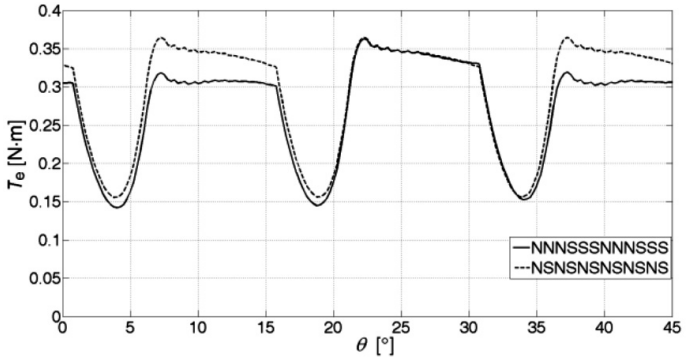

Fig. 7. Electromagnetic torque T_e as a function of the rotor position θ at rotor speed n = 3000 rpm for configuration NSNS in two variants

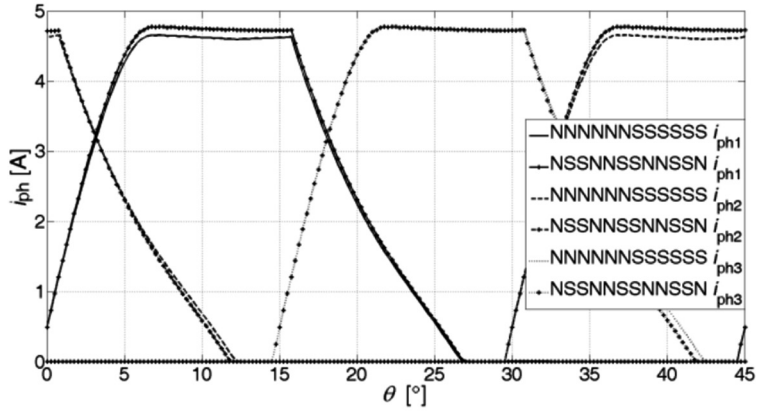

Fig. 8. Phase currents i_{ph} as functions of the rotor position θ at speed n = 3000 rpm for configuration NNSS in two variants

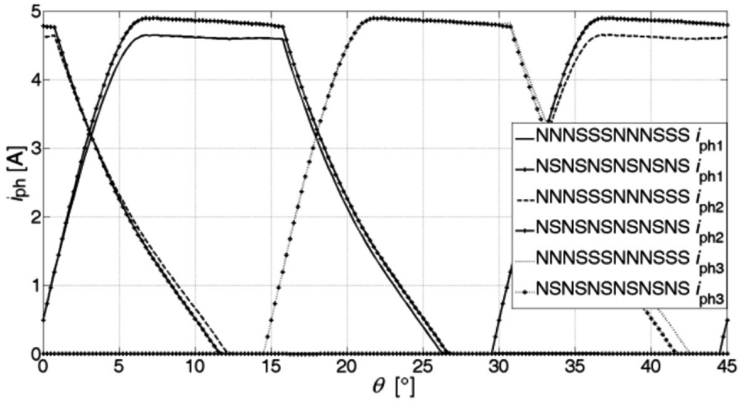

Fig. 9. Phase currents i_{ph} as functions of the rotor position θ at speed n = 3000 rpm for configuration NSNS in two variants

5. Laboratory tests

Laboratory tests were carried out in two stages. In the first stage, static characteristics (torque and flux) were determined for both examined configurations. Figure 10 presents a plot of the electromagnetic torque average value T_{eav} as a function of current I for both configurations, i.e. NNSS and NSNS.

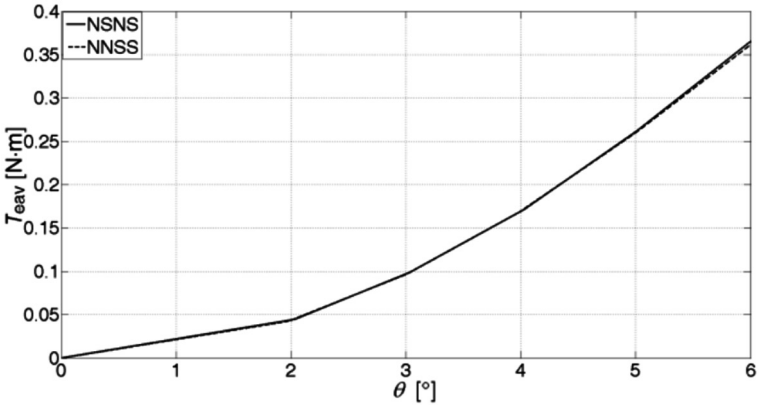

Fig. 10. Electromagnetic torque average value T_{eav} as a function of current I for configurations NNSS and NSNS

As can be observed, the motor torque characteristics obtained in laboratory conditions are almost independent from the configuration type (either NNSS or NSNS). Similar results were obtained on the grounds of the numerical model.

In the second stage of the test, mechanical characteristics of the tested motor were determined and waveforms of its selected parameters were registered. The laboratory setup is shown in Fig. 11.

In view of limitations imposed by the maximum rotation speed of the incremental encoder, the supply voltage value was much lower than the motor's nominal voltage. In the measuring and data acquisition system, the Yokogawa WT1600 six-channel digital power meter equipped with MOTOR module was used. A PC was used for data acquisition and control of the load torque applied to the motor.

At the supply voltage U_{dc} = 60 V, turn-on angle $\theta_{on} = -1.25°$, and turn-off angle $\theta_{off} = 15°$, mechanical characteristics of the motor were determined for configuration NNSS in variant NNNNNNSSSSSS and configuration NSNS in variant NSNSNSNSNSNS (Fig. 12).

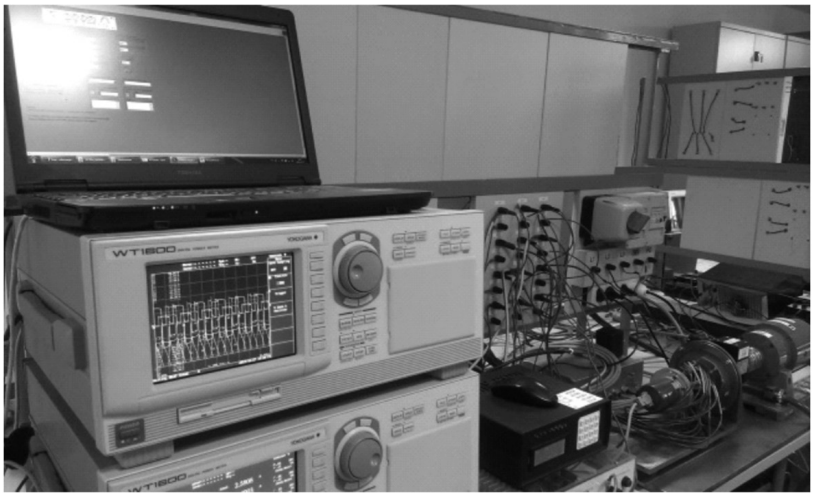

Fig. 11. A view of the laboratory setup

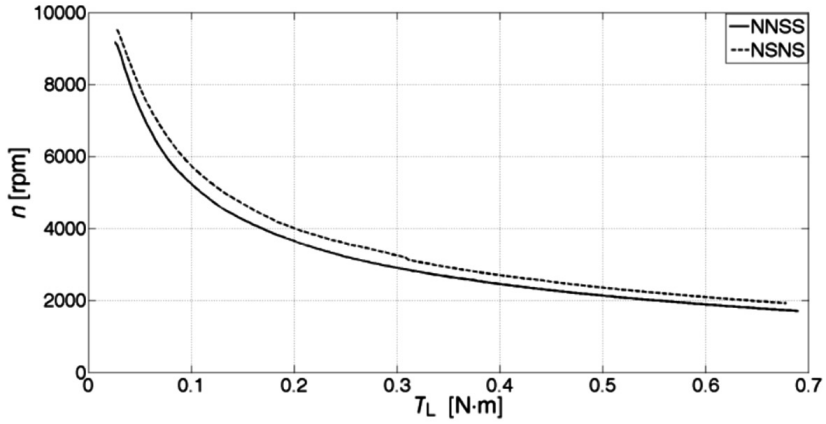

Fig. 12. Rotor speed as a function of load T_L for configurations NNSS (variant NNNNNNSSSSSS) and NSNS (variant NSNSNSNSNSNS)

As can be observed, mechanical characteristics obtained for these two configurations (in selected variants) do not coincide. Configuration NSNS in variant NSNSNSNSNSNS offers higher value of torque on the motor shaft at the same rotor speed with respect to configuration NNSS in variant NNNNNNSSSSSS. This confirms results of simulations obtained earlier for the similar motor operation condition. In an obvious way, this translates into noticeably higher efficiency of the motor than has been observed in laboratory conditions (Fig. 13).

The maximum obtained motor efficiency was 64.5% (at n = 5057 rpm) in the case of configuration NNSS and 67% for configuration NSNS (at n = 5120 rpm). The registered waveforms of phase currents i_{ph}, the mechanical characteristics of which are presented in Fig. 12, are shown in Fig. 14 (NNSS) and Fig. 15 (NSNS) at the motor speed n = 3000 rpm.

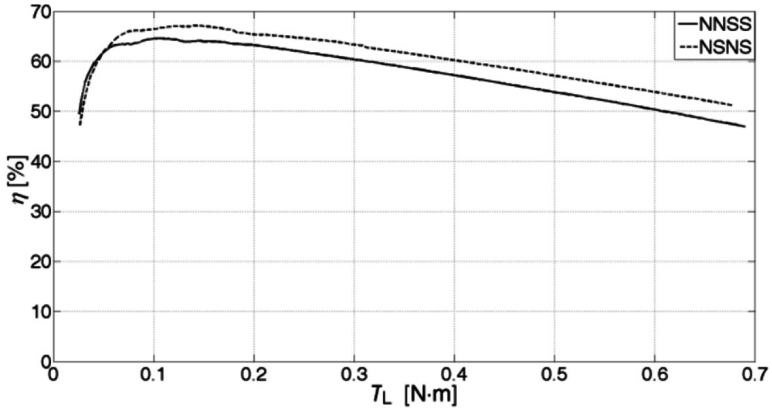

Fig. 13. Motor efficiency as a function of load torque T_L for configurations NNSS (variant NNNNNNSSSSSS) and NSNS (variant NSNSNSNSNSNS)

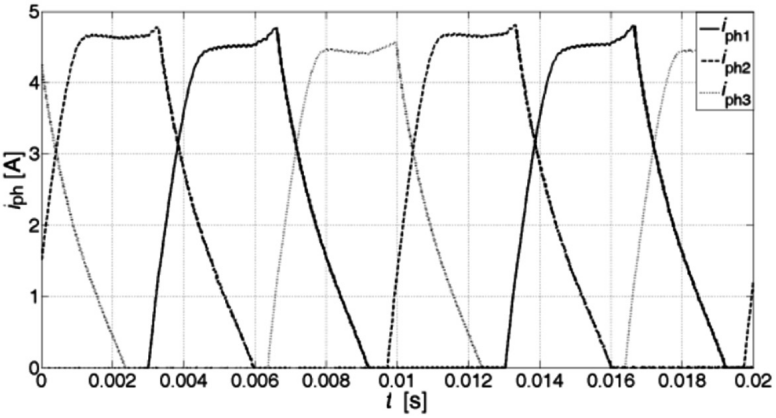

Fig. 14. Phase current waveforms i_{ph} at the motor speed n = 3000 rpm for configuration NNSS in variant NNNNNNSSSSSS

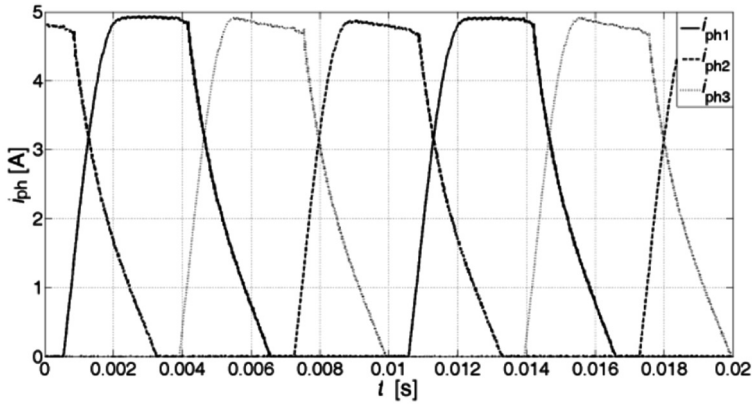

Fig. 15. Phase current waveforms i_{ph} at the motor speed n = 3000 rpm for configuration NSNS in variant NSNSNSNSNSNS

In general, the obtained waveforms of currents i_{ph} confirm results obtained from simulations. However, it should be clearly stated that the differences occurring in waveforms of even a single configuration result not only from the presence of magnetic couplings. A quite important effect is in this case related to the magnetic asymmetry that was not taken into account in the simulation model.

6. Summary

In this paper, results of a study on a three-phase 12/8 switched reluctance motor were presented with various configurations of pole winding connections of individual phases. The windings were connected in series in all cases. From the point of view of static characteristics, the pole winding configuration type (either NNSS or NSNS) does not make any practical difference. Both torque characteristics and flux characteristics almost coincide. Fundamental differences occur in values of magnetic fluxes representing couplings between individual phases. The configuration of NNSS type is characterized by values of magnetic couplings that are several time lower. Simulations performed with the use of a field-circuit model proved that configuration NSNS is more susceptible to the effect of magnetic couplings. This is noticeable especially in the case where, for example, the NNNSSSNNNSSS variant was used. Configuration NNSS is less susceptible to the effect of magnetic couplings. At the same time, in the case of the NNSS configuration, slightly lower values of phase currents and the produced electromagnetic torque were obtained. Laboratory tests confirmed results of simulations in scope of both static characteristics and phase current waveforms. Undoubtedly, the most favourable case is configuration NSNS in the NSNSNSNSNSNS variant. However, only slightly worse results were obtained in the case of the NNSS configuration in variant NSSNNSSNNSSN. Phase current waveform patterns are influenced not only by magnetic couplings from neighbouring phases but also by the way in which the phases are arranged with respect to each other. Moreover, laboratory tests revealed quite a significant effect of magnetic asymmetry between individual phases. This phenomenon is clearly visible in Figs. 14 and 15.

References

[1] Miller T.J.E., *Faults and unbalanced force in the switched reluctance machine*, IEEE on Industry Applications, 1995, Vol. 31(2), pp. 319–328.

[2] Ferreira C.A., Jones S.R., Heglund W.S., Jones W.D., *Detailed design of a 30-kW switched reluctance starter/generator system for a gas turbine engine application*, IEEE Trans. Ind. Appl., 1995, Vol. 31(3), pp. 553–561.

[3] Pochanke A., *Modele obwodowo-polowe pośrednio sprzężone silników bezzestykowych z uwarunkowaniami zasilania. Monografia* [*Indirectly coupled circuit-field models for brushless motors with conditioned supply. A monograph*], Oficyna Wydawnicza Politechniki Warszawskiej, Warszawa 1999.

[4] Miller T.J.E., *Electronic control of switched reluctance machines*, Newnes, 2001.

[5] Li J., Sun H., *Modeling and simulations of four-phase 8/6 switched reluctance motor with an improved winding configuration*, International Conference on Computer Science and Software Engineering, 2008, Vol. 4, pp. 1045–1048.

[6] Bogusz P., Korkosz M., Prokop J., *Wyznaczanie charakterystyk statycznych maszyn reluktancyjnych przełączalnych* [*Determination of static characteristics of switched reluctance machines*], Zeszyty Problemowe — Maszyny Elektryczne, 2005, No. 72, pp. 53–58.

[7] *Flux 11.1 Documentation*, 2012, Cedrat Group.

TECHNICAL TRANSACTIONS | **CZASOPISMO TECHNICZNE**
ELECTRICAL ENGINEERING | ELEKTROTECHNIKA
1-E/2015

PIOTR BOGUSZ*, MARIUSZ KORKOSZ*, PIOTR WYGONIK**

STUDIES OF THE PERMANENT MAGNET DC MACHINE

BADANIA MASZYNY PRĄDU STAŁEGO Z MAGNESAMI TRWAŁYMI

Abstract

A hybrid drive of an unmanned aerial vehicle uses two mechanically coupled drives. In one of the drives, an electrical machine is used. Its role is not only limited to a motoring operation, e.g. during achieving the flight ceiling. The electric machine changes its operation into generating after reaching the flight ceiling, this allows not only meeting current electrical energy demands but also battery recharging. This paper presents the results of laboratory tests of a BLDC machine in motoring and generating operation. Mechanical characteristics of the motor for different supply voltages and external characteristics for generator were determined. The possible energy conversion efficiencies for both motoring and generating operations were determined.

Keywords: *BLDC machine*, *hybrid drive*, *motoring operation*, *generating operation*

Streszczenie

Napęd hybrydowy bezzałogowego aparatu latającego wykorzystuje dwa napędy sprzężone ze sobą mechanicznie. W jednym z napędów stosuje się maszynę elektryczną. Jej rola nie ogranicza się tylko do pracy silnikowej w trakcie np. osiągania pułapu przelotowego. Po osiągnięciu pułapu przelotowego maszyna elektryczna przechodzi w stan pracy generatorowej, umożliwiając nie tylko pokrywanie bieżącego zapotrzebowania na energię elektryczną, ale również doładowywanie baterii akumulatorów. W niniejszym artykule przedstawiono wyniki badań laboratoryjnych maszyny prądu stałego z magnesami trwałymi w zakresie pracy silnikowej i prądnicowej. W wyniku badań wyznaczono charakterystyki mechaniczne badanej maszyny przy pracy silnikowej dla różnych napięć zasilających oraz wyznaczono charakterystyki zewnętrzne maszyny pracującej w zakresie pracy generatorowej. Określono możliwe do osiągnięcia sprawności przetwarzania energii w obu stanach pracy.

Słowa kluczowe: bezszczotkowa maszyna prądu stałego z magnesami trwałymi, napęd hybrydowy, praca silnikowa, praca generatorowa

DOI: 10.4467/2353737XCT.15.036.3836

* Ph.D. Eng. Piotr Bogusz, D.Sc. Ph.D. Eng. Mariusz Korkosz, Faculty of Electrical and Computer Engineering, Rzeszow University of Technology.

** Ph.D. Eng. Piotr Wygonik, Faculty of Mechanical Engineering and Aeronautics, Rzeszow University of Technology.

1. Introduction

Nowadays, an integral part of hybrid drives are electric machines. In many cases, these machines operate both as motors and generators. This is the specification of the hybrid drive, in which part of the kinetic energy of the vehicle is recovered during braking and is then converted into electrical energy. This energy is stored in batteries and used during acceleration or driving uphill. Intensive work on the development of hybrid drive systems used in unmanned aerial vehicles (UAVs) is currently being conducted [1–6]. In this type of drive, an electric motor operates as a motor during climbing and delivers additional power to the propeller. It can also drive the propeller alone, a so-called quiet drive. The demand for power during the flight on a specific ceiling is much smaller than when climbing. Thus, the excess of combustion engine power can be used to charge the battery through the electric machine operating as a generator. In the case of electric and hybrid drives, high efficiency at the smallest possible size is required, especially for UAV.

The aim of this paper is an evaluation of the parameters of the electric machine with permanent magnets as a hybrid drive in motoring and generating operation. The mechanical characteristics for the motoring operation and the external characteristics for the generating operation were determined. The efficiency of the machine for both states was determined.

2. Hybrid drive of the UAV

To improve the efficiency of the combustion engine in the UAV drive, a parallel hybrid drive can be used. In the case of the parallel hybrid drive, there are three options:

- drive with a common shaft,
- drive with a clutch,
- drive through the planetary gear.

The simplest solution and occupying the least amount of space is the hybrid drive with a common shaft. However, its disadvantage is a lack of independent operation of the electric motor and combustion engine. In this solution, there is no possibility of independent operation of the electric motor. The drive with the clutch, which disconnects the combustion engine from the rest of the drive, requires a precise coupling of the combustion engine and the electric motor, e.g. through an electromagnetic clutch. The solution with the planetary gear provides an independent operation of the electric motor, but requires more space and deteriorates the efficiency of the entire drive. Figure 1 shows a block diagram of an exemplary hybrid drive with a gear designed for UAVs. The laboratory test stand of the hybrid drive is shown in Fig. 2.

In the hybrid drive system, the permanent magnet DC machine (BLDCM) was used. The used construction of the BLDCM has an external rotor. This solution leads to a reduction of dimensions of the machine and provides the increased value of the produced electromagnetic torque while reducing the weight of the machine. The disadvantage of this solution is a reduced durability of the motor compared to classical solutions with inner rotor. Table 1 lists the selected geometrical dimensions and parameters of the tested machine.

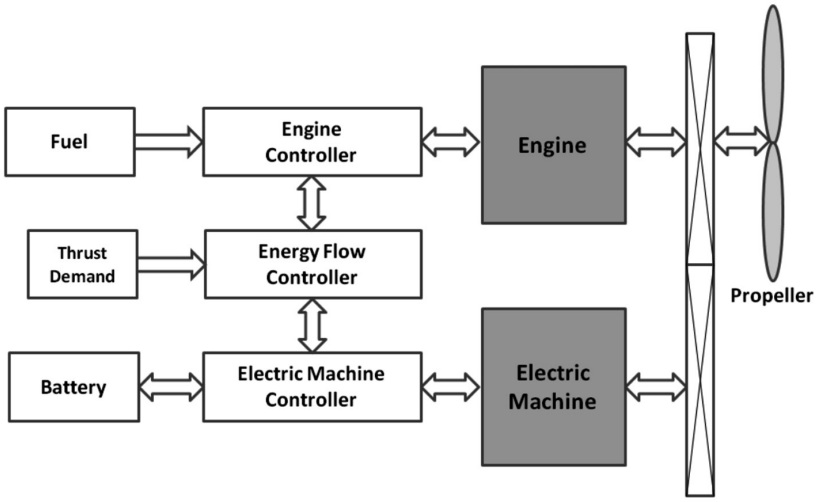

Fig. 1. Block diagram of a hybrid drive with a gear designed for UAV

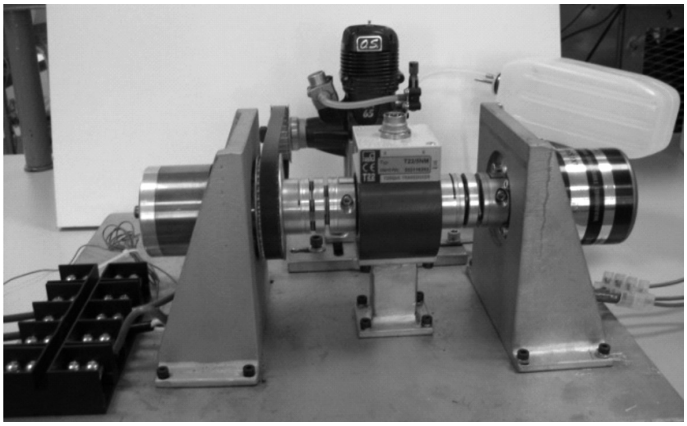

Fig. 2. Laboratory test stand of the hybrid drive

Table 1

Selected parameters and geometrical dimensions of the tested machine

Supply voltage [V]	24–42
No. of phases	3
Winding configuration	triangle
No. of stator poles	12
No. of rotor poles	14
Constant k_V [V/1,000 rpm]	5.84
Phase resistance R_{ph} [Ω]	0.042
No. of turns of winding per pole	18
Rotor outer diameter [mm]	53
Packet length of the stator [mm]	45
Permanent magnets	neodymium
Magnetic sheet of the stator	anisotropic

3. Static characteristics

3.1. Cogging torque

In the laboratory conditions, the cogging torque T_{Coog} of the BLDC machine in a function of the rotor position θ was determined (Fig. 3). Due to the anisotropy of the magnetic steel used in the magnetic circuit of the stator, the cogging torque has significant value, which varies from +0.3 Nm to -0.25 Nm. By using the anisotropy steel, the variation period of the cogging torque decreased from 84 (for the isotropy steel) to 14. The maximum value of the cogging torque also increased significantly.

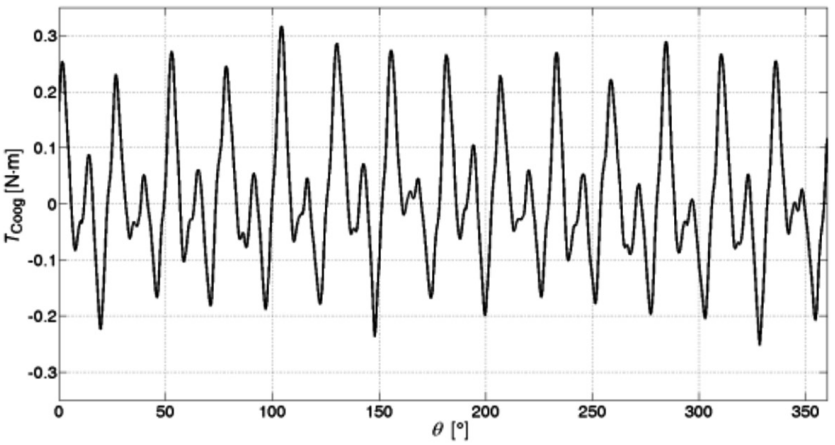

Fig. 3. Relation of cogging torque in a function of the rotor position

3.2. Electromagnetic torque

In order to determine the influence of the anisotropy of the used magnetic material on the generated torque, the measurements for three possible cases of motor phases supply, i.e. *Ph*1–*Ph*2, *Ph*2–*Ph*3 and *Ph*3–*Ph*1 with a constant value of current $I = 21$ A were carried out. Figure 4 shows the relationship of the electromagnetic torque T_e in a function of the rotor position θ for all three cases of motor phases supply.

The *Ph*1–*Ph*2 variant has the most preferred shape of the torque characteristics. Nevertheless, the torque characteristics are far from being desirable. The influence of anisotropy of the magnetic steel on the torque characteristic is quite significant. This causes significant electromagnetic torque ripples at constant value of current in the windings. In the parallel hybrid drive, it is not a significant disadvantage because the motor is directly coupled with the propeller which has a large moment of inertia. Therefore, torque ripples not only from the combustion engine, but also from the electrical motor, are compensated by the dynamic torque of the rotating propeller.

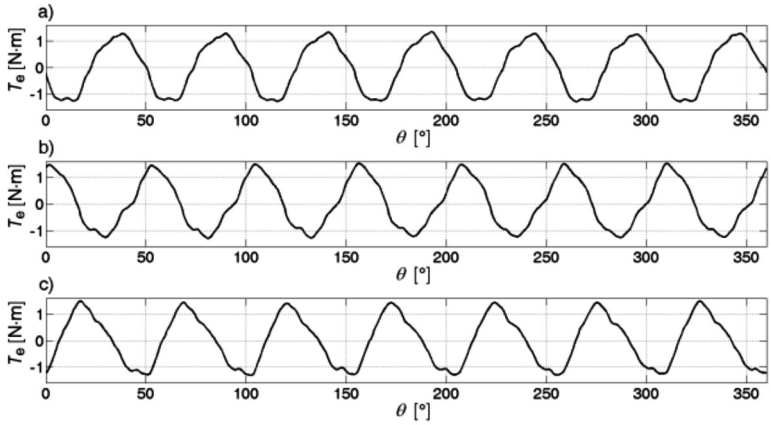

Fig. 4. Relation of the electromagnetic torque T_e in a function of the rotor position at $I = 21$ A for a) *Ph*1–*Ph*2, b) *Ph*2–*Ph*3 and c) *Ph*3–*Ph*1

4. Motoring operation

Mechanical and efficiency characteristics were determined on a laboratory test stand equipped with a stabilized DC power supply (60 V, 110 A), a power analyzer with a motor module (WT1600), a torque meter and a computer used for data acquisition. The programmable load was connected to the load machine to achieve the work with constant voltage, current and power. In the motor control system, a dedicated power supply system with a built-in algorithm of sensorless detection of the rotor position was applied.

The measurement system was configured to determine the motor efficiency, overall efficiency of the drive system or efficiency of the supply system. Particular characteristics were determined at different supply voltages. The designed drive will be powered by battery. Due to the intended application of this drive in different models of UAV, the power will be provided from lithium-polymer battery packs of 8, 9 or 10 cells. The choice will depend on the intended flight range and available space for batteries in the UAV model. Thus, studies of the drive were carried out in the voltage range from 26 V to 42 V. A block diagram of the measuring system is shown in Fig. 5.

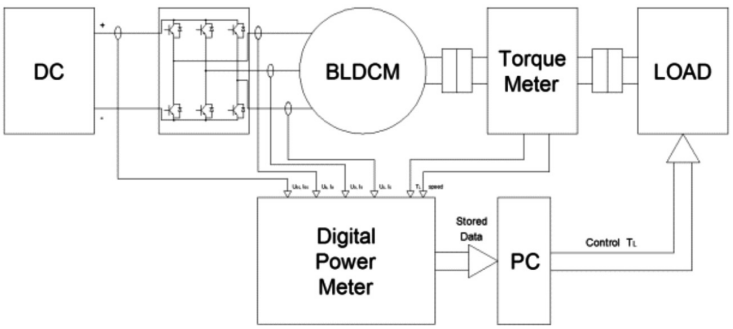

Fig. 5. Block diagram of the measuring system of BLDC machine working as a motor

The dependence of the motor speed n in a function of the load torque T_L at different supply voltages is shown in Fig. 6.

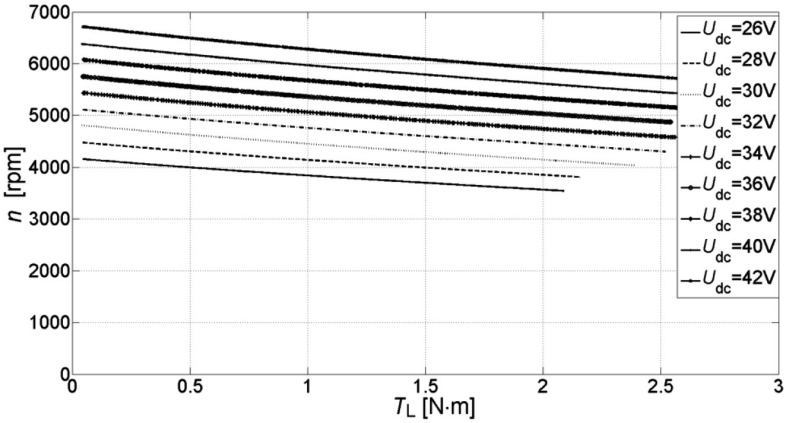

Fig. 6. The characteristics of $n = f(T_L)$ determined for different values of voltage U_{dc}

As can be seen on Fig. 6, speed decreases noticeably with increasing load torque. This results from an extensive measurement system which uses a direct measurement of all currents with the power analyzer. To measure all currents, long cables are used to connect the power analyzer with motor and control systems and to connect the power analyzer with the power supply. This solution leads to significant voltage drops in cables.

The determination of characteristics in the full range of load torque changes was precluded by acceptable parameters of the dynamometer. Below the speed of 6000 rpm, the allowable torque load had to be reduced because of the possibility of the dynamometer damage. This is evident on the obtained mechanical characteristics (Fig. 6). The relationship of the drive efficiency η in a function of the load torque T_L for the limiting voltage values is shown in Fig. 7.

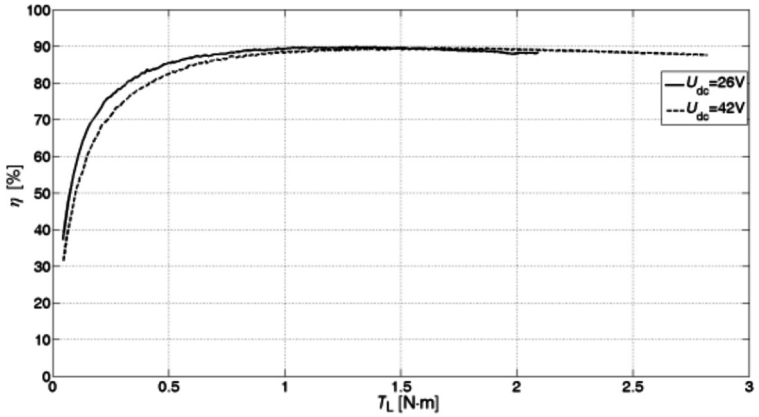

Fig. 7. Relation of the overall efficiency η in a function of the load torque T_L

The efficiency η of the tested drive system reaches 89%. The efficiency of the motor is only slightly higher (91%) due to the high efficiency of the supply system.

A slightly higher efficiency was achieved at the supply voltage U_{dc} = 42 V. This is natural because with the increasing supply voltage, the impact of voltage drops in power electronics components of power supply system decreases.

5. Generating operation

A block diagram of the measurement system of the generating operation is shown in Fig. 8.

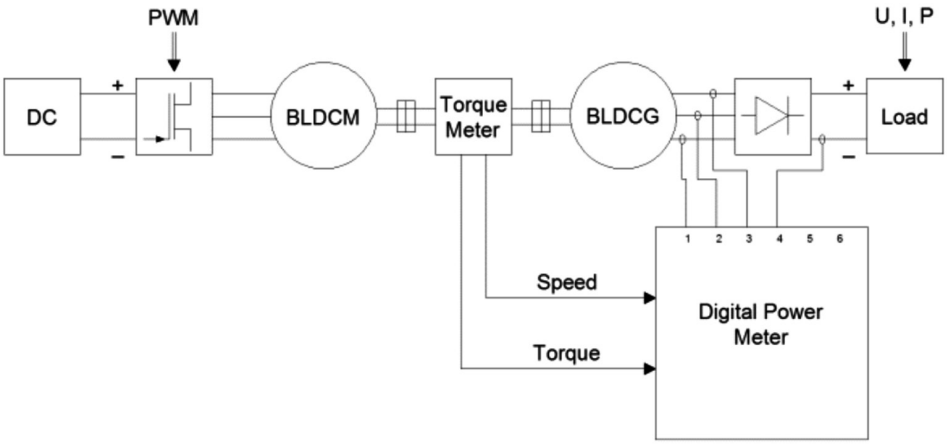

Fig. 8. The block diagram of the measurement system of the BLDC generator

Waveforms of the induced voltages were obtained without loading the tested machine. The wire induced voltages obtained at a speed n = 3000 rpm are shown in Fig. 9.

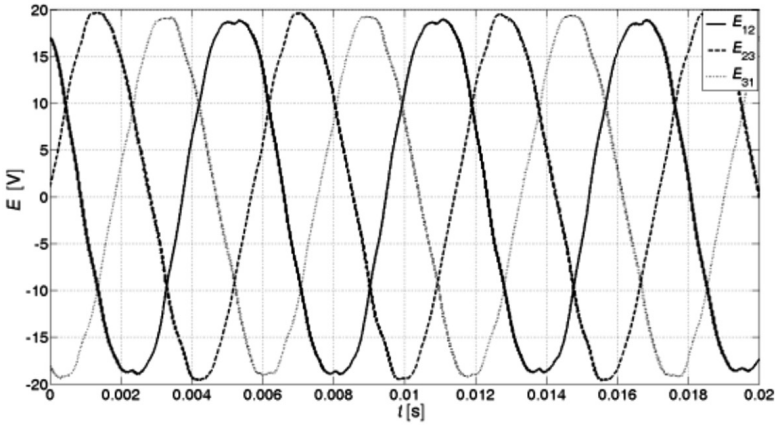

Fig. 9. Waveforms of the wire induced voltages at speed n = 3000 rpm

As one can see, the wire voltages and torque characteristics differ significantly from the desired waveforms. Only in the case of the wire voltage E_{12} is the obtained shape close to the trapezoidal one. Two other voltages differ significantly from the trapezoidal shape. This is the effect of the anisotropy of the used magnetic material of the stator.

The output voltage of the generator is important from the point of view of battery charging. In the laboratory conditions, the studies forcing the constant value of voltage U_{dc} = const on the output of the generator through the programmable load were conducted. The load current I_{dc} (after rectifier circuit) was increasing with increases to the rotational speed. The relationship of the load current I_{dc} in a function of rotational speed n at a constant value of voltage of U_{dc} = const is shown in Fig. 10.

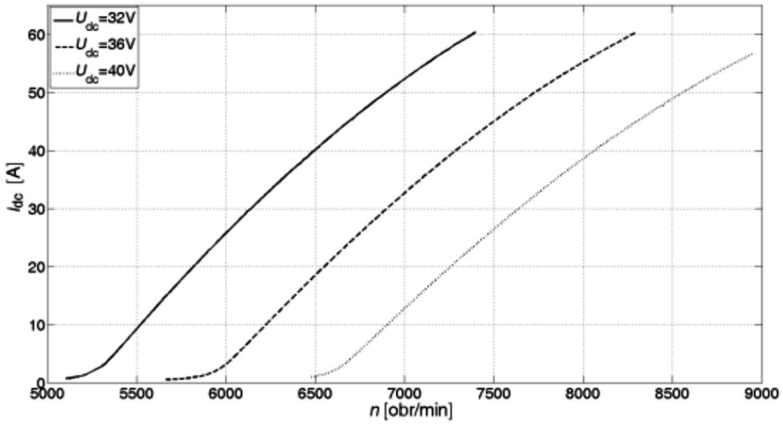

Fig. 10. Relationship of the load current of the I_{dc} generator in a function of rotational speed n at a constant output voltage U_{dc} = const

The control of the machine speed n is required to obtain the specified value of the load current of the generator at the given output voltage. It is easy to notice that by keeping a constant output voltage, the relationship between the I_{dc} current and the rotational speed n is not linear. The resulting efficiency η of the machine operating as a generator at a constant output voltage in a function of generator load current I_{dc} is shown in Fig. 11.

With the increase of the output voltage of the generator, the overall efficiency of the system also increases. The maximum efficiency of the generator with the rectifier system was 87.5% (generator – 91.5%). The effective operation range of the generator requires a current load no less than $I_{dc} > 10$ A. Below this value, regardless of the output voltage of the generator, the overall efficiency reduces significantly.

The obtained stiffness of the external characteristics of the machine operating as a generator is not satisfactory. With the increase of the load current there is a significant voltage drop at the rectifier terminals. Maintaining a constant voltage at the output of the rectifier requires an increase in rotational speed (Fig. 10). An overall efficiency of the machines in this state does not exceed 88% and is lower than during the motoring operation. The Li-Po cells (lithium-polymer) itended for use have significant limitations (the maximum value of charging current). Thus, the actual efficiency of the machine in the generating operation will not exceed 80% due to operation at low load current.

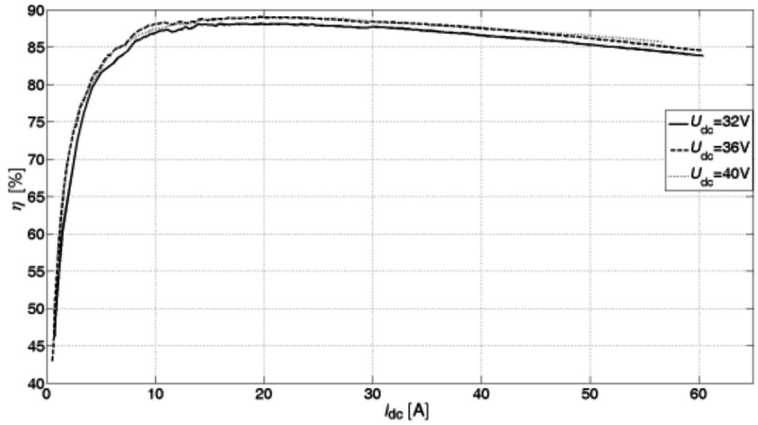

Fig. 11. Relationship of the efficiency η in a function of load current I_{dc} at a constant output voltage U_{dc} = const

6. Conclusions

In this paper, the results of laboratory studies of a BLDC machine in motoring and generating operation were presented. In the tested machine, an anisotropic magnetic sheet steel was used. The type of magnetic steel has an influence on the value of the generated cogging torque, shapes of torque characteristics and induced voltages. This introduces additional electromagnetic torque ripples in the tested motor. However, the resulting overall efficiency of the machine in motoring operation exceeds 89% and the motor efficiency of about 91%. In the generating operation, overall efficiency was significantly lower and does not exceed the value of 88%. The influence on the deterioration in the efficiency of the machine in the generating operation has a rectifier circuit whose efficiency decreases with the increase of the load current. The efficiency of the power system (rectifier) attached to the machine during the generating operation is a few percent lower than that of the controller attached to the machine operating as a motor, due to the fact that during the motoring operation, the MOSFET transistors have a higher efficiency compared to the rectifier diodes, which operate at the generating operation. If the machine works as a generator intended for UAV, the goal working point of the drive should be considered. In this state, the output voltage of the rectifier circuit should not be less than the maximum voltage of battery. Only then is it possible that the batteries can be fully recharged.

References

[1] Hodkinson R., Fenton J., *Lightweight Electric/Hybrid Vehicle Design*, Reed Educational and Professional Publishing Ltd, 2001.

[2] Gawale A., Pant R., *Paper 2004-01-design studies of power plant system of non-rigid airships*, Aerosp. Eng. Dept., Indian Inst. Technol. Bombay, Mumbai, India 2004.

[3] Glassock R., Hung J.Y., Gonzalez L.F., Walker R.A., *Multimodal hybrid powerplant for unmanned aerial systems (UAS) Robotics*, Twenty-Fourth Bristol International Unmanned Air Vehicle Systems Conference, March 30th to April 1st 2009, Bristol, United Kingdom.

[4] Gaide D., Humbargar C., Larrabee D., Marshman J., Petersen E., Serani E., Wormer E., *Hybrid electric integrated optimized system (helios); design of a hybrid propulsion system for aircraft*, Univ. Colorado, Boulder, CO, USA, Tech. Rep. AIAA 900675, 2011.

[5] Recoskie S., Fahim A., Gueaieb W., Lanteigne E., *Experimental testing of a hybrid power plant for a dirigible UAV*, J. Intell. Robot. Syst., 2012, Vol. 9764, pp. 69–81.

[6] Recoskie S., Fahim A., Gueaieb W., Lanteigne E., *Hybrid Power Plant Design for a Long-Range Dirigible UAV*, Mechatronics, IEEE/ASME Transactions, 2014, Vol. 19, Issue 2, pp. 606–614.

Additional information:
The work done within the research project 'Technologies of hybrid power drive of light or unmanned aerial vehicles' – DZP/INNOLOT-1/2020/2013.

TECHNICAL TRANSACTIONS | **CZASOPISMO TECHNICZNE**
ELECTRICAL ENGINEERING | ELEKTROTECHNIKA
1-E/2015

ŽELMÍRA FERKOVÁ*

INFLUENCE OF THE ARRANGEMENT AND SIZES OF MAGNETS ON THE COGGING TORQUE OF PMSM

WPŁYW ROZMIESZCZENIA ORAZ ROZMIARU MEGNESÓW NA MOMENTY ZACZEPOWE W SILNIKACH SYNCHRONICZNYCH Z MAGNESAMI TRWAŁYMI

Abstract

Two-phase permanent magnet synchronous motors are discussed in this paper and the influence of the magnet sizes on cogging torque (CT) is explored. The cogging torque has been calculated using ANSYS/Maxwell software. In more detail, influences of the magnet size, their positioning and orientation to the CT in two basic rotor types were studied. The cogging torque waveform for critical dimensions has been considered using the FFT analysis. The first rotor type is with semi-arc shaped magnets located on the rotor surface. The second motor type features magnets embedded in its rotor. The shape of the stator magnetic circuit has been predetermined.

Keywords: *cogging torque*, *permanent magnet synchronous motor*, *two-phase motor*

Streszczenie

W artykule omawiane są dwufazowe silniki synchroniczne z magnesami trwałymi oraz analizowany jest wpływ rozmiarów magnesów na momenty zaczepowe. Momenty zaczepowe zostały obliczone za pomocą oprogramowania ANSYS/Maxwell. W szczególności rozpatrywany jest wpływ rozmiaru magnesów, ich ustawienia i orientacji na momenty zaczepowe dla dwóch podstawowych typów wirników. Kształt momentów zaczepowych dla krytycznych rozmiarów został przeanalizowany z użyciem analizy FFT. Pierwszy analizowany typ wirnika zawiera wygięte magnesy zlokalizowane na powierzchni wirnika. Drugi typ silnika zawiera magnesy wbudowane w wirnik. Kształt obwodu magnetycznego stojana został z góry określony.

Słowa kluczowe: *momenty zaczepowe*, *silniki synchroniczne z magnesami trwałymi*, *dwufazowe silniki*

DOI: 10.4467/2353737XCT.15.037.3837

* Ph.D. Eng. Želmíra Ferková, Department of Electrical Engineering, Faculty of Electrical Engineering and Informatics, Technical University of Košice, Slovakia.

1. Introduction

In recent years, the utilisation of permanent magnet synchronous motors has dramatically increased. The advantage of excitation with permanent magnets (PM) is the resulting absence of Joule losses in excitation and especially the elimination of sliding contact. The disadvantage is that excitation is uncontrollable and the recently increasing price of magnets presents an issue as well.

Analysed in the present article is a two-phase two-pole motor with permanent magnets (NdFeB, H_c = –849 000 A/m, B_r = 1.125 T). A ready-made stator stack has been used. The shape and number of stator slots could not be changed.

2. Permanent Magnet Synchronous Motor

In the steady state, behaviour of a two-phase synchronous machine can be described by use of the equations below:

$$\mathbf{U}_1 = R_1\mathbf{I}_1 + \mathrm{j}X_d\mathbf{I}_{1d} + \mathrm{j}X_q\mathbf{I}_{1q} + \mathbf{U}_f \tag{1}$$

$$\mathbf{I}_1 = \mathbf{I}_{1d} + \mathbf{I}_{1q} \tag{2}$$

where:
R_1 – phase resistance,
X_d – d-axis synchronous reactance,
X_q – q-axis synchronous reactance,
$\mathbf{U}_1$ – input voltage,
$\mathbf{I}_1$ – one phase current,
$\mathbf{I}_{1d}$ and $\mathbf{I}_{1q}$ – d and q axis stator currents,
$\mathbf{U}_f$ – voltage (EMF) induced by magnetic excitation flux of the rotor.

Phasor diagrams of over-excited and under-excited motors are presented in Fig. 1. The equations clearly imply induced voltage $\mathbf{U}_f$ of the synchronous machine influences on its behaviour. This depends on the number of turns and the arrangement of the stator winding as well as on the arrangement and size of magnets.

Moreover, the placement of magnets affects the reactance X_d and X_q.

For the PMSM electromagnetic torque, it holds that:

$$T_e = \frac{2}{\omega_{\text{synch}}}\left[\frac{U_1 \cdot U_f}{X_d}\sin\theta + \frac{U_1^2}{2}\left(\frac{1}{X_q} - \frac{1}{X_d}\right)\sin(2\theta)\right] \tag{3}$$

where:
U_1 – the effective values of phase voltage,
U_f – the voltage induced by excitation,
θ – the loading angle [2],
T_e – the electromagnetic torque that neglects CT.

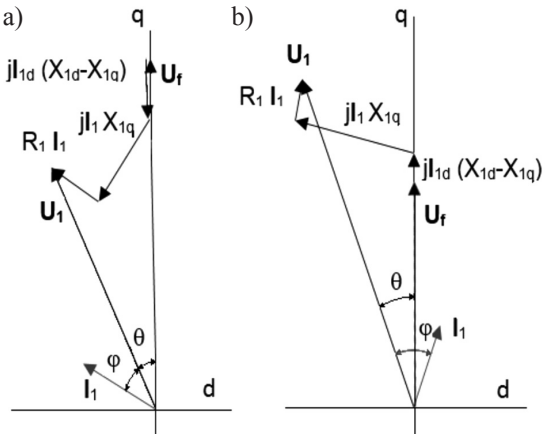

Fig. 1. Phasor diagrams of PMSM, a) over-excited motor, b) under-excited motor

3. Dynamic Model of PMSM

The *d-q* dynamic model is expressed in a rotating frame that moves at a synchronous speed ω_r. The general equation of PMSM working as a motor is as follows:

$$\frac{\mathrm{d}i_d}{\mathrm{d}t} = \frac{u_d}{L_d} - \frac{Ri_d}{L_d} + \frac{L_q}{L_d} p\omega_r i_q \tag{4}$$

$$\frac{\mathrm{d}i_q}{\mathrm{d}t} = \frac{u_q}{L_q} - \frac{Ri_q}{L_q} + \frac{L_d}{L_q} p\omega_r i_d - \Phi \frac{p\omega_r}{L_q} \tag{5}$$

$$T_e = \frac{3}{2} p\left[\Phi i_q + (L_d - L_q) i_d i_q\right] \tag{6}$$

where:
i_d and i_q – the *d* and *q* axis stator currents,
L_d and L_q – the *d* and *q* axis inductances,
u_d and u_q – the *d* and *q* axis stator voltages,
R – phase resistance,
p – the number of pole pairs,
ω_r – the rotor angular speed,
Φ – excitation flux created by the PM.

Electromagnet torque with considered CT is:

$$T_e' = T_e + T_c \tag{7}$$

T_c – depends on stator/rotor angular position.

ANSYS/Maxwell simulation explored the impact of the permanent magnet volumes and arrangement on the cogging torque. Two types of design were chosen, with both motors being two-pole versions.

Type A has rotor surface-mounted magnets. The magnets are semi-arc shaped (rotor surface-mounted magnets). With this type, it can be anticipated that the reactance X_d and X_q are identical.

Type B has two poles made of six magnets embedded in the rotor (Fig. 2). The width, thickness and angles among the magnets of one pole were altered.

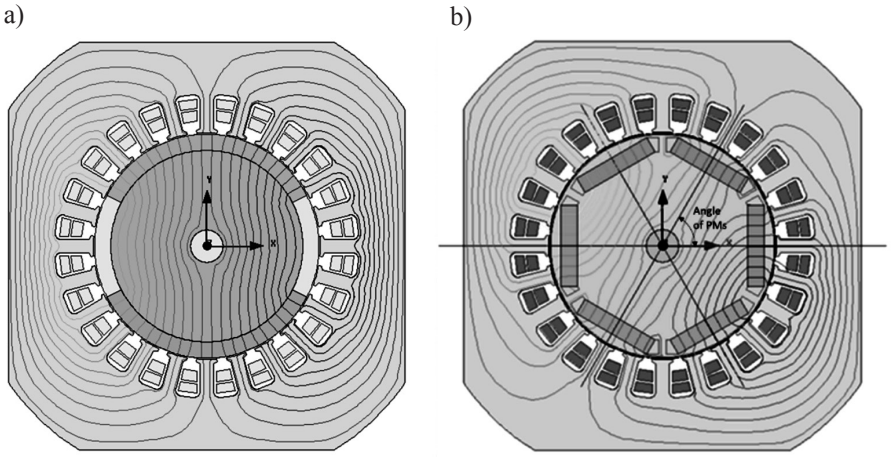

Fig. 2. Design types explored: a) A – motor with rotor surface-mounted magnets, b) B – motor with tangentially embedded magnets.
Dimension of rotor: D_{rot} = 55 mm, rotor length = 26 mm, air gap = 0.5 mm

4. Impact of the Magnet Geometry upon Cogging Torque

When designing 2-pole and 2-phase synchronous motors with permanent magnets, the cogging torque (CT) issue is emerging as more seriously than in the three-phase machines with PM. In this case, the situation becomes worse due to the fact that the magnetic circuit of the stator cannot be changed. The stator has a concentric winding.

The oscillation frequency of the cogging torque depends on the number of slots and is given by the following equation [2]:

$$f_c = \frac{z_1}{p} \cdot f \tag{8}$$

where:
z_1 – the number of stator slots, z_1 = 24,
p – the number of pole pairs,
f – the input frequency, f = 50 Hz.

Analytical methods for calculating the cogging torque usually neglect the magnetic flux through the stator slot and the saturation of the magnetic circuit. The cogging torque can be computed by the derivative of magnetic energy W produced by permanent magnets with respect to the rotor position angle α:

$$T_c = \frac{\mathrm{d}W}{\mathrm{d}\alpha} \tag{9}$$

Upon adjustment and introduction of coordinate x that represents the air gap length, we have arrived at the equation below:

$$T_c = \frac{D_{2\mathrm{out}}}{2}\frac{\mathrm{d}W}{\mathrm{d}x} \tag{10}$$

where $\alpha = 2x/D_{2\mathrm{uot}}$. It is anticipated that the rotor outer diameter is roughly equal to the stator inner diameter $D_{2\mathrm{out}} \approx D_{1\mathrm{in}}$.

In addition to f_c frequency in the timeline of the CT frequencies that are related to the arrangement of magnets can be found.

The waveform of CT can be, if disregarded is saturation of the magnetic circuitry, described by equation [5]:

$$M_c(\alpha) = \sum_{k=1}^{\infty} M_k \cdot \sin(k \cdot z_1\alpha + \varphi_k) \tag{11}$$

where:
z_1 – the number of stator slots,
M_k – the related harmonic's amplitude,
φ_k – the phase shift of the respective harmonic,
α – the rotor position.

The cogging torque can by minimised by a proper design [2]. Measures taken in the motor design to minimise the torque ripple include:

- elimination of stator slots,
- skewed slots,
- special shape slots and stator laminations,
- selection of the number of stator slots with respect to the number of poles,
- decentred magnets,
- skewed magnets,
- shifted magnet segments,
- selection of width,
- direction-dependent magnetization of permanent magnets.

ANSYS/Maxwell 2D cogging torque was calculated for the given magnetic circuit of the stator, for two principal rotor types (types A and B; Fig. 2), and for various shapes of magnets.

In type A, which has two arched magnets on the surface of the rotor, the thickness (HM) and also the magnet central angle represented by the *pole embrace* were changed. *Pole embrace* = 1 corresponds to a central angle of 180° and a *pole embrace* = 0.5 corresponds to 90°.

In type B, which is made of 6 magnets forming 2 poles, the magnet thickness (HM), magnet width (SM), and arrangement of magnets that was characterised by the angle between one pole magnets were changed. (Fig. 2b).

In both cases, the magnet length equals the length of the magnetic circuit.

Type A

The dependence of CT from pole embrace is shown in Fig. 3. Multiples of the groove spacing (slot pitch) are represented by the dashed line. The smallest values and the minimum CT are for:

$$Pole\ embrace \approx (\pi - k2\pi/z_1 + \alpha_{od})/\pi \tag{12}$$

where:

$2\pi/z_1$ – slot pitch in degrees ($2\pi/z_1 = 15°$),

k – integer ($k = <1.5>$),

α_{od} – corresponds to 1/4 of the angle corresponding with the slot opening.

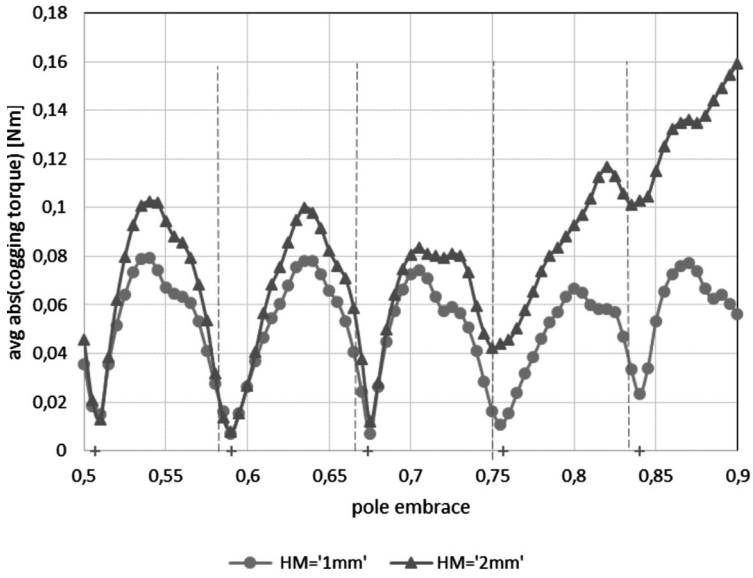

Fig. 3. Average value of absolute values of CT as depending on the pole embrace (HM-thicknesses of magnets)

The smallest CT value can be seen with *pole embrace* = 0.59. This corresponds with the magnet central angle of 106.2°. Different content of higher harmonics in the cogging torque waveform can be for selected *pole embrace* seen in Fig. 4. Prevailing in local max values is the frequency of 1200 Hz (equation (6)).

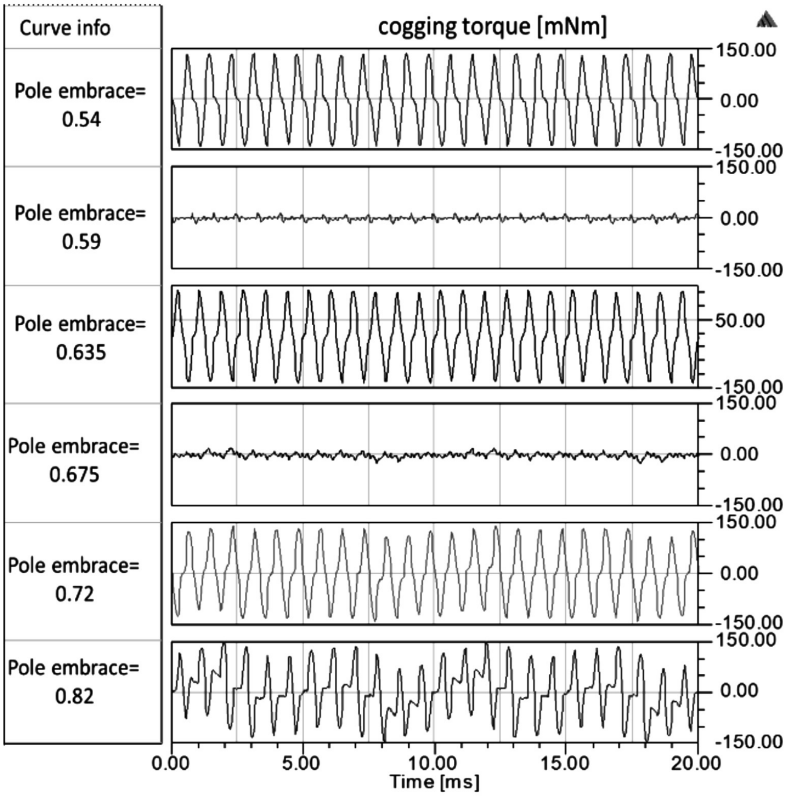

Fig. 4. Cogging torque as a function of time for different *pole embrace*. Rotor speed = 3000 rpm (*pole embrace*: 0.54, 0.59,0.635, 0.675, 0.72, 0.82)

Type B

In this motor type, each pole is composed of three magnets. They were placed in a symmetrical distribution, the angle between the magnets being 60°. Analysis has shown that the arrangement of magnets has significant impact on the cogging torque, and that there exists an angle at which is the cogging torque minimal. CT average value (avgabs[CT]), as depending on the angle between magnets, is shown in Fig. 6. The parameters are the magnet widths (SM) and thicknesses (HM), respectively. The curves show the minimum for the angle of 55°. It is the angle between two magnets of one and the same pole.

The CT waveform dramatically changes with angles to the left and to the right of the minimum. The CT time waveforms for angles of 53°, 55°, and 57° for magnet thicknesses of 3 mm^{-s} and for magnet widths of 18 mm and 19 mm, respectively, are shown in Fig. 7.

The distribution of individual harmonics can be seen in the harmonic analysis shown in Fig. 8. Prevailing are multiples of 1200 Hz. The 1200 Hz frequency is given by the number of slots (equation (8)).

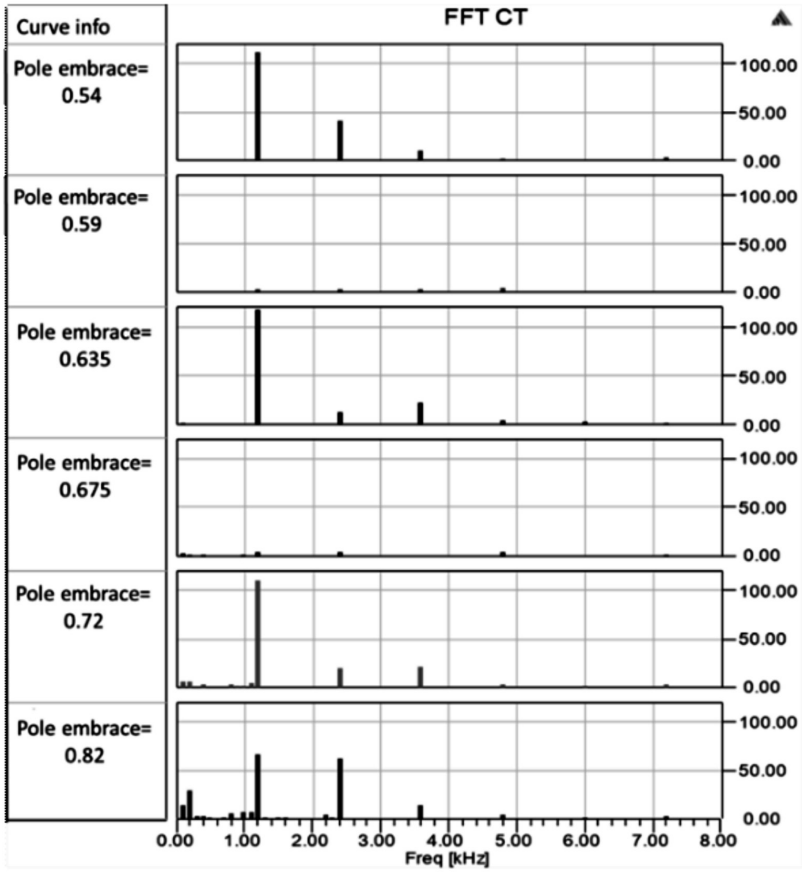

Fig. 5. Harmonic components of the waveform (mag(CT)) given in Fig. 4 (*pole embrace*: 0.54, 0.59, 0.635, 0.675, 0.72, 0.82)

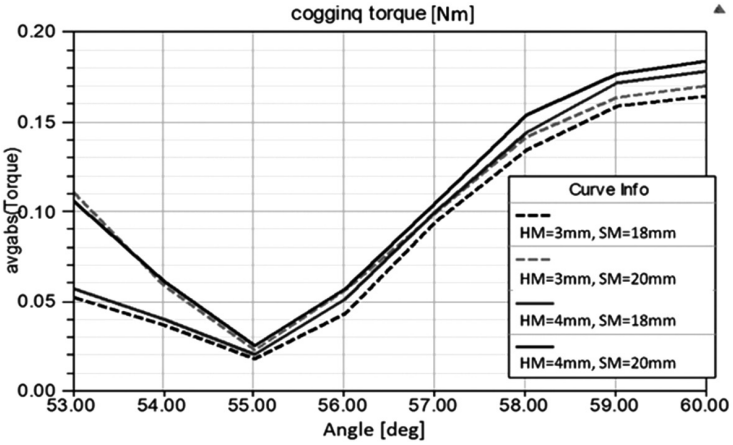

Fig. 6. The average value of the CT (absolute values) depending on the angle between PM (HM – heights of magnets, SM – widths of magnets)

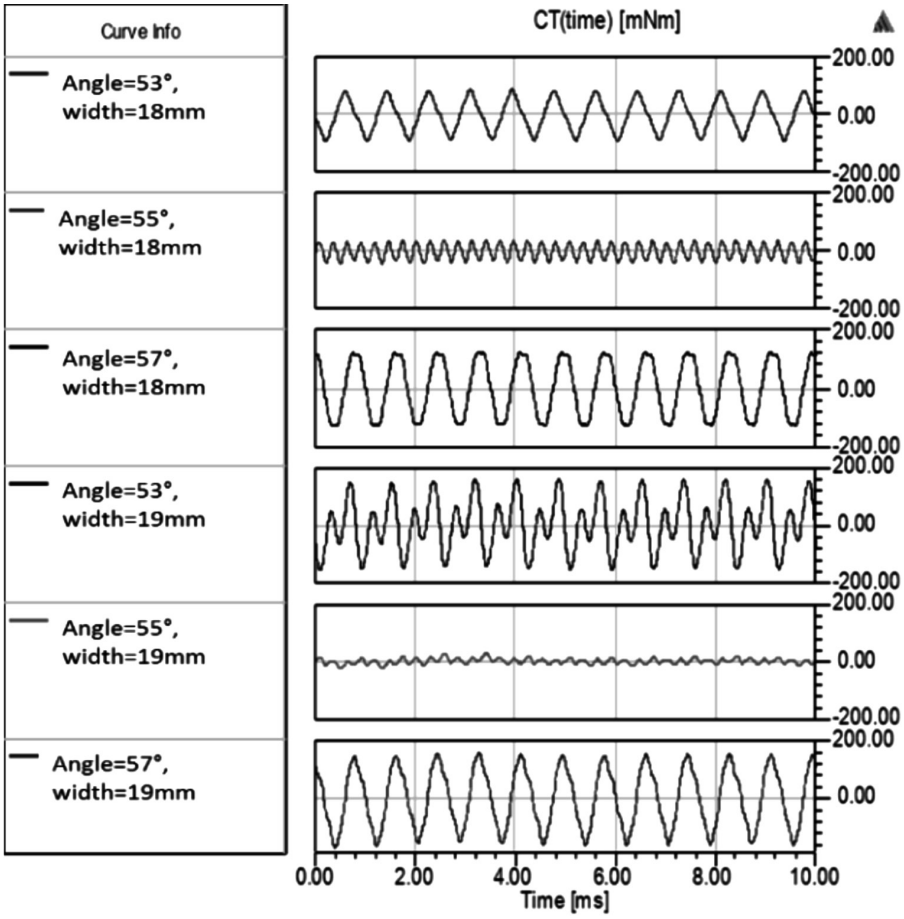

Fig. 7. Cogging torque as function of time for different width of PM and the angle between PM. Rotor speed = 3000 rpm

5. Conclusions

This paper has demonstrated cogging torque dependencies upon the dimensions and geometry of placement of magnets. Fourier analysis of CT waveforms shows a changing spectrum that changes with the arrangement of magnets. Prevailing in both cases are frequencies of f_c = 1200 Hz that are determined by the number of slots, and also multiples of f_c. In areas with a minimum value of CT, these frequencies are significantly suppressed.

Better results, while decreasing cogging torque, can be reached by the skewing of magnets or by the skewing of stator slots. This issue has been resolved although it was not discussed in this article.

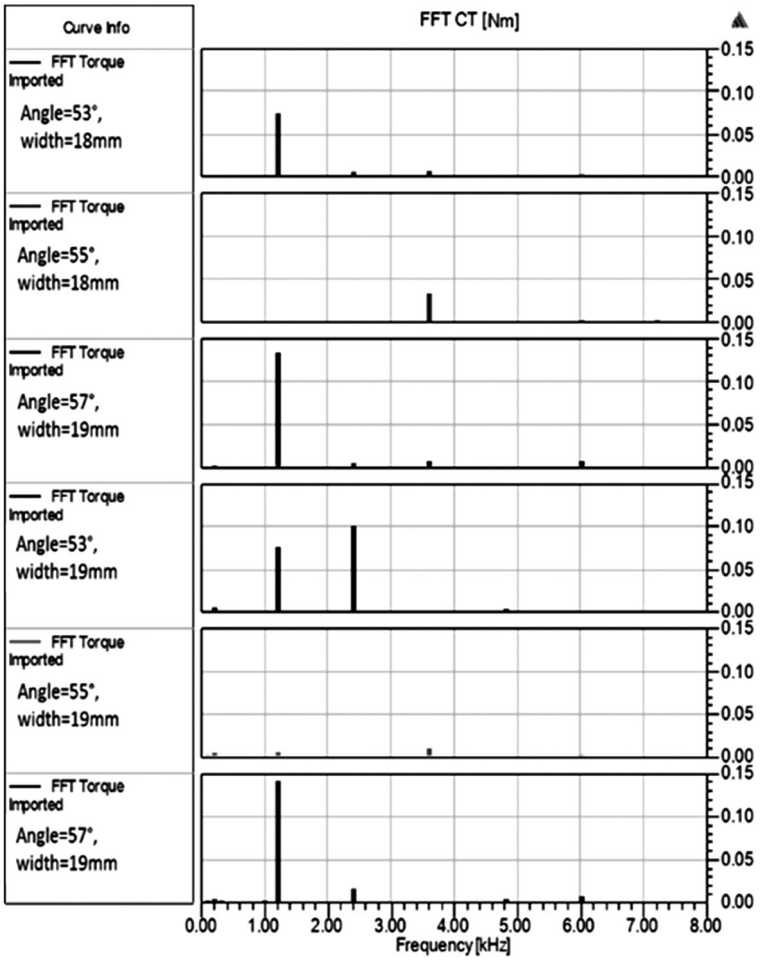

Fig. 8. Harmonic components of the waveform (mag(CT)) given in Fig. 7

Acknowledgement

This work was supported by the Slovak Research and Development Agency under the contract No. SK-CZ-2013-0065 and by the Scientific Agency under the contract No. VEGA 1/0121/15.

References

[1] Pyrhönen L., Jokinenm T., Hrabovcová V., *Design of Rotating Electrical Machines*, John Wiley & Sons, Ltd, 2008.

[2] Gieras J., Wing M., *Permanent Magnet Motor Technology*, Marcel Dekker, USA, 2002.

[3] Gieras J., *Analytical Approach to cogging Torque Calculation of PM Brushless Motors*, IEEE Transactions on Industry Applications, 2004, Vol. 40, No. 5.

[4] Glinka T., *Maszyny elektryczne wzbudzane magnesami trwałymi*, Wydawnictwo Politechniki Śląskiej, Gliwice 2002.

[5] Glinka T., Jakubiec M., *Silniki elektryczne z magnesami trwałymi umieszczonymi na wirniku*, Zeszyty Problemowe – Maszyny Elektryczne, 2005, nr 71, Katowice, p. 103.

[6] Dosiek L., Pillay P., *Cogging Torque Reduction in Permanent Magnet Machines*, IEEE Transactions on Industry Applications, 2007, Vol. 43, No. 65.

[7] Tudorache T., Trifu I., Ghita C., Bostan V., *Improved mathematical model of PMSM taking into account cogging torque oscilations*, Advances in Elektrical and Computer Engineering, 2012, Vol. 12, No. 3, pp. 59–66.

[8] Rosa R., Pistelok P., *The algotithm for the electromagnetic calculations of the concentrated winding permanent magnet synchronous motors*, Zeszyty Problemowe – Maszyny Elektryczne, 2013, nr 4, BORME Komel, Katowice, pp. 161–169.

[9] Mynarek P., Kowol M., *Field-circuit analysis of permanent magnet synchronous motors*, Zeszyty Problemowe – Maszyny Elektryczne, 2014, nr 4, BORME Komel, Katowice, pp. 73–76.

[10] Sekerák P., Hrabovcová V., Pyrhönen J., Kalamen L., Rafajdus P., Onufer M., *Comparison of synchronous motors with different permanent magnet and winding types*, IEEE, Transaction on Magnetics, 2013, Vol. 49, No. 3, ADC, pp. 1256–1263, 9018–9464.

[11] Hruska K., Kindl V., Pechanek R., *Design and FEM analyses of an electrically excited automotive synchronous motor*, 15th International Power Electronics and Motion Control Conference and Exposition 2012, EPE-PEMC 2012 ECCE Europe, art. no. 6397422, pp. LS2e.21–LS2e.27.

[12] Ivančo V., Novotný L., *Mechanika (Mechanics)*, TU Košice, Košice 2010, ISBN 978-80-553-0604-9.

[13] Howe D., Zhu Z.Q., *Cogging torque in permanent magnet machines*, http://www.shef.ac.uk/uni/academic/D-H/eee/md/cogging.html.

[14] Sung S.J., Park S.J., Jang G.H., *Cogging Torque of Brushless DC Motors Due to the Interaction Between the Uneven Magnetization of a Permanent Magnet and Teeth Curvature*, IEEE Transactions on Magnetics, July 2011, Vol. 47, No. 7, pp. 1932–1928.

TECHNICAL TRANSACTIONS | **CZASOPISMO TECHNICZNE**
ELECTRICAL ENGINEERING | ELEKTROTECHNIKA
1-E/2015

SEBASTIAN BERHAUSEN, ANDRZEJ BOBOŃ, ROMAN MIKSIEWICZ*

MEASUREMENT VERIFICATION OF A FIELD-CIRCUIT MODEL OF THE 55.5 MVA HYDROGENERATOR

WERYFIKACJA POMIAROWA MODELU POLOWO-OBWODOWEGO HYDROGENERATORA O MOCY 55,5 MVA

A b s t r a c t

A two-dimensional, field-circuit model of a 55.5 MVA hydrogenerator is presented in the paper. This model takes into account the fractional-pitch stator winding, the rotor damper squirrel-cage, nonlinear magnetization curves and the rotor motion. Verification of the model has been carried out by the comparison of the no-load and short-circuit characteristics computed using the finite element method with those obtained from measurements.

Keywords: *hydrogenerator*, *field-circuit model*, *finite element method*

S t r e s z c z e n i e

W pracy przedstawiono dwuwymiarowy polowo-obwodowy model hydrogeneratora o mocy 55,5 MVA. Model uwzględnia uzwojenie ułamkowe w stojanie, klatkę tłumiącą w wirniku, nieliniowe charakterystyki magnesowania rdzeni magnetycznych i ruch obrotowy wirnika. Weryfikację modelu polowo-obwodowego przeprowadzono na podstawie porównania zmierzonych i obliczonych metodą elementów skończonych charakterystyk biegu jałowego i trójfazowego zwarcia.

Słowa kluczowe: *hydrogenerator*, *model polowo-obwodowy*, *metoda elementów skończonych*

DOI: 10.4467/2353737XCT.15.038.3838

* Ph.D. Eng. Sebastian Berhausen, Ph.D. Eng. Andrzej Boboń, Ph.D. Eng. Roman Miksiewicz, Institute of Electrotechnics and Informatics, Faculty of Electrical Engineering, Silesian University of Technology.

1. Introduction

Synchronous generators installed in a power system operate under variable load conditions resulting from the need to balance the constantly changing demand for power in the system. Therefore, the monitoring of the current operating conditions of a generator as well as the ability to predict the behavior of a machine under different operating and load conditions becomes more and more important. The majority of scientific research studies addresses high-power turbogenerators. In the literature, much less attention is paid to hydrogenerators [2, 7, 8]. Hydrogenerators, like turbogenerators, are modernized during long-term operation to increase their rating power. There is therefore a need for research of those generators, not only in terms of the possibility of increasing power, but also their influence on the power system operation. Such research is often carried out by simulation programs in which mathematical models of hydrogenerators and turbogenerators are expressed in the *d*-*q* coordinate system.

Due to the large number of starts and stops in a daily cycle, hydrogenerators installed in pumped-storage power plants have to meet high requirements. Such machines must operate as a generator and a motor. This is why the design solutions of their rotors are more complex than those of turbogenerators. The stator windings of hydrogenerators often have a non-integer number of slots per pole and per phase, which is rare in turbogenerators of typical construction.

The field methods for calculating electromagnetic quantities of electrical machines under different operating conditions, using the finite element method (FEM), are currently the most accurate calculation methods, since they enable taking into account the influence of many factors neglected in approximate circuit calculations. In this paper, there is presented the measurement verification of a two-dimensional, field-circuit model of a HV832732/32 hydrogenerator installed in the pumped-storage power plant in Żydowo. The measurement verification was based on the comparison of no-load and three-phase symmetrical short-circuit characteristics determined experimentally with those calculated by FEM.

Calculations of static characteristics were carried out based on the distributions of electromagnetic fields obtained from solving the diffusion equations describing arbitrarily time-varying fields by FEM. Calculations of the generator steady state have to be preceded by calculations of the transient state. Therefore, they are time-consuming, require a large memory and considerable processing power of a computer. The assumed two-dimensional, field-circuit model of the generator takes into account all essential factors affecting the calculated characteristics, among others, the motion of the rotor as well as electromotive forces induced in the windings and damper squirrel-cage by higher harmonics of the magnetic field.

2. The field-circuit model of a hydrogenerator

The field-circuit model of a synchronous machine consists of differential equations with partial derivatives describing the distribution of the magnetic field inside the machine and differential equations with ordinary derivatives describing the voltage-current relationships in the electric circuits of the windings [3, 4].

The space-time distribution of the electromagnetic field in the machine is described by the equation for the magnetic vector potential **A**:

$$\mathrm{rot}\frac{1}{\mu}\mathrm{rot}\mathbf{A} = -\gamma\frac{\partial \mathbf{A}}{\partial t} \tag{1}$$

where:
γ – conductivity,
μ – magnetic permeability.

In the two-dimensional model, the magnetic vector potential has one component only. The average value of the flux linked with the *k*-th winding is expressed by the relationship

$$\Psi_{\mathrm{k}} = \sum_{\mathrm{i}} \frac{l_{\mathrm{e}}}{S_{\mathrm{i}}} \int_{s_{\mathrm{i}}} A_i \, \mathrm{d}s_i \tag{2}$$

where:
A_i – average value of the potential in the cross-section of the winding conductor,
S_i – surface area of the winding conductor,
l_{e} – effective length of the machine.

The Kirchhoff equation describing the electromagnetic state of the *k*-th winding is of the form:

$$u_k = R_k i_k + \frac{\mathrm{d}\Psi_k}{\mathrm{d}t} \tag{3}$$

Where u_k, i_k, Ψ_k – instantaneous values of the voltage, current and flux linkage of the *k*-th winding.

A salient-pole synchronous machine operating in Żydowo Pumped Storage Power Plant was the object of the investigations. The field-circuit calculations were carried out using Transient solver of Ansys Maxwell 2D software [1]. The ratings of the machine for the generator and motor operation are given in Table 1.

Table 1

Ratings of hydrogenerator HV832732/32

Quantity	Motor operation	Generator operation
S_n	55.5 MVA	71.5 MVA
P_n	48.3 MW	61.5 MW
I_n	3050 A	3900 A
I_{fn}	985 A	995 A
$\cos\varphi_n$	0.87 i	0.95 p
U_n = 10.5 kV, n_n = 187.5 rpm		

The tested hydrogenerator was a salient-pole (32 poles) and low-speed machine. A three-phase two-layer winding of two parallel branches and a non-integer number of slots per pole and phase (fractional winding, $q = 3.5$) is placed in 336 slots of the stator. In salient-pole machines, such a winding provides a lower harmonic content in the induced stator voltage [5, 8]. Due to a different number of slots occupied by the phase bands of the stator winding under successive poles, the region of analysis cannot be divided into symmetrical parts and the sizes of solved equations FEM cannot be reduced [8]. The analysis was performed for the half of the machine cross-section. In the pole shoes of the rotor poles, there are 8 bars of the damper squirrel-cage short-circuited on both sides of the rotor by short-circuiting rings.

In the developed computational model of the hydrogenerator, there was taken into account:

- two-dimensional distribution of the electromagnetic field in the generator cross-section comprising one pole pitch of the machine,
- nonlinear single-valued magnetization characteristics of the stator and rotor cores,
- constant speed of rotor rotation,
- currents induced in the rotor damper-squirrel cage and conducting elements of the rotor,
- influence of the harmonics of saturation, permeance and magnetomotive forces of the windings.

The skin effect in the stator windings and excitation winding was neglected.

The external electric circuits of the hydrogenerator, connected to the modelled windings in the field part, are shown in Fig. 1. They contain the resistances and leakage inductances of stator and excitation winding ends as well as the resistances and leakage inductances of the segments of the short-circuiting rings which short-circuit the bars of the damper squirrel-cage in the rotor. The values of these parameters were determined from the design relationships [9]. The switches (W) presented in Fig. 1 were open during the determination of the no-load characteristic and closed during the determination of the three-phase short-circuit characteristic.

The zero Dirichlet boundary condition for the vector magnetic potential was assumed on the outer surface of the stator and the inner surface of the rotor yoke. Symmetry conditions were imposed on the surface separating the two halves of the cross-section.

The rotational motion of the rotor was modeled in Maxwell software by means of the special object ‘band’ [1] comprising all rotating elements of the rotor. The electromagnetic field was calculated in two separate coordinate systems, motionless in relation to the stator and rotor, respectively.

The considered cross-section of the generator computational model was discretized using triangular finite elements of second order. The computational model contained about 127 000 finite elements. In magnetostatic calculations, the number of finite elements was twice as large since the full machine model was used for investigations. A fragment of the hydrogenerator cross-section and the finite element mesh are presented in Fig. 2.

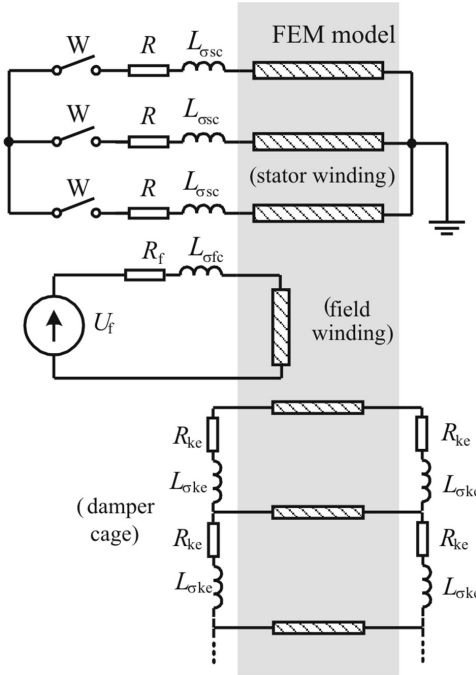

Fig. 1. External circuits connected to the hydrogenerator field model

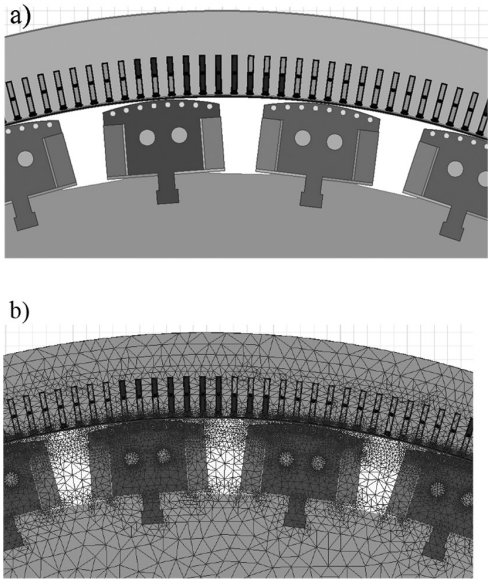

Fig. 2. Fragment of the hydrogenerator cross-section (a) and finie element mesh (b)

3. Field calculation results and measurement verification

The developed field-circuit model of the hydrogenerator was used for calculations of the no-load and three-phase symmetrical short-circuit characteristics. Individual points of the characteristics were determined based on instantaneous values of the appropriate voltages, currents and magnetic fluxes in the steady state after finishing the initial transient state.

3.1. The no-load characteristic

The no-load characteristic was determined based on a series of analyses of the electromagnetic field distribution for successive values of the excitation current at the open switch (*W*) of the stator winding (Fig. 1).

Figure 3a) shows the distribution of the magnetic flux density amplitude in the hydrogenerator cross-section in the steady state at no-load at the selected time instant.

In the steady state of a hydrogenerator operating at no-load, the currents induced by higher harmonics of the magnetic field, including subharmonics of the field generated by the fractional winding of the stator, flow in the damping circuits of the rotor [5]. To investigate their influence on the values of the voltages induced in the stator winding, there were calculations carried out whilst taking into account and neglecting the effect of the currents in-

duced in the damper squirrel-cage. Based on the calculations, it was stated that the influence of these currents on the no-load characteristic was negligibly small. The differences in the stator voltage, invisible on the no-load characteristic, are equal to about 40 V on the curved part of the characteristic (Fig. 4). The contents of harmonics in the generator stator voltage is small. Figure 5 shows the amplitudes of higher harmonics, calculated by FEM, in the phase and line-to-line voltage of the generator operating at no-load, related to the amplitude of the first harmonic. The third harmonic of the amplitude equal to 1.76% of the first harmonic amplitude is dominant in the phase voltage. The values of the other harmonics do not exceed 0.25% of the first harmonic amplitude. However, they are uncertain due to the fact that they are comparable with the level of numerical errors. The relative harmonic content of the phase voltage calculated up-to 40-th harmonic from the waveforms of the stator voltage equals [6]:

$$\mathrm{THD} = \frac{\sqrt{\sum_{k=2}^{n} U_k^2}}{U_1} = \begin{cases} 1.807 - \text{for the phase voltage} \\ \\ 0.286 - \text{for the line-to-line voltage} \end{cases} \tag{4}$$

Where U_1, U_k – rms value of the first and k-th harmonic of the stator voltage.

From the comparison of the measured and calculated by FEM no-load characteristics, it follows that the field-circuit model represents the saturation of magnetic cores and higher harmonics of the magnetic field with a strong degree of accuracy.

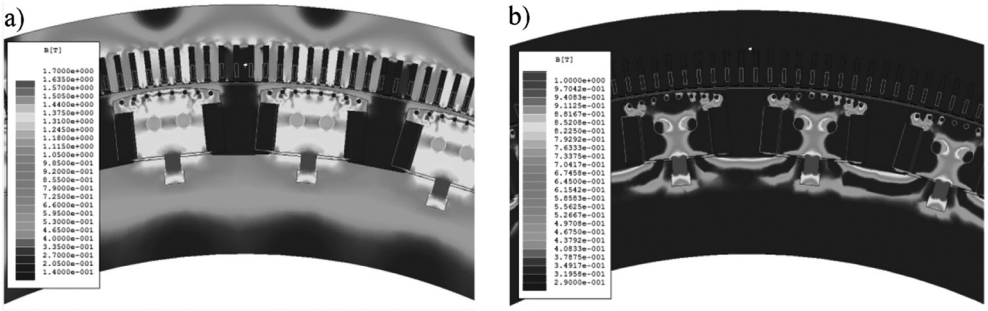

Fig. 3. Distribution of the magnetic flux density amplitude in the hydrogenerator cross-section in steady state at no-load (a) and symmetric short-circuit (b).

To shorten the calculation time, the no-load characteristics are often calculated based on the distributions of magnetostatic fields for given excitation currents. The voltage induced in the stator is calculated with the use of the relationships valid for the circuit model of a mono-harmonic machine. Figure 6 presents the no-load characteristic calculated by means of the magnetostatic solver of Ansys Maxwell. Compared to the calculations based on the generator field-circuit model for transient states, in the magnetostatic calculations the machine model does not take into account the rotational motion of the rotor and electromotive forces induced in the windings and damper squirrel-cage by higher harmonics of the field. The visible differences between the characteristics in the saturation region are equal to about 5%.

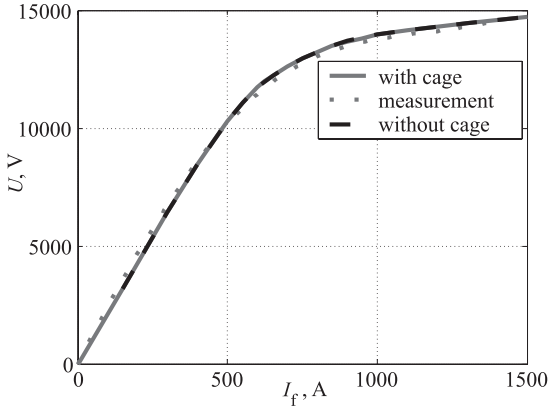

Fig. 4. Comparison of the no-load characteristic when taking into account and neglecting the effect of the damper squirrel-cage with the measured characteristic

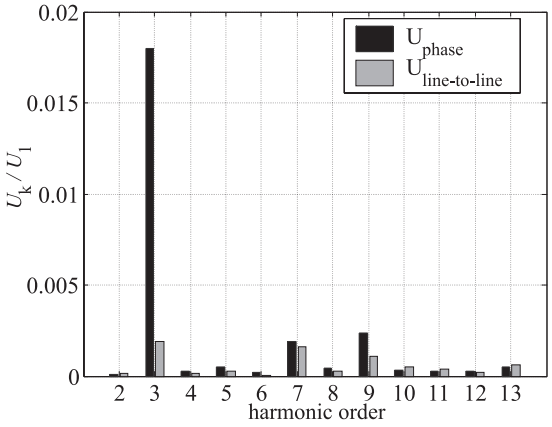

Fig. 5. Amplitudes of higher harmonics of the phase and line-to-line voltage of the stator related to the first harmonic amplitude at no-load

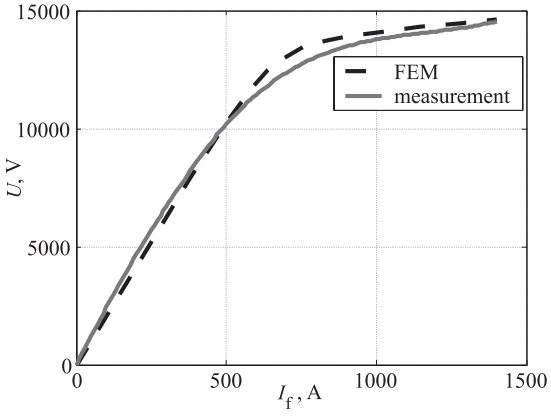

Fig. 6. Comparison of the no-load characteristic determined based on calculations of magnetostatic fields (FEM) and measurements

3.2. The three-phase symmetrical short-circuit characteristic

The three-phase symmetrical short-circuit characteristic was determined on the basis of a series of analyses of the electromagnetic field for successive values of the excitation current at the short-circuited stator winding. The computational model of the machine contains the circuit of three star-connected phases of the stator windings, short-circuited at terminals, connected to the field model FEM (Fig. 1). Figure 3b) shows the distribution of the magnetic flux density amplitude in the hydrogenerator cross-section at the steady-state symmetrical short-circuit at selected time instant. The comparison of the short-circuit characteristic calculated by FEM with that measured in Żydowo Power Plant is presented in Fig. 7.

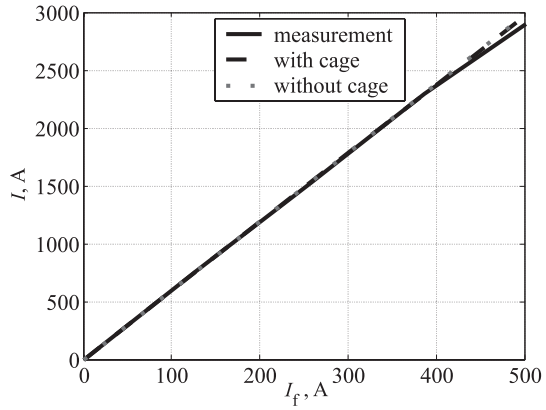

Fig. 7. Comparison of the calculated and measured three-phase symmetrical short-circuit characteristic of the hydrogenerator

From the carried out FEM calculations, it follows that the influence of the damper squirrel-cage on the rms values of the short-circuit currents is negligibly small under the analyzed operating conditions of the turbogenerator (Fig. 7).

The comparison of the calculated and measured characteristics recorded in Żydowo Power Plant proves the correctness of the modelled stator winding and rotor electric circuits.

4. Remarks and conclusions

The presented two-dimensional field-circuit hydrogenetaor model with a non-integer number of slots per pole and per phase in the stator includes all essential factors influencing the calculation accuracy. These factors are: nonlinearity of magnetization characteristics of magnetic cores; higher space and time harmonics of the magnetic field; rotational motion of the rotor; effect of currents induced in the damper squirrel-cage; conducting elements of the rotor.

The investigated hydrogenerator is a multipolar machine with a fractional pole pitch stator winding. To use the symmetry conditions enabling a reduction of the size of the solved system of equations FEM, the computational model should not comprise one pole pitch only, which is possible in machines with an integer number of slots per pole and per phase. This model should contain a greater number of pole pitches, dependent on the kind of a fractional winding.

The comparison of the no-load and short-circuit characteristics calculated based on this model with the measured characteristics proved the usefulness of the model for analyses of different states of generator operation. In particular, the agreement of the calculated and measured no-load characteristics confirms the correctness of modelling the phenomenon of saturation of magnetic cores and higher harmonics of the magnetic field. Whereas the agreement of the calculated and measured short-circuit characteristics confirms the correctness of modelling the stator winding and the electric circuits of the rotor.

The calculations of the no-load characteristic based on the distributions of the magnetostatic field can be loaded with a few percent error resulting from neglecting the effect of higher harmonics induced in the stator winding.

In the model, there are solved the diffusion equations, which is time-consuming, especially when the purpose of calculations is to determine the quantities in the steady state.

The field-circuit model of the hydrogenerator verified by measurements will be used for determining the parameters of circuit models of synchronous generators in further works by the authors of this paper.

References

[1] Ansys, Inc., *Ansys Maxwell 16.0 Online Help*, 2012.

[2] Arkkio A., Ahtiainen J., Lindgren O., *Finite Element Analysis for Hydrogenerators*, SME 1999, Prace Naukowe „Elektryka", z. 111, Oficyna Wydawnicza Politechniki Warszawskiej, Warszawa 1999, pp. 27–36.

[3] Berhausen S., Boboń A., Paszek S., *Estimation of Synchronous Generator Model Parameters Based On Analysis of Disturbance Waveforms Under Load Conditions with Use of the Finite Element Method*, Zeszyty Problemowe – Maszyny Elektryczne, BOBRME Komel, 2013, cz. II, nr 100(4), Katowice, pp. 13–18.

[4] Berhausen S., Boboń A., Paszek S., *Verification of a Field-Circuit Model of a Synchronous Generator Using Measured Transient Waveforms*, XIV Międzynarodowa Konferencja Naukowa „Aktualne Problemy w Elektroenergetyce", t. 1: *Systemy elektroenergetyczne: Modelowanie i badania symulacyjne*, APE 2009, Jurata, pp. 103–110.

[5] Dubicki B., *Electrical Machines. Alternating Current Windings, Vol. II*, Państwowe Wydawnictwo Naukowe, Warszawa 1953.

[6] Fuchs E.F., Masoum M.A.S., *Power Quality in Power Systems and Electrical Machines*, Academic Press, Elsevier, 2008.

[7] Nitta T., Okada T., *Analysis of Damper Winding Current of Synchronous Generator Due to Space Subharmonic M.M.F.*, IEEE Transaction on Magnetics, Nov. 1983, Vol. 19, No. 6, pp. 2643–2646.

[8] Schmidt E., Grabner Ch., Traxler-Samek G., *Reactance Calculation of a 500 MVA Hydro-Generator using a Finite Element Analysis with Superelements*, Proceedings of the IEMDC 2001, MIT, Cambridge, Boston, USA, 17–20 June 2001, pp. 838–844.

[9] Turowski J., *Electromagnetic Computations of Electrical Machines and Devices*, WNT, Warszawa 1982.

The authors thank to the company 'ENERGA WYTWARZANIE' for permission to publish the measurement data of the hydrogenerator used for investigations.

TECHNICAL TRANSACTIONS | **CZASOPISMO TECHNICZNE**
ELECTRICAL ENGINEERING | ELEKTROTECHNIKA
1-E/2015

GRZEGORZ KAMIŃSKI, PAWEŁ GÓRALSKI*

THE INFLUENCE OF GEOMETRIC DIMENSIONS ON TORQUE VALUE IN A COMPLEX MOTION COMMON MAGNETIC CIRCUIT ELECTRIMAGNETIC CONVERTER

WPŁYW GEOMETRII NA WIELKOŚCI MOMENTÓW OBROTOWYCH WYTWARZANYCH W ELEKTROMECHANICZNYM PRZETWORNIKU POŁOŻENIA O RUCHU ZŁOŻONYM OPARTYM NA STRUKTURZE RADIALNEJ

Abstract

The article presents the results of the impact of various geometric dimensions of torque in a complex motion electromechanical converter. The converter differs from the conventional radial structure motor in that it has two rotors, an inner and an outer, and excitation by a common stator which is located between them. The use of such a system introduces different size ratios relative to the normal external rotor motor. The result is that the shape of the torque curve of the outer rotor is different from the one in the internal rotor. This article presents a study on the impact of individual items in the course of time – this relied upon a comparison of several hundred configuration dimensions.

Keywords: *electrical machines*, *influence of geometric dimensions on torque value*

Streszczenie

W artykule przedstawiono wyniki badania wpływu poszczególnych wymiarów geometrycznych na moment obrotowy w elektromechanicznym przetworniku położenia o ruchu złożonym. Przetwornik różni się od konwencjonalnego silnika w strukturze radialnej tym, że posiada dwa wirniki, wewnętrzny i zewnętrzny, a wzbudzający je wspólny stojan znajduje się pomiędzy nimi. Zastosowanie takiego układu wprowadza inne proporcje wymiarów w stosunku do zwykłego silnika z zewnętrznym wirnikiem. Powoduje to, że kształt krzywej momentu wirnika zewnętrznego różni się od uzyskanego w wirniku wewnętrznym. W niniejszym artykule przedstawiono badania wpływu poszczególnych elementów na przebieg momentu, które polegały na porównaniu kilkuset konfiguracji wymiarów. Omówiono zasadę porównania rozbieżnych co do wartości wyników jedną zależnością kryterialną.

Słowa kluczowe: *maszyny elektryczne*, *wpływ geometrii na moment obrotowy*

DOI: 10.4467/2353737XCT.15.039.3839

* Prof. D.Sc. Ph.D. Eng. Grzegorz Kamiński, M.Sc. Eng. Paweł Góralski, Faculty of Electrical Engineering, Institute of Electrical Machines, Warsaw University of Technology.

1. Introduction

The development of computerized numerical control technologies inspires the creation of new complex motion electromechanical converters. The device presented herein allows simultaneous, independent linear and rotary shaft motion. The applied solution with a common magnetic circuit allowed the replacement of two motors with one. Accurate information is described in [1–4]. The main target of the common magnetic circuit is a reduction of device dimensions compared to the dual motor application. This requirement forces a height reduction of the outer part of the device and different parameter values in comparison to the inner part which is presented in Fig. 1. The result of usage of different parameter values was a disadvantageous torque distribution. To find appropriate solutions, several studies were performed.

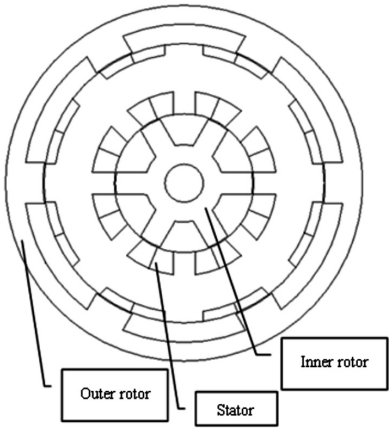

Fig. 1. Cross-section of the complex motion electromechanical converter

2. Research description

The study consisted of a 576 dimension configuration examination which was made on a filed model of a common circuit complex motion motor based on SRM philosophy. Every configuration test was to outer rotor torque registration, with energized proper coils in few rotor position from 0–0.5 range. Calculations were made in FEMM4.2 and Matlab software. The all parameter descriptions and range of change are shown in Table 1 and Fig. 3.

Table 1

No.	Coefficients	Description	Range
1	*kr*	Diameters coefficient	1.4–1.8 step 0.2
2	gamS2	Parameter specifying stator tooth width	0.2–0.5 step 0.1
3	*ks*2	Parameter specifying stator yoke height	0.2–0.5 step 0.1
4	*krr*2	Parameter specifying rotor yoke height	0.3–0.6 step 0.1
5	*kr*2	Parameter specifying the middle of air gap (in align rotor position)	0.4–0.6 step 0.1

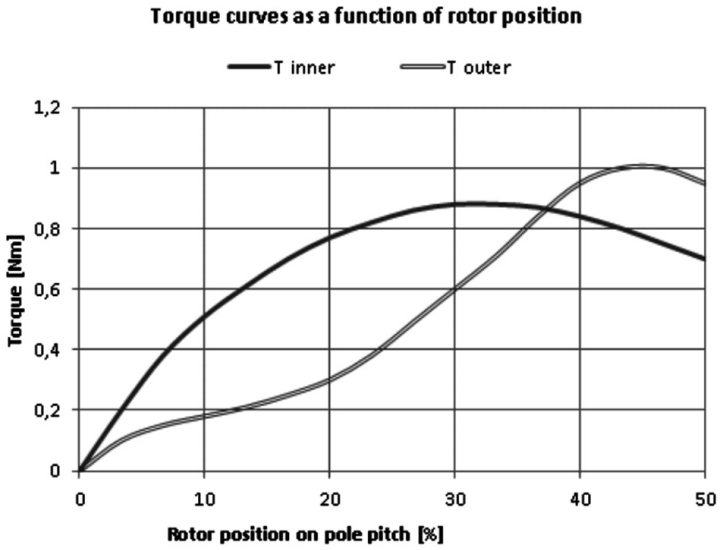

Fig. 2. Distribution of torques

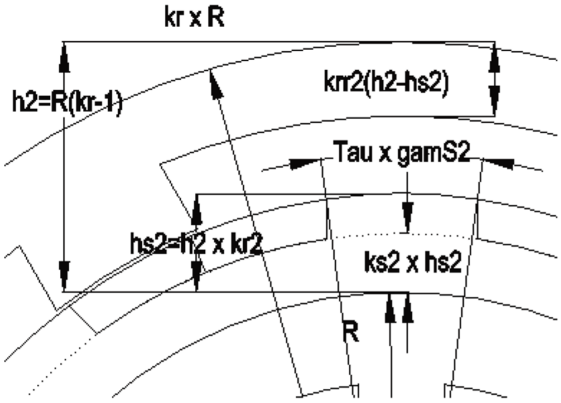

Fig. 3. Decision-making dimensions, and parameters

The result of the test was a torque matrix. For a qualitative comparison of the results, the average values were determined. In the next step, every configuration ripple factor was calculated. It was difficult to draw conclusions from data given in that form. Presentation of two related values as a function of five variables needs other form then spatial waveforms. It was considered that the mean value and ripple factor should be scaled by the maximum achieved values. For those values where the diameter coefficient was changed, should be scaled locally – this was to avoid comparing cases from different categories. Finally, it was decided to use a ratio of scaled coefficient of torque to ripple factor one, as a comparison criteria.

$$f_{\text{criterion}} = \frac{\dfrac{T_{\text{avg}}(n)}{\max\left(T_{\text{avg}}\right)}}{\dfrac{k_t(n)}{\max\left(k_t\right)}} \tag{1}$$

Where:
n – number of case,
T_{avg} – torque mean value of case n,
$\max(T_{\text{avg}})$ – maximum value of T_{avg} for range constant kr factor range.

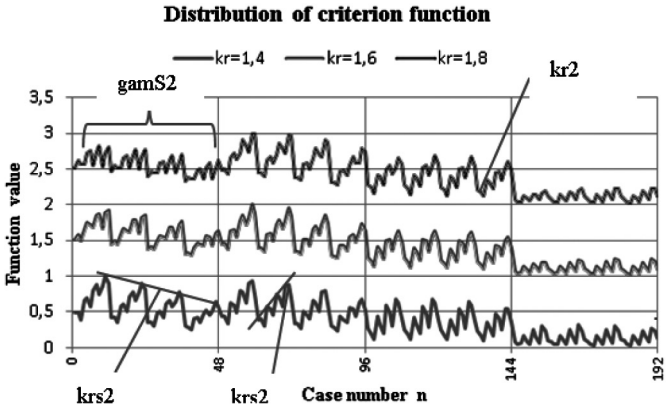

Fig. 4. Distribution of criterion function, for kr = 1.6 values increased +1, for kr = 1.8 values increased +2

There is course of criterion function presented in Fig. 4. There can be seen four areas of visible changes. The first is 1–48 range, where gamS2 parameter is 0.2, the second is 49–96 range for gamS2 = 0.3, the third is 97–144 for gamS2 = 0.4, the fourth 145–192 for gamS2 = 0.5. Based on this figure, the following conclusions can be drawn.

The pole width should be well-fitted to the diameter coefficient *kr*. This means that for small values of *kr*, the number of poles or phases should be increased. In every case, the number cycle per revolutions increases.

Too large a tooth width causes there to be too little space for winding and this results in a small torque value – this explanation is presented in Fig. 5.

Limited winding area comparing to stator tooth causes low flux distribution in the tooth core and too little reluctance change. The influence of the gamS2 parameter is shown in Fig. 6. The further analysis of Fig. 4 points other modulation of criterion function curve where 4 subareas can be found. Describing function fluctuation is caused by *ks*2 parameter. The *ks*2 parameter corresponds to the height of the stator yoke. The reduction of the criterion function is caused by the reduction of the stator yoke height. This situation is shown in Fig. 7. The stator tooth is significantly higher and the flux lines denser. It can also be seen in Fig. 4 that for increasing gamS2 values, *krs*2 parameter has no influence on criterion function.

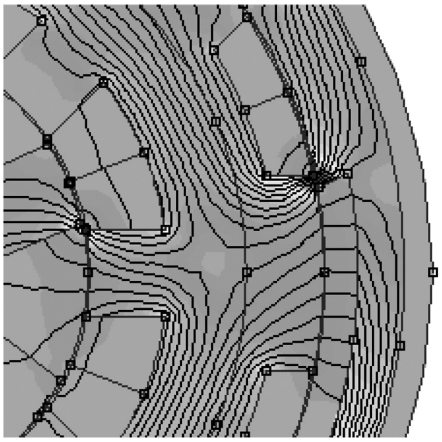

Fig. 5. Distribution of magnetic flux in pole tooth that is too wide. Unaligned rotor position

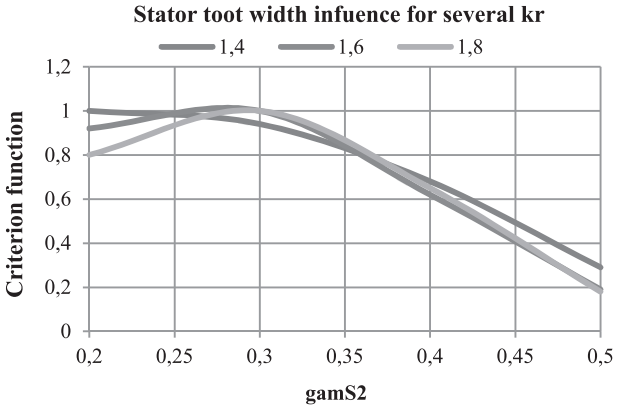

Fig. 6. The influence of stator width on criterion function for several *kr*

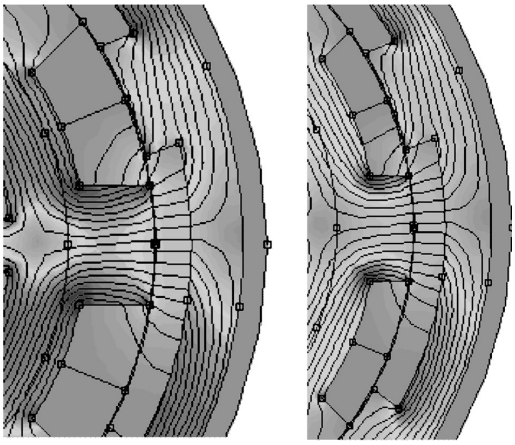

Fig. 7. Distribution of magnetic flux for different *krs*2 parameter values. Left *krs*2 = 0.2, right *krs*2 = 0.5

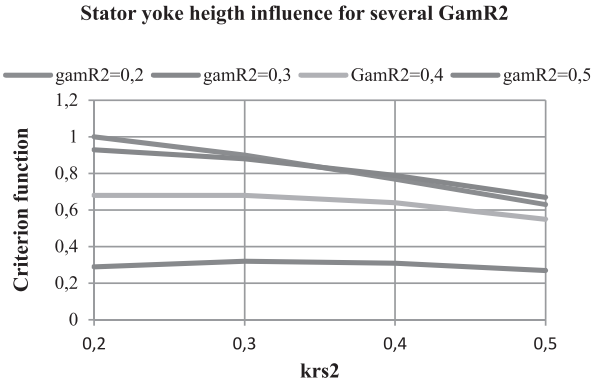

Fig. 8. The influence of stator yoke height for several GamR2

The parameter corresponding to rotor yoke height has a completely different effect on criterion function. The higher the value of *krr*2, the higher the criterion function value.

In Figure 8, the flux distributions in the magnetic core of two configurations are shown. Both constructions differ in the thicknesses of their rotor yokes. The influence of this parameter (*krr*2) can be seen in Fig. 11 where the saturation is shown.

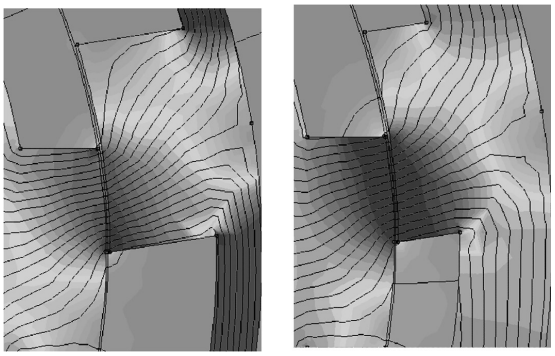

Fig. 9. Distribution of magnetic flux for different *krr*2 parameter values. Left *krr*2 = 0.2, right *krr*2 = 0.6

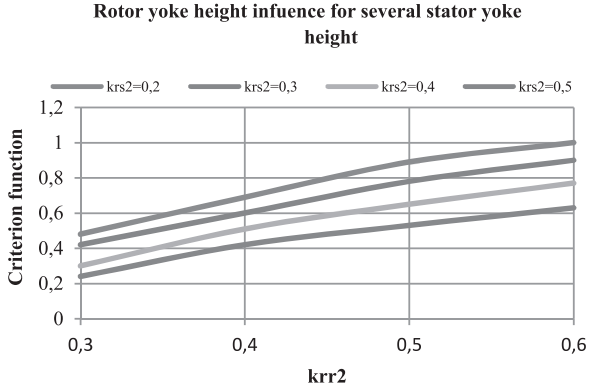

Fig. 10. The influence of rotor yoke height on criterion function for several stator yoke heights

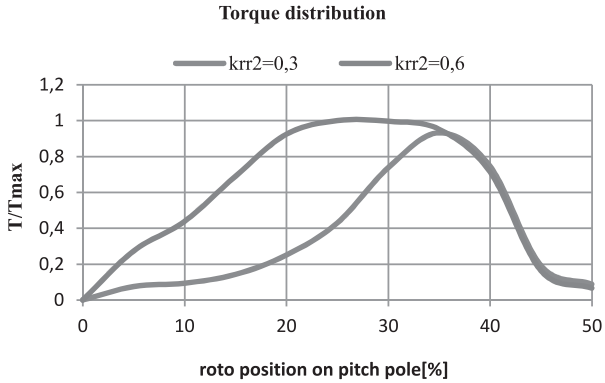

Fig. 11.Torque distributions for different stator yoke heights

It should be noted the description of moment problem by criterion function gives good results.

Another parameter resulting on outer rotor torque is the *kr*2 parameter. This coefficient defines the diameter of the air gap and scale dimensions controlled by krs2 and *krr*2. The influence of the *kr*2 parameter on criterion function is shown on Fig. 12.

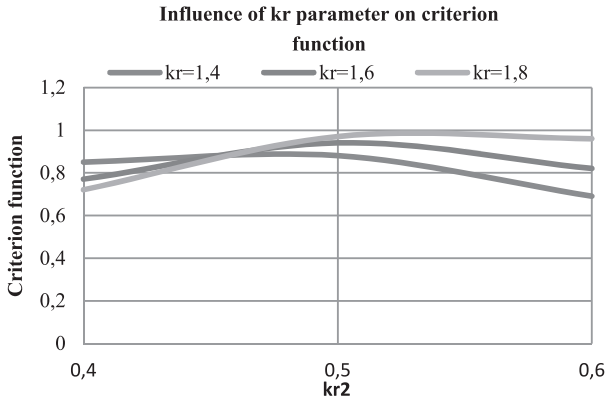

Fig. 12. The influence of *kr*2 parameter on criterion function

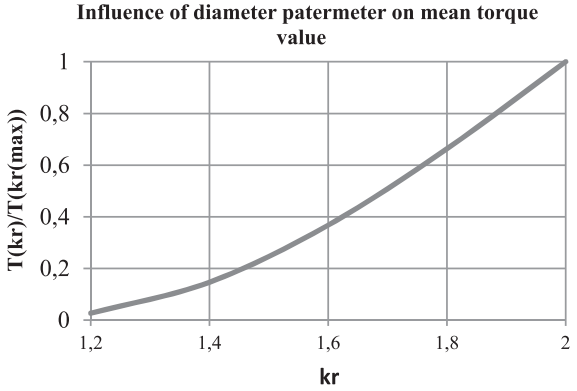

Fig. 13. The influence of *kr* parameter on torque mean value

Based on Fig. 12, it can be stated that the influence of the *kr*2 parameter is connected to the diameter coefficient. The optimum value is 0.5.

The reflections about influences of various parameter on torque ends diameter ratio discussion, which character is parabolic.

3. Summary

In this paper, the influence of various parameters on torque distribution was presented. Moreover, the efficient method of comparing and evaluating configurations was pointed out. A further step will be to analyze both the inner and the outer rotor. Then, in conjunction with criteria [5], the best possible solution for the set of requirements will be chosen.

References

[1] Kamiński G., Góralski P., *Opis prac badawczych nad konstrukcją przetwornika położenia o ruchu złożonym o wspólnym obwodzie magnetycznym*, Prace Naukowe Instytutu Maszyn, Napędów i Pomiarów Elektrycznych Nr 66 Politechniki Wrocławskiej, Studia i Materiały, nr 32, 2012.

[2] Kamiński G., Szczypior J., Koziej J., *Model matematyczny silnika reluktancyjnego przełączalnego z wirnikiem zewnętrznym*, Prace Naukowe Politechniki Warszawskiej, Elektryka, 1998, z. 102, pp. 65–78.

[3] Sochocki R., *Mikromaszyny elektryczne*, Oficyna Wydawnicza Politechniki Warszawskiej, Warszawa 1996.

[4] Kamiński G., Góralski P., *Przetwornik elektromechaniczny o ruchu złożonym*, Zgłoszenie do Urzędu Patentowego PR, nr P-398483.

[5] Kamiński G., Góralski P., *The electromagnetic calculations of complex motioncommon magnetic circuit electromagnetic converter*, Archives of Electrical Engineering, 2014, Vol. 63(1), pp. 125–133.

TECHNICAL TRANSACTIONS | **CZASOPISMO TECHNICZNE**
ELECTRICAL ENGINEERING | ELEKTROTECHNIKA
1-E/2015

ROMAN KROK, MARIAN PASKO*

THE MODERNIZATION OF TURBOGENERATORS AS A METHOD OF DECREASING ELECTRICAL ENERGY PRODUCTION COSTS

MODERNIZACJE TURBOGENERATORÓW SPOSOBEM NA ZMNIEJSZENIE KOSZTÓW PRODUKCJI ENERGII ELEKTRYCZNEJ

Abstract

This paper presents possibilities for reducing the costs of electricity generation as a result of modernizations aimed at increasing the rated power of turbogenerators. Programs for calculating temperature fields in large AC machines have aided work on turbogenerator modernization. Turbogenerators with increased rated power operate in many power plants in Poland and abroad, e.g. in Bulgaria, Finland, Greece, Slovenia, Korea and China. The example of TWW-200-2(2A) turbogenerator modernization is presented. The improved fans with increased capacity have enabled the increase in the turbogenerator rated power by 20%.

Keywords: *costs of electricity generation*, *modernizations of turbogenerators*, *CAD software*

Streszczenie

W artykule przedstawiono możliwości zmniejszenia kosztów produkcji energii elektrycznej w wyniku modernizacji zwiększających moce znamionowe turbogeneratorów. Programy do obliczeń pola temperatury w dużych maszynach prądu przemiennego wspomagają prace związane z modernizacją turbogeneratorów. Turbogeneratory o podwyższonych mocach znamionowych pracują w wielu elektrowniach w Polsce oraz między innymi w: Bułgarii, Finlandii, Grecji, Słowenii, Korei i Chinach. Zaprezentowano przykład modernizacji turbogeneratora TWW-200-2(2A). Udoskonalone wentylatory o zwiększonym wydatku umożliwiły podwyższenie mocy znamionowej turbogeneratora o 20%.

Słowa kluczowe: *koszty wytwarzania energii elektrycznej*, *modernizacje turbogeneratorów*, *programy wspomagające projektowanie*

DOI: 10.4467/2353737XCT.15.040.3840

* Ph.D. D.Sc. Eng. Roman Krok, Prof. D.Sc. Ph.D. Eng. Marian Pasko, Institute of Electrotechnics and Informatics, Faculty of Electrical Engineering, Silesian University of Technology.

1. Introduction

Lots of scientific institutions all over the world conduct research aimed at decreasing the costs of electrical generation and ensuring the proper quality of electrical energy. To aid the national economy, it seems advisable to reinforce power units in power stations during modernization.

In Poland, as in many other countries, a significant role in the generation of electrical energy is played by turbogenerators. The results of implemented research show that an increase of power of steam turbines by even 20% does not usually require much structural modification. The most difficult technical issue is how to modernize turbogenerators in order to increase their power and, at the same time, to increase their durability and improve operational reliability.

The calculations and measurements conducted for a lot of turbogenerators show that the introduction of structural modifications makes it possible to increase power output. The rated power of the turbogenerator is mostly restricted by full thermal utilization of stator, excitation windings and stator core. Therefore, an increase of turbogenerators' power first of all requires the introduction of changes ensuring improvement in the cooling of active elements. The allowable load of turbogenerators in some cases is limited by the heating of terminal elements of the stator core and mechanical stresses occurring during short-circuiting.

The calculated temperature field is used to evaluate new designs of turbogenerators' principal elements. The conducted research has resulted in the elaboration of the modified thermal networks method [1]. This method makes it possible to model the temperature field in large AC machines. The developed software based on this method constitutes the most important element of computer-aided systems for the design of turbogenerators.

2. Modified thermal networks in turbogenerator design

The thermal network method is one of the oldest methods used in the calculation of temperature distribution in electrical machines [1]. The early thermal networks contained only a few nodes, and the resultant sets of equations were solved analytically.

Significant increases in the number of nodes in the thermal network became possible when analog computers were applied for computing and, later on, digital computers. The increase in the number of nodes in the thermal network [2–9] resulted in improved accuracy of calculations. A dedicated node representing average temperature was assigned to each element of the electrical machine engaged in the heat exchange. In the classic approach to the thermal networks method, medium flowing through the cooling duct corresponds to one node representing its average temperature. The drawback of this modelling method is that there is no possibility of calculating the temperature distribution in elements of the electrical machine and the streams of the cooling medium flowing through these elements.

In very long cooling ducts of turbogenerators' active elements, the difference of medium temperatures between input and output may even reach several tens of kelvins. This leads to the emergence of very high non-uniformities of temperature distribution inside cooled elements. The approximate values of average temperatures of active elements, calculated by thermal network methods, are insufficient for a full assessment of the turbogenerator's thermal condition.

The novel method of modified thermal networks [10] makes it possible to model temperature distribution in medium streams in cooling ducts and inside the active elements of the turbogenerator. This is possible both for steady and transient thermal states.

In order to create a modified thermal network for steady-state conditions, active elements of the turbogenerator (excitation winding wires, stator bars etc.) are classified in accordance with the heat flow direction into differential zones (Fig. 1). Next, one thermal node is assigned to each active element. The nodes of the thermal network are connected by thermal conductances.

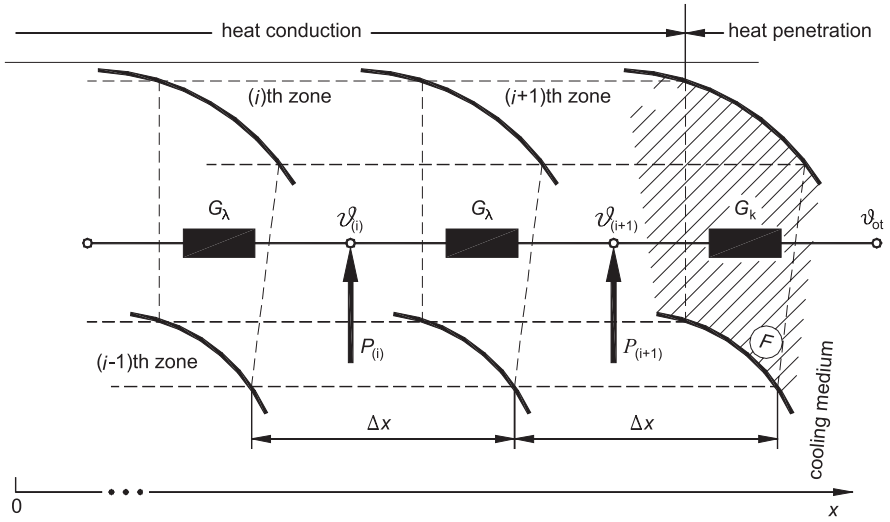

Fig. 1. Thermal network for element divided into differential zones in the thermal steady state

The conductance for thermal flux flowing between neighbouring differential zones due to conduction (Fig. 1) has been determined from the formula:

$$G_{\lambda} = \frac{\lambda_x \cdot F}{\Delta x} \tag{1}$$

where:

λ_x – specific thermal conductivity of the elemental material in the direction of the x axis,
F – area of face dividing neighbouring zones.

The conductance for thermal flux being removed from the face of the differential zone to the cooling medium coursing round it (Fig. 1) has been determined from the formula:

$$G_k = \alpha_k \cdot F \tag{2}$$

where:

α_k – heat removal factor,
F – area of face from which heat is removed to the cooling medium.

Additional power losses dependent on temperature are present in nodes representing differential zones singled out inside winding wires (Fig. 1):

$$P_{(i)} = P_o \cdot (1 + \alpha \cdot \vartheta_{(i)}) \qquad P_o = k_d \cdot j^2 \cdot \rho_o \cdot V \tag{3}$$

where:

P_o – power losses in the singled out zones at the reference temperature (in the models reference temperature was assumed to be 0°C),
α – temperature coefficient of the winding wire material,
$\vartheta_{(i)}$ – average temperature of *i*-th zone,
k_d – coefficient of additional losses,
j – average current density,
ρ_o – resistivity of the wire winding material at the reference temperature,
V – volume of singled out zones.

A novel thermal network for fluid or gas stream flowing in the cooling duct of the electrical machine has been presented in [1]. This network contains equivalent current sources (Fig. 2), with capacities equal to thermal powers carried by the cooling medium flowing in the duct:

$$P_{m(i)} = \dot{m}\, c_p\, \vartheta_{m(i)} \tag{4}$$

where:

$\dot{m}$ – mass flow of cooling medium,
c_p – medium's specific heat at constant pressure,
$\vartheta_{m(i)}$ – medium's average temperature in *i*-th differential zone singled out within the duct.

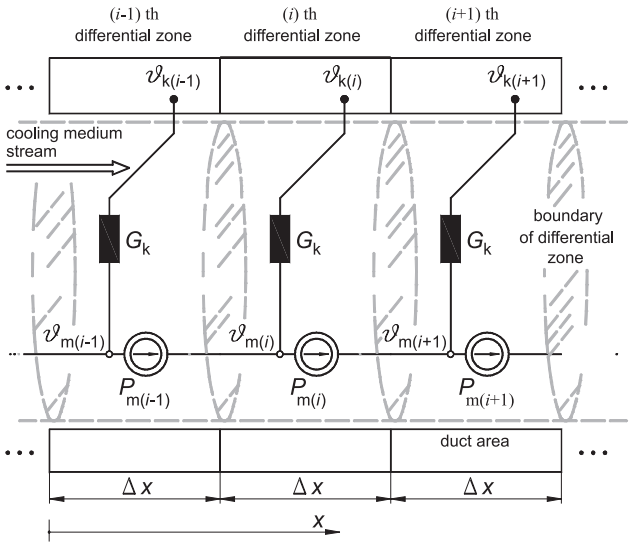

Fig. 2. Thermal network for medium stream flowing in the cooling duct of the electrical machine in thermal steady state

Increasing the mesh density (i.e. the partitioning of constructional elements of the electrical machine into differential zones) improves the accuracy of numerical calculations. At the same time, increase in the number of thermal network nodes must lengthen the calculation time. The optimum value of the Δx parameter, which determines the number of differential zone partitions of the constructional element and cooling duct, may be resolved by investigating the sensitivity of the solution (i.e. calculated temperature distributions in the element and medium stream) to its changes. For each generated modified thermal network we ran a series of calculations of temperature distribution, gradually decreasing the value of the Δx parameter.

When continued decreasing of this parameter at some point does not cause any further change in the calculated temperature greater than the assumed accuracy of numerical calculations (this accuracy has been assumed to be equal to 0.1 K), then the number of partitions obtained as a result of discretization is declared to be optimum. The optimum division of the element into differential zones ensures the achievement of the proposed accuracy of numerical calculations at the lowest possible number of singled out differential zones. The obtained results have not been compared with classic relative sensitivity according to Bode:

$$S_{\Delta x}^{R} = \frac{\partial R}{\partial \Delta x} \cdot \frac{\Delta x}{R} \tag{5}$$

where:
Δx – width of differential zone,
R – change in temperature distribution.

3. Example of TWW-200-2(2A) turbogenerator modernization

The developed computer software based on the modified thermal networks has been used in working out the plans of numerous modernizations of turbogenerators rating from 6 to 560 MW. These modernizations have been later implemented by TurboCare Poland S.A. in Lubliniec. The modernizations were aimed at increasing power with simultaneous rises in turbogenerator reliability.

In this section, we present the modernization of the TWW-200-2(2A) type turbogenerator. As a result of introducing constructional changes, we obtained an increase in the turbogenerator's power from 200 to 240 MW, i.e. by 20%, the rated power factor was unchanged. In addition, these modifications improved the operational reliability and lengthened the turbogenerator's durability.

The initial research related to modernization of this turbogenerator type, targeted at an increase of its power and aided by the modified thermal networks method was initiated in 1994. Then, modification in the excitation winding construction was introduced (but the cooling system constructed by the manufacturer [10] was not interfered with) and this caused a decrease in temperature rise of this turbogenerator element (it must be noted that excitation winding is the most utilized thermal element of the turbogenerator). As a result, we obtained an increase in the turbogenerator's power from 200 to 220 MW, while the rated power factor was unchanged. Thermal measurements of the modernized turbogenerator confirmed the effects anticipated in the modernization draft, i.e. the desired increase in power.

In order to increase turbogenerator power even more, we decided to introduce an axial cooling system in the excitation winding. Figure 1 shows the cross-section of the rotor slot with visible axial ducts, and Fig. 2 shows the network of cooling ducts for a quarter of the excitation winding coil.

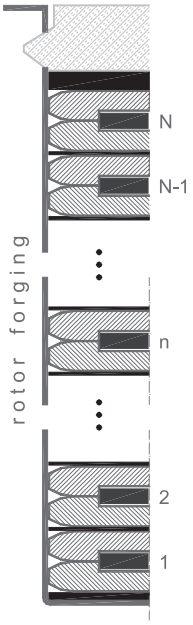

Fig. 3. Cross-section of rotor slot

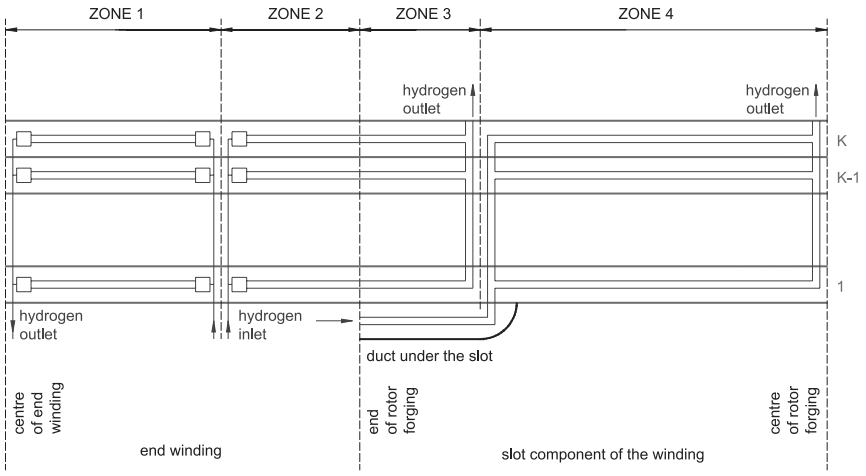

Fig. 4. Network of cooling ducts in one quarter of the excitation winding coil

Cold hydrogen flowing out of the cooler is forced under the covers by the fans. The wires of the excitation winding located near the end of the rotor forging contain holes, through which

hydrogen runs into the axial ducts. One stream of hydrogen flows through the axial ducts in the direction of the end winding centre, and from there, it flows out by the outlet holes. The second hydrogen stream flows through axial ducts in the windings in the direction of the rotor forging. The slot wedges and winding wires contain radial outlet ducts (located at some length from the end of the rotor forging), and through these, the coolant stream flows out to the rotor gap. The third hydrogen stream flows through ducts under the slots and then runs into the axial ducts in the winding wires through radial holes. This stream then flows out through radial holes in the winding wires and slot wedges near the centre of the rotor forging and goes into the rotor gap.

New fans were designed and constructed for the modernized turbogenerator; they were additionally equipped with rear guide blades. The comparative measurements in the aerodynamic tunnel showed that efficiency of new fans with rear guide blades is 24% higher than that of original fans.

Construction of the new axial fan with rear guide blades is shown in Fig. 5; fan blades (3) are fixed to the fan rotor (1), and rear guide blades (5) are located in the fan housing (4).

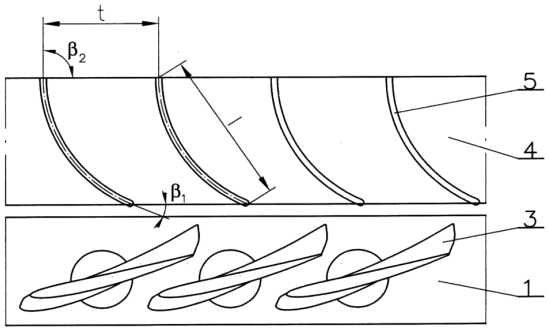

Fig. 5. Developed view of blade cascades of fan rotor and guide blades

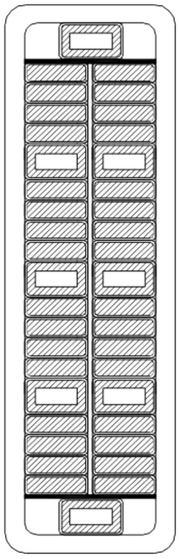

Fig. 6. Cross-section of stator winding bar

The stator winding of the modernized turbogenerator is cooled directly with distillate. The winding bars are made of both solid and hollow elementary conductors and distillate flows through them – see Fig. 6. The new bars differ from the original bars both in the number and the dimensions of the elementary conductors. The introduced constructional changes caused a decrease of losses in the turbogenerator stator winding as a result of the decreased additional power losses factor (these power losses are related to current displacement).

The construction of the turbogenerator stator core was unchanged. It is laminated and divided into axial segments; between these segments, radial cooling ducts are located.

Lots of additional changes were introduced into the turbogenerator, the most important were related to the modernization of the terminal elements of the stator core and hydrogen coolers.

Using thermal diagrams for the differential zone singled out in the wire (Fig. 1) and cooling duct (Fig. 2) in the steady state, a modified thermal network for the turbogenerator's excitation winding was created (Fig. 7). This network contained 206 thermal nodes.

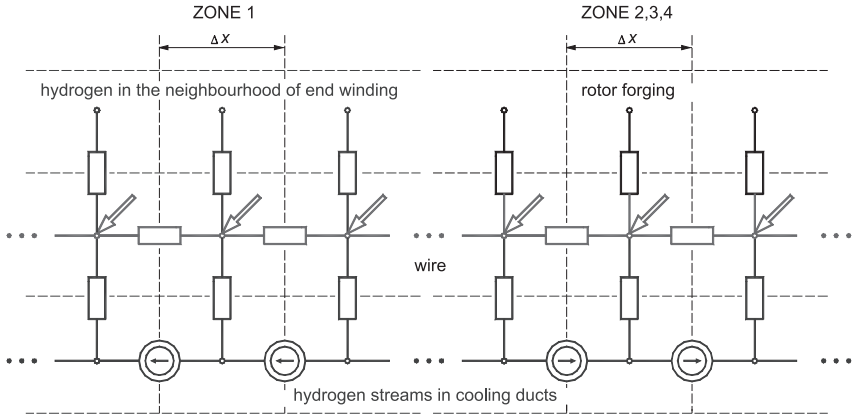

Fig. 7. Modified thermal network for excitation winding in thermal steady state

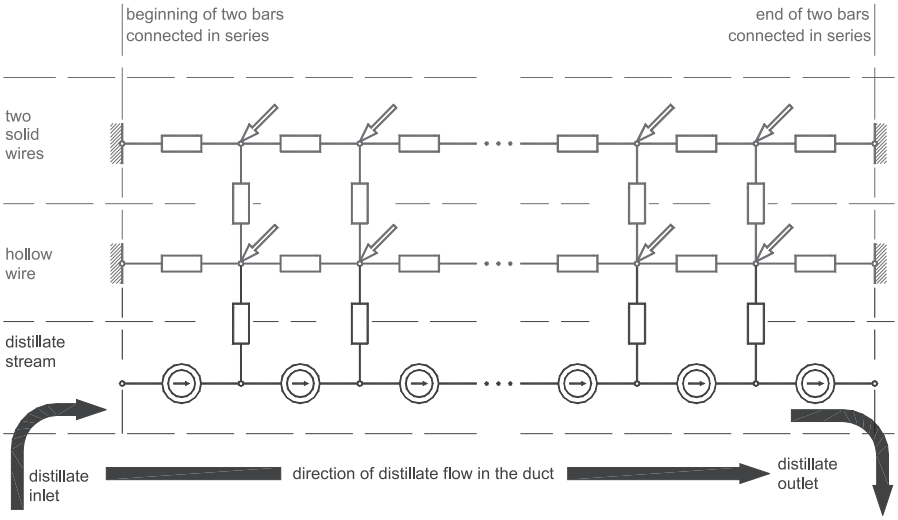

Fig. 8. Modified thermal network for stator winding in thermal steady state

Similar rules were applied in the creation of the modified thermal network for turbogenerator stator winding (Fig. 8). It contained 708 thermal nodes.

Using modified thermal networks, the temperature field in the active elements of the modernized turbogenerator was calculated. The generator was loaded with active power equal to $P = 255$ MW, at rated power factor $\cos\varphi_n = 0.85$ (lagging). An example of the temperature rise distribution in the wires of the excitation winding outer coil and its cooling hydrogen stream is shown in Fig. 9.

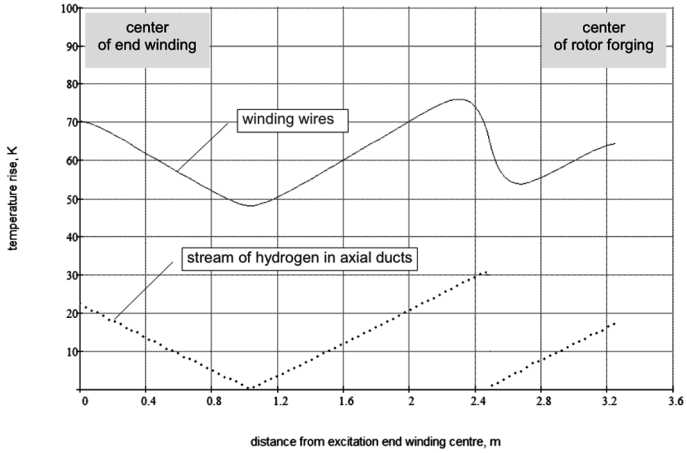

Fig. 9. Distribution of temperature rise in excitation winding outer coil – turbogenerator running at $P = 255$ MW, $\cos\varphi_n = 0.85$ (lag)

The calculated and allowable temperature rises of the active elements of modernized turbogenerator are compared in Table 1. All values relate to turbogenerator loaded with power $P = 255$ MW at rated power factor $\cos\varphi_n = 0.85$ (lagging).

Table 1

Comparison of calculated and allowable temperature rises

Temperature rise [K]	Calculated	Allowable
Average, excitation winding	60.5	70
Maximum, stator winding	36.5	49
Maximum, stator core	13.5	55

On account of the thermal utilization of the active elements, there exists a possibility of increasing the power of the modernized turbogenerator up to even 255 MW (with rated power factor unchanged). The presented modernization scheme was implemented in practice. The manufacturer took into account additional factors limiting the power (in the particular heating of the terminal elements of the stator core and mechanical stresses during short-circuiting) and stated the rated power as equal to 240 MW after moderniza-

tion. It must be noted that after modernization, the temperature rises in the active elements at rated operational conditions are significantly lower than the allowable rises – this fact must result in increased durability. It must also be emphasized that the modified thermal networks used in calculations were verified experimentally. They ensure a high accuracy of representing the temperature distribution in the turbogenerator. The maximum difference between the calculated and measured temperatures was equal to 6.5 K. In view of the complexity of the design of the modelled object, this must be acknowledged as a very satisfactory result.

4. Conclusion

Power stations all over the world try to lower the costs of electricity production. The operators wish to combine necessary repair work on the turbogenerators with modernization in order to increase the rated power and improve operational reliability. Research presented in this paper has resulted in numerous implemented modernizations of turbogenerators for power stations in EU and Asian countries (e.g. China and Korea). In addition, perfecting the design of turbogenerators has helped to eliminate many different types of failures. The modernization of the TWW-200-2(A) turbogenerator described in this paper may be considered a rather interesting case, since a very large increase in rated power was obtained (20%) with a simultaneous decrease of temperature rises in all active elements.

References

[1] Hak J., *Die inneren axialen Wärmewiderstände einer elektrischen Maschine*, Archiv für Elektrotechnik, Heft 1, 1957, pp. 58–76.

[2] Kalander G., *Temperature simulation of a 15 kW induction machine operating at variable speed*, International Conference on Electrical Machines, Manchester, United Kingdom, 1992, pp. 943–947.

[3] Rioul M., *Development of thermohydraulic modelling for the determination of hot spots in the bars and the slot thermal image for the stator 900 MW turbogenerators*, Proceedings of ICEM ’94, Paris, France, 1994, pp. 437–441.

[4] Elleuch M., Poloujadoff M., A *contribution to the modeling of three phase transformers using reluctance*, IEEE Transactions on Magnetics, 1996, No. 32, pp. 335–343.

[5] Mukosiej J., *Universal program for thermal calculation of electric machines by the method of equivalent thermal networks (ETN)*, Proceedings of ICEM ’96, Vigo, Spain, 1996, pp. 377–381.

[6] Tylavsky D.J., Qing He, Jennie Si, McCulla G.A., Hunt J.R., *Transformer top – oil temperature modeling and simulation*, IEEE Transactions on Industry Applications, 2000, Vol. 36, No. 5, pp. 1219–1225.

[7] Swift G., Molinski T.S., Lehn W., A *fundamental approach to transformer thermal modeling – Part I: Theory and equivalent circuit*, IEEE Transactions on Power Delivery, 2001, No. 16, pp. 171–175.

[8] Gurazdowski D., Zawilak J., *Rozkład temperatury w pręcie uzwojenia stojana turbogeneratora*, Zeszyty Problemowe – Maszyny Elektryczne, 2006, nr 75, Komel, pp. 177–184.

[9] Gurjewicz E.I., Filin A.G., *Pole temperatury w uzwojeniu stojana dużego turbogeneratora przy lokalnych uszkodzeniach wewnętrznego wodnego systemu chłodzenia*, Elektriczestvo, 2010, No. 3, pp. 23–29.

[10] Krok R., *Sieci cieplne w modelowaniu pola temperatury w maszynach elektrycznych prądu przemiennego*, Monografia, Wydawnictwo Politechniki Śląskiej, Gliwice 2010.

TECHNICAL TRANSACTIONS | **CZASOPISMO TECHNICZNE**
ELECTRICAL ENGINEERING | ELEKTROTECHNIKA
1-E/2015

PAWEŁ IDZIAK, MARIUSZ BARAŃSKI, WIESŁAW ŁYSKAWIŃSKI*

COMPARED ANALYSIS OF LSPMSM AND SQUIRREL-CAGE MOTOR EXPLOITATION WITH VARIABLE ROTATIONAL SPEED

ANALIZA PORÓWNAWCZA SILNIKÓW SYNCHRONICZNEGO MAGNETOELEKTRYCZNEGO O ROZRUCHU WŁASNYM I INDUKCYJNEGO PRACUJĄCYCH Z REGULOWANĄ PRĘDKOŚCIĄ

Abstract

In this paper, the steady-states operation of a line start permanent magnet synchronous motor (LSPMSM) and a squirrel-cage motor have been compared. The stator of a Sg 100L-4B type, 3 kW induction motor, was used in both structures. The squirrel cage in the rotor of the LSPMSM is made from copper. The influence of the frequency change of the supply voltage on the motor's efficiency and current as well as the power factor has been examined.

Keywords: *permanent magnet synchronous motor*, *asynchronous motor*, *power factor*, *efficiency*, *variable rotational speed*

Streszczenie

W artykule porównano pracę w stanie ustalonym dwóch silników: synchronicznego magnetoelektrycznego z klatką rozruchową (LSPMSM) oraz indukcyjnego klatkowego (IM). W obu konstrukcjach wykorzystano stojan silnika indukcyjnego typu Sg 100L-4B o mocy 3 kW. W silniku synchronicznym zastosowano klatkę rozruchową wykonaną z miedzi. Zbadano wpływ zmiany częstotliwości napięcia zasilającego oba silniki na sprawność, współczynnik mocy i prąd pobierany z sieci.

Słowa kluczowe: *silnik synchroniczny magnetoelektryczny*, *silnik indukcyjny*, *współczynnik mocy, sprawność*, *regulowana prędkość obrotowa*

DOI: 10.4467/2353737XCT.15.041.3841

* Ph.D. D.Sc. Eng. Paweł Idziak, Ph.D. Eng. Mariusz Barański, Ph.D. D.Sc. Eng. Wiesław Łyskawiński, Electrical Machines and Mechatronics, Faculty of Electrical Engineering, Poznan University of Technology.

1. Introduction

In order to reduce the operating costs of electric drives, induction motors are more frequently being replaced with permanent-magnet synchronous motors (PMSM), which with the same dimensions, provide a greater power efficiency and power factor [10]. In recent years, many interesting structures of these motors have been developed i.e. with a surface mounted permanent magnet [7, 9]. A disadvantage of the PMSM is that it necessitates the use of power converters during start-up, which increases the total cost of the drive. This cost can be minimized by using a synchronous motor adapted to start when directly connected to the supply voltage (Line Start Permanent Magnet Synchronous Motors – LSPMSM). Studies on this type of motor have been conducted in many research centers [3, 4, 6, 8].

This paper presents the results of the analysis of selected power parameters. The effects of changes in the motor's speed: permanent magnet synchronous and squirrel-cage induction motors on efficiency, power factor and current in the stator windings were tested. Changes in rotor speed were achieved by supplying the motors with an adjustable frequency.

The present paper is a continuation of the work carried out by the authors on the development of a new construction and testing of the LSPMSM [1, 2, 5].

2. Structure of examined motors

A squirrel-cage motor (IM) and line start permanent magnet synchronous motor were tested. In the considered constructions, the stator and frame of a 4 pole, Sg 100L-4B type, 3 kW induction motor, were used. The rated line to line supply voltage of the base IM was equal to 400 V (star connection) and the nominal speed was equal to 1415 rpm. The stator consisted of 36 slots and was wound with a single layer 3 phase winding. The rotor cage had 28 bars manufactured from aluminium (Fig. 1a). In the rotor of the LSPMSM, the bars were placed over a *U* arrangement of N42SH magnets embedded into the laminated rotor core (Fig. 1b).

Figure 2 shows the complete structure of both of the rotors of the considered motors.

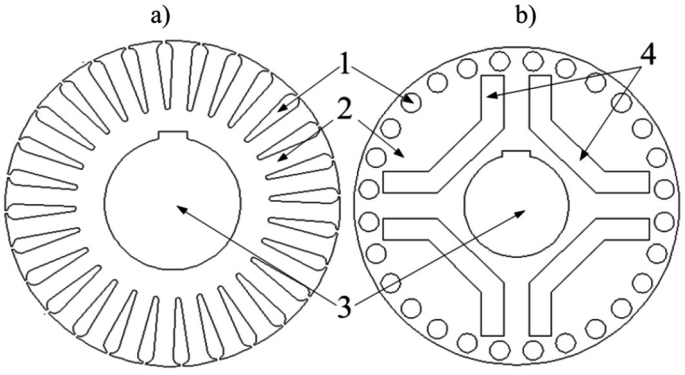

Fig. 1. The structures of rotors: a) IM, b) LSPMSM
(1 – rotor bars, 2 – rotor core, 3 – shaft, 4 – magnets)

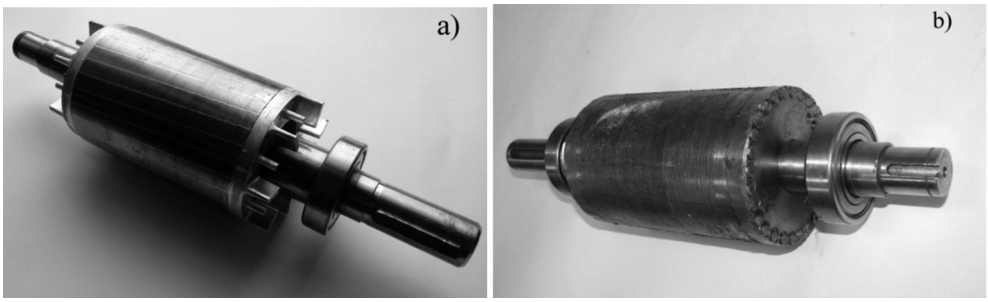

Fig. 2. Rotor of a) squirrel-cage motor and b) LSPMSM with a squirrel-cage manufactured from copper

3. Results

Measurements were performed by supplying the motors with an adjustable frequency, while maintaining the condition U/f = const. The influence of the load torque on the motor efficiency η, power factor cosφ as well as phase current I were examined. The results for the selected frequencies for the IM and the LSPMS motor are shown in Figs. 3 and 4 respectively.

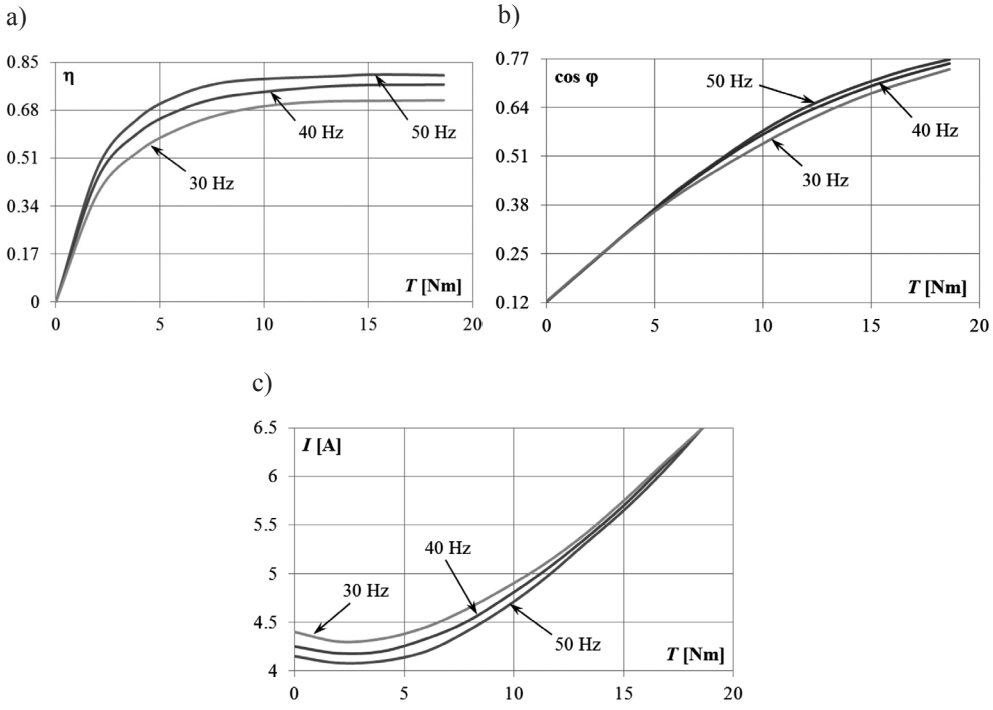

Fig. 3. Efficiency (a), power factor (b) and phase current (c) vs. load torque of the IM

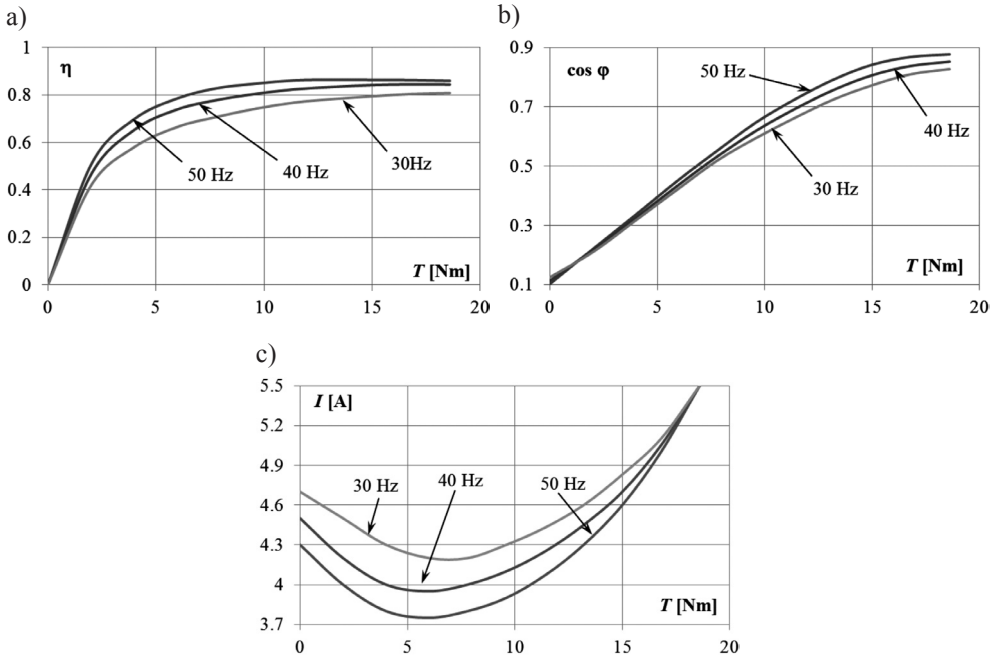

Fig. 4. Efficiency (a), power factor (b) and phase current (c) vs. load torque of the LSPMSM

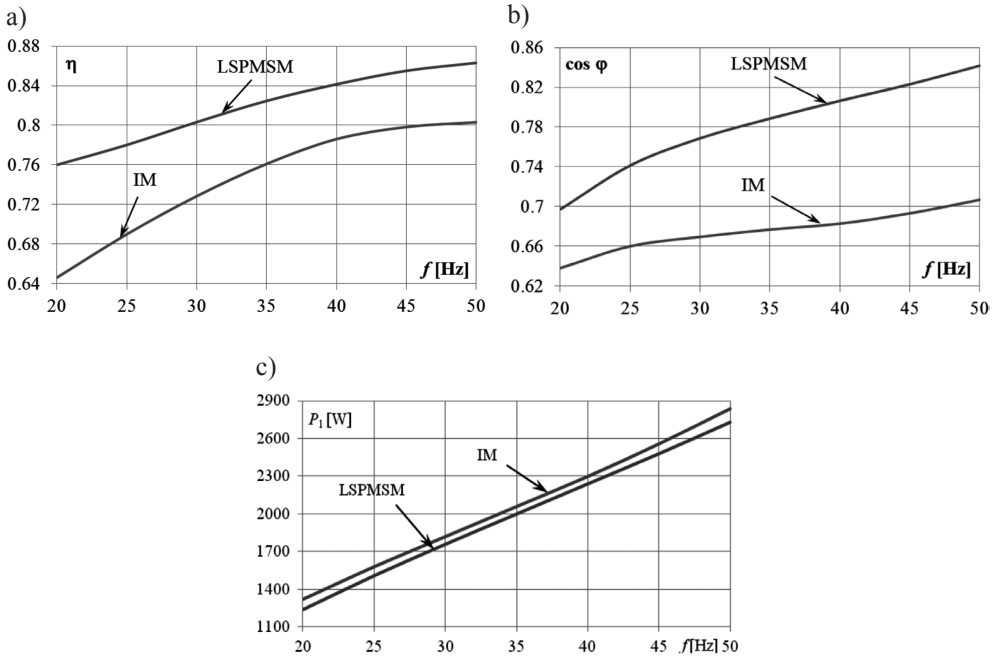

Fig. 5. Efficiency (a), power factor (b) and input power (c) vs. load torque of the IM as well as the LSPMSM

Measurements were also performed for motors supplied with an adjustable frequency at a constant load torque of T = 15 Nm. The influence of the frequency changes on the motor efficiency η, power factor cosφ as well as the input power P_1 is presented in Fig. 5. In order to compare the obtained functional parameters of both the considered motors in these operating conditions, the values of efficiency, power factor, currents in stator winding and useful power P_u are summarized in Table 1.

Table 1

Selected functional parameters in the steady state obtained during laboratory tests at T = 15 Nm and selected frequencies

Parameters	IM			LSPMSM		
	30 Hz	40 Hz	50 Hz	30 Hz	40 Hz	50 Hz
η [-]	0.728	0.786	0.803	0.803	0.842	0.863
cosφ [-]	0.669	0.683	0.707	0.769	0.806	0.842
I [A]	5.7	5.7	5.7	4.8	4.7	4.6
P_u [W]	1325	1808	2280	1414	1885	2356

4. Conclusions

The effective parameters of the LSPMSM are better than those of the induction motor. The power factor and efficiency of a motor with permanent magnets are significantly higher than those obtained from the induction motor. These parameters increase in both structures along with an increase in frequency. The effective current value of the LSPMSM in a steady--state with a load torque of over 10 Nm is also lower by approx. 10–20 % than that of the induction motor for the same load of both machines.

Based on the obtained results of the research, it can be concluded that synchronous motors with permanent magnets exhibit higher efficiency and higher power than induction motors. It has been shown that they can successfully replace induction motors as drive systems with frequency control. For this reason, this type of machinery should be implemented for production and operation.

References

[1] Barański M., Idziak P., Królikowski W., Łyskawiński W., *Analiza stanów pracy silników indukcyjnego i synchronicznego magnetoelektrycznego o rozruchu bezpośrednim*, Zeszyty Problemowe – Maszyny Elektryczne, 2013, nr 99, BOBRME Komel, pp. 227–232.

[2] Barański M., Szeląg W., Jędryczka C., Mikołajewicz J., Łukaszewicz P., *Analiza i badanie silnika synchronicznego o rozruchu bezpośrednim i magnesach w wirniku rozłożonych w kształcie litery U*, Przegląd Elektrotechniczny, 2013, R. 89, nr 2b, pp. 107–111.

[3] Ding T., Takorabet N., Sargos F.M., *Design and analysis of different line-start PM synchronous motors for oil-pump applications*, IEEE Transactions on Magnetics, 2009, Vol. 45, No. 3, pp. 1816–1819.

[4] Fei W., Luk K.P.C., Ma J., Shen J.X., Yang G., A *high-performance line-start permanent magnet synchronous motor amended from a small industrial three-phase induction motor*, IEEE Transactions on Magnetics, 2009, Vol. 45, No. 1, pp. 4724–4727.

[5] Idziak P., Barański M., Łyskawiński W., Kowalski K., *Ocena wybranych parametrów energetycznych modelowych silników prądu przemiennego małej mocy o różnych konstrukcjach wirnika*, Zeszyty Problemowe – Maszyny Elektryczne, 2013, nr 100, BOBRME Komel, pp. 53–57.

[6] Knight A.M., McClay C.I., *The design of high-efficiency line-start motors*, IEEE Transactions on Industry Applications, 2000, Vol. 36, No. 6, pp. 1555–1562.

[7] May H., Palka R., Paplicki P., Szkolny S., Canders W.-R., *Modified concept of permanent magnet excite synchronous machines with improved high-speed features*, Archives of Electrical Engineering, 2011, Vol. 60, No. 4, pp. 531–540.

[8] Miller T.J.E., Popescu M., Cossar C., McGilp M.I., Strappazzon G., Trivillin N., Santarossa R., *Line start permanent magnet motor: single-phase steady-state performance analysis*, IEEE Transactions on Industry Applications, 2004, Vol. 40, No. 2, pp. 516–525.

[9] Młot A., Korkosz M., Łukaniszyn M., *Iron loss and eddy-current loss analysis in a low-power BLDC motor with magnet segmentation*, Archives of Electrical Engineering, 2012, Vol. 61, No. 1, pp. 33–46.

[10] Zawilak T., Antal L., *Porównanie silnika indukcyjnego oraz synchronicznego z magnesami trwałymi i rozruchem bezpośrednim – badania eksperymentalne*, Zeszyty Problemowe – Maszyny Elektryczne, 2007, nr 77, BOBRME Komel, pp. 277–282.

TECHNICAL TRANSACTIONS | **CZASOPISMO TECHNICZNE**
ELECTRICAL ENGINEERING | ELEKTROTECHNIKA
1-E/2015

ŁUKASZ SIENKIEWICZ*, JEAN-FRANÇOIS ROUCHON**,
MIECZYSŁAW RONKOWSKI*, GRZEGORZ KOSTRO*

A NEW PROTOTYPE OF PIEZOELECTRIC BENDING RESONANT TRANSDUCER FOR ANALYSIS OF SOFT TISSUES PROPERTIES

NOWY PROTOTYP REZONANSOWEGO PRZETWORNIKA PIEZOELEKTRYCZNEGO DO ANALIZY WŁAŚCIWOŚCI TKANEK MIĘKKICH

Abstract

This paper is devoted to a new piezoelectric bending resonant transducer prototype dedicated to the characterization of the mechanical properties of soft tissue. A general description of the actuator's structure is presented including the basic principles of the measurement. The chosen geometry of the prototype is discussed and compared with the existing version. Constitutive equations are presented for the active and passive layer of the cantilever transducer. The prototype is verified by means of finite element method analysis. Results of the static and modal analysis are presented and discussed.

Keywords: *piezoelectric transducer*, *sensor*, *actuator*, *resonant transducer*, *finite element method*

Streszczenie

W niniejszym artykule opisano nowy prototyp rezonansowego przetwornika piezoelektrycznego przeznaczony do pomiaru właściwości mechanicznych tkanek miękkich. Przedstawiono ogólny opis struktury aktuatora wraz z wyjaśnieniem podstawowej zasady pomiaru. Podano cechy geometryczne projektowanego prototypu, a następnie porównano go do już istniejącego. Sformułowano równania konstytutywne dla warstwy aktywnej oraz pasywnej przetwornika. Prototyp zweryfikowano metodą elementów skończonych. Zaprezentowano oraz skomentowano wyniki symulacji statycznej i modalnej.

Słowa kluczowe: *przetwornik piezoelektryczny*, *sensor*, *aktuator*, *przetwornik rezonansowy*, *metoda elementów skończonych*

DOI: 10.4467/2353737XCT.15.042.3842

* M.Sc. Eng. Łukasz Sienkiewicz, D.Sc. Ph.D. Eng. Mieczysław Ronkowski, Ph.D. Eng. Grzegorz Kostro, Department of Electrical and Control Engineering, Power Electronics and Electric Machines Group, Gdansk University of Technology.

** D.Sc. Ph.D. Eng. Jean-François Rouchon, Prof. of the INPT-ENSEEIHT-LAPLACE (Laboratoire Plasma et Conversion d'Energie), Toulouse, France.

1. Introduction

From the time of their discovery in 1880, piezoelectric materials have found applications in various fields of industry and services. Piezoelectric transducers are used for measuring a wide variety of mechanical and thermal parameters including: effort; pressure; acceleration; weight; angular speed; moments; deformations; temperature etc. Considering accuracy, in many cases these devices surpass transducers based on other detection principles. Nowadays, piezoelectric transducers are used in medicine and bioengineering for ultrasonic tomography, pulse measurements, tone measurements, urology, ophthalmology, etc. This work describes the continuation of research activities dedicated to a piezoelectric resonant transducer intended for dermatological application. Details of the measurement system as well as state of the art can be found in [1, 2].

This paper is organized as follows: section 2 presents the problem under research in a qualitative manner; basic requirements for the designed transducer are shown, as well as the main differences between the prototypes; section 3 describes the measurement system in a more quantitative way; constitutive equations are presented for the cantilever sensor/actuator; the principle of operation is described; section 4 presents the numerical model of the transducer and the results of finite element method analysis; section 5 presents remarks and conclusions on the investigated prototype.

2. Description of piezoelectric sensor actuator

The main objective of the project is the design and analysis of a piezoelectric resonant, bending sensor/actuator intended for measuring the mechanical properties of soft tissues, such as their rigidity, flexibility and viscosity.

A dynamic indentation method for the measurement of mechanical properties is used in this study. This technique is based upon registering the force applied on the surface of the material as a function of the displacement imposed by the indenter. In addition to a static force, vibrations are injected on the surface of the tested sample. A spherical indentation device is located at the free end of the developed piezoelectric cantilever sensor/actuator working in resonance conditions.

A resonant piezoelectric sensor is a device with an element vibrating at resonance which changes its output frequency, i.e. the mechanical resonance frequency, as a function of a physical parameter – this is proved to have major advantages over other physical resolution principles. Resonant sensors with various excitation and detection techniques have been reported in the literature and each one has its own advantages and disadvantages. Smart materials, in particular piezoelectric materials for excitation and detection, have numerous advantages like strong force, low actuation voltage, high energy efficiency, linear behavior, high acoustic quality, high speed and high frequency. In the design of resonance piezoelectric sensors, a sensor/actuator in collocation is usually used and provides a stable performance [5]. A new prototype of a developed piezoelectric sensor/actuator should meet a number of requirements based on the analysis of human skin properties:

- stimulation method with sufficient sensitivity for measuring mechanical quantities, such as stiffness and elasticity (e.g. indentation method),
- the maximum deflection at the free end of the actuator, which corresponds to the depth of skin's penetration, should be less than 5 mm,
- the maximum force applied to the tested tissue should not exceed 1 N,
- the frequency of the stimulation should be in the range perceivable by the skin receptors – that is below 1500 Hz,
- simple electromechanical structure with compact dimensions,
- possibility of implementation of the structure on a stylus [6].

Firstly, to better fulfill the compact dimensions condition, the new prototype is 40% smaller than the first transducer. The total active length is now only 60 mm, the width is 10 mm for the piezoelectric ceramics, and is only 1.5 mm thick. On the other hand, the indentation device (a rigid sphere) is now bigger, with a diameter of 16 mm, which contributes to better sensitivity for measured quantities. Material for the active layer had been changed to PZT-401 ceramic, due to its better electro-mechanical coupling and lower dielectric losses. Also, the area for the electrodes has been rearranged. Thanks to the sectorization of the ceramics, there are five areas dedicated to sensing and actuating at a desired resonance frequency. The middle three are dedicated to sensing/actuating the first and the third mode, while the other two are dedicated for the second resonant mode. The new prototype is located in Fig. 1.

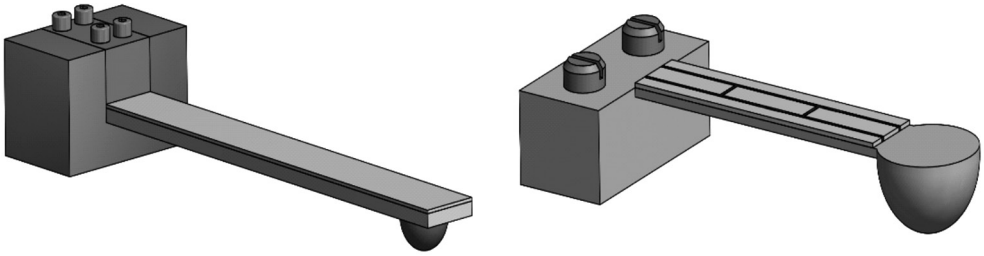

Fig. 1. Comparison of two prototypes of cantilever sensor/actuator. Right – first prototype; left – newest prototype (size is not scaled)

3. Analytical description of the transducer

General constitutive equations for piezoelectric material can be presented in the form of a matrix, describing the relationship between the following pairs of quantities: (***S***, ***E***); (***S***, ***D***); (***T***, ***E***); (***T***, ***D***). Choosing ***T*** and ***E*** as independent variables, constitutive relations take form of:

$$\begin{aligned} (S) &= \left[s^E \right] \cdot (T) + [d]^t \cdot (E) \\ (D) &= [d] \cdot (T) + \left[\varepsilon^T \right] \cdot (E) \end{aligned} \tag{1}$$

where:
($\boldsymbol{S}$) – the six-dimensional strain vector,
($\boldsymbol{T}$) – the vector of stresses,
($\boldsymbol{D}$) – the three-dimensional electric displacement vector,
($\boldsymbol{E}$) – the electric field vector,
[$\boldsymbol{s}^{E}$] – the six by six compliance matrix evaluated at constant electric field,
[$\boldsymbol{d}$] – the three by six matrix of piezoelectric strain coefficients,
[$\boldsymbol{\varepsilon}^{T}$] – the three by three dielectric constant matrix evaluated at constant stress.
T – represents the stress induced by the combined mechanical and electrical effects [3].

Before writing the constituent equations for the piezoelectric cantilever (bending transducer), it is necessary to adopt the following convention for the crystal axes of the piezoelectric material: the polarization vector defines 3rd or z direction; the 1st and 2nd directions (x, y directions) are mutually perpendicular to the 3rd direction; the z direction is perpendicular to the large surface of the piezoelectric element. When an external voltage, V, is applied across the electrodes such that the external electric field, E_3, is anti-parallel to the polarization of the piezoelectric element, the piezoelectric material will expand in the plane perpendicular to E_3 and contract in the direction of E_3 if $d_{31} < 0$ and $d_{33} > 0$. Taking the above assumptions into consideration; the constitutive equations for the piezoelectric cantilever sensor/actuator (1), with polarization along the 3rd direction, can be reduced from matrix form into the following:

$$\begin{aligned} S_1^a &= s_{11}^{E,a} T_1^a - d_{31} E_3 \\ -D_3^a &= d_{31} T_1^a - \varepsilon_{33}^T E_3 \end{aligned} \tag{2}$$

For the passive layer, a non-piezoelectric, elastic material can be used. For this layer, it can be written:

$$S_1^p = s_{11}^p T_1^{\mathrm{p}} \tag{3}$$

where s_{11} represents compliance under mechanical stress. Both T_1^a and T_1^p are transverse stresses acting on the y-z planes of the elements and are linear functions of the distances from the neutral axis, z_a and z_p, as given in the following:

$$\begin{aligned} T_1^a &= -\Gamma^a z_a \\ T_1^p &= -\Gamma^p z_p \end{aligned} \tag{4}$$

where Γ^a and Γ^p are proportionality constants. The neutral axis of the bender doesn't coincide with the joined surface [3].

The active, piezoelectric layer (superscript a) is bonded to a passive, elastic layer (superscript p). When the voltage is applied across the thickness of the active layer, a longitudinal and transverse strain appears. The elastic layer opposes the transverse strain and the asymmetry of the whole structure leads to a bending deformation. A basic rectangular cantilever transducer under deformation is located in Fig. 2. To benefit from the indentation function, a small rigid sphere (an indentation device) is glued to the free end of the sensor/actuator.

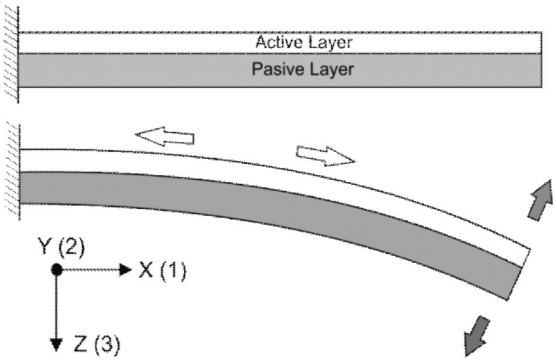

Fig. 2. Principle of operation: piezoelectric material extension resulting in the bending movement of cantilever actuator

The total deflection of the free end of the transducer is a function of material characteristics (piezoelectric and elastic properties), the supply voltage and the geometric dimensions. Without the force acting at the free end, the total deformation can be expressed as follows:

$$\delta_0 = -3L^2 \frac{\beta\eta(1+\eta)}{h_s(1+4\beta\eta+6\beta\eta^2+4\beta\eta^3+\beta^2\eta^4)} d_{31}E_3 \tag{5}$$

where:
E_a, E_p – Young modules of piezoelectric and the elastic layer in [N/m^2],
h_a, h_p – thicknesses of the piezoelectric and the elastic layer in [m],
L – length of the transducer in [m],
d_{31} – piezoelectric coefficient in [m/V],
E_3 – electric field in [kV/m],
with $\beta = E_a/E_p$ and $\eta = h_a/h_p$.

The piezoelectric sensor/actuator is equipped with a spherical rigid probe – the indentation device (Fig. 3). Such a design grants the possibility of verification of the obtained results (by means of an electromechanical impedance analysis, which is explained in detail in [1] and [2]) with the classic Hertzian contact mechanics theorem. Knowing the normal force acting on an elastic surface, as well as the properties of the spherical indenter, it is possible to assess the Young modulus of the elastic material as well as the stiffness of the contact

$$\delta = \sqrt[3]{\frac{9}{16}\frac{F_N^2}{RE^{*2}}} \tag{6}$$

$$\frac{1}{E^*} = \frac{1-\nu_1^2}{E_1} + \frac{1-\nu_2^2}{E_2} \approx \frac{1-\nu_2^2}{E_2} \tag{7}$$

Where:

δ – the penetration depth,

F_N – the normal force acting on the surface,

R – the radius of the sphere,

E_1, E_2, ν_1, ν_2 – Young and poisons coefficients for the rigid sphere and the elastic material surface respectively.

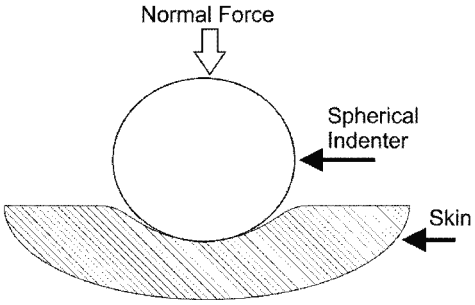

Fig. 3. Schematic description of the indentation method: rigid sphere acting on a soft tissue with the normal force F_N

4. Simulation analysis

In this paragraph, we will present results of the verification of the proposed piezoelectric transducer by means of the finite element method. This analysis will include a short description of the numerical model of the sensor/actuator, as well as results of static and modal simulations aiming to check if the performance of the designed prototype is up to the required level. Computations were made using a user-defined numerical model and boundary conditions in a finite element method package ANSYS.

The definition of piezoelectric material requires permittivity (or dielectric constants), the piezoelectric matrix and the elastic coefficient matrix to specify the properties of the material [7]. The permittivity matrix specifies the relative permittivity values. The permittivity values represent the diagonal components ε_{11}, ε_{22}, ε_{33} respectively of the permittivity matrix ε^s. The superscript *S* indicates that the constants a2re evaluated at a constant strain. The piezoelectric matrix can be defined as a piezoelectric stress matrix **[*e*]** or a strain matrix **[*d*]**. Matrix **[*e*]** is usually associated with the input of anisotropic elasticity in the form of the stiffness matrix **[*c*]**, while **[*d*]** is associated with the compliance matrix **[*s*]**. The elastic coefficients matrix (6x6 symmetric matrix) specifies the stiffness **[*c*]** or compliance **[*s*]** coefficients [4].

The numerical model of the cantilever transducer can be divided into two main parts – the passive layer of the bender and the indentation device (hemisphere), which are created from one solid block of steel. The second part of the transducer includes the active layer built from sectorized piezoelectric ceramics. For this part, hard PZT-401 ceramics were chosen due to their high resistance to depolarization and low dielectric losses under high electric drive. This type of material is especially suited for high power transducers and power generating bending systems. The meshed geometry of the transducer is provided in Fig. 4.

Table 1

Properties of materials used in the FEM model

Layer	Passive	Active
Material	Steel	PZT-401
Height	$h_p = 1$ mm	$h_a = 0.5$ mm
Density	$\rho = 7850$ kg/m^3	$\rho = 7600$ kg/m^3
Young modulus	$E_p = 21 \cdot 10^{10}$ N/m^2	$E_a = 12.89 \cdot 10^{10}$ N/m^2
Poisson Coefficient	$\nu_p = 0.3$ [–]	$\nu_a = 0.31$ [–]
Piezoelectric strain coefficients	–	$d_{33} = 315$ pm/V $d_{31} = 132$ pm/V $d_{15} = 511$ pm/V
Dielectric constant	–	$K_{33}^T = 1395$ [–]

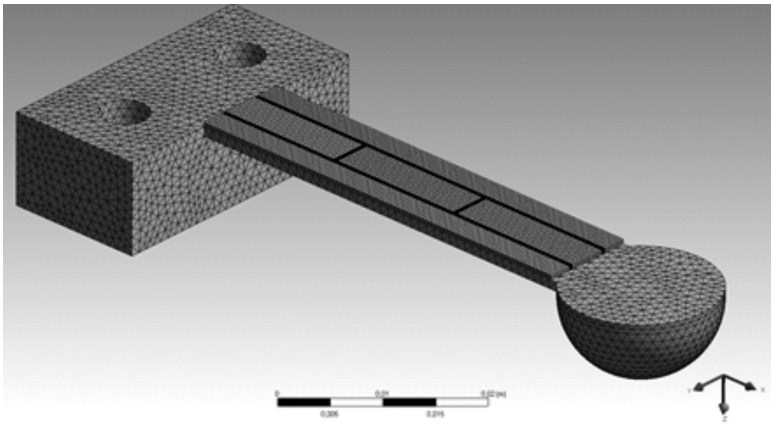

Fig. 4. Meshed numerical model of cantilever transducer. Piezoelectric layer is sectorized into five regions for sensing and actuation

During the static analysis, piezoelectric ceramics were supplied with a DC voltage of 200 V. The structure was fixed at the bottom of the base. The deformation was measured along the *z* axis, and it corresponded to the normal excitation of the material's surface. Depending on how many sectors of the active layer were supplied with voltage, the deformation of the transducer ranged from 21.99 µm to 49.79 µm. Those values could be related to a maximal deflection at the state of resonance using the quality factor *Q*. Considering the fact that the described sensor/actuator has a *Q*-factor below 100, its maximal deformation meets the requirements described in section 2. The static, bending deformation is illustrated in Fig. 5.

The other design requirements were tested with modal analysis. The aim of which was to determine the vibration characteristics of a structure, including its natural frequencies, mode shapes and participation factors (the amount of a mode participates in a given direction). Three basic natural frequencies were extracted. Each of those corresponded to a deformation in a different direction (axis). First resonant mode was the bending movement in the *z* axis, which is normal to the tested material. The second was the torsion deformation (the tip of

spherical indenter – probe is moving in the *y* axis). The third natural frequency was linked to a 'wave' movement of the transducer, which caused the probe to move in the direction aligned with the *x* axis (Fig. 6).

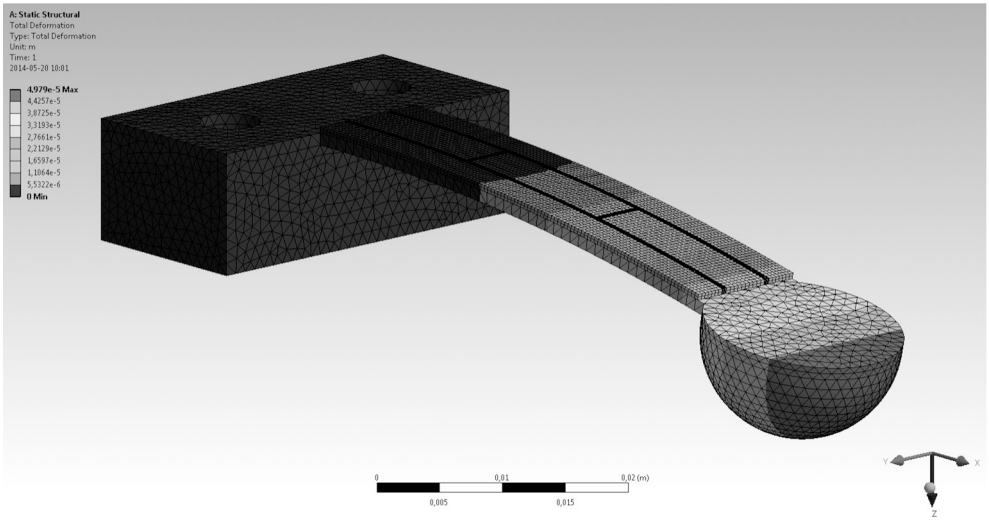

Fig. 5. Results of static simulation: cantilever sensor/actuator supplied with 200 V DC. Basic bending deformation

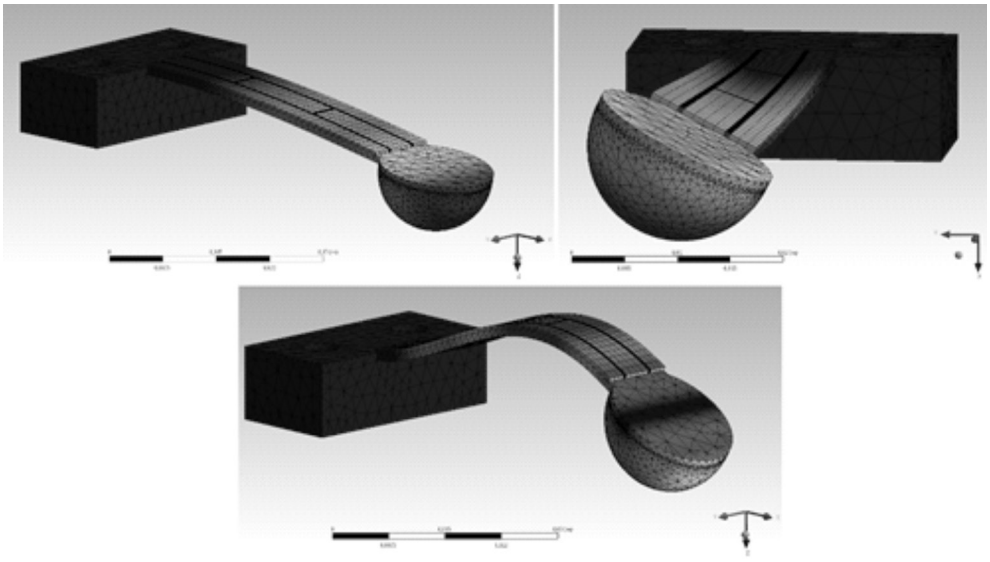

Fig. 6. Results of modal simulation: first three natural frequencies and corresponding deformations of the cantilever transducer. Upper left: first mode – bending movement; upper right: second mode – torsional movement; lower: third mode – 'wave' movement. The amplitude of deformations **is not** to scale

Moreover, for each natural frequency of the actuator, the indentation sphere and tested material create different contact surfaces. This contributes to varying conditions of friction and sliding between the spherical indenter and sample to be characterized. Piezoelectric actuators, generally characterized by a low amplitude of vibration, work in the area of partial slip, since the contact area is often greater than the vibration amplitude. Under those conditions, the coefficient of friction of the sphere/surface contact may change depending on the mode in question. This property can serve as a way to tune the deformations of the transducer to meet the specific requirements of the measurement of mechanical properties of materials.

To establish frequency values of resonance and anti-resonance for each mode of the transducer, boundary conditions of the model had to be defined accordingly:

- Resonance – electromechanical impedance becomes minimum; $Z \rightarrow 0$; short-circuit: voltage on both electrodes set to 0.
- Anti-resonance – electromechanical impedance becomes maximum; $Z \rightarrow \infty$; open circuit; voltage not defined [4].

Table 2

Results of modal analysis: resonance and anti-resonance frequencies for the first three working modes of the sensor/actuator

Mode number	Resonance frequency [Hz]	Anti-resonance frequency [Hz]
1	133.91	135.84
2	772.91	775.83
3	1337.4	1358.7

Deformations corresponding to frequencies listed above are illustrated in Fig. 5. Depending on the frequency of the supply voltage the cantilever sensor/actuator can produce movement in each axis. This property is quite interesting considering the characterization of the mechanical properties of soft materials, where different kinds of movement can be used in extracting different quantities. Moreover, the highest value of resonant frequency is well below the required threshold of 1500 Hz (Table 2).

5. Conclusions

The aim of the paper was to present a new prototype of the piezoelectric cantilever transducer with improved geometry and electromechanical properties, while comparing with the first one. The presented analysis has proved that such a design has met most of the requirements specified for the measurement system of mechanical quantities describing soft tissues. Those are: compact dimensions and the simple electromechanical structure welcome in a portable device; adequate levels of produced deformation; force and operating frequency; most importantly, sufficient sensitivity for measurement of mechanical properties of viscoelastic materials (at the current stage of research – soft polymers; ultimately – human skin tissue).

Furthermore, the described prototype profits from the dynamic indentation method described in the literature, used for the measurement of elastic and viscous properties of human skin.

The presented considerations in the paper have proved the importance of choosing the resonance mode of the actuator on the mechanical contact between the indenter and the sample. Therefore, the right choice of working mode of the sensor/actuator will allow or greatly facilitate the measurement of mechanical properties of soft tissues.

In further works, it is planned to fabricate the considered prototype and to carry out experimental verification by an impedance measurement and a comparison with the existing prototype.

Acknowledgement

Part of this research has been carried out in the frame of the "Advanced PhD": The Center for Advanced Studies – the development of interdisciplinary doctoral studies at the Gdansk University of Technology in the key areas of the Europe 2020 Strategy.

The project is co-financed by the European Union within the European Social Fund – Human Capital Operational Programme (HC OP).

www.AdvancedPhd.pg.gda.pl

References

[1] Sienkiewicz Ł., Rouchon J.-F., Ronkowski M., Kostro G., Ryndzionek R., *Identification of the mechanical properties of the skin by electro-mechanical impedance analysis of resonant piezoelectric actuator*, IECON 2013, Vienna, pp. 3940–3945.

[2] Sienkiewicz Ł., Rouchon J.-F., Ronkowski M., *Design and analysis of a piezoelectric resonant sensor/actuator for measuring the aging process of human skin*, Zeszyty Problemowe – Maszyny Elektryczne, 2013, nr 100, pp. 83–89.

[3] Smits J.G., Choi W.C., *The constituent equations of piezoelectric heterogeneous bimorphs*, IEEE Ultrasonics Symposium, 1990, pp. 1275–1278.

[4] Dalessandro L., Rosato D., *Finite-element analysis of the frequency response of a metallic cantilever coupled with a piezoelectric transducer*, IEEE Trans. on Instrumentation and Measurement, 2005, Vol. 54, No. 5, pp. 1881–1891.

[5] Sharapov V., *Piezoceramic Sensors*, Microtechnology and MEMS, Springer 2011.

[6] Pailler C., Zahouani H., *Analysis of adhesive behaviour of human skin in vivo by year indentation test*, International Tribology, 2006, Vol. 39, pp. 12–21.

[7] Lange R., Scampoli S., Ansari N., Shaw D., *Piezoelectric Fan Modeling FSI Analysis using ANSYS and CFX*, International ANSYS Conference, Pittsburgh, USA 2008.

TECHNICAL TRANSACTIONS | **CZASOPISMO TECHNICZNE**
ELECTRICAL ENGINEERING | ELEKTROTECHNIKA
1-E/2015

PIOTR GAJEWSKI, KRZYSZTOF PIEŃKOWSKI*

ANALYSIS OF A WIND ENERGY CONVERTER SYSTEM WITH PMSG GENERATOR

ANALIZA PRZEKSZTAŁTNIKOWEGO SYSTEMU ELEKTROWNI WIATROWEJ Z GENERATOREM PMSG

Abstract

This article presents a variable-speed converter system for wind energy conversion. The considered system consists of a wind turbine with a permanent magnet synchronous generator (PMSG), a machine-side converter, a grid-side converter and control circuits. Mathematical models of the components of the wind energy system are described. The control algorithms of the converter systems based on the vector methods of control are also described. The considered wind energy system were studied by digital simulation. The simulation results are presented and discussed.

Keywords: *wind turbine*, *PMSG generator*, *control systems*, *simulation studies*

Streszczenie

W niniejszym artykule przedstawiono przekształtnikowy system elektrowni wiatrowej o zmiennej prędkości. Rozpatrywany system składa się z turbiny wiatrowej z generatorem synchronicznym z magnesami trwałymi (PMSG), przekształtnika maszynowego, przekształtnika sieciowego i układów sterowania. Opisano modele matematyczne poszczególnych elementów systemu elektrowni wiatrowej. W algorytmach sterowania przekształtników energoelektronicznych zastosowano wektorowe metody sterowania. Przeprowadzono badania symulacyjne rozpatrywanego systemu przekształtnikowego elektrowni wiatrowej. Wykonane badania symulacyjne potwierdziły prawidłowość pracy układów sterowania i dużą dokładność sterowania.

Słowa kluczowe: *elektrownia wiatrowa*, *generator PMSG*, *systemy sterowania*, *badania symulacyjne*

DOI: 10.4467/2353737XCT.15.043.3843

* M.Sc. Eng. Piotr Gajewski, D.Sc. Ph.D. Eng. Krzysztof Pieńkowski, Prof. WrUT, Department of Electrical Machines, Drives and Measurements, Faculty of Electrical Engineering, Wroclaw University of Technology.

1. Introduction

The world's development of energy generation from renewable sources has increased significantly in recent years. The biggest development of renewable sources is wind energy conversion system (WECS). An increasing trend is to stimulate research in the field of energy conversion in order to optimize receiving the largest values of energy from the wind.

Wind turbines can be classified into fixed-speed and variable-speed turbines [4, 5, 8]. The main advantages of the systems with variable-speed turbines are: increased wind energy output, the possibility to achieve maximum power conversion efficiency and reduced mechanical stress. Most of the major wind turbine manufacturers are now developing wind turbine systems based on variable-speed operation.

In WECS, mechanical energy of the wind turbine is converted in electrical energy with the help of an appropriate electrical generator. In the future, permanent magnet synchronous generators (PMSG) will predominate in small and large power wind turbines due to the possibility of multipole designs that eliminate the need for gearboxes [2, 4, 6].

A typical wind energy conversion system consists of: wind turbine; electrical generator; power converters; control circuits. The currently developed configuration of wind power system is presented in Fig 1. The figure shows the system in which the directly driven or geared driven PMSG generator is connected to the AC grid via a full capacity power converter system. The converter system includes a machine side converter (MSC) and grid side converter (GSC) connected in a back-to-back converter configuration.

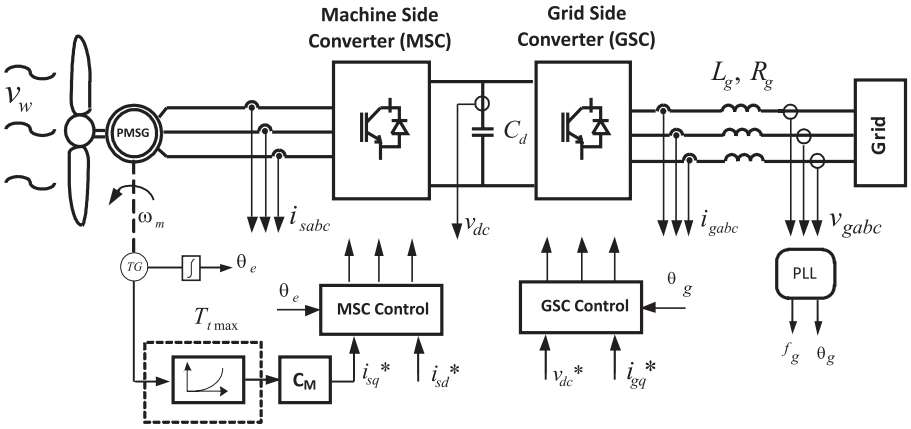

Fig. 1. Configuration of variable-speed wind turbine system with direct-driven PMSG and full-capacity converters

The aim of this paper is to analyze the converter system of a permanent magnet synchronous generator connected to a wind turbine under varying wind speeds in order to investigate the effectiveness of the wind energy conversion systems. The paper is divided into 7 sections as follows: in section 2 and 3 the wind turbine model and PMSG model are presented; sections 4 and 5 are dedicated to the description of the control system of the MSC and GSC converters; the simulation results of considered WECS are presented in Section 6; the article finishes with research conclusions.

2. Model of Wind Turbine

The wind turbine converts the wind energy into rotational mechanical energy. Wind turbine output power P_t and wind turbine output torque T_t are given by the following equations [1–5]:

$$P_t = 0.5 \cdot \rho A \cdot C_p(\lambda, \beta) \cdot v_w^3 \tag{1}$$

$$T_t = 0.5 \cdot \rho R A \cdot C_p(\lambda, \beta) \cdot v_w^2 / \lambda \tag{2}$$

where:

ρ – air density,
$A = \pi R^2$ – area swept by the rotor blades,
C_p – power coefficient of the wind turbine,
$\lambda = R\omega_m / v_w$ – tip speed ratio,
β – blade pitch angle,
v_w – wind speed,
R – radius of the turbine blade,
ω_m – angular speed of turbine rotor.

The power coefficient C_p as a function of tip speed ratio λ, and blade pitch angle β is shown in Fig. 2a). The wind turbine can produce maximum power when the turbine operates at a maximum value of C_p, i.e. at $C_{p\max}$. Therefore, it is necessary to keep the rotor speed at an optimum value of the tip speed ratio, λ_{opt}. If the wind speed varies, the speed of the rotor turbine should be adjusted to follow the wind speed changes.

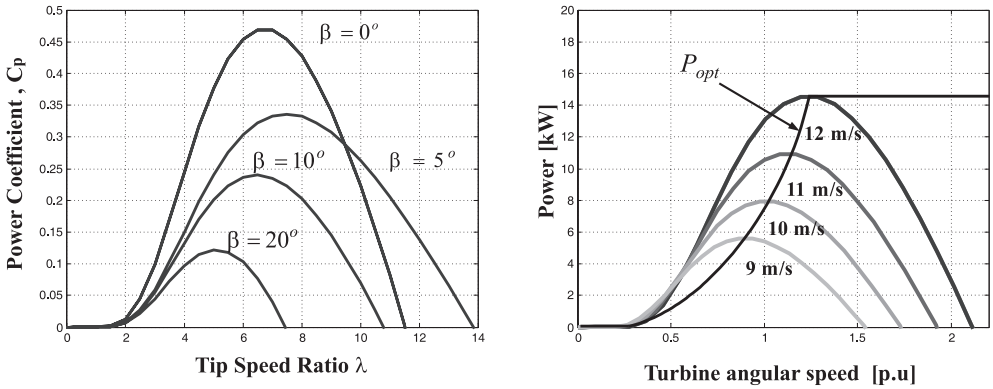

Fig. 2. Characteristics of the wind turbine: a) C_p curves as function of λ and β, b) wind turbine power curves at various wind speeds

The mechanical rotor power generated by the turbine as a function of the rotor speed for different wind speeds is shown in Fig. 2b). The optimum power curve P_{opt} shows how max-

imum energy can be captured from the fluctuating wind. The function of the control system with maximum power-point tracking (MPPT) is to keep the operation of the turbine on this curve, as the wind velocity varies.

3. The Model of Permanent Magnet Synchronous Generator

In the PMSG model, the following basic assumptions have been considered: the electrical and magnetically symmetry; the magnetic flux is sinusoidal distributed along the air gap; no saturation; no damping winding. Mathematical equations of PMSG are formulated in the synchronous rotating reference frame *d-q*, by aligning the *d*-axis with the direction of the rotor flux. Voltage equations of the generator have the following form [1, 2, 6, 7]:

$$v_{sd} = R_s i_{sd} + L_d \cdot p i_{sd} - \omega_e L_q i_{sq} \tag{3}$$

$$v_{sq} = R_s i_{sq} + L_q \cdot p i_{sq} + \omega_e L_d i_{sd} + \omega_e \psi_{PM} \tag{4}$$

where: $$\omega_e = n_p \cdot \omega_m \,,\ p = \mathrm{d}/\mathrm{d}t \tag{5}$$

u_{sd}, u_{sq} – the stator voltages in the *d-q* axis,
i_{sd}, i_{sq} – the stator currents in the *d-q* axis,
L_d, L_q – the *d-q* axis stator inductances,
ψ_{PM} – rotor flux linkage established by permanent magnets,
R_s – resistance of the stator winding,
ω_e, ω_m – electrical and mechanical angular speed of the PMSG generator,
n_p – number of pole pairs of the PMSG generator,

The expression for the electromagnetic torque of the PMSG has the form:

$$T_e = (3/2) n_p [\psi_{PM} i_{sq} + (L_d - L_q) i_{sd} i_{sq}] \tag{6}$$

For a non-salient-pole machine, the stator direct and quadrature inductances L_d and L_q are equal, so the electromagnetic torque equation then takes the form:

$$T_e = (3/2) n_p \cdot \psi_{PM} i_{sq} \tag{7}$$

The mechanical equation of motion is given as:

$$T_t - T_e = J \cdot p\omega_m \tag{8}$$

where T_t, J – the referred to the side of generator shaft: the output torque of wind turbine and the total equivalent inertia, respectively.

4. The Model of Control System of Machine Side Converter

The machine-side converter regulates the active power and speed of the PMSG generator. The block scheme of the control system of the MSC [1, 4, 5, 8] is presented in Fig. 3.

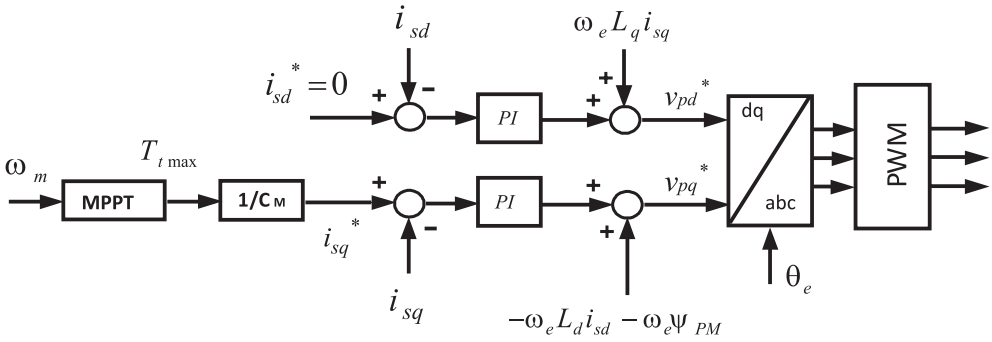

Fig. 3. Control diagram of the Machine Side Converter

In the control system, the principle of maximum power point tracking (MPPT) has been applied. The operation with maximum power is achieved through optimal control of the maximum torque generated by the wind turbine $T_{t\max}$, according to the equation:

$$T_{t\max} = 0.5\rho A C_{p\max} (R/\lambda_{opt})^3 \omega_w^2 = K_M \cdot \omega_m^2 \tag{9}$$

where K_M is a constant determined by the wind turbine characteristic [8].

In order to obtain the maximum power generated by the PMSG, the references components of the stator current i_{sq}^* can be calculated as:

$$i_{sq}^* = C_M T_{t\max} \tag{10}$$

where $C_M = 2/(3n_p\psi_{PM})$ – coefficient to convert the value of torque into the reference current.

The MSC control system is based on a rotor flux field orientation. The position of the rotor flux vector θ_e is obtained from the encoder or from the conversion of the signal from the speed sensor. The *d*-axis stator current reference i_{sd}^* is always set to zero in order to achieve the maximum torque at the minimum stator current and to achieve a linear relationship between the magnitude of the stator current and the electromagnetic torque of the generator. The *q*-axis stator current reference i_{sq}^* is achieved through the operation of the MPPT block on the base of the measured mechanical turbine speed ω_m. The measured stator phase currents of the PMSG are transformed into *dq*-axis currents, i_{sd} and i_{sq}, defined in the rotor flux synchronous frame. The *dq*-axis stator currents, i_{sd} and i_{sq}, are compared with the reference stator currents, i_{sd}^* and i_{sq}^*, respectively. The error signals are sent to two PI controllers.

The state variables of the PMSG are cross-coupled because in equations (3) and (4), the derivate of *d*-axis stator current i_{sd} is related to both *d* and *q*-axis variables, as is the *q*-axis

stator current i_{sq}. To solve these problems, the decoupling signals are added to the PI output signals, as shown in Fig. 3. The resultant signals, v_{pd}^{*} and v_{pq}^{*}, are the *dq*-axis reference voltages for the MSC control. These two reference voltages are then transformed to three-phase reference voltages and are sent to the block of the PWM generation for the MSC.

5. The Model of the Control System of the Grid Side Converter

The grid side converter GSC feeds generated energy into the AC grid, keeps the DC link voltage stable and adjusts the quantity of the active and reactive powers delivered to the AC grid during wind variation. There are many strategies used to control the grid side converter [1–4, 8]. The control method presented in this paper is known as the grid voltage oriented control (VOC). The principle of the VOC control is based on the state equations for the grid-side circuits of the GSC converter. The state equations expressed in the *dq* rotating synchronous reference frame have the form:

$$v_{gd} = R_g i_{gd} + L_g \cdot p i_{gd} - \omega_g L_g i_{gq} + v_{gcd} \tag{11}$$

$$v_{gq} = R_g i_{gq} + L_g \cdot p i_{gq} + \omega_g L_g i_{gd} + v_{gcq} \tag{12}$$

where:
v_{gd}, v_{gq} – *d-q* components of the grid voltage vector,
i_{gq}, i_{gq} – *d-q* components of the grid current vector,
v_{gcd}, v_{gcq} – *d-q* components of the voltage vector of the grid side converter,
L_g, R_g – inductance and resistance of the grid filter,
ω_g – angular frequency of the grid voltage.

The grid-side converter controls the active and reactive power of the AC grid. The general equations describing the active and reactive power are as follows:

$$P = (3/2)(v_{gd} i_{gd} + v_{gq} i_{gq}), \quad Q = -(3/2)(v_{gd} i_{gq} + v_{gq} i_{dg}) \tag{13}$$

The VOC control of GSC is based on the orientation of the grid voltage vector such that the *d*-axis of the synchronous reference frame is aligned with the grid voltage vector. The grid voltage vector only has *d*-axis component v_{gd}, while the *q*-axis component v_{gq} is equal to zero. The phase locked loop (PLL) estimates the angle θ_z of the grid voltage vector, for the coordinates transformation. In the frame system oriented with the grid voltage vector, the active and reactive power will be proportional to i_{gd} and i_{gq} respectively:

$$P = (3/2)\, v_{gq}\, i_{gd}, \quad Q = -(3/2)\, v_{gd} i_{gq} \tag{14}$$

Hence, the active power *P* can be controlled by the *d*-component of the converter current, i_{gd}, whereas the reactive power *Q* can be controlled by the *q*-component of the converter current, i_{gq}.

The block scheme of the VOC control system of the grid-side converter GSC is presented in Fig. 4. In the system, there are three feedback control loops – two inner current loops for the control of the *dq*-axis grid currents, i_{gd} and i_{gq}, and one outer voltage feedback loop for the control of the DC voltage of the GSC, v_{dc}. The inputs of the control system are: v^*_{dc}, which is the reference dc-link voltage and Q^*, which is the reference for the reactive power, which can be set to zero for unity power operation, a negative value for leading power operation, or a positive value for lagging power factor operation. The PI controller for DC voltage control generates the *d*-axis current reference i^*_{gd}, which represents the active power of the system. The *q*-axis current reference i^*_{gq} is calculated on the basis of the set value of the reference for the reactive power Q^*.

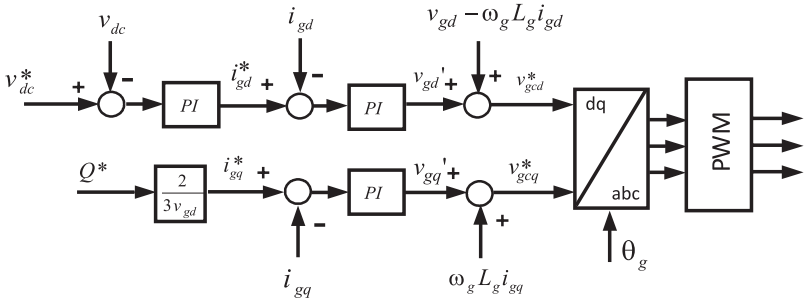

Fig. 4. Control diagram of the Grid Side Converter

The measured phase currents of the grid are transformed into *dq*-axis currents, i_{gd} and i_{sq}, defined in the grid voltage vector oriented synchronous frame. The *dq*-axis grid currents, i_{gd} and i_{sq}, are compared with reference grid currents, i^*_{gd} and i^*_{gq}, respectively. The error signals are sent to two PI controllers. The state variables of the GSC system are cross-coupled because in the equations (11) and (12), the derivate of the *d*-axis grid current i_{gd} is related to both the *d* and *q*-axis grid variables, as is the *q*-axis grid current i_{gq}. To solve these problems, the decoupling signals are added to the PI output signals, as shown in Fig. 4. The resultant signals, v^*_{gcd} and v^*_{gcq}, are the *dq*-axis reference voltages for the output AC circuits of GSC. These two reference voltages are then transformed to three-phase reference voltages of GSC and are sent to the block of PWM generation for the GSC.

6. Simulation studies

In order to evaluate the performance of wind energy converter system, a set of simulation studies has been performed. The model of the wind energy conversion system with control systems has been implemented in MATLAB/Simulink. Digital simulation studies were made for the system with the wind turbine, 3-phase PMSG (with parameters: P_N = 6 kW; R_s = 0.425 Ω; ψ_{PM} = 0.433 Wb; L_d = 8.4 mH; L_q = 8.4 mH; n_p = 5) and machine and grid-side converter (in back-to-back configuration). The FOC control with zero *d*-axis current was considered for the MSC converter and the VOC control with unity power factor for GSC converter.

The chosen results of simulation studies [4, 5] are presented in Figs. 5–10.

Figure 5 shows the considered stochastic time waveforms of wind speed acting on the wind turbine. The time variations of the mechanical torque of the wind turbine and the electromagnetic torque of the PMSG generator are presented in Figs. 6 and 7, respectively. It can be stated that both torque waveforms reflect the variations of the wind speed. Figure 8 presents the time waveform of the voltage v_{dc} in the DC link of the back-to-back converter system. The voltage v_{dc} is quite constant at variations of wind speed. It shows good performance of control circuits.

Figure 9 presents the response of the stator current vector components i_{sd}, i_{sq} in the *dq*-axis reference frame. The component i_{sd} of the stator current vector is kept at zero by the controller to achieve proportionality to the electromagnetic torque of the PMSG. The time values of the component i_{sq} stator current vector are fluctuated according to the wind speed changes. Figure 10 shows as an example, the time waveform of the stator phase current i_{sa} of the PMSG. The variable wind speed causes suitable changes of magnitude of the stator phase current. The presented simulation waveforms confirmed the good performance of the WECS and the quick response of the control systems.

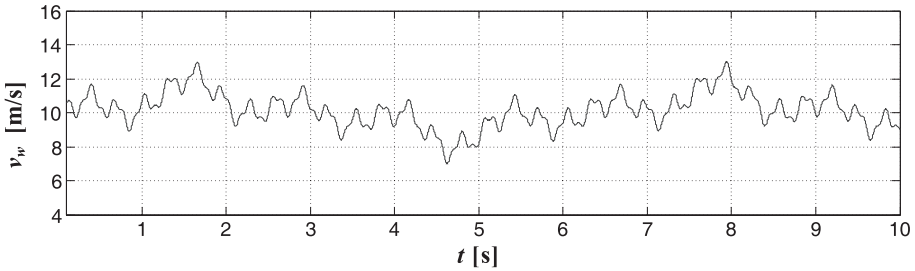

Fig. 5. Time variations of wind speed

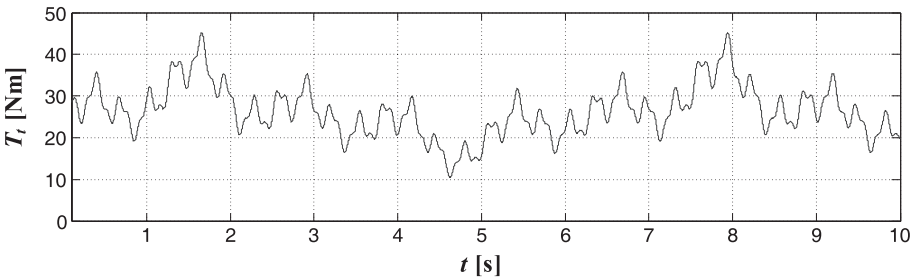

Fig. 6. Simulated waveform of mechanical torque T_t of wind turbine

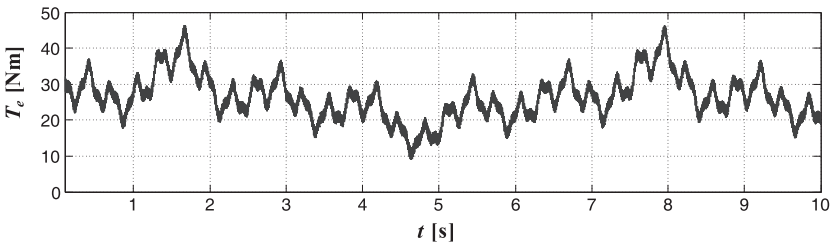

Fig. 7. Simulated waveform of electromagnetic torque T_e of PMSG

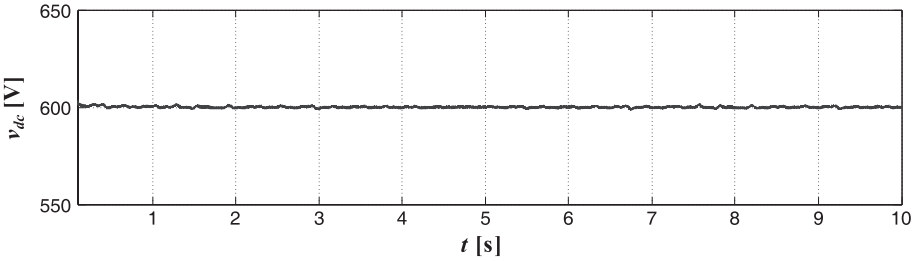

Fig. 8. DC link voltage waveform

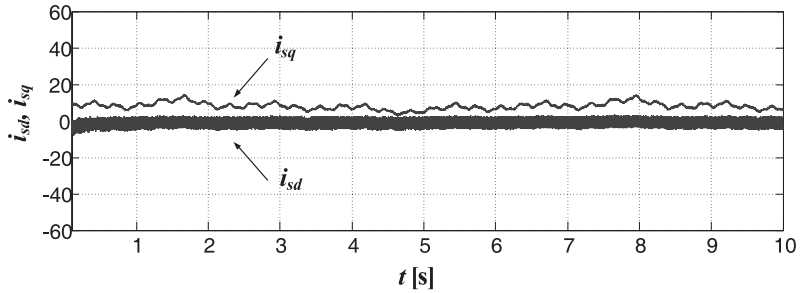

Fig. 9. Waveforms of controlled stator current vector components i_{sd}, i_{sq} of PMSG

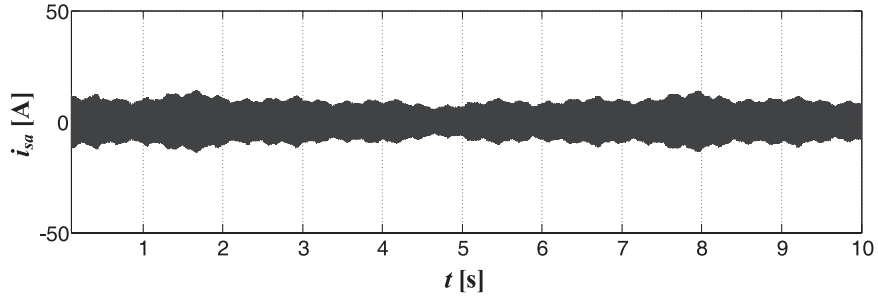

Fig. 10. Waveform of stator phase current i_{sa} of PMSG

7. Conclusions

Control strategies for a variable speed wind turbine with a PMSG have been presented in this paper. Systems with PMSG has many advantages: operation at high power factor; high efficiency; high torque to current ratio. In this paper, two methods of control have been investigated – FOC with MPPT for machine side converter and VOC for grid side converter. FOC with MPPT allows the use of optimal control of maximum torque generated by the wind turbine. VOC control is a simple method and allows keeping the DC link voltage to reference value and to adjust the quantity of the active and reactive powers delivered to the AC grid during wind variation.

Simulation studies demonstrate, that a wind turbine with PMSG, based on the vector control of back-to-back converter systems can effectively accomplish the wind turbine control objectives with superior performance of the system under both steady and variable wind conditions. The simulation results demonstrate that the control systems work very well and show very good dynamic and steady-state performance.

References

[1] Errami Y., Ouassaid M., *Modelling and Control Strategy of PMSG Based Variable Speed Wind Energy Conversion System*, International Conference on Multimedia Computing and Systems (ICMCS), 2011, pp. 1–6.

[2] Haque E., Negnevitsky M., Muttaqi K., A *Novel Control Strategy for a Variable – Speed Wind Turbine With a Permanent Magnet Synchronous Generator*, IEEE Transaction on Industry Applications, 2010, Vol. 46, No. 1, pp. 331–339.

[3] Hemeida A., Farag W., Mahgoub O., *Modeling and Control of Direct Driven PMSG for Ultra Large Wind Turbines*, World Academy of Science, Engineering and Technology, 2011, Vol. 59, pp. 621–626.

[4] Gajewski P., Pieńkowski K., *Analiza elektrowni wiatrowej z generatorem PMSG*, Zeszyty Problemowe – Maszyny Elektryczne, 2014, nr 3(103), pp. 31–36.

[5] Gajewski P., Pieńkowski K., *Modelowanie i analiza elektrowni wiatrowej z generatorem PMSG*, Prace Naukowe Instytutu Maszyn, Napędów i Pomiarów Elektrycznych Politechniki Wrocławskiej, Nr 69, Studia i Materiały 33, 2013, pp. 207–221.

[6] Li S., Haskew T.A., Swatloski R.P., Gathings W., *Optimal and Direct-Current Vector Control of Direct-Driven PMSG Wind Turbines*, IEEE Transactions on Power Electronics, 2012, Vol. 27, No. 5, pp. 2325–2337.

[7] Mahersi E., Kheder A., Mohamed M., *The Wind Energy Conversion System Using PMSG Controlled by Vector Control and SMC Strategies*, International Journal of Renewable Energy Research, 2013, Vol. 3, No. 1, pp. 41–50.

[8] Wu B., Yongqiang L., Navid Z., Samir K., *Power Conversion and Control of Wind Energy*, A John Wiley & Sons, INC., Publication, 2011.

TECHNICAL TRANSACTIONS | **CZASOPISMO TECHNICZNE**
ELECTRICAL ENGINEERING | ELEKTROTECHNIKA
1-E/2015

SEBASTIAN SZKOLNY, OLGIERD MAŁYSZKO*

HARDWARE-IN-THE-LOOP SIMULATOR FOR TESTING WIND TURBINE GENERATORS

SYMULATOR TYPU *HARDWARE-IN-THE-LOOP* DO TESTOWANIA GENERATORÓW TURBIN WIATROWYCH

Abstract

This paper presents research issues of electric generators using systems of the Hardware-in-the--Loop (HIL) type. Using the HIL system, it is possible to reproduce the actual operating conditions of wind turbines working with different types of generators in a laboratory environment. This approach easily and economically allows analyzing the hardware and software controlling the operation of the generator. This system has been implemented on the sbRIO National Instruments controller cooperating with regenerative frequency converter with DTC control of ABB. The paper presents all the components of this system and discusses their operation.

Keywords: *generator*, *wind turbine*, *simulator*, *test stand*

Streszczenie

W niniejszym artykule przedstawiono problematykę badań generatorów elektrycznych z wykorzystaniem systemów typu *Hardware-in-the-Loop* (HIL). Za pomocą systemu HIL możliwe jest odzwierciedlenie w środowisku laboratoryjnym rzeczywistych warunków działania turbin wiatrowych współpracujących z różnymi typami generatorów. Takie podejście pozwala na szybkie i ekonomiczne przygotowanie stanowiska badawczego do analizy działania sprzętu, jak i oprogramowania sterującego pracą generatora w warunkach zbliżonych do rzeczywistych. System ten został zaimplementowany na sterowniku sbRIO firmy National Instruments współpracującym z przemiennikiem częstotliwości ze sterowaniem DTC firmy ABB. W pracy przedstawiono ważniejsze składniki tego systemu i omówiono ich działanie.

Słowa kluczowe: *generator*, *turbina wiatrowa*, *symulator*, *stanowisko badawcze*

DOI: 10.4467/2353737XCT.15.044.3844

* Ph.D. Eng. Sebastian Szkolny, Ph.D. Eng. Olgierd Małyszko, Department of Power Systems and Electrical Drives, Faculty of Electrical Engineering, West Pomeranian University of Technology, Szczecin.

1. Introduction

Electric power produced by wind turbines is strongly dependent on wind speed. As a result, the amount of production is rather unpredictable [5]. This behavior of wind turbines connected to the power system affects its stability.

In addition, modern wind turbines include such devices as voltage and frequency converters. As a result, the generated power contains a lot of harmonic current and voltage.

In order to determine parameters such as the characteristics of the generated active and reactive power, flickers or harmonics are necessary to carry out the relevant tests. The tests must be performed in a wide range of parameter changes. Such research can take months, and generate significant cost.

An interesting solution to this problem is to conduct research using HIL (Hardware-in--the-Loop) simulation methods [7, 8, 11, 13–15].

The idea of a HIL simulation system is to replace real systems with a simulation platform. This simulation platform is equipped with an interface for connecting the simulator with real devices. In the proposed solution, the wind turbine and its control systems are simulated by the HIL system. The simulation platform is connected with a real generator by an asynchronous motor. The torque of the asynchronous motor is controlled by the simulation platform. The simulated process must be described by the relevant mathematical models. The model is described in this paper.

Using the HIL system, it is possible to reproduce the actual operating conditions of wind turbines working with different types of generators in the laboratory environment. This approach easily and economically allows analysis of the hardware and software controlling the operation of the generator.

2. The test stand

In 2008, at the Faculty of Electrical Engineering of West Pomeranian University of Technology in Szczecin, the Research Group for Power Transmission Lines and Unconventional Power Plants Analysis was set up (the authors of this paper are its members). The team deals with an analysis of the possibilities of connecting renewable energy sources to the power system, as well as the technical aspects of the decentralized power generation [2–4]. Team experience gained in this field led to the start of a new research topic and led to a decision to build the test stand for simulating the operation of the wind turbine. For this purpose, the dynamometric stand built in the parent department of the authors within the framework of a research project [1] was used.

This test stand is equipped with a driving system consisting of a high speed asynchronous motor type CM-5-7 (Fig. 1) and inverter with direct torque control (DTC) type ACS 800 (Fig. 2) both devices are manufactured by ABB.

Using this set, it is possible to get a torque on the shaft of the generator of about 100 Nm. The limitation is caused only by the torque sensor DataFlex 32/100. The maximum instantaneous torque equals 300 Nm (Fig. 3). It can be obtained up to its rated speed of 4000 rpm.

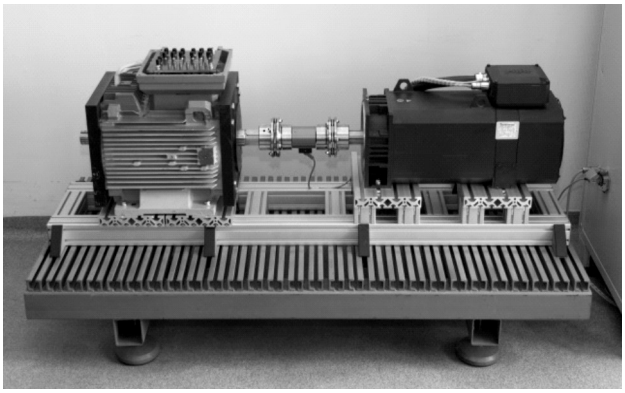

Fig. 1. The dynamometer used to build a wind turbine emulator

Fig. 2. The inverter ACS 800 and the controller NI sbRIO 9606

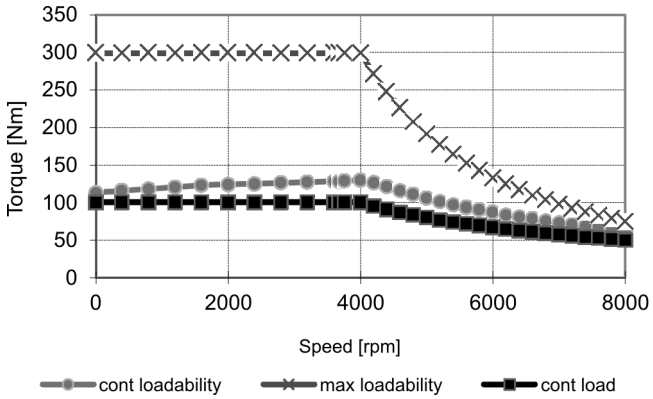

Fig. 3. Mechanical characteristics of the drive used for the construction of the dynamometer

Rated power of the motor equals 54 kW, maximum speed of 8000 rpm and the moment of inertia of 0.15 kgm^2.

The NI sbRIO-9606 controller is used as a master control system. It is joined with the NI 9683 card by RMC connector. The NI 9683 card is used for the transmission of both analog and digital signals. The main task of the NI sbRIO-9606 controller is to control the dynamometer according to the given operation algorithm. In this case, it is the wind turbine simulator.

3. The control algorithm

The most important issue concerning the construction of the wind turbine simulator is modelling the wind speed variability in a virtual environment. This is necessary because the amount of electrical energy produced by wind turbine depends on wind speed.

3.1. Model Wind

In the analysis of a wind turbine operation in the power system, it is assumed that the variability of the wind speed can be modeled using the following methods: the method of the sum of harmonics; the method of step changes or incremental changes; the method of stochastic variables [5]. For the construction of the test stand, the first method was used (i.e. the sum of harmonics). In addition, wind gusts are also included. Such a model of wind can be described by the following relationships [5]:

$$V(t) = V_0\left(1 + \sum_k A_k \sin(\omega_k t)\right) + V_g(t) \tag{1}$$

where:

V_0 – the average value of the wind speed [m/s] (assumed 9 m/s),

A_k, ω_k – amplitude [m/s] and pulsation [rad/s] of the k-th harmonic of wind speed,

$V_g(t)$ – wind gusts, which are described by the following equation [5] [m/s],

$$V_g(t) = \frac{2V_{g\max}}{1 + e^{-4(\sin(\omega_g t)-1)}} \tag{2}$$

where:

$V_{g\max}$ – amplitude of wind gusts [m/s],

ω_g – speed of wind gusts [rad/s].

In practice, it is assumed that the frequency of wind speed harmonics is in the range 0,1, …, 10 Hz while the amplitude of wind gusts can be up to 10 m/s with a period in the range of 10–50 sec. An example of these relationships implemented in LabView is shown in Fig. 4 and an example of wind speed variability for sample parameters is shown in Fig. 5.

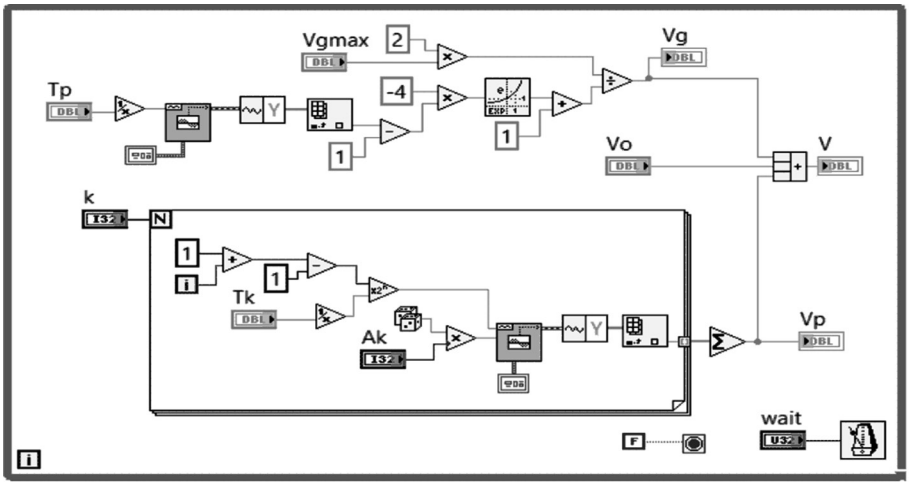

Fig. 4. A subprogram (subVI) generating the wind speed variability

3.2. Power of the wind turbine

The value of the power produced by the wind turbine can be described by the following mathematical model [9, 10, 12]:

$$P_w(V) = \begin{cases} 0 & V < V_{ci} \\ aV^3 - bP_r & V_{ci} \le V < V_r \\ P_r & V_r \le V < V_{co} \\ 0 & V_{co} \le V \end{cases} \tag{3}$$

where:
P_w – electric power generated by the wind turbine [W],
P_r – rated power of wind turbine [W],
V_{ci}, V_r, V_{co} – cut-in, nominal and cut-out wind speed [m/s],
a, b – coefficients which depend on construction of the turbine.

This model determines the average value of the power produced by the wind turbine depending on wind speed. However, at a given wind speed, the real wind turbine may produce different values of electrical power. This is shown in Fig. 6.

Furthermore, in the case of the flicker analysis or the quality parameters of electric power, the model described by the equations (3) is insufficient. This is because it does not take into account a number of phenomena affecting these parameters – e.g. wind turbine power changes caused by a mechanical vibrations associated with moving blades of the wind wheel in front of the tower of wind turbine, the asymmetry of the wind wheel or vibration of blades [5]. Therefore, it is necessary to accurately model these phenomena.

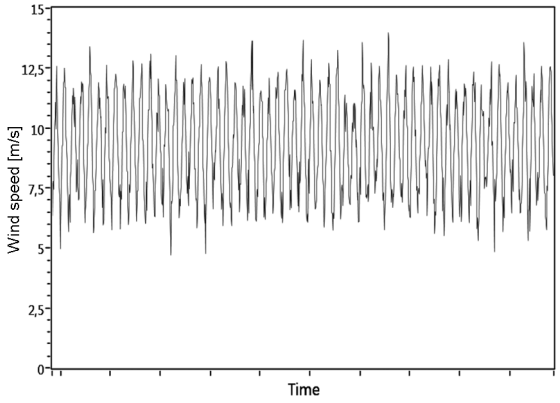

Fig. 5. An example of the variability of wind speed

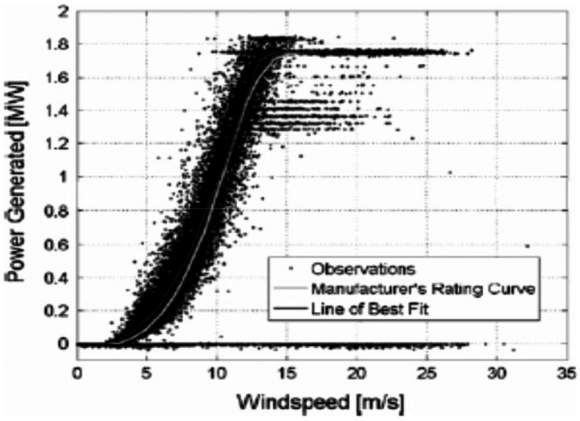

Fig. 6. The actual value of the power generated by the real wind turbine [6]

The mutual relationships between the mathematical descriptions of individual phenomena can be presented in the form of a diagram, this is shown in Fig. 7. Each of the blocks shown in this diagram describes one of the phenomena and is described by a separate subprogram (subVI). A set of these subprograms creates the structure of a program written in LabView environment.

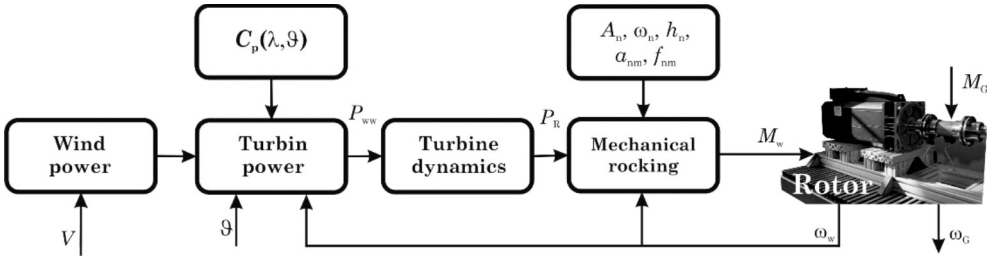

Fig. 7. Structure of wind turbine model

The first block (defined as the mechanical power of the wind turbine obtained from the wind flow) can be described by the following equation [5, 10]:

$$P_{WW} = 0{,}5 \cdot c_P(\lambda, \vartheta) \cdot \rho A V^3 \tag{4}$$

where:

$\rho = \rho_0 - 1.194 \cdot 10^{-4} H$ – air density [kg/m^3],
$\rho_0 = 1{,}225$ kg/m^3 – the air density at sea level at $T = 288$ K,
H – height of the location of a wind turbine above sea level [m],
A – swept area [m^2],
V – wind speed [m/s],
$c_P(\lambda, \vartheta)$ – a coefficient which describes the characteristic of the turbine for the coefficient of blade pitch ϑ and specific speed λ.

Implementation of this relationship in the LabView environment is shown in Fig. 8

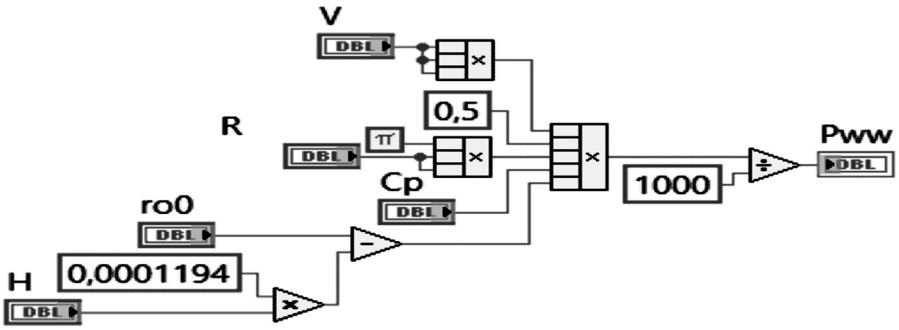

Fig. 8. A subprogram (subVI) defining the value of the power produced by the wind turbine

The coefficient c_p identifying the characteristics of the turbine can be described by the following relationship [5, 10]:

$$c_P(\lambda, \vartheta) = c_1 \left(\frac{c_2}{\Lambda} - c_3 \vartheta - c_4 \vartheta^x - c_5 \right) e^{-\frac{c_6}{\Lambda}} \tag{5}$$

where:

c_1–c_6 – coefficients (sample values taken from [5, 16]: $c_1 = 0.5$, $c_2 = 116$, $c_3 = 0.4$, $c_4 = 0$, $c_5 = 5$, $c_6 = 21$),
Λ – parameter which is described by the following formula:

$$\frac{1}{\Lambda} = \frac{1}{\lambda + 0.08\vartheta} - \frac{0.035}{1 + \vartheta^3} \tag{6}$$

where:

ϑ – blade pitch angle [rad],

$\lambda = \dfrac{\omega R}{V}$ – specific speed,

ω – angular velocity of the turbine rotor [rad/s],

R – radius of the rotor [m].

The code calculating the value of the coefficient c_p written in G-language is shown in Fig. 9.

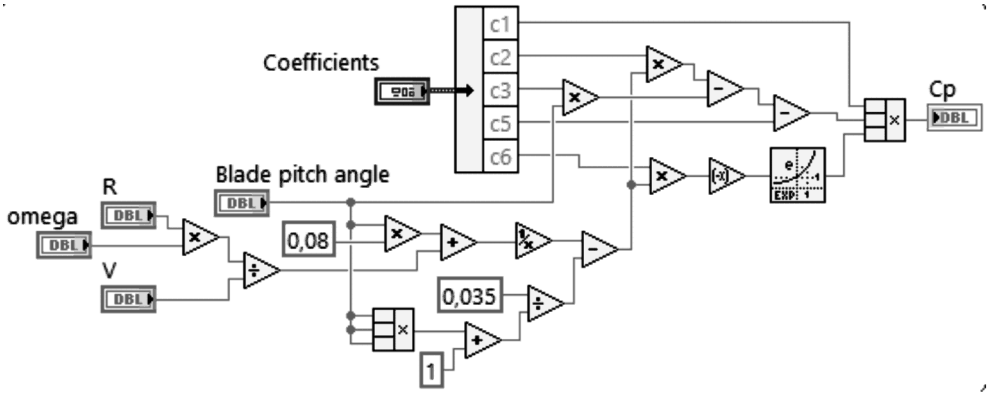

Fig. 9. The subprogram (SubVI) defining the coefficient C_p

3.3. Dynamics of the wind turbine

In real operating conditions, there are a number of phenomena associated with the impact of wind on the turbine blades. For this reason, it is necessary to take into account the dynamics of the wind turbine. The dynamics can be described by the following transmittance [5, 10]:

$$\frac{P_R}{P_{WW}} = K_W \frac{1 + sT_{W1}}{1 + sT_{W2}} \tag{7}$$

Typical values of these parameters for medium power wind turbines with a power control system using a drag effect are as follows [5]: $K_W = 1$, $T_{W1} = 3.3$ s, $T_{W2} = 0.9$ s.

3.4. Mechanical vibration

The quality of the produced electrical energy is mainly influenced by the variability of the wind speed. However, for better accuracy, the mechanical vibration of wind turbines must be also taken into account. These torsional oscillations are transmitted to the shaft, and then to the generator. As a result, electrical energy generated by the wind turbine and transmitted to the power system contains a number of harmonic current and voltage.

The most important factors which affect the mechanical vibration of wind turbines are as follows: the asymmetry of the wind wheel; change of power of wind turbine caused by mechani-

cal vibrations associated with moving blades of the wind wheel in front of the tower of wind turbine; vibrations of the blades which are dependent on their structure and size [5, 17].

Taking into account the mechanical vibration of wind turbines, the mechanical power on the shaft of the wind turbine can be described by the following equation [5]:

$$P_W = P_R\left(1+\sum_{k=1}^{3} A_k\left(\sum_{m=1}^{2} a_{km} g_{km}(t)\right)h_k(t)\right) \tag{8}$$

$$g_{km}(t) = \sin\left(\int_0^t m\omega_k(\tau)d\tau + \phi_{km}\right) \tag{9}$$

where:

A_k, ω_k, $h_k(t)$, g_{km}, φ_{km} – value, pulsation, modulation, distribution and phase of the k-th type of power swings,

m – number of harmonics,

a_{km} – normalized value of g_{km}.

3.5. Model of gear

The next element taking part in the conversion of wind energy into electric energy is the gear. This consists of: pitch control; wind wheel; shaft; generator rotor; gear (not included in wind turbines with low-speed generators). The dynamics of this system can be described by the following differential equations [5]:

$$\begin{cases} \dfrac{d\delta_W}{dt} = \omega_W - \omega_{W0} = \Delta\omega_W \\ \dfrac{d\delta_G}{dt} = \omega_G - \omega_{G0} = \Delta\omega_G \\ J_W \dfrac{d\Delta\omega_W}{dt} = M_W - K\left(\delta_W - \dfrac{\delta_G}{\upsilon}\right) - D\left(\Delta\omega_W - \dfrac{\Delta\omega_G}{\upsilon}\right) \\ J_G \dfrac{d\Delta\omega_G}{dt} = M_G + \dfrac{K\left(\delta_W - \dfrac{\delta_G}{\upsilon}\right) + D\left(\Delta\omega_W - \dfrac{\Delta\omega_G}{\upsilon}\right)}{\upsilon} \end{cases} \tag{10}$$

where:

ω_{W0}, ω_{G0} – the wind wheel speed and the generator rotor speed in a steady state [rad/s],

J – moment of inertia [kg·m^2],

M – mechanical moment [kg·m^2/s^2],

D – damping coefficient [kg·m^2/s],

K – stiffness coefficient [kg·m^2/s],

δ – angle [rad],

υ – gear ratio [–].

The index *W* refers to the wind wheel side, and the index *G* refers to the gear side of the generator rotor.

All of these elements of the wind turbine model may affect the quality of the produced electrical energy.

The proposed model of wind turbine allows analyzing the influence of individual parameters of the used mathematical model on the quality parameters of the generated electrical energy. This test stand can be also used in every stage of the wind turbine design and optimization.

4. Conclusions

This paper presents a Hardware-in-the-Loop type simulator used for the laboratory testing of wind turbine generators. Using this simulator, it is possible to reproduce the actual operating conditions of wind turbines with different types of generators in the laboratory. This approach allows an easy, economical and rapid analysis of both devices and their control software. This system has been implemented at sbRIO controller manufactured by National Instruments. This controller cooperates with the inverter with DTC control (manufactured by ABB). Furthermore, the use of the LabView graphical programming environment creates enormous opportunities for research prototype generators and converters of electric energy cooperating with wind turbines.

References

[1] Pałka R., Szkolny S., *Stanowisko do badania napędów elektrycznych z komputerowym systemem pomiarowym*, Zeszyty Problemowe – Maszyny Elektryczne, 2013, nr 100k, cz. I, pp. 83–88.

[2] Małyszko O., Zeńczak M., *Balance of reactive power in wind power farms*, Przegląd Elektrotechniczny, 2012, R. 88, nr 10a, pp. 19–21.

[3] Małyszko O., Szkolny S., Zeńczak M., *Elektroenergetyczna automatyka zabezpieczeniowa w systemie elektroenergetycznym z farmami wiatrowymi*, Wiadomości Elektrotechniczne, 2010, t. 78, nr 4, pp. 16–19.

[4] Małyszko O., Szkolny S., Zeńczak M., *Zastosowanie przewodów wysokotemperaturowych przy podłączaniu farm wiatrowych*, Wiadomości Elektrotechniczne, 2010, t. 78, nr 4, pp. 28–29.

[5] Lubośny Z., *Elektrownie wiatrowe w systemie elektroenergetycznym*, WNT, Warszawa 2007.

[6] Potter C.W., Gil H., McCaa J., *Wind power data for grid integration studies*, IEEE PES general meeting 2007.

[7] Song Y.D., Zhang Z.Y., Peng Li, Wang W.L., Qin M., *Robust adaptive variable speed control of wind power systems without wind speed measurement*, Journal of Renewable and Sustainable Energy, 2013, No. 5.

[8] Vlad C., Bratcu A.I., Munteanu I., Epure S., *Real-time replication of a stand-alone wind energy conversion system: Error analysis*, International Journal of Electrical Power & Energy Systems, February 2014, Vol. 55, pp. 562–571.

[9] Martinez F., Herrero L.C., Santiago P., *Open loop wind turbine emulator*, Renewable Energy, March 2014, Vol. 63, pp. 212–221.
[10] Ruihong Yu, Yanqin Li, Jianxian Cai, *Maximum Power Point Tracking from a Wind Turbine Emulator Using a DC-DC Converter Controlled*, International Journal of Control and Automation, 2014, Vol. 7, No. 1, pp. 117–128.
[11] Lee J.K., Park J.Y., Oh K.Y., Park J.S., *Development of Wind Turbine Simulator for Generator Torque Control*, World Academy of Science, Engineering and Technology, 2011, Vol. 58, pp. 162–165.
[12] Rahelo B., Hofmann W., Gluck M., *Emulation of the Static and Dynamic Behaviour of a Wind-turbine with a DC-Machine Drive*, 35th Annual IEEE Power Electronics Specialists Conference Aachen, Germany, 2004, pp. 2107–2112.
[13] Song S.H., Byoung-Chang J., Lee H.I., Kim J.J., Oh J.H., Venkataramanan G., *Emulation of output characteristics of rotor blades using a hardware-in-loop wind turbine simulator*, Twentieth Annual IEEE Applied Power Electronics Conference and Exposition, APEC 2005, 6–10 March 2005, Vol. 3, pp. 1791–1796.
[14] Lopes L., Lhuilier J., Mukherjee A., Khokhar M., *A Wind Turbine Emulator that Represents the Dynamics of the Wind Turbine Rotor and Drive Train*, IEEE 36th Power Electronics Specialists Conference, PESC '05, 16–16 June 2005, Recife, pp. 2092–2097.
[15] Schoder K., Langston J., Steurer M., *Commissioning of MW-Scale Power Hardware-in-the-Loop Interfaces for Experiments with AC/DC Converters*, 39th Annual Conference of the IEEE Industrial Electronics Society, IECON, 10–13 Nov. 2013, Vienna, pp. 5364–5367.
[16] Paepen S., De Koker K., Adams P., Coussens P., *Industrial drive based wind simulator for small wind turbine optimisation*, International Conference on Clean Electrical Power, ICCEP, 14–16 June 2011, Ischia, pp. 786–790.
[17] Dolan D., Lehn P.W., *Real-Time Wind Turbine Emulator Suitable for Power Quality and Dynamic Control Studies*, International Conference on Power Systems Transients (IPST '05), 19–23 June 2005, Montreal, Canada, Paper No. IPST05-074.
[18] Szkolny S., Małyszko O., *Symulator typu Hardware-In-The-Loop do testowania generatorów turbin wiatrowych*, Zeszyty Problemowe – Maszyny Elektryczne, 2014, nr 103, cz. I, pp. 269–274.

TECHNICAL TRANSACTIONS | **CZASOPISMO TECHNICZNE**
ELECTRICAL ENGINEERING | ELEKTROTECHNIKA
1-E/2015

UWE SCHUFFENHAUER, NORBERT MICHALKE*

CALCULATION METHODS FOR EDDY CURRENT LOSSES WITH THE EXAMPLE OF A PERMANENT MAGNET EXCITED SYNCHRONOUS MACHINE INSIDE THE THRESHING CYLINDER OF A COMBINE HARVESTER

METODY OBLICZANIA STRAT OD PRĄDÓW WIROWYCH NA PRZYKŁADZIE MASZYNY SYNCHRONICZNEJ WZBUDZANEJ MAGNESAMI TRWAŁYMI WEWNĄTRZ MŁOCKARNI KOMBAJNU ZBOŻOWEGO

Abstract

Electrical drives become more and more interesting for many applications in mobile machines including farming equipment. In this paper, the electromagnetic design of a threshing cylin der for an electrical combine harvester with a function-fitted external rotor and an inner stator is shown. Special attention will be paid to the calculation of the eddy current losses within the magnets through different FEM methods. The influence on the losses of segmentation of magnets in tangential and axial directions is shown.

Keywords: *synchronous machines*, *finite element methods*, *mobile working machine*

Streszczenie

Napędy elektryczne stają się coraz bardziej atrakcyjne również w aplikacjach maszyn ruchomych, włączając w to również maszyny rolnicze. W niniejszym artykule omówiona została konstrukcja młockarni dla elektrycznego kombajnu zbożowego z zewnętrznym wirnikiem i wewnętrznym stojanem. Szczególną uwagę zwrócono na obliczenia strat prądów wirowych w obrębie magnesów z użyciem obliczeń MES. Pokazany został wpływ segmentacji magnesów w kierunku stycznym oraz osiowym na straty.

Słowa kluczowe: *maszyny synchroniczne*, *metoda elementów skończonych*, *maszyny pracujące w ruchu*

DOI: 10.4467/2353737XCT.15.045.3845

* M.Sc. Eng. Uwe Schuffenhauer, Prof. D.Sc. Eng. Norbert Michalke, Faculty Electrical Engineering, University of Applied Sciences, Dresden.

1. Introduction

By the expansion of drive engineering into broader areas, for instance electric mobility, the requirements enlarge opposite the classic industry drives. The drives must show a high degree of effectiveness in a wide operating range, whereas high torque and power density just as low mass and volume are demanded. These requirements are frequently connected with the specifications of construction and mechanical use, more difficult cooling and environmental conditions as well as safety aspects. Frequently, not only are permanent excited synchronous motors of high power densities favoured, but also high-speed asynchronous machines as well as further new approaches such as transversal flux machines which utilize new materials and technologies. Similar standards are valid for mobile applications, of which not only the traction drive but as in the case of mobile working machines, the drive of working elements and individual functions should be also carried out electrically. Associated with this, there is a development project aimed at electrifying the rotary drives of a combine harvester. Figure 1 shows as an example the individual functional drive with an inner stator and the stroke strips cut to size to an electrical threshing cylinder of a combine mounted directly on the outer rotor [1]. This solution is embedded in the roadmap of a new concept for an electrical combine in cooperation with the Chair of Agricultural Systems and Technology (AST) of the TU Dresden [2].

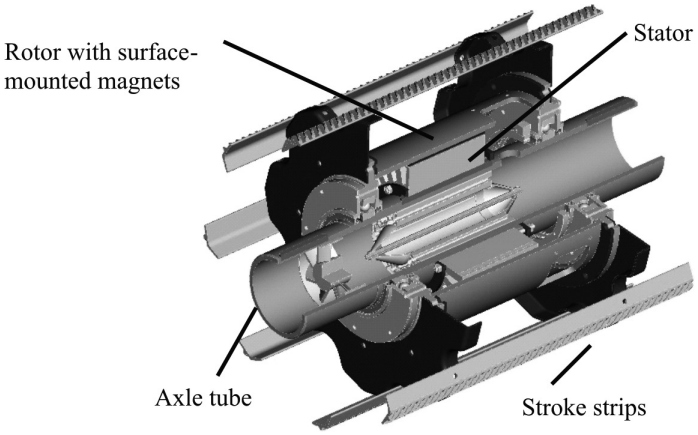

Fig. 1. Electrical threshing cylinder of a combine harvester

The application of decentralized electrical individual functional drives gives the opportunity for various working functions, saves design space, and simplifies the power transfer in the mechanical drive torque distribution. This simultaneously prepares the energy concept for the future. Moreover, the electrical drives with their possibilities for speed and torque control up to the reversible operation and good control response are leading to new technological potential.

The construction of the threshing cylinder requires a suitable cooling concept. For the stator, active air cooling is realized by cooling profiles in the axle tube. Furthermore, the warming of the rotor and particularly the magnets is problematic and requires an optimization of the construction and calculation of the losses already in the design phase. The employed methods are introduced and compared there, where special attention is paid towards the eddy

current losses into the surface-mounted magnets. The methods of the analytical and numerical loss calculation are known essentially [3] and are permanently developed further. The knowledge of the necessary technical or physical parameters is always problematic as well as the modelling and computation efforts plus restrictions of the physical effects implemented in the software. Under application of the usual segmentation of the magnet for limitation of the losses [4] different computation methods are applied to the introduced threshing cylinder.

2. Innovative Materials

Requirements in the field of electric mobility necessitate the search for materials with special physical and technological properties. Magnetically soft materials for electrical machines are a compromise at the demand for a high repletion polarization, low coercivity hysteresis and low eddy current losses. The magnetic sheet steel used in classic electrical machine engineering forms a good compromise of these properties each at mature production technology. An innovation stimulus comes in this juncture by completely new materials or technologies like cobalt based alloys or powder composite materials. Co-alloys show the highest saturation polarization and furthermore, have high mechanical strength and hardness values at their disposal. The materials, originally developed for aircraft construction are, however, very expensive in comparison with standard electric metals.

Magnetically soft powder composite materials, at which the spreading of the eddy currents isn't limited by the material thickness but by the particle size, show comparatively bad magnetization behaviour. The production technology, however, allows the pressing of exactly fitting complicated parts which make a three-dimensional flux direction possible due to their magnetic isotropy. Figure 2 shows the contrary trend for the magnetization behaviour $B = f(H)$ and the losses $p_{spez} = f(B)$ for two selected laminas and the new materials Vacoflux and Somaloy.

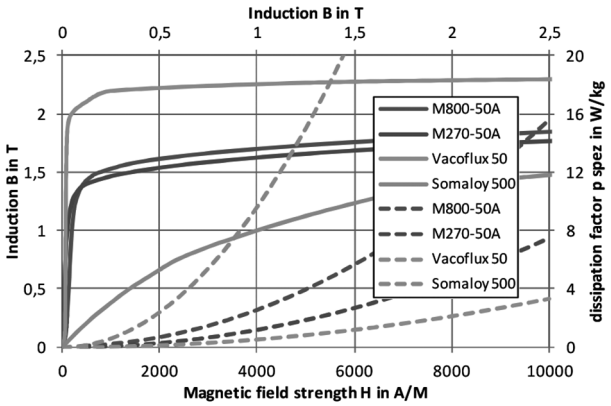

Fig. 2. Magnetization and loss characteristics

Magnetically hard materials offer optimization capacity as well. In principle, only rare earth magnets like NdFeB are possible for this performance category from electrical machines as

shown in Fig. 3. The first types have a considerably higher energy density. The magnets with lower induction show, however, advantages in the field of irreversible demagnetization. In particular, the surface magnets in high-performance engines are endangered by the armature cross-field on the pole edges at increased rotor temperatures and bad heat dissipation.

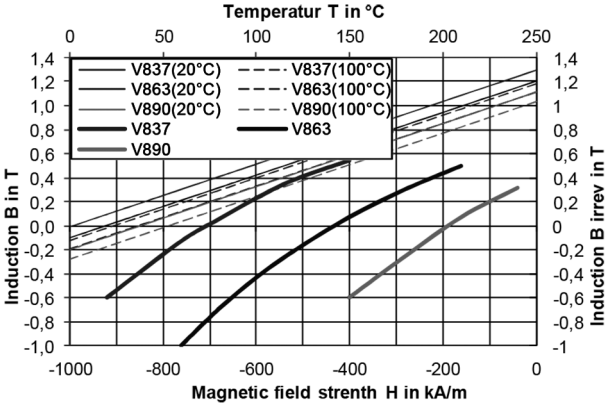

Fig. 3. Linearized demagnetization characteristic and maximum temperature for NdFeB magnets

Knowledge of the characteristics of losses dependent on induction and frequency is of decisive importance for the electromagnetic calculation and for efficiency and warming estimation.

3. Analytical and composite methods of computation with 2D FEM

Losses in electrical machines arise from friction in the windings by Joule heat, in the magnetic circuit by magnetic reversal and in form of mechanical losses. Magnetic reversal losses arise from hysteresis and eddy currents, which one specific loss component each can be indicated for. The eddy currents themselves produce a magnetic field and react field-displacing onto the original field. The depth δ is defined as a value where the electrical or magnetic field strength has decreased under the influence of the eddy currents on the *e*-th part of its surface value. It is described according to [5] as the penetrating measure.

$$\delta = \frac{1}{\beta} = \frac{1}{\sqrt{\pi \cdot f \cdot \kappa \cdot \mu}} \tag{1}$$

where:

μ – the permeability $\mu = \mu_0 \cdot \mu_{rel}$,

κ – the specific electrical conductivity.

The penetrating measure therefore depends on the electrical conductivity κ and the relative permeability μ_{rel} of the material.

The limit, above which a considerable weakening of the field appears because of field displacement, is the critical frequency f_g. For areas of the thickness d it is valid:

$$f_g = \frac{1}{\pi \cdot \kappa \cdot \mu \cdot d^2} \tag{2}$$

After that, the reaction by eddy currents doesn't play a role in the iron because of the use of a thin laminated steel sheet and in the magnets because of the low conductance, but it has to be taken into account in construction elements. The specific loss factor p_{wb} for eddy current losses is

$$p_{wb} = \frac{1}{24} \cdot \frac{\kappa}{\rho} \cdot d^2 \cdot \omega^2 \cdot \hat{B}^2 \cdot F(x) \tag{2}$$

$$\text{with } F(x) = \frac{3}{x} \cdot \frac{\sinh x - \sin x}{\cosh x - \cos x} \text{ and } x = d \cdot \beta = d \cdot \sqrt{\pi \cdot f \cdot \kappa \cdot \mu}$$

where ρ is the specific gravity.

For small values of x follows $F(x) \approx 1$ and the equation changes for the loss factor.

$$p_{wb} = \frac{1}{24} \cdot \frac{\kappa}{\rho} \cdot d^2 \cdot \omega^2 \cdot \hat{B}^2 \tag{4}$$

The so calculated loss factor is valid for sheets on the condition that the thickness is much smaller than the other dimensions, it is potentially too high with an increasing material thickness. Nevertheless, this way is usual to determine the losses in solid parts. These losses can assume considerable values at high frequencies in solid material, for example, the losses in surface mounted magnets in voltage system converters supplied synchronous machines [6] or asynchronous machines [7]. A reduced penetration depth by eddy currents has to be taken into account as described above.

The specific loss factor can be approximately calculated for metals and other conductive materials. If taken into account, however, the frequency dependent penetration depth, this leads in the iron to a reduction of the material effectively concerned so. The loss factors form the basis for the fast analytical calculation of the electrical machine together with the manufacturer's material properties. The disadvantage is the number of simplifications like the summarizing calculation of the induction for typical areas of the magnetic circuit, the only partial consideration of saturation conditions and the leakage. Harmonic wave appearances are not taken into consideration; additional effects are summarized in allowance factors.

The induction maxima actually appearing are adequately determined in every element of the magnetic circuit by a stationary FEM calculation. Only an instantaneous value of the induction is included, though, the actual maxima can be higher. Harmonic wave appearances are included in the calculation, however, they find their expression in the evaluation only according to tendency in the average value of the induction and this is always assigned to

the fundamental. The rotor evaluation would deliver only a statement about the amount of induction but not about its change because the fundamental as a constant component cannot be separated from the harmonic waves.

Therefore, this way a method of computation is used for the iron and additional losses including calculation of the amount and the distribution of the stator and rotor losses from the transient FEM calculation. In every field element, the actually appearing harmonic field waves and sub-harmonics are determined by means of evaluation of the transient field course by a discrete Fourier analysis. The loss calculation is carried out for every element. The calculated losses are summarized for both laminated and solid parts of the magnetic circuit and summed up in loss zones about all elements. The obtained loss sums contain the influence of the fundamental one and of the harmonics arising by the winding and the slots.

$$P_{Vfe} = \sum_{e} \sum_{\nu'} P_{fe,e,\nu'} \left(p_{wb}, \hat{B}_{e,\nu'}, f_{\nu'} \right) \tag{5}$$

where:

$\hat{B}_{e,\nu'}$ – the induction in an element for the harmonic ν',
$f_{\nu'}$ – the frequency for the harmonic ν'.

Firstly, these combined methods were applied on the integrated threshing cylinder (nominal power P_n = 30 kW, maximum performance P_{max} = 60 kW at a speed of n_{max} = 1000 obr/min). A permanent excited synchronous motor with an outer rotor was chosen for an optimal function integration of the engine into the predefined threshing cylinder. The winding is performed as a concentrated one in tooth coil technology. This leads to relatively little winding heads with shorter axial lengths and lower copper losses. A disadvantage is the deviation of the stator field from the sine form with additional high and sub-harmonics (Fig. 4).

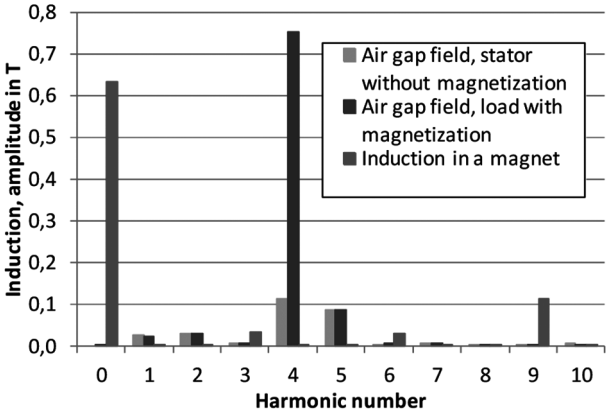

Fig. 4. Harmonic spectrum of the field curve without magnetization on load, analysis in the magnet

In the stator, the 4th harmonic dominates which as armature cross-field adds up with the magnetization of the rotor to the basic wave field and rotates synchronously with this. It shows itself as a direct component in one point of a magnet in the rotor in the analysis of

the transient load calculation (Fig. 5). However, a wave dominates, at which the distinctive 5th harmonic of the stator is contrary formed itself in the rotating rotor as 9th harmonic of the fundamental and causes the corresponding losses there.

The really occurring harmonics and sub-harmonics of each element are obtained by transient calculation. The calculation of stator and rotor losses is carried out by harmonic analysis of the time course and following the loss calculation using the value of the harmonics. The results are summarized over all elements of the regarded area. Figure 5 shows the distribution of the loss density by the effect of the harmonic wave fields in the outer rotor on the right and additional in the stator iron.

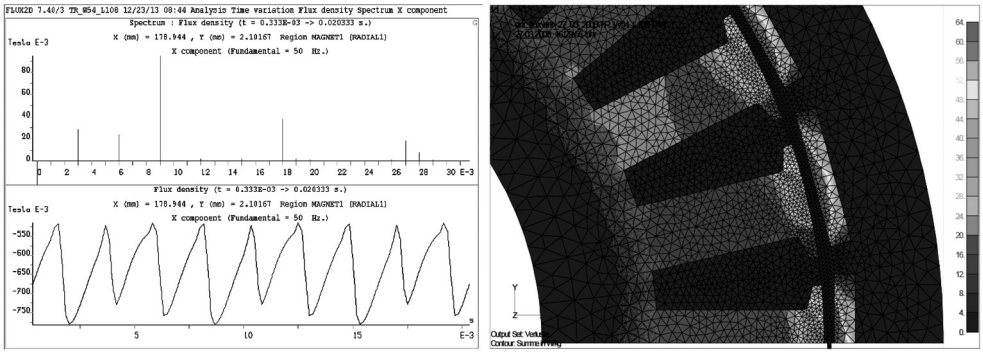

Fig. 5. Induction course in one point of magnet and the resulted loss distribution in the iron and the magnets

The loss calculation in the rotor and the inactive parts of the magnetic circuit is possible using the developed method for the calculation of the core losses by harmonic waves using the results of transient FEM calculation. It can be utilized for new designs of machines with a high degree of accuracy. By this method, not only the loss sum but also its distribution (Fig. 5) is very well determinable so that these results can be combined with a more detailed heating calculation and make adapted cooling methods possible.

4. New methods of the 3D FEM

The 2D-FEM has the restriction that the eddy current losses only are concluded from the analytically well-founded effect of the calculated electromagnetic fields and moreover, the reaction of the eddy currents to the magnetic field cannot be taken into account. These disadvantages should be overcome by the 3D-FEM calculation.

The simulation software Ansys® offers an extensive library with element types for the solution of several types of physical task formulations. In the present task of calculation of the eddy currents, the use of a new edge element is forced for the solution of the dynamic field calculation instead of the element used for quasi-static electromagnetic calculations explicitly [8]. This element has an electrical degree of freedom (DOF) at the corner node in addition to the electromagnetic one. It is suitable for the calculation of the eddy currents and

losses with the restriction that a transient analysis but no harmonious one is possible with nonlinear material. Furthermore, permanent magnets aren't permitted in the harmonic analysis. Besides the stator winding, the magnets of the rotor are defined as a solid conductor with the material properties 'relative permeability' and 'resistance' in order to make possible the calculation of the eddy currents (Fig. 6, highlighted areas). The solution must be carried out at the still-standing rotor under impression either the harmonics in the electrical circuit or the field harmonic waves at the air-gap.

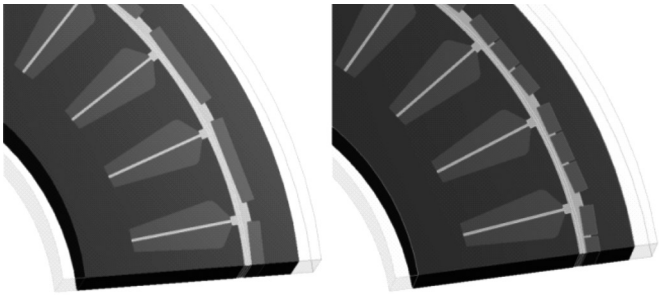

Fig. 6. 3D-FEM-Modell with magnet segmentation

A coupling of the FEM problem with the calculation of the electrical circuit is possible if in a transient calculation time functions of current or voltage should be provided or even if discreet construction elements like leakage inductances whose modelling exceeds the possibilities of a 3D-FEM model should be included in a calculation. The extended functions are integrated into the sequence of modelling, solution and post-processing by means of macros. The losses calculated this way are represented for different variants of the segmentation (Fig. 7) and are compared with the described analytical approach.

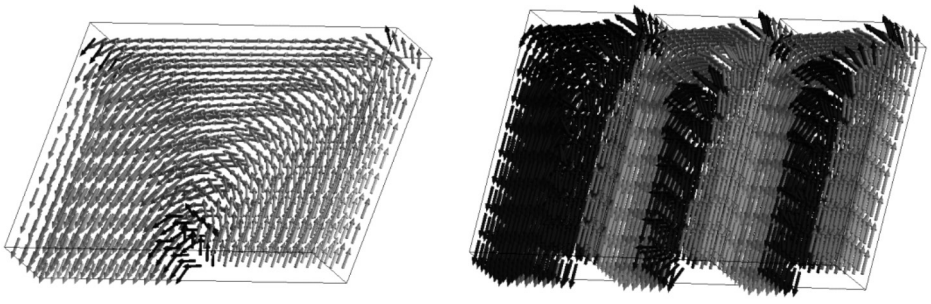

Fig. 7. Eddy currents in a magnet, model part, maximum current density 3.43 A/mm² and in a three times segmented magnet, maximum current density 1.89 A/mm²

The eddy current losses per element are found out by means of the calculated current density. All of the eddy current losses of a component or the data set from several components arise from the sum P_{Vfe} with the element current density J_e:

$$P_{Vfe} = \sum_e \rho_{el} \cdot V_e \cdot J_{e,ges}^2 \quad \text{with} \quad J_{e,ges}^2 = J_x^2 + J_y^2 + J_z^2 \tag{6}$$

where:
V_e – the element volume,
J_e – the element current density with their components.

For the predefined application, the effect of the segmentation of the permanent magnets was examined in a tangential and axial direction. This is a usual measure whose effectiveness, however, depends on the concrete geometric conditions and appearing field harmonics. Figure 8 represents the eddy currents appearing in the magnet.

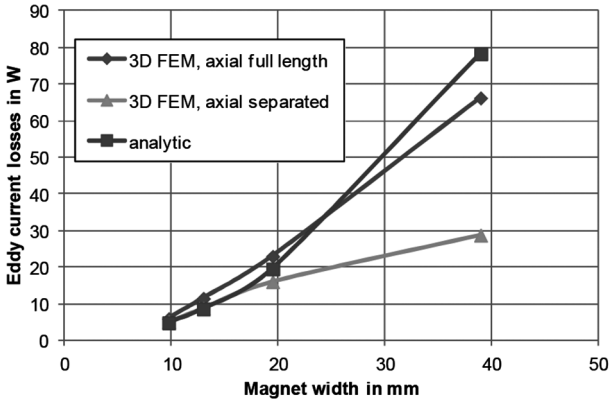

Fig. 8. Magnet losses as a function of the segmentation

A comparison for different degrees of the segmentation with the analytical approach described above shows that the connections are represented by tendency correctly in all variants, the real 3D-FEM calculation, however, better reflects the concrete geometry conditions.

5. Results

Three times in tangential and two times in radial direction segmented magnets were realized for the rotor of the threshing cylinder motor. Ultimately, technological and economic reasons influence the decision. A view into the outer rotor is shown in Fig. 9.

For the threshing cylinder engine, the eddy current losses of the magnets are calculated in Flux2D at 351 W and for the segmented magnets in Ansys®3D at 277 W. These values are approximately within the range of a third of the core losses at a total electrical efficiency of 96% for the designed machine.

With the introduced methods, there are several practical ways by which the losses in the magnets can be calculated analytically combined with a transient 2D-FEM calculation or by a transient and harmonic analysis with a real eddy current calculation in 3D-FEM. These are applied both to the analysis of other drives of the combine harvester and in direct projects with manufacturers of electrical machines.

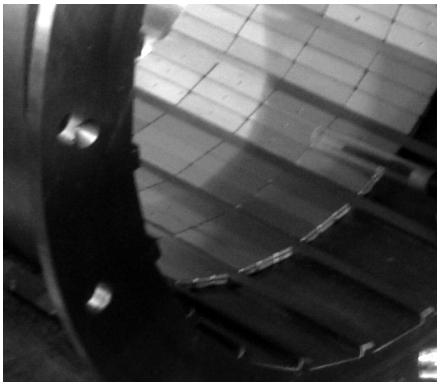

Fig. 9. View into the rotor with segmented magnets

References

[1] Aumer W., Bernhardt G., Lindner M., Michalke N., Kuss H., Schuffenhauer U., *Selbstfahrende Erntemaschine mit elektrisch angetriebener Dreschtrommel*, Schutzrecht WO 2010/122055 A1.

[2] Herlitzius Th., Aumer W., Lindner M., Bernhardt G., Kuß H., Michalke N., Schuffenhauer U., *System Integration and Benefits of Electrical Solutions in Mobile Machines*, ECPE-Seminar, More Electric Vehicle, München, 30. und 31.03.2009.

[3] Küpfmüller K., Kohn G., *Theoretische Elektrotechnik und Elektronik*, Springer-Verlag, 2000.

[4] Bode C., Canders W.-R., *Advanced Calculation of Eddy Current Losses in PMSM with tooth windings*, XIX International Conference on Electrical Machines – ICEM 2010, Rome.

[5] Mirzaei M., Binder A., Deak C., *3D Analysis of Circumferential and Axial Segmentation Effect on Magnet Eddy Current Losses in Permanent Magnet Synchronous Machines with Concentrated Windings*, XIX International Conference on Electrical Machines – ICEM 2010, Rome.

[6] Polinder H., Hoeijmakers M.J., *Eddy-current losses in the segmented surface-mounted magnets of a PM machine*, IEE Proc.-Electr. Power Appl., May 1999, Vol. 146, No. 3.

[7] Green T.C., Hernandez C.A., Smith A.C., *Losses in grid and inverter supplied induction machine drives*, IEEE Proc. Electr. Power Apll., 2003, Vol. 150, No. 6.

[8] Hanke M., Otto J., *Elektromechanische Antriebe, simuliert mit ANSYS*, antriebspraxis, 04/2009.

TECHNICAL TRANSACTIONS | **CZASOPISMO TECHNICZNE**
ELECTRICAL ENGINEERING | ELEKTROTECHNIKA
1-E/2015

ANDRZEJ BYTNAR*, SŁAWOMIR WRÓBLEWSKI**

ONLINE DIAGNOSTICS OF THE TECHNICAL CONDITION OF THE TURBOGENERATOR STATOR CORE SUSPENSION

DIAGNOSTYKA ONLINE STANU TECHNICZNEGO ZAWIESZENIA RDZENIA W KORPUSIE STOJANA TURBOGENERATORA

Abstract

This paper presents a method for the continuous technical diagnostic of the core suspensions at selected measurement points of the turbogenerator stator. The method extends diagnostic capabilities of a turbogenerator vibration monitoring system which has been designed with the participation of the authors of this paper and applied within the Polish power industry. This method uses two indicators (suppression and vibration harmonic contribution in suspension nodes) whose values are calculated from acquired and processed data in a given turbogenerator operation period. There has been four value ranges proposed for the indicators. The ranges define a technical condition of a stator suspension (very good, good, acceptable, bad) including two alarm ranges. Each technical condition is presented as a colourful area on an idle and active power plot. This enables the quick identification of machine operation areas, which reveals the weakened technical condition of a stator component.

Keywords: *turbogenerator*, *diagnostics*, *suspension*, *technical condition*

Streszczenie

W niniejszym artykule przedstawiono metodę ciągłej automatycznej wibracyjnej diagnostyki stanu technicznego elementu zwieszenia rdzenia stojana w wybranych punktach pomiarowych stojana turbogeneratora. Rozszerza ona możliwości diagnostyczne systemu monitoringu wibracji turbogeneratora, który został opracowany i wdrożony w energetyce polskiej przy współudziale autorów niniejszego artykułu [12]. W metodzie tej wykorzystano dwa wskaźniki oceny (tłumienia i udziału harmonicznych wibracji w węzłach zawieszenia), których wartości są wyznaczane w zadawanym okresie pracy turbogeneratora z przetworzonych i gromadzonych danych pomiarowych w systemie monitoringu. Dla wskaźników zaproponowano cztery przedziały wartości określające stan techniczny elementu zawieszenia rdzenia (bardzo dobry, dobry, przejściowo dopuszczalny, zły), w tym dwa stany alarmowe. Każdy stan techniczny przedstawiany jest w postaci innego barwnego obszaru na wykresie mocy czynnej i biernej turbogeneratora. Umożliwia to szybką identyfikację obszarów pracy maszyny, w których zachodzi znaczący proces pogarszania się stanu technicznego elementu zawieszenia rdzenia stojana.

Słowa kluczowe: *turbogenerator*, *diagnostyka*, *zawieszenie*, *stan techniczny*

DOI: 10.4467/2353737XCT.15.046.3846

* D.Sc. Ph.D. Eng. Andrzej Bytnar, The Institute of Power Engineering, Warszawa.
** Ph.D. Eng. Sławomir Wróblewski, Ericpol Sp. z o.o., Łódź.

1. Introduction

It is known that turbogenerator stator core elements are vulnerable to damage during operation with a variable load of active and reactive power. The damage is mainly caused by vibrations (Fig. 1) [5].

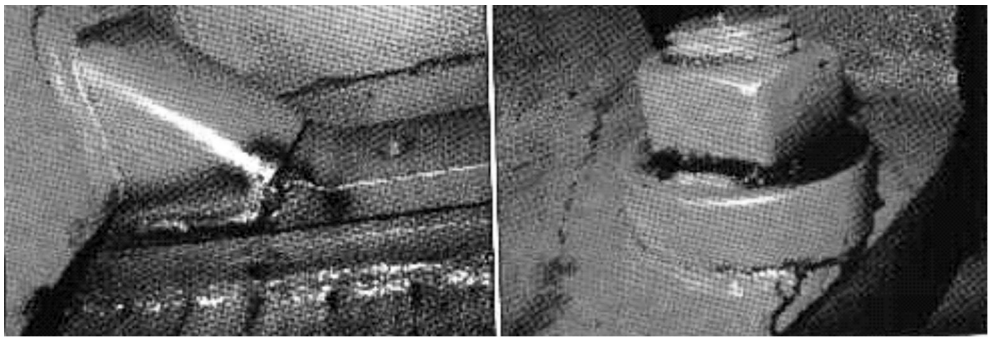

Fig. 1. Examples of suspension components' damage in the body of the stator core of a large turbogenerator

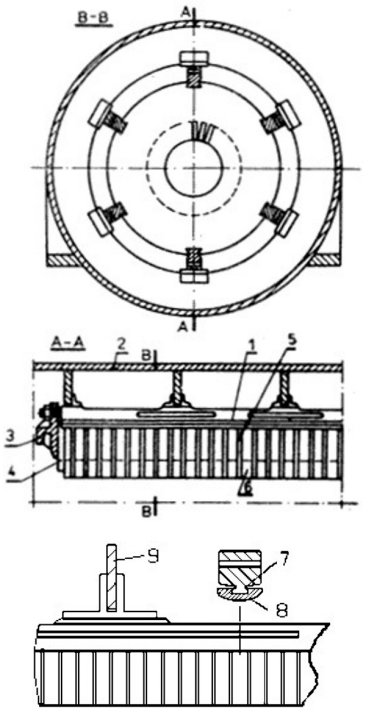

Fig. 2. Elastic suspension in the turbogenerator stator core [1]: 1 – a bar pulling elastic suspension elements of the core; 2 – core; 3 – retaining ring; 4 – platen; 5 – radial ventilation duct; 6 – stator lamination stack; 7 – a fragment of the pulling bar; 8 – notch in the plates of the yoke core; 9 – lateral wall (a rib) of the stator

High vibration levels are very often present in the turbogenerator stator core, especially in its active part. The vibrations are mainly caused by the meaningfully lowered pressure of the stator lamination stack. They can penetrate into a stator housing, its foundation and the building foundation – this is considered to be a serious threat.

The core is elastically suspended in the stator frame in modern constructions of large two-pole turbogenerators. This suspension type is used to suppress the vibrations in the stator core and in the foundations. There is a wide array of suspension types used in turbogenerators [1, 2, 11, 12] (Fig. 2). The core suspension damage caused by vibration phenomena appears very often during turbogenerator exploitation and there are a number of pieces of research dedicated to that phenomena [3–7, 13].

2. Turbogenerator Suspension Design Guidelines

The elastic suspension is so designed that vibrations between the stator core and the housing, caused by the basic harmonic of 100 Hz, are suppressed at least three times (9.5 dB).

The highest admissible vibration level is specified by recommendations – construction standards for turbogenerators [8] and indirectly by vibration standards for non-rotating machine parts [9].

On the basis of vibration phenomena analysis and visualization of particular stator suspension parts in the stator core of large turbogenerators, a new method of continuous automatic vibration diagnostics of the stator core technical condition has been designed.

3. Analysis of Vibrations Transferred through the Core Suspension

Analysis of electromagnetic phenomena and vibration measurements of turbogenerators shows that the rms value of the vibration of the stator components in the low frequency band of approx. 10 to 1 kHz (in accordance with the standard parameters for the assessment of the turbogenerator bearing technical condition) depend mainly on: active induction in the rotor gap; coupling induction of a stator; rotor end winding dissipation; the stiffness of vibrating elements.

The values of the vibration excitation forces depend on the value and type of electrical load P; Q of the turbogenerator (induction dissipation is considerably increased in the area of underexcitation). Also, the rigidity of the structural elements in the nodes (associated with excessive clearances, microcracks, etc.) may change in the existing real power load area as a result of the action of the synchronous torque. A mechanical shock (the measured vibration harmonics) appears in damaging components. The shock frequency in ‘clocked’ with a main force of 100 Hz making turbogenerator vibrations.

Pairs of accelerometers placed on the outer planes of the stator core and on the housing in the same cross-sections (described by a clock scale) (Fig. 3) allow the identification and analysis of the vibration signal transferred between the pairs. Inner sensors are mounted with screws anchored in the core radial channels and outer ones are mounted with neodymium magnet holders with a lifting strength of 30 kG.

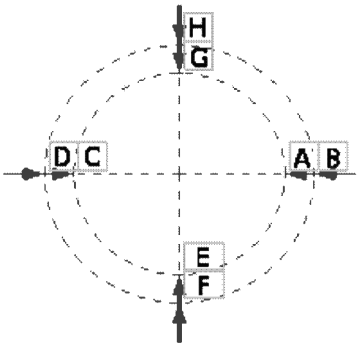

Fig. 3. Distribution of vibration sensors on the outer surface of the stator yoke and on the body in the cross-section of the stator: A, E, C, G – sensors on the yoke core; B, F, D, H – sensors on the housing

Such a distribution of accelerometers allows calculating a new suspension technical condition state indicator from the vibration signals.

It has been found that when the suspension is operating correctly, the core vibrations are transmitted into the stator housing almost without distortion. However, when weakening of the mounting in the structural nodes appears, higher harmonic velocity vibrations are generated and their parameters can be used in the diagnostics (Fig. 4).

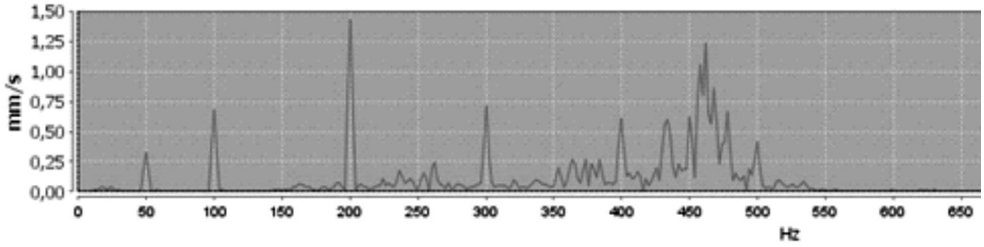

Fig. 4. Velocity vibration harmonics in the lower frequency band on the housing; $P \approx 211$ MW and $Q \approx 36$ MVar 230 MW turbogenerator

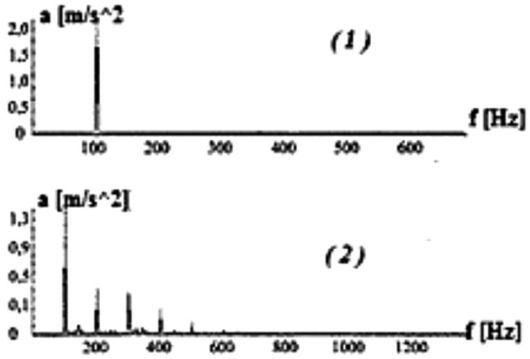

Fig. 5. Acceleration vibration plots of the stator suspension at turbogenerator rated duty (1) – correctly operating core suspension, (2) – weakness in the nodes of the suspension mounting

The research results of vibrations on the stator housing surface (Fig. 5, [2]) confirm that phenomena.

4. Estimation of the Technical Condition of Suspension Components

So far, however, there is no method of evaluating the technical condition of the core suspension while the turbogenerator is operating. The authors have therefore attempted to create it on the basis of numerous vibration studies of the core yoke, the stator body, the stator frame and the suspension inspection during repairs of various turbogenerators.

Attenuation rate and vibration harmonics transfer indicators (between described reference points, e. g. A and B; H and G Fig. 2) have been introduced to estimate the technical condition of i-th element of stator suspensions:

- **τ(i)** (a basic indicator, formula (1)), attenuation rate indicator taking into account the frequency band 10–1000 Hz [13],
- **λ(i)** (a supplemental indicator, determining the harmonic contribution; formula (2)) taking into account the frequency band 10–1000 Hz without 100 Hz component.

$$\tau_{(i)} = \sqrt{\sum_{k=10\text{Hz}}^{1000\text{Hz}} \left(v_{(i)\text{inner}(k)} / v_{(i)\text{outer}(k)} \right)^2} \tag{1}$$

Where:
$v(i)\text{outer}(k)$ – k-th harmonic velocity on the stator housing (e.g. sensor A),
$v(i)\text{inner}(k)$ – k-th harmonic velocity on the stator core (e.g. sensor B),
k – k-th harmonic.

$$\lambda_{(i)} = \frac{\sqrt{\left(\sum_{k=10\text{Hz}}^{1000\text{Hz}} v^2_{(i)\text{inner}(k)} \right) - v^2_{(i)\text{inner}(100\text{Hz})}}}{\sqrt{\left(\sum_{k=10\text{Hz}}^{1000\text{Hz}} v^2_{(i)\text{outer}(k)} \right) - v^2_{(i)\text{outer}(100\text{Hz})}}} \tag{2}$$

where numerator and denominator – geometric sum of k-th harmonic values without 100 Hz respectively on the stator housing and core.

Attenuation rate **τ(i)** and vibration harmonics transfer **λ(i)** indicators have been determined on the basis of vibration and visualizing the survey of turbogenerator components (Table 1).

The values of **λ(i)** are similar to those used in Russia [4].

At the given P; Q load of the turbogenerator, technical condition of the i-th suspension component is estimated by comparing the value **τ(i)** (calculated using the formula (1)) to the criteria values (Table 1), completed with +/– signs: '1+'; '2+'; '3+' or '1-'; '2-'; '3-' in cases when value **λ(i)*p*** (calculated using the formula (2)) is in a different range of the approved grading scale.

Table 1

Criteria values of attenuation rate indicator $\tau_{(i)}$ and vibration harmonics transfer $\lambda_{(i)}$

Values of the indicators	Technical condition of the suspension
$\tau_{(i)} > 3$	Very good
$\lambda_{(i)} < 1$	
$3 \geq \tau_{(i)} > 1.5$	good
$1 \leq \lambda_{(i)p} < 1.5$	
$1.5 \geq \tau_{(i)} > 0.5$	temporarily permissible
$1.5 \leq \lambda_{(i)} \leq 3$	(alarm I)
$\tau_{(i)} \leq 0.5$	bad
$\lambda_{(i)p} \geq 3$	(alarm II)

When the technical condition of *i*-th element of the suspension is mapped into four colours in the permissible load plot, the mentioned signs increment or decrement the calculated value of **τ(i)** by 10% of the average value of the lower and upper range (good and temporarily permissible) or of the minimal lower value (very good and bad) of the given criteria range for every sign value of the supplemental number. In extreme cases, evaluation of the technical condition can be changed, for example, from 'temporarily permissible' to good.

Values of criteria indicators will be verified on the basis of future complex turbogenerator research.

5. Continuous Automatic Evaluation of the Technical State of Suspension in the Body of the Stator Core

For the purposes of the existing vibration monitoring system for turbogenerators [12], algorithms for the automatic determination of the values of the indicators (attenuation and harmonic transfer) and creating the technical condition of *i*-th element maps have been developed. These have been applied in the form of a computer programme.

Suspension *i*-th element points in the cross-section are automatically identified (Fig. 3) thanks to the machine model which was previously saved in a database.

The values of the indicators are calculated according to formula (1) and (2) for each pair of adjacent points lying in the same stator cross-section. For example, for points A, B, C, and D in Fig. 2. The technical condition of *i*-th stator elements are presented as coloured areas (rectangles) on the turbogenerator load plot (*P*-*Q* plane). The size of each area is defined when defining the parameters of the map.

Depending on the predefined machine type, each area contains a resulting indicator value in the given range of active and reactive power. For example, the areas can be sized to 3 MVar/3 MW and presenting the worst value or the last value for the defined time span (Fig. 6). The areas can be zoomed in on to look closer into the surrounding.

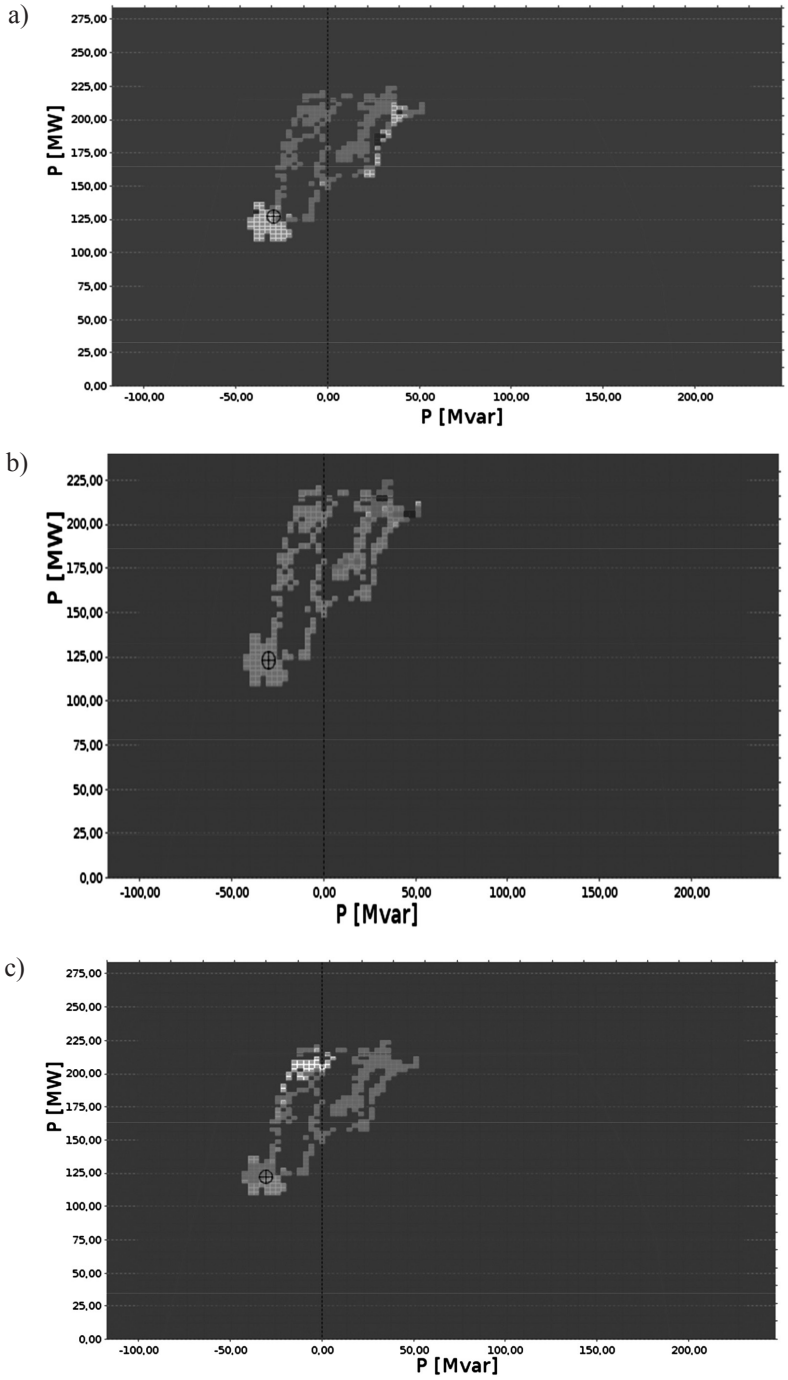

Fig. 6. Maps of the technical condition of three different suspension components in the body of the stator core turbogenerator of 230 MW, a) ring side; 9 o'clock, b) ring side; 3 o'clock, c) ring side; 12 o'clock, dark gray – very good, gray – good, light gray – temporarily permissible, very light gray – bad

Such a presentation allows pointing out the turbogenerator components with reduced technical quality and the areas on the *P-Q* plain which affect the stator condition in the most destructive way. Due to this, the first general analysis can be done in quickly.

6. Conclusions

1. The technical condition of turbogenerators operating in a diurnal cycle of variable loads should be continuously monitored during the turbogenerator exploitation to allow effective elimination of damage at a very early stage.
2. The presented method of automatic continuous assessment of the technical condition of the stator suspension expands the conventional turbogenerator diagnostics.
3. The next task is the design of complex computer software on the basis of the presented algorithms to support a modern turbogenerator diagnostic system.

References

[1] Bytnar A., *Wybrane zagadnienia z konstrukcji i eksploatacji turbogeneratorów*, Wydawnictwo Politechniki Warszawskiej, Warszawa 1983.

[2] Dement'ov V.I. et al., *Obnaruženie defektov statora turbogenertora po parametram vibroakustičeskih kolebanij ego stal'nyh konstrukcji*, Êlektričestvo, 2005, No. 12.

[3] Kumaraswamy S. et al., *Standardization of Absolute Vibration Lewel and Damage Factors for Machinery Health Monitoring*, Proceedings of Vetomac – 2, 16–18 December 2002.

[4] Kuznecov D.V., Šandyvin M.I., *Primenenie metodov vibrokomtrolja dla ocenki sostojanija uprugoj podveski serdečnika statora turbo-generatora*, Élektričeskie Stancii, 2007, No. 10.

[5] Kuznecov D.V. et al., *Vyjavlenie i ustranienie defektov podveski serdečnika statora mošnych turbogeneratorov*, Élektričeskie Stancii, 2012, No. 9.

[6] Maksimov L.V., *Vibrations of the stator of a turbogenerator with elastic suspension of the core using tangential rods*, Scientific-Research Institute of the LPÉO of the Élektrosila, Leningrad, Translated from Prikladnaya Mekhanika, January 1980, Vol. 16, No. 1, pp. 94–98.

[7] Nazolin A.L., Poljakov V.I., *Osobiennosti raboty uzlov kreplenija serdečnika statora turbo-generatora*, Élektričeskie Stancii, 2007, No. 6.

[8] Standard PN-80/B-03040.

[9] Standard ISO 10816-1(1995E).

[10] Patent PL 73909 B2.

[11] Patent PL 54535.

[12] Wróblewski S., Bytnar A., Pietrzak P., *Projektowanie systemów diagnostyki wibracyjnej turbogeneratora*, Wiadomości Elektrotechniczne, 2011, Vol. LXXIX, No. 11.

[13] Wróblewski S., Bytnar A., *Analiza stanu technicznego zawieszenia rdzenia w korpusie stojana turbogeneratora*, Zeszyty Problemowe – Maszyny Elektryczne, 2013, nr 100(4), BOBRME Komel.

TECHNICAL TRANSACTIONS | **CZASOPISMO TECHNICZNE**
ELECTRICAL ENGINEERING | ELEKTROTECHNIKA
1-E/2015

ALEKSANDER LEICHT, KRZYSZTOF MAKOWSKI*

THE EMPLOYMENT OF A SINGLE-PHASE CAPACITOR INDUCTION MOTOR FOR STAND-ALONE GENERATING OPERATION

ZASTOSOWANIE JEDNOFAZOWEGO SILNIKA INDUKCYJNEGO Z POMOCNICZYM UZWOJENIEM KONDENSATOROWYM DO AUTONOMICZNEJ PRACY GENERATOROWEJ

Abstract

The paper presents a two-dimensional field-circuit model of a two-winding, single-phase induction machine operating as single-phase, self-excited induction generator. The model takes remnant magnetism and magnetization characteristics of the stator and rotor core into account. Results of simulations and experiments are presented, i.e. waveforms of voltages during self-excitation, their dependence on rotor slot opening, influence of capacitances and different capacitor topologies on self-excitation, as well steady-state values of generator voltages and currents at no-load operating conditions. Terminal voltage and currents in stator windings as a function of rotor speed and capacitances of capacitors for resistive loads are also presented. The possibility of directly supplying a single-phase induction motor from the generator as a dynamic load were also investigated. Obtained simulation and experimental results show the need for use of semi-closed rotor slots to ensure conditions for successful self-excitation. The obtained simulation results were validated experimentally on the laboratory setup.

Keywords: *induction generator*, *single-phase*, *self-excitation*, *field-circuit modeling*

Streszczenie

W artykule przedstawiono dwuwymiarowy model polowo-obwodowy dwuuzwojeniowej, jednofazowej maszyny indukcyjnej pracującej jako samowzbudny generator indukcyjny. Model ten uwzględnia (w sposób uproszczony) istnienie remanentu magnetycznego w rdzeniu maszyny oraz charakterystyki magnesowania blach pakietów stojana i wirnika. Zaprezentowane zostały wyniki badań symulacyjnych oraz eksperymentalnych – przebiegi napięć podczas procesu samowzbudzenia generatora w zależności od szerokości otwarcia żłobków wirnika, z uwzględnieniem wpływu pojemności i układów kondensatorów w uzwojeniach generatora na przebieg procesu samowzbudzenia oraz na wartości ustalone napięć i prądów w stanie jałowym. Przedstawiono także zmiany napięcia na zaciskach generatora i w uzwojeniu wzbudzenia oraz prądów stojana w zależności od prędkości obrotowej generatora oraz zastosowanych pojemności i układów kondensatorów w uzwojeniach stojana przy obciążeniu rezystancyjnym i przy zasilaniu jednofazowego silnika indukcyjnego. Uzyskane wyniki symulacji i pomiarów wskazują na konieczność zastosowania w wirniku jednofazowego samowzbudnego generatora indukcyjnego żłobków półzamkniętych w celu zapewnienia warunków do zainicjowania procesu samowzbudzenia. Otrzymane na drodze symulacji charakterystyki zostały pozytywnie zweryfikowane na stanowisku laboratoryjnym.

Słowa kluczowe: *generator indukcyjny*, *jednofazowy*, *samowzbudzenie*, *modelowanie polowo-obwodowe*

DOI: 10.4467/2353737XCT.15.047.3847

* M.Sc. Eng. Aleksander Leicht, D.Sc. Ph.D. Eng. Krzysztof Makowski, prof. of WrUT, Department of Electrical Engineering, Chair of Electrical Machines, Drives and Measurements, Wroclaw University of Technology, Poland.

1. Introduction

Single-phase, self-excited induction generators (SPSEIG), driven by internal combustion engines, small wind or hydro turbines can be used as an additional or reserve source of electrical energy in households or in remote areas. Induction generators are characterized by their simple construction (i.e. brushes and permanent magnets are not used), and their low cost of manufacturing, maintenance and ruggedness when compared with synchronous and DC generators. Considerate interest in induction generators was observed, since renewable energy sources became a viable alternative to conventional sources [1–8]. Most of the available works deal with three-phase SEIG, while a two-winding, single-phase induction machine may also be successfully utilized [1, 2, 5]. The single-phase induction machine may operate as a self-excited induction generator, when its main and auxiliary windings are electrically separated and an excitation capacitor is connected to its auxiliary (excitation) winding. The main winding becomes a load winding, to which the load is connected. In the majority of available papers, steady-state and transient analysis is done with the help of a classical circuit model – equivalent circuit for steady state and *dq* model for transients [1, 3, 5]. Classical models are convenient, however, lumped parameter based analysis greatly simplify the phenomena associated with varying magnetic flux in the machine's core, e.g. self-excitation, skin effect or saturation. The use of a two-dimensional field circuit model, based on the finite element method, allows for precise determination of parameters and transient and steady-state characteristics, taking into account the phenomena associated with the varying magnetic field [11]. Design and analysis of SEIG, which operates when the magnetic core is saturated, may be effectively performed by using a field-circuit model [8, 9]. For the first time, this model was applied to the single-phase self-excited induction generator in [6, 7], where the residual magnetism was modeled as a weak permanent magnet embedded in the rotor core.

The paper presents the examination of performance of the single-phase self-excited induction generator by simulation and experiments with both no-load and load conditions.

2. Field-circuit model of the generator

The physical support for the study is represented by a two-phase induction machine, designed for motor operation, characterized by the main data – rated power of 1.1 kW, rated voltage of 230 V, 4 poles. The physical symmetry and electromagnetic periodicity allows for the reduction of the two-dimensional computation domain to half of the cross-section (two pole pitches) of the machine, as shown in Fig. 1. The finite element mesh includes about 20 thousand second-order triangular and quadrangular elements. The computation domain is delimited by the outer surface of the stator core and inner surface of the rotor core. Zero magnetic flux boundary conditions are applied to those surfaces.

The stator windings of the generator are unsymmetrical, the single-layer, two-phase copper windings: main winding (marked by *M* in Fig. 1) is the output winding of the generator, and the load is connected to its terminals, while the auxiliary winding (*A* in Fig. 1) operates as the excitation winding with excitation capacitor connected to its terminals. The aluminum rotor cage consists of 30 bars, placed in semi-closed slots, the width of the slot opening b_r = 1 mm.

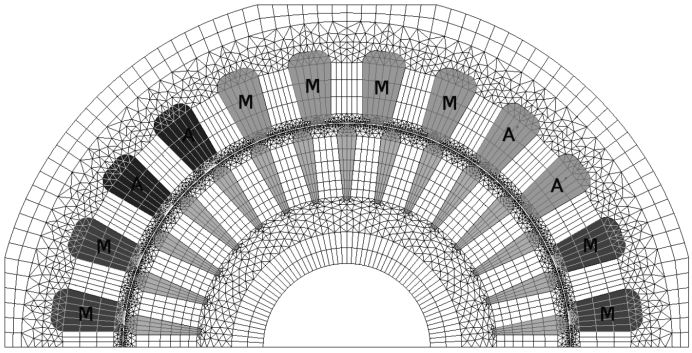

Fig. 1. Two-dimensional field model of the SPSEIG

An electrical circuit associated with the field model is depicted in Fig. 2 – this consists of the following components:

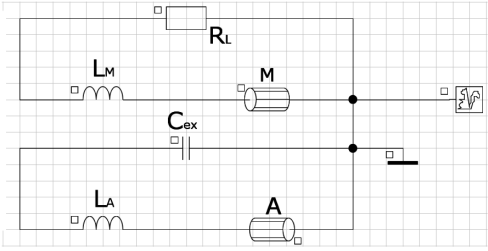

Fig. 2. Circuit part of the field-circuit model of the SPSEIG

- *M* and *A* are respective phases of the winding; these components are direct couplings between circuit and field parts of the model,
- L_M and L_A are leakage inductances of stator winding end connections,
- C_{ex} is the excitation capacitor,
- R_L is the load resistance,
- The squirrel symbol in Fig. 2 represents a macro-circuit used to model the cage rotor, consisting of rotor bars (field-circuit couplings), along with resistances and leakage reactances of the inter-bar section of short-circuit rings (circuit components).

The magnetic field in different parts of the generator's cross-section may be described by the following equations:

$$curl\left(\nu \cdot curl\mathbf{A}\right) = \begin{cases} \mathbf{J_S} & \text{in stator winding} \\ \mathbf{J_S} - \sigma \cdot \partial\mathbf{A} / \partial t & \text{in rotor bars} \\ 0 & \text{in airgap and magnetic core} \end{cases} \tag{1}$$

where:
$\boldsymbol{A}[0,0,A(x,y,t)]$ – the magnetic vector potential,
$\boldsymbol{J}_s[0,0,J_s(x,y,t)]$ – the current density in the stator slots,
v – the magnetic reluctivity of the core,
σ – the electric conductivity.

Field computations were performed with the non-linear magnetization characteristics of the stator and rotor core taken into account.

The simulation results have been validated using the laboratory set-up, which comprises the SPSEIG, driven by a three-phase motor fed by frequency inverter. A view of the tested machine as a main part of the laboratory set-up is shown in Fig. 3.

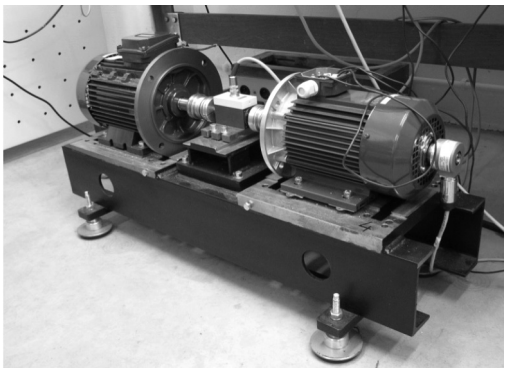

Fig. 3. Laboratory set-up for experimental study of the SPSEIG

3. Self-excitation of single-phase induction generator

3.1. Modeling of residual magnetism

Contemporary available FEM software programs, including Cedrat Flux2D, do not allow taking magnetic hysteresis into account, therefore, three approximate methods of modeling the remnant flux density were applied:

1. Placing the source of magnetic flux (non-zero boundary condition) on the inner diameter of rotor core
2. Placing a thin layer of current in the airgap
3. Initiating the magnetic flux as a result of current flowing in the auxiliary winding while the excitation capacitor discharges.

The values of magnetic flux, current density and initial capacitor voltage in respective methods have been chosen to obtain terminal voltages corresponding to remnant voltage measured in the experiments. Simulation results of self-excitation for each method for a topology with two capacitors (C_{sh} = 15 μF, C_{ex} =30 μF) are shown in Fig. 4. For each method, the steady-state voltage is close to the rated voltage, however, the time needed for voltage build-up is different for every method. The third method was employed for further study, as time of voltage build-up for this is closest to the experimental results (Fig. 4d)).

An influence of the rotor slot opening and its width on self-excitation process is illustrated in Fig. 5. For the wider slot opening the longer is the build-up time of the stator voltage. Width of rotor slot opening does not significantly affect the RMS value of the terminal voltage.

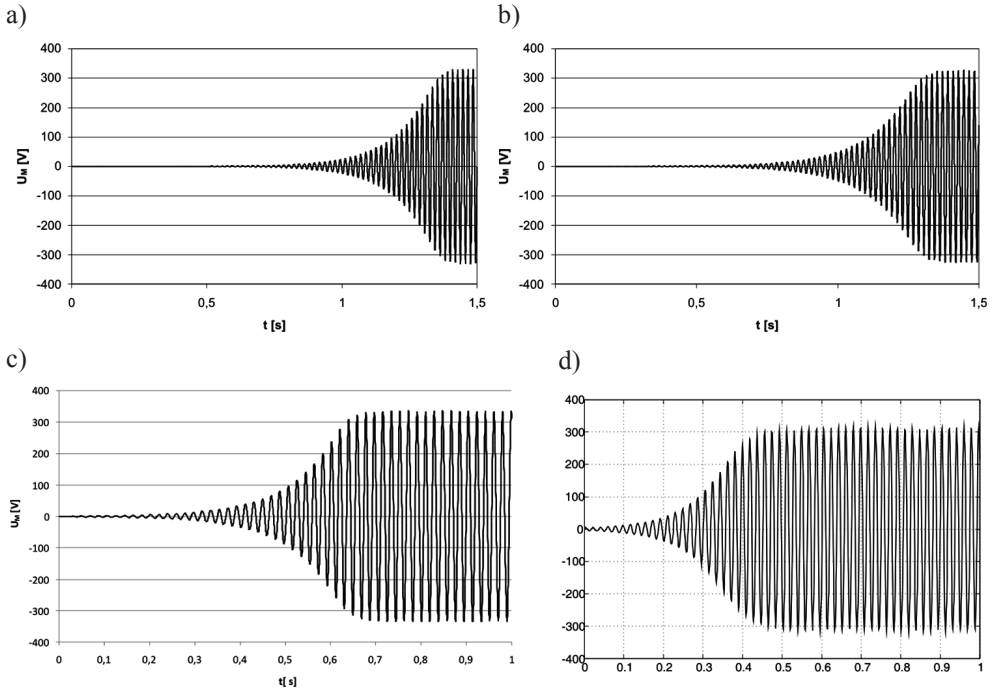

Fig. 4. Main winding voltage during self excitation: residual magnetism modeled by: a) the 1st method; b) 2nd method; c) 3rd method; d) measurement

3.2. Significance of rotor slot opening for self-excitation process

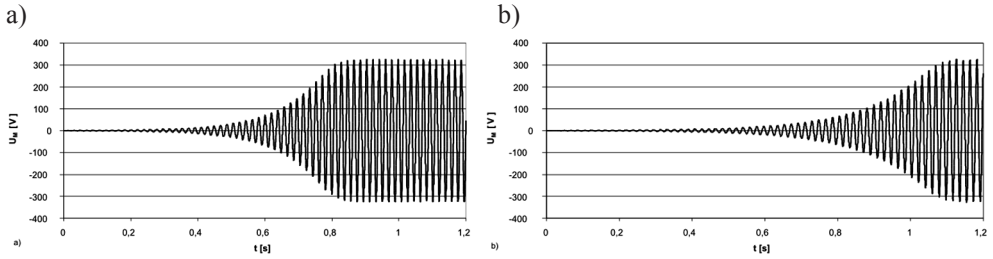

Fig. 5. Main winding voltage waveform during self-excitation: a) b_r = 0.5 mm; b) b_r = 2 mm

In small power induction motors, closed rotor slots are often used to reduce noise, torque pulsations and starting current due to large leakage rotor reactance. When closed rotor slots are used in induction generator, voltage build-up may not take place, because the magnetic flux induced by the stator currents passes through bridges above the rotor slots, as shown in Fig. 6a), and does not induce currents in the rotor bars. The resultant magnetic flux does not increase and the voltage in the stator windings die out, i.e. the voltage build-up does not take place. Figure 7 shows experimental results for the machine with closed rotor slots. The pre-charged excitation capacitor is switched at the instant of time 0.1 s. The induced low voltage

visible at the beginning of the waveform is the result of residual flux density in the rotor core. The capacitor discharges after being switched on, and self-excitation does not occur – the voltages settles at a level dependent upon the remnant flux.

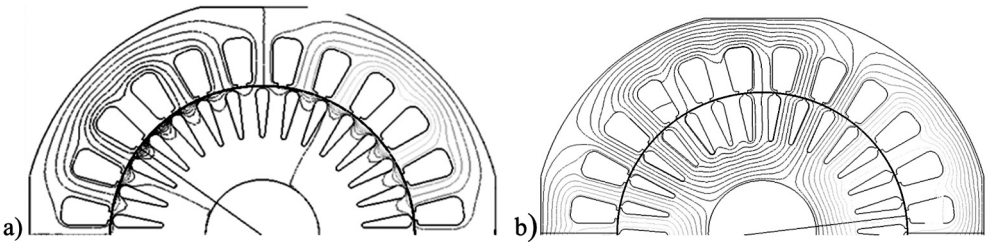

Fig. 6. Magnetic flux lines in SPSEIG: a) closed rotor slots; b) semi-closed rotor slots

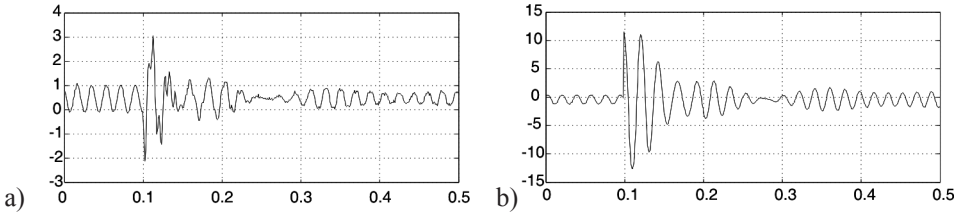

Fig. 7. Voltage waveforms during unsuccessful voltage build-up – experimental results: a) main winding voltage; b) auxiliary winding voltage

4. Influence of capacitor's capacitances and prime mover speed on no-load voltages and currents

Figures 8a)–c) show the dependence of no-load voltages in the main and auxiliary windings and auxiliary winding current on the prime mover rotational speed and excitation capacitance C_{ex} for capacitor topology with excitation capacitor only, as shown in Fig. 8d). As might be expected, terminal voltage U_M is strongly dependent on the rotor speed and capacitance C_{ex}, and it is not possible to obtain a voltage close to the rated value (230 V), even for large capacitances and speeds far exceeding the synchronous speed of the machine as the magnetic core is deeply saturated. Limits of speed and capacity below which self-excitation will not take place can be read from Fig. 8, i.e. C_{ex} = 30 μF for n = 1380 rpm and C_{ex} = 25 μF for n = 1380–1560 rpm. It should be noted that auxiliary winding voltage U_A reaches levels exceeding the rated value.

Applying shunt capacitor to the main stator winding (Fig. 9e)) improves operating conditions by the more efficient exploit of both the windings and the iron core. Simulation and experimental results for the topology with excitation and shunt capacitors are shown in Fig. 9 (C_{ex} = 30 μF). This solution allows obtaining rated terminal voltage. It is seen that the shunt capacitance C_{sh} has no major effect on the main winding current I_M of the generator and it is possible to control terminal voltage by modulation of the shunt capacitance.

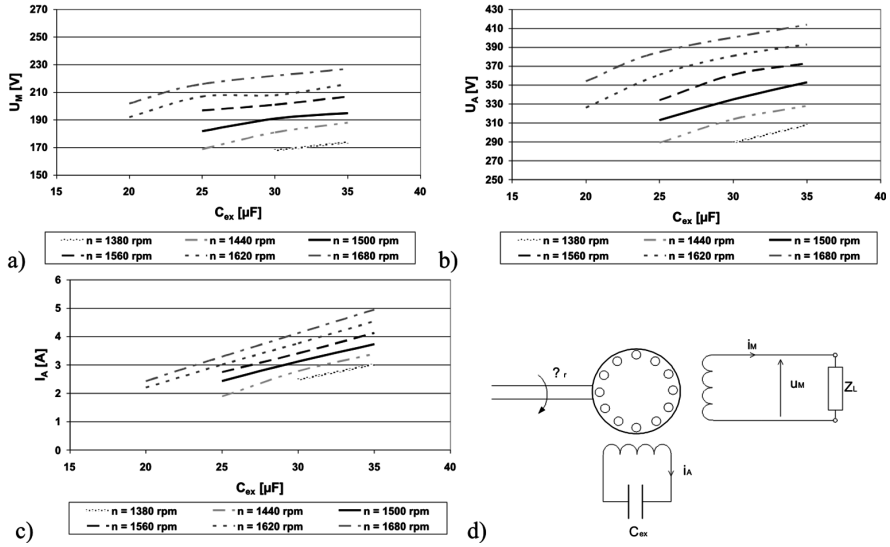

Fig. 8. No-load characteristics of the generator for different values of C_{ex} and rotor speed, for the topology with excitation capacitor only: a) main winding voltage U_M; b) auxiliary winding voltage U_A; c) auxiliary winding current I_A; d) connection scheme

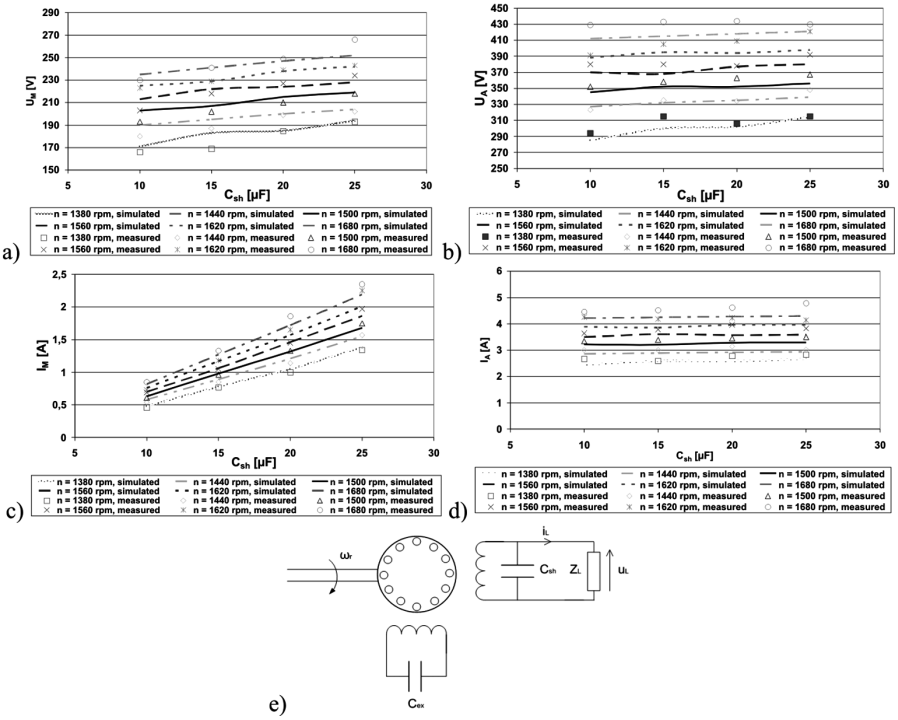

Fig. 9. No-load characteristics of the generator for different values of C_{sh} and rotor speed, for the shunt capacitor topology: a) main winding voltage U_M; b) auxiliary winding voltage U_A; c) main winding current I_M; d) auxiliary winding current I_A; e) capacitor connection scheme

5. Load characteristics of SPSEIG

Simulation and experimental results presented in Fig. 10 show that the SPSEIG with the shunt capacitor in the main winding may operate stably with a resistive load up to approximately 50% of the machine's rated power, while with the resistant-inductive load, the range of stable operation decreases with decreasing the power of the factor of the load (Fig. 10c)).

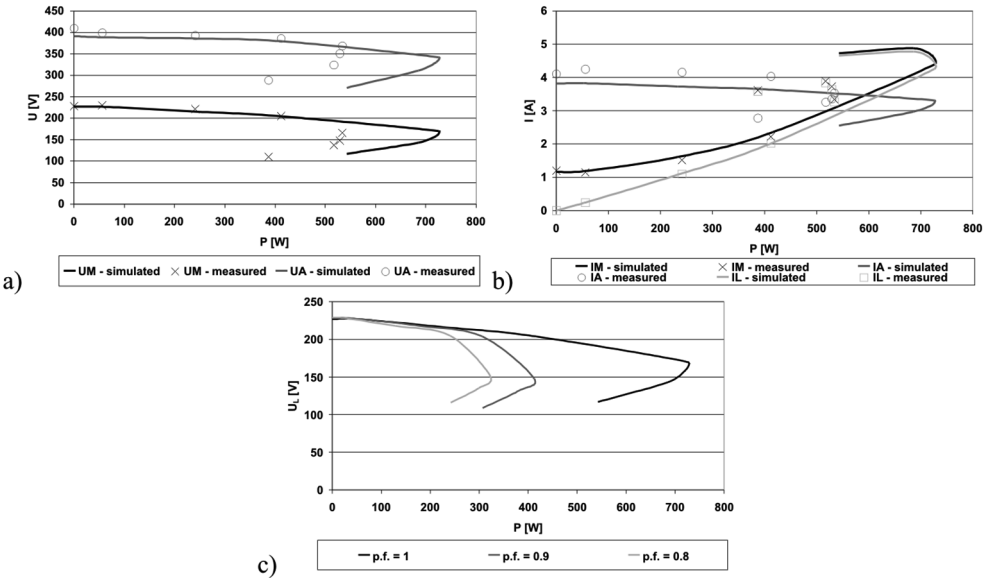

Fig. 10. Voltages and currents versus output power of the SPSEIG with shunt capacitor topology: a) main (U_M) and auxiliary (U_A) winding voltage for resistive load; b) main winding (I_M), auxiliary winding (I_A), and load current (I_L) for resistive load; c) terminal voltage for different power factors

Load range of the SPSEIG may be easily extended by applying the short-shunt capacitor topology (Fig. 11) – the generator may be loaded up to the rated power when the load is purely resistive. For the resistant-inductive load output power of the generator, as in the previous case, decreases after power factor decreasing.

Figure 12 shows voltage and current waveforms of the SPSEIG with shunt topology measured during switching of the dynamic load – the single-phase capacitor induction motor of rated power P_n = 90 W. During motor start-up, a terminal voltage drop and current increase may be noticed, as the induction motor intakes reactive power from the generator. If the SPSEIG is to supply induction motors, e.g. small pumps, special attention should be paid, because too large a starting current may demagnetize the generator leading to terminal voltage collapse. Simple remedial measures, like a damping resistor, may be used to limit the starting current of the induction motor.

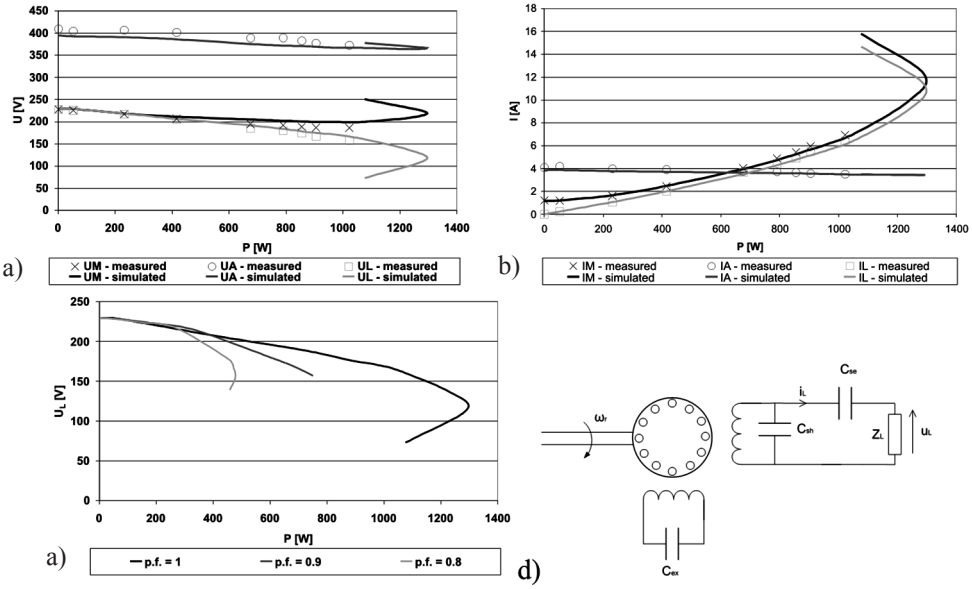

Fig. 11. Voltages and currents versus output power of the SPSEIG with short-shunt capacitor topology: a) main (U_M) and auxiliary (U_A) winding voltage for resistive load; b) main winding (I_M), auxiliary winding (I_A), and load current (I_L) for resistive load; c) terminal voltage for different power factors; d) capacitor connection scheme

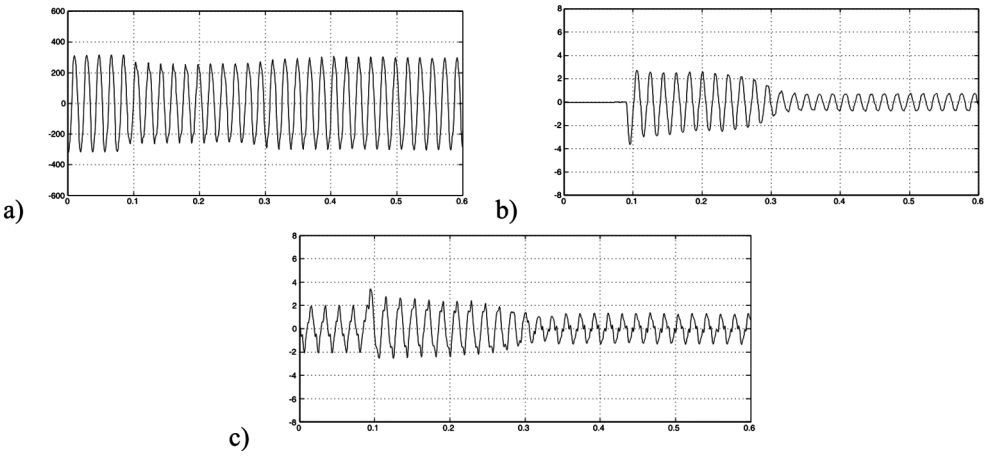

Fig. 12. Measured voltage and current waveforms of the generator before and after switching of an induction motor: a) terminal voltage, b) load current, c) main winding current

6. Conclusions

In the paper, the FEM-based, field-circuit model of single-phase, self-excited induction generator was presented. An investigation of the single-phase induction machine designed as the induction motor in respect to possible employment as an autonomous self-excited induction generator was presented. Analysis of the influence of the rotor slot opening showed that semi-closed rotor slots should be used to ensure self-excitation of the generator by remnant magnetic flux in the rotor left from previous operation events. In the case of closed rotor slots of the tested machine, the relatively weak remnant flux density does not induce currents in the rotor cage, so the self-excitation process can not be initiated. The detailed study shows that, for a resistive load, the short-shunt capacitor topology provides stable operation conditions up to the rated power of the machine. The possibility of directly supplying the single-phase capacitor induction motor from the generator as a dynamic resistant-inductive load was also presented. The simulation results obtained by the field-circuit model of the generator were successfully verified by laboratory tests.

References

[1] Murthy S.S., Singh B., Sandeep V., *A Novel and Comprehensive Performance Analysis of a Single-Phase Two-Winding Self-Excited Induction Generator*, IEEE Transactions on Energy Conversion, March 2012, Vol. 27, No. 1, pp. 117–127.

[2] Leicht A., Makowski K., *Self-excitation analysis of a single-phase induction generator*, XVI International Symposium on Electromagnetic Fields in Mechatronics, Electrical and Electronic Engineering, ISEF, Ohrid, Macedonia, Sept. 12–14, 2013.

[3] Makowski K., Leicht A., *Analysis of operation of a single-phase self-excited induction generator by a field-circuit model*, XVI International Symposium on Electromagnetic Fields in Mechatronics, Electrical and Electronic Engineering, Ohrid, Macedonia, Sept. 12–14, 2013.

[4] Leicht A., Makowski K., A *single-phase induction motor operating as a self-excited induction generator*, Archives of Electrical Engineering, 2013, Vol. 62(3), pp. 361–373.

[5] Ojo O., Omozusi O., Jimoh A.A., *The operation of an inverter-assisted single-phase induction generator*, IEEE Transactions on Industrial Electronics, Jun 2000, Vol. 47, No. 3, pp. 632–640.

[6] Rajanathan C.B., Edward A.J.G., Hu G., *Finite element study of a single phase induction generator*, Sixth International Conference on Electrical Machines and Drives, 1993, Conf. Publ. No. 376, pp. 252–257.

[7] Rajanathan C.B., Watson B.J., *Simulation of a single phase induction motor operating in the motoring, generating and braking modes*, IEEE Transactions on Magnetics, May 1996, Vol. 32, No. 3, pp. 1541–1544.

[8] Tudorache T., Melcescu L., Paturca S.V., *Finite Element Analysis of Self-Excited Induction Generator for Isolated Small Power Wind Turbines*, International Conference on Clean Electrical Power, ICCEP ’07, 21–23 May, 2007, pp. 656–661.

[9] Sawetsakulanond B., Kinnares V., *Design, analysis, and construction of a small scale self-excited induction generator for a wind energy application*, Energy, December 2010, Vol. 35, Issue 12, pp. 4975–4985, ISSN 0360-5442.

[10] Björnstedt J., Sulla F., Samuelsson O., *Experimental investigation on steady-state and transient performance of a self-excited induction generator*, Generation, Transmission & Distribution, December 2011, IET, Vol. 5, No. 12, pp. 1233–1239.

[11] Kumbhar G.B., Kulkarni S.V., Escarela-Perez R., Campero-Littlewood E., *Applications of coupled field formulations to electrical machinery*, COMPEL, 2007, Vol. 26, Issue 2, pp. 489–523.

TECHNICAL TRANSACTIONS | **CZASOPISMO TECHNICZNE**
ELECTRICAL ENGINEERING | ELEKTROTECHNIKA
1-E/2015

PAWEŁ ZALAS, JAN ZAWILAK*

GENTLE SYNCHRONIZATION OF TWO-SPEED HIGH-POWER SYNCHRONOUS MOTOR OUT OF OVER SYNCHRONOUS SPEED

ŁAGODNA SYNCHRONIZACJA DWUBIEGOWEGO SILNIKA SYNCHRONICZNEGO DUŻEJ MOCY Z PRĘDKOŚCI NADSYNCHRONICZNEJ

Abstract

This paper presents an analysis of the synchronization process of the high-power, two-speed synchronous motor out of over synchronous speed. A method of increasing the effectiveness of synchronization by applying a change system of polarization of the field circuit supply DC voltage is proposed. The process of synchronization from the stator supply voltage is also analyzed. The influence of the periodic reduction value of the supply voltages on the synchronization processes was also investigated. The proposed synchronization method can be applied during the synchronization processes of line start permanent magnet synchronous motors with a two-stage start-up.

Keywords: *electrical machines*, *synchronous motor*, *synchronization*, *FEM calculation*

Streszczenie

W artykule przedstawiono analizę procesu synchronizacji silnika synchronicznego dużej mocy z prędkości nadsynchronicznej. Zaproponowano metodę zwiększającą skuteczność tego procesu dzięki zastosowaniu układu zmiany polaryzacji napięcia wzbudzenia. Analizowano przebieg procesu synchronizacji wzbudzonej maszyny od strony sieci zasilającej stojan. Zbadano również wpływ okresowego zmniejszenia wartości napięć zasilających podczas procesu synchronizacji na jego przebieg i skuteczność. Zaproponowana metoda synchronizacji może zostać zastosowana podczas procesów synchronizacji silników synchronicznych o wzbudzeniu od magnesów trwałych (LSPMSM) i rozruchu dwustopniowym.

Słowa kluczowe: *maszyny elektryczne*, *silnik synchroniczny, synchronizacja*, *obliczenia MES*

DOI: 10.4467/2353737XCT.15.048.3848

* Ph.D. Eng. Paweł Zalas, Prof. D.Sc. Ph.D. Eng. Jan Zawilak, Department of Electrical Machines, Drives and Measurements, Faculty of Electrical Engineering, Wroclaw University of Technology.

1. Introduction

The use of switchable armature and field magnet windings in electromagnetically excited high-power synchronous motors allows for the design of two-speed motors with two synchronous speeds, and synchronous motors with a two-stage start-up and one rated speed. Salient-pole synchronous motors are mostly employed in the drive systems of the main-ventilation fans in deep mines. Two-speed drive motors are generally used, usually built as a result of the modernization of one-speed motors and significantly improving the starting properties by reducing starting currents and unfavorable mechanical stresses. The step change of speed achieved by changing the number of motor magnetic field poles [2, 9] ensures sufficient capacity control and results in a significant reduction of the power consumed by the fan. Major savings can be made and the total mining costs can be reduced through the rational use of the fans' capacity [2]. One of the machines is a two-speed synchronous motor of type GAe 1716/20t - its main specifications are presented in Table 1.

Table 1

The ratings of two-speed synchronous motor GAe 1716/20t

Rated power	kW	2600	1200
Stator voltage	V	6000 YY	6000 Y
Stator current	A	292	186
Field voltage	V	86	78
Field current	A	337	300
Rotational speed	rpm	375	300
Power factor	-	$0.9_{poj.}$	$0.77_{ind.}$
Efficiency	%	95.5	81.0

The synchronization process of the motor to a lower synchronous speed does not always proceed properly, therefore, studies have been conducted [7, 8] focusing on developing solutions that improve the course of this process, both out of over and under synchronous speed.

Developing methods of synchronization out of over the synchronous speed, in particular through switching supply voltages to the stator windings of the excited synchronous motor, can also be applied during gentle synchronization processes of line start permanent magnet synchronous motors with two-stage start-ups [1, 3]. The proposed two-stage method for starting-up the LSPMSM type motors significantly improves the starting properties of these machines and the synchronization process started above the rated synchronous speed may proceed gently.

This paper presents the results of numerical synchronization calculations for a selected model of the two-speed high-power salient-pole synchronous motor, realized from the field magnet side and the supply network side of the stator.

2. Analysis of synchronization processes

A specially developed field-circuit model of the two-speed motor type GAe 1716/20t [6, 7] was used to analyze the synchronization process of the motor.

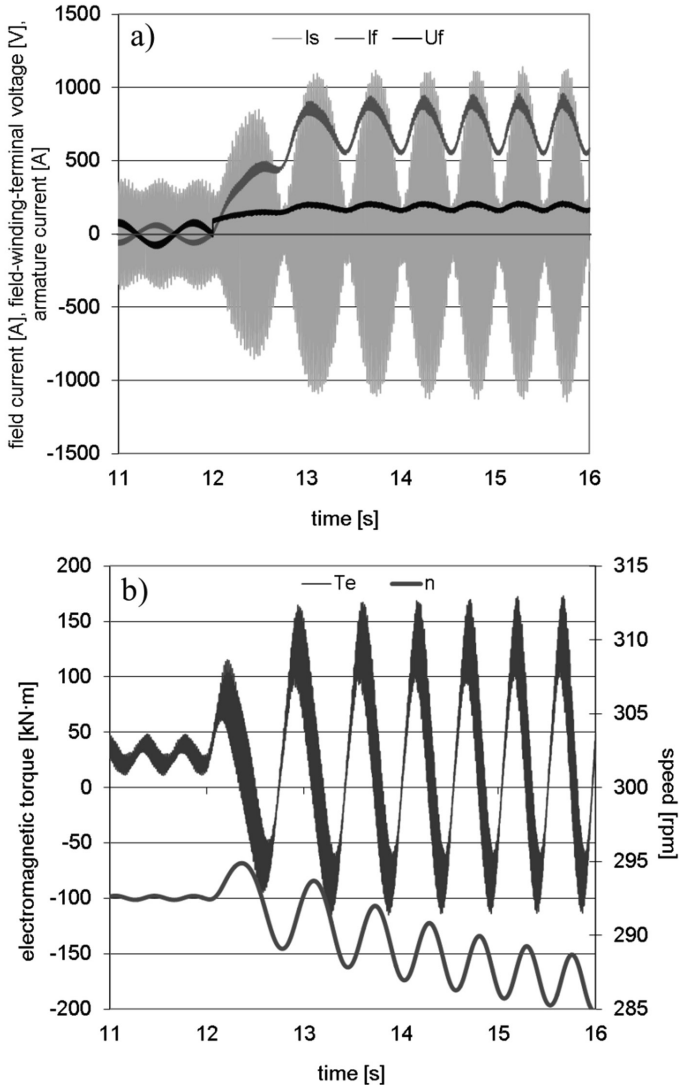

Fig. 1. Waveforms of the quantities during motor synchronization started at: $n \approx 293$ rpm and field current forcing, $p = 10$

To verify the calculation model, measurements of the actual motor installed in a mine fan station and the corresponding calculations were carried out [7]. A comparison of the calculation results with the measurements showed the field-circuit model of the GAe 1716/20t

two-speed synchronous motor to be correct and suitable for further investigation of the phenomena occurring during the operation of motors of this type.

Figures 1–5 show the calculated waveforms of armature phase A, current I_s, field current I_f, field-winding-terminal voltage U_f (a), electromagnetic torque and rotational speed (b) during synchronization processes at the lower rotational speed ($p = 10$) of the motor. The calculations were performed for load torque 0.8 T_N. This corresponds to the load which the WPK 5.3 fan constitutes with its control unit flaps fully opened. The resultant moment of inertia of the fan drive system: $J_r \approx 40\,000$ kg·m^2 [7, 8] was used in the calculations.

Figure 1 shows the calculated waveforms of the quantities during motor synchronization started at an angle of $\delta = 0^{\circ}$ and field current forcing of 2.5 I_{fn}, where δ is the angle between the stator field axis and the rotor field axis [5].

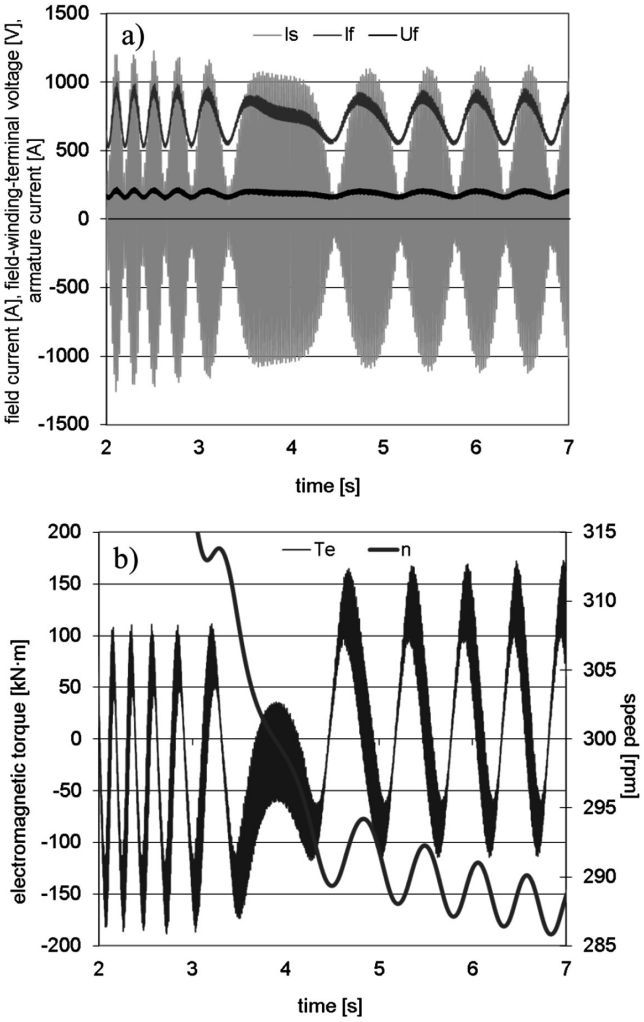

Fig. 2. Waveforms of the quantities during motor synchronization started at: $n \approx 370$ rpm and field current forcing, $p = 10$

According to Fig. 1, despite the selection of a proper synchronization initiating instant and the field current forcing, no effective synchronization is achieved. The calculation results show that for the adopted motor operating conditions, regardless of the choice of an instant of connecting the field voltage, synchronization processes started below the synchronous speed proceed ineffectively.

Figure 2 shows the calculated waveforms of the quantities during motor synchronization started at a rotational speed of $n \approx 370$ rpm (above the rated synchronous speed for $p = 10$) and field current forcing of 2.5 I_{fn}.

An accidental instant of connecting DC voltage to the field winding, despite the initiation of the process in proper operating conditions and the field current forcing, resulted in no effective synchronization. Switching the field voltage for such a high value of the rotational speed (above the synchronous speed) also causes adverse surges of stator currents (Fig. 2a)) and considerable electromagnetic torque fluctuations (Fig. 2b)).

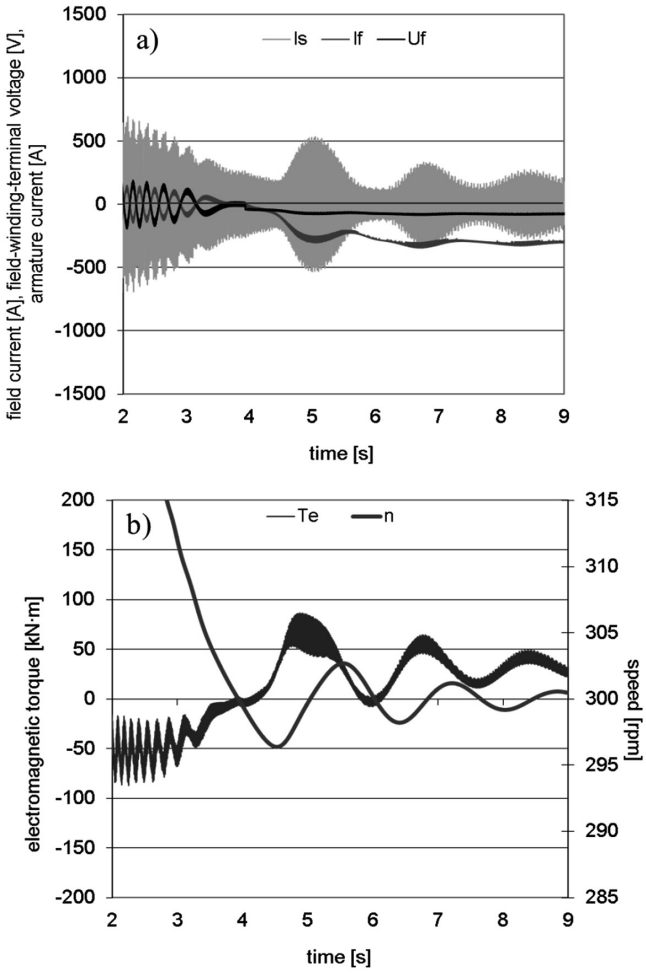

Fig. 3. Waveforms of the quantities during motor synchronization started at $n \approx 300$ rpm with the polarization change system of the field circuit supply DC voltage, $p = 10$

Lack of steady-state operation in the process of synchronization started above the synchronous speed makes it difficult to control the course of this process. The characteristic operating point of the motor, whose appointment is not difficult, is a change in the rotational speed from over to under synchronous speed. A significant increase in the probability of an effective and gentle motor synchronization out of over the synchronous speed provided by the use of the transistor switch [7], allowing the changing of the polarization of the field circuit supply DC voltage [8]. The polarization of this voltage is selected at the instant when the motor reaches the synchronous speed, providing conditions in which the DC current is added to the corresponding value of the field current caused by the AC voltage induced in the field magnet winding [4]. This increases the resultant value of the field current, thereby increasing the pull-in torque. The calculation results of the synchronization process realized by switch-

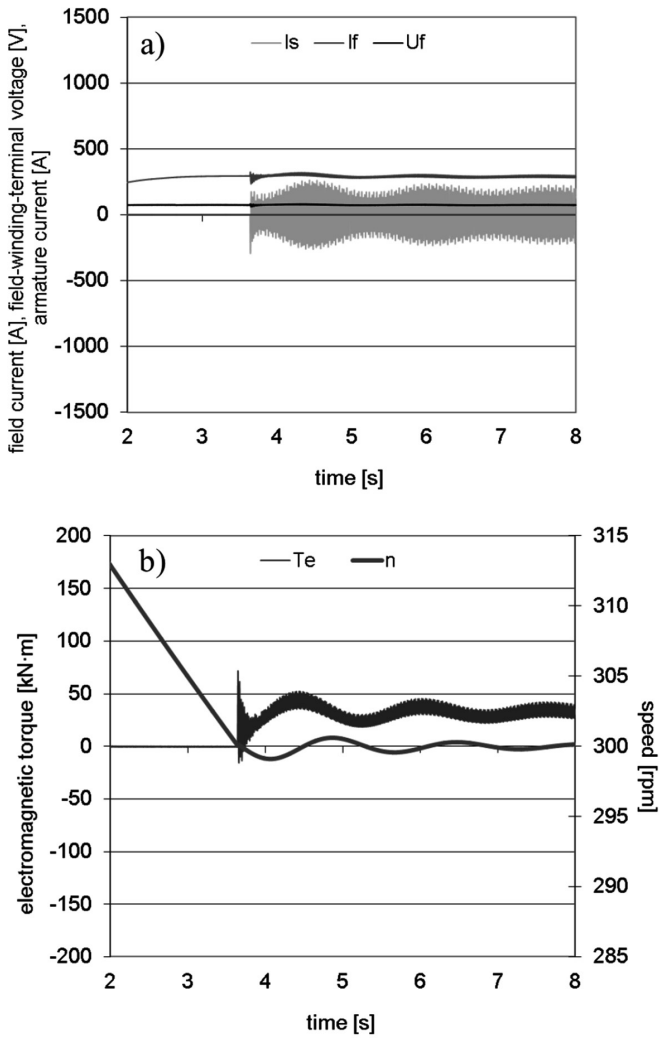

Fig. 4. Waveforms of the quantities during motor synchronization started at: $n \approx 300$ rpm and initial angle of the rotor 10 deg, $p = 10$

ing the rated value of the field voltage at the instant when the motor reaches the synchronous speed with the polarization change system of the field circuit supply DC voltage, for the same operating conditions as before, are shown in Fig. 3.

The synchronization process out of over the synchronous speed can also be realized from the supply network side of the stator of the excited synchronous machine. Switching the rated value of the field voltage is realized in the conditions of asynchronous operation, above the synchronous speed and switching voltages of the stator windings is executed at the instant when the motor reaches the rated synchronous speed. However, there is a problem of synchronizing the motor with the power network voltages. The electromotive forces induced through the rotor electromagnetic field in the phase armature windings do not allow uncontrolled switching of the windings on the supply voltages. The calculation results of the

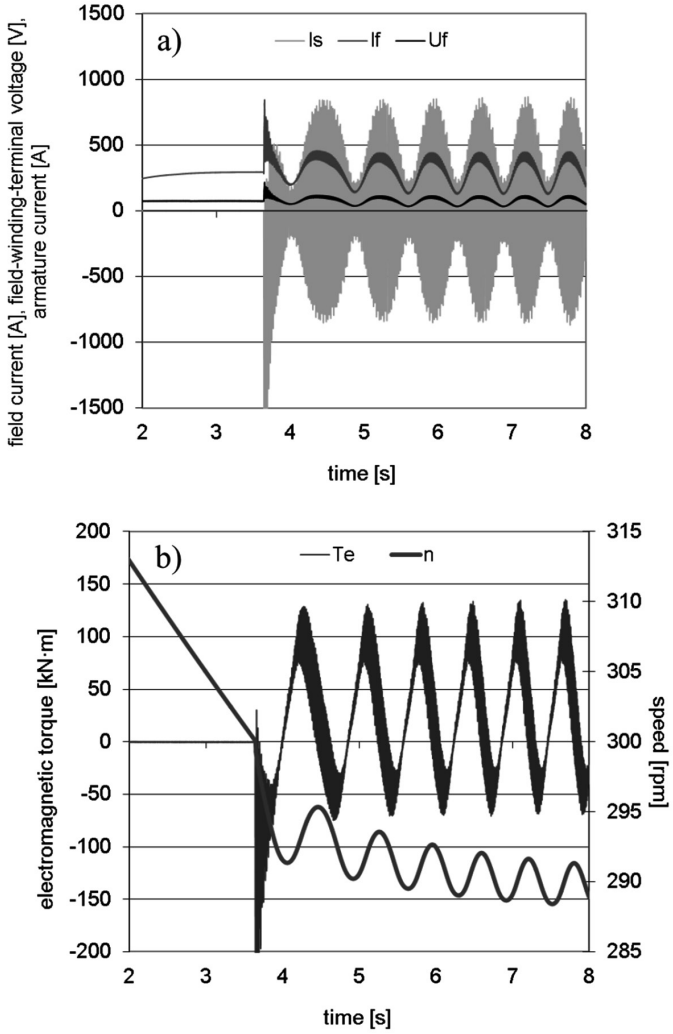

Fig. 5. Waveforms of the quantities during motor synchronization started at: $n \approx 300$ rpm and initial angle of the rotor 150 deg, $p = 10$

switching process to a lower rotational speed of the two-speed synchronous motor for two different initial angular positions of the rotor are shown in Figs. 4 and 5.

The proposed synchronization method (Fig. 4) through controlled switching voltages of the stator windings provides effective synchronization and a considerable reduction of armature current, electromagnetic torque and rotational speed fluctuations – this reduces mechanical impacts on the transmission shaft. The synchronization process of the motor proceeds more gently (Fig. 4) than in the use of classical methods of implementation of this process and the field current forcing [7].

Accidental switching of the voltages to the stator windings (Fig. 5) may cause ineffective synchronization processes and result in adverse transients with significant risks to electrical circuits and the mechanical system. This issue requires further study.

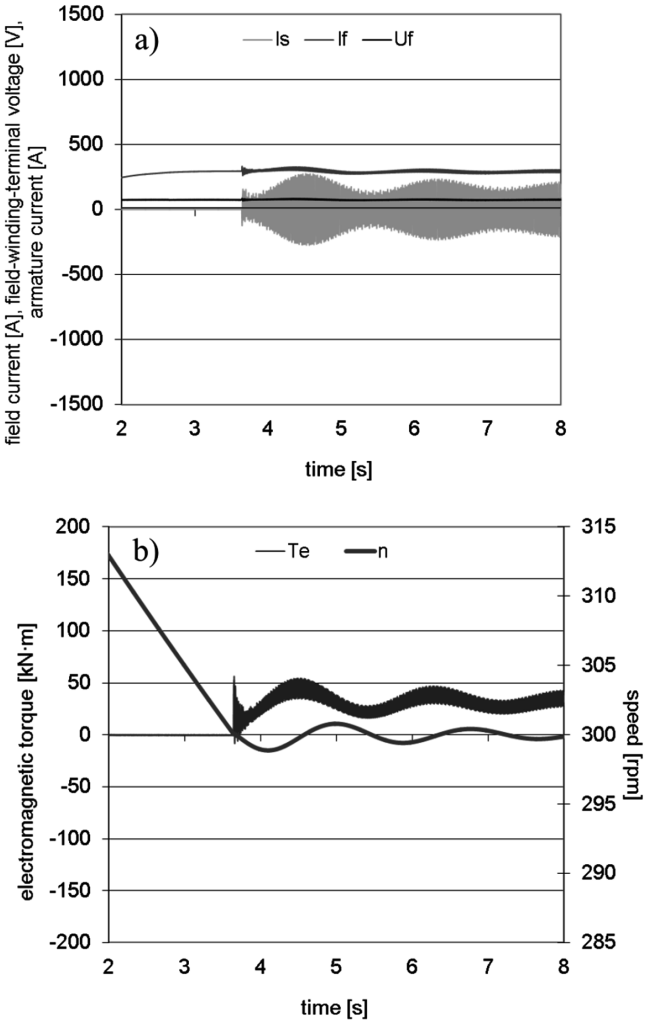

Fig. 6. Waveforms of the quantities during motor synchronization started at: $n \approx 300$ rpm, initial angle of the rotor 10 deg and reduction value of the supply voltages by 15%, $p = 10$

The field-circuit model of the motor was also used to calculate the processes of synchronization for the previously adopted operating conditions, taking into account the occurring periodic reduction value of the supply voltages. The periodic reduction of the stator voltages during the synchronization process by 15% (Fig. 6) and 20% (Fig. 7) was used in the calculations. In both cases (Figs. 6 and 7), the gentle synchronization process out of over the synchronous speed, realized by the controlled switching of power supply voltages to the stator windings, proceeds efficiently and smoothly.

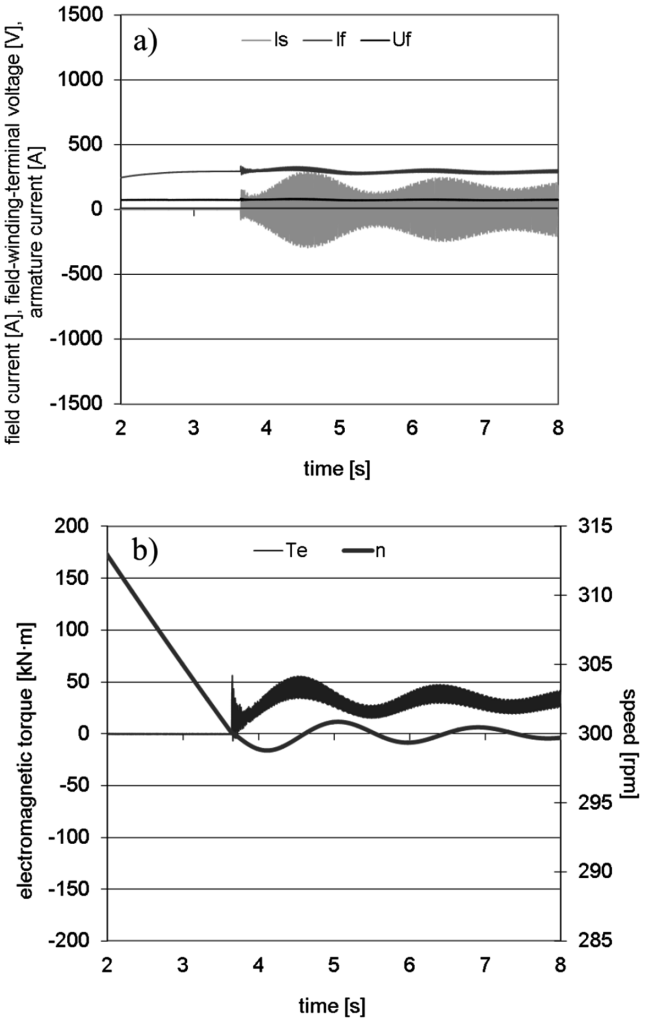

Fig. 7. Waveforms of the quantities during motor synchronization started at: $n \approx 300$ rpm, initial angle of the rotor 10 deg and reduction value of the supply voltages by 20%, $p = 10$

3. Conclusions

The synchronization process of the two-speed large-power synchronous motors out of over the synchronous speed, realized through switching the proper polarization of the field circuit supply DC voltage at the instant when the motor reaches the rated synchronous speed, proceeds effectively and gently, without using the field current forcing. The synchronization process out of over the rated synchronous speed realized through the controlled switching of voltages to the stator windings provides effective synchronization and a considerable reduction of armature currents and electromagnetic torque fluctuations. Due to the use of proposed synchronization methods, the motor can be synchronized when loaded with a torque higher than the torque at synchronization with classical methods of implementation of this process and field current forcing of 2.5 I_{fn}.

References

[1] Aliabad A.D., Mirsalim M., Ershad N.F., *Line-Start Permanent-Magnet Motors: Significant Improvements in Starting Torque, Synchronization, and Steady-State Performance*, IEEE Transactions on Magnetics, 2010, Vol. 46, Issue 12, pp. 4066–4072.

[2] Antal L., Zawilak J., *Testing of a two-speed synchronous motor*, Prace Nauk. IMNiPE PWr. nr 63, Studia i Mat. nr 29, 2009, pp. 17–29.

[3] Cistelecan M.V., Popescu M., Melcescu L., Tudorache T., *Three phase line start claw poles permanent magnet motor with pole changing winding*, Power Electronics, Electrical Drives, SPEEDAM, International Symposium on Automation and Motion, 2008, pp. 245–249.

[4] Paszek W., *Dynamika maszyn elektrycznych prądu przemiennego*, Wydawnictwo Helion, Gliwice 1998.

[5] Sobczyk T., *Łagodna synchronizacja silników synchronicznych dużych mocy z asynchronicznego stanu pracy*, XX SME, Maszyny synchroniczne, Kazimierz Dolny 1984, pp. 28–29.

[6] Zalas P., Zawilak J., *Dwubiegowy silnik synchroniczny w ujęciu polowo-obwodowym*, Prace Nauk. IMNiPE PWr. nr 56, Studia i Materiały nr 23, 2003, pp. 65–77.

[7] Zalas P., Zawilak J., *Gentle synchronization of two-speed synchronous motor with asynchronous starting*, Electrical Engineering (Berlin), 2012, Vol. 94, No. 3, pp. 155–163.

[8] Zalas P., Zawilak J., *Synchronizacja silników synchronicznych napięciem przemiennym*, SME 2008, Prace Nauk. IMNiPE PWr. nr 62, Studia i Mat. nr 28, 2008, pp. 542–548.

[9] Zawilak J., *Uzwojenia zmiennobiegunowe maszyn elektrycznych prądu przemiennego*, Prace Naukowe IMiNE PWr. 1986.

TECHNICAL TRANSACTIONS | **CZASOPISMO TECHNICZNE**
ELECTRICAL ENGINEERING | ELEKTROTECHNIKA
1-E/2015

DARIUSZ KAPELSKI, BARTOSZ JANKOWSKI, MAREK PRZYBYLSKI,
BARBARA ŚLUSAREK*

THE INFLUENCE OF CRYOGENIC TEMPERATURES ON THE CHARACTERISTICS OF A BRUSHLESS MOTOR

WPŁYW TEMPERATURY KRIOGENICZNEJ NA CHARAKTERYSTYKI SILNIKA BEZSZCZOTKOWEGO

Abstract

This article presents the results of a study on the magnetic properties of soft magnetic powder composites at room temperature and at liquid nitrogen temperature. The properties of a magnetoelectric motor with the power of 0.75 kW at room temperature and cryogenic temperatures are also presented in this article. The study of magnetic properties showed that magnetization curves at 20°C and -195.8°C temperatures are almost the same. Iron loss in the composite at liquid nitrogen temperature increased significantly in comparison to loss at room temperature. The study of the magnetoelectric motor showed that the back electromotive force at liquid nitrogen temperature decreases insignificantly in comparison to the back electromotive force at room temperature. Electromagnetic torque at liquid nitrogen temperature increases in comparison to room temperature.

Keywords: *electrical machines*, *powder metallurgy*, *cryogenic condition*

Streszczenie

W artykule przedstawiono wyniki badań właściwości magnetycznie miękkich kompozytów proszkowych oraz parametry silnika magnetoelektrycznego o mocy 0,75 kW w temperaturze pokojowej i kriogenicznej. Badania właściwości magnetycznych kompozytów pokazały, że krzywe magnesowania określone w temperaturach 20°C i -195,8°C są zbliżone, natomiast straty mocy w schłodzonym kompozycie proszkowym znacznie się zwiększyły. W badaniach silnika magnetoelektrycznego wykazano nieznaczne zmniejszenie siły elektromotorycznej i przyrost momentu elektromagnetycznego w czasie pracy silnika w temperaturze ciekłego azotu w stosunku do parametrów w temperaturze pokojowej.

Słowa kluczowe: *maszyny elektryczne, metalurgia proszków*, *warunki kriogeniczne*
DOI: 10.4467/2353737XCT.15.049.3849

* M.Sc. Eng. Dariusz Kapelski, Ph.D. Eng. Bartosz Jankowski, Ph.D. Eng. Marek Przybylski, Prof. D.Sc. Ph.D. Eng. Barbara Ślusarek, Tele & Radio Research Institute, Warsaw.

1. Introduction

Electric drives for cryogenic temperatures below -150°C such as liquid gases: e.g. nitrogen, hydrogen, helium and natural gas are applied more often in the industry. Among others, cryogenic drives are applied in the cars supplied with hydrogen, rocket engines, cooling apparatus, devices for the storage and transportation of liquefied natural gas. Devices for storage, transport and processing should be employed in pumps and electric drives working in the atmosphere of liquefied gases. Electric machines applied in modern pumps of liquefied gases usually work whilst immersed and liquefied gas flows through the gap between the stator and the rotor.

Articles [1–2] show results of the study of a three phase induction motor working as a part of a pump immersed in liquefied natural gas. The article [3] presents computer simulations of a high voltage squirrel cage induction motor with 1 MW power working in liquefied natural gas (LNG) at a temperature of -162°C. The study showed that the induction motor immersed in liquid gas develops higher maximum torque and less change of rotational speed than the induction motor working at room temperature. The disadvantage of the cooled motor is a smaller starting torque resulting from lower resistance of an aluminum squirrel cage. Article [4] shows the study of a magnetoelectric motor applied for a pump drive of fuel in a new cryogenic drive for a rocket with low thrust.

Temperature changes of soft and hard magnetic materials lead to changes of their physical properties. The authors in publications [5] showed the results of measurements of magnetic properties of non-oriented steel sheets in cryogenic conditions. It was observed that at low magnetic field strengths, magnetic induction is lower in cryogenic conditions than at room temperature. At high magnetic strengths, magnetic induction is insignificantly higher for cryogenic conditions than at room temperature. The results of the measurements presented in article [6] showed that in liquid nitrogen immersion of iron based soft magnetic composites, their magnetic permeability is lower and their total loss is increased compared to when at room temperature.

In the case of Nd-Fe-B, permanent magnets lowering their temperature leads to an increase in remanence and coercivity. Manufacturers' catalogues of permanent magnets usually present the temperature coefficients of remanence and coercivity only for changes from 20°C to 100°C. For sintered Nd-Fe-B permanent magnets, values of the temperature coefficient of remanence is from -0.08 to -0.11%/K depending on the composition of the alloy. The temperature coefficient of coercivity of polarization of sintered Nd-Fe-B permanent magnets is from -0.5 to -0.6%/K. For isotropic bonded permanent magnets, the temperature coefficient of remanence is from -0.11 to -0.14%/K, for coercivity of magnetic polarization, the coefficient is about -0.4%/K [7].

In Tele and Radio Research Institute, the changes of magnetic parameters of bonded permanent magnets obtained from the Nd-Fe-B powder, type MQP-B produced by Magnequench Company, compressed and bonded by epoxy resin were measured. The measurements of the magnetic properties were carried out in a liquid nitrogen atmosphere at a temperature of -195.8°C and at room temperature. The temperature coefficient of remanence is -0.17%/K, whereas the coefficient of intrinsic coercivity is -0.39%/K determined for room and liquid nitrogen temperature [8].

The main aim of research was to determine the magnetic property changes of soft magnetic materials on parameters of the magnetoelectric motor.

2. Methodology of research

2.1. The research of magnetic properties of soft magnetic composites

The samples for the research were manufactured from commercially available soft magnetic powder called Somaloy 500 with the addition of lubricating binder LB1. The particles of iron powder are covered with a bonding agent that also ensures electrical insulation between particles. The composite samples were obtained by the cold compression moulding of powder with 800 MPa pressure. The green compacts that are mechanically weak were cured in air atmosphere at a temperature of 200°C for 60 minutes. The ring shaped samples for the magnetic measurements had the following dimensions: outer diameter 75 mm, inner diameter 55 mm, and height 10 mm.

The magnetization curves and the total power loss P_{tot} were measured by the measurements of dynamic hysteresis loops according to the IEC 60404-6 standard. The measurements of a hysteresis loop were carried out by the AMH-20K-HS system manufactured by the Laboratorio Elettrofisico Walker LDJ Scientific. The total power loss was determined for the frequency from 50 to 600 Hz for the amplitude of induction B_{max} = 1.0 T. The maximum error of measurements of total loss equals 3%. During the measurements of the magnetic properties, the back electromotive force induced in the measuring coil was sinusoidal with the shape coefficient equal to 1.111 ± 0.006. The measurements were conducted at room temperature and at liquid nitrogen temperature.

2.2. Measurements of properties of the brushless electric motor with the composite stator

Parts of the stator were cut using electric discharge machining from cylinders with a diameter of 63 mm and a height of 22.5 mm manufactured from Somaloy 500 + 0.6% LB1 (Fig. 1).

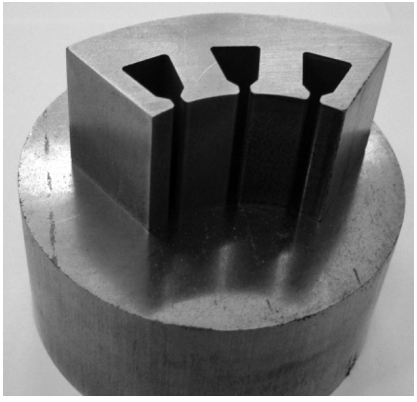

Fig. 1. Part of a stator and a half-finished product from iron powder composite

The obtained stator parts were glued with two component epoxy glue. In the research, the 4 pole motor with permanent magnets with 0.75 kW power and rotational speed 18 000 rpm was analyzed. The structure of this motor is presented in Fig. 2 [9].

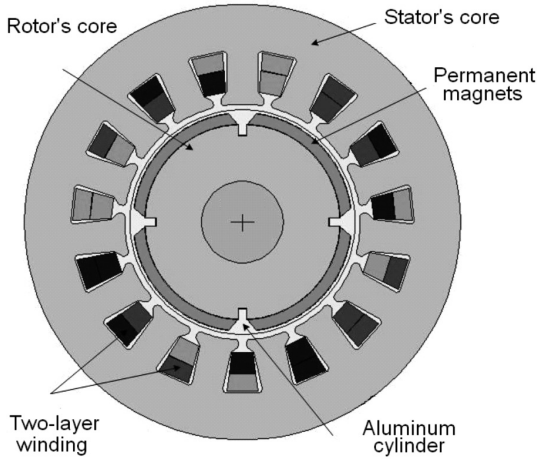

Fig. 2. The structure of analyzed motor

The analyzed electric motor consists of a stator with 15 slots, the rotor a 4 sintered Nd-Fe-B permanent magnets produced by Vacuumschmelze (VAC 669AP) and an aluminum cylinder. Typical parameters of permanent magnets obtained from the manufacturer's catalogue are the following: B_r = 1.16 T; H_{Cb} = 885 kA/m; H_{cJ} = 2000 kA/m; $(BH)_{\max}$ = 255 kJ/m^3. The temperature coefficient of remanence α_{Br} = -0.085%/°C, the temperature coefficient of coercivity β_{HcJ} = -0.57%/°C with changes of temperature from 20°C to 100°C. The analyzed motor should have higher magnetic flux density in the air gap resulting from lower temperature of permanent magnets in cryogenic temperatures. The motor has a two-layered, frictional-slotted winding with q = 1¼ slots for a pole and a phase. A commercial motor housing from the motor manufactured by the Motor and Controller company, model MBL-92FT-300HA was used.

The measurements of parameters of the motor in the liquid nitrogen immersion needed the application of type C4 bearings with the enhanced bearing slackness. Before the assembly, sealants and lubricant were removed from bearings using acetone. The courses of interfacial back electromotive force and the electromagnetic torque in the function of rotor's position were measured. The back electromotive force was determined for the two rotational speeds of 1000 and 1500 rpm. During the measurements of the back electromotive force, the measured motor's rotor was moved by the three phase induction motor Skh-56-6B with the LG SV-iG5A inverter. The recording of the back electromotive force was carried out by the digital scope Tektronix TDS 210. The course of the electromagnetic torque was measured at the supply of the motor with direct current in brushless DC mode ($i_a = -i_b$ and $i_c = 0$). The measurements were done for two values of supply current i_a = 3 A and i_a = 5 A. DC supply GW Instek PSP-2010 was used in the research. The electromagnetic torque was registered with MW 2006-3S device co-working with the MT-3Nm torque meter manufactured by the Roman Pomianowski's Electronics Laboratory. During the recording of the electromagnetic torque, the measured motor was connected with 1 phase W&W Motor YJF61/16 with a gear-motor and the rotational speed was 0.8 rpm. Measurements were done at room temperature and next at the temperature of liquid nitrogen.

3. Results of measurements

In the first part of the research, the magnetic properties of soft magnetic composites were measured. The magnetization curves at 50 and 600 Hz frequency at room temperature and at liquid nitrogen temperature were measured. The magnetization curves almost overlap (Fig. 3).

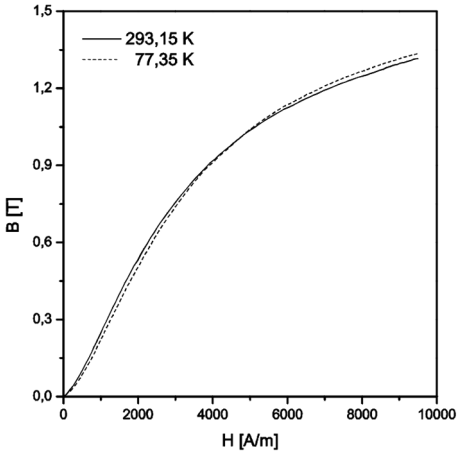

Fig. 3. The magnetization curves of powder soft magnetic composites measured at room and liquid nitrogen temperature, f = 50 Hz

The magnetization curves differ only in the speed increase of magnetic induction B which causes differences in the maximum magnetic permeability of the iron magnetic composite. Maximum magnetic permeability was equal to 215 for the temperature of 20°C and 202 for the temperature of -195.8°C at the frequency 50 Hz and 600 Hz.

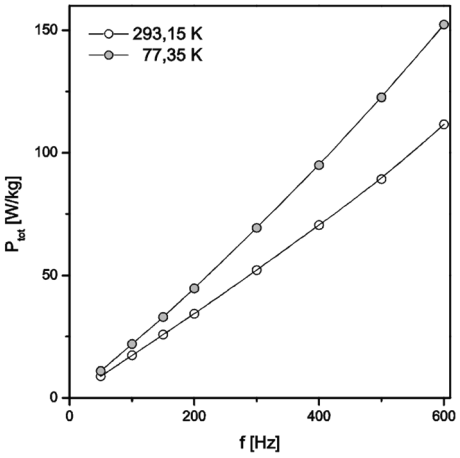

Fig. 4. The total power loss of iron soft magnetic composites measured at room and liquid nitrogen temperature, B_{max} = 1.0 T

The decrease in the sample's temperature to -195.8°C caused an increase of total power losses P_{tot} in the magnetic core. The increase in the loss of eddy currents is caused by the decrease of the resistivity of the material. The increase of coercivity causes the increase of hysteresis loss and magnetization energy due to a decrease of crystal lattice oscillations and a decrease of domain wall movements [8]. For example, at the magnetization frequency 50 Hz, the total power loss at liquid nitrogen temperature is about 25% higher than at room temperature, whereas at the frequency 600 Hz, it is more than 35% (Fig. 4).

In the second part of the research, the interfacial back electromotive force and electromagnetic torque was measured as a function of the angle of the rotor's rotation.

The analyzed magnetoelectric motor has asinusoidal back electromotive force at the 1000 rmp (Fig. 5a)) and 1500 rpm (Fig. 5b)) at room temperature and at liquid nitrogen temperature.

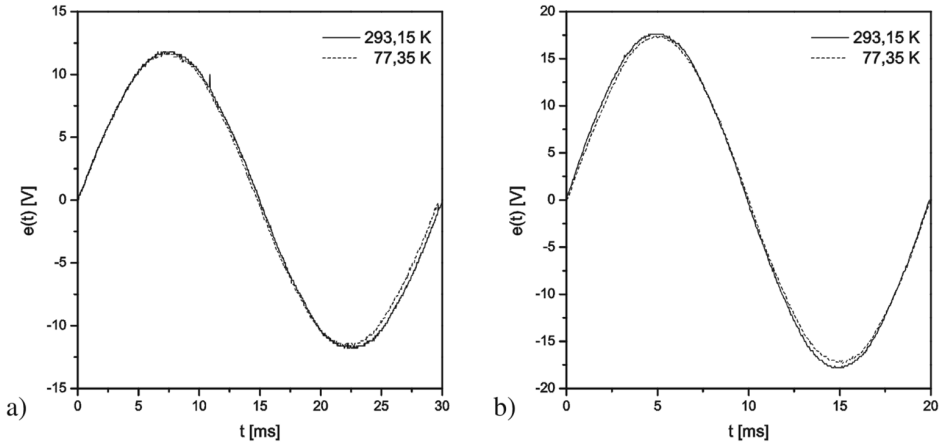

Fig. 5. The back electromotive force at the rotational speed: a) 1000 rpm, b) 1500 rpm measured at room temperature and liquid nitrogen temperature

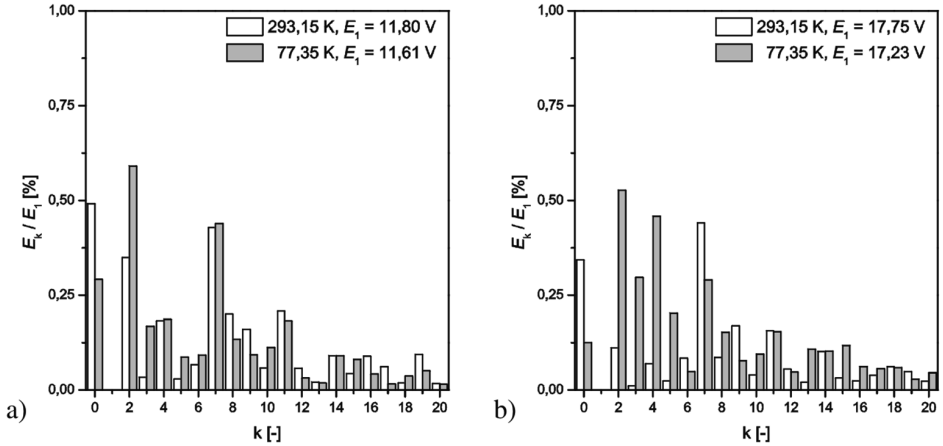

Fig. 6. Higher harmonics E_k in relation to the first harmonic E_1 at the rotational speed: a) 1000 rpm, b) 1500 rpm at room and liquid nitrogen temperature

After cooling the motor to liquid nitrogen temperature, the first harmonic of the back electromotive force decreases at the rotational speed 1000 and 1500 rpm but the change does not exceed 3%. Harmonics of 2, 3, 4 and 5 order increase their values (Figs. 6a) and b)). This effect leads to changes of total harmonic distortion (THD) coefficient. THD coefficient determined for rotational speed 1500 rpm at room temperature is equal 0.84%, whereas at liquid nitrogen temperature, it is 1.16%.

Table 1 shows the average rectified, effective-root mean square and maximum values of induced back electromotive forces for room temperature and liquid nitrogen temperature. Table 1 also presents shape and peak factors.

Table 1

Average rectified, effective-root mean square and maximum values, shape and peak factors of back electromotive forces

Room temperature (20°C)					
n (rpm)	U_{arv} (V)	U_{rms} (V)	U_m (V)	k_{rms} (-)	k_{peak}
1500	11.33	12.57	17.60	1.109	1.401
1000	7.52	8.35	11.80	1.110	1.414
Liquid nitrogen temperature (-195.8°C)					
1500	10.96	12.19	17.40	1.112	1.428
1000	7.41	8.22	11.80	1.109	1.436

The shape of the generated electromagnetic torque is sinusoidal (Figs. 7a) and b)).

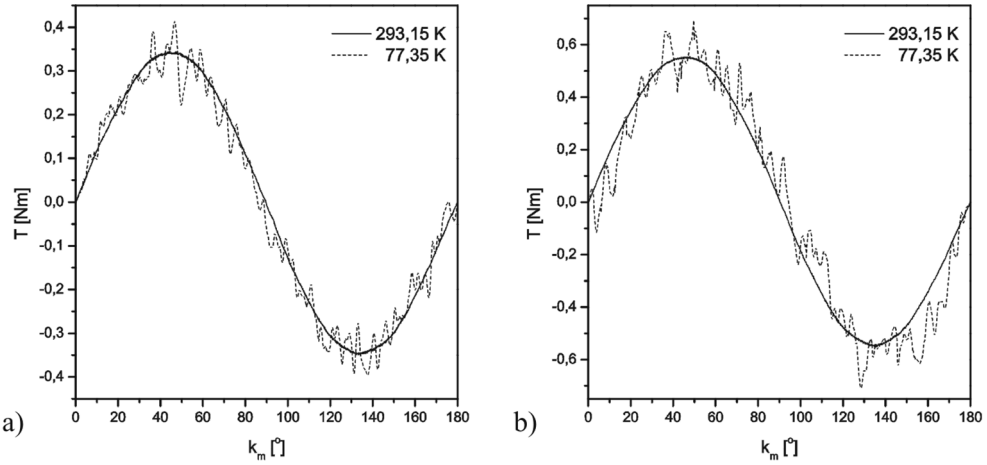

Fig. 7. The electromagnetic torque for: a) i_a = 3 A, b) i_a = 5 A measured at room and liquid nitrogen temperature

At the temperature of –195.8°C, unfavorable torque fluctuations caused by a bearing in a socket between a motor and a torque meter are seen in Figs. 7a) and b). This effect causes higher harmonics increase (Figs. 8a) and b)).

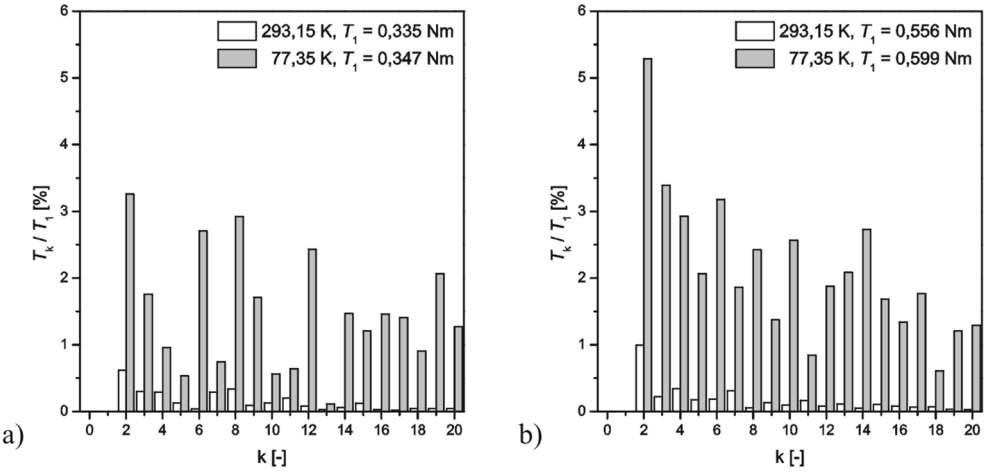

Fig. 8. Higher harmonics of electromagnetic torque T_k in relation to the first harmonic T_1 for: a) i_a = 3 A, b) i_a = 5 A measured at room temperature and at liquid nitrogen temperature

After the decrease of the temperature to liquid nitrogen temperature, an increase of the first harmonic of electromagnetic torque by 3% and 7% for i_a = 3 A and i_a = 5 A respectively, can be seen. In turn, the coefficient of total harmonics distortion THD described at room temperature changes from 1.44% at i_a = 3 A to 1.33% at i_a = 5 A.

4. Conclusions

The influence of temperature on the characteristics of the magnetoelectric motor with a stator manufactured from iron soft magnetic composites are presented in the article. Results of measurements of magnetic properties of soft magnetic composites showed that the influence of temperature on magnetization curves is very small. Significant differences can be observed in the measurements of total power losses at room temperature and at liquid nitrogen temperatures. The increase of total losses is caused by the increase of eddy current loss due to the lower resistivity of the iron based composite and increase of hysteresis loss due to higher coercivity of the iron based composite.

The back electromotive force induced in the motor after cooling in liquid nitrogen insignificantly decreases its value. Simultaneously, the increase of higher harmonics 2, 3, 4 and 5 can be observed.

It is observed increase of its first harmonic of electromagnetic torque after decrease of temperature of a motor. However, parasitic torque from bearings would not allow precise analyses.

The research shows that powder soft magnetic composites can be applied in devices working at cryogenic temperature conditions. Measurements of dynamic parameters of the analyzed motor should be the final tests of application of the powder magnetic composites in cryogenic temperatures.

References

[1] Kołowrotkiewicz J., Barański M., Szeląg W., Długiewicz L., *FE analysis of induction motor working in cryogenic temperature*, COMPEL – The International Journal for Computation and Mathematics in Electrical and Electronic Engineering, 2007, Vol. 26, No. 4, pp. 952–964.

[2] Barański M., Szeląg W., *Finite-element analysis of transient electromagnetic-thermal phenomena in a squirrel-cage motor working at cryogenic temperature*, IET Science, Measurement & Technology, 2012, Vol. 6, Issue 5, pp. 357–363.

[3] Azarewicz S., Śniegoń S., Węgliński B., *Influence of active materials on the parameters of cryogenic motor*, Proceedings from XIX Symposium Electromagnetic Phenomena in Nonlinear Circuits, 28–30 June, 2006, Maribor, Slovenia, pp. 73–74.

[4] Długiewicz L., Kołowrotkiewicz J., Szeląg W., Ślusarek B., *Permanent magnet synchronous motor to drive propellant pump*, International Symposium On Power Electronics, Electrical Drives, Automation And Motion, 19–22 June, 2012, Sorrento, Italy, pp. 822–826.

[5] Azarewicz S., Buniowski A., Węgliński B., *Research of behaviour of electrical sheets in cryogenic temperatures*, Proceedings from XVIII Symposium Electromagnetic Phenomena in Nonlinear Circuits, June 28–30, 2004, Poznań, Poland, pp. 61–62.

[6] Jankowski B., Kapelski D., Karbowiak M., Przybylski M., Ślusarek B., *Influence of cryogenic temperature on magnetic properties of soft magnetic composites*, Powder Metallurgy, 2014, Vol. 57, Issue 2, pp. 156–160.

[7] MS-Schramberg company website (http://www.magnete.de/en/products.html) (access: 3.02.2015).

[8] Karbowiak M., Jankowski B., Kapelski D., Przybylski M., Ślusarek B., Gromek J., *Measurements of magnetic properties of Nd-Fe-B bonded permanent magnets at a temperature of liquid nitrogen*, XXII Symposium on Electromagnetic Phenomena in Nonlinear Circuits, 26–29 June, 2012, Pula, Croatia.

[9] Wojciechowski R.M., Jędryczka C., Łukaszewicz P., Kapelski D., *Analysis of high speed permanent magnet motor with powder core material*, COMPEL – The International Journal for Computation and Mathematics in Electrical and Electronic Engineering, 2012, Vol. 31, Issue 5, pp. 1528–1540.

TECHNICAL TRANSACTIONS | **CZASOPISMO TECHNICZNE**
ELECTRICAL ENGINEERING | ELEKTROTECHNIKA
1-E/2015

AGNIESZKA BANACH*, WITOLD MAZGAJ**

SPECIFIC POWER LOSS OF TYPICAL DYNAMO STEEL SHEETS

STRATNOŚĆ TYPOWYCH BLACH PRĄDNICOWYCH

Abstract

In typical dynamo steel sheets, the magnetization process can have a two-fold character. In parts of the dynamo sheets which refer to the stator core of induction motors the magnetization process has a rotational character. On the other hand, the axial magnetization occurs mainly in the stator teeth. This paper discusses the specific power loss of typical dynamo sheets and its dependence on the magnetization frequency and on the maximum value of the flux density in dynamo sheets. Anisotropic properties of these sheets were taken into consideration. Special attention was given to understanding the dependency of the magnetization direction on specific power loss. The measured specific power losses of two selected dynamo sheets were compared with results obtained on the basis of analytical formulas.

Keywords: *anisotropy*, *dynamo steel sheets*, *specific power loss*

Streszczenie

Proces magnesowania w typowych blachach prądnicowych może mieć dwojaki charakter. W częściach blach, które odnoszą się do rdzenia stojana maszyn indukcyjnych, proces magnesowania ma charakter obrotowy. Natomiast magnesowanie osiowe występuje głównie w zębach stojana. Niniejszy artykuł dotyczy stratności typowych blach prądnicowych oraz ich zależności od częstotliwości przemagnesowania i maksymalnej wartości indukcji występującej w blachach prądnicowych. Specjalną uwagę poświęcono zależności stratności od kierunku magnesowania w płaszczyźnie blachy. Zmierzone wartości stratności dla dwóch wybranych blach prądnicowych zostały porównane z wartościami stratności, które wyznaczono na podstawie wzorów analitycznych.

Słowa kluczowe: *anizotropia*, *blachy prądnicowe*, *stratność*

DOI: 10.4467/2353737XCT.15.050.3850

* M.Sc. Eng. Agnieszka Banach, Institute of Electrical Engineering and Computer Science, Cracow University of Technology.

** D.Sc. Ph.D. Eng. Witold Mazgaj, Institute of Electromechanical Energy Conversion, Faculty of Electrical and Computer Engineering, Cracow University of Technology.

1. Introduction

Dynamo steel sheets are mainly used in constructions of stators and rotors of induction and synchronous motors. In stator cores, the magnetization process has mainly an elliptical character, but in stator teeth, axial magnetization occurs very often. When a dynamo sheet has isotropic properties, the power losses in particular stator teeth are the same. However, most dynamo sheets have certain anisotropic properties in terms of both their magnetic properties and power losses. This means that the amount of specific power loss depends on the direction of the magnetic field changes on the sheet plane with respect to the rolling direction in the given dynamo sheet.

It is worth underlining that dynamo steel sheets are quite often used in constructions of cores of small power transformers. For this purpose, the *E* and *U* sheet shapes for transformer cores are cut out from these sheets. Worse magnetic properties in directions other than the rolling direction of dynamo sheets cause decreases in the value of the resultant magnetic flux in the transformer core. Inferior magnetic properties in directions other than the rolling direction of dynamo sheets could lead to decreased values of the resultant magnetic flux in the transformer core.

2. Calculation of the specific power loss in steel sheets

Accurate calculations of power losses in magnetic circuits of electrical machines and transformers continue to be an important research area. It is well known that total power losses are treated as a sum of hysteresis losses, eddy current losses, and excess losses which are caused by the so-called domain eddy currents in electrical steel sheets [1–3]. The reasons for power losses during the axial and rotational magnetization processes are similar, but their calculation varies considerably due to different mechanisms of each process. In practice, losses occurring in steel sheets are given per mass unit and they are referred to as specific power losses. Unlike losses in the rotational magnetization, power losses occurring during the axial magnetization can be estimated by using analytical formulas. The general formula determining the hysteresis specific power loss has the well-known form [4–6]:

$$p_h = \eta \, f \, B_m^x \tag{1}$$

where:

- η – constant whose value depends on the given electrical steel sheets (frequently it is equal to 0.038),
- f – frequency of magnetic field changes,
- B_m – maximum value of the flux density during the magnetization process,
- x – exponent which is equal to 1.6 in the Steinmetz's formula or 2.0 in the Richter's formula [4].

In some cases, concerning the calculation of the specific hysteresis power loss, the following relation is used [6]:

$$p_h = \xi \, f \, B_m^2 \, \frac{1}{kd} \, \frac{shkd - \sin kd}{chkd + \cos kd} \tag{2}$$

where:
ξ – coefficient depending on the given electrical sheet,
d – thickness of the given dynamo sheet,
k – coefficient determined as $k = \sqrt{0.5 \, \omega \, \mu \, \gamma}$,
ω – pulsation $2\pi f$,
μ – magnetic permeability,
γ – conductivity of the given dynamo sheet.

It is worth underlining that hysteresis losses are also calculated with the use of a chosen hysteresis model. An interesting approach concerning the determination of hysteresis losses occurring in induction machines supplied by voltage source inverters is proposed in [7].

The specific power loss of 'classical' eddy currents are usually estimated with the use of the formula [4–6]:

$$p_{ed} = \frac{\gamma \, \pi^2 \, d^2 \, f^2 \, B_m^2}{6} \tag{3}$$

where all parameters are defined in the previous relations.

It should be remembered that the discussed formulas have been formulated assuming a constant value of magnetic permeability. However, for most dynamo sheets, the magnetization characteristic has a curvature when values of flux densities are about 1 T. Due to this, the magnetic permeability does not have a constant value in the whole range of changes of the magnetic flux density. Additionally, in dynamo sheets with the thickness of 0.5 mm or more, the distribution of the magnetic field is not homogeneous when the frequency is equal to 50 Hz or higher. It is necessary to stress that none of the above-mentioned formulas take into account the dependence of power losses on magnetization direction.

Many problems in the estimation of power losses in electrical steel sheets occur during calculations of losses caused by the so-called domain eddy currents. These micro currents appear around the moving domain walls. The model of domain wall motion proposed by Pry and Bean allows us to estimate these losses but only in transformer sheets which usually have an ordered grain structure [8]. However, grains in typical dynamo sheets are arranged randomly. Thus, most of these sheets have certain anisotropic properties [9]. At this point the method worked out by G. Bertotti, who has proposed statistical approach to estimate the eddy current losses [2, 10], should be mentioned. He assumed that the movement of the domain walls during the magnetization process consists of random jumps in the iron crystals of the dynamo sheet. He treated fragments of these walls as certain magnetic objects.

Estimation of power losses during the rotational magnetization is a qualitatively different problem. Determination of these losses is much more difficult than calculations of losses during the axial magnetization. Until now, analytical formulas allowing us to simply estimate power losses under rotational magnetization have not been formulated. These power losses are determined with the use of the basic formula, which is widely presented in [2, 3, 11]. It is

necessary to stress that the total power losses occurring in the magnetic circuits of electrical machines are determined with the use of a chosen machine model, where special attention is paid, for example, to calculations of additional losses caused by higher harmonics [12].

3. Dependence of the specific power loss on magnetization direction

Dynamo steel sheets should have isotropic properties. However, different magnetic measurements show that most dynamo sheets have a certain anisotropy, both in terms of the magnetization curves and power losses. These anisotropic features have been confirmed by crystallographic studies on the possible occurrence of textures in dynamo sheets. On the one hand, the magnetization process occurs most easily along the rolling direction in the given sheet; on the other hand, power losses are the biggest when the magnetization process takes place along the transverse direction with respect to the rolling direction. An analysis of the dependence of the specific power loss on the magnetization angle was carried out on the basis of the magnetic measurements, because up until now, formulas which would allow us to calculate the hysteresis and eddy current losses whilst taking into account the magnetization angle have not yet been carried out. Measurements were performed for two selected typical dynamo sheets marked as M530-50A, one of which is produced in the Czech Republic, and the other in South Korea. Figure 1 presents values of the specific power loss in both dynamo sheets as the dependence on the magnetization angle*. Measurements were performed for the following frequencies: 25 Hz; 50 Hz; 75 Hz; 100 Hz. The specific power losses are presented for the flux density values 1.0 T. and 1.5 T (as is usually determined in standards), and they were approximated by means of the second-degree curves.

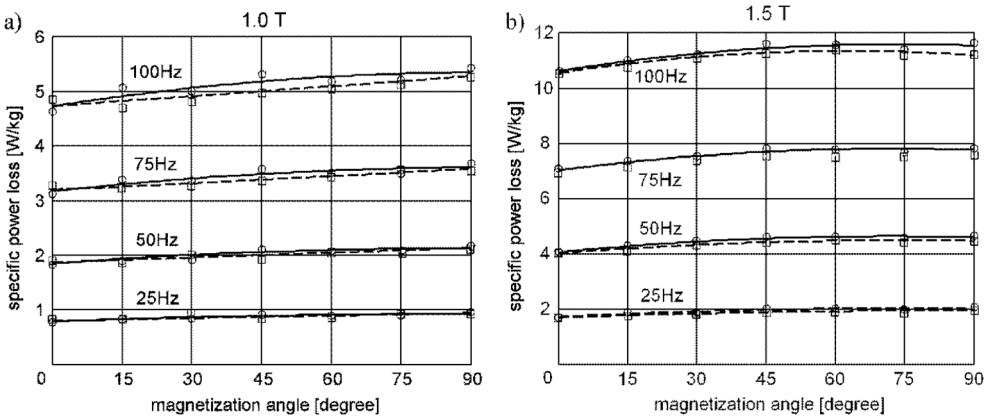

Fig. 1. Specific power loss for Czech and Korean dynamo sheets: a) B_m = 1.0 T; b) B_m = 1.5 T; continuous lines – Czech dynamo sheet, dashed lines – Korean dynamo sheet, circles and squares denote the measured values of the Czech sheet and the Korean sheet, respectively

* Magnetic measurements were carried out in Laboratory of Magnetic Measurements in Stalprodukt SA, Bochnia (Poland).

Higher values of the specific total power loss occur during the magnetization along directions on the sheet plane which significantly differ with respect to the rolling direction. Differences of the specific power losses may be higher than ten percent with respect to the rolling direction. It can be assumed that bigger hysteresis specific power loss in these directions are the direct cause of greater total specific power loss. Figure 2a) presents hysteresis loops of the Czech dynamo sheet for three magnetization directions and for the flux density 1.0 T. In turn, Fig. 2b) shows hysteresis loops when the maximum value of the flux density was equal to 1.5 T; in this case, hysteresis loops measured along the direction of 45 and 90 degrees are almost the same. Due to magnetic anisotropy, hysteresis loops measured along directions inclined 45 or 90 degrees with respect to the rolling direction are wider than hysteresis loops in the rolling direction.

The Korean dynamo sheet has similar properties to the Czech dynamo sheet (Fig. 3).

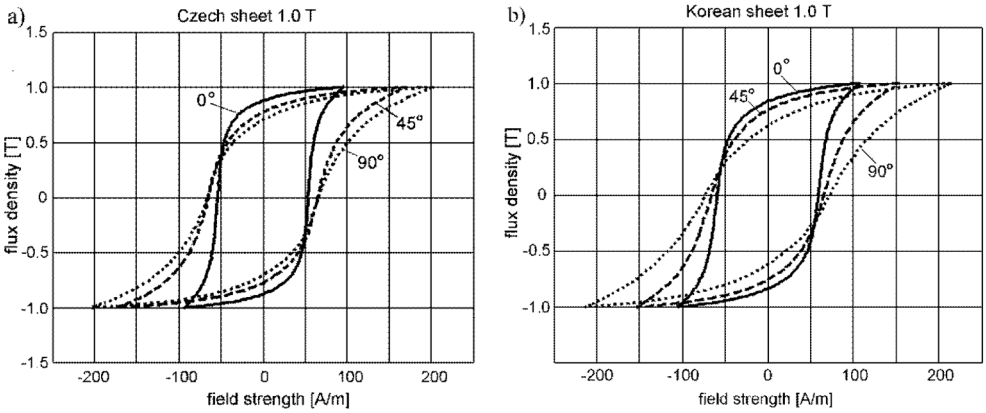

Fig. 2. Hysteresis loops for B_m = 1.0 T: a) Czech sheet, b) Korean sheet

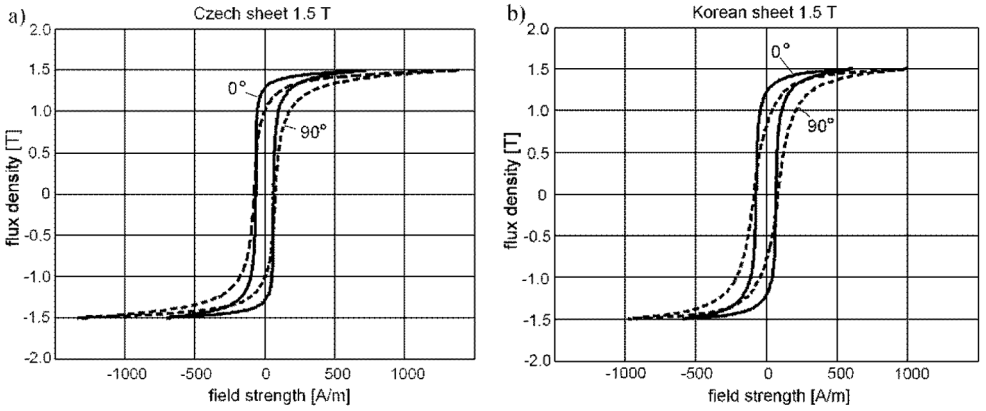

Fig. 3. Hysteresis loops for B_m = 1.5 T: a) Czech sheet, b) Korean sheet

Table 1 presents, by way of example, hysteresis specific power losses for both of the tested dynamo sheets in seven magnetization directions. Hysteresis specific power losses in the transverse direction are about twenty percent higher than specific power losses determined in

the rolling direction. Both the magnetic anisotropy and the loss anisotropy are caused by the occurrence of certain textures, this is a characteristic property of most dynamo steel sheets [9]. This means that a certain amount of grains have a privileged crystallographic orientation. It should be noted that the standards define the acceptable anisotropy of power losses in the range 10 to 14%. It is worth noting that losses for directions higher than 45 degrees with respect to the rolling direction are practically the same.

On the basis of magnetic measurements, the losses caused by eddy currents were determined as the differences between measured total power losses and hysteresis losses, wherein the latter were the product of the hysteresis losses per cycle and the magnetization frequency. Measurements performed for two mentioned dynamo sheets, and estimations carried out on the basis of the measured results show that generally, power losses caused by eddy currents do not depend on the direction of the magnetic field changes when values of the flux density are not higher than 1.0 T and the frequency does not exceed 50 Hz. These losses decrease with increases of the magnetization angle for higher frequencies and higher values of the flux density occurring in the given dynamo sheet. Figure 4 presents specific power losses caused by eddy currents as a dependence of the magnetization angle.

Table 1

Hysteresis specific power loss in W/kg

Magnetization angle	Czech sheet		Korean sheet	
	1.0 T	1.5 T	1.0 T	1.5 T
0°	0.025	0.055	0.026	0.055
15°	0.027	0.060	0.026	0.056
30°	0.028	0.062	0.028	0.060
45°	0.030	0.066	0.029	0.063
60°	0.030	0.067	0.030	0.065
75°	0.030	0.067	0.031	0.064
90°	0.031	0.066	0.032	0.065

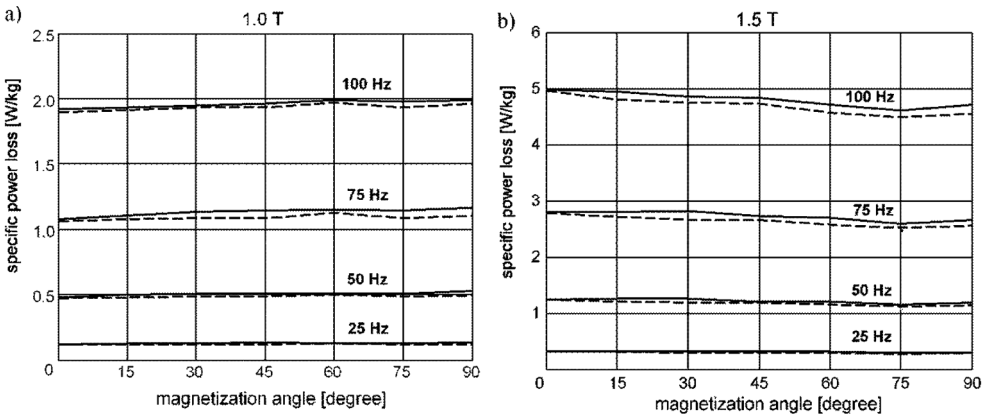

Fig. 4. Specific power loss caused by eddy currents: a) for B_m = 1.0 T; b) B_m = 1.5 T; continuous lines – Czech dynamo sheet, dashed lines – Korean dynamo sheet

4. Comparison between measured and calculated specific power losses

In many papers, it is concluded that the measured losses are significantly bigger than the calculated losses. As mentioned in Chapter 2, reasons of these differences are the so-called domain micro eddy currents which occur around moving domain walls. However, these remarks refer first of all to the transformer steel sheets. Their grains, and thus their domains, may have an area of several square centimeters. On the other hand, the average size of grains in dynamo sheets is in the range of 60 to 100 μm, and in the majority, grains are arranged randomly. The occurrence of the excess losses in the dynamo sheets is rather a controversial issue. Although

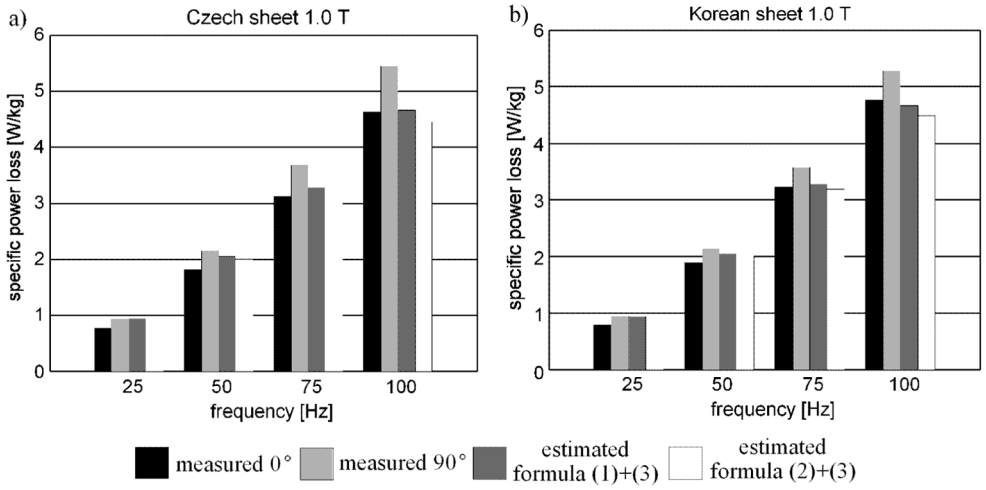

Fig. 5. Measured and calculated specific power loss for B_m = 1.0 T: a) Czech dynamo sheet, b) Korean dynamo sheet

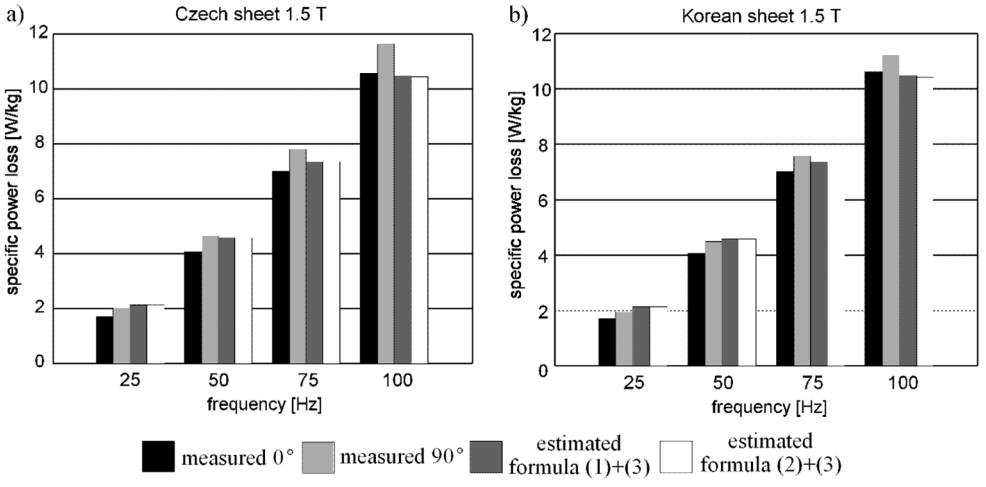

Fig. 6. Measured and calculated specific power loss for B_m = 1.5 T: a) Czech dynamo sheet, b) Korean dynamo sheet

G. Bertotti showed that the measured losses in a certain dynamo sheet are bigger than calculated losses [1], the research carried out for some typical dynamo sheets does not generally confirm this fact. It is obvious that the value of the calculated losses depends on the applied formulas in estimation of the hysteresis and eddy current losses. Figure 5 presents comparisons between the measured losses and the estimated losses during the axial magnetization along the rolling (0°) and transverse direction (90°). The latter losses are calculated for two cases. In the first one, hysteresis losses were estimated with the use of formula (1) (Richter formula) and in the second case, relation (2) was applied. In both cases, eddy current losses are estimated by means of formula (3). Estimated values of power losses depend significantly on coefficients which concern the given soft magnetic material. To reduce the differences between measured and calculated losses, we assumed that the coefficient η in formula (1) and the coefficient ξ in (2) are smaller than is proposed in the literature and they both are equal to 0.035. It should be stressed once again that the above mentioned formulas do not take into account the direction of the magnetization process. The smallest errors between the values of themeasured and estimated losses occur when the power losses are estimated with the use of the sum of formulas (1) and (3). However, these errors amount to 10–20 percent. Similar differences between the losses occur also for the Korean dynamo sheet.

5. Conclusions

Determination of the total specific power loss in typical dynamo sheets with the use analytical formulas without taking into account the magnetization angle can cause errors of even up to 20 percent. Differences in the specific power losses for individual magnetization directions are caused by the presence of anisotropy properties. It may be assumed that this is due to higher hysteresis losses for the magnetization directions other than the rolling direction. However, the formulation of more general conclusions requires studies of a larger number of typical dynamo steel sheets.

Further research should aim at deriving such analytical formulas relating to hysteresis losses that could take into account the magnetization direction. These studies should also include a dependence of eddy current losses on the magnetization angle for frequencies higher than 50 Hz. Specific power losses obtained by means of different analytical relations should also be compared with the values estimated with the use of the general formula. In further research works, attention should be also given to the exceed losses and their dependence on magnetic parameters of dynamo steel sheets.

This paper was supported by research grant No DEC-2011/01/B/ST7/04479: 'Modelling of nonlinearity, hysteresis, and anisotropy of magnetic cores in electromechanical converters with rotating magnetic field' financed by the National Science Centre, (Poland).

References

[1] Bertotti G., *General Properties of Power Losses in Soft Ferromagnetic Materials*, IEEE Transactions on Magnetics, 1988, Vol. 24, No. 1, pp. 621–630.

[2] Pfützner H., *Rotational Magnetization and Rotational Losses of Grain Oriented Silicon Steel Sheets – Fundamental Aspects and Theory*, IEEE Transactions on Magnetics, 1994, Vol. 30, No. 5, pp. 2802–2807.

[3] Tumański S., *Handbook of magnetic measurements*, CRC/Taylor & Francis, Boca Raton 2011.

[4] Dąbrowski M., *Analiza obwodów magnetycznych. Straty mocy w obwodach*, PWN, Warszawa–Poznań 1981.

[5] Heck C., *Magnetic materials and their applications*, Butterworths, London 1974.

[6] Turowski J., *Elektrodynamika techniczna*, WNT, Warszawa 2014.

[7] Fratila M., Benabou A., Tounzi A., Dessoude M., *Improved iron loss calculation for non-centered minor loops*, COMPEL, 2013, Vol. 32, No. 4, pp. 1358–1365.

[8] Pry R.H., Bean C.P., *Calculation of the energy loss in magnetic sheet materials using a domain model*, Journal of Applied Physics, 1958, Vol. 19, No. 3, pp. 532–533.

[9] Mazgaj W., Warzecha A., *Influence of electrical steel sheet textures on their magnetization curves*, Archives of Electrical Engineering, 2013, Vol. 62(245), No. 3, pp. 425–437.

[10] Bertotti G., *Physical interpretation of eddy current losses in ferromagnetic materials. I. Theoretical considerations*, Journal of Applied Physics, 1985, No. 57(6), pp. 2110–2117.

[11] Attalah K., Howe D., *Calculation of the rotational power loss in electrical steel laminations from measured H and B*, IEEE Transactions on Magnetics, 1993, Vol. 29, No. 6, pp. 3547–3549.

[12] Vogel R., Kulig S., *Rotor surface losses in an I-converter-fed synchronous generator considering saturation*, COMPEL, 2011, Vol. 30, No. 3, pp. 1035–1046.

TECHNICAL TRANSACTIONS | **CZASOPISMO TECHNICZNE**
ELECTRICAL ENGINEERING | ELEKTROTECHNIKA
1-E/2015

TOMASZ WĘGIEL, ADAM WARZECHA, WITOLD MAZGAJ*

MODELLING OF A PERMANENT MAGNET ELECTRICAL MACHINE WITH STATOR CORE ANISOTROPY

MODELOWANIE MASZYN ELEKTRYCZNYCH WZBUDZANYCH MAGNESAMI TRWAŁYMI Z ANIZOTROPOWYM RDZENIEM STOJANA

Abstract

This article deals with the methodological aspects of the modelling and field analysis of machines with surface mounted permanent magnets on the rotor, taking into account the anisotropic properties of the stator core. These considerations are intended to show the effect of anisotropy on the structure of the mathematical model of the machine and answer the question of whether if based on classical modelling, it is possible to take into account the rotational magnetization phenomena. The results explain the question, how the magnetic anisotropy effect at rotational magnetization is important from an exploitation point of view.

Keywords: *magnetic anisotropy*, *PM synchronous machine*

Streszczenie

Temat podjęty w pracy dotyczy metodycznych aspektów modelowania oraz analiz wyników obliczeń polowych maszyn z powierzchniowo montowanymi magnesami trwałymi na wirniku z uwzględnieniem anizotropii magnetycznej rdzenia stojana. Rozważania te mają na celu pokazanie wpływu anizotropii na strukturę modelu matematycznego maszyny i udzielenie odpowiedzi na pytanie, czy przy oparciu się na klasycznych założeniach stosowanych w modelowaniu obwodowym możliwe jest jej uwzględnienie. Przedstawione wyniki obliczeń polowych wykonane dla maszyny modelowej pozwalają określić, na ile efekt anizotropii przy magnesowaniu obrotowym jest istotny z punktu widzenia eksploatacyjnego.

Słowa kluczowe: *anizotropia magnetyczna*, *maszyna synchroniczna z magnesami trwałymi*

DOI: 10.4467/2353737XCT.15.051.3851

* D.Sc. Ph.D. Eng. Tomasz Węgiel, D.Sc. Ph.D. Eng. Adam Warzecha, D.Sc. Ph.D. Eng. Witold Mazgaj, Institute of Electromechanical Energy Conversion, Cracow University of Technology.

1. Introduction

The phenomenon of rotational magnetization is usually omitted in 'classical' models of electrical machines [1]. Studies considered in this paper refer to the modelling of machines which have permanent magnets (PM) mounted on the rotor surface. Anisotropic properties of the stator core can be taken into account with the assumption of linear magnetization characteristics along the rolling direction (RD) and the transverse direction (TD). On the one hand, these considerations are intended to show the influence of the anisotropy on the structure of a mathematical model of a given machine. On the other hand, we expect the answer as to whether it is possible to take into account the anisotropy based on classical assumptions of the circuit modelling.

The Lagrangian formalism is one of the most convenient methods for the circuit modelling of electrical machines [2, 3]. This formalism also refers to machines which have permanent magnets in their structure – under the assumption of certain general conditions. For today's rare earth magnets (NdFeB types) we can assume that the operating point of the permanent magnet moves along an unambiguous demagnetization curve caused by the impact of winding currents. Thanks to this assumption, we obtain possibilities of using the Lagrangian formalism for modelling machines with permanent magnets, even for cases where the magnetic circuit has anisotropic properties.

The total co-energy which occurs in the magnetic circuit of the permanent magnets machine (PMM) is a sum of the co-energy $E_{0\Theta}$ generated by winding currents and the co-energy E_{0PM} generated by permanent magnets in a currentless state. For typical constructions of PMMs, the equivalent air gap is relatively wide. Therefore, we can consider that corrections which allow modelling the anisotropic properties refer to the magnetic field excited by permanent magnets. As a result of the stator core anisotropy, differences between the magnetic permeability μ_{rFeRD} in the rolling direction RD and permeability μ_{rFeTD} in the transverse direction TD occur. The function of the field co-energy and the function of the equivalent air gap width should be appropriately modified with respect to the classical considerations [4, 5]. Determination of the mathematical model parameters of the machine with surface-mounted permanent magnets on the rotor, which describe the magnetic anisotropy of the stator core, requires finite element analysis FEA of the magnetic field.

Studies which present the results of research in this area concern mainly synchronous motors, and they focus on the impact of the stator core anisotropy on the cogging torque [6, 7]. Frequently, these studies relate to modelling methods of magnetic anisotropy in cores constructed of oriented or non-oriented steel sheets [8, 9]. Effects caused by magnetic core anisotropy were presented in [10]. Machines with permanent magnets are characterized by relatively high values of the air gap width. Thus, influence of the stator core anisotropy can be considered in the linear range with the use of formulations given in [2].

2. Lagrange's equations of the machine excited by permanent magnets

As it was previously mentioned, the total magnetic field co-energy which occurs in the magnetic circuit of the PMM is a sum of the co-energy of introduced through winding currents and the co-energy generated by permanent magnets in the currentless state. A general form of this function for a three-phase machine can be written as follows:

$$E_0(\varphi, i_1, i_2, i_3) = E_{0\Theta}(\varphi, i_1, i_2, i_3) + E_{0\mathrm{PM}}(\varphi) \tag{1}$$

where:

$E_{0\Theta}(\varphi, i_1, i_2, i_3)$ – co-energy introduced into the system through the winding currents in the presence of magnets,

$E_{0\mathrm{PM}}(\varphi)$ – co-energy introduced into the system by PM in currentless state.

Lagrange's equations of the model of the PMM can be written in the following form:

$$\frac{\mathrm{d}}{\mathrm{d}t}\frac{\partial E_{0\Theta}(\varphi, i_1, i_2, i_3)}{\partial i_i} = u_i - R_\mathrm{s} \cdot i_i \quad \text{for} \quad i = 1,2,3$$

$$J\frac{\mathrm{d}^2\varphi}{\mathrm{d}t^2} = \frac{\partial E_{0\Theta}(\varphi, i_1, i_2, i_3)}{\partial \varphi} + \frac{\partial E_{0\mathrm{PM}}(\varphi)}{\partial \varphi} + T_\mathrm{l} - D\frac{\mathrm{d}\varphi}{\mathrm{d}t} \tag{2}$$

Iron cores of the stator and rotor have a very high magnetic conductivity with respect to the air and magnet materials. Therefore, in classical considerations, it is usually assumed that the energy concentration of the magnetic field occurs mainly in the volume of the air gap and the permanent magnets. This means that the magnetic voltage drops in iron yokes of the given machine can be neglected. In order to take into account the effect of the stator core anisotropy, we should resign from classical assumptions and take into account magnetic voltage drops in iron parts of the stator and the rotor. It is worth underlining that differences between the iron magnetic permeability in the rolling direction (RD) and the permeability in the transverse direction (TD) occur during the rotational magnetization.

The easiest way to take into account the magnetic voltage drops in iron is to add these drops to the magnetic voltage drops occurring in the air gap, on this basis, the magnetic field distribution should be corrected. The consequence of this approach is the local increase of the air gap width for the transverse direction (TD). Thus, the co-energy function should be appropriately modified with respect to classical electrical machines.

3. Magnetic field distribution in PMM with taking into account the anisotropy

The equivalent air gap of the PMM is relatively large. Therefore, it can be assumed that the local increase of the air gap, which represents the anisotropy in the TD axis, occurs mainly for magnetic field lines associated with the flux of the permanent magnet. Inductances of the simplest models of classical machines are calculated on the basis of the distribution of the field radial component in the air gap, because it is possibly due to the specific structure of the magnetic circuit. The geometry of the magnetic circuit of the PMMs is varied and not always simple relations, which are sufficiently accurate for conventional machines, can be used for machines with permanent magnets. Regardless of winding inductances, for these machines the linkage fluxes and the co-energy should be determined as a dependence on the rotational angle in currentless state.

Firstly, this paper focuses on machines with a cylindrical rotor which has surface mounted magnets. For this case, in analytical models of the magnetic field distribution in the air gap, the geometry of the magnetic circuit is characterized by a function of the unit permeance [2–5]. For machines with a smooth surface air gap, these formulas are relatively simple. However, this problem gets complicated when the anisotropy of stator steel sheets need to be taken into account. In order to show the methodology of analysis of the field distribution in the air gap, we used a model of the PMM with a smooth stator (Fig. 1).

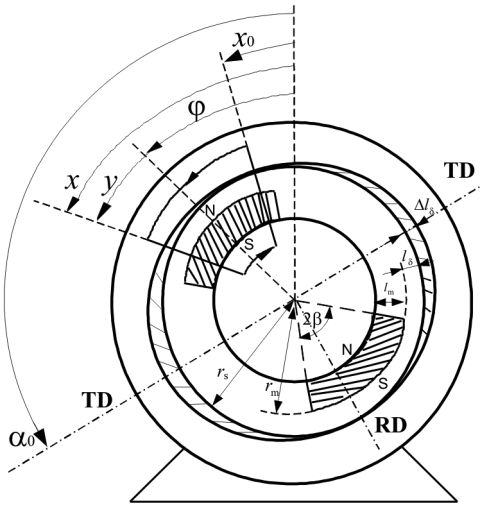

Fig. 1. Cross-section of the PMM with the stator anisotropy

We assumed that the demagnetization curve of the permanent magnet is linear $B_m = B_r + \mu_0 \cdot \mu_{rm} \cdot H_m$; this approximation is widely acceptable for today's rare earth permanent magnets. The form of Ampere's law for the selected contour marked in Fig. 1 allows us to formulate a relationship which describes a simplified one-dimensional field distribution in the air gap of the given PMM:

$$B(x,\varphi,i_1,i_2,i_3) = B_\Theta(x,\varphi,i_1,i_2,i_3) + B_{\mathrm{PM}}(x,\varphi) \tag{3}$$

where:

$$B_\Theta(x,\varphi,i_1,i_2,i_3) = \Theta_s(x,i_1,i_2,i_3) \cdot \lambda(x,\varphi) + C_\Theta(x,\varphi,i_1,i_2,i_3) \tag{4}$$

$$B_{\mathrm{PM}}(x,\varphi) = B_{\mathrm{m}}(x-\varphi)\frac{\lambda(x,\varphi)}{\lambda_{\delta\mathrm{m}}} + C_{\mathrm{PM}}(x,\varphi) \tag{5}$$

$B_\Theta(x,\varphi,i_1,i_2,i_3)$ – radial component of the magnetic field density distribution generated by winding currents along the circumference of the air gap,

$B_{\mathrm{PM}}(x,\varphi)$ – radial component of the magnetic field density distribution in the air gap generated by permanent magnets,

$\lambda_{\delta m} = \dfrac{\mu_0}{l_\delta + l_m / \mu_{rm}}$ – unit permeance for machines with stator smooth cylindrical surface,

$\Theta_s(x, i_1, i_2, i_3)$ – magnetomotive force (MMF) distribution of the stator windings,

$B_m(x-\varphi)$ – function describing one-dimensional distribution of the magnetic flux density along the circumference in the PMM in the currentless state.

The coefficients C_Θ and C_{PM} in formulas (4), (5), which result from Gauss's law for magnetism, are equal to zero in the considered cases. In general, a magnetic circuit can be characterized by the unit permeance function $\lambda(x, \varphi)$, the distribution of which can be written in the form of a double Fourier series [3]:

$$\lambda(x,\varphi) = \sum_{m\in M} \sum_{n\in N} \lambda_{m,n} \cdot e^{\mathrm{j}mx} \cdot e^{\mathrm{j}n\varphi} \tag{6}$$

The function of the unit permeance allows modelling of the real shape of the magnetic circuit, therefore in the general case, sets M and N in the formula (6) can include all integers. The function of the magnetic field distribution in the one-dimensional model in the currentless state (smooth stator and anisotropy is neglected) is the function of one variable.

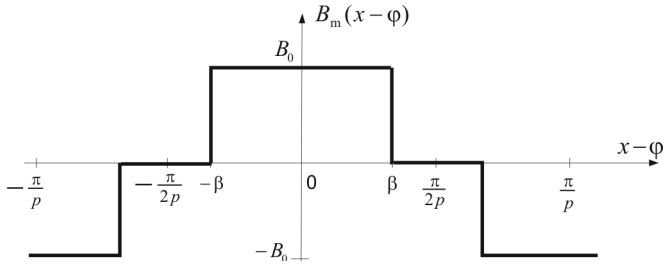

Fig. 2. Flux density distribution in the air gap in a slotless machine without taking into account the stator core anisotropy

The coefficients of the Fourier series of the field distribution function presented in Fig. 2 can be determined on the basis of the following formulas:

$$B_m(x-\varphi) = \sum_{\varsigma\in Q} B_{m\varsigma} \cdot e^{\mathrm{j}\varsigma(x-\varphi)} \tag{7}$$

where:

$$Q = \{\ldots -5p, -3p, -p, p, 3p, 5p \ldots\};\ B_{m\varsigma} = \frac{2}{\pi}\frac{B_0}{\varsigma} p \cdot \sin(\varsigma \cdot \beta);\ B_0 = B_r \frac{l_m / \mu_{rm}}{l_m / \mu_{rm} + l_\delta}$$

For special cases, when it is assumed a smooth cylindrical surface of the stator and a uniform air gap, the function of the unit permeance (6) of the anisotropic machine only becomes dependent on x because properties of permanent magnets are similar to air properties ($\mu_{rm} \cong 1$):

$$\lambda(x,\varphi) = \lambda(x) = \frac{\mu_0}{l_\delta + \Delta l_\delta(x) + l_m / \mu_{rm}} \tag{8}$$

where: $\Delta l_\delta(x)$ is a function which increases the equivalent width of the air gap due to the occurrence of magnetic voltage drops caused by the anisotropy of the stator core.
Thus, for anisotropic cores with smooth surfaces of the stator and the rotor, the set M contains harmonics {…, –4, –2, 0, 2, 4, …}, however, the set N only contains the zero harmonic {0}:

$$\lambda(x) = \sum_{m \in M} \lambda_{m,0} \cdot e^{\mathrm{j}mx} \tag{9}$$

The consequence of this assumption is the fact that the inductances of the stator windings do not depend on the rotation angle, and the PM flux density distribution in the air gap takes a simplified form:

$$B_{\mathrm{PM}}(x,\varphi) = \sum_{m \in M} \sum_{\varsigma \in Q} B_{m\varsigma} \frac{\lambda_{m,0}}{\lambda_{\delta m}} e^{\mathrm{j}(m+\varsigma)x} \cdot e^{-\mathrm{j}\varsigma\varphi} \tag{10}$$

4. Form of the co-energy function of the PMM whilst taking into account the anisotropy

For methodological purposes, the form of the co-energy function is presented for a simplified case of the anisotropic machine with smooth cylindrical surfaces of the stator and the rotor. The functions of the winding characteristics have an additional element which represents the flux linkage produced by PM $\psi_{\mathrm{PM}a}(\varphi)$; this flux depends on the rotation angle φ. For example, the relationship between the flux and the current of the a winding can be written as follows:

$$\psi_a(\varphi, i_1, i_2, i_3) = L_{a1} \cdot i_1 + L_{a2} \cdot i_2 + L_{a3} \cdot i_3 + \psi_{\mathrm{PM}a}(\varphi) \tag{11}$$

As a consequence, the co-energy component dependent on winding currents takes the following form [2]:

$$E_{0\Theta}(\varphi, i_1, i_2, i_3) = \frac{1}{2} \sum_{a=1}^{3} \sum_{b=1}^{3} L_{ab} \cdot i_a \cdot i_b + \sum_{a=1}^{3} \psi_{\mathrm{PM}a}(\varphi) \cdot i_a \tag{12}$$

In order to determine the characteristics of the windings (flux dependences), we assumed that the Fourier spectrums contain the v harmonic which belong to the P set. Elements of

this set for the windings with an integer number of slots per pole and phase are as follows: $P = \{\ldots, -5p, -3p, -p, p, 3p, 5p, \ldots\}$. Furthermore, we assumed that windings *a* and *b*, which have w_s number of turns, are characterized by winding factor $k_u^{|\nu|}$. Thus, inductances can be determined on the basis of the relation [2–4]:

$$L_{ab} = \sum_{\nu \in P} \sum_{m \in M} Q_1 \frac{2 r_s \cdot l_c}{\pi} \frac{(w_s)^2 \cdot k_u^{|\nu|} \cdot k_u^{|\nu+m|}}{|\nu| \cdot |\nu + m|} \lambda_{m,0} \cdot e^{j(\nu+m)x_a} \cdot e^{-j\nu x_b} \tag{13}$$

where:

l_c – equivalent axial length of the given machine,

Q_1 – parameter depends on elements of the *P*, *M* sets and it is defined as follows:

$$Q_1 = \begin{cases} 1 \Leftrightarrow \forall \nu, \forall m, \nu \in P \wedge m \in M \wedge (\nu + m) \in P \\ 0 \qquad \text{in opposite case} \end{cases} \tag{14}$$

For the three-phase stator, the angles between winding magnetic axes are equal to:

$$x_a = (a-1)\frac{2\pi}{3p}, \; x_b = (b-1)\frac{2\pi}{3p} \text{ for } a, b = 1, 2, 3$$

The component of the magnetic flux which is linked with a winding in currentless state is written as [2]:

$$\psi_{\mathrm{PM}\,a}(\varphi) = \sum_{\varsigma \in Q} \sum_{m \in M} D_1 \frac{2\, r_s\, l_c}{\lambda_{\delta m}} B_{m\varsigma} \frac{w_s\, k_u^{|\varsigma+m|}}{|\varsigma + m|} \lambda_{m,0} \cdot e^{j(\varsigma+m)x_a} \cdot e^{-j\varsigma\varphi} \tag{15}$$

Parameter D_1 depends on the content of sets *P*, *Q*, *M* and it is defined as:

$$D_1 = \begin{cases} 1 \Leftrightarrow \forall \varsigma, \forall m, \varsigma \in Q \wedge m \in M \wedge (\varsigma + m) \in P \\ 0 \qquad \text{in opposite case} \end{cases} \tag{16}$$

The co-energy component which is independent of winding currents is associated with areas of energy occurrence (air gap, permanent magnets). Analytical calculation of the co--energy in the currentless state is not a simple task when real shapes of the magnetic circuit need to be taken into account. We propose a simplified approach which is based on 1-D field distribution. If the previously defined function of the unit permeance function (6) is taken into account, the co-energy component for the currentless state takes the form:

$$E_{0\mathrm{PM}}(\varphi) = \frac{r_m\, l_c}{2} \int_0^{2\pi} \frac{\left[B_{\mathrm{PM}}(x, \varphi)\right]^2}{\lambda(x, \varphi)} \, \mathrm{d}x \tag{17}$$

In the particular case in which the simplified forms of the permeance function (6) and the flux density distribution are taken into consideration, we obtain the relationship describing the co-energy in the currentless state in the following form:

$$E_{0\mathrm{PM}}(\varphi) = \frac{l_c \cdot r_m}{2(\lambda_{\delta m})^2} \int_0^{2\pi} [\lambda(x,\varphi) \cdot B_m(x-\varphi)^2] \, \mathrm{d}x \tag{18}$$

where:

$$B_m(x-\varphi)^2 = \sum_{k \in K} B_{mk}^2 \cdot \mathrm{e}^{\mathrm{j}k(x-\varphi)} \tag{19}$$

$$K = \{...-4p,-2p,0,2p,4p,...\}; \;\; B_{mk}^2 = \begin{cases} \dfrac{2}{\pi}(B_0)^2 \cdot p \cdot \beta & \text{for} \quad k = 0 \\ \dfrac{2}{\pi}\dfrac{(B_0)^2}{k} p \cdot \sin(k \cdot \beta) & \text{for} \quad k \neq 0 \end{cases} \tag{20}$$

After taking into account relationships (18), (19) and (20), and formal mathematical operations, we obtain the simplified formula describing the co-energy in the currentless state:

$$E_{0\mathrm{PM}}(\varphi) = \frac{\pi \cdot l_c \cdot r_m}{(\lambda_{\delta m})^2} \, \mathrm{Re}\,\{\sum_{k \in K} \lambda_{-k,0} \cdot B_{mk}^2 \cdot e^{-\mathrm{j}k\varphi}\} \tag{21}$$

5. Field calculations of the PMM whilst taking into account the anisotropy

Field analysis was carried out with the use of the MagNet package for the model of the exemplary machine which is shown in Fig. 1 under the assumption that the magnetization characteristics of iron and permanent magnets are linear. The anisotropy was taken into account by introducing appropriately different values of the magnetic permeability of the stator core for the rolling direction ($\mu_{r\mathrm{FeRD}}$ = 10 000) and for the transverse direction (μ_{rFeRD} = 5000). The assumption of the linear characteristics was related to methodological aspects of the analysis, these were intended to emphasize only the influence of the phenomenon of the anisotropy.

The basic construction parameters of the considered machine are as follows: external radius of the stator yoke – 120 mm; internal radius of the stator yoke r_s = 71 mm; packet length l_c = 100 mm; number of stator slots Z_s = 36; opening width of the stator slots 4 mm; number of pole pairs p = 1; double-layer winding composed of a 12 serial elementary coils; number of coils forming a one pair of poles – 6; total number of stator turns w_s = 120; stator winding pitch – 15; external radius of the rotor core – 64 mm; internal radius of the rotor core – 27 mm; length of the air gap over the magnet l_δ = 2 mm; thickness of the magnet l_m = 5 mm; PM angular pitch 2β = 120°; parameters of the PM: B_r = 1.1 T; H_c = 827.6 kA/m; μ_{rm} = 1.1.

Test calculations were performed on the basis of the field model of the two-poles machine – this model was formulated in the MagNet 2D Static and is shown in Fig. 3. In the first step, magnetic field distributions in the air gap of machines with the isotropic and anisotropic stator were compared.

a) b)

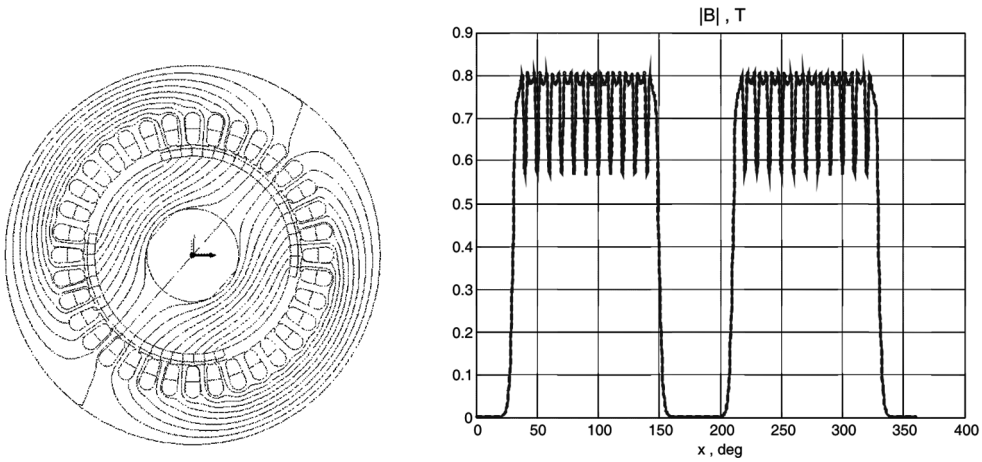

Fig. 3. Diagram of the magnetic field lines for the anisotropic machine core a) and the distribution of the radial component module of the flux density in the air gap ($\varphi = \pi/2$, $\alpha_0 = \pi/2$) b) isotropic case – dashed line, anisotropic case – continuous line

The results shown in Fig. 3b) indicated that the influence of the anisotropy on the field distribution in the gap is practically unnoticeable. For this reason, further studies focused on integral values of the magnetic field i.e. the co-energy and linkage fluxes of the windings in the currentless state.

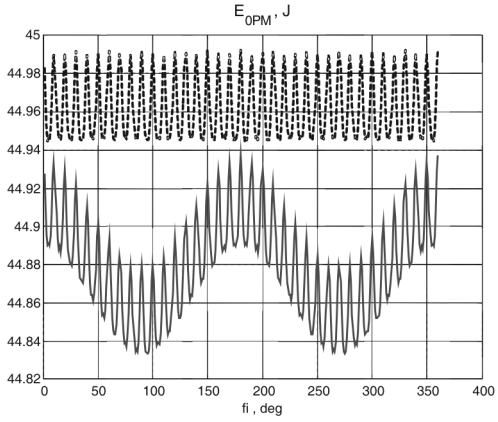

Fig. 4. Changes of co-energy as a function of the angular position of the PM rotor with respect to the stator in the currentless state; isotropic case – dashed line, anisotropic case – continuous line

Figure 4 shows a comparison of changes of the co-energy function according to rotor positions in the currentless state. When the stator is anisotropic, the co-energy function also contains the second harmonic in addition to the constant component and slot harmonic. The Fourier spectrum of this function is presented in Figs. 5a) and b); values of amplitudes are given in (dB) with respect to the accepted reference level of 0.1 mJ.

a) b)

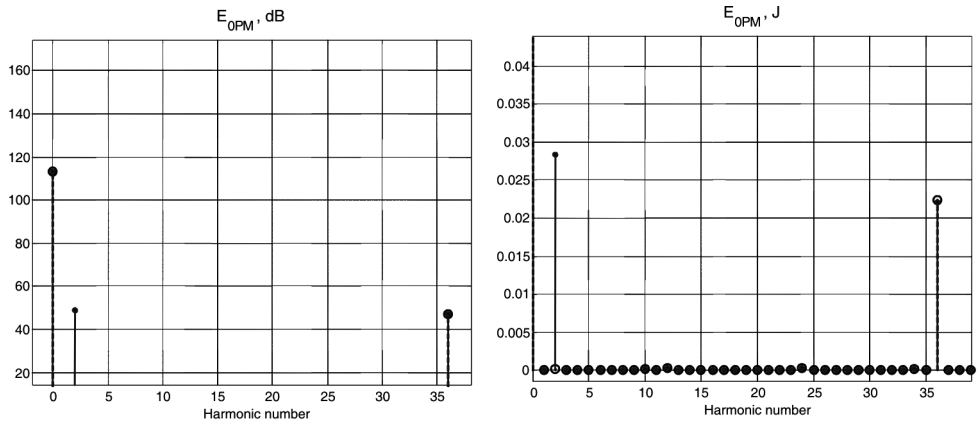

Fig. 5. Amplitude spectrum of the co-energy function in (dB) and variable components of the co-energy in energy unit (J) isotropic case – dashed line O, anisotropic case – continuous line •

The amplitude of the second harmonic of the co-energy is close to the level of the 36th slot harmonic, which has practically the same value in both cases, as is shown in Fig. 5.

In the next step, the asymmetry degree of the induced voltages in the stator windings was examined. The basis for the analysis were FEA results recalculated for the rotor speed which corresponds to a frequency of 50 Hz. Waveforms of induced voltages, which are shown in Fig. 6a), have small but noticeable differences in the amplitudes for the basic harmonic.

a) b)

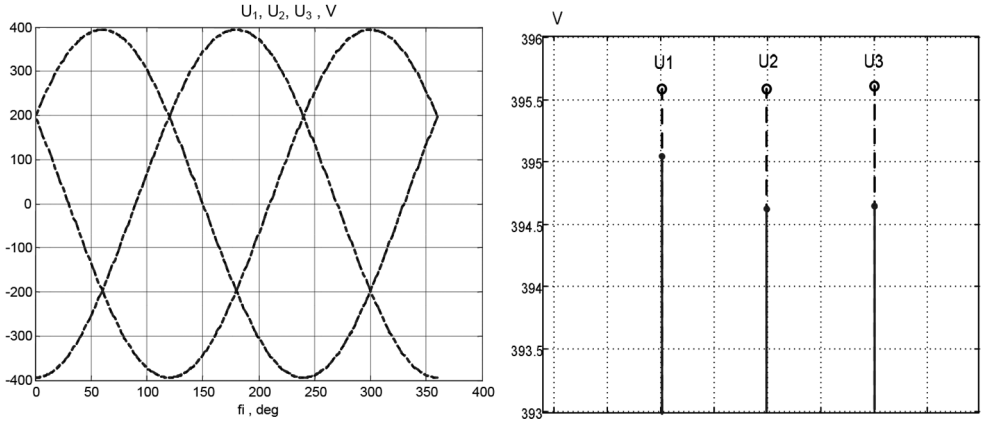

Fig. 6. Time waveforms of voltages induced in stator windings a) and amplitudes for base harmonic of particular phases b) isotropic case – dashed line O, anisotropic case – continuous line •

From the comparison of amplitude values of the basic harmonic of the phase voltages (Fig. 6) it follows that the anisotropy of the stator core voltage introduces an asymmetry in phase 1 at 0.5 V with respect to phase 2 and 3. A very important aspect in PMMs is the occur-

rence of the cogging torques. The calculation results of these torques are shown in Figs. 7a) and b) – numerical analysis was carried out with the use of the virtual work method.

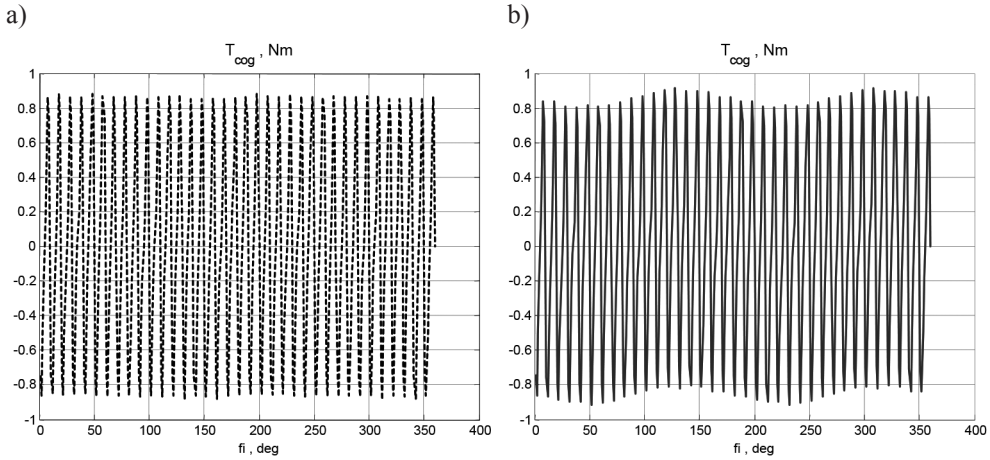

Fig. 7. Cogging torque produced for changes of rotor position: a) isotropic case, b) anisotropic case

Harmonic analysis of these torques (Fig. 8) shows that the second harmonic caused by the anisotropy is about ten times smaller than the harmonics caused by the stator slotting. However, the variable component of the co-energy caused by the anisotropy is comparable with the component associated with the stator slotting.

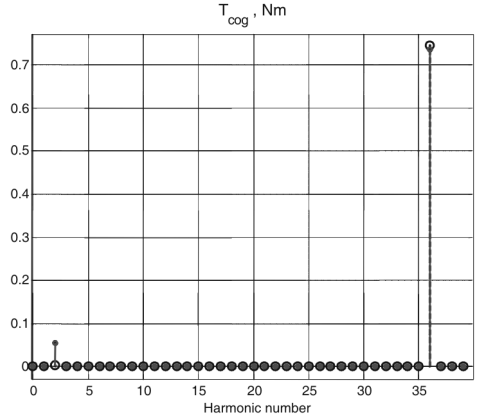

Fig. 8. Amplitude spectra of the cogging torque, isotropic case – dashed line O, anisotropic case – continuous line •

6. Components of the permeance function caused by the anisotropy

Due to the specificity of the magnetic circuit of the PMMs with the anisotropic stator, analytical relationships [2] describing the unit permeance function, which are sufficiently accurate for isotropic machines, need to be complemented with components allowing us to model the anisotropy. Based on the results of the distribution of the co-energy function obtained by FEA, additional components of the unit permeance function caused by the anisotropy can be determined qualitatively. This mainly concerns the second harmonic, which is confirmed by Figs. 5a) and b). For the model two-poles machine with the anisotropic stator and the smooth cylindrical rotor, the form of the simplified one-dimensional distribution of the unit permeance function can be written as follows:

$$\lambda(x) \approx \lambda_{0,0} + 2\lambda_{2,0} \cdot \cos(2x) + \cdots \tag{22}$$

For such a defined function of the unit permeance, we can formulate a Fourier series which approximates the co-energy function in the currentless state whilst taking the anisotropy into account:

$$E_{0\,\mathrm{PM}}(\varphi) \approx E_0 + E_2 \cdot \cos(2\varphi) + \cdots \tag{23}$$

The coefficients of the first terms of this series are defined as:

$$E_0 = \frac{2l_c \cdot r_m \cdot (B_0)^2}{(\lambda_{\delta m})^2} \lambda_{0,0} \cdot \beta \quad E_2 = \frac{4l_c \cdot r_m \cdot (B_0)^2}{(\lambda_{\delta m})^2} \frac{\lambda_{2,0}}{2} \cdot \sin(2\beta) \tag{24}$$

Taking into account the co-energy components in the currentless state determined on the basis of FEA, we obtain basic coefficients of the distribution of the unit permeance function which correspond to anisotropy:

$$\lambda_{0,0} = 1.96 \cdot 10^{-4} \frac{H}{m^2};\ \frac{\lambda_{0,0}}{\lambda_{\delta m}} = 1.02;\ \lambda_{2,0} = 1.47 \cdot 10^{-7} \frac{H}{m^2};\ \frac{\lambda_{2,0}}{\lambda_{\delta m}} = 0.77 \cdot 10^{-3}$$

7. Conclusions

Methodological aspects of the modelling presented in this paper show possibilities of how to take into account the phenomenon of the rotational magnetization in stator core of PMM. In order to include the anisotropy into the machine model, we must determine the corrections of the unit permeance function which are important for the second harmonic of its distribution. Determination of these corrections is only possible through modelling of the field distribution using numerical methods FEA. As a result, we can show the influence of the anisotropy on the form of the co-energy function in the currentless state and stator winding characteristics.

The proposed mathematical model of the anisotropic machines, despite significant simplifications, gives us the possibility to perform calculations the results of which may be useful from an operational point of view. Results of field calculations show that for the machine with assumed structure of the magnetic circuit characteristic effects are poorly unnoticeable. The asymmetry of induced phase voltages during a generator operation is at a level of 0.2%, and the cogging torque, important for motor operation, is smaller of one order than the torque caused by stator slotting. Despite such weak effects, we can obtain their qualitative compatibility with the effects which are predicted on the basis of the analytical description in field calculations. As a consequence, it proved possible to determine additional coefficients of the distribution of the unit permeance function caused by the anisotropy – these coefficients complete the basic classical parameters of the mathematical model. The presented research has been carried out for a two-pole machine because the anisotropic effects are then the strongest.

It is worth underlining that the presented conclusions can be dissimilar with respect to switching machines with different relationships between numbers of stator teeth and rotor poles and different dimensions of slots and teeth.

Acknowledgements

This paper was supported by research grant No DEC-2011/01/B/ST7/04479: ‘Modelling of nonlinearity, hysteresis, and anisotropy of magnetic cores in electromechanical converters with rotating magnetic field’ financed by the National Science Centre (Poland).

References

[1] Warzecha A., Sobczyk T., Mazgaj W., *Matematyczny opis silnika indukcyjnego z anizotropią magnetyczną rdzenia*, Zeszyty Problemowe – Maszyny Elektryczne, 2013, nr 100, pp. 123–128.

[2] Węgiel T., *Space harmonic interactions in permanent magnet generators*, Monograph 447, Wydawnictwo Politechniki Krakowskiej, 2013.

[3] Sobczyk T., *Metodyczne aspekty modelowania matematycznego maszyn indukcyjnych*, WNT, Warszawa 2004.

[4] Sobczyk T., Drozdowski P., *Inductances of electrical machine winding with a nonuniform air-gap*, Archiv fur Elektrotechnik, 1993, No. 76, pp. 213–218.

[5] Heller B., Hamata V., *Harmonic Field Effect in Induction Machines*, Elsevier Scientific, New York 1977.

[6] Gašparin L., Černigoj A., Fišer R., *Additional cogging torque components due to asymmetry in stator back iron of PM synchronous motors*, The International Journal for Computation and Mathematics in Electrical and Electronic Engineering, COMPEL, 2011, Vol. 30, No. 3, pp. 894–905.

[7] Yamaguchi S., Daikoku A., *Cogging torque calculation considering magnetic anisotropy for permanent magnet synchronous motors*, The International Journal for Computation and Mathematics in Electrical and Electronic Engineering, COMPEL, 2004, Vol. 23, No. 3, pp. 639–646.

[8] Tamaki T., Fujisaki K., Wajima K., Fujiwara K., *Comparison of Magnetic Field Analysis Methods Considering Magnetic Anisotropy*, IEEE Transactions on Magnetics, 2010, Vol. 46, No. 2, pp. 187–190.

[9] Higuchi S., Takahashi Y., Tokumasu T., Fujiwara K., *Comparison Between Modeling Methods of 2-D Magnetic Properties in Magnetic Field Analysis of Synchronous Machines*, IEEE Transactions on Magnetics, 2014, Vol. 50, No. 2.

[10] Warzecha A., Mazgaj W., *Główne efekty wywoływane anizotropią magnetyczną rdzenia w silniku indukcyjnym*, WZEE-2013, Rzeszów–Czarna 2013.

TECHNICAL TRANSACTIONS | **CZASOPISMO TECHNICZNE**
ELECTRICAL ENGINEERING | ELEKTROTECHNIKA
1-E/2015

PRZEMYSŁAW KRZYK, NATALIA PRAGŁOWSKA-RYŁKO, MACIEJ SUŁOWICZ*

APPLICATION OF INTERPOLATED DISCRETE FOURIER TRANSFORM METHOD IN THE DIAGNOSTICS OF CAGE INDUCTION MOTORS

ZASTOSOWANIE METODY INTERPOLOWANEJ DYSKRETNEJ TRANSFORMATY FOURIERA DO DIAGNOSTYKI SILNIKÓW INDUKCYJNYCH KLATKOWYCH

Abstract

This paper compares the accuracy of the multi-frequency stator phase current spectrum estimation. This is as a development of considerations made in [1]. In this paper, the authors added to previous results for the classic Discrete Fourier Transform method and the two-point interpolated DFT method (IpDFT), new results obtained by three-point IpDFT method's algorithm. The analysis was made for slip spectrum component which is used for cage damage detection. To minimize the spectrum leakage effect, the selected Rife-Vincent Class I windows (RVCI) were used. The article focuses on the effectiveness of spectral component estimation in function of the used method, type of time window and measurement time. Values of errors of frequency and amplitude estimations are presented on graphs. The authors compared theoretical considerations with the case of real stator current of an asynchronous motor with a broken cage. This article can be used as a base for further studies on the diagnosis of induction motors.

Keywords: *Discrete Fourier Transform (DFT)*, *two and three-point IpDFT method*, *estimation of signal parameters*, *spectral leakage*, *time windows RVCI*, *diagnosis of electrical motors*

Streszczenie

Niniejszy artykuł przedstawia porównanie dokładności estymacji parametrów dla sygnału wieloharmonicznego. Artykuł jest rozszerzeniem rozważań zawartych w pracy [1]. Autorzy poszerzyli poprzednie badania wykonane dla klasycznej metody DFT i interpolowanej dwupunktowej metody DFT o kolejny algorytm – trzypunktową metodę interpolowanego DFT. Analizę przeprowadzono dla częstotliwości poślizgowej widma, którą stosuje się najczęściej do detekcji uszkodzeń silnika. W celu ograniczenia wpływu przecieku widma użyto wybranych okien Rife'a–Vincenta klasy I (RVCI). Niniejszy artykuł koncentruje się na skuteczności estymacji składowych widma w zależności od użytej metody, wykorzystanego okna czasowego i czasu pomiaru. Wartości błędów estymacji częstotliwości i amplitudy zostały przedstawione na wykresach. Autorzy porównali wyniki rozważań teoretycznych z rzeczywistym przypadkiem uszkodzenia klatki silnika indukcyjnego. Tekst ten może stanowić podstawę dalszych badań dotyczących doskonalenia metod diagnostyki silników indukcyjnych.

Słowa kluczowe: *Dyskretna Transformata Fouriera*, *dwu- i trzypunktowa metoda IpDFT*, *estymacja parametrów sygnału*, *przeciek widma*, *okna czasowe RVCI*, *diagnostyka silników elektrycznych*

DOI: 10.4467/2353737XCT.15.052.3852

* Ph.D. Eng. Przemysław Krzyk, M.Sc. Eng. Natalia Pragłowska-Ryłko, Institute of Electrical Engineering and Computer Science, Cracow University of Technology.
Ph.D. Eng. Maciej Sułowicz, Institute of Electromechanical Energy Conversion, Cracow Iniversity of Technology.

1. Introduction

Diagnostics of electrical motors is a widely used and developed branch of research nowadays [2–10]. The early detection of irregularities in the functioning of machines can reduce operating costs associated with unexpected failures reducing and life of equipment [2–10].

Time-frequency analysis is successfully used for the diagnostics of electrical machines. One of the basic methods is voltage and current spectral analysis by the classic DFT method [2–10]. For asynchronous motors, spectral analysis of stator phase current commonly uses a method based on the amplitude estimation of the spectrum component with the sliding-frequency $(1 - 2s)f_0$.

The accuracy of the estimated signal parameters such as amplitude and frequency, significantly determines the diagnosis quality level of electrical machines. A significant decrease of the accuracy of the DFT method occurs when a spectral leakage appears, i.e. a transfer of power from one frequency to other frequencies.

In the case of spectral leakage, extension of measurement time and adjusting by time windows are commonly used [11]. In literature, one can find methods based on increasing frequency resolution by adding zero samples at the end of the signal [12–14]. Another way of minimizing the spectral leakage, which determines the estimation error of the signal parameter, is the spectrum interpolation by two or three-point interpolated DFT methods (2p IpDFT and 3p IpDFT). These methods effects in increasing of accuracy estimation of lobe peak position [15].

In this paper, the classic DFT methods with two and three-point (2p and 3p) IpDFT are compared. The authors analysed values of the estimated parameters of the sliding harmonic calculated by all three methods, using Rife–Vincent class I windows (RVCI) of selected orders. A previous comparison of DFT with only the two-point IpDFT method is available in [1].

2. RVCI time windows

Time windows can be separated into cosine and non-cosine windows [13]. In this paper, the authors analyzed just the cosine Rife–Vincent Class I windows (RVCI) [13], which were defined by the formula:

$$w_n = \begin{cases} \sum_{m=0}^{M} (-1)^m A_m^w \cos\left(\frac{2\pi}{N} mn\right) & \text{if } 0 \le n < N \\ 0 & \text{if } 0 > n \vee n \ge N \end{cases} \tag{1}$$

where:

w_n – cosine Rife–Vincent Class I windows (RVCI),
N – length of the window (number of samples),
A_m^w – amplitude of the m harmonic for cosine window of M order (for $M = 0$ RVCI window is rectangular and for $M = 1$, window is Hanning).

In this paper the authors used cosine Rife–Vincent Class I windows (RVCI) [13] of the first and the third order for $M = 1$ and $M = 3$ respectively.

3. Analysis of signal parameter estimation using the IpDFT methods

The description of algorithms for the two and three-point IpDFT method in this chapter was based on [13, 16–19].

The interpolated DFT method uses two or three adjacent bins from the DFT spectrum. Bins with the maximum modules (two or three, depending on the selected IpDFT method – 2p or 3p), allow the correction δ [13]. The coefficient δ makes a correction of bin frequency ω_k to signal frequency ω_0:

$$\omega_0 = \left(k \pm \delta\right)\frac{2\pi}{N}, 0 < \delta \le 0.5 \tag{2}$$

3.1. Two-point IpDFT method

The two-point IpDFT method is based on two bins from the DFT spectrum with the maximum modules. In other words, the IpDFT method consists on determining the ratio of DFT bins modules with the greatest amplitude, analyzed by using the time window shape. As a result, one obtains the following dependence: $v_n = w_n x_n$, where v_n is windowed signal and x_n is a sinusoidal signal. The following formulas are based on the transformations made in [13].

For RVCI windows of order $M = 0, 1, 2, \ldots$, using the two-point interpolated DFT method, one calculates correction δ by the formula [16–18]:

$$\delta = \frac{(M+1)|V_{k+1}| - M|V_k|}{|V_k| + |V_{k+1}|} \tag{3}$$

where V_k is DFT spectrum.

Correction δ is used for estimation of the bin pulsation ω_0 and bin amplitude $|V(\omega_0)|$ respectively:

$$\omega_0 = \left(k \pm \frac{(M+1)|V_{k+1}| - M|V_k|}{|V_k| + |V_{k+1}|}\right)\frac{2\pi}{N} \tag{4}$$

$$\left|V\left(\omega_0\right)\right| = \frac{2\pi}{\sin\left(\delta\pi\right)}\frac{|V_k|}{S_k} \tag{5}$$

where:

$$S_{k+n} = \left|\sum_{m=-M}^{M}\frac{(-1)^{m+n}A'_m}{\delta-\left(m+n\right)}\right| \tag{6}$$

and:

$$\begin{cases} A'_m = A_0^w \text{ if } m = 0 \\ A'_m = \dfrac{A_{|m|}^w}{2} \text{ if } m \neq 0 \end{cases} \tag{7}$$

3.2. Three-point IpDFT method

The three-point IpDFT method uses three bins modules with the greatest amplitude from the DFT spectrum. According to [13], for the three-point IpDFT method and RVCI windows, one obtains the correction δ:

$$\delta = (M+1)\frac{|V_{k+1}| - |V_{k-1}|}{2|V_k| + |V_{k-1}| + |V_{k+1}|} \tag{8}$$

which is again used for estimating the bin pulsation ω_0 and bin amplitude $|V(\omega_0)|$ respectively:

$$\omega_0 = \left(k \pm (M+1)\frac{|V_{k+1}| - |V_{k-1}|}{2|V_k| + |V_{k-1}| + |V_{k+1}|} \right)\frac{2\pi}{N} \tag{9}$$

$$|V(\omega_0)| = \frac{2\pi}{\sin(\delta\pi)}\frac{|V_{k-1}| + 2|V_k| + |V_{k+1}|}{S_{k-1} + 2S_k + S_{k+1}} \tag{10}$$

where S_{k+n} is defined in formula .

4. Comparison of classic DFT method with two and three-point IpDFT method

In this section, the authors present the analysis for the simulated multi-frequency signal and the real case of the current signal from a damaged asynchronous motor.

4.1. Almost periodic signal

In order to investigate the error level using IpDFT methods, the authors allowed a spectral leakage occurrence. The spectral leakage can be obtained for a near periodic signal (a signal which does not contain an integer number of periods).

The analysis was based on the multi-frequency waveform with ten major harmonics and five sliding harmonics. The signal was defined by:

$$\begin{aligned} & f = (k - ls) f_0 \\ & for \begin{cases} k = 0; & l = 1,2,...,5 \\ k = 1,2,...,10; & l = -5,-4,...,5 \end{cases} \end{aligned} \tag{11}$$

Waveform from was characterized by $f_p/sf_0 \in \mathbf{R}\backslash\mathbf{Q}$ and $f_p/f_0 \in \mathbf{R}\backslash\mathbf{Q}$, where f_p – sampling frequency.

The signal specified in equation has irrational values of f_0 and s:

$$f_0 \cong 50.054327 \text{ Hz}$$

$$f_0 \cong 0.015643.$$

A measuring time of 100 seconds was chosen. Measuring points were selected for: 1, 2, 5, 10, 20, 50 and 100 seconds. The assumed sampling frequency is 10 kS/s. The results are presented on graphs, with a logarithmic scale.

The authors compared the error value of the bin estimation parameter, for frequency $(1 - 2s)f_0$. Error values were received from the classic DFT method and the two and three-point interpolation. This paper compares results depending on the measurement time length, obtained after using the DFT method and two and three-point IpDFT methods. For the analysis RVCI windows of order: first (Hanning, $M = 1$) and third ($M = 3$) were used.

Results for the case when the sampling frequency was not a multiple of sf_0 (f_p/sf_0 and f_p/f_0 are irrational numbers), are presented in Figs. 1–2. Figures 1–2 include analysis from DFT method and two and three-point IpDFT methods.

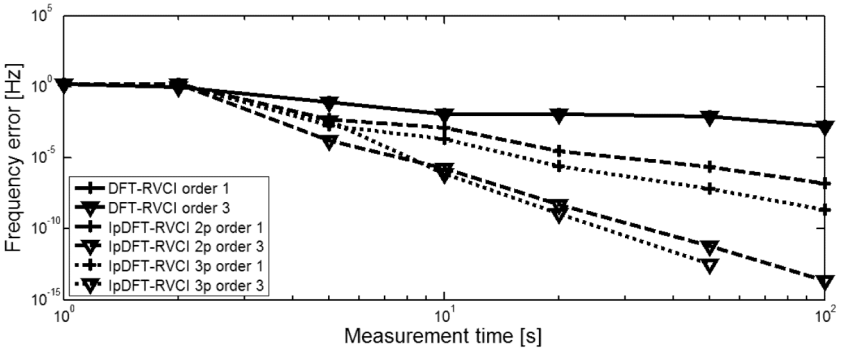

Fig. 1. Comparison of frequency error for DFT, two and three-point IpDFT method for chosen time windows

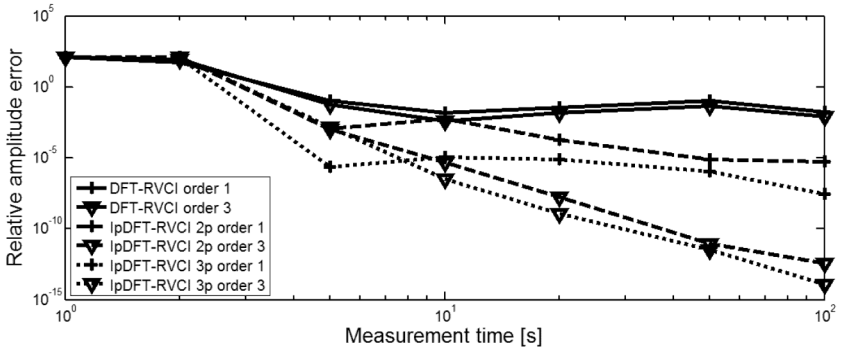

Fig. 2. Comparison of amplitude error for DFT, two and three-point IpDFT method for the chosen time windows

In the case of the frequency measurement, Fig. 1 exactly presents how the increase of the window order reduced the estimation error. It occurred for both IpDFT methods.

In the case of the classic DFT method, the window order had much less effect on the accuracy improvement.

For amplitude estimation and measurement time less than five seconds, the signal spectral analysis was practically impossible. It was caused by the spectral leakage. For measurement time longer than five seconds, the error value for IpDFT methods started to decrease. In the case of the classic DFT method, the error varied slightly during the entire measurement. Errors of measured parameters obtained from the classic DFT method can be reduced by proper selection of the windows order and the length of measurement time.

In the case of the two and three-point interpolated DFT method, the above mentioned selection can further help to reduce the measurement error [13]. Using a window of the third order, in the case of the amplitude estimation, reduces the relative measurement error value to the order of magnitude 10^{-13} for two-point IpDFT and up to 10^{-14} for three-point IpDFT.

Results obtained in Figs. 1–2 show that the two and three-point DFT interpolation method significantly improved the estimated signal parameters accuracy. This difference, however, was noticeable for measurement time longer than five seconds. For measurement time shorter than two seconds, measurement error was unacceptable for all three analyzed methods.

The authors did not use a rectangular window. For the near periodic signal, the leakage from the main bin for the rectangular window was minimal. Whereas there was a significant impact of the leakage spectrum from side lobes. Leakage from the main bin can be reduced by using a time window starting from the first order window. Figures 1–2 showed that the three-point interpolated DFT method gave better results than the classic DFT and two-point IpDFT methods for both windows of the first and third order, with measurement time extension.

4.2. Current analysis of a motor with a damaged cage

In this section, the authors present an analysis of the current signal from the transducer LEM, type HY-5, measuring one of motor phase currents with a damaged cage. The measurement was performed on the range 10 V with a resolution of 16 bits and a sampling frequency of 10 kS/s. The measurement time was 180 seconds. For frequency analysis, we used a 50 second time period, which was determined at 0.1 s. In this part, the results for the analyzed signal with the first and the third order RVCI windows are presented. For the rectangular window, the spectrum leakage was significant. This fact caused that the obtained measurement data were characterized by a high volatility and have not been presented in the article. The case of a signal spectrum with RVCI window of order 1, corresponding to the Hanning window, is presented in Fig. 3a). The signal spectrum with RVCI window of order 3 is shown in Fig. 3b).

Figure 3a) shows an extension of the main lobe and a decrease of spectrum leakage for the first order RVCI window. The reduction of spectrum leakage allowed for relatively stable measurements of signal parameters. For the third order RVCI window, Fig. 3b) shows that the main lobes were wider than in the previous cases, and some smaller value ripples disappeared. Graphs from Fig. 4 present the average value of lubricant harmonic frequency according to the first sample time. RVCI window of the first and the third order were used. All graphs are shown below, including results for the classic DFT method and the two and three-point interpolated DFT methods.

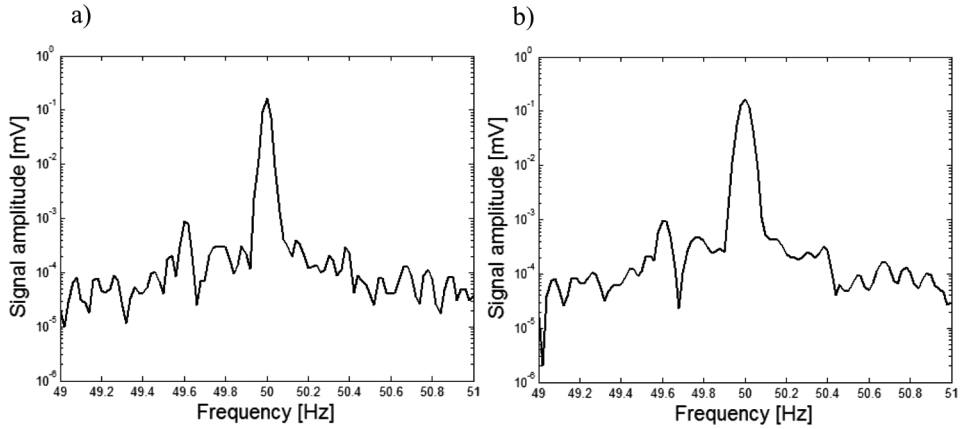

Fig. 3. Waveform of amplitude spectrum of current for the RVCI window: a) of the first order window; b) of the third order window

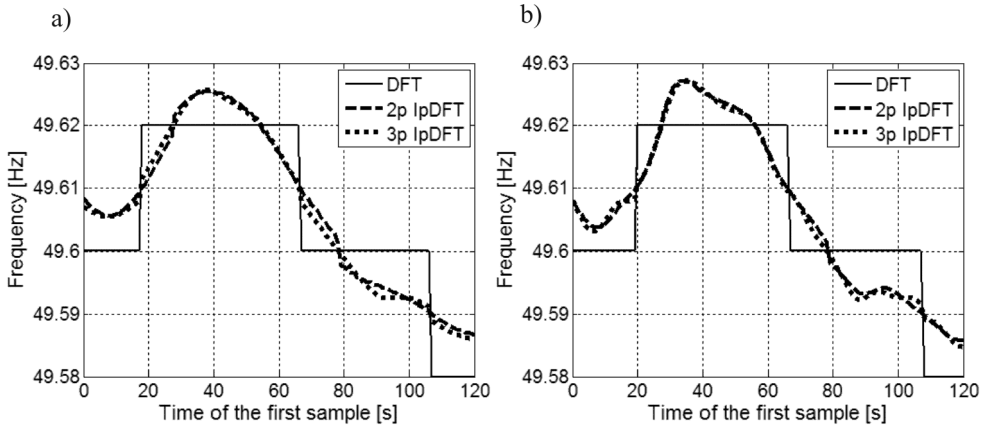

Fig. 4. Waveform of the average frequency value of the lubricant harmonic according to time of the first sample for the RVCI window: a) of the first order; b) of the third order

The analysis shows that the frequency resolution of the classic DFT method was 1/(50s) = 0.02 Hz and was significantly lower than for both IpDFT methods. In addition, in the case of IpDFT methods, small fluctuations in the frequency value could be observed. For the classic DFT method, the step change of frequency was connected with the step change of the curve slope angle (second derivative discontinuity).

In Figure 5, the authors present the average value of lubricant harmonic amplitude, according to the first sample time for the RVCI window of the first and the third order.

Figure 5 shows that the value fluctuations occurred while using all presented methods, but for two and three-point IpDFT, they were significantly lower. What is more, both IpDFT methods consistently did not produce less amplitude value than the DFT method. The value difference is greater when the difference of the estimated frequency increases.

Furthermore, the curve of amplitude for the two-point IpDFT method was smoother than for the DFT method. In addition, the amplitude curve for the three-point IpDFT method

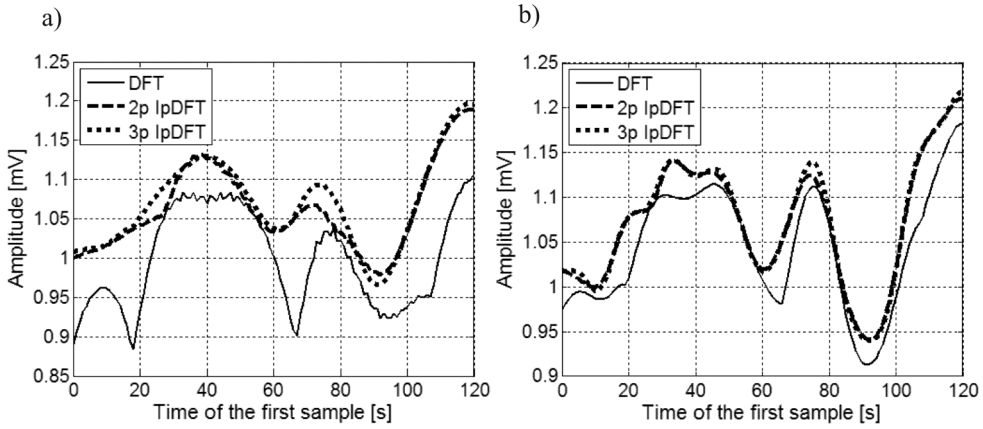

Fig. 5. Waveform of average amplitude of the lubricant harmonic depending on the first sample time for the RVCI window: a) of the first order; b) of the third order

had almost all ripples reduced. This made the three-point IpDFT more accurate in comparison with both mentioned methods. Comparing just the two and three-point IpDFT methods for the first order RVCI window, one can notice that the three-point IpDFT method gives smoother curves than the two-point IpDFT method.

Basing on Figs. 4b) and 5b), one can conclude that there is a minimization of fluctuation results for both frequency and amplitude. The obtained results were correlated with the results for the first order window. In addition, one can see the details of dynamic waveforms. As in the case of the first order window, IpDFT methods did not give less amplitude value than the classic DFT method. The difference grew with the increase of the estimated frequency. In addition, at the points of the step frequency changes, the increase of the window order had not completely wiped out a step change of the curve angle slope of the DFT waveform.

From the results one concludes that both IpDFT methods allowed estimating the lubricant harmonic value $(1 - 2s)f_0$ with a significantly higher resolution and less error than with the classic method of DFT. In addition, the window order increase allowed decreasing the spectral leakage, thereby reducing fluctuations in the received data and thus the measurement error.

Both two and three-point IpDFT methods gave quite similar results in the case of the third order RVCI window.

5. Conclusions

A comparative analysis of the advantages of different DFT methods in the diagnosis of the asynchronous motor has been achieved. It is shown how using the two and three-point IpDFT method improved the estimation accuracy of the parameters for $(1 - 2s)f_0$ bin. It is recommended to apply IpDFT methods in the case of testing low loaded engines, where the slip is uncontrolled, which implicates almost-periodic stator current.

Both two and three-point IpDFT methods can be effectively used in the diagnosis of electric machines. Particularly, the three-point IpDFT method can be the most useful because of

better fluctuation elimination. For respectively long measurement time, in the case of the real current signal from motor with damaged cage, the three-point IpDFT method gives the most reliable results from all compared methods in this article.

Moreover according to the results of the multi-frequency signal analysis, low order windows should be used for short measurement time. Analogously high order windows should be used for longer measurement time (high amount of samples). Using additionally adjusted time windows and extension of measurement time, error associated with the occurrence of the leakage spectrum can be reduced. The performed physical experiment confirmed the results obtained through simulation.

References

[1] Krzyk P., Sułowicz M., Pragłowska-Ryłko N., *Zastosowanie IpDFT do diagnostyki silników asynchronicznych*, Zeszyty Problemowe – Maszyny Elektryczne, 2014, nr 103, BOBRME Komel, pp. 293–300.

[2] Kowalski C.T., Kanior W., *Ocena skuteczności analiz FFT, STFT i falkowej w wykrywaniu uszkodzeń wirnika silnika indukcyjnego*, Prace Naukowe Instytutu Maszyn, Napędów i Pomiarów Elektrycznych Politechniki Wrocławskiej, nr 60, Wrocław 2007.

[3] Rusek J., *Komputerowa analiza maszyny indukcyjnej z wykorzystaniem bilansu harmonicznych*, Uczelniane Wydawnictwa Naukowo-Dydaktyczne AGH, Kraków 2000.

[4] Zając M., *Metody falkowe w monitoringu i diagnostyce układów elektromechanicznych*, seria: Inżynieria Elektryczna i Komputerowa, Monografia nr 371, Politechnika Krakowska, Kraków 2009.

[5] Thomson W.T., Fenger M., *Current signature analysis to detect induction motor faults*, IEEE Ind. Appl. Mag., 2001, Vol. 7, No. 4, pp. 26–34.

[6] Głowacz A., Głowacz Z., *Diagnostics of induction motor based on analysis of acoustic signals with application of FFT and classifier based on words*, Archives of Metallurgy and Materials, 2010, Vol. 55, Issue 3, pp. 707–712.

[7] Weinreb K., Sułowicz M., Petryna J., *Kompleksowa analiza uszkodzeń wirnika w maszynach indukcyjnych metodą rozdziału widma prądu stojana*, Zeszyty Problemowe, 2000, nr 61, BOBRME, Katowice, pp. 233–238.

[8] Weinreb K., Sułowicz M., Węgiel T., *Nieinwazyjna diagnostyka wirnika maszyny asynchronicznej*, Zeszyty Problemowe, 2004, nr 69, BOBRME, Katowice, pp. 35–40.

[9] Weinreb K., *Обнаружение динамического эксцентриситета и обрыва стержней клетки в асинхронном двигателе методом спектрального анализа тока статора. Научно-технические ведомости СПбГПУ*, Основной выпуск, 2008, №1(53), pp. 119–126.

[10] Sobczyk T.J., Weinreb K., Węgiel T., Sułowicz M., Warzecha A., Maciołek W., *Ocena skuteczności diagnostyki wirników silników klatkowych na podstawie widma prądów*, Materiały 13. Konferencji Energetyki „Energetyka – modernizacja i rozwój", Kliczków, 10–12.09.2003, pp. 167–176.

[11] Harris F.J., *On the use of windows for harmonic analysis with the discrete Fourier transform*, Proc. IEEE, Jan. 1978, Vol. 66, pp. 51–83.

[12] Zieliński T.P., *Cyfrowe przetwarzanie sygnałów, od teorii do zastosowań*, WKŁ, Warszawa 2005.
[13] Duda K., *Fourierowskie metody estymacji widm prążkowych*, Wydawnictwa AGH, Kraków 2011.
[14] Oppenheim A.V., Schafer R.W., Buck J.R., *Discrete-Time Signal Processing*, 2nd Edition, Prentice-Hall, 1999.
[15] Schoukens J., Pintelon R., Van hamme H., *The Interpolated Fast Fourier Transform: A Comparative Study*, IEEE Trans. Instrum. Meas., April 1992, Vol. 41, No. 2, pp. 226–232.
[16] Jain V.K., Collins W.L., Davis D.C., *High-Accuracy Analog Measurements via Interpolated FFT*, IEEE Trans. Instrum. Meas., June 1979, Vol. 28, No. 2, pp. 113–122.
[17] Grandke T., *Interpolation Algorithms for Discrete Fourier Transforms of Weighted Signals*, IEEE Trans. Instrum. Meas., June 1983, Vol. 32, No. 2, pp. 350–355.
[18] Andria G., Savino M., Trotta A., *Windows and interpolation algorithms to improve electrical measurement accuracy*, IEEE Trans. Instrum. Meas., 1989, Vol. 38, pp. 856–863.
[19] Offelli C., Petri D., *Interpolation Techniques for Real-Time Multifrequency Waveform Analysis*, IEEE Trans. Instrum. Meas., February 1990, Vol. 39, No. 1, pp. 106–111.

TECHNICAL TRANSACTIONS | **CZASOPISMO TECHNICZNE**
ELECTRICAL ENGINEERING | ELEKTROTECHNIKA
1-E/2015

KRZYSZTOF LUDWINEK*

FEMM UTILISATION IN REPRESENTATION OF INDUCTANCE DISTRIBUTIONS IN A SALIENT POLE SYNCHRONOUS GENERATOR CIRCUITAL MODEL IN NO-LOAD STATE

WYKORZYSTANIE FEMM DO ODWZOROWANIA ROZKŁADÓW INDUKCYJNOŚCI MODELU OBWODOWEGO GENERATORA SYNCHRONICZNEGO JAWNOBIEGUNOWEGO W STANIE BIEGU JAŁOWEGO

Abstract

This paper concerns a circuital model of a 5.5 kVA salient pole synchronous generator with damping bars, with and without the rotor skew. The paper presents an influence of the stator to rotor self and mutual inductance distribution on the induced voltages in the no-load steady state. Inductance distributions used in the circuital model are determined in the FEMM program for linear and nonlinear magnetic circuit. Simulation and experimental verification are presented.

Keywords: *synchronous generator*, *inductance distributions*, *induced voltages*

Streszczenie

W artykule przedstawiono wpływ rozkładów indukcyjności własnych i wzajemnych uzwojeń stojana i wirnika na indukowane napięcia w stanie biegu jałowego generatora synchronicznego jawnobiegunowego o mocy 5,5 kVA z klatką tłumiącą na wirniku bez skosu oraz ze skosem. Rozkłady indukcyjności użyte w modelu obwodowym wyznaczono w programie FEMM dla liniowego i nieliniowego obwodu magnetycznego. Przedstawiono wyniki badań symulacyjnych i eksperymentalnych.

Słowa kluczowe: *generator synchroniczny*, *rozkłady indukcyjności*, *indukowane napięcia*
DOI: 10.4467/2353737XCT.15.053.3853

* Ph.D. Eng. Krzysztof Ludwinek, Department of Electrical Machines and Mechatronic Systems, Kielce University of Technology.

1. Introduction

Both for a designer and a user, knowing about the harmonic contents of waveforms of induced voltages in the stator winding, a synchronous generator in the no-load and load steady states is very important [1–4]. Generator sets consume more fuel due to the presence of higher harmonic contents in the induced stator voltage and current waveforms. This has negative economic consequences.

In a no-load state, a magnetic flux density in the air gap of a synchronous generator is distorted due to: the influence of the stator and rotor slot opening [5]; the presence of the damping circuits [6]; saturation of the magnetic circuit (mainly low order odd harmonics) [7, 8]; magnetic rotor asymmetry; static and dynamic stator;rotor eccentricity; inside asymmetry [9–13]. Low power salient pole synchronous generators without the rotor (or stator) skew up to several kVA due to a single-layer stator winding have the largest content of higher harmonics (in low power synchronous generators less than 10 kVA dominate single layer windings) [14–19]. No rotor skew and the presence of single-layer stator winding causes a significant increase in higher harmonic order in self and mutual inductance distributions in circuital models of synchronous generators [14–19]. In cases of powering various types of sensitive loads (e.g. UPS, PC computers, notebooks, compact fluorescent lamps and different types of audio-video electronic equipment) the induced stator voltages and the armature currents are very distorted. This case is illustrated in Figure 1, where the comparison of registered waveforms of induced stator voltages u_a and u_b, field voltage U_f and current i_f in no load state for two salient pole synchronous generators with single-layer stator winding with and without the rotor skew are presented. The first generator rated data as follows: S_N = 5.5 VA; U_N = 400 V (*Y*); I_N = 7.9 A; cosφ$_N$ = 0.8; n_N = 3000 rpm; Q_s = 24, p = 1 (number of pole pairs); α_q = 15° (angle of rotor skew). The second generator rated data as follows: S_N = 10 kVA; U_N = 400 V (*Y*); I_N = 14.5 A; cosφ$_N$ = 0.8, n_N = 3000 rpm; Q_s = 24, p = 1, α_q = 0° (without the rotor skew). During the investigations, field winding is powered by a DC voltage source (U_f = const.).

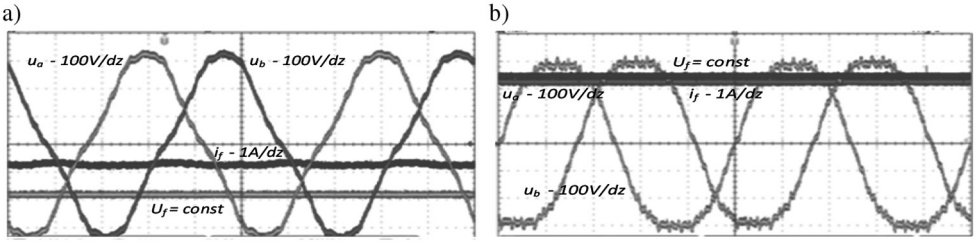

Fig. 1. Comparison of registered induced stator voltages in no load state for two salient pole synchronous generators: a) with the rotor skew, b) without the rotor skew

The total harmonic distortion ($THDu_a$) counted up to the 100th harmonic in the presented waveforms (in Fig. 1) of the induced phase voltages under no-load conditions are [18]:

- with the rotor skew $THDu_{as}$ = 8.41%,
- without the rotor skew $THDu_a$ = 10.21%.

The participation of the higher harmonics in the induced stator voltages is the most visible during the powering of sensitive receivers. The two synchronous generators (with and without the rotor skew) are used for powering a PC set-up (a PC unit, a monitor and a laser jet printer). In Figure 2, comparison of registered waveforms of the distorted load current i_a for the two salient pole synchronous generators with and without the rotor skew are presented. During the investigation, the field winding is powered by a DC voltage source (U_f = const.).

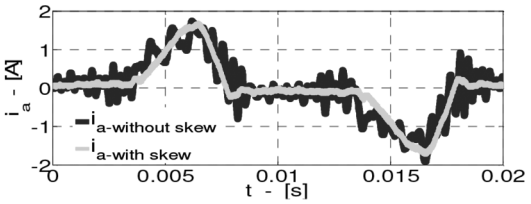

Fig. 2. Comparison of currents of two synchronous generators with and without the rotor skew

In Figure 3, the comparison of load current magnitudes with and without the rotor skew (Fig. 2) due to the Fourier analysis is presented.

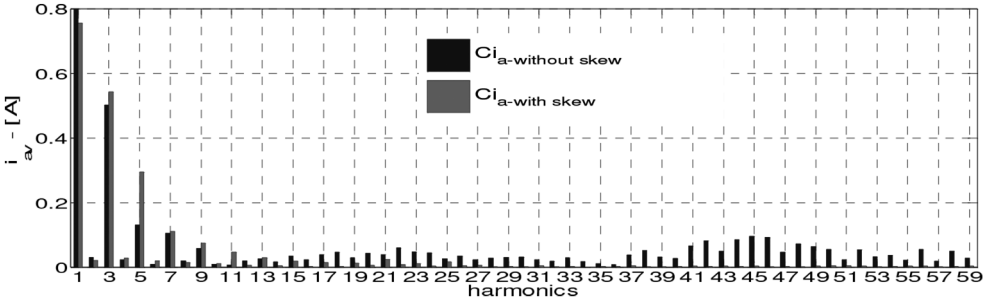

Fig. 3. Comparison of current magnitude harmonics

The total harmonic distortion counted up to the 100th harmonic in the presented waveforms (in Fig. 2) during powering the PC set-up are:

- with the rotor skew $THDi_{as}$ = 80.14%,
- without the rotor skew $THDi_a$ = 84.21%.

Although, from the 14th harmonic the higher harmonic contents are greater for the 10 kVA synchronous generator (without the rotor skew) than for the 5.5 kVA version (with the rotor skew) due to saturation of the magnetic circuit (mainly 3rd and 5th harmonics Figs. 2 and 3 and lower fundamental magnitude for generator with the rotor skew than without the rotor skew), the total harmonic distortion for the synchronous generator with the rotor skew $THDi_{as}$ is equal to 80.14%. It is similar to $THDi_a$ = 84.21% (for the synchronous generator without the rotor skew). In the presented waveforms (in Fig. 2), the harmonic contents can be calculated by the Telephone Harmonic Factor $THFi_a$ (from 14th to the 100th harmonic):

- with the rotor skew $THFi_{as}$ = 44.21%,
- without the rotor skew $THFi_{a}$ = 6.22%.

From presented Figs. 1–3 results, that about a better quality of synchronous generator can decide the harmonic contents in induced stator voltages in the no-load state.

The most important aspect in simulations using a circuital model of a synchronous generator is choosing suitable reference frames and the presence of the damping circuits [5, 6, 8–10, 14–17]. Studies of synchronous generators using circuital models are very popular in the rotor reference frame $dq0$ due to constant inductance distributions. But this assumption (constant inductance distributions) is true if the self and mutual inductances of the stator windings contain only the constant component and the same magnitude of the 2nd harmonic [19]. As shown in [19], for linear and nonlinear magnetic circuit the Park's transformation of the higher harmonics of the stator self and mutual inductance distributions to the $dq0$-axes introduces only additional unnecessary calculations (because not only the self inductance distributions in the $dq0$-axes but also the mutual ones contain higher harmonics) [19].

This paper presents an influence of the stator to rotor self and mutual inductance and derivative distributions on the waveforms of induced phase stator voltages in the no-load steady state of the nonlinear 5.5 kVA salient pole synchronous generator with damping bars on the rotor with and without the skew. In the circuital model, the self and mutual inductance distributions are obtaind using the FEMM program. Detailed analysis of the influence of the rotor skew on the reduction of higher harmonics in self and mutual inductances are presented in [14–19].

2. Model of a salient pole synchronous generator in the stator and rotor natural reference frame

Due to contents of higher harmonics in the self and mutual inductance distributions in the $dq0$-axes, simulations of the induced phase stator voltages u_a, u_b and u_c with a circuital model of a salient pole synchronous generator is easier to carry out in the stator and the rotor natural reference frame [19]. In Figure 4, the equivalent circuit parameters of a salient pole synchronous generator in the no-load state are presented [17].

The circuit model (Fig. 4) consists of the field winding, three phase stator windings (i_a, i_b and i_c are equal to 0) and damping bars (5 bars per pole) with segment of rings. On differential linkage fluxes in no-load state have the influence the electrical angle of the rotor position θ, the field current (i_f) and currents in the equivalent 10 damping bars and ring segments ($i_{r(1)}$, ..., $i_{r(10)}$). As shown in [14], the amplitudes of higher harmonic currents $i_{r(1)v}$, ..., $i_{r(10)v}$ in the no-load steady state of the 5.5 kVA salient pole synchronous generator are very small. In this condition, on the magnetic flux distribution the field winding ampere-conductors have significant influence and the damping bar ampere-conductors can be omitted. So, in the no-load steady state it can be assumed that on the self and mutual inductance distributions have influence only the electrical angle of the rotor position θ and field current i_f.

In the circuital model (Fig. 4), the induced stator phase voltages u_a, u_b, u_c, the field voltage u_f and the induced voltage in the k-th shorted equivalent damping bar can be expressed as [17]:

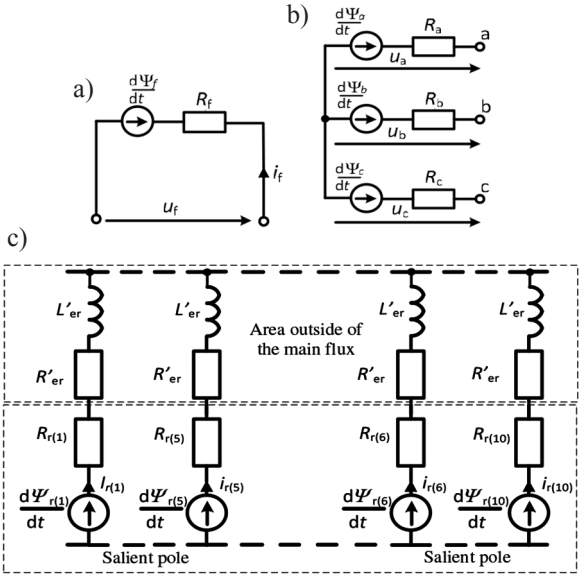

Fig. 4. Equivalent circuit parameters of a salient pole synchronous generator in the stator and rotor natural reference frame a) field winding, b) stator windings, c) damping circuits

$$\frac{\mathrm{d}\psi_a(\theta,i_f)}{\mathrm{d}t}=u_a,\quad \frac{\mathrm{d}\psi_b(\theta,i_f)}{\mathrm{d}t}=u_b,\quad \frac{\mathrm{d}\psi_c(\theta,i_f)}{\mathrm{d}t}=u_c \tag{1}$$

$$\frac{\mathrm{d}\psi_f(\theta,i_f)}{\mathrm{d}t}+R_f i_f=u_f \tag{2}$$

$$\frac{\mathrm{d}\psi_{r(k)}(\theta,i_f)}{\mathrm{d}t}+R_{r(k)}i_{r(k)}+L_{er}\frac{i_{r(k)}}{\mathrm{d}t}=0 \tag{3}$$

$$\frac{\mathrm{d}\theta}{\mathrm{d}t}=p\omega \quad \text{and} \quad i_{r(1)}+i_{r(2)}+\ldots+i_{r(k)}=0 \tag{4}$$

where:

a, b, c, f – indexes of stator windings and field winding,
$\Psi_a, \Psi_b, \Psi_c, \Psi_f$ – stator and field winding linkage fluxes,
u_a, u_b, u_c, u_f – stator phase voltages and field voltage,
R_f – resistance of the field winding,
i_f – field current,
$r(k)$ – index of k-th-damping bar $k = \{1, 2, \ldots, 10\}$,
$\Psi_{r(k)}$ – k-th damping bar linkage flux,
$R_{r(k)}$ – resistance of equivalent damping bar and ring elements.

$$R_{r(k)} = R_{pr} + R_{er}/\{2\sin^2(\alpha_{(k)})\} = R_{pr} + R'_{er},$$

R_{pr}, R'_{er} – resistance of damping bar (in area of main flux) and equivalent ring elements (in area outside of main flux),
$\alpha_{(k)}$ – an angle between the equivalent k-th rotor damping bar (with ring elements) and the rotor reference axis, $\alpha_{(k)} = p\pi/Q_r$,
Q_r – number of rotor bars,
L'_{er} – equivalent inductance of end ring elements, $L'_{er} = L_{er}/\{2\sin^2(\alpha_{(k)})\}$,
$i_{r(k)}$ – current in k-th damping bars and ring elements,
θ – electrical angle of the rotor position $\theta = \theta_m p$,
θ_m – mechanical angle of the rotor position,
ω – electrical angular velocity $\omega = (1/p)\cdot d\theta/dt$.

The differential linkage fluxes can be derived from the following equations:

$$\frac{\mathrm{d}\boldsymbol{\psi}_{sfr}(\theta, i_f)}{\mathrm{d}t} = \frac{\mathrm{d}\theta}{\mathrm{d}t}\frac{\partial \mathbf{L}_{sfr}(\theta,\ i_f)}{\partial\theta}\mathbf{i}_{sfr} + \mathbf{L}_{sfr}(\theta,\ i_f)\frac{\mathrm{d}\mathbf{i}_{sfr}}{\mathrm{d}t} \tag{5}$$

where:
$\mathbf{i}_{sfr}$ – matrix of the stator currents (equal to zero), field current and currents in the equivalent 10 damping bars and ring elements $[0, 0, 0, i_f, i_{r(1)}, \ldots, i_{r(10)}]^T$,
$\boldsymbol{\Psi}_{sfr}$ – matrix of linkage fluxes of stator windings, field winding, and equivalent 10 damping bars $[\Psi_a, \Psi_b, \Psi_c, \Psi_f, \Psi_{r(1)}, \ldots, \Psi_{r(10)}]^T$, whereas $\boldsymbol{\Psi}_{sfr} = \mathbf{L}_{sfr}\mathbf{i}_{sfr}$,
$\mathbf{L}_{sfr}$ – matrix of self and mutual inductances of stator-to-rotor windings and damping bars (and ring elements) can be expressed as:

$$\mathbf{L}_{sfr}(\theta,\ i_f) = \begin{bmatrix} L_a + L_{es} & L_{ab} & L_{ac} & L_{af}(\theta,\ i_f) & L_{ar(1)}(\theta,\ i_f) & \ldots & L_{ar(10)}(\theta,\ i_f) \\ L_{ba} & L_b + L_{es} & L_{bc} & L_{bf}(\theta,\ i_f) & L_{br(1)}(\theta,\ i_f) & \ldots & L_{br(10)}(\theta,\ i_f) \\ L_{ca} & L_{cb} & L_c + L_{es} & L_{cf}(\theta,\ i_f) & L_{cr(1)}(\theta,\ i_f) & \ldots & L_{cr(10)}(\theta,\ i_f) \\ L_{fa}(\theta,\ i_f) & L_{fb}(\theta,\ i_f) & L_{fc}(\theta,\ i_f) & L_f(\theta,\ i_f) + L_{ef} & L_{fr(1)}(\theta,\ i_f) & \ldots & L_{fr(10)}(\theta,\ i_f) \\ L_{r(1)a}(\theta,\ i_f) & L_{r(1)b}(\theta,\ i_f) & L_{r(1)c}(\theta,\ i_f) & L_{r(1)f}(\theta,\ i_f) & L_{r(1)}(\theta,\ i_f) + L_{er} & \ldots & L_{r(1,10)}(\theta,\ i_f) \\ \ldots & \ldots & \ldots & \ldots & \ldots & \ldots & \ldots \\ L_{r(10)a}(\theta,\ i_f) & L_{r(10)b}(\theta,\ i_f) & L_{r(10)c}(\theta,\ i_f) & L_{r(10)f}(\theta,\ i_f) & L_{r(10,1)}(\theta,\ i_f) & \ldots & L_{r(10)}(\theta,\ i_f) + L_{er} \end{bmatrix}$$

where:
L_{af}, L_{bf}, L_{cf} – mutual inductance of the stator windings to the field winding (L_{fa}, L_{fb}, L_{fc}),
$L_{ar(k)}$, $L_{br(k)}$, $L_{cr(k)}$ – mutual inductance of the stator windings to k-th damping bar and ring element ($L_{r(k)a}$, $L_{r(k)b}$, $L_{r(k)c}$),
L_f – self inductance of the field winding,
$L_{fr(k)}$ – mutual inductance of the field winding to k-th damping bar and ring element ($L_{r(k)f}$),
$L_{r(k)}$ – self inductance of k-th damping bar and ring element,
L_{es}, L_{ef}, L_{er} – leakage inductance of stator winding, field winding and ring element.

From relations (1) to (5) in the no-load state, the matrix describing induced stator voltages whilst taking into account 10 damping bars with the ring segments can be expressed as [17]

$$\begin{bmatrix} u_a \\ u_b \\ u_c \end{bmatrix} = \omega \frac{\partial}{\partial \theta} \begin{bmatrix} L_{af}(\theta,\, i_f) & L_{ar(1)}(\theta,\, i_f) & \ldots & L_{ar(10)}(\theta,\, i_f) \\ L_{bf}(\theta,\, i_f) & L_{br(1)}(\theta,\, i_f) & \ldots & L_{br(10)}(\theta,\, i_f) \\ L_{cf}(\theta,\, i_f) & L_{cr(1)}(\theta,\, i_f) & \ldots & L_{cr(10)}(\theta,\, i_f) \end{bmatrix} \begin{bmatrix} i_f \\ i_{r(1)} \\ \ldots \\ i_{r(10)} \end{bmatrix} + \tag{6}$$

$$\begin{bmatrix} L_{af}(\theta,\, i_f) & L_{ar(1)}(\theta,\, i_f) & \ldots & L_{ar(10)}(\theta,\, i_f) \\ L_{bf}(\theta,\, i_f) & L_{br(1)}(\theta,\, i_f) & \ldots & L_{br(10)}(\theta,\, i_f) \\ L_{cf}(\theta,\, i_f) & L_{cr(1)}(\theta,\, i_f) & \ldots & L_{cr(10)}(\theta,\, i_f) \end{bmatrix} \frac{\mathrm{d}}{\mathrm{d}t} \begin{bmatrix} i_f \\ i_{r(1)} \\ \ldots \\ i_{r(10)} \end{bmatrix}$$

From relations (1) to (5) in the no-load state, the matrix describing circuits of the field winding and the equivalent 10 damping bars with the ring segments can be expressed as:

$$\begin{bmatrix} \boldsymbol{u}_f \\ 0 \\ \ldots \\ 0 \end{bmatrix} = \left\{ \omega \frac{\partial}{\partial \theta} \begin{bmatrix} \boldsymbol{L}_f(\theta,\, \boldsymbol{i}_f) + \boldsymbol{L}_{ef} & \boldsymbol{L}_{fr(1)}(\theta,\, \boldsymbol{i}_f) & \ldots & \boldsymbol{L}_{fr(10)}(\theta,\, \boldsymbol{i}_f) \\ \boldsymbol{L}_{r(1)f}(\theta,\, \boldsymbol{i}_f) & \boldsymbol{L}_{r(1)}(\theta,\, \boldsymbol{i}_f) + L_{er} & \ldots & \boldsymbol{L}_{r(1,10)}(\theta,\, \boldsymbol{i}_f) \\ \ldots & \ldots & \ldots & \ldots \\ \boldsymbol{L}_{r(10)f}(\theta,\, \boldsymbol{i}_f) & \boldsymbol{L}_{r(1,10)}(\theta,\, \boldsymbol{i}_f) & \ldots & \boldsymbol{L}_{r(10)}(\theta,\, \boldsymbol{i}_f) + L_{er} \end{bmatrix} + \begin{bmatrix} \boldsymbol{R}_f & 0 & \ldots & 0 \\ 0 & \boldsymbol{R}_{r(1)} & \ldots & 0 \\ \ldots & \ldots & \ldots & \ldots \\ 0 & 0 & \ldots & \boldsymbol{R}_{r(10)} \end{bmatrix} \right\} \begin{bmatrix} \boldsymbol{i}_f \\ \boldsymbol{i}_{r(1)} \\ \ldots \\ \boldsymbol{i}_{r(10)} \end{bmatrix} +$$

$$+ \begin{bmatrix} \boldsymbol{L}_f(\theta,\, \boldsymbol{i}_f) + \boldsymbol{L}_{ef} & \boldsymbol{L}_{fr(1)}(\theta,\, \boldsymbol{i}_f) & \ldots & \boldsymbol{L}_{fr(10)}(\theta,\, \boldsymbol{i}_f) \\ \boldsymbol{L}_{r(1)f}(\theta,\, \boldsymbol{i}_f) & \boldsymbol{L}_{r(1)}(\theta,\, \boldsymbol{i}_f) + L_{er} & \ldots & \boldsymbol{L}_{r(1,10)}(\theta,\, \boldsymbol{i}_f) \\ \ldots & \ldots & \ldots & \ldots \\ \boldsymbol{L}_{r(10)f}(\theta,\, \boldsymbol{i}_f) & \boldsymbol{L}_{r(1,10)}(\theta,\, \boldsymbol{i}_f) & \ldots & \boldsymbol{L}_{r(10)}(\theta,\, \boldsymbol{i}_f) + L_{er} \end{bmatrix} \frac{\mathbf{d}}{\mathbf{d}\square} \begin{bmatrix} \boldsymbol{i}_f \\ \boldsymbol{i}_{r(\square)} \\ \ldots \\ \boldsymbol{i}_{r(\square 0)} \end{bmatrix} \tag{7}$$

In expression (7), the significant simplification of the description of the model (in relation to classical circuit model) is the diagonal matrix of resistance (of field winding and damping bars with ring segments).

3. Determination of the self and mutual inductance distributions

Figure 5 presents magnetic flux distribution lines obtained using the FEMM program [11–14] for the examined nonlinear 5.5 kVA salient pole synchronous generator (with and without the rotor skew with shorted 10 equivalent damping bars) rated: S_N = 5.5 kVA; U_N = 400 V (*Y*); n_N = 3000 rpm; I_N = 7.9 A; cosφ_N = 0.8; p = 1; Q_s = 24; α_q = 15° (factory rotor skew equal to stator slot pitch). In FEMM software, the magnetic field distribution (Fig. 5) and inductance distributions are obtained from current flowing in the field winding (in Fig. 5, two upper and two lower slots on the rotor) as a function of the electrical rotor position an-

gle θ. The calculations are carried out on the basis of the real construction data of the 5.5 kVA synchronous generator in the no load steady state with initial rotor position $\theta_0 = 0$ (Fig. 5). A method of determining the self and mutual inductance distributions in FEMM program is presented in [17].

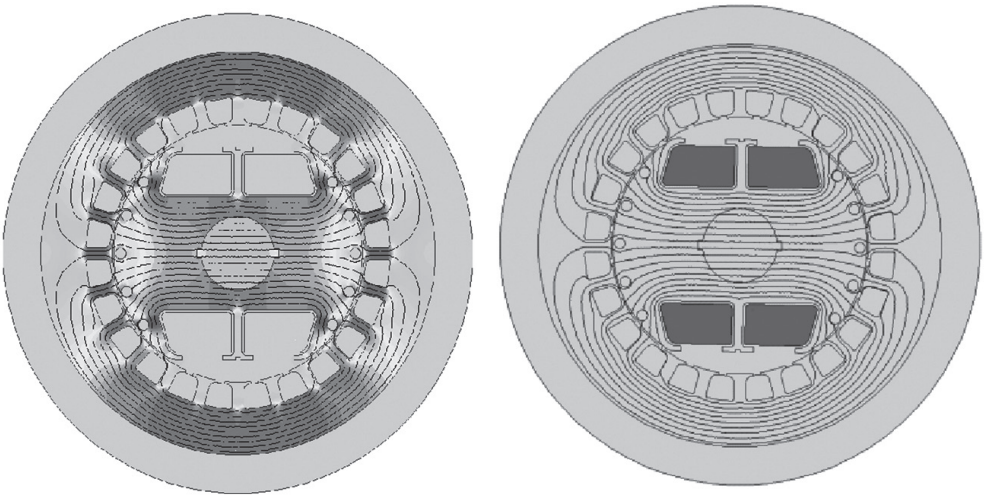

Fig. 5. Distribution lines in the 5.5 kVA salient pole synchronous generator with 10 damping bars in the no-load state a) magnetic flux density, b) current density in the field winding

In the induced stator voltages (6) in the no-load state, one of the most important are stator to field winding inductance distributions. The fundamental components of the induced stator voltages u_{a1}, u_{b1}, u_{c1} are the products of electrical angular velocity ω and mutual inductance derivative distributions ($\partial L_{af1}/\partial\theta$), $\partial L_{bf1}/\partial\theta$), $\partial L_{cf1}/\partial\theta$)) and constant component of the field current i_{f0}. Each phase stator winding gives the product $u_{a1} = \omega(\partial L_{af1}/\partial\theta)i_{f0}$, $u_{b1} = \omega(\partial L_{bf1}/\partial\theta)i_{f0}$, and $u_c = \omega(\partial L_{af1}/\partial\theta)i_{f0}$. In the case of winding, symmetry the voltage magnitudes are equal.

Figures 6–12 contain the next indicates: *s* – index with the rotor skew; *n* – index for nonlinear model. Figure 6 shows the comparison of the stator to field winding mutual distributions for the nonlinear model without the rotor skew (L_{af}). In the case of the nonlinear model, the influence of saturation on the inductance distribution for better visibility is presented from 120° to 240° (Fig. 6b)). The mutual inductance distribution for the nonlinear model with the rotor skew (Fig. 6) is very similar to the model without the rotor skew. The differences are only visible after calculation of the product $\omega\partial L_{afsn}/\partial\theta$ and $\omega\partial L_{afn}/\partial\theta$ (nonlinear model with and without the rotor skew – Fig. 7a)) or the product $\omega\partial L_{afsn}/\partial\theta$ and $\omega\partial L_{afn}/\partial\theta$ in relation to $\omega\partial L_{af1}/\partial\theta$ (fundamental component of linear model – Fig. 7b)) and in higher harmonic contents due to the Fourier analysis (Fig. 8). In Figure 8c), higher harmonic contents from 65^{th} to 75^{th} (in the zoom window from 0 to 1%) are presented.

Figure 9 shows the comparison of the mutual stator to damping bars (5 damping bars per pole) inductance and the inductance derivative distributions without the rotor skew (in relation to the linear one) and higher harmonic contents due to the Fourier analysis (Fig. 10).

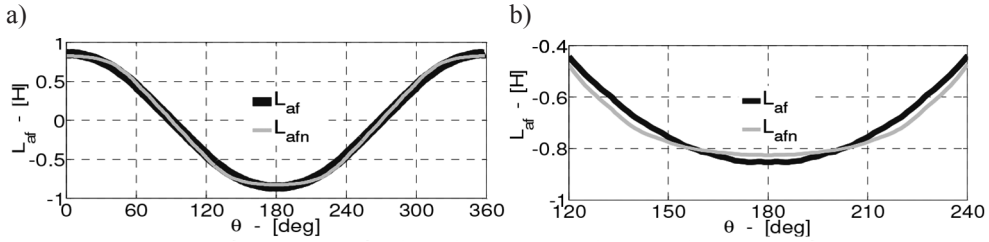

Fig. 6. Comparison of the stator to field winding mutual inductance distributions for the linear and nonlinear model without the rotor skew L_{af} and L_{afn} a) θ = 0°–360°, b) θ =120°–240°

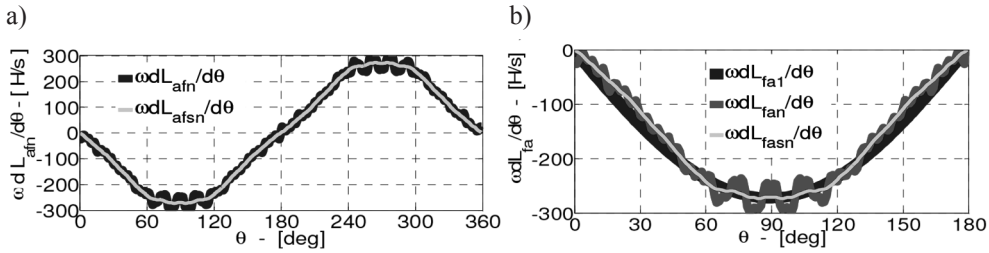

Fig. 7. Comparison of the stator to field winding mutual distributions of the product a) $\omega\partial L_{afn}/\partial\theta$ and $\omega\partial L_{afsn}/\partial\theta$, b) $\omega\partial L_{af1}/\partial\theta$, $\omega\partial L_{afn}/\partial\theta$, and $\omega\partial L_{afsn}/\partial\theta$ (in zoom window from θ = 0° to θ = 180°)

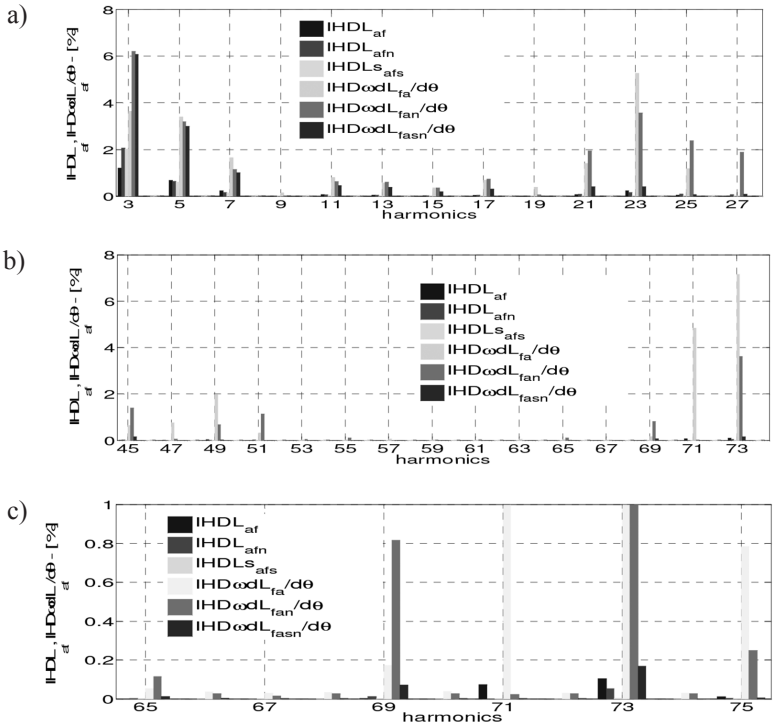

Fig. 8. Comparison of harmonic contents of the stator to field winding mutual inductance and inductance derivative distributions a) from 3rd to 29th, b) from 39th to 63th, c) from 65th to 75th

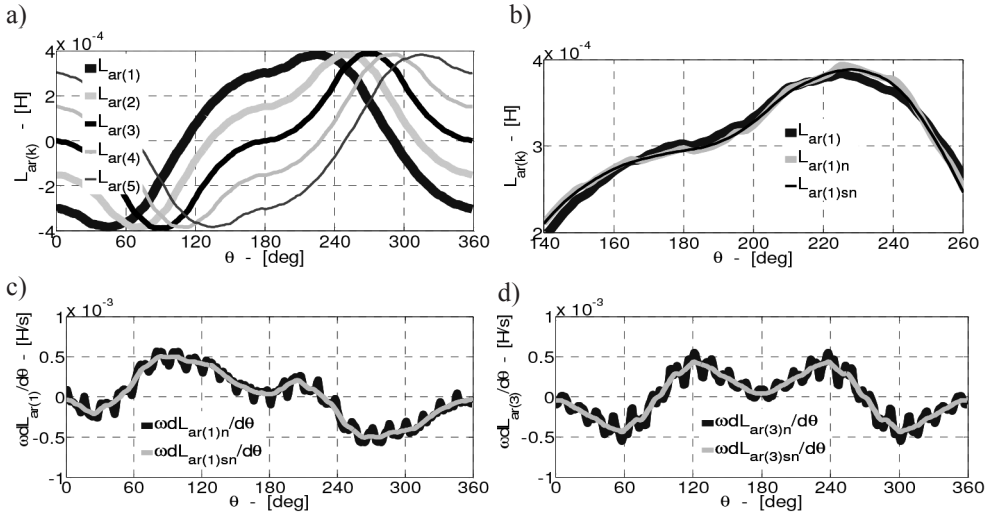

Fig. 9. Comparison of the mutual stator to damping bar inductance and the inductance derivative distributions for the linear and nonlinear model a) $L_{ar(1)}$ - $L_{ar(5)}$, b) $L_{ar(1)}$, $L_{ar(1)n}$, and $L_{ar(1)sn}$ (in zoom window from θ = 140° to θ = 260° for better visibility), c) products of $\omega\partial L_{ar(1)n}/\partial\theta$ and $\omega\partial L_{ar(1)sn}/\partial\theta$, d) products of $\omega\partial L_{ar(3)n}/\partial\theta$ and $\omega\partial L_{ar(3)sn}/\partial\theta$

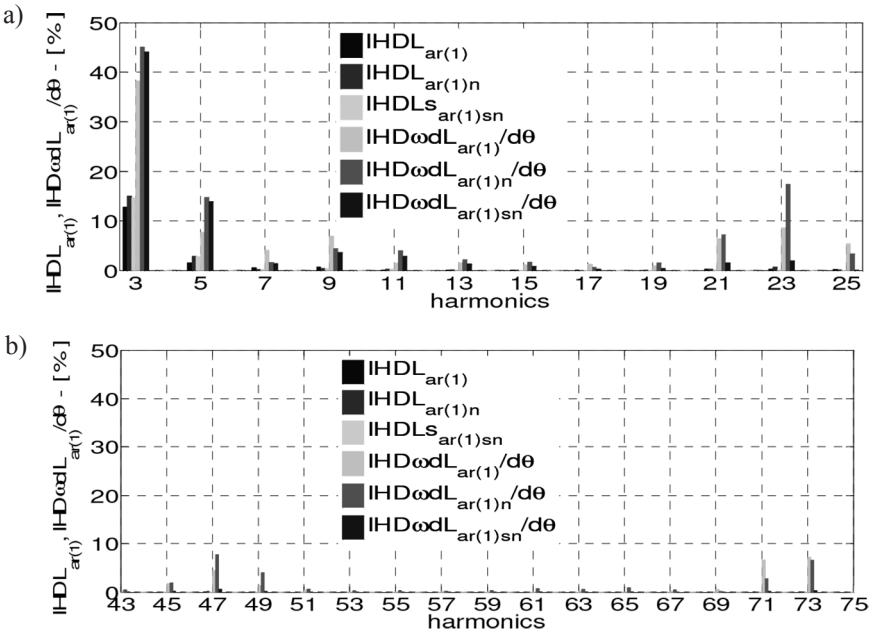

Fig. 10. Comparison of harmonic contents of the stator to damping bar mutual inductance and inductance derivative distributions of a) from 3rd to 25th, b) from 43rd to 75th

In the harmonic spectrum comparison of the mutual inductance and the inductance derivative distributions (Figs. 8 and 10), it can be seen that odd harmonics dominate. The greatest reduction of the higher harmonic order is achieved by the rotor skew. From the harmonic spectrum comparison results, it can be seen that for the examined 5.5 kVA salient pole synchronous generator without the rotor skew, the participation of, for example, the 73rd harmonic of the stator to field winding mutual inductance distribution is very small and is only 0.1% (with relation to the fundamental component Fig. 8c)). In the case of calculating the mutual inductance derivative (Fig. 8), the value is enhanced 73 times by the derivative order value and the participation increases to 7.3% (with respect to the derivative fundamental component). Similarly, the participation of the other higher harmonics that are the most visible in the inductance distributions (Figs. 8 and 10) are enhanced by the derivative order value [16].

In the case of the mutual inductance and the inductance derivative distributions of the stator to rotor damping bar with and without the rotor skew, the most significant is the 3rd harmonic. A skew of the rotor has a significant influence on the reduction in higher-order harmonic [16–19]. So, the lower-order harmonics (for example, caused by the saturation of the magnetic circuit) are only slightly reduced due to the rotor skew (Figs. 8 and 10).

As shown in [15], the field current (7) depends on the method of powering the field winding. Moreover, the field current and currents in 10 damping bars depend on the self and mutual rotor inductance and inductance derivative distributions (7). Figure 11 shows the comparison of the field winding self inductance and the inductance derivative distributions without the rotor skew and higher harmonic contents due to the Fourier analysis.

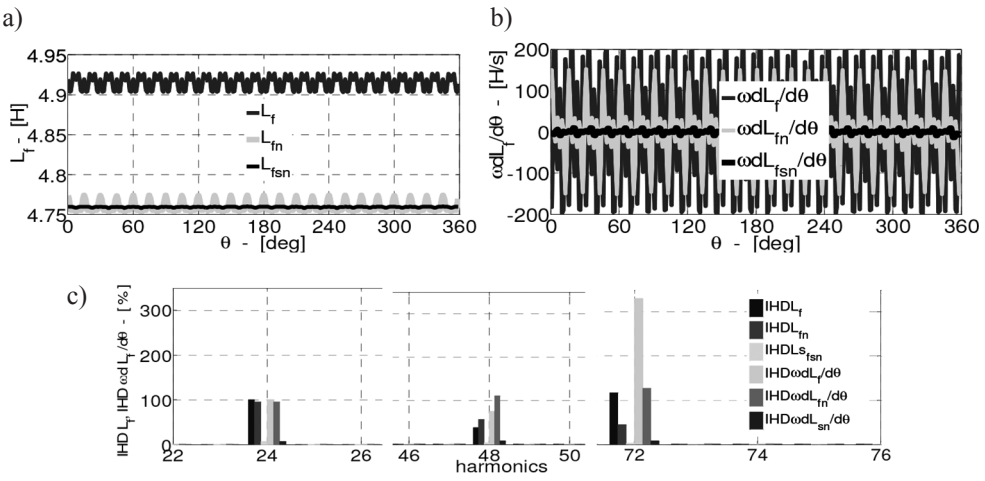

Fig. 11. Comparison of the field winding a) self inductance distributions for linear and nonlinear model, b) products of ω($\partial L_f/\partial\theta$), ω($\partial L_{fn}/\partial\theta$) and ω($\partial L_{fsn}/\partial\theta$), c) detailed harmonic contents of the inductance and inductance derivative distributions for 24th, 48th and 72nd order

In Figure 12, the comparison of the field winding to damping bars mutual inductance distributions $L_{fr(1)n}$ - $L_{fr(5)n}$ ($L_{fr(6)n}$ - $L_{fr(10)n}$), the product of ω($\partial L_{fr(1)sn}/\partial\theta$) and ω($\partial L_{fr(1)n}/\partial\theta$) for nonlinear model (with and without the rotor skew) and the harmonic contents in relation to the constant component of $L_{fr(0)}$ due to the Fourier analysis are presented. The differences be-

tween $L_{fr(1)} - L_{fr(5)}$ ($L_{fr(6)} - L_{fr(10)}$) and $L_{fr(1)n} - L_{fr(5)n}$ ($L_{fr(6)n} - L_{fr(10)n}$) for linear and nonlinear models are very small and therefore, in Fig. 12, is shown only the nonlinear model.

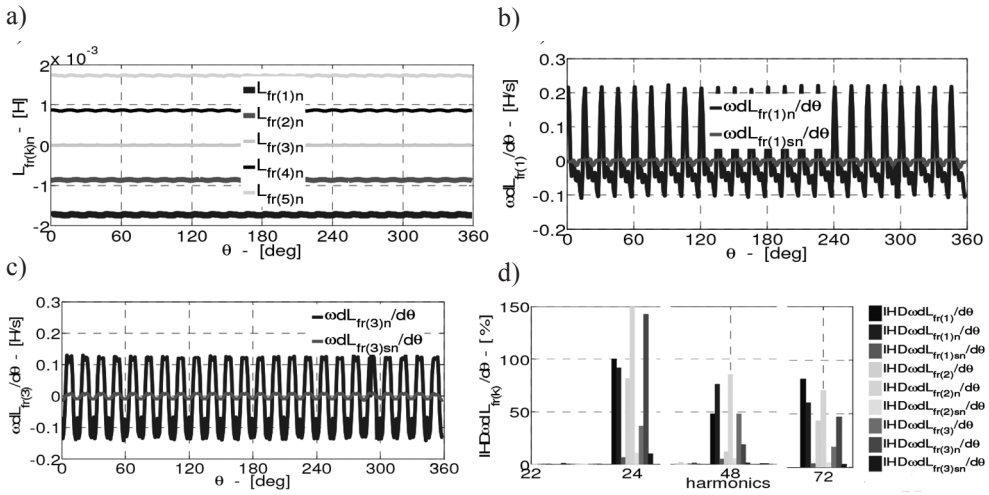

Fig. 12. Distributions of a) the field winding to damping bars mutual inductance, b) products $\omega(\partial L_{fr(1)n}/\partial\theta)$ and $\omega(\partial L_{fr(1)sn}/\partial\theta)$, c) products $\omega(\partial L_{fr(3)n}/\partial\theta)$ and $\omega(\partial L_{fr(3)sn}/\partial\theta)$, d) harmonic contents

4. Numerical simulations using the circuital model

Simulation studies of the influence of the DC voltage powering the field winding on higher harmonic contents in the induced stator phase voltages and the field and damping bar currents under no-load steady state conditions for the examined 5.5 kVA salient pole synchronous generator with and without the rotor skew are obtaind using the circuital model – expressions (6) and (7). Figure 13 shows the transient state of currents in 5 damping bars (per pole) after switching on the DC voltage that is powering the field winding.

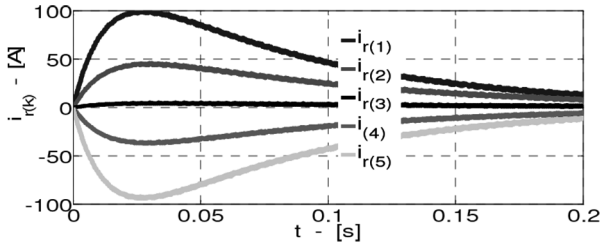

Fig. 13. Transient state of currents in 5 damping bars

Presented in Figs. 14–16, waveforms and harmonic contents are obtaind in an almost steady state. Figure 14 shows current waveforms $i_{r(1)}$ (without the rotor skew) and $i_{r(1)s}$ (with the rotor skew), the current derivatives $\mathrm{d}i_{r(1)}/\mathrm{d}t$ and $\mathrm{d}i_{r(1)s}/\mathrm{d}t$ and harmonic contents due to the Fourier analysis of the nonlinear model.

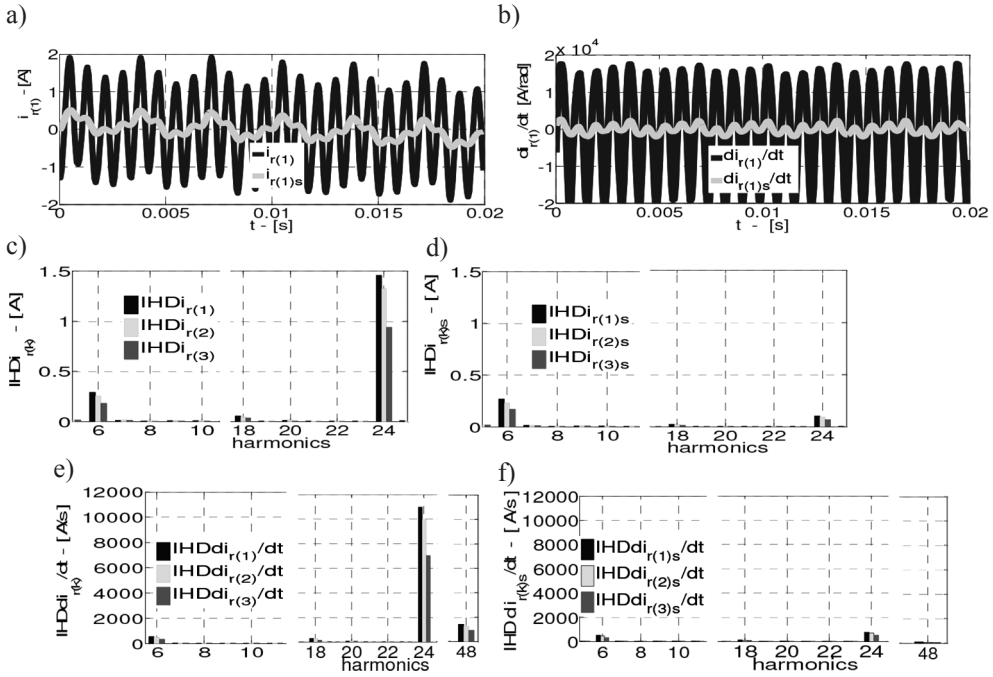

Fig. 14. Comparison of a) the currents $i_{r(1)}$ and $i_{r(1)s}$, b) the derivatives d$i_{r(1)}$/dt and d$i_{r(1)s}$/dt, c) and d) and e) and f) harmonic contents of $i_{r(1),}$ $i_{r(2)}$, $i_{r(3)}$ and $i_{r(1)s}$, $i_{r(2)s}$, $i_{r(3)s}$, d$i_{r(1)}$/dt, d$i_{r(2)}$/dt, d$i_{r(3)}$/dt and d$i_{r(1)s}$/dt, d$i_{r(2)s}$/dt, d$i_{r(3)s}$/dt

Figure 15 shows current waveforms i_f (without the rotor skew) and i_{fs} (with the rotor skew), the current derivatives di_f/dt and di_{fs}/dt and harmonic contents due to the Fourier analysis.

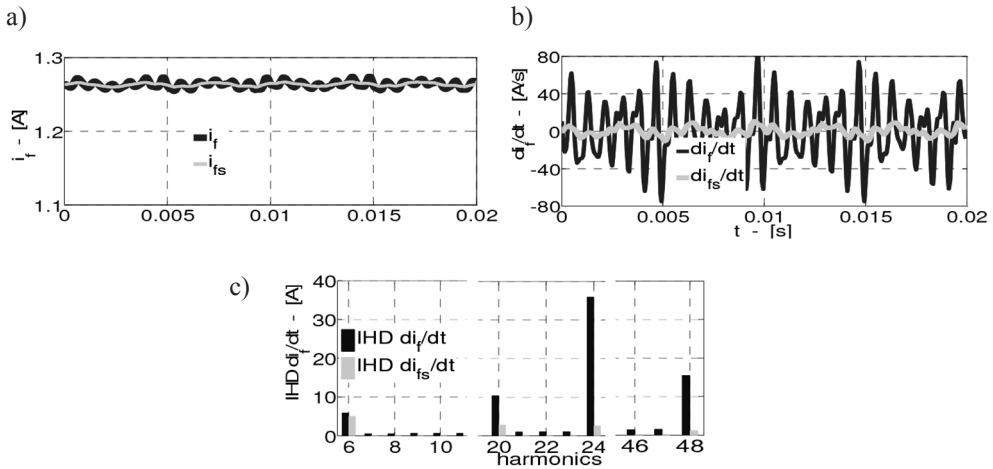

Fig. 15. Comparison of a) current waveforms i_f and i_{fs}, b) derivatives di_f/dt and di_f/dt, c) harmonic contents

As shown in Figs. 14 and 15, due to the presence of the $Q_s = 24$ open stator slots in some damping bars on the rotor $k = \{1, 5, 6, 10\}$ the current derivative $\mathrm{d}\mathbf{i}_{r(k)}/\mathrm{d}t$ for the 24th harmonic has a value of almost 11 kA/s. Moreover, the current derivative $\mathrm{d}\mathbf{i}_f/\mathrm{d}t$ for the same harmonic has a value of almost 36 A/s. This implies in the circuital model that in (6), the product of the stator to rotor mutual inductance distributions and rotor current derivatives (in the model without the rotor skew) have a significant impact on induced stator voltages in the no-load state. For the model with the rotor skew in the waveform of the rotor current derivatives dominate the low order 6th harmonic because the 24th harmonic is reduced due to the rotor skew.

Figure 16 shows the simulation of the induced stator phase voltage waveforms u_{as}, u_{bs}, and u_{cs} and u_a, u_b, and u_c (with and without the rotor skew) when the DC voltage is powering the field winding of the examined nonlinear 5.5 kVA synchronous generator. Moreover, in Fig. 16, the contents of harmonic magnitudes due to the Fourier analysis are presented.

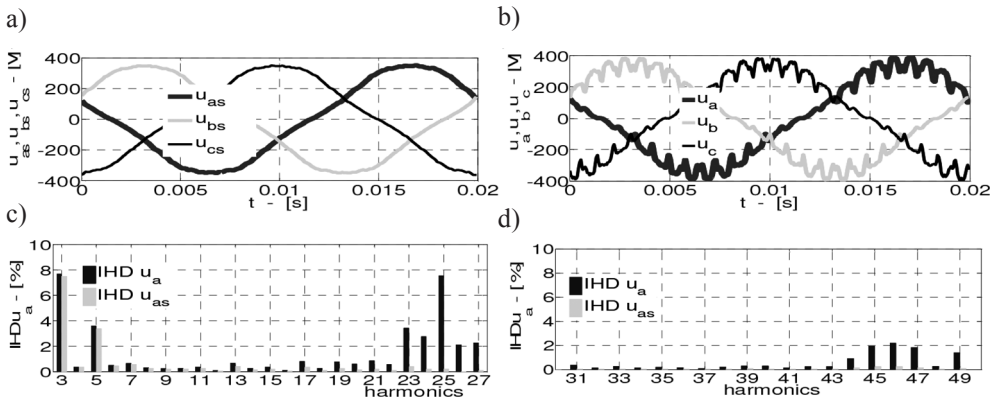

Fig. 16. Induced stator phase voltages under no-load conditions (U_f = const.) a) waveforms for model with the rotor skew, b) waveforms for model without the rotor skew, c) and d) harmonic contents

In the presented waveforms (in Fig. 16), the total harmonic distortion $THDu_a$ for the case of U_f = const. are:

- for the model with the rotor skew $THDu_{as} = 8.39\%$,
- for the model without the rotor skew $THDu_a = 13.73\%$.

5. Experimental verification

Figure 17 shows a measurement set for investigation of the 5.5 kVA salient pole synchronous generator with and without the rotor skew with single layer stator windings. Experimental verifications of the induced stator phase voltages are performed for the three-phase salient pole synchronous generators with the following rated data: $S_N = 5.5$ kVA; $U_N = 400$ V (Y); $I_N = 7.9$ A; $\cos\varphi_N = 0.8$; $n_N = 3000$ rpm; $Q_s = 24$; $p = 1$; $\alpha_q = 0°$; $\alpha_q = 15°$ (with and without the rotor skew). During the investigations, the field winding is powered by a DC voltage source. The induced stator voltages are registered using a four-channel digital oscilloscope.

Figure 18 shows registered waveforms of the induced stator phase voltages under no-load conditions.

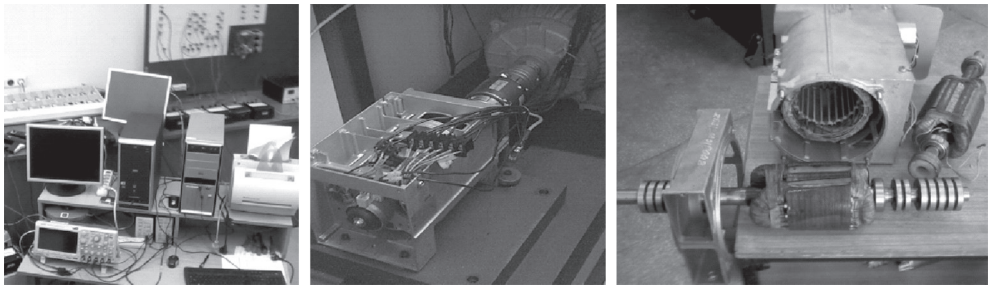

Fig. 17. Measurement set for investigation of the induced stator voltages of the 5.5 kVA salient pole synchronous generator with and without the rotor skew

a) b)

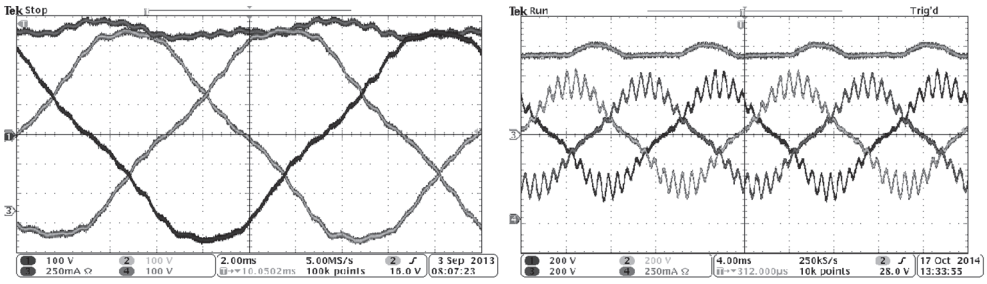

Fig. 18. Registered waveforms of the induced stator phase voltages under no-load conditions for the 5.5 kVA salient pole synchronous generator a) with the rotor skew, b) without the rotor skew

In the presented waveforms (Fig. 18), the total harmonic distortion of the u_{as} and u_a (with and without the rotor skew) for the case of U_f = const. are:

- for the 5.5 kVA synchronous generator with the rotor skew $THDu_{as}$ = 8.29%,
- for the 5.5 kVA synchronous generator without the rotor skew $THDu_a$ = 15.18%.

6. Conclusions

This paper presents the detailed process for determining the induced stator phase voltages whilst taking into account the circuital model of the low power salient pole synchronous generator with and without the rotor skew with damping circuits. This model is based on the self and mutual stator to rotor inductance distributions that are determined by means of the FEMM program. Based on the simulation studies, it can be concluded that in a steady state when powering the field winding from a DC voltage source due to the presence of the damping bars on the rotor:

- without the skew and due to rotor current derivatives (in damping bars and field current) the increase of harmonic content in induced stator voltages is significant and registered $THDu_a$ = 15.18% and simulated $THDu_a$ = 13.73%,
- with the skew reduces the influence of the rotor current derivatives (in damping bars and field current) on the increase of harmonic content in induced stator voltages and registered $THDu_a$ = 8.29% and simulated $THDu_a$ = 8.39%.

Due to the presence of the stator slots (Q_s) in the field current and in the damping bar, currents dominate mainly Q_s-th harmonic. As shown in this paper, for the examined 5.5 kVA synchronous generator, the current derivative $\mathrm{d}\mathbf{i}_r/\mathrm{d}t$ in same damping bars for 24th harmonic (Q_s = 24) has a value of almost 11 kA/s. Although, the magnitude of the stator to damping bar (and part of the two rings) of the mutual inductance distributions $\mathbf{L}_{sr} = [L_{ar(1)}, \ldots, L_{ar(10)}; L_{br(1)}, \ldots, L_{br(10)}; L_{cr(1)}, \ldots, L_{cr(10)}]$ are equal to 0.4 mH, but the product of the $\mathbf{L}_{sr}\mathbf{di}_r/\mathrm{d}t$ has significant influence on the waveforms of the induced stator voltages for the model without a rotor skew.

The main advantages of the circuital modelling (in comparison with simulations using a field model) are the short calculation time, direct and complete control of the influence of every electromagnetic parameter on increasing or reduction of the harmonic contents in the induced stator phase voltages. In the case of a field model simulation of the salient pole synchronous generator with damping circuits with and without the rotor skew, it is difficult to determine which of the electromagnetic parameters have an influence on the induced stator phase voltages.

As shown in this article, FEMM cooperation (in determining the self and mutual inductance distributions) with numerical calculation of the inductance derivative distributions and the simulations in the circuital model give good results similar to experimental ones.

References

[1] Keller S., Xuan M.T., Simond J.J., *Prediction of the no-load voltage waveform of laminated salient pole synchronous generators*, Industry Applications Conference, Fortieth IAS Annual Meeting, 2–6 Oct. 2005, Vol. 4, pp. 2265–2271.

[2] Keller S., Tu Xuan M., Simond J.J., *Computation of the no-load voltage waveform of laminated salient-pole synchronous generators*, IEEE Transactions on Industry Applications, 2006, Vol. 42, No. 306, pp. 681–687.

[3] Glinka T., *Synchronous generators used as reactive power compensators and higher harmonics filters*, Zeszyty Problemowe – Maszyny Elektryczne, 2013, nr 1, Komel, Katowice, pp. 51–62.

[4] May H., Palka R., Paplicki P., Szkolny S., Canders W.R., *Modified concept of permanent magnet excited synchronous machines with improved high-speed features*, Archives of Electrical Engineering, 2011, Vol. 60, No. 4, pp. 531–540.

[5] Skwarczyński J., Weinreb K., *Method of Analysis of Slot Harmonics in the Salient-Pole Synchronous Generators*, International Conference on Electrical Machines (ICEM), Boston, MA, 13–15 August, 1990, pp. 1165–1170.

[6] Vicol L., Banyai A., Viorel I.A., Simond J.J., *On the damper cage bars' currents calculation for salient pole large synchronous machines*, Advances in Electrical and Electronic Engineering, 2008, Vol. 7, No. 1, pp. 165–170.

[7] Moreira J., Lipo T.A., *Modeling of Saturated AC Machines Including Airgap Flux Harmonic Components*, IEEE-IAS Conference Record, 7–12 Oct., 1990, Part 1, pp. 37–44.
[8] Sobczyk T.J., *Mathematical model of synchronous generators accounting for saturation due to the first and the third MMF harmonic*, SME, OWPW, Elektryka, 1999, No. 111, pp. 42–51.
[9] Sobczyk T.J., *Methodology of mathematical modeling of induction machines*, WNT, Warsaw 2004.
[10] Skwarczyński J., *Salient poles inner asymmetries*, Scientific Bulletins of Stanisław Staszic Academy of Mining and Metallurgy, Electrotechnics, Bulletin 16, 1990.
[11] Weinreb K., Sułowicz M., Dziechciarz A., *Application of instantaneous power for rotor eccentricity detection in synchronous motor*, Zeszyty Problemowe – Maszyny Elektryczne, 2014, nr 104, Komel, Katowice, pp. 301–306.
[12] Weinreb K., Sułowicz M., *Noninvasive diagnostics of synchronous machine windings internal asymmetry*, Zeszyty Problemowe – Maszyny Elektryczne, 2007, nr 77, Komel, Katowice, pp. 59–64.
[13] Weinreb K., Węgiel T., Sułowicz M., *Influence of inside asymmetry in asynchronous motor on spectrum of stator currents*, Proceeding of XLIInd International Symposium on Electrical Machines, SME, 3–6 July, 2006, Cracow, Poland, pp. 307–310.
[14] Ludwinek K., *Influence of Representation of the Stator to Rotor Mutual Inductances on the Induced Phase Voltage Waveforms in a Salient Pole Synchronous Generator*, Zeszyty Problemowe – Maszyny Elektryczne, 2014, nr 104, Komel, Katowice, pp. 147–154.
[15] Ludwinek K., *Influence of DC voltage and current of field winding on induced stator voltages of a salient pole synchronous generator*, International Review of Electrical Engineering, 2014, Vol. 9, No. 1, pp. 62–72.
[16] Ludwinek K., *Representation of the mutual inductances in a circuital model of a salient-pole synchronous machine*, Elektro. Info, 2013, No. 9, pp. 103–111.
[17] Ludwinek K., *Representation of the stator to rotor self- and mutual inductances in a salient pole synchronous generator in the no-load state*, Zeszyty Problemowe – Maszyny Elektryczne, 2014, nr 104, Komel, Katowice, pp. 117–124.
[18] Ludwinek K., *An overview of the most important methods of reducing the harmonic content introduced by discretely distributed armature winding*, Elektro. Info, 2014, No. 7–8, pp. 53–57.
[19] Ludwinek K., *Some aspects of representation of inductance distributions in dq0-axes in a salient pole synchronous generator*, Zeszyty Problemowe – Maszyny Elektryczne, 2014, nr 104, Komel, Katowice, pp. 187–184.
[20] http://www.femm.info/wiki/HomePage.

TECHNICAL TRANSACTIONS | **CZASOPISMO TECHNICZNE**
ELECTRICAL ENGINEERING | ELEKTROTECHNIKA
1-E/2015

JOSÉ GREGORIO FERREIRA, TADEUSZ J. SOBCZYK, ADAM WARZECHA*

MULTICRITERIA DIAGNOSIS OF SYNCHRONOUS MACHINE USING THE WELCH METHOD

WIELOKRYTERIALNA DIAGNOSTYKA MASZYNY SYNCHRONICZNEJ Z UŻYCIEM METODY WELCHA

A b s t r a c t

This paper discusses the detection of internal faults in the stator and rotor windings of synchronous machines. Using current signature analysis, it is demonstrated how by using low cost equipment, it is possible to detect the fault by monitoring the currents. The process of detection is totally optimized, and the processing time is enough to identify the fault before the total machine damage. Using the spectrum of the healthy machine as a reference, the followed methodology allows the timely and reliable detection of faults.

Keywords: *synchronous machine*, *spectral analysis*, *fault diagnosis*

S t r e s z c z e n i e

W niniejszym artykule opisano metodę wykrywania wewnętrznych uszkodzeń w uzwojeniach stojana i wirnika maszyny synchronicznej. Przedstawiono sposób zastosowania analizy widmowej monitorowanych prądów do wydzielenia sygnałów o uszkodzeniu. Proces wykrywania jest zoptymalizowany i umożliwia wykrycie uszkodzenia maszyny przed jej zniszczeniem. Wzorcem odniesienia jest widmo prądów maszyny nieuszkodzonej. Zastosowana metodologia zapewnia terminowe i niezawodne wykrywanie błędów.

Słowa kluczowe: *maszyna synchroniczna*, *analiza widmowa*, *diagnostyka uszkodzeń*

DOI: 10.4467/2353737XCT.15.054.3854

* M.Sc. José Gregorio Ferreira, Prof. D.Sc. Ph.D. Eng. Tadeusz J. Sobczyk, D.Sc. Ph.D. Eng. Adam Warzecha, Faculty of Electrical and Computer Engineering, Iinstitute on Electromechnical Energy Conversion, Cracow University of Technology.

1. Introduction

The need to reduce production costs, maximize the return on investment and decrease CO_2 emissions is leading to new ways of operating existing processes and develop new and more integrated industrial processes. These more integrated systems demand continuous information from the assessment of their components. To collect, transmit and process all available data is not a trivial task and must be timely and reliably executed [1].

Addressing technology gaps at the interfaces between the processes, mechanical and electrical domains, and realizing energy savings from integrated operations are factors that motivate and extend research on the multicriteria diagnosis of synchronous machines. In addition, a unique rotor-mounted sensing system was specially designed to collect data from different sensors installed over the rotor [2]. It is strongly believed that this method for acquiring data would allow the reliable detection of faults, even more so when used in combination with an automated monitoring algorithm or process [3].

Synchronous machines (SM) are used mostly in high power operations and as an alternating power source. In general, SM can be found where constant speed operation, power factor control and/or high operating efficiency are required. Moreover, it's high torque characteristics at low speed, and in applications where a wide speed adjusting range is necessary, SM have proven their ability to improve stability in variable-frequency drive applications.

Energy-efficient drive technologies should be well dimensioned, and the control strategy designed according to load conditions. Reducing the input power of the system is a direct way of reducing the cost of production and thus to increase the efficiency of the systems. However, this does not guarantee the availability of the system to meet the requirements of the load. Therefore, it is necessary have systems capable of fault detection and ideally, prediction [4].

Condition monitoring systems are becoming more accurate, and less expensive. Their applications in complex systems allow the assessment of the integrity of the system required for long term scheduling [5]. Loading and maintenance strategies are the two main tasks that directly link the information provided. Trying to minimize the number of unexpected shutdowns, understanding the behaviour and/or the early detection of faults are desirable for every system. Therefore, it seems clear and reasonable to develop algorithms that inform about the assessment of the system allowing a better operation and thus, an improvement in efficiency [6].

2. Motor current signature analysis. Stator and rotor inter-turn fault detection

Initially used to study anomalies and faulty condition in induction motors, the so-called motor current signature analysis (MCSA) has been proven to be a tool for detecting faults such as broken rotor bars, air gap eccentricity, shorted winding, etc [7, 8]. MCSA can identify these problems at an early stage and thus avoid collateral damages or complete failure of the motor.

Detecting stator and rotor winding short-circuits has been analyzed for several years already. In 1996, a novel method of detecting short circuits in both the stator and rotor windings of synchronous generators has been proposed by detecting changes of the harmonic content in the rotor and the stator current spectrum. More recently, new diagnostic tools to determine

when significant insulating aging has occurred have been introduced such as polarization-depolarization current, dielectric spectroscopy and on-line leakage current monitoring [6].

Regarding documentation associated with stator and/or rotor short-circuit faults, most of the available literature relates to the monitoring of failures in synchronous generators [9, 10] or in permanent magnet SM [11]. In [12], the effects of stator interturn short-circuit are analyzed using the field current. The same author as [13] added a rotor search coil voltage signature analysis to identify winding the short-circuit in synchronous motors.

The authors in [14] have developed a mathematical model to study the winding failure of a salient pole synchronous machine calculating the spectra of the stator and field current.

3. Experimental platform configuration

A salient pole synchronous machine (SPSM) ready for non-invasive fault diagnosis tests under different severity levels is available. Running as a generator or as a motor, it is possible to set-up either mechanical or electrical faults or to combine both.

Operated as a motor only; stator and rotor interturn short circuit faults are discussed in this paper. The features of this synchronous machine are described in Table 1.

Table 1

SPSM parameters

Power [kW]	7.5
Voltage [V]	400
Current [A]	15.8
Rotational speed [rpm]	1500
Power factor	0.8
Frequency [Hz]	50
Number stator-slots	42
Field current [A]	8.56
Field voltage [V]	50
Efficiency [%]	85.2
Mass [Kg]	263
Protection level	IP23
Cooling	IS01
Assembly	IM100

The stator of the machine consists of 42 slots with double layer windings. The configuration of the winding can be modified, all the ends of every group of windings are accessible allowing the simulation of many fault conditions to be performed.

All experiments were carried out under the same machine configuration, and special attention was given to guarantee the repeatability of the experiments. The data-set was collected at a sampling frequency of 25 kS/s during two seconds using the Matlab data acquisition toolbox.

A National Instrument NI-USB 6255 acquisition card it is available. The most relevant features are as follows:

– 80 analog inputs (16-bit),
– 125 MS/s single-channel (750 kS/s aggregate).

3.1. Stator short-circuit fault

In Figure 1, a stator winding configuration is presented. Each phase consists of two parallel branches of one group of three coils and another of four coils connected in series. In [15], the utility of the circulating current was used for fault detection in SM.

Simulations of different levels of stator interturn short-circuit were made by placing a variable resistor connected in parallel with the phase 'c' (second parallel branch) in a group of four coils.

Different levels of short-circuit were obtained controlling the deviated current from 0 to 2 amperes, at increments of 0.25 amperes with the motor running at 60% of rated power.

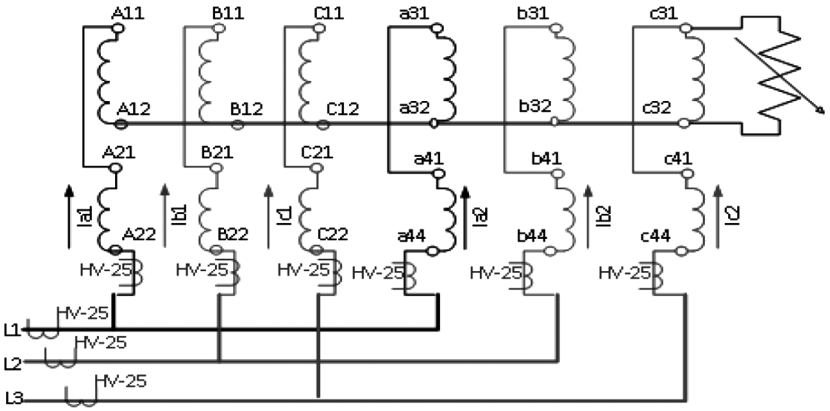

Fig. 1. Stator winding configuration

3.2. Rotor short-circuit fault

The rotor is a salient 2p poles rotor with configurable field winding. In this case, Fig. 2, it is possible to short circuit 90% or 10% of the coils that creates the pole. The experiments were carried out for different set points varying the load of the machine from 0% to 100% of rated power, with the pole four having 90% of shortened coils.

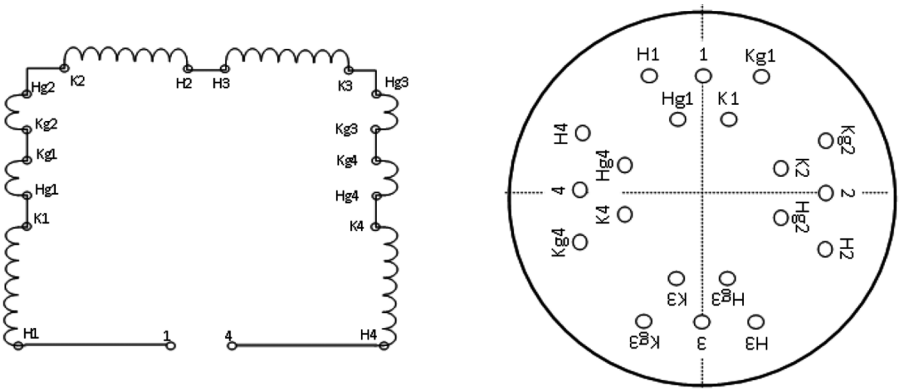

Fig. 2. Rotor winding configuration

4. Preprocessing and statistical analysis of current spectrum

In order to comply with the mathematical requirements, our data was truncated from the first negative to positive zero crossing, and to the last positive to negative zero crossing. Additionally, each signal was centered to have a mean of zero and scaled to have a standard deviation of one using the standardized z-scores MATLAB algorithm. The condition of the second-order stationary was also verified.

Once all mathematical requirements are fulfilled, the next step was classifying them according the level of fault and for each load level. At this point, the data set is ready to be processed.

4.1. Mathematical formulation

We are interested in finding those frequency components that may change when the synchronous motor is running under fault condition. Therefore, all datasets were obtained during only steady-state conditions. The collected signals under this condition, are considered as random signals from a sequence of time samples or just called discrete-time sequence.

$$\left\{ y\left(t\right); t = 0, \pm 1, \pm 2 \ldots \right\} \tag{1}$$

It is assumed to be a sequence of random variables with a zero mean given by the expectation operator $\{E;\, E\{y(t)\} = 0\}$ for all t. The time index t is expressed in units of the sampling interval, that is,

$$y\left(t\right) = y_c\left(t \cdot T_s\right) \tag{2}$$

where:
$y_c(\cdot)$ – is a continuous signal,
T_s – sampling time interval.

and has finite energy;

$$\sum_{t=-\infty}^{\infty} \left| y(t) \right|^2 < \infty \tag{3}$$

Then, the sequence $\{y(t)\}$ possesses a discrete-time Fourier transform (DTDT) defined as:

$$Y(\omega) = \sum_{t=-\infty}^{\infty} y(t) e^{-i\omega t} \quad \text{(DTFT)} \tag{4}$$

Only frequencies below 5 kHz are considered. Hence, effects which might be incurred by the sampling process, such as aliasing, are surely avoided inasmuch as $f_{Nyquist} = 12.5$ kHz.

A random signal usually has a finite average power and therefore, can be characterized by an average power spectral density [16]. The power spectral density (PSD) of a time series $y(t)$ describes how the variance of the data is distributed over the frequency components into which $y(t)$ may be decomposed. Our motivation for considering spectral analysis is to characterize the average power at frequency ω in the signal, given by the formula:

$$\varphi(\omega) = \lim_{N \to \infty} E\left\{ \frac{1}{N} \left| \sum_{t=1}^{N} y(t) e^{-i\omega t} \right|^2 \right\} \tag{5}$$

where

$1/N$ – normalization parameter by N number of points of the available data sequence.

$\varphi(\omega)$ is a periodic function, with the period equal to 2π. Hence, $\varphi(\omega)$ is completely described by its variation in the interval:

$$\omega \in [-\pi, \pi] \text{ (radians per sampling interval)} \tag{6}$$

Alternatively, the PSD can be viewed as a function of the frequency:

$$f = \frac{\omega}{2\pi} \quad \text{(cycles per sampling interval)} \tag{7}$$

Then, from a finite-length record $\{y(1), \ldots, y(N)\}$ of a second-order stationary random process, the premise of our problem is to determine an estimator $\hat{\varphi}(\omega)$ of its power spectral density $\varphi(\omega)$, for $\omega \in [-\pi, \pi]$.

4.2. Spectral estimator, Welch's method

The use of Fast Fourier Transform for the estimation of the power spectrum is a well known technique. A more practical approach is the Discrete-Time Fourier Transform (DTFT). Various improvements have been proposed over the years. For this research, averaged periodograms of overlapped, windowed segments of a time series algorithm, using the so-called Welch's method was implemented. A periodogram here means the DTFT of one segment of

the time series, while modified refers to the application of a time-domain window function and averaging to reduce the variance of the spectral estimates is used.

Motivated by the high variance of the periodogram and based on Bartlett's method, Welch's method, represents an improvement used for estimating the power of a signal at different frequencies. The signal is split up into overlapping segments. *L* data segments of length *M*, overlapping by *D* points [17]. The overlapping segments are then windowed. After setting these parameters, the squared magnitude of each segment is computed and time-averaged – this reduces the variance of the individual power measurements, at the cost of reduced resolution. Furthermore, the 95% confidence intervals are calculated and indicated with the grey area called the 'healthy region'.

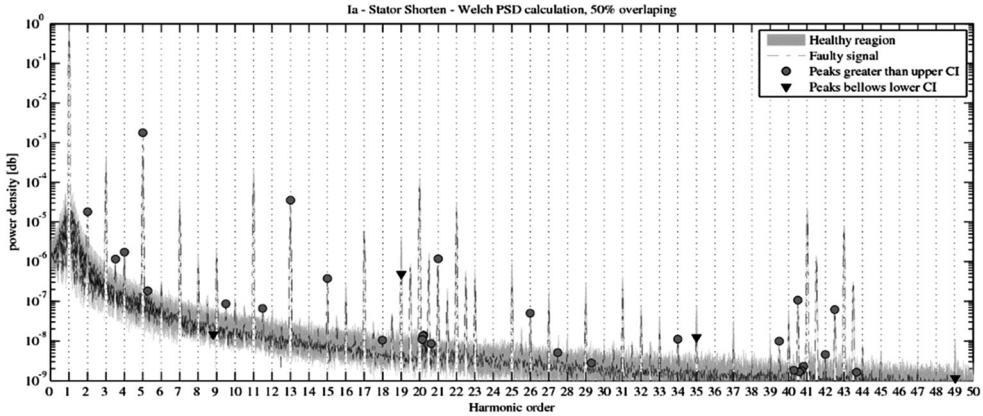

Fig. 3. Power spectral density under fault condition: Stator shorten

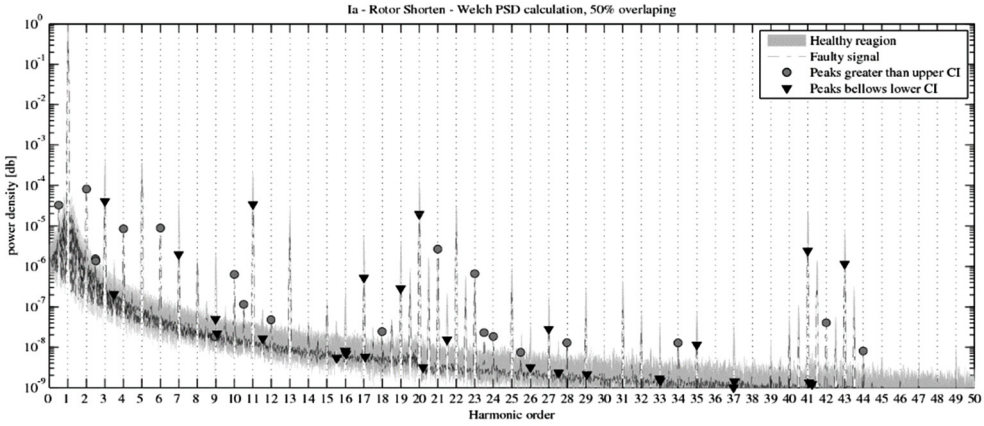

Fig. 4. Power spectral density under fault condition: Rotor shorten

As it is possible to see from Figs. 3 and 4, the PSD of the faulty signal is represented over the healthy region defined by a 95% confidence interval. The peaks greater than the upper confidence interval and below the lower interval are indicated at their respective frequency.

5. Results

In general, properly designed electrical machines and no fault condition, it is expected to have a symmetrical flux distribution in the air gap. All machines have constructional asymmetries. In fact, these asymmetries, have already been exploited to perform fault detection. Consequently, the magnetic field distribution will be affected.

Using the healthy synchronous machine spectrum as a reference, it seems logical to assume that if the amplitude of the measured faulty signals is located outside the confidence intervals, the machine is no longer operating under a symmetrical state. Therefore, a fault condition is detected. When a difference is detected in a particular frequency, and the variations found are not as significant, the level of uncertainty is higher than that established by the confidence intervals.

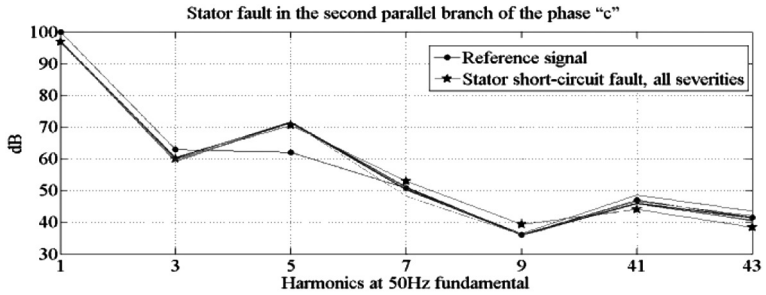

Fig. 5. Stator current harmonics for fault in a parallel branch of the stator winding

In Figure 5, the first odd harmonics and stator-harmonics for the stator fault in the second parallel branch of phase 'c' is presented (See Fig. 1). In Figure 5, it is easy to identify the appearance of a higher peak at 250 Hz for all level off fault. The variation detected is only 10 dB. Therefore, looking at all harmonics levels, it is possible to understand how the amplitude remains constant and under different short-circuit severities for all harmonics with the exception of the fifth harmonic.

Looking at the spectra of the motor running with a fault in the rotor (Fig. 4) it is possible to appreciate how the even harmonics show greater peaks than the upper bound of the machine running on the healthy state. More meaningful are the two side peaks that appear at 25 Hz and 75 Hz.

6. Conclusions

One of the aims of the extended research on Multicriteria diagnosis of synchronous machines is to use available tools in order to identify the associated variables related to faults in the system. This paper has shown how it is possible to on-line detect slow rising short-circuits in the stator and/or rotor by only using a basic data acquisition card connected to a standard PC/laptop using the spectrum of the healthy machine as a reference.

Using Welch's method, it was possible to quantify and determine the variation of the energy around a frequency-bin.

Financial support from the Marie Curie FP7-ITN project "Energy savings from smart operation of electrical, process and mechanical equipment" – ENERGY-SMARTOPS, Contract No: PITN-GA-2010-264940 is gratefully acknowledged.

References

[1] Mechefske C.K., *Machine condition monitoring and fault diagnostics*, Vibration And Shock Handbook, 2005.

[2] Ferreira J.G., Sobczyk T., *Multicriteria diagnosis of synchronous machines – rotor-mounted sensing system. Rotor Signal Collector construction*, UKACC 10th International Conference on Control, 2014.

[3] Marwala T., *Condition monitoring using computational intelligence methods: applications in mechanical and electrical systems*, Springer, 2012.

[4] Smith D.P., *PdM centralization for significant energy savings*, www.reliableplant.com/Articles/Print/15492 (access: 25.10.2013).

[5] Tavner P., Ran L., Penman J., Sedding H., Condition Monitoring of Rotating Electrical Machines, 2008, Vol. 56, The Institution of Engineering and Technology.

[6] Stone G., *Condition monitoring and diagnostics of motor and stator windings-A review*, Dielectrics and Electrical Insulation, IEEE Transactions, 2013, Vol. 20, No. 6, pp. 2073–2080.

[7] Thomson W.T., Gilmore R.J., *Motor current signature analysis to detect faults in induction motor drives-fundamentals, data interpretation, and industrial case histories*, Proccedings of 32rd Turbomachinery Symposium, 2003.

[8] El Hachemi Benbouzid M., *A review of induction motors signature analysis as a medium for faults detection*, Industrial Electronics, IEEE Transactions, 2000, Vol. 47, No. 5, pp. 984–993.

[9] Juárez-Caltzontzin L.L., Trinidad-Hernández G., Asiaín-Olivares T.I., Ruiz-Vega D., *Theoretical and Experimental Analysis of the Short Circuit Current Components in Salient Pole Synchronous Generators*, Proceedings of the 11th Spanish Portuguese Conference on Electrical Engineering (11 CHILE), 2009, Vol. 1.

[10] Shuting W., Yonggang L., Heming L., Guiji T., *The analysis of generator excitation current harmonics on stator and rotor winding fault*, Industrial Electronics, IEEE International Symposium, 2006, Vol. 3, pp. 2089–2093.

[11] Zhaoxia X., Hongwei F., *Stator Winding Inter-Turn Short Circuit and Rotor Eccentricity Diagnosis of Permanent Magnet Synchronous Generator*, Control, Automation and Systems Engineering (CASE), International Conference, 2011, pp. 1–4.

[12] Neti P., Nandi S., *Stator inter-turn fault detection of synchronous machines using field current signature analysis*, Industry Applications Conference, 41st IAS Annual Meeting, Conference Record of the IEEE, 2006, Vol. 5, pp. 2360–2367.

[13] Neti P., Nandi S., *Stator inter-turn fault detection of synchronous machines using field current and rotor search-coil voltage signature analysis*, Industry Applications, IEEE Transactions, 2009, Vol. 45, No. 3, pp. 911–920.

[14] Weinreb K., Drozdowski P., *Detection of Winding Faults of a Salient Pole Synchronous Machine by a Spectral Analysis of Currents*, Proc. ICEM, 1994, Vol. 94, pp. 5–8.

[15] Rodriguez P., Rzeszucinski P., Sulowicz M. et al., *Stator Circulating Currents as Media of Fault Detection in Synchronous Motors*, Diagnostics for Electric Machines, Power Electronics & Drives (SDEMPED), IEEE International Symposium, 2013.

[16] Stoica P., Moses R.L., *Spectral analysis of signals*, Pearson/Prentice Hall, Upper Saddle River, NJ 2005.

[17] Welch P.D., *The use of fast Fourier transform for the estimation of power spectra: a method based on time averaging over short, modified periodograms*, IEEE Transactions on Audio and Electroacoustics, 1967, Vol. 15, No. 2, pp. 70–73.

[18] Drozdowski P., Weinreb K., Węgiel T., *Wykrywanie ekscentryczności wirnika w maszynach synchronicznych poprzez analizę harmoniczną prądów*, Materiały SME, 1995, pp. 206–221.

TECHNICAL TRANSACTIONS | **CZASOPISMO TECHNICZNE**
ELECTRICAL ENGINEERING | ELEKTROTECHNIKA
1-E/2015

RAFAŁ PIOTUCH, RYSZARD PAŁKA*

IPMSM WITH SMC ROTOR – OPTIMIZATION AND EXPERIMENTAL RESULTS

MASZYNA SYNCHRONICZNA Z WIRNIKIEM PROSZKOWYM – OPTYMALIZACJA I WYNIKI EKSPERYMENTALNE

A b s t r a c t

The work presented in this paper relates to an Interior Permanent Magnet Synchronous Motor (IPMSM) experimental results and optimization procedure programed in Matlab and Maxwell environments. The stator of the machine is a conventional stator with distributed winding. The subject of the first optimization stage was the geometry of the IPM machine, concerning average torque value maximization and maximum cogging torque value minimization under physical and technological constraints. The optimized rotor core is made of from Magnetic Powder (SMC). It was tested in a generator regime.

Keywords: *PM electrical machines*, *IPMSM optimization*, *FEM*, *experimental research*

S t r e s z c z e n i e

Artykuł podejmuje temat badań eksperymentalnych oraz optymalizacji maszyn synchronicznych z magnesami zagnieżdżonymi z wykorzystaniem narzędzi Matlab i Maxwell. Stojan badanej maszyny jest typowym stojanem silnika asynchronicznego klatkowego z uzwojeniem rozłożonym. Dokonano optymalizacji geometrii wirnika maszyny, z uwzględnieniem maksymalizacji wartości średniej momentu elektromagnetycznego i minimalizacji maksymalnej wartości momentu zaczepowego oraz ograniczeń geometrycznych i technologicznych. Zoptymalizowany rdzeń wirnika został wykonany z proszku magnetycznie miękkiego. Zaprojektowaną maszynę przebadano w stanie generatorowym.

Słowa kluczowe: *maszyny z magnesami trwałymi*, *optymalizacja*, *MES*, *badania eksperymentalne*

DOI: 10.4467/2353737XCT.15.055.3855

* M.Sc. Eng. Rafał Piotuch, Prof. D.Sc. Ph.D. Eng. Ryszard Pałka, Faculty of Electrical Engineering, West Pomeranian University of Technology in Szczecin.

1. Introduction

To protect the environment, there exists a strong demand to develop very efficient motors with a high torque/mass ratio. Thanks to the rapid advancement of power electronics, material engineering, digital signal processors and control algorithms, PM-excited and switched reluctance motors find more and more applications and have replaced the traction systems of most present hybrid and electrical vehicles because they offer high performance over other DC and AC machines [1–3]. In particular, owing to the development of rare-earth magnets with high energy production, it is possible to develop high power density machines with improved overall efficiency. Furthermore, extended high speed capabilities, demanded in a highway cycle, are achieved thanks to proper rotor geometry designs, and field weakening control strategies [3–8]. Surface and radially-laminated Interior PM synchronous machines with conventional structures have limited or zero flux-weakening capability [5, 6]. Properly designed IPMSMs are capable of operating in CPSR (constant power speed region) – such machines also perform inverse saliency, i.e. the *q*-axis inductance is larger than *d*-axis inductance. Consequently, it provides an additive torque value, reluctance torque, that may be exploited to extend CPSR. Another positive feature of the IPM rotor is that centrifugal forces cannot damage magnets, thus the whole construction is mechanically robust. Small cogging torque reduces noise and mechanical vibrations which causes increased reliability and user-friendly operation [9–13]. PM excited machines can fulfill all the above requirements [1–4].

A proposed geometry has NdFeB magnets oriented in a radial direction. Such structures are referred to as IPM machines [5, 6]. Its rotor is made of Soft Magnetic Powder. The authors have implemented the optimization procedure in the Matlab environment with a genetic algorithm that runs and evaluates FE models using Maxwell (Ansys). After the optimization process, the machine has been built and tested.

2. PMSM mathematical model

Torque generated in IPM machines can be described as follows:

$$T_{em} = \frac{3}{2} \cdot p_b \cdot \left[\Psi_{PM} \cdot I_q + \left(L_d - L_q \right) \cdot I_d \cdot I_q \right] \tag{1}$$

where:
T_{em} – electromagnetic torque average value,
p_b – number of pole pairs,
Ψ_{PM} – PM caused magnetic flux,
I_d, I_q – *d*- and *q*-axis currents,
L_d, L_q – *d*- and *q*-axis inductances.

Electromagnetic torque may be divided into two components. The first term in the equation (1) is the PM torque, and the second term is the reluctance torque which is proportional to difference between stator inductances, L_d and L_q. In the analyzed IPMSM, L_q is higher than L_d (due to the lower reluctance in the *q*-axis direction), because magnetic flux flowing along

the *d*-axis has to cross the air gap and magnet, while the magnetic flux of *q*-axis crosses only air gap. The *d*-axis is also basically magnetized with PM [5, 6]. The inductance difference increases torque and extends CPSR. The mathematical model of IPM machines is commonly defined by the following equation set:

$$U_d = RI_d + \frac{\mathrm{d}\Psi_d}{\mathrm{d}t} - p_b \Omega_m \Psi_q \tag{2a}$$

$$U_q = RI_q + \frac{\mathrm{d}\Psi_q}{\mathrm{d}t} + p_b \Omega_m \Psi_d \tag{2b}$$

$$\Psi_d = L_d I_d + \Psi_{PM} \tag{2c}$$

$$\Psi_q = L_q I_q \tag{2d}$$

where:
U_d, U_q – *d*- and *q*-axis voltages,
R – stator phase winding resistance,
Ψ_d, Ψ_q – *d*- and *q*-axis magnetic fluxes,
Ω_m – mechanical rotor speed.

The control strategy applied for such motors meets several limitations:

$$U_d^{\,2} + U_q^{\,2} \le U_N^{\,2} \tag{3a}$$

$$I_d^{\,2} + I_q^{\,2} \le I_N^{\,2} \tag{3b}$$

where U_N, I_N denote base harmonic voltage and current RMS values.

In high speed regions, a flux developed by magnets gives electro-motive force that exceeds supply voltage (2). Using the classic field weakening method, the main flux is decreased by the *d*-axis negative current (2c) and thus it is possible to stay within the voltage limit (3a). The optimum flux-weakening condition can be written as:

$$I_N = \left| \frac{\Psi_{PM}}{L_d} \right| \tag{4}$$

Such designs are called optimal field-weakening IPM machines and theoretically exhibit unlimited CPSR.

3. Design problem

The case of this study is represented by a 4-pole IPMSM with a fixed stator geometry and winding parameters. The rotor is equipped with NdFeB magnets (B_r = 1.23 T, size: 50x20x40 mm) and is made of SMC (relative permeability of about 40). In contrary to the previous research [11], classical geometry (without magnets segmentation) was chosen in order to achieve high electromagnetic torque value. In IPMSM designs, magnet volume should be rather high and segmented geometry will cause PM flux leakage. A small PM flux leakage is strongly demanded especially for rotors made of SMC (with rather low relative permeability values of 30–100 [2]).

Some of the IPM parameters are kept constant – these are presented in Table 1. Selected design variables were chosen according to the available technological abilities – these are presented in Table 2. The analyzed geometry (optimized geometry without SMC poles) is depicted in Fig. 1.

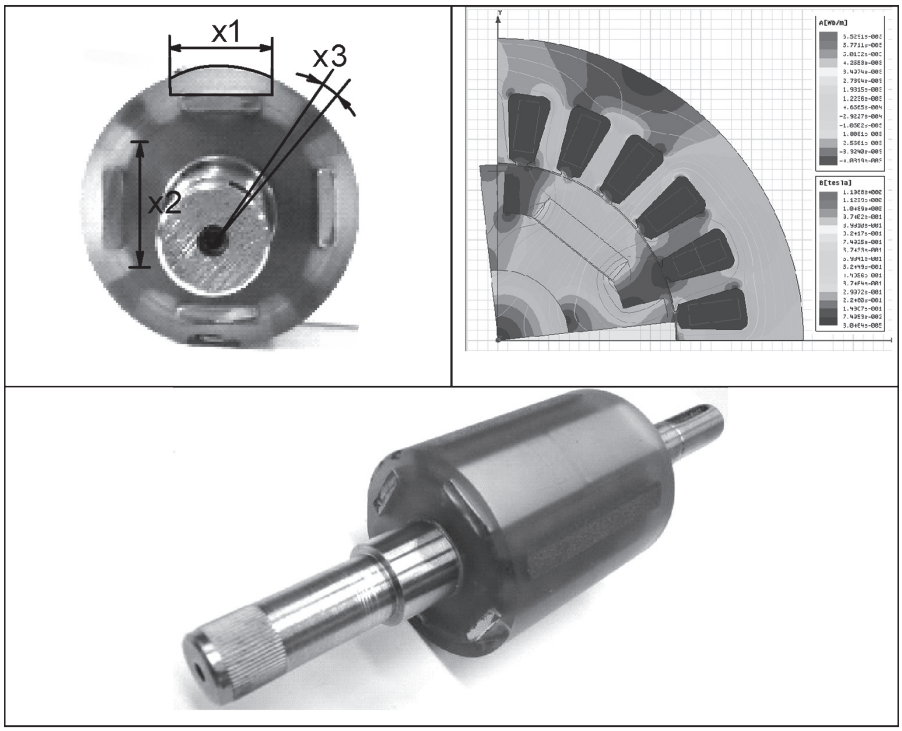

Fig. 1. Initial rotor geometry (without iron poles)

Table 1

Machine parameters

Rotor outer diameter [mm]	Air gap length [mm]	Stator outer diameter [mm]	Rotor length [mm]	Nominal current [A]	Phase resistance 20° [Ohm]
67.5	1.5	120	55	1.6	12.7

Table 2

Design variables constraints

$x1$ [mm] Pole width	$x2$ [mm] Cutter width	$x3$ [deg] Tooth angle
5–26	13–16	0–20

4. Optimization process

In the optimization procedure, a genetic algorithm (GA) was used. This heuristic technique based on a struggle between individuals, commonly known as GA, mimics natural selection that exists in nature were the strongest individuals survive, because they fit to the present demanding [11, 13]. Details of the used genetic algorithm have been given in [14].

The optimization problem described in the paper is a typical multi-objective optimization problem (MOP) subject to a set of constraints. For the proposed geometry, the following objective functions are defined:

$$f_1(x) = \max(T_{cogg}(\varphi)) \tag{5a}$$

$$f_2(x) = -\text{mean}(T_{em}(\varphi)) \tag{5b}$$

where:
T_{cogg} – cogging torque,
T_{em} – electromagnetic torque,
φ – rotor angle.

All the above quantities should be minimized. After solving the MOP, a set of optimal non-dominated solutions were generated creating a Pareto front shown in Fig. 2. This is a set

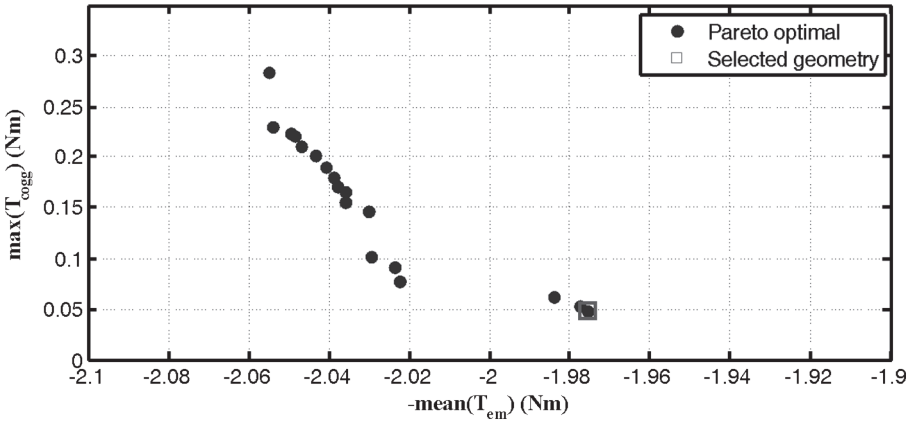

Fig. 2. Pareto front

of models that acts as an area for a selection of best individual. The final selection should be made taking into account other features that the motor should have [1, 11] – in this particular design problem, the highest possible difference between L_d and L_q values as well as proper L_d value (4). Details of the presented methodology are described in [11]. The GA have used 30 individuals in each population and 30 generations. The whole optimization process lasted for about 15 h on a high performance PC. The results of the optimization are shown in Fig 2. One individual that was designed and created for experimental evaluation is also depicted.

5. Experimental results

For the experimental evaluation of the machine parameters and characteristics, a proper test-stand has been designed (Fig. 3). It consists of the optimized IPM prototype and a B&R servo motor (8LSA44 – 451 W, 3000 rpm) clutched and mounted on a aluminum plate, a torque meter, load resistors, voltage and current meters and a digital oscilloscope. The B&R was controlled via an application developed for Power Panel 45.

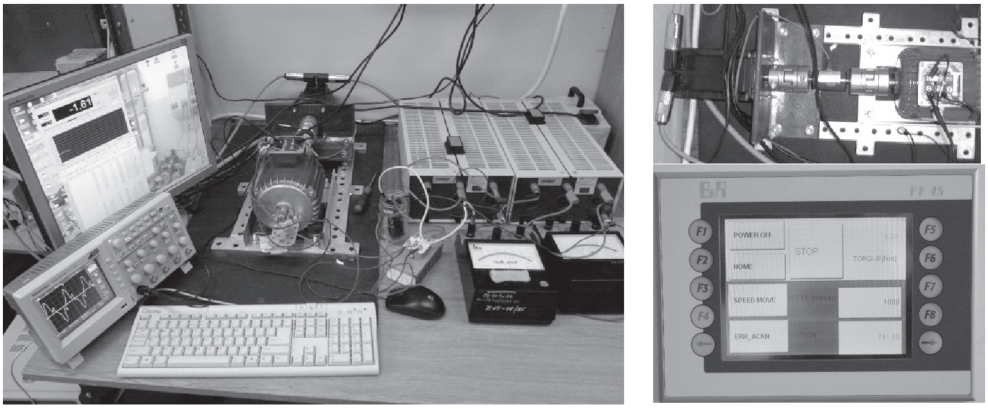

Fig. 3. Test stand

All crucial parameters of the optimized rotor are shown in Table 3.

Table 3

Optimized Design variables values

$x1$ [mm] Pole width	$x2$ [mm] Cutter width	$x3$ [deg] Tooth angle
25.2	15.5	6.5

Cogging torque was measured for various rotor positions. Experimental and simulation results are presented in Fig. 4.

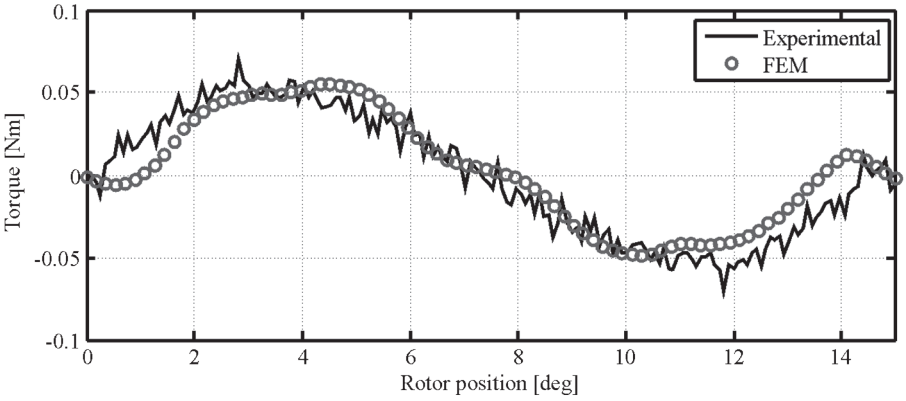

Fig. 4. Cogging torque waveform

Inductance was measured with the scheme shown in Fig. 5.

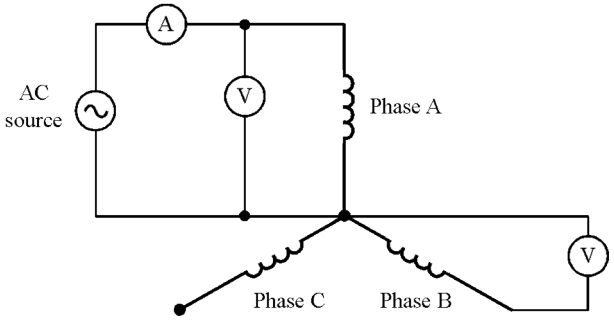

Fig. 5. Inductance measurement scheme

The inductances values were calculated with the following formulas:

$$L_A(\varphi) = \frac{\sqrt{\left(\frac{U_A}{I_A}\right)^2 - R^2}}{2\pi f} \tag{6a}$$

$$L_{AB}(\varphi) = \frac{U_B}{(2\pi f) I_A} \tag{6b}$$

where:
U_A, U_B – A and B phase RMS voltage value,
L_A, L_{AB} – self and mutual inductance,
f – AC source frequency.

Figure 6 shows self and mutual inductances for different rotor positions and two AC currents – nominal and 1.5 times the nominal value. It occurred that the machine was not saturated – for different currents there was nearly any change in the inductance values. This was caused by the relatively big air-gap length.

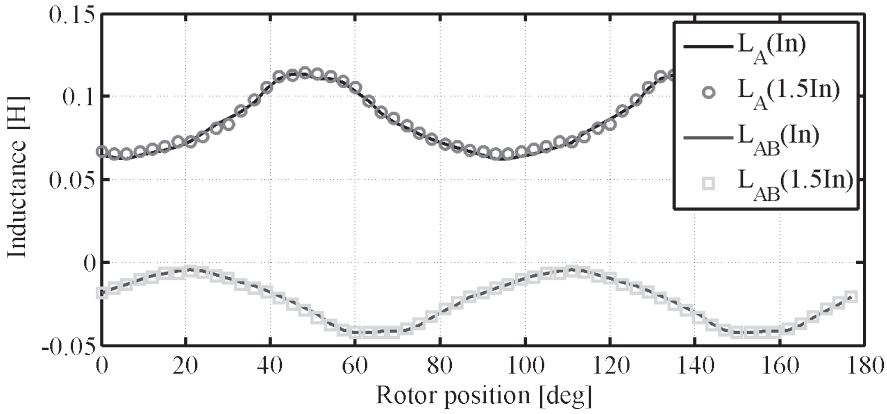

Fig. 6. Measured inductances for different current values

The calculated values of self and mutual inductances during simulation were increased with the end-connection inductance value. The results for the nominal current value are presented in Fig. 7.

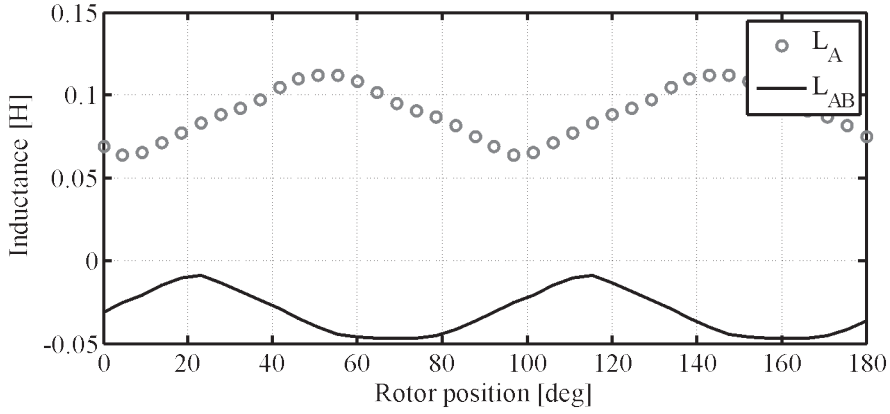

Fig. 7. FEM calculated inductances for nominal current

After simple mathematical calculations, L_d and L_q values may be obtained [15]. The value of L_d was 65 mH and L_q was 150 mH. Small inductance in the *d*-axis cannot assure proper field-weakening capabilities according to equation (5). Its small value is caused by the small permeability of the SMC and large air-gap length. Efficiency of the generator was 91% for 1500 rpm rotor speed and nominal current, so it was 19% higher than for the IM motor with

the same stator and windings. During the experimental tests, torque for different current values was also evaluated. Two phases were connected in series and supplied with a DC current. For each rotor position, the shaft was stalled and the torque value was measured. A comparison between simulation and experimental results for nominal current is presented in Fig. 8.

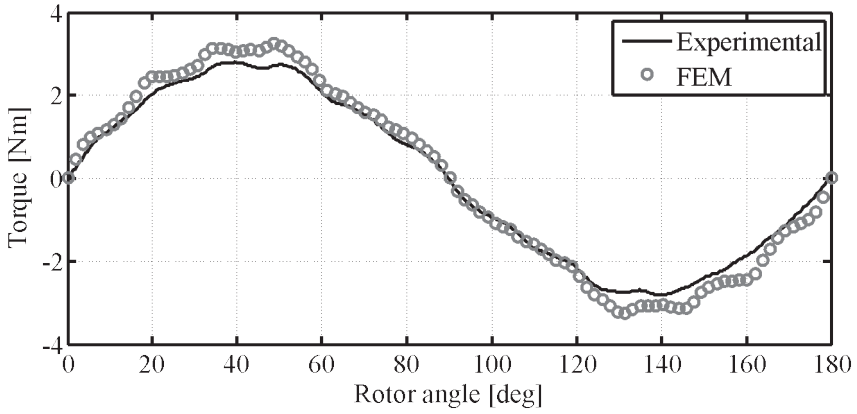

Fig. 8. Torque waveforms for nominal current

6. Summary

The authors applied Maxwell and Matlab tools for the SMC rotor geometry optimization process of the interior permanent magnet synchronous motor. The connection between these two packages allowed a flexible FE model geometry definition and analysis as well as effective results evaluation. The simulation points out the benefits of the optimization using a genetic algorithm.

Simulation results were verified on the experimental test stand. Efficiency, mechanical torque, cogging torque and L_d and L_q values have been measured.

The prototype offered very high nominal efficiency (about 91%) with very small maximum cogging torque value (about 0.05 Nm – 2% of nominal value). All these features were achieved due to PM excitation and the rotor made of SMC. A negligible influence of the current on *d*- and *q*-axis inductances values was observed. A serious disadvantage of such solutions is the small value of L_d, which results in limited field-weakening capabilities – further work will be focused on better high speed features of IPM with SMC. Surely, this could be achieved with optimized rotor geometry and higher relative permeability of used magnetic powder.

During simulation and experimental tests, the authors encountered several problems. The first was to apply proper mesh settings in order to shorten the whole optimization calculation time, and assure correct FEM calculation results. Particularly, the mesh should be more dense in the air gap region, and thinner over the stator and rotor cores. Secondly, the simulation did not consider any losses, it caused a difference between the measured and simulated torque values of approximately 10%. The main problem during experimental tests was to assure a nominal temperature of windings.

References

[1] Di Barba P., Mognaschi M.E., *Industrial design with multiple criteria: shape optimization of a permanent-magnet generator*, IEEE Transaction on Magnetics, 2009, Vol. 45, No. 3, pp. 1482–1485.

[2] Paplicki P., *The new generation of electrical machines applied in hybrid drive car*, Electrical Review, 2010, Vol. 86, No. 6, pp. 101–103.

[3] May H., Pałka R., Paplicki P., Szkolny S., Wardach M., *Comparative research of different structures of a permanent-magnet excited synchronous machine for electric vehicles*, Electrical Review, 2012, No. 12a, pp. 53–55.

[4] Di Barba P., Mognaschi M.E., Pałka R., Paplicki P., Szkolny S., *Design optimization of a permanent-magnet excited synchronous machine for electrical automobiles*, International Journal of Applied Electromagnetics and Mechanics, IOS Press, 2012, Vol. 39, No. 1–4, pp. 889–895.

[5] Stumberger B., Hamler M., Trlep M., Jesenik M., *Analysis of Interior Permanent Magnet Synchronous Motor Designed for Flux Weakening Operation*, IEEE Transaction on Magnetics, 2001, Vol. 37, No. 5, pp. 3644–3647.

[6] Pałka R., Piotuch R., *FEM based IPMSM optimization*, Problem Issues – Electrical Machines, 2014, Vol. 104, No. 4, pp. 99–104.

[7] Paplicki P., Piotuch R., *Improved Control System of PM Machine with Extended Field Control Capability for EV Drive*, Mechatronics-Ideas for Industrial Application, Springer, part. I, 2015, Vol. 317, pp. 125–132.

[8] Putek P., Paplicki P., Pałka R., *Topology optimization of rotor poles in a permanent-magnet machine using level set method and continuum design sensitivity analysis*, COMPEL, Vol. 33, Issue 3, pp. 711–728.

[9] Putek P., Slodička M., Paplicki P., Pałka R., *Minimization of cogging torque in permanent magnet machines using the topological gradient and adjoint sensitivity in multi-objective design*, International Journal of Applied Electromagnetics and Mechanics, 2012, Vol. 39, No. 1–4, pp. 933–940.

[10] Putek P., Paplicki P., Slodička M., Pałka R., Van Keer R., *Application of topological gradient and continuum sensitivity analysis to the multi-objective design optimization of a permanent-magnet excited synchronous machine*, Electrical Review, 2012, Vol. 88, No. 7a, pp. 256–260.

[11] Caramia R., Piotuch R., Pałka R., *Multiobjective FEM based optimization of BLDC motor using Matlab and Maxwell scripting capabilities*, Archives of Electrical Engineering, 2014, Vol. 63(1), pp. 115–124.

[12] Putek P., Paplicki P., Pałka R., *Low Cogging Torque Design of Permanent Magnet Machine Using Modified Multi-Level Set Method With Total Variation Regularization*, IEEE Transaction on Magnetics, 2014, Vol. 50, No. 2, pp. 657–660.

[13] Paplicki P., *Design optimization of the electrically controlled permanent magnet excited synchronous machine to improve flux control range*, Electronika ir electrotechnika, 2014, Vol. 20, No. 10.

[14] Deb K., Pratap A., Agarwal S., Meyarivan T., A *fast and elitist multiobjective genetic algorithm: NSGA-II*, IEEE Transactions On Evolutionary Computation, April 2002, Vol. 6, No. 2.

[15] Shchur I., Rusek A., *Simulation modelling of synchronous motor with permanent magnets on the base of results of field research*, Problem Issues – Electrical Machines, 2013, Vol. 93, No. 3, pp. 189–195.

TECHNICAL TRANSACTIONS | **CZASOPISMO TECHNICZNE**
ELECTRICAL ENGINEERING | ELEKTROTECHNIKA
1-E/2015

MICHAŁ RADZIK*, TADEUSZ J. SOBCZYK**

ANALYSIS OF A SYNCHRONOUS MACHINE DRIVEN BY AN INTERNAL-COMBUSTION ENGINE

ANALIZA PRACY MASZYNY SYNCHRONICZNEJ NAPĘDZANEJ PRZEZ SILNIK SPALINOWY

Abstract

The steady state response of a synchronous machine to the torque with angle dependent pulsating component is of great practical importance for the piston drive. Determining such a response is not easy due to the necessity of solving the system of nonlinear differential equations. This paper describes an algorithm that allows directly determining the steady states of a synchronous machine driven by an internal combustion engine (e.g. diesel engine). To create such an algorithm, the harmonic balance method and the iterative Newton–Raphson procedure are used. This approach allows obtaining steady-state solutions directly in the frequency domain. Exemplary calculations are performed for synchronous generators derived from the four-stroke internal combustion engine.

Keywords: *synchronous machines*, *steady-state performance*, *harmonic balance method*

Streszczenie

Reakcja maszyny synchronicznej na moment napędowy zależny od kąta obrotu wirnika ma duże znaczenie praktyczne dla napędów tłokowych. Określenie rozwiązania ustalonego nie jest łatwe ze względu na konieczność rozwiązywania układu nieliniowych równań różniczkowych. W niniejszym artykule opisano algorytm pozwalający na bezpośrednie wyznaczanie stanu ustalonego w maszynie synchronicznej napędzanej przez silnik spalinowy. Algorytm ten opiera się na metodzie bilansu harmonicznych oraz wykorzystuje procedurę iteracyjną Newtona–Raphsona. Pozwala to na uzyskanie rozwiązania ustalonego bezpośrednio w dziedzinie częstotliwości w postaci szeregu Fouriera. Przykładowe obliczenia przeprowadzono dla prądnicy pracującej synchronicznie na sieć sztywną i napędzanej momentem mechanicznym pochodzącym od spalinowego silnika czterosuwowego.

Słowa kluczowe: *maszyny synchroniczne*, *stany ustalone*, *metoda bilansu harmonicznych*

DOI: 10.4467/2353737XCT.15.056.3856

* Ph.D. Eng. Michał Radzik, Technical Institute, State Higher Vocational School in Nowy Sacz.
** Prof. D.Sc. Ph.D. Eng. Tadeusz J. Sobczyk, Institute on Electromechanical Energy Conversion, Cracow University of Technology.

1. Introduction

This paper considers the performance of synchronous generators driven by internal combustion engines, mainly by diesel engines. These are commonly used as small or medium power electric sources. The characteristic features of such a drive is the pulsating torque of the driven engine due to the pulsating nature of the forces acting on the pistons in the cylinders, these are caused by the changeable pressure of a medium in cylinders. This causes the angle depended torque, which generates the speed ripples, even if the generator is running synchronously [2]. The second independent phenomenon causing the speed ripples is a variation of the total moment of inertia of the whole piston drive with the angle of rotation [3]. The resulting fluctuations of the torque acting on the synchronous generator shaft are a function of the shaft's rotational angle. It generates oscillations in the angular velocity of the synchronous generator. In turn, it has a direct impact on the oscillations of the power angle ϑ of the synchronous generator. Also, the winding's currents reflect on those oscillations by new components. In practice, in order to counteract this, the amplitude of the alternating component in torque is reduced to a minimum, most often through multiplication of the number of cylinders and selection of an appropriate tact of work for each cylinder [4].

Determining the steady-state of a synchronous generator when the oscillation of the angular speed has an impact on the winding currents requires solving the generator electrical equations together with the equation of rotary motion. However, such a set of differential equations is nonlinear. The most popular method is a numerical integration of that equation set. As a result, the steady-state solution in the time domain could be obtained. To find useful measures of currents and torque, i.e. mainly their Fourier spectra, additional signal processing is necessary, this can be complicated because steady-state performances are quasi-periodic in such cases. The steady-state in a considered case can be directly determined in the frequency domain using the harmonic balance method for nonlinear systems presented in [5]. This allows finding a steady-state for the synchronous generator directly in the frequency domain, when the period of the alternating component of mechanical torque is known. This algorithm, after some modifications, can also be applied to determine a steady-state when the external mechanical torque is a periodic function of the rotation angle.

This paper presents the steady-state analysis of a salient-pole synchronous generator running synchronously and driven by a four-stroke internal-combustion engine [2]. The basic model of synchronous machines was used assuming linearity of the magnetic circuit when the stator windings are supplied by the balanced voltage source and the field winding is supplied by a DC voltage source. The steady-state equations combining both electrical and mechanical equations were formulated by the harmonic balance method and the Newton–Raphson algorithm was used to solve them. The results are presented in the form of the Fourier spectra of all generator currents as well as the power angle.

2. Formulation of harmonic balance equations for a synchronous machine

The harmonic balance method [6] operates within the complex Fourier series. Therefore, the synchronous machine equations are presented at a specially chosen rotating coordinate system (0,+,–) [6]. For those coordinates, the three phase voltages and stator currents are

represented by complex time functions and in steady-states they can be described by the complex Fourier series. Resulting equations in (0,+,-) coordinates take the forms: the electrical equations (1a) and the mechanical equation (1b), in which notations follow [6]:

$$\begin{bmatrix} u^{+} \\ u^{-} \\ U_f^{'} \\ 0 \\ 0 \end{bmatrix} = \begin{bmatrix} R_s i^{+} \\ R_s i^{-} \\ R_f^{'} i_f^{'} \\ R_D^{'} i_D^{'} \\ R_Q^{'} i_Q^{'} \end{bmatrix} + \frac{\mathrm{d}}{\mathrm{d}t} \begin{bmatrix} \psi^{+} \\ \psi^{-} \\ \psi_f^{'} \\ \psi_D^{'} \\ \psi_Q^{'} \end{bmatrix} + \mathrm{j}\Omega_s \begin{bmatrix} \psi^{+} \\ -\psi^{-} \\ 0 \\ 0 \\ 0 \end{bmatrix} \tag{1a}$$

$$J \frac{\mathrm{d}^2 \varphi}{\mathrm{d}t^2} + D \frac{\mathrm{d}\varphi}{\mathrm{d}t} = T_{em} + T_m(\varphi);\ T_{em} = \mathrm{j}p\ (i^{-}\psi^{+} - i^{+}\psi^{-}) \tag{1b}$$

The balanced stator voltages are represented in these coordinates by constant values:

$$u^{+} = u^{-} = \sqrt{\tfrac{3}{2}} U \tag{2}$$

The list of unknown functions for equations (1a, b) is: $i^{+}(t)$; $i^{-}(t)$; $i_f'(t)$; $i_D'(t)$; $i_Q'(t)$; rotor rotation angle $\varphi(t)$. The harmonic balance method allows qualitatively and quantitatively predicting periodic or quasi-periodic solutions in steady-states. The rotation angle $\varphi(t)$ is not periodic in time and must be replaced by some periodic function. At a synchronous speed, the angle $\varphi(t)$ can be substituted by its fluctuations $\Delta\varphi(t)$ defined by the formula:

$$\varphi(t) = \left(\Omega_s / p\right) \cdot t + \Delta\varphi(t) \tag{3}$$

where:
Ω_s – pulsation of supplied voltages,
p – pole-pair number.

The mechanical equation (1b) takes new form:

$$J \frac{\mathrm{d}^2 \Delta\varphi}{\mathrm{d}t^2} + D \frac{\mathrm{d}\Delta\varphi}{\mathrm{d}t} = T_{em} + T_m(t) - D\ \left(\Omega_s / p\right) \tag{4}$$

Combining (1a) and (4) into one set, the resulting vector equation takes the form:

$$\frac{\mathrm{d}^2}{\mathrm{d}t^2} \mathbf{F}_2(\mathbf{x}) + \frac{\mathrm{d}}{\mathrm{d}t} \mathbf{F}_1(\mathbf{x}) + \mathbf{F}_0(\mathbf{x}, t) = 0 \tag{5}$$

in which the vector of unknown functions **x** has the form:

$$\mathbf{x} = \left[i^{+} \quad i^{-} \quad i_{\mathrm{f}}^{'} \quad i_{\mathrm{D}}^{'} \quad i_{\mathrm{Q}}^{'} \quad \Delta\varphi \right]^{T} \tag{6}$$

And $\mathbf{F}_n(\mathbf{x})$ are vectors of functions with respect to $\mathbf{x}$.

Due to periodicity of the mechanical torque generated by the combustion engine and keeping in mind the assumption that the generator runs synchronously, all variables in vector $\mathbf{x}$ will be periodic too with the period of the forced torque and consequently the functions in vectors $\mathbf{F}_1(\mathbf{x})$, $\mathbf{F}_2(\mathbf{x})$ and $\mathbf{F}_0(\mathbf{x}, t)$ are also periodic. To use the harmonic balance method for the equation (5), all of them should be presented in the form of the complex Fourier series (7) and (8) with the period $T_x = 2\pi/\Omega_x = 1/f_x$, i.e. the period of the oscillating component of the driven torque:

$$\mathbf{x} = \sum_{k=-\infty}^{\infty} \mathbf{X}_k e^{\mathrm{j}k\Omega_x t} = \sum_{k=-\infty}^{\infty} \begin{bmatrix} I_k^+ \\ I_k^- \\ I_{f,k}^{'} \\ I_{D,k}^{'} \\ I_{Q,k}^{'} \\ \varphi_k \end{bmatrix} \cdot e^{\mathrm{j}k\Omega_x t} \tag{7}$$

$$\mathbf{F}_n = \sum_{k=\infty}^{\infty} \mathbf{F}_{n,k} e^{\mathrm{j}k\Omega_x t} = \sum_{k=\infty}^{\infty} \begin{bmatrix} F_{n,k}^1 \\ F_{n,k}^2 \\ F_{n,k}^3 \\ F_{n,k}^4 \\ F_{n,k}^5 \\ F_{n,k}^6 \end{bmatrix} \cdot e^{\mathrm{j}k\Omega_x t}; \quad n \in \{0,1,2\} \tag{8}$$

Substituting the series (7) and (8) into equation (5) and comparing coefficients for the same basic functions on both sides, a set of non-linear algebraic (9) is obtained. It has an infinite number of equations and an infinite number of variables, which are the Fourier coefficients of the series (7).

$$-\mathrm{diag}\begin{bmatrix} \vdots \\ \Omega^2 \\ 0 \\ \Omega^2 \\ \vdots \end{bmatrix} \cdot \begin{bmatrix} \vdots \\ \mathrm{F}_{2,1} \\ \mathrm{F}_{2,0} \\ \mathrm{F}_{2,-1} \\ \vdots \end{bmatrix} + \mathrm{diag}\begin{bmatrix} \vdots \\ \mathrm{j}\Omega \\ 0 \\ -\mathrm{j}\Omega \\ \vdots \end{bmatrix} \cdot \begin{bmatrix} \vdots \\ \mathrm{F}_{1,1} \\ \mathrm{F}_{1,0} \\ \mathrm{F}_{1,-1} \\ \vdots \end{bmatrix} + \begin{bmatrix} \vdots \\ \mathrm{F}_{0,1} \\ \mathrm{F}_{0,0} \\ \mathrm{F}_{0,-1} \\ \vdots \end{bmatrix} = \begin{bmatrix} \vdots \\ 0 \\ 0 \\ 0 \\ \vdots \end{bmatrix} \tag{9}$$

The matrix $\mathbf{\Omega} = 2\pi f_x \mathbf{E}$ is created by the unity matrix $\mathbf{E}$ with dimensions [6 × 6]. Below, simplified notation is used by introducing the so-called vector and matrix representations of the complex Fourier series [6]. As a result, equation (9) takes the form:

$$-(\mathbf{\Omega})^2 \cdot \mathbf{F}_2 + \mathrm{j} \cdot \mathbf{\Omega} \cdot \mathbf{F}_1 + \mathbf{F}_0 = 0 \tag{9a}$$

3. Iterative algorithm of finding steady-state solutions for a synchronous machine

The equation (9a) constitutes an infinite set of non-linear algebraic equations with the infinite number of variables. It can only be solved numerically by using an iterative procedure when the number of equations and number of variables are reduced to finite one, i.e. reducing the number of considered harmonics in the Fourier series (7) and (8) to sufficiently high. In this paper, the Newton–Raphson iterative procedure was used given by the general formula:

$$\mathbf{x}^{i+1} = \mathbf{x}^{i} - \mathbf{J}(\mathbf{x}^{i})^{-1} \cdot \mathbf{F}(\mathbf{x}^{i}) \tag{10}$$

The matrix $\mathbf{J}(\mathbf{x})$ and the vector $\mathbf{F}(\mathbf{x})$ are the respective matrix and vector representation and they are determined by the formulas below:

$$\mathbf{F}(\mathbf{x}) = -\left(\boldsymbol{\Omega}\right)^{2} \cdot \mathbf{F}_{2}(\mathbf{x}) + \mathrm{j} \cdot \boldsymbol{\Omega} \cdot \mathbf{F}_{1}(\mathbf{x}) + \mathbf{F}_{0}(\mathbf{x}) \tag{11}$$

$$\begin{aligned} \mathbf{J}(\mathbf{x}) = \frac{\partial \mathbf{F}(\mathbf{x})}{\partial \mathbf{x}} &= -\left(\boldsymbol{\Omega}\right)^{2} \cdot \frac{\partial \mathbf{F}_{2}(\mathbf{x})}{\partial \mathbf{x}} + \mathrm{j} \cdot \boldsymbol{\Omega} \cdot \frac{\partial \mathbf{F}_{1}(\mathbf{x})}{\partial \mathbf{x}} + \frac{\partial \mathbf{F}_{0}(\mathbf{x})}{\partial \mathbf{x}} = \\ &= -\left(\boldsymbol{\Omega}\right)^{2} \cdot \mathbf{F}_{d,2}(\mathbf{x}) + \mathrm{j} \cdot \boldsymbol{\Omega} \cdot \mathbf{F}_{d,1}(\mathbf{x}) + \mathbf{F}_{d,0}(\mathbf{x}) \end{aligned} \tag{12}$$

The matrices $\mathbf{F}_{d,k}(\mathbf{x})$ (for k = 1, 2, 3) are calculated based on the functions in the vectors $\mathbf{F}_{1}(\mathbf{x})$, $\mathbf{F}_{2}(\mathbf{x})$ and $\mathbf{F}_{0}(\mathbf{x}, t)$.

$$\mathbf{F}_{d,n}\left(\mathbf{x}\right) = \frac{\partial \mathbf{F}_{n}\left(\mathbf{x}\right)}{\partial \mathbf{x}} = \begin{bmatrix} \frac{\partial f_{n,1}}{\partial i^{+}} & \frac{\partial f_{n,1}}{\partial i^{-}} & \frac{\partial f_{n,1}}{\partial i_{f}^{'}} & \frac{\partial f_{n,1}}{\partial i_{D}^{'}} & \frac{\partial f_{n,1}}{\partial i_{Q}^{'}} & \frac{\partial f_{n,1}}{\partial \Delta\varphi} \\ \frac{\partial f_{n,2}}{\partial i^{+}} & \frac{\partial f_{n,2}}{\partial i^{-}} & \frac{\partial f_{n,2}}{\partial i_{f}^{'}} & \frac{\partial f_{n,2}}{\partial i_{D}^{'}} & \frac{\partial f_{n,2}}{\partial i_{Q}^{'}} & \frac{\partial f_{n,2}}{\partial i\Delta\varphi} \\ \frac{\partial f_{n,3}}{\partial i^{+}} & \frac{\partial f_{n,3}}{\partial i^{-}} & \frac{\partial f_{n,3}}{\partial i_{f}^{'}} & \frac{\partial f_{n,3}}{\partial i_{D}^{'}} & \frac{\partial f_{n,3}}{\partial i_{Q}^{'}} & \frac{\partial f_{n,3}}{\partial \Delta\varphi} \\ \frac{\partial f_{n,4}}{\partial i^{+}} & \frac{\partial f_{n,4}}{\partial i^{-}} & \frac{\partial f_{n,4}}{\partial i_{f}^{'}} & \frac{\partial f_{n,4}}{\partial i_{D}^{'}} & \frac{\partial f_{n,4}}{\partial i_{Q}^{'}} & \frac{\partial f_{n,4}}{\partial \Delta\varphi} \\ \frac{\partial f_{n,5}}{\partial i^{+}} & \frac{\partial f_{n,5}}{\partial i^{-}} & \frac{\partial f_{n,5}}{\partial i_{f}^{'}} & \frac{\partial f_{n,5}}{\partial i_{D}^{'}} & \frac{\partial f_{n,5}}{\partial i_{Q}^{'}} & \frac{\partial f_{n,5}}{\partial \Delta\varphi} \\ \frac{\partial f_{n,6}}{\partial i^{+}} & \frac{\partial f_{n,6}}{\partial i^{-}} & \frac{\partial f_{n,6}}{\partial i_{f}^{'}} & \frac{\partial f_{n,6}}{\partial i_{D}^{'}} & \frac{\partial f_{n,6}}{\partial i_{Q}^{'}} & \frac{\partial f_{n,6}}{\partial \Delta\varphi} \end{bmatrix}; \quad n \in \{0,1,2\} \tag{13}$$

Details of calculating the individual components of expressions (11), (12) and (13) after each iteration are described in [7]. The problem of selecting the starting point for the iterative algorithm is also discussed in that paper.

4. The results of numerical calculations

The iterative algorithm was implemented in MATLAB. Calculations were provided for the synchronous machine with rated data $P_N = 1250$ kW, $U_N = 6$ kV, $\cos\varphi_N = 0.9$, $n_N = 750$ rpm, $J_s = 250$ kg · m^2. It was assumed that $I'_f = 0.95I'_{fN}$ and that the mean value of the torque was equal to the rated torque. The spectra of the phase stator current and load angle were selected as the most representative measures of the generator properties.

Numerical tests were done to study the influence of the moment of inertia and the number of combustion engine pistons on the performance of the synchronous generator. As a reference, the case when a torque performance versus rotary angle is as in Fig. 1, i.e. represents the torque of a four-stroke internal combustion engine [2].

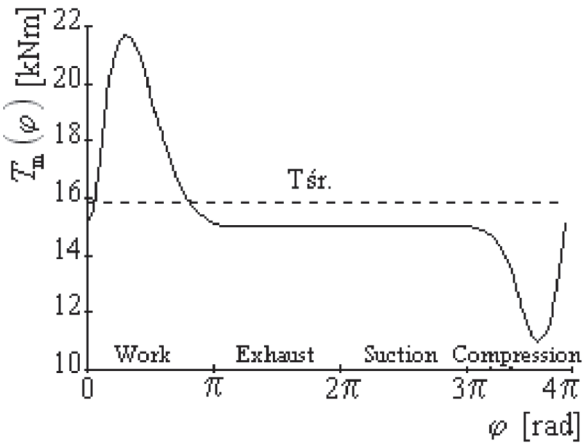

Fig. 1. The torque of the four-stroke internal combustion engine [2]

Figures 2 and 3 present the influence of the moment of inertia on the spectra of the stator phase current and the load angle. The amplitudes of the individual components are done in decibels due to significant differences in their values. The spectrum of the phase stator current $i_a(t)$ given by the formula:

$$i_a(t) = \sum_{k=-N}^{N} I_k \cdot \cos\left[\left(\Omega_s + k \cdot \left(\Omega_s / 2p\right)\right)t + \alpha_k\right] \tag{14}$$

is shown in Fig. 2. The component I_0 with network frequency $f_0 = 50$ Hz dominates in this spectrum. Frequencies of other harmonics take the values according to relationships $f_s = f_s + k \cdot (f_s/2p)$, in which p is the generator pole-pair number. From Fig. 2, it follows that if the moment of inertia grows twice, the spectrum of the stator current changes significantly and only the component with network frequency f_s do not change. The first additional components I_{-1} and I_1 are almost 20 dB smaller to the main harmonic I_0 for basic case and are reducing by 10 dB when the moment of inertia is growing twice. For sequent components I_{-2} and I_2, the same tendencies can be observed and they achieve the levels of 2% and 1% of I_0, respectively.

Generally, the growing moment of inertia twice additional components in the stator currents are reducing more than twice and only the basic harmonic I_0 does not change. So, fluctuations of the stator current are reduced, which could be expected.

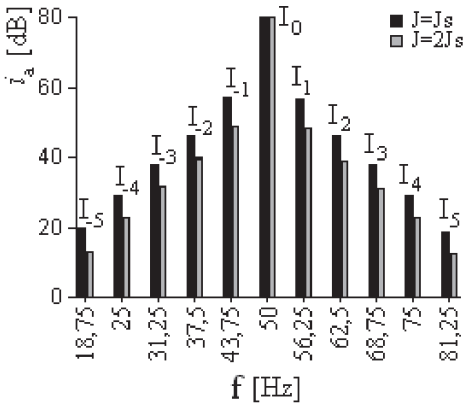

Fig. 2. Spectrum of phase stator current for two different moments of inertia

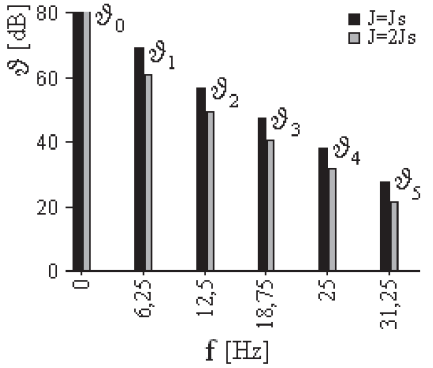

Fig. 3. Spectrum of the power angle for two different values of the moment of inertia

The spectrum of the power angle in Fig. 3, which is done by the formula:

$$\vartheta(t) = \vartheta_0 + \sum_{k=1}^{N} \vartheta_k \cdot \cos\left[\left(k \cdot \left(\Omega_s / 2p\right)\right)t + \beta_k\right] \tag{15}$$

contains components with frequencies $f_k = k \cdot (f_s/2p)$. The component ϑ_0 represents the mean value of the power angle and the amplitudes of sequent components decrease but not as fast as in the stator current spectrum. When increasing the moment of inertia twice, the mean value of the power angle is not changed, whereas the amplitudes of the other harmonics are reduced by over 50%. This means that fluctuations of the angular velocity of the synchronous generator driven by the combustion engine can be reduced by increasing the total moment of inertia, which is in line with expectations.

Improving the uniformity of the mechanical torque of an internal combustion piston engine is commonly achieved by increasing the number of cylinders. For the confirmation of the validity of such a statement, the performance of the mechanical torque versus angle was changed as is shown in Fig. 4. It was found from the curve in Fig. 1 adding two curves respectively shifted, but keeping the mean value. The differences to the mean value decrease and change the Fourier spectrum of the torque. It allows showing the influence of a number of cylinders on the steady-state. Results of calculations are shown in Fig. 5 and Fig. 6.

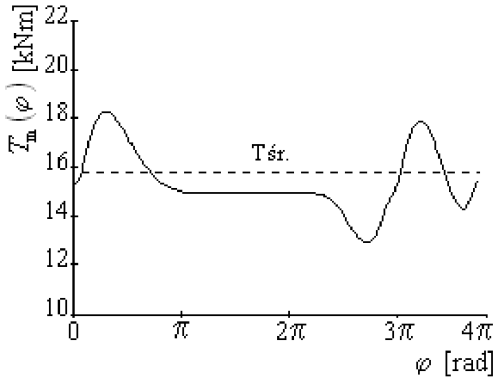

Fig. 4. Mechanical torque of the four-stroke internal combustion engine with double the number ○of the cylinders

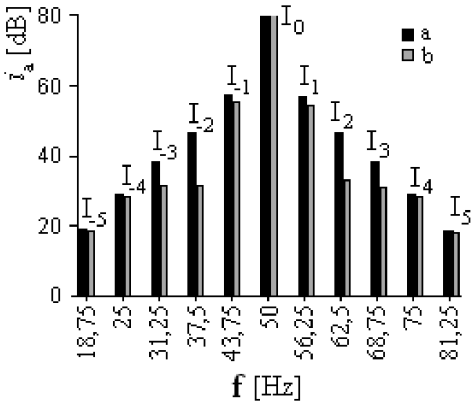

Fig. 5. Spectrum of phase stator currents for: a) four-stroke internal combustion engine, b) four-stroke internal combustion engine with doubled number of cylinders

The spectrum of the phase stator current in Fig. 5 confirms that all higher harmonics are more or less reduced. The most limited are components I_2 and I_{-2} with frequencies of 62.5 Hz and 37.5 Hz respectively, which dropped nearly five times. This means that the stator currents become really close to being sinusoidal.

The spectra of the power angle for those two cases are presented in Fig. 6. All harmonics are decreasing too when the number of cylinders is doubled, beside the mean value. The

second harmonics and higher are reduced significantly – this means that the power angle fluctuations are practically mono-harmonic.

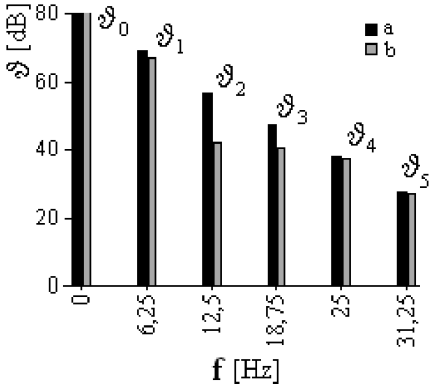

Fig. 6. Spectrum of the power angle for: a) four-stroke internal combustion engine, b) four-stroke internal combustion engine with double the number of cylinders

The developed algorithm also determines the spectra of the field current, of currents of equivalent damping windings and also of the angular velocity but these results are not presented in this paper.

5. Conclusions

The algorithm presented in this paper allows the direct steady-state analysis of synchronous generators driven by a piston engine, which is a source of angle dependent torque. Such an electromechanical system is described by a set of nonlinear differential equations and direct steady-state analysis is extremely complicated. In this paper, the steady-states equations have been created by the harmonic balance method. They have a form of an infinite set of algebraic equations with an infinite number of unknowns. To solve them, the Newton–Raphson iterative algorithm was developed for those equations, when limited to finite dimensions.

Numerical tests show that the presented algorithm is rather effective and allows directly determining the Fourier spectra of generator currents and mechanical variables. This ability of the algorithm can also be applied for determining the spectra in cases of internal faults in generators or faults in the mechanical part of a drive when the angle dependent distortions of the torque are generated. Detail properties of the Fourier spectra in faulty states can be useful for diagnostic purposes using motor current signature analysis.

References

[1] Laudyn D., Pawlik M., Strzelczyk F., *Elektrownie*, WNT, Warszawa 2000.

[2] Anuszczyk J., *Maszyny elektryczne w energetyce. Zagadnienia wybrane*, WNT, Warszawa 2005.

[3] Jagiełło A., *Systemy elektromechaniczne dla elektryków*, Wydawnictwo Politechniki Krakowskiej, Kraków 2008.
[4] Laible Th., *Die Theorie der Synchronmaschine im nichtstationären Betrieb*, Springer-Verlag, Berlin–Göttingen–Heidenberg 1952.
[5] Sobczyk T.J., Radzik M., *Algorytm bezpośredniego określania stanów ustalonych w maszynach synchronicznych z uwzględnieniem równania ruchu metodą bilansu harmonicznych*, Zeszyty Problemowe – Maszyny Elektryczne, 2009, nr 83, BOBRME Komel, pp. 83–88.
[6] Sobczyk T.J., *Metodyczne aspekty modelowania matematycznego maszyn indukcyjnych*, WNT, Warszawa 2004.
[7] Radzik M., *Algorytm bezpośredniego określania stanów ustalonych w maszynach synchronicznych z uwzględnieniem równania ruchu*, praca doktorska, Cracow University of Technology, Cracow 2011.
[8] Radzik M., Sobczyk T.J., *Analiza pracy maszyny synchronicznej napędzanej silnikiem tłokowym*, Zeszyty Problemowe – Maszyny Elektryczne, 2014, nr 103(3), Wyd. Instytut Maszyn i Napędów Elektrycznych (KOMEL), pp. 217–222 (SME 2014).

TECHNICAL TRANSACTIONS | **CZASOPISMO TECHNICZNE**
ELECTRICAL ENGINEERING | ELEKTROTECHNIKA
1-E/2015

GRZEGORZ KAMIŃSKI, RAFAŁ JAKUBOWSKI, EMIL KUPIEC*

COOLING METHODS OF LINEAR MOTORS FOR PRT DRIVE

SPOSOBY CHŁODZENIA SILNIKÓW LINIOWYCH DO NAPĘDU PRT

Abstract

This paper presents thermal calculations and tests of a linear induction motor for a model of a personal rapid transit vehicle drive. Various air and liquid cooling systems are analyzed. Laboratory test results of selected solutions are presented. The thermal equivalent circuit model of selected solutions were made. The calculation results were compared with the test results and the most effective solution was selected.

Keywords: *linear induction motor*, *thermal tests of electrical machines*, *thermal analysis*

Streszczenie

Praca dotyczy obliczeń i badań cieplnych indukcyjnego silnika liniowego przeznaczonego do napędu modelu pojazdu systemu *Personal Rapid Transit*. Przeanalizowano różne układy chłodzenia powietrznego oraz cieczowego. Przeprowadzono badania wybranych rozwiązań układu chłodzenia na rzeczywistym układzie. Wykonano modele matematyczne w postaci sieci cieplnej wybranych rozwiązań. Wyniki badań porównano z wynikami obliczeń oraz wybrano najefektywniejsze rozwiązanie układu chłodzenia rozpatrywanego silnika liniowego.

Słowa kluczowe: *silnik indukcyjny liniowy*, *badania cieplne maszyn elektrycznych*, *obliczenia cieplne*

DOI: 10.4467/2353737XCT.15.057.3857

* Prof. D.Sc. Ph.D. Eng. Grzegorz Kamiński, M.Sc. Eng. Rafał Jakubowski, M.Sc. Eng. Emil Kupiec, Institute of Electrical Machines, Faculty of Electrical Engineering, Warsaw Universitety of Technology.

1. Introduction

In recent years, constructors' interest in drive implementations using linear motors has increased. Linear motors, due to their ability to convert electrical energy directly to the thrust force of linear motion, are becoming more popular in propulsion systems. In this article, a linear induction motor (LIM) applied as drive for vehicle of personal rapid transit (PRT) system is presented. PRT is an idea of the public transportation system based on small vehicles moving on a special track which perform automated point-to-point transportation of passengers with no stops [1]. A single sided flat linear induction motor with short primary part mounted on vehicle and aluminum reaction plate with back-iron on the track was used as the drive unit [2]. The LIM inductor has open structure and its vulnerable parts, such as end-winding connections, are located nearly to the track structure. Ensuring reliability of operation of this machine in outdoor conditions requires adequate mechanical protection for its parts. Measures used for this purpose should allow for effective heat loss dissipation.

Motor operation in the drive of the PRT vehicle is characterized by a high variability of generated thrust (frequent starts and stops) and variable cooling conditions due to driving speed and high ambient temperature range. Therefore, during the design, it is important to pay particular attention to thermal problems occurring in this type of machine.

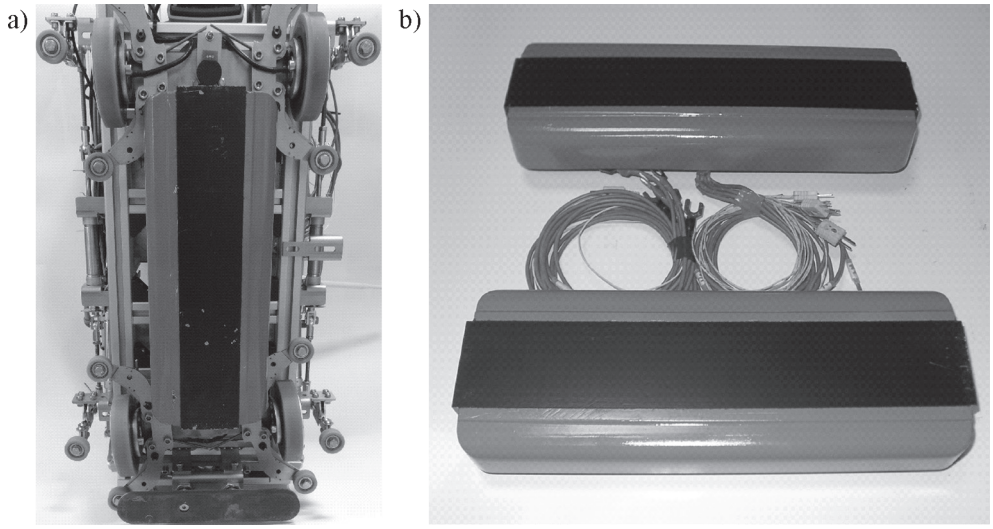

Fig. 1. PRT vehicle model: a) bottom view, b) inductor of the LIM

The article presents a few technical solutions for cooling system for linear induction motors with the short primary part destined for the PRT vehicle model drive.

A model of a PRT vehicle driven by a linear motor is shown in Fig. 1. It consist of an inductor mounted to the vehicle body and bogie, which provides an appropriate air gap between the inductor and the track, keeps the vehicle on the track and supports the change of direction of movement at junctions.

2. Cooling methods of linear motors for PRT drive

The following methods of LIM cooling destined for the PRT drive model have been proposed:

- natural convection – the inductor is not equipped with an additional cooling system, heat transfer occurs only through natural convection (Fig. 1a),
- forced convection – fans are installed on the outer surface of the inductor yoke with a vane system directing air flow over the yoke and end-winding connections surfaces (Figs. 2 and 3a),
- free or forced convection – an inductor with a radiator created by the diversity of the dimensions of the inductor yoke steel sheets (Fig. 4a) or by bending the core sheets (Fig. 4b),
- forced convection with liquid cooling medium – inductor with heat exchanger and liquid cooling system.

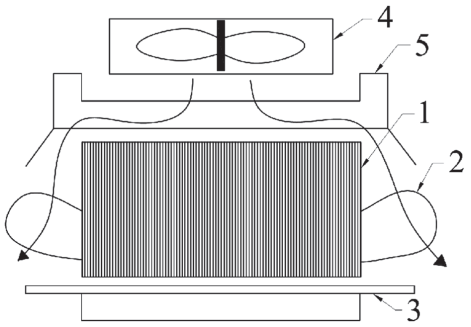

Fig. 2. LIM inductor with convection forced by fans: 1 – core, 2 – end-winding connections, 3 – aluminum reaction plate with back-iron, 4 – fan, 5 – vanes system directing air flow

a) b)

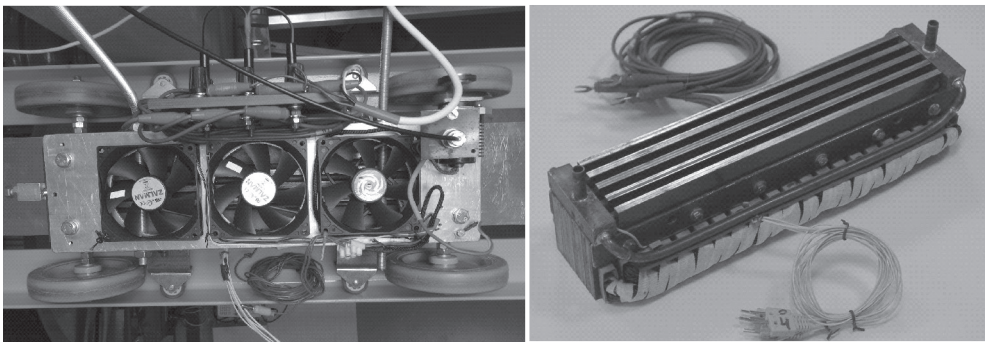

Fig. 3. Model of LIM inductor: a) with convection forced by fans, b) with liquid heat exchanger

An exchanger can be formed by using inductor stack sheets in shapes that ensure the formation of sealed cooling channels and collector channels (Fig. 5) by embedding exchanger pipes into the yoke and end-winding (Fig. 3b) or by using hollow conductors for the inductor winding.

By analyzing the structural terms of the presented cooling methods, it should be noted that the use of LIM solutions with natural cooling creates the necessity of increasing the dimensions of the machine relative to the solutions with forced cooling. An LIM cooling system with a radiator created by differentiated or bended yoke sheets causes an increase in the volume of the motor which in turn causes a larger space in the vehicle reserved for the drive. The solution which provides a compact design of the LIM is a system with a liquid heat exchanger (in the form of pipes with coolant or hollow conductors).

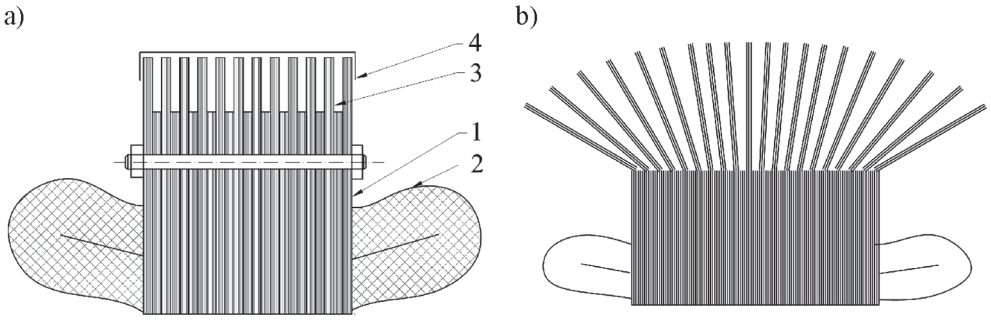

Fig. 4. Inductor with radiator: a) formed by differentiated core sheets, 1 – core, 2 – end-winding connections, 3 – core sheet of various sizes, 4 – cover with vanes system, b) bending core sheet

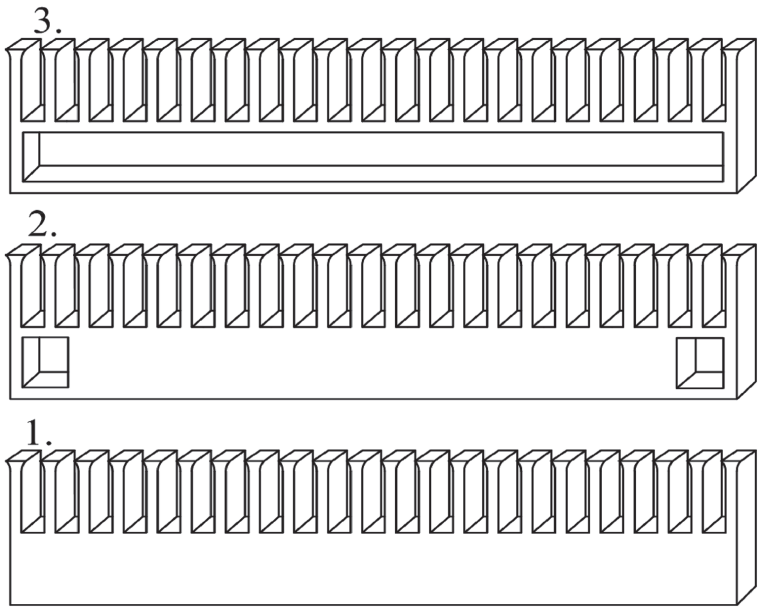

Fig. 5. LIM cooling system with liquid heat exchanger constructed by the use of various steel sheets: 1 – core sheet, 2 – sheets with channels collector, 3 – steel sheets with cooling channel

3. Thermal model of linear motor

A parametrical thermal model of an inductor of geometric dimensions shown in Fig. 7 was build. It enables making the calculations for the cooling system with free convection, forced convection and water cooling.

The geometry of the inductor core was simplified to straight teeth without rounded corners of the slots bottom and without teeth shoes – holes for core pressing and mounting bolts were omitted. The geometry of the thermal model is described by the following list of parameters: h_{ds} – inductor tooth height; b_d – tooth width; b_Q – slot width; h_j – inductor yoke height; l_{Fe} – length of inductor stack – along the cross-section; l_s – length of inductor.

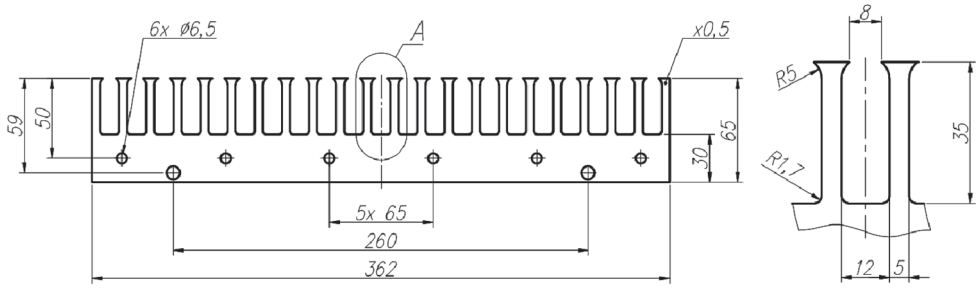

Fig. 7. Dimensions of inductor core model

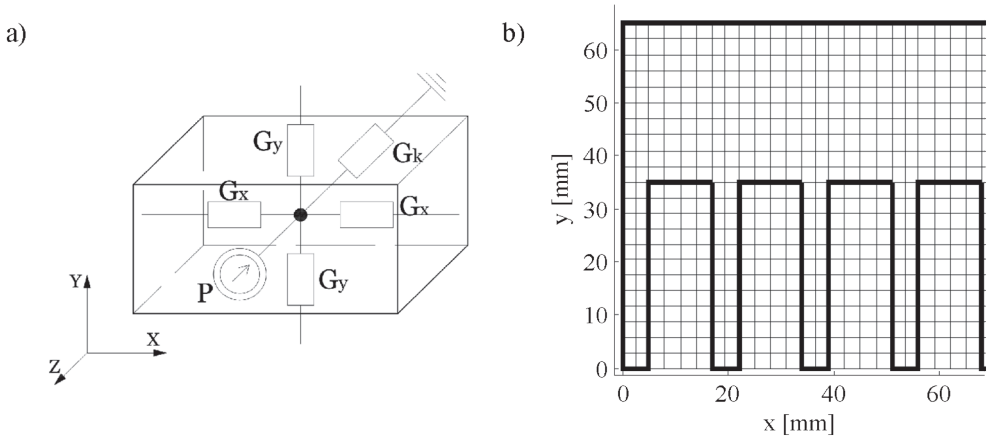

Fig. 8. a) The elementary volume of thermal network and b) fragment of thermal model mesh for the exemplary discretization parameters: $n_{xQ} = 4$, $n_{xd} = 2$, $n_{yj} = 10$, $n_{ydQ} = 12$

Due to the symmetry of the LIM along the length of the core and along the width of the stack, the thermal model of the motor represents 1/4 of physical model. The thermal network method was used for modeling steady state temperature distribution in the LIM structure [3–6]. Temperature differences across the width of the stack were neglected, this allowed building a two-dimensional thermal network. The thermal model was divided into elementa-

ry volume by *ZX* and *ZY* planes of length equal to the width of the stack. The division of the model was described by the following discretization parameters: n_{xQ} – number of nodes in *X*-axis, in area of one slot; n_{xd} – number of nodes in *X*-axis, in area of one tooth; n_{yj} – number of nodes in the *Y*-axis, in area of yoke; n_{ydQ} – number of nodes in *Y*-axis, in teeth and slots area. As a result of discretization, the model was divided into an elementary volume. The fragment of the model with an exemplary discretization is shown in Fig. 8b).

Figure 8a) shows the view of the thermal network model elementary volume described by the following parameters: G_x – thermal conductance in *X*-axis; G_y – thermal conductance in *Y*-axis; G_k – thermal conductance to the coolant medium; *P* – heat source power flowing into volume.

In the presented model, heat transfer to the other elements and to the ambient cooling medium by conduction and convection was taken into account but emission, due to its small contribution to heat transfer, was ignored. Convection occurs in heat transfer from the side and top surface of the inductor yoke to the ambient air or the liquid cooling medium and from the surface of the teeth top and slots to the air gap. In the remaining parts of the LIM, heat transfer occurs by conduction. The power losses in winding and core are here the heat sources. Power losses in the inductor winding were calculated based on winding resistance and the set up currents. Power losses in the yoke and inductor core teeth were determined in the design calculations.

Thermal networks were solved by a method analogous to the nodal potential method used in the electrical networks. Conduction and convection conductance were matched into conductance matrix *G*. Power losses and heat fluxes are matched in sources vector *P*. The system of equations with unknown temperatures ϑ, has the following form:

$$G \cdot \vartheta = P \tag{1}$$

A description of the formulation and solution thermal network algorithm is presented in [4, 5].

4. Thermal tests of linear motor model

Thermal tests of the linear induction motor for the PRT driver were performed for three constructions of the inductor:

- inductor 1 – inductor with impregnated winding,
- inductor 2 – inductor with winding impregnated with resin – monolithic inductor (Fig. 1b),
- inductor 3 – monolithic inductor with liquid heat exchanger (Fig. 3b).

The tested physical models of the inductor were equipped with temperature sensors at the following points: T_1 – bottom of the slot; T_2 – between layers of winding; T_3 – under winding wedge; T_4 – in end-winding; T_5 – between heat exchanger pipe and stack; T_w – temperature of water in exchanger. Sensors T_5 and T_w were only used in the inductor with a liquid heat exchanger. Heating tests were performed for three inductor constructions at various cooling conditions:

– inductor 1 with natural cooling,
– inductor 1 with forced convection,
– inductor 2 with natural cooling,
– inductor 2 with forced convection,
– inductor 3 with liquid cooling system,
– inductor 3 with liquid cooling system without radiator fan.

100°C was set as the temperature limit for the LIM model. A series of heating tests for different values of the stator current were performed until a steady state or temperature limit had been reached. Heating test of inductor 3 for inductor winding current $I = 6$ A and working cooling system is shown in Fig. 9.

In Figure 10, heating curves of inductor physical models for presented cooling conditions were compared.

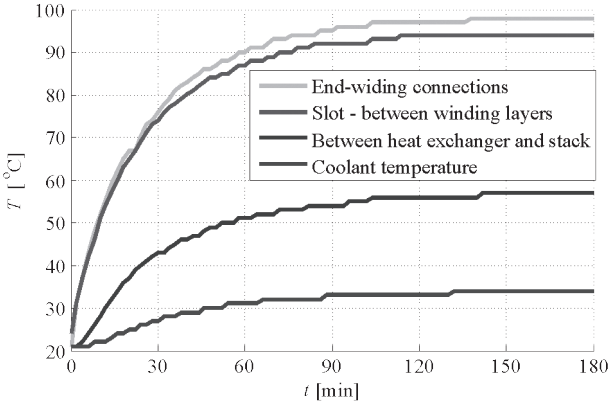

Fig. 9. Temperature vs. time of monolithic inductor supply current $I = 6$ A with working cooling system

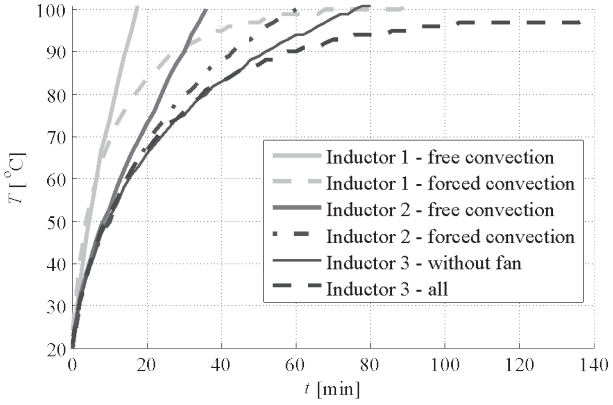

Fig. 10. Comparison of heating curves presented version of LIM supplied with current $I = 6$ A

Through the use of the liquid cooling system, there was a possibility to achieve more than a double increase in inductor heat transfer capacity from inductor elements (from 122 W to 300 W), owing to this, the continuous current for this version of the inductor is $I = 6$ A. The same

power losses (~ 300 W) can dissipate air forced convection cooling system of inductor 1. In the case of failure of the radiator fan of inductor 3, power losses possible to dissipate decreases to 236 W. Inductor 3 has a higher time constant in comparison to inductor 1. When analyzing heating curves, it should be noted that the increase in power losses in the LIM inductor during its heating, may result in deforming the heating curve from the exponential curve.

5. Thermal calculations of the linear motor model

A series of thermal calculation models with free, forced, and water cooling were performed. In Figure 11, the distribution of average temperature along the length of the inductor core on specific core heights for inductor 3 with working cooling system and supplied current $I = 6$ A is shown.

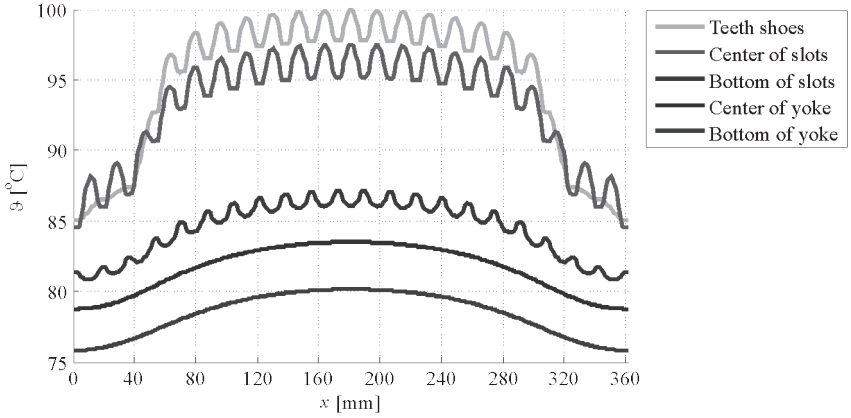

Fig. 11. Temperature distribution in the longitudinal section of the LIM model for current $I = 6$ A and forced water cooling

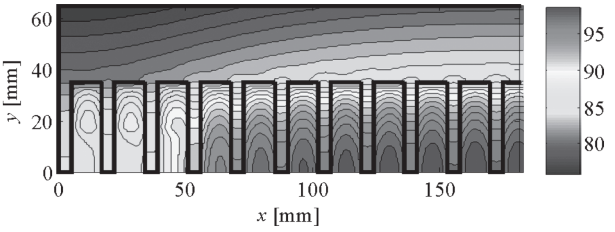

Fig. 12. Temperature map of half of longitudinal section of LIM model for current $I = 6$ A and forced water cooling

Figure 12 shows the temperature map at half of the longitudinal section of the inductor.

The local temperature increases correspond to inductor slots that generate the most losses. Lower temperature of core edges result from the winding scheme of the machine. In three peripheral slots at the end of inductor stack, there was only one layer of winding – due to this,

these regions had generated half of the heat losses. The highest temperature value occurs in the central axis of the slot. The temperature between the layers of winding in the middle slot of inductor 3 cooled by water is 98°C and this is close to the result obtained from measurements.

In order to establish the relationship between the maximum temperature of the inductor winding and the supply current for air and water cooling methods, a series of calculations of the LIM thermal network model were made. Calculation results are shown in Fig. 13.

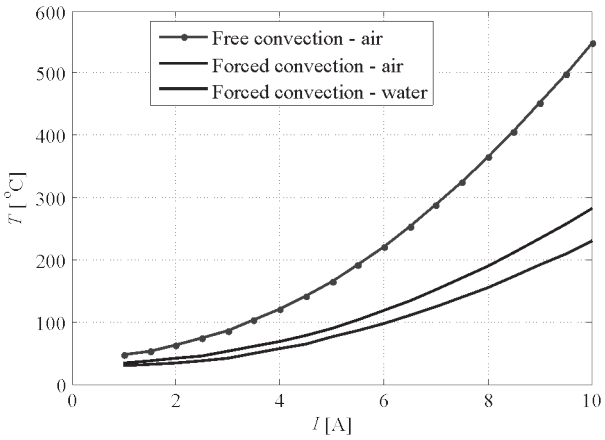

Fig. 13. Dependence maximum temperature in LIM model on inductor current for three cooling methods

The current increase causes a disproportional increase in maximum temperature. Increasing cooling intensity decreases the temperature value.

6. Summary

The paper presents selected methods of cooling LIM designed for the model of the PRT vehicle driver. Results of research and calculations of the physical model of LIM were presented.

The calculation results correspond to a large extent with the results of research. The occurring differences between measured and calculated values of temperature are caused by simplified assumptions in the mathematical model and the difficulty in obtaining proper thermal conductivity data and convection coefficient, which is strongly dependent on the temperature and the characteristic dimensions of heat sink surface.

The use of active cooling methods of the inductor allows more than a double increase in value of drained power losses from its inside and thus a corresponding increase in rated thrust force. It should be noted that in the water cooling system, there occurs the relatively large temperature difference between the winding (primary source of heat) and the heat exchanger, which means high resistance in this part of the thermal circuit. Reducing value of this thermal resistance by transferring heat exchanger on the bottom of the slots or making the winding of the hollow conductor makes it possible to further improve the efficiency of the drain heat losses from the inductor.

References

[1] Fitcher D., *Individualized automatic transit and the city*, Chicago, Illinois 1964.
[2] Kamiński G., Herbst A., *Porównanie wyników elektromagnetycznych obliczeń polowych 2D i 3D dla jednostronnego indukcyjnego silnika liniowego*, Zeszyty Problemowe – Maszyny Elektryczne, 2011, nr 93, pp. 109–112.
[3] Szczypior J., Jakubowski R., *Układ chłodzenia i obliczenia cieplne maszyny z magnesami trwałymi i zewnętrznym wirnikiem*, Zeszyty Problemowe – Maszyny Elektryczne, 2014, nr 103, pp. 151–156.
[4] Krok R., *Sieci cieplne w modelowaniu pola temperatury w maszynach elektrycznych prądu przemiennego*, Monografia, Wydawnictwo Politechniki Śląskiej, Gliwice 2010.
[5] Szczypior J., Jakubowski R., *Obliczenia cieplne w bezrdzeniowej maszynie dyskowej z magnesami trwałymi o chłodzeniu bezpośrednim*, Zeszyty Problemowe – Maszyny Elektryczne, 2009, nr 83, pp. 59–66.
[6] Szczypior J., Jakubowski R., *Metody bezpośredniego chłodzenia uzwojenia w bezrdzeniowej maszynie dyskowej z magnesami trwałymi*, Zeszyty Problemowe – Maszyny Elektryczne, 2010, nr 88, pp. 109–115.

TECHNICAL TRANSACTIONS | **CZASOPISMO TECHNICZNE**
ELECTRICAL ENGINEERING | ELEKTROTECHNIKA
1-E/2015

JAN SZCZYPIOR, RAFAŁ JAKUBOWSKI*

THERMAL CALCULATIONS AND TESTING OF EXTERNAL ROTOR PERMANENT MAGNET MACHINE

OBLICZENIA I BADANIA CIEPLNE MASZYNY Z MAGNESAMI TRWAŁYMI I ZEWNĘTRZNYM WIRNIKIEM

Abstract

The work concentrates on the thermal calculations and tests of the permanent magnet machine with an external rotor and cooled with liquid flowing around the inner surface of the stator frame. The distribution of the temperature in the cross-section of the machine, obtained as a result of the thermal net solutions in a steady state is presented. The calculation results are compared with the test results.

Keywords: *outer rotor PM electrical machines*, *thermal calculations*, *thermal tests of electrical machines*

Streszczenie

W pracy przedstawiono model do obliczeń cieplnych i stanowisko do badań maszyny z magnesami trwałymi i zewnętrznym wirnikiem, w której wewnętrzna powierzchnia korpusu stojana jest chłodzona cieczą. Zaprezentowano rozkład temperatury w przekroju poprzecznym maszyny otrzymany w wyniku rozwiązania zastępczej sieci cieplnej, w stanie ustalonym. Wyniki obliczeń porównano z wynikami badań.

Słowa kluczowe: *maszyna elektryczna z magnesami trwałymi*, *obliczenia cieplne*, *badania cieplne*

DOI: 10.4467/2353737XCT.15.058.3858

* Ph.D. Eng. Jan Szczypior, M.Sc. Rafał Jakubowski, Institute of Electrical Machines, Faculty of Electrical Engineering, Warsaw University of Technology.

1. Introduction

The work refers to the permanent magnet machine with an outer rotor designed for the direct drive of an electric vehicle. Knowledge of the temperature distribution inside the machine is needed for the proper design of the magnetic circuit and cooling system. Parameters of neodymium magnets worsen with the increase of temperature. Cooling systems should ensure that the maximum and average temperature in the magnets and winding are not exceeded. These temperatures are the input data for electromagnetic calculation which gives the design and operational parameter of the machine.

Vehicle requirements and the first version of the machine construction are presented in [1]. The machine has continuous power of 5 kW at a speed of 330 rev/rpm. Additionally, the machine must ensure a triple torque overload and a 70% increase of speed. The machine presented in this paper is different to the machine discussed in [1] with regard to:

– bearing system, which provides easier access and regulation of bearing slackness,
– design of disk and rotor body which allows increasing the maximum speed,
– seal system, which improves its efficiency and reliability.

Construction of the presented machine is shown in Fig. 1, a view of the built prototype is shown in Fig. 2.

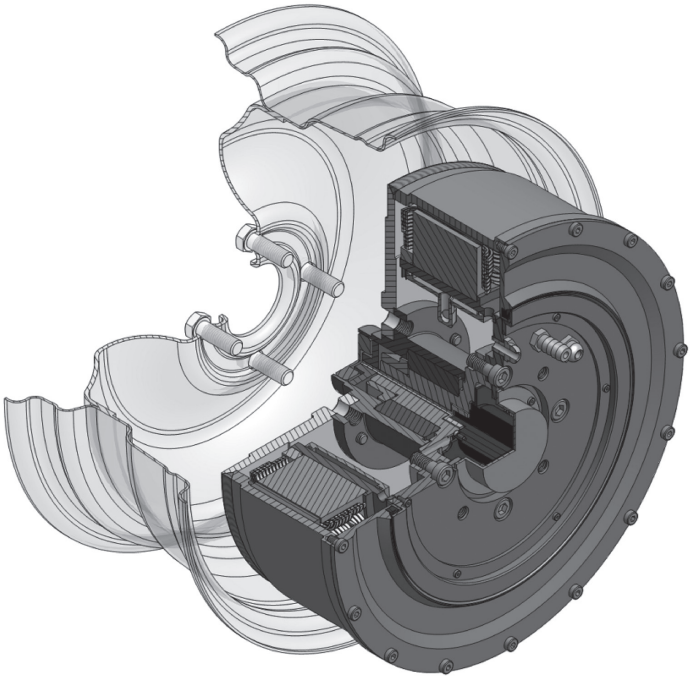

Fig. 1. Construction of machine

Thermal model of machine including stator and cooling channel is presented in [2].

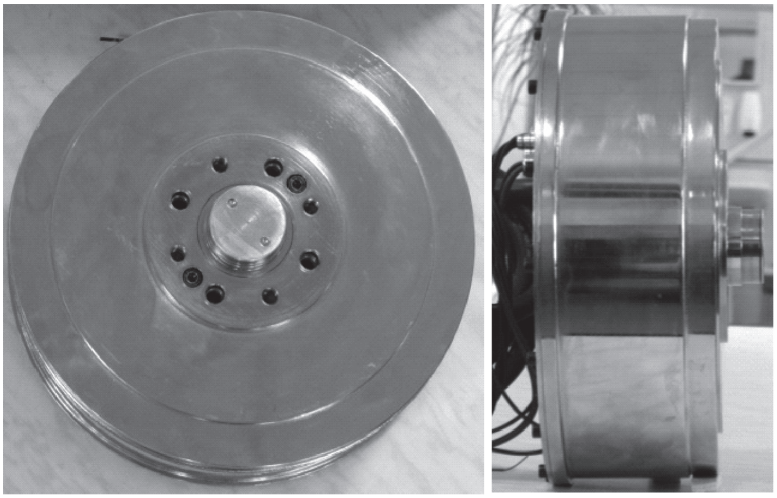

Fig. 2. View of built prototype

In this paper, two methods of cooling were compared. A cooling solution with two parallel circuits (inlet to the channel at the bottom and outlet at the top), which is considered in this work, enabled lower temperatures and easier channel venting. Initial tests of the built prototype have shown that the thermal model should also include the rotor. The reason for this is that the power losses generated were due to flux pulsation in the magnets and yoke. Moreover, rotating the outer rotor is cooled by the air. What is more, heat transfer from the stator disk to the structure which mounts it to the stand or vehicle suspension, was observed and taken into consideration.

In the following part of the paper, the thermal model of the machine and results of calculations are presented, which are than compared with measurements made on the research stand.

2. Thermal model of the machine

In order to model the temperature distribution in the machine in a thermal steady state, thermal network was used [3–6]. By ignoring differences in the temperature along the length of the machine, a two-dimensional thermal model of half machine from the inlet to the outlet of the cooling medium was built. The modelled half of the machine was divided into elementary volumes by planes *RZ* i *Z*ϑ. These volumes have the same thickness, which equals l_s – length of the stator packet. Elementary volumes in the teeth area have a constant width and rectangular prism shape, the remaining volumes have shape of the ring sector. The dimensions of the elementary volumes were made dependent from parameters of the design and discretization.

To the set of design parameters belong: Q_s – number of stator slots; r_{re} – outer rotor radius; h_{jr} – height of rotor yoke; h_m – magnets height; α_e – pole magnet fill factor; δ – thickness of the air gap; r_{se} – stator outer radius; h_{ds} – stator tooth height; b_d – stator tooth width; h_{js} – height of the stator yoke; d_{szp} – thickness of gap between stator and body; g_{ks} – thickness of stator body wall; h_k – height of cooling channel.

Division into the elements of the modelled area define the list of the following parameters: n_{rjs} – number of layers in stator yoke along radius; n_{rd} – numbers of layers in slot and tooth along radius; n_{rm} – number of layers in permanent magnet along radius; n_{rjw} – number of layers in rotor yoke along radius; n_{fid} – number of divisions around angle in tooth area; n_{fiq} – number of divisions around angle in slot area. Angle division parameters in slot-tooth area are passed on to remaining areas of the machine. The areas of the cooling channel with medium, stator frame, air gaps between stator packet body and air gaps between stator and rotor, was modelled as a single layer in the radial direction. Due to this, a parametric thermal model of the machine which allows easily changing the design parameters was obtained. A fragment of the thermal network from the model of half of the machine for exemplary division is shown in Fig. 3.

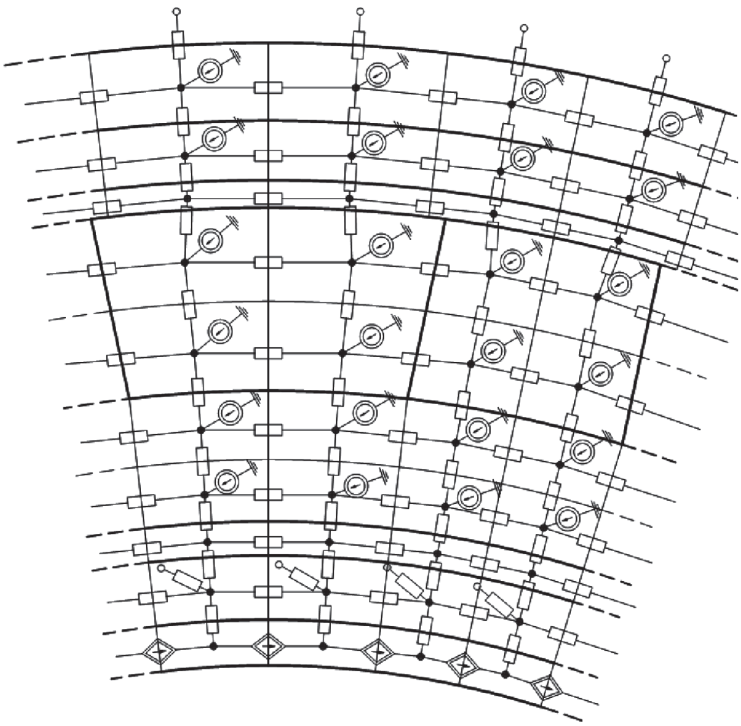

Fig. 3. Fragment of thermal network of machine

The model takes into account heat transfer to other elements and to the surroundings through conduction and convection (emission was omitted). Convection occurs during heat transfer from channel faces to the cooling medium, from stator and rotor surfaces to the air-gap, and from the rotor surface to the surrounding air. In the remaining parts of the machine, heat transfer occurs by conduction.

Power losses generated in winding, in the stator core, in the rotor core, and in the magnets are here the heat sources. Power losses in the windings were determined on the basis of winding resistance and assumed currents. Stator core losses were determined in design calculations. Rotor core losses and losses in magnets were determined based on the mechanical power of

the machine which drives the tested machine during no load test. Knowing power generated in different regions of machine, power losses emitted in elementary volumes were determined.

The set-point temperature of cold water in the model is the reference temperature. Branches in the outer layer of the rotor and stator body are connected with reference temperature. Power losses and heat fluxes in the branches connected to the reference temperatures are heat sources in the thermal network which flow into the nodes. The heat exchange in the channel was modelled as sources of heat flux controlled by temperature of liquid [3, 5].

The thermal network was solved by using a method analogous to the nodal potential method used in electrical networks. In thermal networks, potentials correspond to temperature and heat fluxes correspond to currents or power losses. According to this method, conduction and convection conductance was matched in thermal self-conductance matrix **G** (sum of conductance attached to a given node) and mutual ones (existing between adjacent nodes). Power losses and heat fluxes in branches connected to reference temperatures $\mathfrak{P}$, were matched in source vector **P**. The equation system with unknown temperatures, has the form:

$$\mathbf{G} \cdot \mathfrak{P} = \mathbf{P} \tag{1}$$

The program for building and solving the thermal model of the machine was written in Matlab. The program allows graphical visualization of results in the form of graphs and maps of temperature. A detailed description of algorithm of formulation and the solution of the thermal network is presented in [4 and 5].

3. Results of calculations

In thermal calculations presented in [2], it was assumed that the thermal conductance coefficient in the channel can range from 500 to 2000 W/m^{2}K. The value of this coefficient depends on the geometry of the channel, liquid velocity, thermal conductivity, viscosity and liquid density. Accordingly, the value of this coefficient is often determined experimentally. In order to find the dependence α_k on the liquid velocity and temperature for three coolant flow rates 0.25, 0.5 and 1 l/minute Reynolds number was calculated [7]:

$$Re = \frac{\rho u d}{\eta} \tag{2}$$

where:

ρ – density of liquid [kg/m3],
η – coefficient of dynamic viscosity of liquid [Pa·s],
u – average linear speed [m/s],
d – equivalent diameter of channel [m], equal $4S_k/b_k$ – S_k – channel cross-section, b_k – circumference of channel.

Calculations were made for water. Density, coefficient of dynamic viscosity and conductivity of water were made conditional on temperature in the range from 10 to 60°C. The value of the Reynolds number in all cases was lower than 2100. This means that the flow is laminar. Next, the Prandtl number was calculated:

$$Pr = \frac{c\eta}{\lambda} \tag{3}$$

where:
c – specific heat [J/kg·K],
λ – thermal conductivity [W/m·K] of water, as a temperature function.

With laminar flow, the Nusselt number is determined as:

$$Nu = C(Re\,Pr\,l_k / d)^n \tag{4}$$

where l_k is channel length.

Value of C and n depend on the product value in brackets (4). Calculated values of the product were greater than 13, therefore $C = 1.86$, $n = 0.33$. Based on the Nusselt number, the heat transfer coefficient in the channel was calculated.

$$\alpha_k = \frac{C(Re\,Pr\,l_k / d)^n \lambda}{d} \tag{5}$$

Calculation results were shown in Fig. 4. The figure shows that α_k increases non-linearly depending on the liquid temperature and velocity.

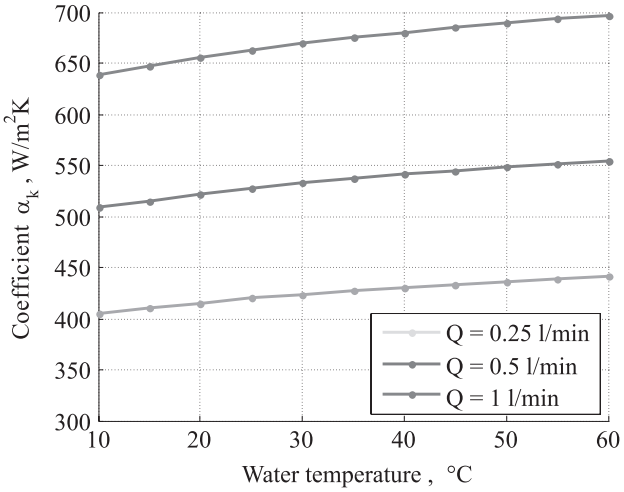

Fig. 4. Dependence of coefficient α_k on liquid temperature and discharge

Calculated values of α_k were used in thermal calculation for the same flow rate of liquid in the channel and for 1.8 times overload of the machine. This overloading was determined in such a way that the maximum temperature of the winding for the smallest liquid flow was close to 120°C. Despite a much greater allowable winding temperature (200°C), such a temperature

was adopted as the maximum due to the adverse effect of temperature on magnet parameters. For easier comparisons of calculation results with research results, the same temperature of cold water was set up (26.5°C). Results of calculations at a flow equal to 0.25 l/min is shown in Fig. 5a) and b), and at a flow equal to 0.5 and 1 l/min, in Fig. 6a) and b).

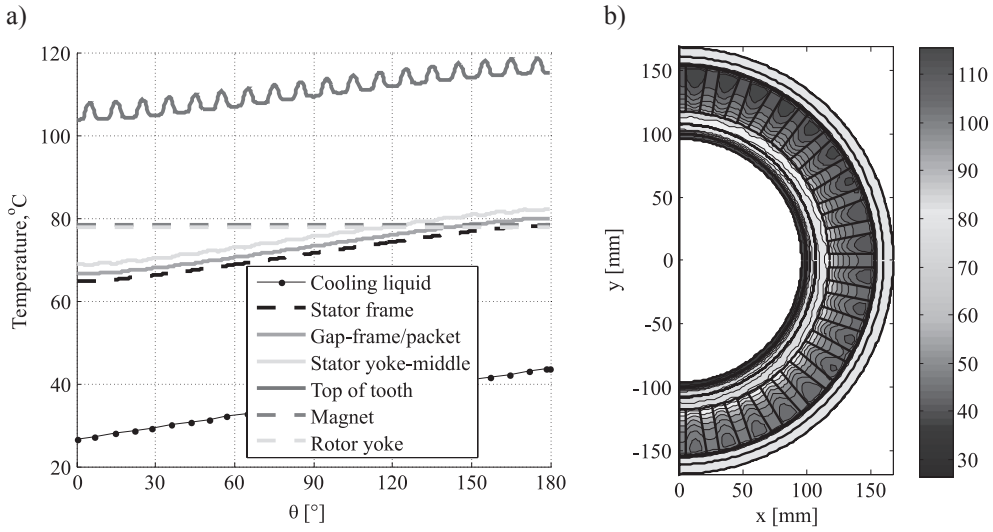

Fig. 5. Temperature distribution in: a) selected areas of constant radius and angle in the range of 0 to 180°, at a flow of liquid 0.25 l/min, b) cross-section of the machine at liquid flow 0.25 l/min

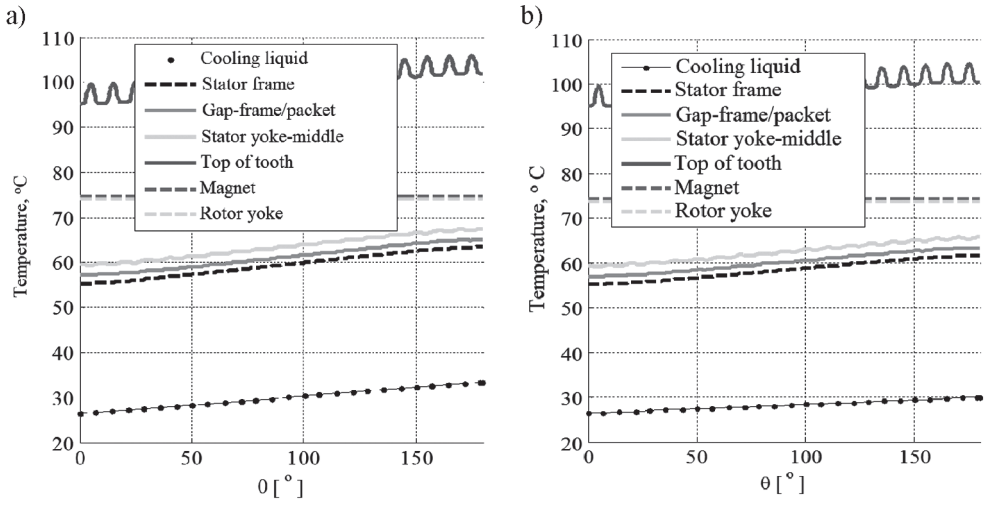

Fig. 6. Temperature distribution in selected areas of constant radius and angle in the range of 0 to 180°, at a flow of liquid: a) 0.5 l/min, b) 1 l/min

4. Machine research

Research of the built prototype was performed on the stand shown in Fig. 7a). The machine was installed in a handle and connected by a system of flexible coupling and a torque meter with a DC machine equipped with a planetary gear. The tested machine was cooled by distilled water in a closed system consisting of a pump with a regulated flow cooling channel inside the stator frame, the flowmeter and the radiator with a fan. 12 type LM135 temperature sensors was placed in the machine. The sensors were placed on two coils located closest to the inlet and outlet of liquid.

a) b)

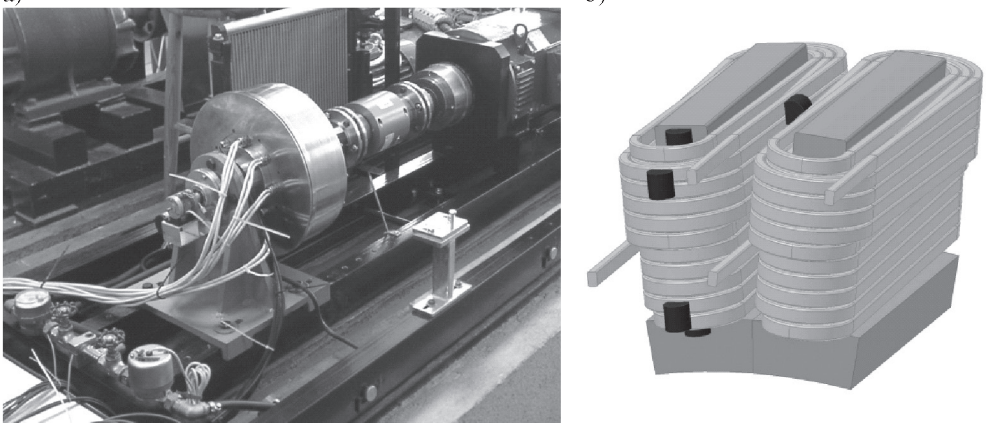

Fig. 7. a) The stand for research of the machine, b) Arrangement of temperature sensors in the coil located closest to the liquid outlet

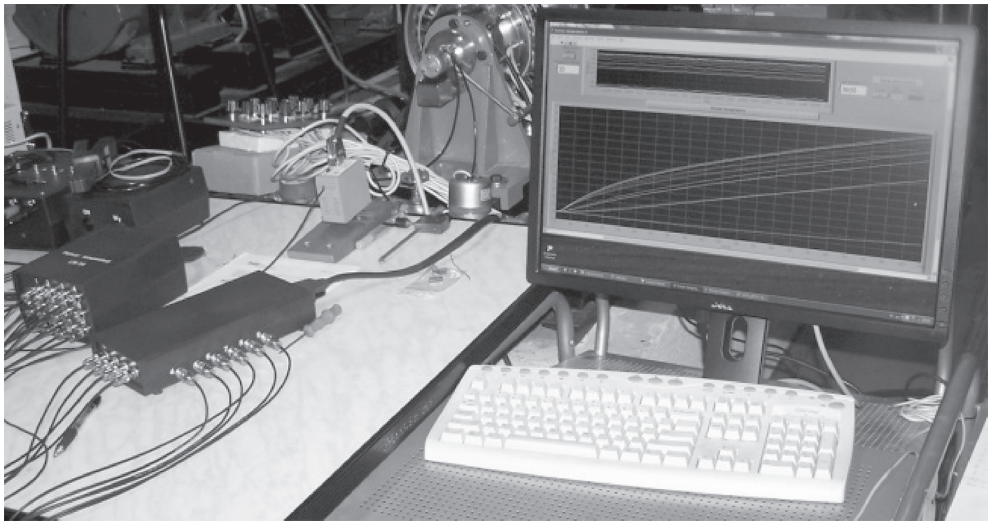

Fig. 8. System for temperature recording

Sensor arrangement in one coil area is shown in Fig. 7b). The remaining 2 sensors measured the temperature of the liquid flowing in and out of the machine.

The measured temperatures were registered using a measuring data card NI PCI 6251 connected to a computer and a specially developed virtual instrument. This device allows simultaneous recording of temperature from 12 sensors in set-up time. Signals from sensors were read at frequency 1 kHz. In order to reduce the number of data points and eliminate random noises, measurements were averaged over 1 sec. Temperature from each sensor calculated in this way was saved in the form of a file. After each results recording, in graphic window of control panel of the instrument current temperature dependence as a function of time were displayed, Fig. 8.

Research was performed in generator state of machine. The machine was driven by a DC motor and loaded with regulated resistance. Three heating tests were performed for the flow rate of liquid in channel (0.25, 0.5 and 1 l/min) and in overload (1.8), same as in the calculation. The time of each test was limited to 120 minutes. After this time, temperatures were practically steady. The maximum temperature in the winding was indicated by the sensor attached to the coil in the middle of the machine length. The maximum temperature dependences on time in the coil located at the outlet (solid lines) and the coil placed near the cooling liquid inlet (dashed line) are shown in Fig. 9. This figure shows that for liquid flow of 0.25 l/min, maximum temperature of the winding is approximately 118°C and is close to the calculated temperature shown in Fig 5a). From Figs. 9, 5a), 6a) and b) show that increases in liquid flow above 0.5 l/min cause a slight reduction in the maximum temperature of the winding. With increasing the flow from 0.5 to 1 l/min the temperature was reduced by only approx. 3°C, while the increase in the flow from 0.25 to 0.5 l/min reduced the temperature by about 10°C.

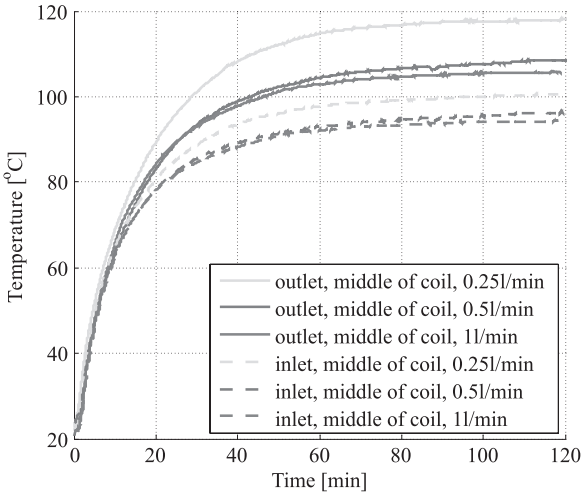

Fig. 9. Maximum temperature of the coil located at the outlet (solid lines) and the coil adjacent to the inlet of the cooling liquid (dashed lines) for different liquid flow rates

Figure 10 shows the dependence of temperature of the liquid flowing in and out of the machine over time. The maximum temperatures are close to the calculated temperatures of hot water from Figs. 5a), 6a) and b). Figures 9 and 10 show that the differences of liquid

temperature are close to the differences of the winding temperature, wherein with increasing speed of liquid, a slight increase in the differences of winding temperatures relative to differences of liquid temperature can be observed.

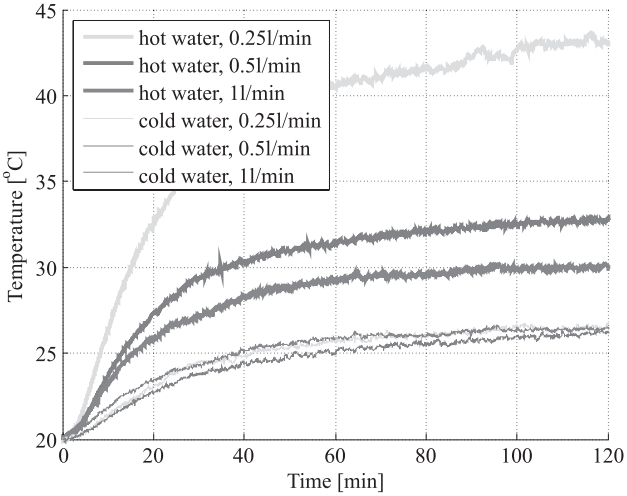

Fig. 10. Temperature of hot and cold liquid at different flow rates

5. Summary

The paper presents a parametric thermal model of the machine with a permanent magnet and external rotor. This model allows determining the temperatures of individual elements of the machine depending on the load and speed of the liquid flow in the cooling channel. The correctness of the model was confirmed by good quantitative correspondence of the calculation results to the test results.

The performed calculation and conducted research suggest that dependence of the maximum winding temperature on the liquid velocity in the channel is highly nonlinear. During determining the optimal liquid flow (as low as possible, which will provide adequate cooling effectiveness), the decreasing power losses in the winding caused by the decreasing temperature and the winding resistance should be compared with the increase in power losses needed to produce the greater liquid flow. In the presented machine, it is the speed approx. 0.5 l/min.

References

[1] Szczypior J., Jakubowski R., *Konstrukcja maszyny do napędu samochodu elektrycznego o specjalnych wymaganiach*, Prace Naukowe Instytutu Maszyn, Napędów i Pomiarów Elektrycznych Politechniki Wrocławskiej, Nr 66/2012, t. 2, pp. 396–407.

[2] Szczypior J., Jakubowski R., *Układ chłodzenia i obliczenia cieplne maszyny z magnesami trwałymi i zewnętrznym wirnikiem*, Prace Naukowe Instytutu Maszyn, Napędów i Pomiarów Elektrycznych Politechniki Wrocławskiej, Nr 66/2012, t. 2, pp. 408–417.
[3] Krok R., *Sieci cieplne w modelowaniu pola temperatury w maszynach elektrycznych prądu przemiennego*, Monografia, Wydawnictwo Politechniki Śląskiej, Gliwice 2010.
[4] Szczypior J., Jakubowski R., *Obliczenia cieplne w bezrdzeniowej maszynie dyskowej z magnesami trwałymi o chłodzeniu bezpośrednim*, Zeszyty Problemowe – Maszyny Elektryczne, 2009, nr 83, BOBRME Komel, pp. 59–66.
[5] Szczypior J., Jakubowski R., *Metody bezpośredniego chłodzenia uzwojenia w bezrdzeniowej maszynie dyskowej z magnesami trwałymi*, Zeszyty Problemowe – Maszyny Elektryczne, 2010, nr 88, BOBRME Komel, pp. 109–115.
[6] Gurazdowski D., Zawilak J., *Rozkład temperatury w pręcie uzwojenia stojana turbogeneratora*, Zeszyty Problemowe – Maszyny Elektryczne, 2006, nr 75, pp. 177–183.
[7] Domański R., Jaworski M., Kołtyś J., Rebow W., *Wybrane zagadnienia z termodynamiki w ujęciu komputerowym*, PWN, Warszawa 2000.

TECHNICAL TRANSACTIONS | **CZASOPISMO TECHNICZNE**
ELECTRICAL ENGINEERING | ELEKTROTECHNIKA
1-E/2015

MARCIN SZCZYGIEŁ, KRZYSZTOF KLUSZCZYŃSKI*

ROTARY-LINEAR INDUCTION MOTOR BASED ON THE STANDARD 3-PHASE SQUIRREL CAGE INDUCTION MOTOR – CONSTRUCTIONAL AND TECHNOLOGICAL FEATURES

SILNIK INDUKCYJNY OBROTOWO-LINIOWY NA BAZIE STANDARDOWEGO 3-FAZOWEGO SILNIKA KLATKOWEGO – CECHY KONSTRUKCYJNE I TECHNOLOGICZNE

Abstract

Induction motors with some degrees of freedom (more than one) belong to unconventional drives which offer wider possibilities of motion than traditional drives. These motors constitute a small group of electric drives, however, new requirements for mechatronic devices are the cause of growing interest in their steady and regular development. As far as rotary-linear motors are concerned, they can be used in devices dedicated to mixing and drilling ensuring both rotary and linear movements. Because of the complex construction of such motors, their manufacturing process is expensive. In order to reduce these costs, the authors develop and propose the concept of the 3-phase rotary-linear machine built-up on the basis of a standard 3-phase squirrel-cage motor. This approach results in the significant reduction of manufacturing costs through the use of prefabricated parts (e.g. complete stator, stack of stator sheets, motor housing), as well as allowing the partial adoption of technologies used for standard induction motors.

Keywords: *squirrel cage induction motor*, *rotary-linear induction motor*, *design and technology process*

Streszczenie

Silniki indukcyjne o wielu stopniach swobody są napędami niekonwencjonalnymi, które charakteryzują się szerszymi możliwościami ruchu niż tradycyjne napędy realizujące wyłącznie ruch liniowy lub ruch obrotowy. Prognozuje się szerokie zastosowanie silników obrotowo-liniowych jako napędów niekonwencjonalnych w urządzeniach, w których moduł obrotowy odgrywa rolę napędu głównego (roboczego) urządzenia, a moduł liniowy odgrywa rolę aktuatora o ruchu postępowym (napędu pomocniczego pozycjonującego końcówkę roboczą). Taki napęd może być wykorzystany przede wszystkim w urządzeniach do mieszania i mielenia. Ze względu na nietypową budowę silników indukcyjnych obrotowo-liniowych i konieczność zastosowania niestandardowych technologii ich proces produkcji jest kosztowny. W celu ograniczenia kosztów ich wytwarzania zaproponowano koncepcję budowy 3-fazowego silnika indukcyjnego obrotowo-liniowego na bazie elementów składowych 3-fazowego silnika indukcyjnego klatkowego. Postępowanie to opisano w sposób szczegółowy na przykładzie 3-fazowego silnika klatkowego typu ShR90X-8M produkowanego seryjnie. Takie podejście powoduje znaczące obniżenie kosztów wytwarzania silnika o 2 stopniach swobody dzięki wykorzystaniu gotowych elementów 3-fazowego silnika indukcyjnego (w szczególności: kompletnego stojana, pakietu blach, korpusu silnika), a równocześnie umożliwia dostosowanie technologii wytwarzania takiego złożonego przetwornika elektromechanicznego do istniejącego procesu produkcyjnego 3-fazowych silników indukcyjnych.

Słowa kluczowe: *silnik indukcyjny klatkowy*, *silnik obrotowo-liniowy*, *konstrukcja i technologia wykonania*

DOI: 10.4467/2353737XCT.15.059.3859

* Ph.D. Eng. Marcin Szczygieł, Prof. D.Sc. Ph.D. Eng. Krzysztof Kluszczyński, Department of Mechatronics, Faculty of Electrical Engineering, Silesian University of Technology.

1. Introduction

Rotary-linear motors (motors with two degrees of freedom denoted as 2DoF motors) belong to unconventional drives which offer wider possibilities of motion than traditional drives. Especially as they enable the formation of a spiral (helical) rotor trajectory which in conventional drives can be obtained only with the help of additional mechanical components (Fig. 1a)). Of course, they can also work as a rotary or as linear motor which is presented in Fig. 1b) and c) respectively. As regards their application, they can be used for instance in a wide range of devices dedicated to the mixing and drilling process. Such an application in a mixing machine is shown in Fig. 2. From the viewpoint of the manipulator theory, the rotary module works as a main drive unit and a linear module plays the role of a linear actuator responsible for positioning the working tool (stirrer). Another possible application in the drilling machine is presented in Fig. 3.

Different types of rotary-linear motors have different principles of operation: asynchronous [1–4]; synchronous with permanent magnet (PMSM) [3, 4]; ultrasonic motors (USM) [5]; switched reluctance motors (SRM) [6]; brushless DC motors (BLDC) [7].

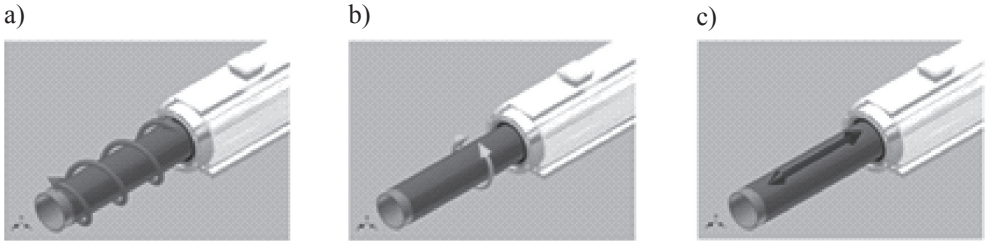

Fig. 1. Trajectories of motion realized by the rotary-linear motor: a) trajectory of the spiral motion (when both linear and rotary modules are supplied), b) trajectory of rotary motion (when only rotary module is supplied), c) trajectory of linear motion (when only linear module is supplied)

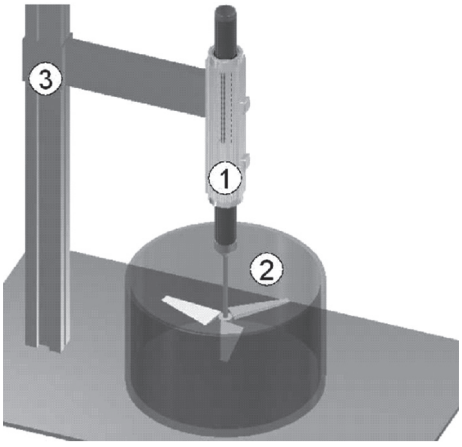

Fig. 2. Examplary application of rotary-linear motor in mixing machine: 1 – rotary-linear motor, 2 – working tool, 3 – stand

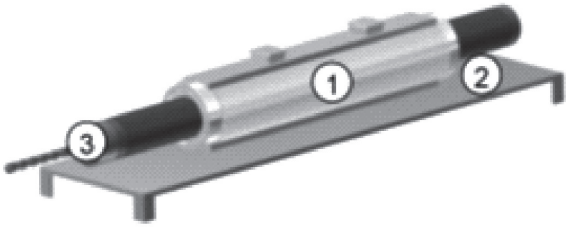

Fig. 3. Examplary application of rotary-linear motor in drilling machine: 1 – rotary-linear motor, 2 – stand, 3 – working tool

2. Constructional features

The 3-phase rotary-linear motor requires 2 types of windings: 3-phase distributed winding (which generates rotating circular magnetic field and is responsible for rotary motion); 3-phase ring winding (which generates travelling magnetic field and is responsible for linear motion).

As far as their location in the 2DoF motor is concerned, there are 2 main possibilities presented in Figs. 4 and 5, respectively.

Motor with one common stator is compact but more complicated. Both distributed and ring windings are located in the common stator and have a common magnetic circuit. The horizontal conductors of a distributed winding and the vertical conductors of a ring winding are mutually perpendicular. This means that the magnetic field density vector in the air-gap of the machine has two perpendicular components relating to the circular and travelling magnetic fields, respectively. Such a 2-dimentional magnetic field requires special construction of a rotor (bar-crossed rotor) [6]. Of course, it is possible to replace this rotor by a solid or tubular rotor which can also interact with both components of the magnetic field [5].

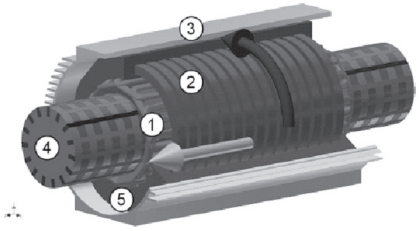

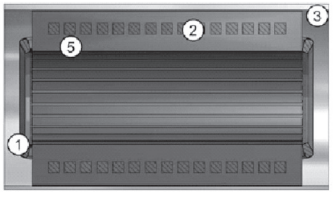

Fig. 4. 2DoF induction motor with one common stator: a) general view, b) cross-section of stator, c) bar-crossed rotor: 1 – winding which generates the rotating circular magnetic field, 2 – ring winding which generates the travelling magnetic field, 3 – housing, 4 – rotor, 5 – common iron core

The motor with two stators has a simpler construction but its total length is usually greater. The two autonomous stators are equipped in two separate windings which can act with a bar-crossed, solid or tubular rotor. The winding located in the first stator (which is called the linear module LM) is responsible for linear motion and the winding located in the secondary stator (called the rotary module RM) is responsible for rotary motion. It is assumed that the both modules can work autonomously.

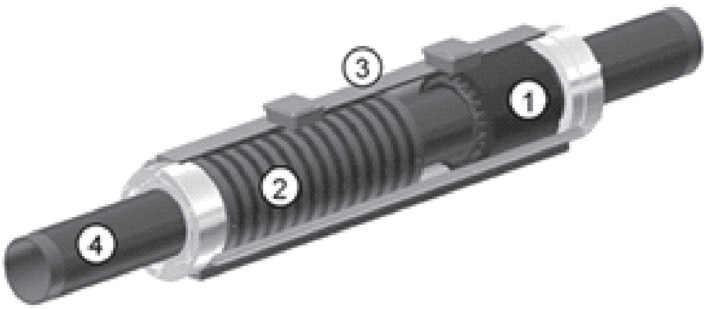

Fig. 5. 2DoF induction motor with two stators: 1 – stator which generates the rotating circular magnetic field, 2 – stator which generates the travelling magnetic field, 3 – housing, 4 – rotor

3. General description of the prototype built on the basis of the induction motor ShR90X-8M

Because of the unconventional construction of the rotary-linear induction motors, non-standard technologies have to be usually employed and, as a consequence, their production process is expensive in comparison with the normal manufacturing process. In order to reduce manufacturing costs, the authors develop and propose the concept of the 3-phase rotary-linear induction motor based on the components of a factory-manufactured 3-phase squirrel cage induction motor.

This approach results in a significant reduction in manufacturing costs through the use of ready-made components (e.g. a complete stator, the motor housing), and at the same time, allows the incorporation of existing technology used in the production process of 3-phase motors.

The main assumed goal during the designing of the 3-phase induction rotary-linear motor was to use as great a number of ready-made components as possible in the 3-phase factory-manufactured squirrel cage induction motor. This assumption results in a relatively cheap and simple production process.

The induction rotary-linear motor elaborated in the Department of Mechatronics at the Silesian University of Technology was made of components normally used for manufacturing the ShR 90X-8M motor. The squirrel-cage motor used as the basis for the new construction has the following specifications: P_N = 750 W; U_N = 400 V; I_N = 2.7 A; n_N = 670 rpm; $2p = 4$; $Q_S = 24$.

3.1. The design of rotary module RM

As has seen in Fig.6, the stator of the module RM is the same as the stator of the 3-phase squirrel-cage motor (including both the magnetic core and the 3-phase distributed winding).

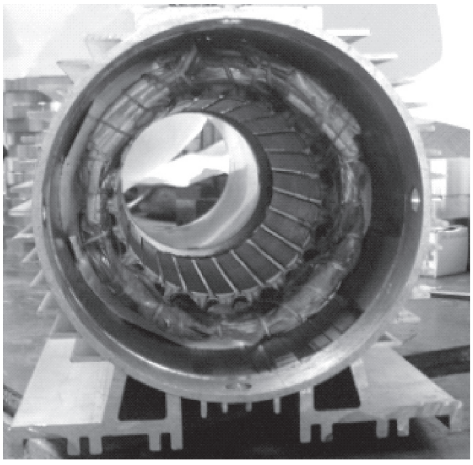

Fig. 6. Module RM – stator ShR 90X-8M after mounting in the housing of the rotary-linear motor

The stator core consist of 240 sheets with a thickness of 0.5 mm (including insulation) made of isotropic electrical tape V600-50A DIN 46400. The stator winding of module RM is a single-layer winding with number of turns $N_s^R = 428$.

3.2. The design of the linear module LM

In order to construct the linear module LM, it is necessary to have sheets of the standard motor which are non-slotted (Fig. 7a) and b)) – this means that during their manufacturing in a factory it is necessary to omit the technological process of slot cutting (Fig. 7a)). The stator of the LM module consists of 13 stacks of the above mentioned non-slotted iron sheets (Fig. 7b)) forming 13 'laminated ferromagnetic rings' (one of which is presented in Fig. 7a)) having an external diameter equal to the external diameter of the basic stator (Fig. 6). These 13 'laminated ferromagnetic rings' (Fig. 7a)) are separated by 12 'solid ferromagnetic rings' (Fig. 8a)) whose external diameter is the same as the diameter of the basic stator. Because of the difference in the internal diameters of the 'laminated rings' and the 'solid rings' (Fig. 8a)), 12 slots are formed in which the ring winding (Fig. 8b)) can be put (Fig. 8c)). From the electromagnetic point of view, the 'laminated ferromagnetic rings' play the role of big teeth and the 'solid ferromagnetic rings' play the role of yokes.

The general view of linear module LM consisting of 13 'laminated rings', 12 'solid rings' and 12 coil rings is presented in Fig. 9a) (computer visualization). The photo of the finished stator of the linear module LM (being part of the constructed prototype) is presented in Fig. 9b).

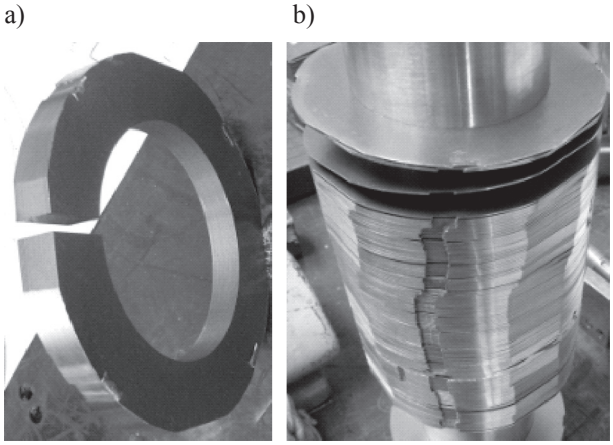

Fig. 7. Iron sheet used in construction of linear module LM of 2DoF motor and non-slotted ‘laminated ring’ which formed teeth of module LM: a) ‘laminated ring’, b) non-slotted stator iron sheet

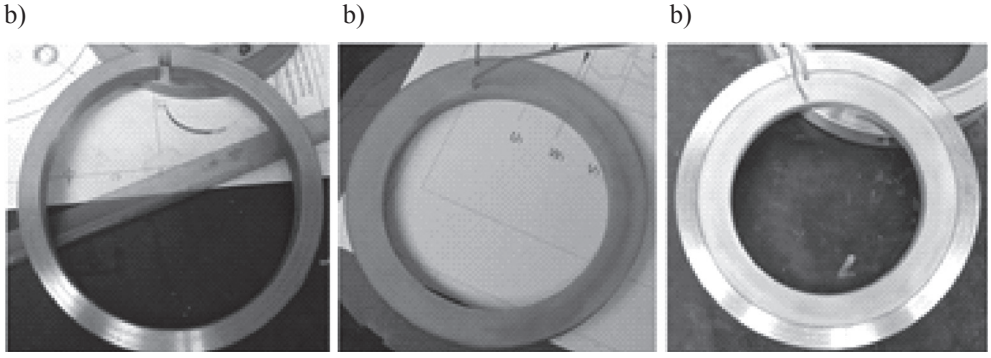

Fig. 8. Constructional components of LM module: a) ‘solid ferromagnetic ring’, b) ring winding, c) ring winding placed in ‘solid ferromagnetic ring’

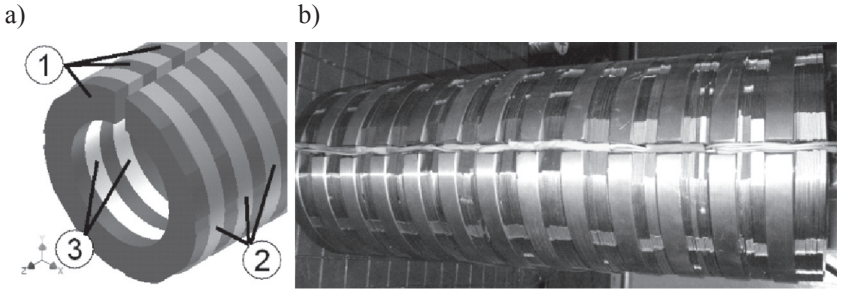

Fig. 9. Module LM: a) perspective computer view, b) constructed prototype

3.3. Design of the rotor with a solid conductive layer

The magnetic circuit of rotor in the rotary-linear induction motor is a steel tube made of structural steel R65, which has been coated with a copper layer having a thickness $\Delta_{Cu} = 0.5$ mm, coated in an electrolytic method (Fig. 10).

In the known solutions of rotary-linear induction motors designers usually use solid rotors. Solid rotor is much heavier and has a large moment of inertia. Because of that oscillations of the electromagnetic torque in a motor are not observed during its start. It should be noted, however, that the use of massive rotor significantly increases the mechanical time constant of the motor. It also requires the design of the bearing with much greater strength, capable of delivering large forces and moments acting in the supporting point of the rotor.

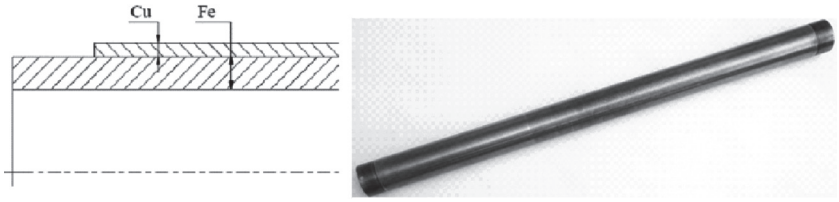

Fig. 10. Tubular rotor of 2DoF induction motor (cross-section and real view)

3.4. Construction of motor housing

The body of an rotary-linear induction motor is made of profiled aluminium tube, normally used in the manufacture of motors ShR-8M 90X IMB version (Fig. 11).

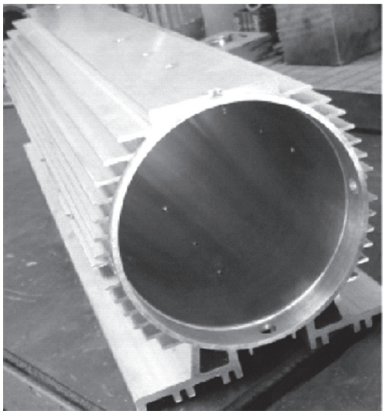

Fig. 11. The housing of an rotary-linear induction motor

The considerable length of the housing is the reason for applying a tight fitting in the RM module and in the LM module. The value of the fitting for the RM module is equal to 135H7/n6 and value of fitting for LM module equals ∅135H7/p6. Additionally, to make sure that the

construction is sufficiently stiff, numerous screws are used. The number of screws joining the housing with the RM module is equal to 8 and in the presented prototype, is the same as the number of screws joining the housing with the LM module.

3.5. Construction of rotary-linear bearing system

One of possible solutions for a bearing system (Figs. 12 and 13) is to use a truck. The truck mounted on the slide enables a rotor to move forward, to move backward, as well as to rotate around its axis. Another possibility for a bearing system is to put the rotor directly on an internal surface of bearings. Such a solution requires special material extremely resistant to abrasion, for instance Teflon. Because the external diameter of the designed motor was out of the standardised diameters of the factory-manufactured Teflon bearings, it was necessary to elaborate a bespoke solution for the bearing system consisting of two rolling bearings and a plain bearing made of polymer PA T-27MHS. This concept is presented in Fig. 12.

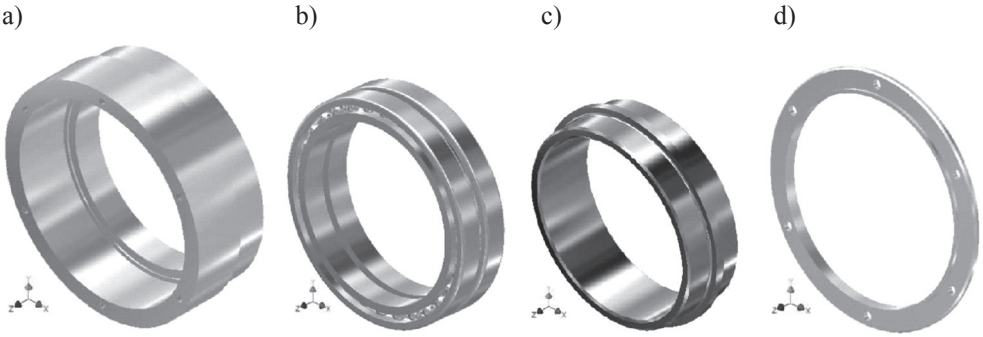

Fig. 12. The rotary-linear bearing system: a) front cover, b) two ball bearings (with parameters: static nominal load C_0 = 22.8 kN; dynamic nominal load C = 19.9 kN; fatigue load limit P_U = 0.93 kN; speed limit n_{max} = 3000 rpm), c) plain bearing made of polymer PA T-27MHS, d) locking ring

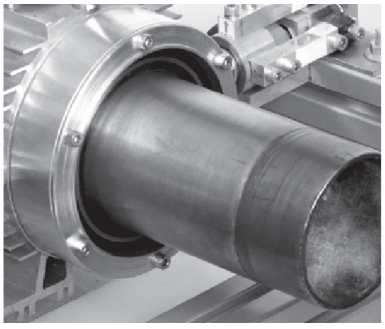

Fig. 13. The photo of mounted rotary-linear bearing system

4. Design methodology

The design methodology based on an analytical circuit model and on a field model implemented in the FEMM program. As regards the former method, the equivalent circuit of an induction motor with a solid rotor [8–10] is presented in Fig. 14.

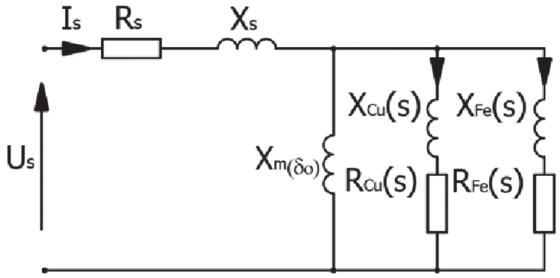

Fig. 14. The equivalent circuit of an induction motor with solid rotor [8–10]

The impedance of the rotor with the solid conductive layer (referred to the stator) is given by the following formula:

$$Z_r' = \frac{\dfrac{j\,\omega\,\mu_{Fe}}{\kappa_{Fe}\,\tau_p}\dfrac{l_{Fe}}{\tanh\left(\kappa_{Fe}\,\Delta_{Fe}\right)}\;\dfrac{j\,\omega\,\mu_{Cu}}{\kappa_{Cu}\,\tau_p}\dfrac{l_{Fe}}{\tanh\left(\kappa_{Cu}\,\Delta_{Cu}\right)}}{\dfrac{j\,\omega\,\mu_{Fe}}{\kappa_{Fe}\,\tau_p}\dfrac{l_{Fe}}{\tanh\left(\kappa_{Fe}\,\Delta_{Fe}\right)} + \dfrac{j\,\omega\,\mu_{Cu}}{\kappa_{Cu}\,\tau_p}\dfrac{l_{Fe}}{\tanh\left(\kappa_{Cu}\,\Delta_{Cu}\right)}}\;\frac{m_s}{m_r}\left(\frac{N_s\,k_{ws}}{N_r\,k_{wr}}\right)^2 \quad (1)$$

where:

κ_{Fe}, κ_{Cu} – attenuation coefficients (for iron and copper),
Δ_{Fe}, Δ_{Cu} – thickness of layers (for iron and copper),
μ_{Fe}, μ_{Cu} – the relative permeability (for iron and copper),
l_{Fe} – length of iron core,
τ_p – pole pitch,
m_s – number of phase of stator,
m_r – number of phase of solid rotor equal the number of poles $2p$,
N_s – number of turns of stator,
N_r – number of turns of rotor (for solid rotor $N_r = 0.5$),
k_{ws}, k_{wr} – winding coefficients,
ω – pulsation.

As far as the latter method is concerned, the special procedure in Lua language for the FEMM program (Finite Elements Method for Magnetics) is employed. It enables determining the spatial distribution of the magnetic field in the machine and, in consequence, allows calculating electromechanical curves – torque vs. slip $T_e = f(s)$ and force vs. slip $F_e = f(s)$, as well as phase current vs. slip $I_s = f(s)$.

Exemplary spatial distributions of the magnetic field in the RM module at standstill (the blocked rotor) and at no load state, are presented in Fig. 15. The highest saturation points occur on the surface of the tubular rotor and are equal to about B_{max} = 2 T for both of the considered states.

a) b)

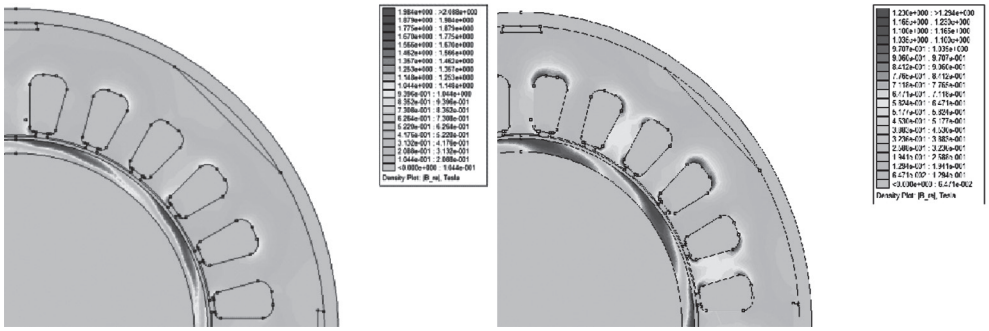

Fig. 15. The exemplary distribution of magnetic field in the module RM: a) blocked rotor state, b) no load state

Exemplary spatial distributions of magnetic field in the LM module at standstill and at no load state, are depicted in Fig. 16. The highest saturation points occur on the surface of the tubular rotor and equal to about B_{max} = 2 T for the case of the blocked rotor and to about B_{max} = 1.6 T for the case of no load state, respectively.

a) b)

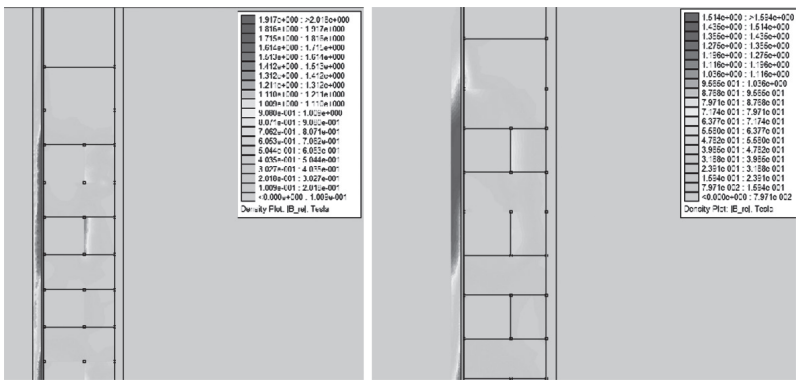

Fig. 16. The exemplary distribution of magnetic field in the module LM: a) blocked rotor state, b) no load state

Based on the above field calculations, the curves – electromagnetic torque vs. slip $T_e = f(s)$ and stator current vs. slip $I_s^R = f(s)$ for the module RM are determined (Fig. 17). Analogously, the curves – electromagnetic force vs. slip $F_e = f(s)$ and stator current vs. slip $I_s^L = f(s)$ for the module LM are calculated and presented in Fig. 18.

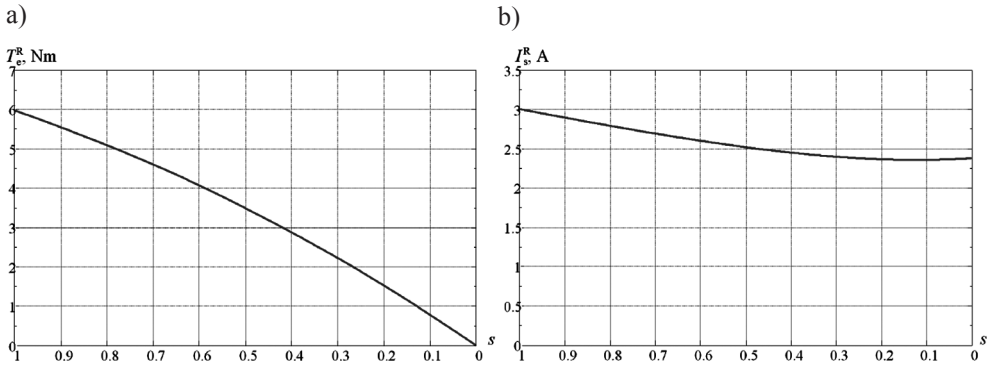

Fig. 17. The electromagnetic torque vs. slip curve $T_e = f(s)$ and stator current vs. slip curve $I_s^R = f(s)$ of module RM

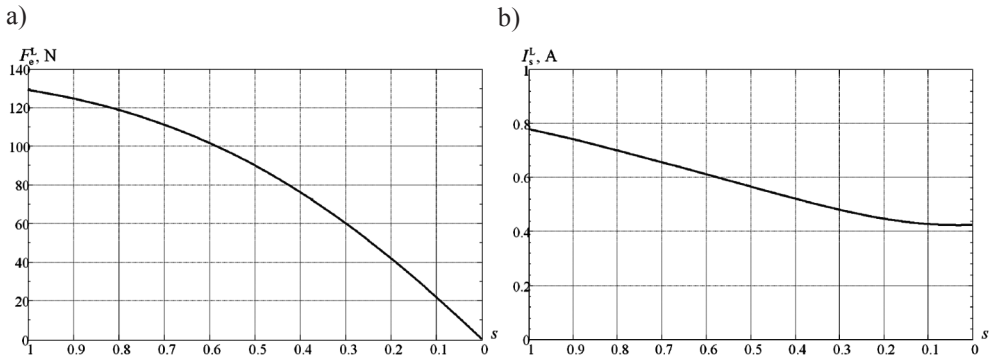

Fig. 18. The electromagnetic force vs. slip curve $F_e = f(s)$ and stator current vs. slip curve $I_s^L = f(s)$ of module LM

Both methods – the analytical method based on the equivalent circuit of an induction motor with a solid rotor and the field method based on the procedure in Lua language for FEMM program are employed in the designing process of the constructed prototype.

5. Conclusions

The idea of converting the conventional (factory-manufactured) squirrel-cage induction motor in the non-conventional rotary-linear induction motor is very useful. It allows the producers of the electrical machines to widen, in an easy way and without considerable investment, their offer by putting on the market a new non-conventional rotary-linear actuator. On the other hand, this concept can be effectively developed in an academic laboratory by advanced students on their own. The goal, which can be easily achieved in the university, is a new educational laboratory stand combined with students' training and satisfaction.

References

[1] Szczygieł M., *Modelowanie silnika indukcyjnego o dwóch stopniach swobody ruchu oraz badanie jego właściwości eksploatacyjnych przy wykorzystaniu magnetoreologicznego hamulca obrotowo-liniowego*, Ph.D. Thesis, Silesian University of Technology, Gliwice 2011.

[2] Szczygieł M., Trawiński T., Pilch Z., Kluszczyński K., *Modeling the bench for electromechanical devices with two degrees of freedom*, Przegląd Elektrotechniczny (Electrical Review), 2009, No. 12.

[3] Kamiński G., *Motors with rolling rotors*, WPW, Warszawa 2003.

[4] Mendrela E., Fleszar J., Gierczak E., *Modeling of induction motors with one and two degrees of mechanical freedom*, Kluwer Academic Publishers, Boston 2003.

[5] Mashimo T., Toyama S., *Micro Rotary-Linear Ultrasonic Motor for Endovascular Diagnosis and Surgery*, IEEE International Conference on Robotics and Automation, Pasadena, CA, USA 2008,

[6] Pan J.F., Cheung N.C., Guang-zhong Cao, *Investigation of a rotary-linear switched reluctance motor*, XIX International Conference on Electrical Machines (ICEM), 2010.

[7] Bolognesi P., Taponecco L., *A Novel 2-Freedom-Degrees Brushless Motor*, 0-7803-7369-3/02 2002 IEEE.

[8] Dabrowski M., Gieras J.F., *Induction Motors with Solid-Rotor*, PWN, Warszawa 1977.

[9] Gieras J.F., Eastham A.R., Dawson G.E., *Performance calculation for single-sided linear induction motors with a solid steel reaction plate under constant current excitation*, IEE Proceedings Electric Power Applications, 1985, Vol. 132.

[10] Gieras J.F., Saari J., *Performance calculation for a High-Speed Solid-Rotor Induction Motor*, IECON, Phoenix, Arizona, USA 2010.

TECHNICAL TRANSACTIONS | **CZASOPISMO TECHNICZNE**
ELECTRICAL ENGINEERING | ELEKTROTECHNIKA
1-E/2015

MAREK CIURYS, IGNACY DUDZIKOWSKI*

ANALYSIS OF A BRUSHLESS DC MOTOR INTEGRATED WITH A HIGH-PRESSURE VANE PUMP

ANALIZA SILNIKA BEZSZCZOTKOWEGO ZINTEGROWANEGO Z WYSOKOCIŚNIENIOWĄ POMPĄ ŁOPATKOWĄ

A b s t r a c t

A new design of a brushless direct current motor is introduced in this paper. In the BLDC motor, a high-pressure vane pump is built into the rotor. The motor is excited by neodymium magnets. Its nominal power is 2.5 kW. The motor is built in such a way that the magnetic field does not penetrate the pump. A magnetic structure field analysis of the motor was performed. Demagnetization resistance of the magnets was determined. By the use of time stepping, finite element method waveforms of the electrical and mechanical parameters in the BLDC motor–inverter system were determined.

Keywords: *electrical machines*, *BLDC motors*, *magnetic structure*, *transients*

S t r e s z c z e n i e

Opracowano nową konstrukcję silnika bezszczotkowego (BLDC), w którego wirnik wbudowana jest wysokociśnieniowa pompa łopatkowa. Silnik wzbudzany magnesami neodymowymi ma moc 2,5 kW. Zbudowany jest w taki sposób, aby pole magnetyczne nie wnikało do wnętrza pompy. Przeprowadzono polową analizę obwodu magnetycznego silnika. Wyznaczono odporność magnesów na odmagnesowanie. Metodą polowo-obwodową wyznaczono przebiegi czasowe wielkości elektrycznych i mechanicznych w układzie silnik–przekształtnik.

Słowa kluczowe: *maszyny elektryczne*, *silniki bezszczotkowe*, *obwód magnetyczny*, *przebiegi czasowe*

DOI: 10.4467/2353737XCT.15.060.3860

* Ph.D. Eng. Marek Ciurys, Prof. D.Sc. Ph.D. Eng. Ignacy Dudzikowski, Faculty of Electrical Engineering, Department of Electrical Machines, Drives and Measurements, Wroclaw University of Technology.

1. Introduction

In existing drive systems with vane pumps, the connection between the pump and the electric motor is usually rendered through an elastic clutch and a mounting flange [2]. This solution is by far the most common [6] in the construction of hydraulic power units. Some simplification of the construction is the direct connection of the pump shaft to the electric motor shaft without a clutch and mounting flange. Such a solution is called a close coupled motor pump group [7]. In all of these solutions, the pump and the motor are two separate components.

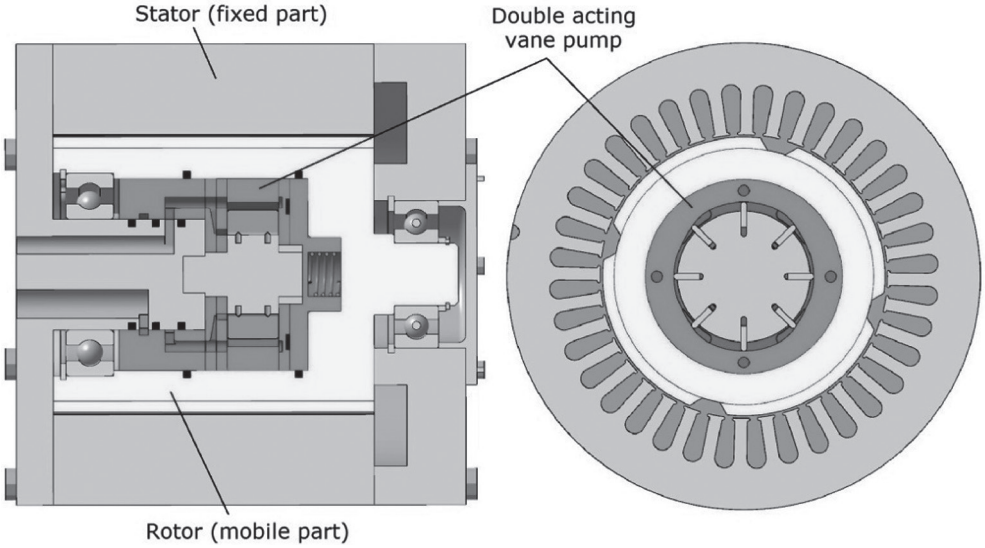

Fig. 1. Design sketch of the double vane pump integrated with the BLDC motor [2]

In this paper, a new design solution for an electrical motor is presented. In this solution (Figs. 1 and 2), the hydraulic pump is built into the rotor of the brushless direct current motor (BLDC motor). This issue has not been analyzed in the available literature.

The stator of the motor is a part of the body of the whole device and the rotor of the electric motor causes rotation of the pump housing. The internal part of the pump (with the vanes) is non-movable. Due to a lack of rotation, the vanes are pressed to the cam ring with spring elements [2].

Electrical drive systems with permanent magnet motors have the highest energy efficiency, the highest power value per unit mass, a large durability and a very good dynamic range [1–5]; therefore, a BLDC motor has been used in the proposed construction of the motor integrated with the vane pump.

The flow of the vane pump is controlled by an electrical motor power converter unit through changing the rotational speed of the motor (by the PWM method). This solution allows the simplification of the hydraulic control systems and reducing the cost of their implementation. The integrated vane pump motor construction has a compact design. The pump is located inside the rotor of the motor, which together with the stator, is an acoustic cover.

Such a solution is therefore characterized by a reduced noise level with respect to the existing, conventional drive systems with vane pumps.

The disadvantage of this solution is the risk of penetration of the magnetic flux into the pump. This could cause the magnetization of metal particles that may be present in the fluid of the hydraulic system. To avoid this, the magnetic structure of the integrated motor-pump construction should be designed in such a way that the magnetic flux does not penetrate the interior of the pump with the liquid.

2. Magnetic structure of the electrical motor

A brushless direct current motor was designed with a power level of P = 2.5 kW at rotational speed n = 3000 rpm and a supply voltage of U = 220 V. High-energy neodymium magnets of N33UH type have been applied. The maximum operating temperature of the magnets is 180°C. The outer diameter of the stator is 135 mm and the packet length is 95 mm.

The required resistance to demagnetization in the heated state (120°C) was provided by permanent magnets with a thickness of 3.5 mm. In order to eliminate the penetration of the magnetic flux into the pump, a non-magnetic sleeve was placed on the outer casing of the pump (Fig. 2).

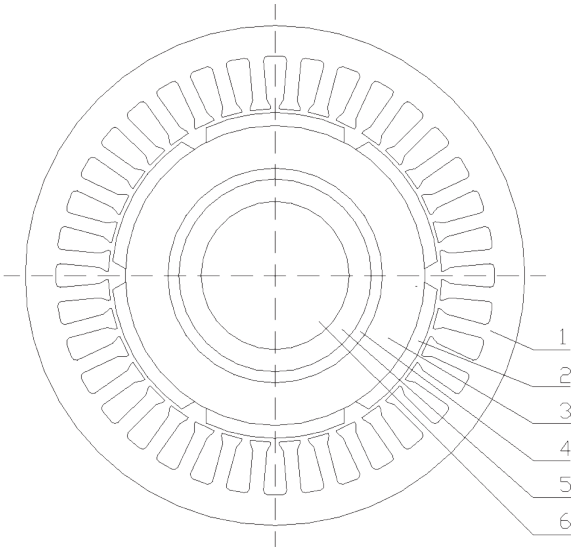

Fig. 2. Cross section of the magnetic structure: 1 – stator sheet, 2 – permanent magnet, 3 – rotor yoke, 4 – non-magnetic sleeve, 5 – casing of the pump, 6 – the interior of the pump (with liquid)

To reduce the size and the weight of stator and rotor, a magnetic structure with 3 pole pairs was used. Computations of the magnetic structure were made by use of Maxwell software. The symmetry of the magnetic circuit was taken into account, hence the computational analysis was performed for the region of one pole pitch.

3. Results of the field computations of the magnetic structure

The aim of the computational analysis was to design a magnetic structure in which the magnetic flux produced by the magnets does not penetrate the interior of the vane pump. To eliminate this phenomenon, a non-magnetic sleeve was applied between the rotor yoke and the casing of the pump (Figs. 2 and 4).

Computational analysis was performed at different values of non-magnetic sleeve thickness. The outer diameter of the pump and the thickness of its steel casing are constant. With changes in the thickness of the non-magnetic sleeve, changes of the rotor yoke thickness occur.

The performed computational analysis shows that the value of the flux density in the interior of the pump is only 13.9 μT when the 3 mm non-magnetic sleeve is applied. This value is smaller than the value of the magnetic field on the surface of the earth (which is approximately 50 μT [8]). Non-magnetic sleeves of a smaller thickness cannot eliminate the phenomenon of the magnetic flux penetration of the interior of the pump.

Due to the fact that the fluid in the hydraulic system can heat up to a temperature of approximately 90°C, the operating temperature of the magnets has been assumed at $\vartheta_m = 120°C$. For the selected 3.5 mm magnet height, the maximum current that does not cause demagnetization is 112 A. This is 6.8 times more than the maximum instantaneous value of the current at steady-state (at the rated load torque). Examples of the computation results are shown in Figs. 3–6.

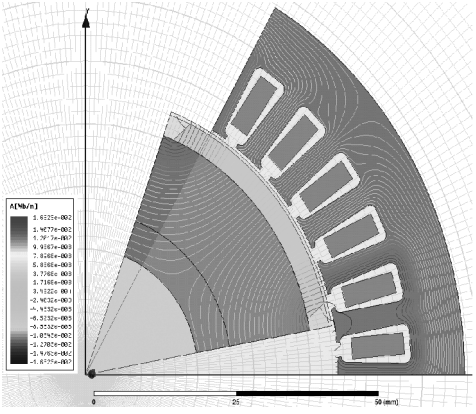

Fig. 3. Flux lines of the motor without the non-magnetic sleeve

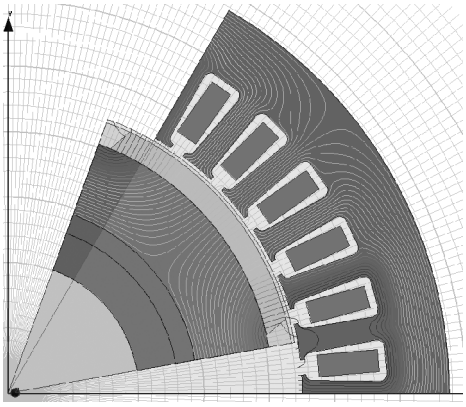

Fig. 4. Flux lines of the motor with the 3 mm non-magnetic sleeve

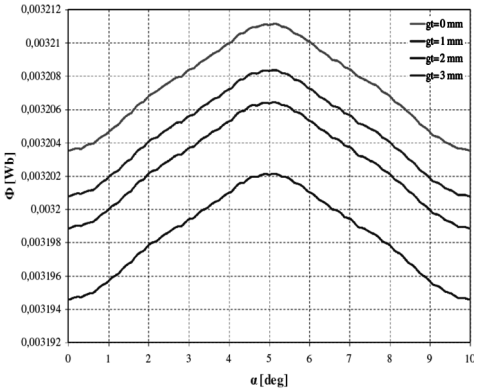

Fig. 5. Magnetic flux versus angle of rotation at different non-magnetic sleeve thicknesses: g_t = 0; 1; 2 and 3 mm

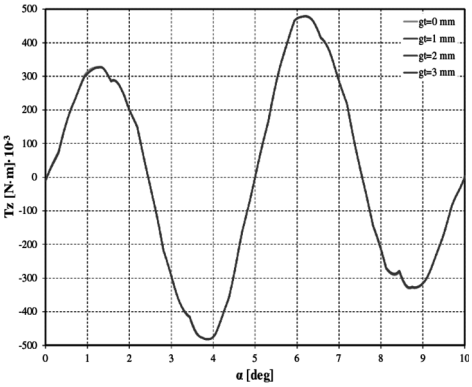

Fig. 6. Cogging torque versus angle of rotation at different non-magnetic sleeve thicknesses: g_t = 0; 1; 2 and 3 mm

4. Field-circuit computations

4.1. Time stepping finite element field-circuit model of the motor with converter

To determine transients of the electrical and mechanical parameters of the designed motor, a time stepping finite element field-circuit model of the motor with a converter was developed in the Maxwell software. The field part of the model is shown in Fig. 3.

The circuit part of the model includes the power supply, the converter and the BLDC motor. The end leakage inductance and resistance of the winding as well as the influence of the temperature on the permanent magnet parameters, the converter diodes and transistors parameters and the armature winding resistance were all considered.

The circuit model of the motor with the converter is shown in Fig. 7, where the symbols stand for: *RA*, *RB*, *RC* – the resistance of the motor winding phases; *EA*, *EB*, *EC* – the summary electromotive force induced in the motor winding phases (including the emf of self and mutual inductance and the emf of rotation). *LAp*, *LBp*, *LCp* are the end leakage inductances of the motor winding phases and *SA*1, *SB*1, *SC*1, *SA*2, *SB*2, *SC*2 stand for transistor switches of the converter; *D*1, …, *D*6 are feedback diodes (model of an ideal *p-n* junction) of the converter, and *R*1, ..., *R*6 are the internal resistances of the converter feedback diodes, V_Uzas is the supply voltage. The circuits with the *VA*, *VB*, *VC*, *VnA*, *VnB*, *VnC*, *RA*1, *RA*2, *RB*1, *RB*2, *RC*1, *RC*2 elements are used to control the transistor switch operation as a function of the rotor position. The resistance of the motor winding phases is 77 mΩ and the end leakage inductance of the motor winding phases is 36 μH.

The main equations of the BLDC motor mathematical model are as follows:

$$u_a = RA_\vartheta \cdot i_a + LA_p \frac{\mathrm{d}i_a}{\mathrm{d}t} + EA(t) \tag{1}$$

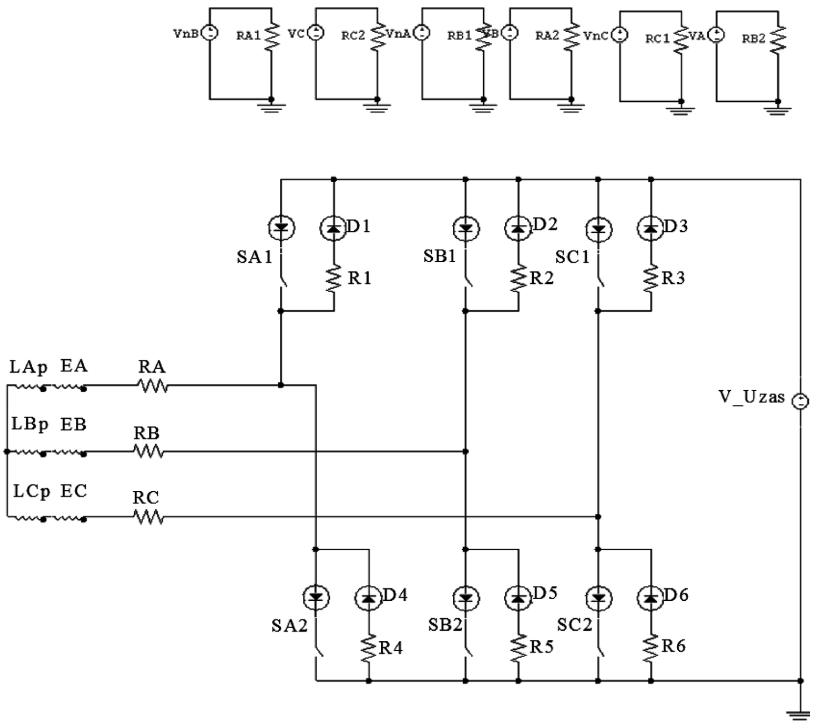

Fig. 7. Circuit model of the BLDC motor with converter

$$u_b = RB_\vartheta \cdot i_b + LB_p \frac{\mathrm{d}i_b}{\mathrm{d}t} + EB(t) \tag{2}$$

$$u_c = RC_\vartheta \cdot i_c + LC_p \frac{\mathrm{d}i_c}{\mathrm{d}t} + EC(t) \tag{3}$$

where:

u_a, u_b, u_c – the instantaneous values of the voltages of *a*, *b* and *c* phases,
RA_ϑ, RB_ϑ, RC_ϑ – the resistance of the armature winding phases at ϑ temperature,
i_a, i_b, i_c – stand for the instantaneous values of the currents in the armature windings of *a*, *b* and *c* phases.

The summary electromotive forces $EA(t)$, $EB(t)$, $EC(t)$ induced in the motor winding phases include the emf of self and mutual inductance and the back emf:

$$EA(t) = L\frac{\mathrm{d}i_a}{\mathrm{d}t} + M\frac{\mathrm{d}i_b}{\mathrm{d}t} + M\frac{\mathrm{d}i_c}{\mathrm{d}t} + e_a \tag{4}$$

$$EB(t) = L\frac{\mathrm{d}i_b}{\mathrm{d}t} + M\frac{\mathrm{d}i_a}{\mathrm{d}t} + M\frac{\mathrm{d}i_c}{\mathrm{d}t} + e_b \tag{5}$$

$$EC(t) = L\frac{\mathrm{d}i_c}{\mathrm{d}t} + M\frac{\mathrm{d}i_a}{\mathrm{d}t} + M\frac{\mathrm{d}i_b}{\mathrm{d}t} + e_c \tag{6}$$

where:
e_a, e_b, e_c – the instantaneous values of back emfs induced in the armature winding phases,
L – the self-inductance of the one armature winding phase (without the end leakage inductance),
M – the mutual inductance of the armature winding phases.

The equation of the currents at the star node of the motor is shown below:

$$i_a + i_b + i_c = 0 \tag{7}$$

The instantaneous value of the electromagnetic torque of the motor equals:

$$T_e(t) = \frac{e_a \cdot i_a + e_b \cdot i_b + e_c \cdot i_c}{\omega} \tag{8}$$

The instantaneous value of the rotor mechanical speed ω is represented in (9):

$$\omega = \frac{\mathrm{d}\alpha}{\mathrm{d}t} \tag{9}$$

where α is the angle of rotation.

The equation of motion for the system is as follows:

$$T_e(t) - T_{tm}(t) - T_o(t) = J\frac{\mathrm{d}\omega}{\mathrm{d}t} + \frac{\omega}{2}\frac{\mathrm{d}J}{\mathrm{d}t} \tag{10}$$

where:
T_o(t) – the instantaneous value of the load torque,
J – moment of inertia of the motor with the rotating part of the vane pump,
$T_{tm}(t)$ – stands for the instantaneous value of friction torque of the motor:

$$T_{tm}(t) = \frac{\Delta P_m(\omega)}{\omega} \tag{11}$$

where $\Delta P_m(\omega)$ are the windage and friction loss as the function of ω speed.

For the analysed drive system, $\frac{\mathrm{d}J}{\mathrm{d}t} = 0$, hence the equation of motion is as follows:

$$T_e(t) - T_{tm}(t) - T_o(t) = J\frac{\mathrm{d}\omega}{\mathrm{d}t} \tag{12}$$

The instantaneous value of the mechanical torque of the motor is:

$$T(t) = T_e(t) - T_{tm}(t) \tag{13}$$

4.2. Results of the time stepping finite-element computations

For the final motor magnetic structure (with the 3 mm non-magnetic sleeve), waveforms of the electrical and mechanical parameters of the motor have been computed. The computations have been performed for the system with the motor current limit at the value of 4 I_{max}, where I_{max} is the maximum value of the phase current at the steady state at the nominal load torque. Examples of the computation results obtained at the nominal load torque (T_o = 7.96 N·m) are shown in Figs. 8–16.

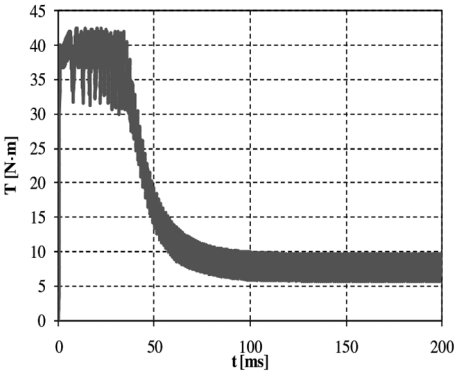

Fig. 8. Transient of the motor mechanical torque at the start-up

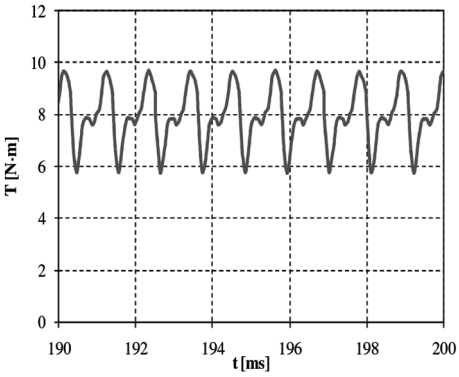

Fig. 9. Mechanical torque of the motor at the steady state

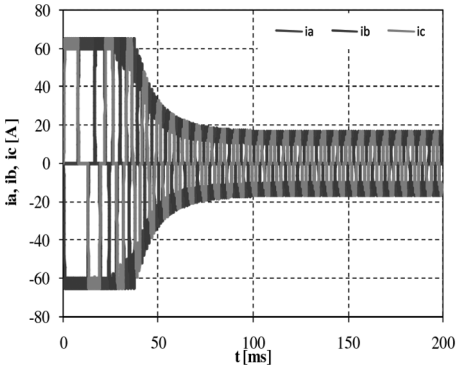

Fig. 10. Waveforms of the phases currents at the motor start-up

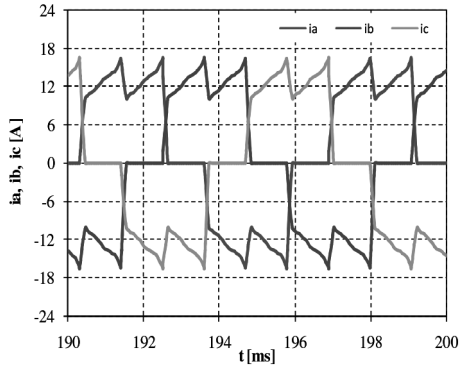

Fig. 11. Waveforms of the phases currents at the steady state

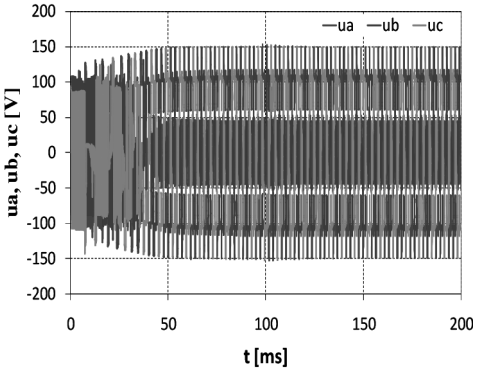

Fig. 12. Waveforms of the phases voltages at the motor start-up

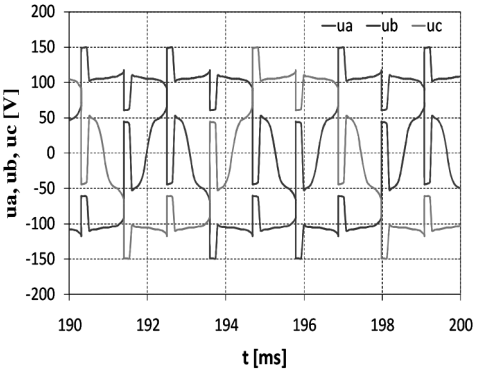

Fig. 13. Waveforms of the phases voltages at the steady state

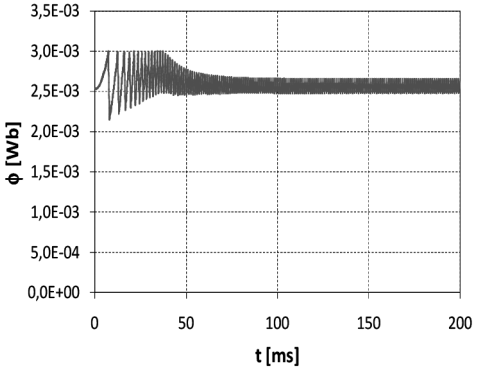

Fig. 14. Magnetic flux in the air-gap at the motor start-up

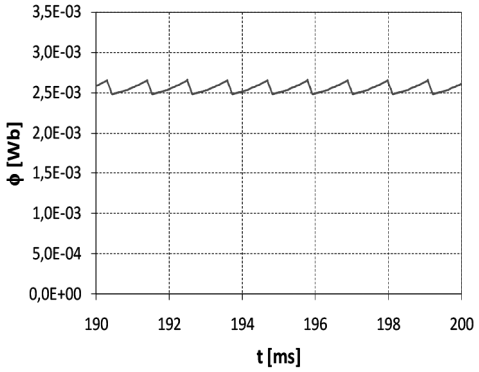

Fig. 15. Magnetic flux in the air-gap at the steady state

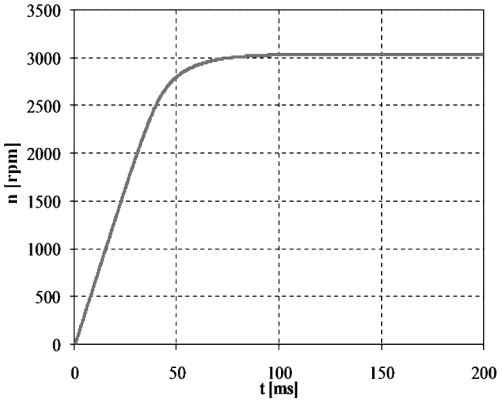

Fig. 16. Rotational speed at the motor start-up

5. Conclusion

A new design for a permanent magnet motor has been reported in this paper. In this motor, a high-pressure vane pump is built into the rotor. In order to eliminate the phenomenon of magnetic flux penetration through the pump, a non-magnetic sleeve was used in the rotor of the electric motor (on the outer steel casing of the pump).

FEM computations of the motor magnetic structure at different non-magnetic sleeve thicknesses were performed. The computational analysis has shown that the non-magnetic sleeve of 3 mm is the best solution. For this thickness, the value of the flux density in the outer steel casing of the pump is 11 mT. It provides a bypass for the magnetic flux and protects against penetration of the magnetic flux into the interior (with liquid) of the pump. The value of the flux density in the interior of the pump is only 13.9 μT. This value is smaller than the value of the magnetic field on the surface of the earth, which is approximately 50 μT [8]. Such a small value of flux density in the liquid of the pump eliminates the danger of magnetization of the metallic particles that may be present in the liquid due to wear of the hydraulic system components.

The decrease of the magnetic flux value in the developed magnetic structure with the non-magnetic 3 mm sleeve is approximately 0.3%. The rise of the temperature of the magnets from 20°C to 120°C causes more than a 3.5-fold decrease of their demagnetization resistance. This confirms that the resistance to demagnetization should be analysed at the highest operating temperature.

Waveforms of the electrical and mechanical parameters of the motor have been computed for the final magnetic structure (with the non-magnetic 3 mm sleeve). The computations have been performed for the system with the motor current limit at a value of 4 I_{max}, where I_{max} is the maximum value of the phase current at the steady-state, at the nominal load torque. The preliminary analysis has shown that the mass of the integrated electrical motor pump system is about 40% smaller than the mass of the conventional solution with the separate pump and motor which are presented, for example, in [2, 6, 7].

References

[1] Dudzikowski I., Ciurys M., *Commutator and brushless motors excited by permanent magnets*, Publishing House of the Wroclaw University of Technology, Wroclaw 2011.
[2] Fiebig W., Dudzikowski I., Ciurys M., Kuczwara H., *Vane Pump integrated into an Electric Motor*, The 9th International Fluid Power Conference, 9 IFK, March 24–26, 2014, Aachen, Germany.
[3] Gieras J.F., *Advancements in Electric Machines*, Springer 2008.
[4] Gieras J.F., Wing M., *Permanent Magnet Motor Technology*, Marcel Dekker, Inc., New York–Basel 2002.
[5] Glinka T., *Permanent magnet electrical machines*, Publishing House of the Silesian University of Technology, Gliwice 2002.
[6] Stryczek S., *Hydrostatic drive*, Vols. 1, 2, WNT, Warsaw 1993.
[7] *Parker Hannifin catalog*.
[8] *Moon and distant quasars facilitate first measurement of magnetic field in Earth's core*, University of California, Berkeley (published: Monday, December 20, 2010).

This work has been financed by The Polish National Centre for Research and Development, project number 208471.

TECHNICAL TRANSACTIONS | **CZASOPISMO TECHNICZNE**
ELECTRICAL ENGINEERING | ELEKTROTECHNIKA
1-E/2015

MACIEJ GWOŹDZIEWICZ, JAN ZAWILAK*

SIX-POLE SINGLE-PHASE LINE START PERMANENT MAGNET SYNCHRONOUS MOTOR

SZEŚCIOBIEGUNOWY JEDNOFAZOWY SILNIK SYNCHRONICZNY Z MAGNESAMI TRWAŁYMI O ROZRUCHU BEZPOŚREDNIM

A b s t r a c t

This paper deals with the results of experimental investigation into a six-pole single-phase line start permanent magnet synchronous motor. The influence of the running capacitor capacitance on the motor running properties was investigated. The influence of the starting capacitor capacitance and its switch-off time on the motor starting properties was investigated.

Keywords: *electric machines*, *single-phase motor*, *permanent magnet*, *high efficiency motor*

S t r e s z c z e n i e

W artykule przedstawiono wyniki badań eksperymentalnych jednofazowego silnika synchronicznego z magnesami trwałymi o liczbie biegunów $2p = 6$. Zbadano wpływ pojemności kondensatora pracy na właściwości eksploatacyjne silnika.

Słowa kluczowe: *maszyny elektryczne*, *silnik jednofazowy*, *magnesy trwałe*, *silnik wysokosprawny*

DOI: 10.4467/2353737XCT.15.061.3861

* Ph.D. Eng. Maciej Gwoździewicz, Prof. D.Sc. Ph.D. Eng. Jan Zawilak, Faculty of Electrical Engineering, Wroclaw University of Technology.

1. Introduction

The norm IEC 60034 part 30 orders the electrical motor producers to produce electrical motors with minimum factor of the efficiency. The goal of this command is to minimize electrical energy consumption through the minimizing of electrical motor power losses. Nowadays, this norm ranges low-voltage electric motors with rated power 0.75 kW $\leq P_n \leq$ 375 kW and the number of pole pairs $2p$ = 2; 4; 6. The new project of the norm assumes widening of the electrical motor rated power range up to 0.12 kW $\leq P_n \leq$ 1000 kW, the number of pole pairs up to $2p$ = 2; 4; 6; 8 and including multi-phase motors (also single-phase motors).

Polish and World producers of electric motors responded to the norm requirements by designing and producing high-efficiency three-phase motors which fulfil the norm by achieving the minimum factor of efficiency. The electrical motor producers respond did not include single-phase motors which are not yet included by the norm.

If the new norm project IEC 60034 part 30 was valid, no single-phase motor produced nowadays would fulfil the norm requirements.

In articles [1, 5, 6], the possibility of building a single-phase line start permanent magnet synchronous motor was proven. The single-phase line start permanent magnet synchronous motor would achieve much better running properties than the single-phase induction motor. Taking into account the modern electrical motor development, we can suppose that in the case of restricted new requirements of producing electrical motors, producers of single-phase motors will be forced to design and produce single-phase line start permanent magnet synchronous motors.

2. Construction of six-pole single-phase permanent magnet synchronous motors

In Maxwell software, two circuit-field models of single-phase line start permanent magnet synchronous motors were built. The models were based on the mass production four-pole single-phase induction motor type SEh 80-4B supplied by a voltage of U_n = 230 V 50 Hz. The

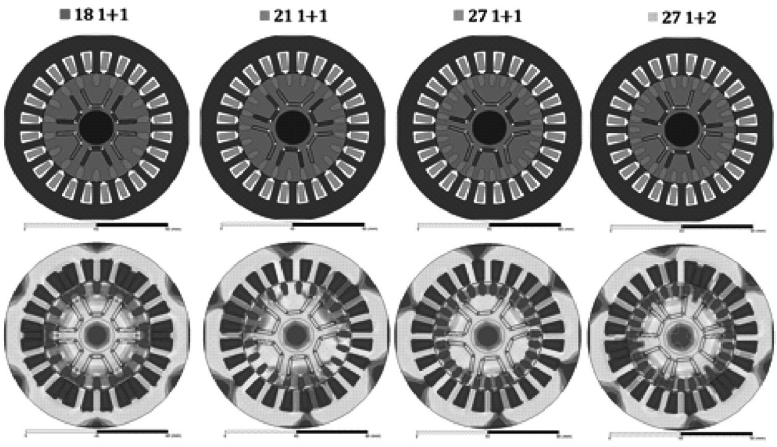

Fig. 1. Cross-sections and magnetic field distributions in built models of six-pole single-phase line start permanent magnet synchronous motor

motor winding was rewound. Cross-sections of the models and magnetic field distributions are shown in the Fig. 1. Neodymium magnet N38SH with remanence induction B_r = 1.24 T and magnetic field coercivity H_{cb} = 990 kA/m was chosen for the excitation. The methodology of the single-phase line start permanent magnet synchronous motor design was revealed in article [3]. Papers [2, 4, 7] were also helpful for the designer.

The motor needs two capacitors, a run-capacitor and a start-capacitor. The best running properties for both motors were obtained for run-capacitor capacitance C_{run} = 50 μF. Starting capacitor capacitance C_{start} = 100 μF is enough capacitance for the motor self-starting with a time switch-off relay which switches off the starting capacitor after motor synchronization.

The design process of the motor was divided into two steps. During the first step, the influence of the motor construction on the back EMF induced by permanent magnets in the motor main winding was investigated. The results are presented in Fig. 2. During the second

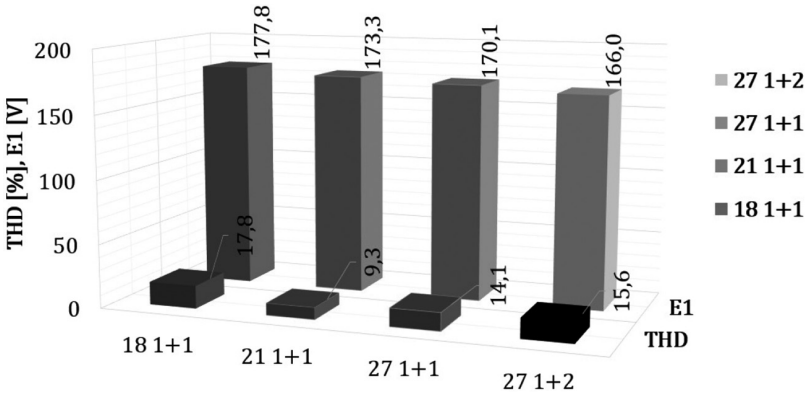

Fig. 2. Influence of the motor construction on the 1st harmonic RMS value and total harmonic distortion of the back EMF induced by permanent magnets in the motor's main winding

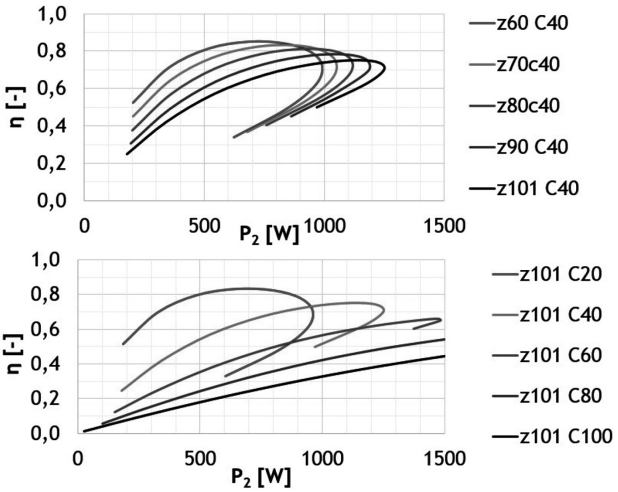

Fig. 3. Influence of the number of the auxiliary winding turns and running capacitor capacitance on the motor efficiency curve

step, the influence of the motor auxiliary winding parameters on the motor performances was investigated. The results are shown in Fig. 3.

On the basis of the obtained results, the physical model of the six-pole single-phase line start permanent magnet synchronous motor was built. The model is presented in Fig. 4. The rotor has 21 bars. The die cast squirrel cage of the rotor is made from aluminum.

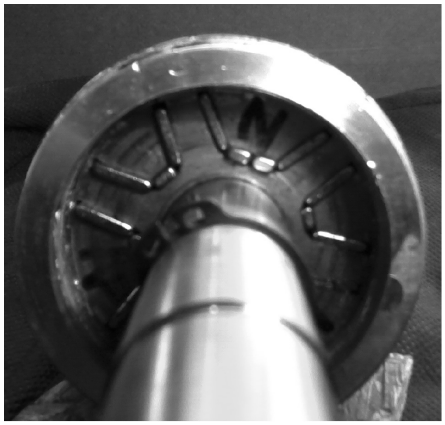

Fig. 4. Rotor of the physical model of the six-pole single-phase line start permanent magnet synchronous motor

3. The motor performance

The influence of the running capacitor capacitance on motor performance was investigated. The results are shown in Fig. 5. An increase in the running capacitor capacitance causes an increase in the maximum load power, a decrease of the motor efficiency of the low load and an increase in the motor efficiency of the high load.

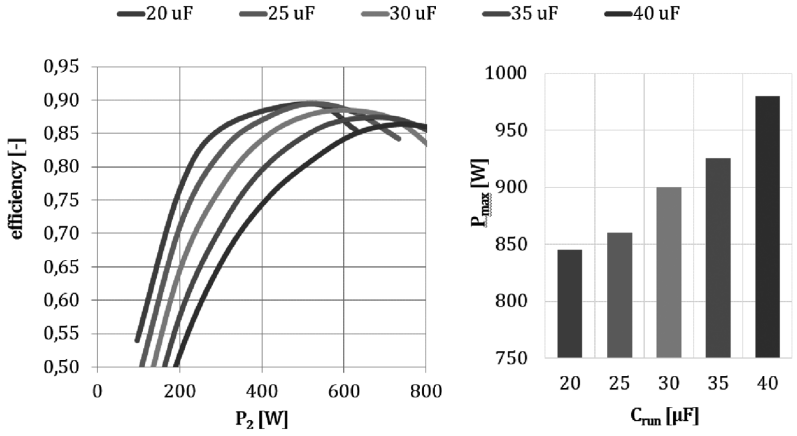

Fig. 5. Influence of the running capacitor capacitance on motor performance

The starting process of the motor is presented in Fig. 6. The starting capacitor (C_{start} = 110 μF) was switched off by the time relay after 0.5 s. The starting capacitor was switched off after synchronization.

The motor performance is shown in Table 1. A comparison of the built motor physical model with a single phase induction motor manufactured by the electric motor producers is presented in Table 2. Single-phase line start permanent magnet synchronous motor efficiency is extremely high in comparison with single-phase induction motor efficiencies.

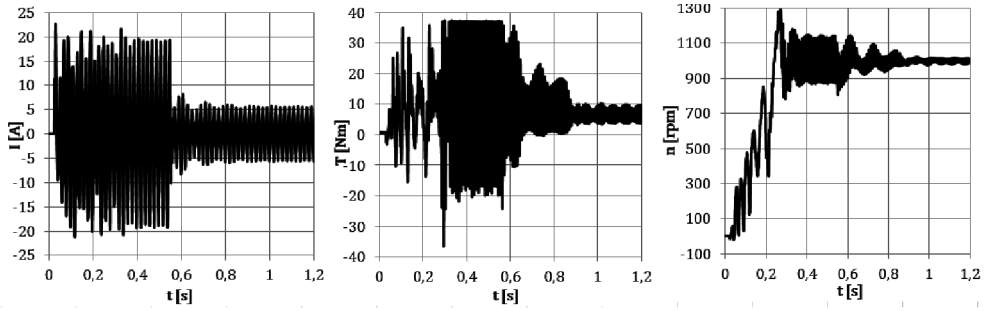

Fig. 6. Starting process of the six-pole single-phase line start permanent magnet synchronous motor

Table 1

Six-pole single phase line start permanent magnet synchronous motor performance

Parameter	Unit	Value
U_n	V	230
P_n	W	**650**
n_n	rev/min	**1000**
I_n	A	3.49
η_n	%	**87.1**
$\cos\varphi_n$	-	0.93
T_{max}/T_n	-	1.3
$\Delta T_{winding}$	°C	30
ΔT_{rotor}	°C	26
C_{run}	μF	25
C_{start}	μF	110
m	kg	9.9

Table 2

Comparison of six-pole single phase PMSM with six-pole single phase induction motors produced by the world electric motor manufacturers

Motor	P_n [W]	n_n [rpm]	η_n [%]	m [kg]
Single-phase PMSM	650	1000	87.1	10.5
Producer A	735	1140	65	28
Producer A	650	900	67.5	11.5

4. Conclusions

The six-pole single phase line start permanent magnet synchronous motor has very high efficiency. It is the main advantage of the motor. The main drawback is the starting capacitor which is needed for self-starting. The time relay which switches off the starting capacitor should work after the motor synchronization. The construction of the six-pole single phase motor presented in the article is both energy-saving and material-saving. The built motor has an IE4 efficiency class – the highest class nowadays.

References

[1] Fei W., Luk P.C.K., Ma J., Shen J.X., Yang G., *A High-Performance Line-Start Permanent Magnet Synchronous Motor Amended From a Small Industrial Three-Phase Induction Motor*, Magnetics, IEEE Transactions, 2009.

[2] Fengbo Q., Zhipeng L., Shukang C., Weili L., *Calculation and simulation analysis on starting performance of the high-voltage line-start PMSM*, Computer Application and System Modeling (ICCASM), International Conference, 2010.

[3] Gwoździewicz M., Zawilak J., *Comparison of properties of single-phase line start permanent magnet synchronous motors with W and VV shape permanent magnet arrangements. Experimental results*, Zeszyty Problemowe – Maszyny Elektryczne, 2013.

[4] Kurihara K., Kubota T., Nitawaki D., *Rotor Design for High Starting Performance of a Self-Starting Single-Phase Permanent-Magnet Motor*, Przegląd Elektrotechniczny, 2012, nr 7b.

[5] Miller T.J.E., Popescu M., Cossar C., McGilp M., Strappazzon G., Trivillin N., Santarossa R., *Line-Start Permanent Magnet Motor Single-Phase Steady-State Performance Analysis*, IEEE Transactions on Industry, Vol. 40, Issue 2, pp. 516–525, 2004.

[6] Rahman M.A., Osheiba A.M., Kurihara K., Jabbar M.A., Hew Wooi Ping, Kai Wang, Zubayer H.M., *Advances on Single-Phase Line-Start High Efficiency Interior Permanent Magnet Motors*, IEEE Transactions on Industrial Electronics, Vol. 59, Issue 3, pp. 1333––1345, 2012.

[7] Zhao Q., Wang X., Yu S., Zhang D., An Z., Tang R., *Study and design for large line-start permanent magnet synchronous motors*, Electrical Machines and Systems, ICEMS, 2003.

TECHNICAL TRANSACTIONS | **CZASOPISMO TECHNICZNE**
ELECTRICAL ENGINEERING | ELEKTROTECHNIKA
1-E/2015

TADEUSZ GLINKA*, ARTUR POLAK*, ADAM DECNER*, ANDRZEJ SIKORA**

EQUIVALENT CIRCUITS USED IN THE DIAGNOSTICS OF INSULATION IN POWER TRANSFORMERS

SCHEMATY ZASTĘPCZE WYKORZYSTYWANE W DIAGNOSTYCE IZOLACJI TRANSFORMATORÓW ENERGETYCZNYCH

Abstract

An equivalent circuit of the insulation system in power transformers comes in many forms. In tests for the dielectric loss tangent (tgδ) of the main insulation, the equivalent circuit has been simplified to two-terminal *RC* series connected or parallel connected circuits. For direct current tests of groundwall insulation modelling, two two-terminals circuits are required – one for charging and shorting, the other for the voltage recovering after shorting. The model turn-to-turn insulation may also be presented by two-terminal circuits. The parameters of the two-terminal circuit can be determined by direct current. The tested winding is energized by DC voltage, the current is interrupted and the voltage waveform on the terminals of the winding is recorded. The parameters of turn-to-turn insulation (equivalent circuit parameters) are calculated from the voltage waveform and they can be used for diagnostic purposes.

Keywords: *power transformer*, *main insulation*, *turn-to-turn insulation*, *equivalent circuit*

Streszczenie

Schemat zastępczy układu izolacyjnego transformatorów energetycznych ma wiele postaci. W badaniach stratności tgδ izolacji głównej schemat zastępczy upraszcza się zwykle do dwójników *RC*, połączonych równolegle bądź szeregowo. W badaniach izolacji głównej napięciem stałym odwzorowywanie układu izolacyjnego wymaga już dwóch dwójników: jednego dla ładowania i zwarcia, a drugiego dla napięcia powrotnego po krótkotrwałym zwarciu. Izolację międzyzwojową można także odwzorowywać dwójnikiem. Parametry tego dwójnika można wyznaczać prądem stałym. Uzwojenie badane zasila się prądem stałym, a następnie wyłącza się prąd i rejestruje przebieg napięcia na uzwojeniu. Z przebiegu napięcia oblicza się parametry izolacji międzyzwojowej (parametry schematu zastępczego), które można wykorzystać do celów diagnostycznych.

Słowa kluczowe: *transformator energetyczny*, *izolacja główna*, *izolacja międzyzwojowa*, *schemat zastępczy*

DOI: 10.4467/2353737XCT.15.062.3862

* Prof. D.Sc. Ph.D. Eng. Tadeusz Glinka, Ph.D. Eng. Artur Polak, Ph.D. Eng. Adam Decner, Institute of Electrical Drives and Machines KOMEL, Katowice.

** Ph.D. Eng. Andrzej Sikora, Faculty of Electrical Engineering, Silesian University of Technology, Gliwice.

1. Introduction

Insulation systems comprised of cables, transformers, electrical machines and other electrical devices are multi-layered. Electrical phenomena appearing inside the insulation system are adopted to the equivalent circuits, as shown in the literature. There is no simple equivalent circuit for the insulation system. For example, Г. Вайда [5] gives several different versions of alternative schemes. One of the simplest examples of the insulation is the insulation of a single conductor cable in a metal screen. Even this simple insulation system is characterized by spatial distribution and for this reason, it is represented by the equivalent circuit with distributed parameters. It can be illustrated by a two-terminal circuit with an internal ladder structure which consists of capacitances and resistances connected as shown in Fig. 1.

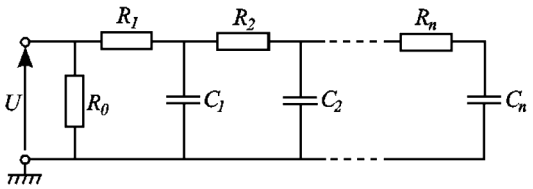

Fig. 1. Equivalent circuit of the insulation system, the example

The transformer insulation system is more complicated, it can be distinguished: turn--to-turn insulation, the insulation between the windings of the upper and lower voltage and the insulation to the core. In Figure 2, an equivalent circuit of the transformer is shown. However, there is no universal equivalent circuit which would be perfect for all phenomena

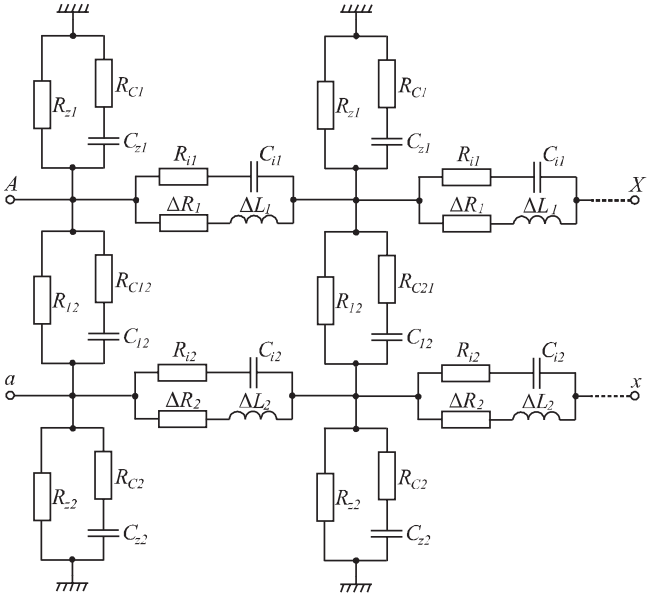

Fig. 2. An equivalent circuit of the transformer insulation system including groundwall and turn-to-turn isolation

appearing in the insulation system, especially during fast transients. The equivalent circuit shown in Fig. 2 is well constructed for an electrical phenomena appearing in the system during the normal operational state of the transformer. This scheme, according to the needs, can be simplify to a two-terminal *RC* circuit.

Equivalent circuit of the insulation system shown in Fig. 2 consists of two orthogonal circuits – groundwall and turn-to-turn insulation. These circuits can be used during the receipt tests as well as diagnostic tests.

2. Examination of the main transformer insulation

2.1. Testing the insulation with AC voltage

Tests of insulation with AC voltage are made each time the transformer is new or after repair or during the diagnostic. The program of receipt tests of the transformer, in accordance with Standard [3] and the Instruction of Exploitation [4] includes the measure of impedance of insulation system X_x, the measure of dielectric loss factor tgδ and the dielectric strength test. The impedance value of the insulation system X_x is used, inter alia, to determine the rated power of the transformer used in the dielectric strength test. During the diagnostic test of the transformer with alternating voltage, the dielectric loss factor tgδ is usually measured. In this case, the equivalent circuit is simplified to a two-terminal circuit with clustered parameters C_x, R_x, connected in parallel or in series, as shown in Figs. 3 and 4. These tests are usually carried out on one winding and the other windings and frame are grounded. In this case, the capacitance C_x is calculated from the equivalent circuit (Fig. 2). Similarly, the resistance is also calculated from the equivalent circuit (Fig. 2).

$$\begin{aligned} C_X &= F(R_{Z1}, R_{Z2}, R_{C1}, R_{C2}, R_{12}, R_{C12}, C_{Z1}, C_{Z2}, C_{12}) \\ R_X &= F(R_{Z1}, R_{Z2}, R_{C1}, R_{C2}, R_{12}, R_{C12}, C_{Z1}, C_{Z2}, C_{12}) \end{aligned} \tag{1}$$

The formulas for calculation of the capacitance C_x and the resistance R_x do not include the parameters of turn-to-turn insulation R_{iz}, C_{iz}, so the insulation system is orthogonal.

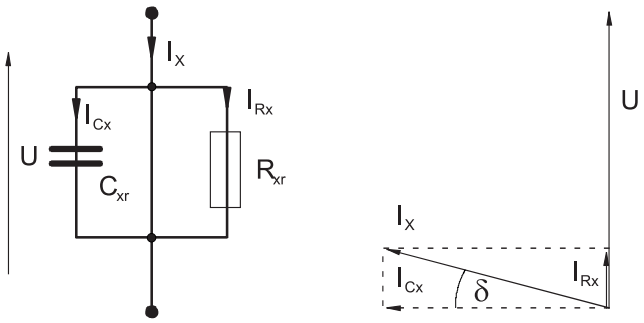

Fig. 3. The parallel equivalent circuit of the insulation system and the definition of angle δ

In parallel equivalent circuits, the dielectric loss factor tgδ is calculated as:

$$\text{tg}\delta = \frac{I_{RX}}{I_{CX}} = \frac{1}{\omega R_{xr} C_{xr}} \tag{2}$$

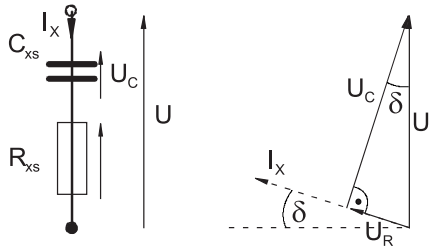

Fig. 4. Serial equivalent circuit of the insulation system and the definition of angle δ

In serial equivalent circuits, the dielectric loss factor tgδ is calculated as:

$$\text{tg}\delta = \frac{U_R}{U_C} = \omega C_{xs} R_{xs} \tag{3}$$

2.2. Testing the insulation with DC voltage

The equivalent circuit of the insulation system tested with DC voltage must contain at least three elements: two resistances and capacitance, as shown in Fig. 5.

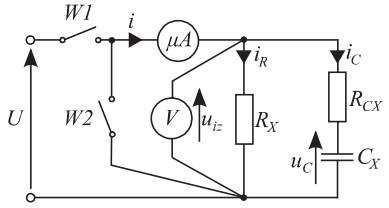

Fig. 5. Interpretation of the charging and discharging of the insulation

The test of insulation with DC voltage consists of switching the voltage U_0 at the time $t = 0$, on uncharged insulation systems and recording the current waveform $i(t)$ and the voltage waveform $u_{iz}(t)$ in the measurement circuit shown in Fig. 5. The transient condition lasts from 60 to 600 s. This time depends on the rated voltage of the winding insulation system and its volume. After determining the current level at time t_1, the voltage U_0 is switched off (switch $W1$) and the insulation system is short (switch $W2$). The short time of the insulation system lasts until t_2 and is $\Delta t_z = t_2 - t_1$. The time difference Δt_z can range from a few to tens of seconds. It depends on the rated voltage of the winding, the volume of the insulation system and its technical condition. The voltage on the internal capacitance of the insulation system during the short time period is reduced to a value U_{C2}. After opening the insulation system at the time t_2 (switch $W2$), the voltage on the insulating system $u_{iz}(t)$ recovers to the maximum

value U_{max}, which is achieved at the time t_3. In the literature, this voltage is also known as the return voltage. Then, the return voltage is slowly reduced to zero. The insulation system discharges itself. The waveforms of the voltage on the insulation system $u_{iz}(t)$ and the current $i(t)$, which are measurable, and the voltage on the capacitance $u_C(t)$, which is not measurable, are presented in Fig. 6. The current i_c is also unmeasurable.

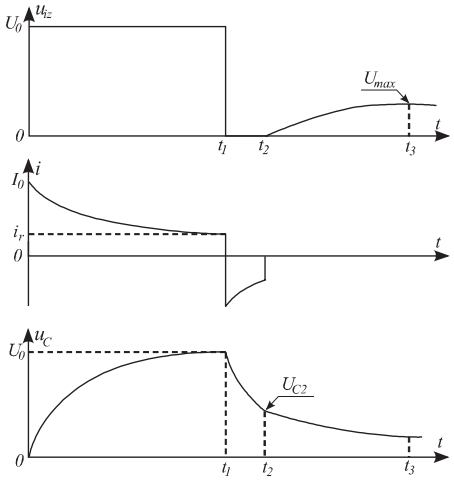

Fig. 6. Waveforms for voltage on insulation system $u_{iz}(t)$, the charging current $i(t)$ and the voltage on the capacitance of the insulation system $u_C(t)$

The voltage waveform $U_{iz}(t)$ and current waveform $i(t)$ in the time interval $0 \le t < t_1$, are correctly simulated using the equivalent circuit shown in Fig. 5. Based on this circuit, equations describing the charging of the insulation system can be calculated as:

$$\begin{aligned} u_{iz}(t) &= U_0 \\ i(t) &= I_R + (I_0 \_ I_R)e^{-t/T_1} \\ u_C(t) &= U_0(1-e^{-t/T_1}) \\ T_1 &= R_{CX}C_X \end{aligned} \tag{4}$$

From the steady value of the current I_R, the resistance of the insulation system is determined, this is called $R_{60} = R_x$. From the current measurement after 15 and 60 seconds, from the time the voltage was switched on, i.e. $I_{15} = i_{(t=15)}$, $I_{60} = i_{(t=60)}$ the absorbency index R_{60} / R_{15} is calculated.

$$\begin{aligned} \frac{i_{(t=15)}}{i_{(t=60)}} &= \frac{I_{15}}{I_{60}} = \frac{R_{60}}{R_{15}} \\ R_{15} &= \frac{U_0}{I_{15}} \\ R_{60} &= \frac{U_0}{I_{60}} \end{aligned} \tag{5}$$

From the electrotechnics point of view, the resistance R_{15} is calculated from the circuit (Fig. 5), is a complex, but in practice the resistance R_{15} is calculated from the measured values – equation (5).

The voltage waveform $U_{iz}(t)$ and the current waveform $i(t)$ in the time interval $t_1 \le t < t_2$, are also correctly simulated using the equivalent circuit shown in Fig. 5. Based on this scheme, the equations describing the discharging of the insulation system can be calculated as:

$$\begin{aligned} u_{iz}(t) &= 0 \\ i(t) &= -(I_0 - I_R)e^{-t/T_1} \\ u_C(t) &= -U_0 e^{-t/T_1} \\ T_1 &= R_{CX} C_X \end{aligned} \tag{6}$$

The capacitance C_x of the insulation system is not completely discharged. The capacitance C_x (Fig. 5) has some electric charge Q_C. At the time t_2, the insulation system is open. After opening switch $W2$, the voltage on the insulation system $u_{iz}(t)$ recovers. The course of the recovery voltage is continuous, from zero to the value $U_{\max}$. The value $U_{\max}$ for the insulating system occurs at time t_3. The equivalent circuit of the insulation system shown in Fig. 5 does not present the course of the recovery voltage in time interval $t_2 \le t < t_3$. In this case, the course of the recovery voltage can be described by another simple equivalent circuit. The scheme is shown in Fig. 7.

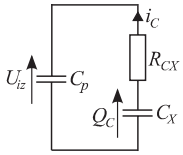

Fig. 7. Equivalent circuit of the insulation system to interpret the recovery voltage

In accordance with the equivalent circuit shown in Fig. 7, the course of the recovery voltage on the insulation system in the interval $t_2 \le t < t_3$, can be approximated by the equations:

$$\begin{aligned} u_{iz}(t) &= U_{\max}(1 - e^{-t/T_2}) \\ i_C(t) &= \frac{C_p U_{\max}}{T_2} e^{-t/T_2} \\ T_2 &= R_{CX}(C_X + C_p) \end{aligned} \tag{7}$$

The time interval $t_3 \le t < \infty$, is a time when the insulation system discharges itself, the voltage $u_{iz}(t)$ decreases from value $U_{\max}$ to zero. The course of voltage $u_{iz}(t)$, can be simulated by the equivalent circuit shown in Figs. 7 and also 5. Using the equivalent circuit from Fig. 5, the equations which describe the self-discharging of the insulation system can be calculated as:

$$\begin{aligned} u_{iz}(t) &= U_{\max} e^{-t/T_3} \\ T_3 &= (R_X + R_{CX}) C_X \end{aligned} \tag{8}$$

All determinations of equations (4) to (7) are shown in Figs. 5–7.

3. Determination of turn-to-turn insulation condition of transformer

The determination of turn-to-turn condition of transformers insulation is an unsolved problem. Most of the failures known to authors, have their beginnings in the turn-to-turn insulation fault, resulting in a shorting. Exposure to surges in the turn-to-turn isolation can come from the supply side and from the consumers of the electricity. There are many surge-generating sources. In the power transformers, which are directly connected to the generator, the sudden turning off of the receiver results in the increase of the generator's voltage.

The winding of the transformer has spread parameters – capacitance, inductance and resistance, for the voltage wave. The voltage wave induces damped electromagnetic oscillations and its distribution and the maximum value changes over time and quickly disappears. However, the most exposing on the damage are turns which are close to the leads. Even if a wave voltage is small, but often repeated, there is a high probability to reduce the dielectric strength of the turn-to-turn insulation of the first turns of the winding and these are the places, which are shorting the most.

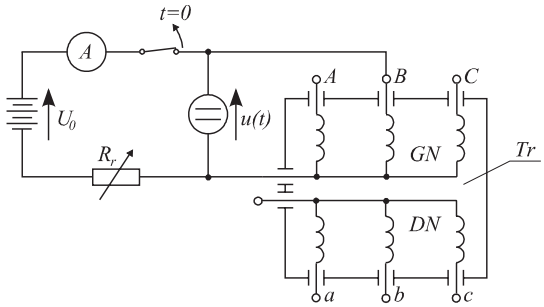

Fig. 8. A measurement diagram for testing the turn-to-turn insulation of the power transformer

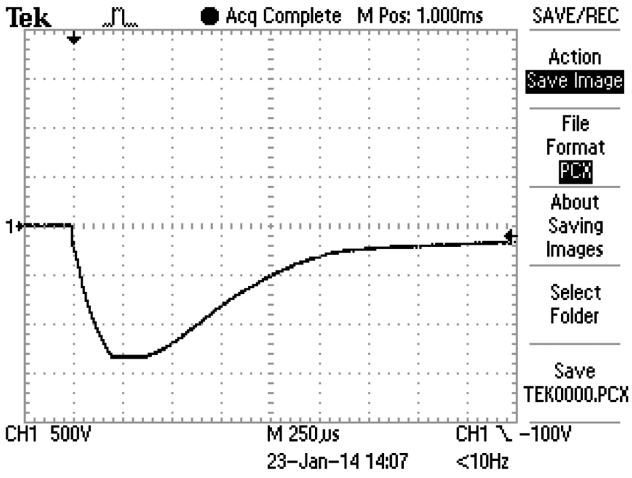

Fig. 9. The voltage waveform $U(t)$ on the terminals of phase B after switching off the current $I = 50$ mA

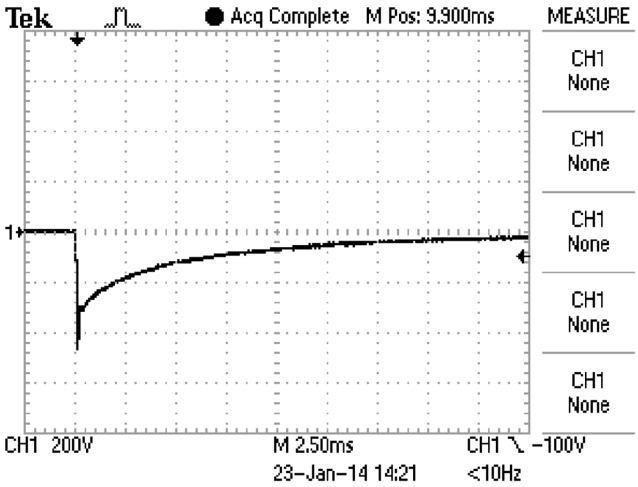

Fig. 10. The voltage waveform $U(t)$ on the terminals of phase B after switching off the current $I = 50$ mA, when an additional turn is short

The capacitance of turn-to-turn insulation and the diagnostic tests of these kinds of insulation can be performed with DC voltage. The measurement diagram is shown in Fig. 8. The phase B of winding GN was fed with a direct current, which had a value of $I = 50$ mA. After the current reached a steady value, the source was turned off, and the voltage waveform $U(t)$ on the terminals of phase B were recorded with an oscilloscope. The voltage $U(t)$ is shown in Figs. 9 and 10.

The maximum value (Fig. 9) $U_{max} = 1340$ V was obtained at the time $t = 0.26$ ms after switching the current off. The time constant of the first part of the wave is $T_1 = 0.177$ ms, the time constant of the second part of the wave is $T_2 = 1.22$ ms.

The maximum value (Fig. 10) $U_{max} = 464$ V was obtained at the time $t = 0.06$ ms after switching current off. The time constant of the first part of the wave is $T_1 = 0.043$ ms, the time constant of the second part of the wave is $T_2 = 4.05$ ms.

The voltage waveforms shown in Figs. 9 and 10 grows from zero to the value U_{max}, and then decreases to zero. These waveforms are determined by the parameters of winding resistance R and inductance L and turn-to-turn insulation parameters capacitance C_{iz} and resistance of insulation R_{iz} (Fig. 2). Voltage rises from zero to value U_{max} during the time interval $0 < t \leq \Delta t$. For this interval, the equivalent circuit shown in Fig. 11 can be assigned.

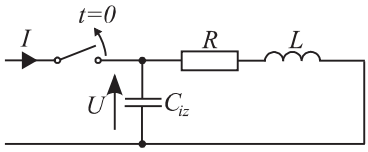

Fig. 11. Equivalent circuit corresponding to conduct the voltage across the winding in the time interval $0 < t \leq \Delta t$

The rise of the voltage waveform can be approximated by the exponential function:

$$U(t) = U_{\max}(1 - e^{-t//T_1})$$
$$T_1 = \frac{1}{U_{\max}} \int_0^{\infty} [U_{\max} - U(t)]dt \tag{9}$$

The capacitance of turn-to-turn insulation in transformer insulation system can be determined with the energy contained in the inductance L and transferred to the capacitor C_{iz}:

$$0.5LI^2 = 0.5C_{iz}U_{\max}^2 \tag{10}$$

The capacitance C_{iz} is a little bit higher than the real one, because in equation (10), it was assumed that all energy of the inductance L is transferred to capacitance C_{iz} and does not include energy dissipation on resistance R at the time Δt.

For the time interval $\Delta t < t < \infty$, the equivalent circuit corresponding to reduce the voltage to zero, is shown in Fig. 12.

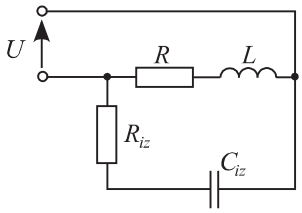

Fig. 12. Equivalent circuit corresponding to the voltage waveform in the time interval $\Delta t < t < \infty$

The decrease of the voltage value to zero, for the time $t > \Delta t$ can be approximated by an exponential function. The time constant T_2 of the exponential function is calculated from the area under the waveform of the voltage $U(t)$, then the resistance of insulation R_{iz} is calculated:

$$U(t) = U_{\max} e^{-t//T_2}$$
$$T_2 = \frac{1}{U_{\max}} \int_{\Delta t}^{\infty} U(t)dt \tag{11}$$
$$R_{iz} = \frac{T_2}{C_{iz}}$$

Table 1

Summary of turn-to-turn insulation parameters

Figure	L	I	$U_{\max}$	$U_{\max}/I$	T_1	T_2	C_{iz}	R_{iz}
	H	**mA**	**V**	**kV/A**	**ms**	**ms**	**nF**	**kΩ**
11	18.00	50	1340	26.80	0.177	1.22	25.0	49
12	0.11	50	464	9.28	0.043	4.05	1.3	—
13	14.00	50	1180	23.60	0.246	1.06	25.0	42

The parameters of turn-to-turn insulation system: capacitance C_{iz} and resistance R_{iz}, were calculated from the waveforms of voltage $U(t)$ (Figs. 9 and 10) and shown in Table 1. As is presented in Table 1, voltage U_{max} or (U_{max} / I) time constants T_1, T_2, capacitance C_{iz} can be used for diagnostic purposes.

4. Conclusions

Power transformer insulation system include the groundwall and turn-to-turn insulation. The electrical parameters of the insulation system are distributed. Electric equivalent circuits of this type of insulation systems may be approximated with two-terminal circuits with an internal ladder structure (Fig. 2). Simplified two-terminal circuits are used in practice during the diagnostic tests of insulation system. Those simplified circuits are built with clustered *RC* parameters. The structure of this scheme is chosen to correctly simulate the real waveforms of the current and voltage during the diagnostic tests of the insulation system. Diagnostic tests of the groundwall insulation of the power transformers are well developed [1, 2]. This article shows only the dielectric loss factor tgδ and recovery voltage, as they have a direct relationship with the equivalent circuit of the insulation system. The article does not discuss the issue of partial discharges and oil testing.

A new proposition, in relation to those known from literature, is a diagnostic test of turn--to-turn insulation. It is proposed that for diagnostic purposes, the voltage waveform on the terminals of winding after switching off the current was used. During the switching off of the current, the voltage induced in each coil is identical. Such tests may be recommended in the receipt tests of the transformer, as an attempt to voltage surges. The short-circuit inside the insulation system affects the value of the inductance as well as the capacitance and resistance of the turn-to-turn insulation. Voltage waveforms $U(t)$ and the results summarized in Table 1 show that it is possible to perform such tests as receipt tests of the new or repaired transformer. These results [voltage U_{max} or (U_{max} / I) time constants T_1, T_2, capacitance C_{iz}], can be used as reference data in the turn-to-turn insulation diagnostic tests performed in subsequent years of transformer operation.

References

[1] Jezierski E., *Transformatory*, WNT, Warszawa 1975.
[2] Kazimierski M., Olech W., *Diagnostyka techniczna i monitoring transformatorów*, Wydawnictwo Energopomiar-Elektryka Sp. z o.o., Gliwice 2013.
[3] Polska norma PN-IEC 76-1/Ak: 1998. *Transformatory. Wymagania ogólne*.
[4] *Ramowa Instrukcja Eksploatacji Transformatorów*, ZPBE Energopomiar-Elektryka, Gliwice 2012.
[5] Вайда Г., *Исследования изоляции*, Энергя, Москва 1968.

CONTENTS